OKÜ Fen Bilimleri Enstitüsü Dergisi
5(Özel Sayı): 1-14, 2022

OKU Journal of The Institute of Science and Technology, 5(Special Issue):1-14, 2022

Osmaniye Korkut Ata Üniversitesi Fen Bilimleri Enstitüsü Dergisi

Osmaniye Korkut Ata University Journal of The Institute of Science and Technology

Fatigue Analysis of Welded Tubular Steel T-Joints

Gokhan YUCEL[1*], Tugrul TALASLIOGLU[2]

[1,2]Osmaniye Korkut Ata University, Faculty of Engineering, Department of Civil Engineering, 80010, Osmaniye

[1]https://orcid.org/0000-0002-2675-4607
[2]https://orcid.org/0000-0002-8075-4130
*Corresponding author: gokhan.yucel@osmaniye.edu.tr

Research Article

Article History:
Received: 08.12.2021
Accepted: 13.01.2022
Published online:23.02.2022

Keywords:
Fatigue
Wind turbine
Lattice structure
T-joint
Finite element modeling

ABSTRACT

Fatigue damage occurs in steel joints exposed to repeated loads during their service life. Even if the design of lattice tubular structures that make up the steel skeletal structures is carried out according to certain regulations, the evaluations for determining the most critical fatigue damage in these structures are limited. Moreover, the discrete geometric configurations of trusses make it difficult to accurately predict fatigue damage. In this study, fatigue analyzes were performed on the planar T-joint sample with two different methods and under different boundary and loading conditions. Three-dimensional finite element models and three-dimensional welded joint detail were created to perform more accurate analysis. As a result, it has been determined that the fixed type support increases the fatigue life due to the increase in rigidity.

T-Birleşimli Borusal Kaynaklı Çelik Yapının Yorulma Analizi

Araştırma Makalesi

Makale Tarihçesi:
Geliş tarihi: 08.12.2021
Kabul tarihi:13.01.2022
Online Yayınlanma: 23.02.2022

Anahtar Kelimeler:
Yorulma
Rüzgar türbini
Kafes yapı
T-birleşim
Sonlu elemanlar modellemesi

ÖZET

Servis ömürleri içerisinde tekrarlı yüklere maruz kalan çelik birleşimlerde yorulma hasarları meydana gelmektedir. Çelik iskeletli yapıları oluşturan kafes boru şeklinde yapıların tasarımı belirli yönetmeliklere göre gerçekleştirilse de bu yapılardaki en kritik yorulma hasarının belirlenmesine yönelik değerlendirmeler kısıtlıdır. Dahası, kafes yapıların ayrık geometrik konfigürasyonları yorulma hasarının doğru bir şekilde tahmin edilmesini zorlaştırmaktadır. Bu çalışmada düzlemsel T-birleşim örneği üzerinde iki farklı yöntemle ve farklı sınır ve yükleme koşullarında yorulma analizleri gerçekleştirilmiştir. Üç boyutlu sonlu elemanlar modelleri ve üç boyutlu kaynaklı birleşim detayı daha gerçekçi analizler gerçekleştirmek için oluşturulmuştur. Sonuç olarak sabit tipli mesnetlemenin rijitlik artışı sebebiyle yorulma ömrünü artırdığı tespit edilmiştir.

To Cite: Yücel G., Talaslıoglu T. Fatigue Analysis of Welded Tubular Steel T-Joints. Osmaniye Korkut Ata Üniversitesi Fen Bilimleri Enstitüsü Dergisi 2022; 5(Özel sayı): 1-14.

Introduction

The tubular lattice structures, which of joints are connected using a welding process are widely utilized to support the wind turbines due to having the more basic configuration, lower construction cost and easily renewable ability. Although their structural resisting capacity is determined in accordance with the appropriate design limitations, the assessment of their fatigue capacity is

generally limited. Fatigue is an accumulative damage formation at any joints of the tubular lattice construction, which is caused by the repetitive loading application. Thus, the progression of fatigue is resulted with a localized damage without giving any warning at the beginning of repetitive loads. This complicated mode of failure has not been completely solved due to being managed by the fatigue mechanism depending on a crack dependent formation. Although the crack theory is solely well understood, the plasticity, which occurs during the propagation of crack, prevents establishing the fundamentals of a unique fatigue mechanism.

The fatigue phenomenon was firstly concerned by German Engineer August Möhler in the 18th century in a way of examining the failure reasons of steel profiles utilized in the railroad network. Although there does not exist a certain study to lay down the theoretical basis of fatigue damage in the 19th century, the first attempt in associating the fatigue formation with the crack issue became in the 20th century (Mann, 1970). The extensive review of fatigue failure is found in references (Cui, 2002; Fuštar et al., 2018; Wei et al., 2018; Feng et al., 2021; Gao and Liu, 2021; Hosseini et al., 2021).

The crack growth in the seam-welded structures is unfortunately influenced by some environmental factors, for example, the boundary and loading conditions, the surface quality, discontinuities in the weld geometry and weld geometric shapes, etc. This variety in the environmental factors causes to use the different fatigue assessment approaches in order to predict more accurately the fatigue lifetime of the welded structural system. Therefore, the different fatigue lifetime determination methods have been taken their places in the national or international design codes, for example, International Institution of Welding (IIW) (Hobbacher, 2019), Japanese (Japanese Society of Steel Construction (JSSC) 2012), British (BSI 1993) and Eurocode 3 (UNI EN 2005), etc.

In general, the stress and strain responses of structural elements are the main determinative factors for the prediction of fatigue lifetime. While the use of stress responses for the estimation of fatigue lifetime becomes to be more appropriate for low-cycle loading conditions, the high-cycle loading conditions require the use of the strain responses for a more accurate fatigue lifetime prediction. Particularly, the stress-based fatigue approaches are mostly utilized in the welded structural systems. The stress-based fatigue approaches are not only categorized depending on the use of stress type, for example, “nominal” (one of its types, “critical plane”), “structural stress” etc., but also the status of crack propagation (Lee et al., 2011). In fact, these categorizations of stress-based fatigue approaches are interacted. In general, whereas the structural stress-based fatigue approaches (SSF) are utilized at the initial level of crack, the critical plane stress-based approaches (CPF) at the micro-crack growth give more accurate results for the fatigue lifetime. It is noted that the principles of linear elastic fracture mechanics are also utilized depending on the propagation status of crack (Pinto et al., 2015; Jia and Hanbin, 2019).

Although the nominal stress-based approaches have relatively simple and practical features due to being mesh-independent, these approaches are generally resulted with more diverged estimation of fatigue lifetime for complex structures due to requiring a further fatigue category. Particularly,

BS7608 as the provisions of British code (BSI 1993) prefers to estimate the fatigue lifetime using the nominal stress-based fatigue approach. The structural stress-based approaches achieve to obtain acceptable accuracy results through a little Finite Element modeling effort. However, it requires to use an appropriate size and arrangement of finite element. Furthermore, the crack propagation is only tackled for the weld toe (Aygul, 2013).

In certain engineering fields, for example, automotive engineering, the metal mechanical components are successfully designed against fatigue failure. However, the estimation of fatigue damage of steel constructions in structural engineering is resulted with a relatively diverged fatigue lifetime at the end of high computing cost. Because, the entire structural system is modelled using the certain finite elements, for example, plate, shell, or solids. Furthermore, it has to take into account of being represented its structural system as a discrete structural system instead of a unique mechanical component.

Moreover, the uncertainties, which are arisen from the nature of its discrete structural system, the variety in both the loading and boundary conditions and its joint connection types prevent obtaining a certain fatigue lifetime prediction considering the damage evaluation.

The primary reasons behind the fatigue damage are associated with the pre-and post-design stages in the construction of steel skeletal systems. While the fatigue lifetime in the pre-design stage is estimated depending on only the local part of steel skeletal construction instead of its entire construction in a way of omitting the manufacturing–related shortcomings, the lacks in the sustainable observations of steel constructional system throughout its existence lifetime against the fatigue damage are mostly encountered in the post-design stage. Particularly, it is noted that there also exist some attempts on the determination of loading conditions for the fatigue estimation of steel skeletal structures (Kajolli, 2013; Maheswaran, 2014).

Thus, this paper attempts to investigate the influence of using different loading and boundary conditions on the fatigue lifetime evaluation of typical T-joint in the steel skeletal structure. Particularly, it is also proposed to find out the critical welding regions of T-joint concerned with the fatigue failure under the different loading and boundary conditions. For this purpose, a sensitivity analysis of fatigue lifetime depending on the repetitive loading application is carried out.

Finite Element Modeling and Structural Analysis of Tubular T-joint

Generation of the Finite element mesh: Finite element analysis carried out using a well-known software Abaqus, 2019. The geometry and mesh of the tubular joint model are shown in Figure 1. The finite elements, which represent the parent plate, are formed using Abaqus Element named C3D8. The finite element model consists of 33335 nodes and 16626 elements in total. Since the stress levels are being in elastic limit under loads that cause fatigue, only elastic material properties were assigned. Young's modulus and Poisson's ratio were assigned to be 210 GPa and 0.3, respectively. The finite

element sets in the model for the fatigue analysis described in the next section and element numbers for two different sets are given in Figure 2.

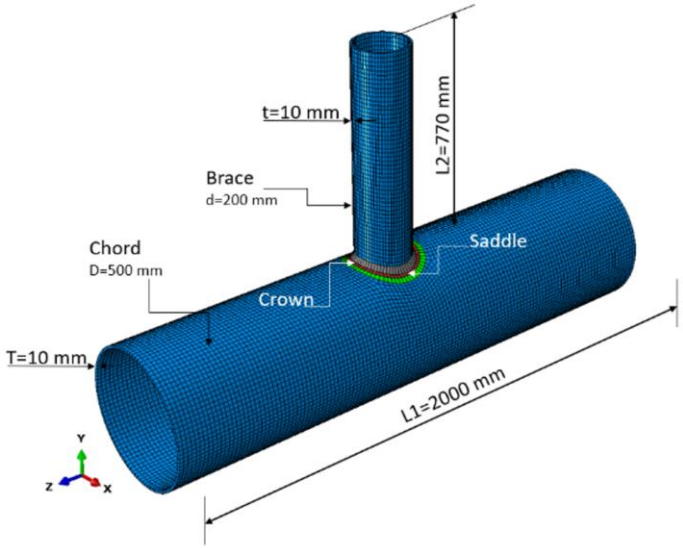

Figure 1. Geometry and finite element mesh of tubular T-joint

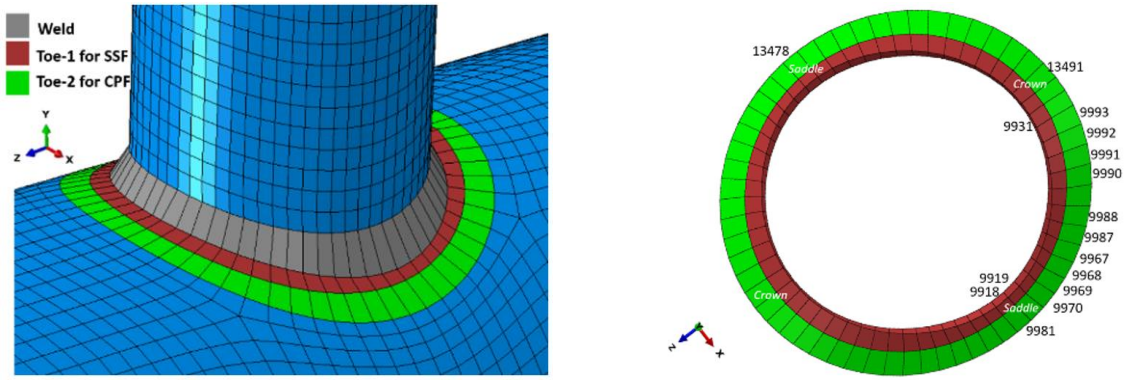

(a) (b)

Figure 2. Element sets (a) and some of the element numbers for Toe-1 and Toe-2 sets (b)

Modeling of the weld profile: To obtain proper local stiffness and so the stress distribution, three-dimensional weld geometry is also modeled (see Figure 2). Weld geometry was created considering the specifications given in the structural welding code ASW D1.1 (American Welding Society, 2015). With a reference to the brace and chord selected in 10 mm thickness, the finite element mesh size was determined as 10 mm and for the welding zone, C3D6 wedge elements are defined.

Establishment of Boundary and Loading Set Models: In this study, the influence of using different loading and boundary conditions on the fatigue lifetime evaluation of typical T-joint in the steel skeletal structure is examined. For this purpose, 6 different boundary types, which of connections are pinned and/or fixed are tackled for the simulation of T-joint (see Figure 3). Furthermore, 14 different loading scenarios, which of each represents a different loading combination are also purposed for each

of these 6 different boundary conditions. In this regard, two different cases, which of each has a lower and higher magnitude are utilized to represent both axial and bending loadings. While each of the loading cases for the boundary types is presented in Table 1, the loading magnitudes and their combinations for these loading set models are tabulated in Tables 2 and 3. It is noted that the boundary types BT4, BT5, and BT6 seem to be more rigid with respect to ones, BT1, BT2, and BT3.

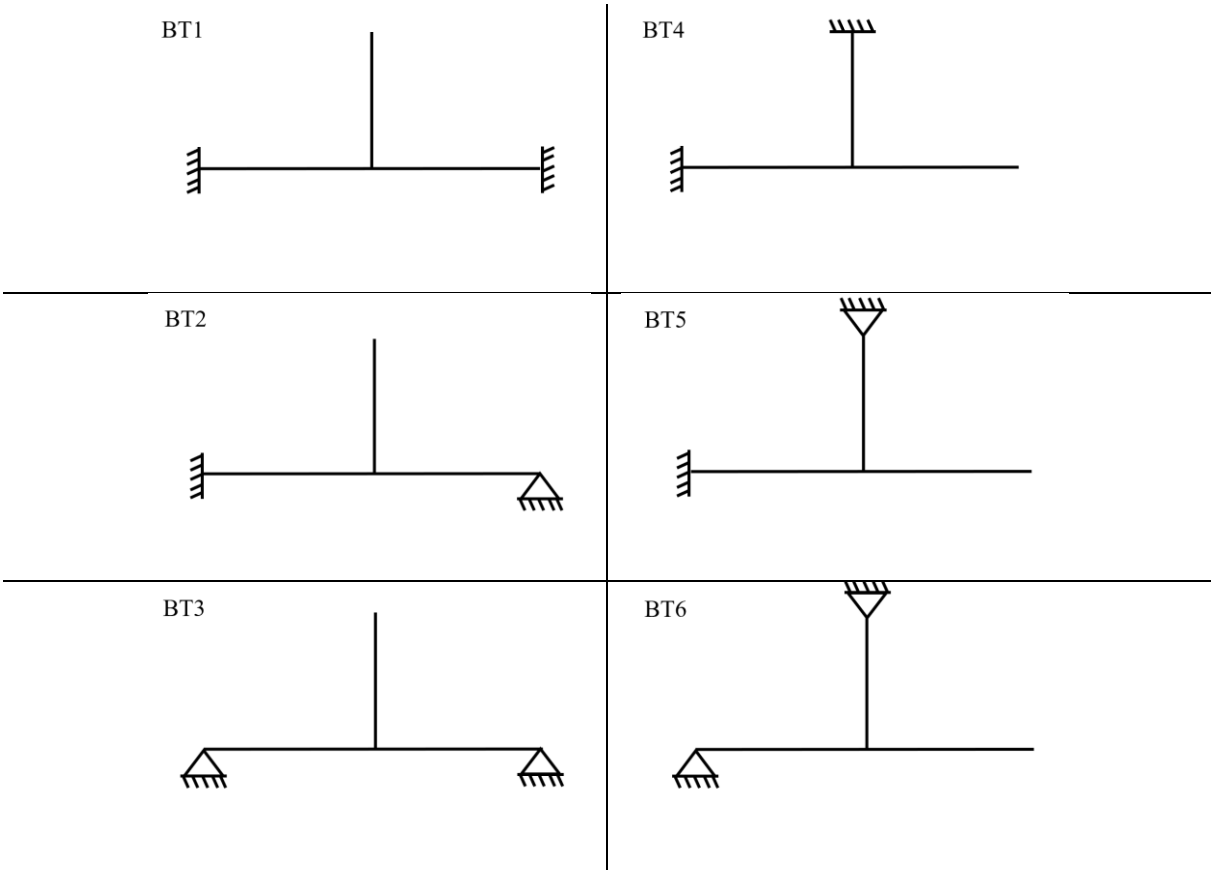

Figure 3. Boundary conditions set models and corresponding abbreviations

Structural Analysis Approach: As the nature of fatigue analysis, a linear type of structural analysis has to be computed the elastic structural response for the external static loads. In this study, the linear perturbation analysis as a structural analysis approach is employed to calculate the structural response corresponding to the base state of the finite element model, which is determined from the initial boundary and loading conditions. The main feature of linear perturbation analysis is its ability to be performed from time to time for the general response steps. This feature provides a big contribution for the computation of structural responses in case of any instability state of the purposed structural system.

Table 1. Loading conditions for each of boundary condition set models

Boundary Types (BT)	Load Conditions Utilized in Loading Patterns		
	Axial Tension force (P)	In-plane bending (M_x)	Out-of-plane bending (M_y)
BT 1-2-3	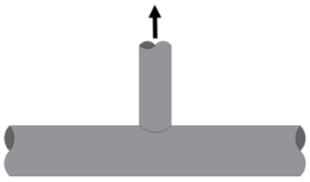	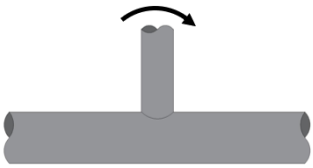	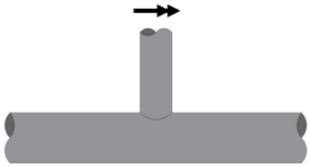
BT 4-5-6			

Table 2. Magnitudes of loadings for each of boundary condition set models

Boundary Type (BT)	P_1 (kN)	P_2 (kN)	M_{x1} (kNm)	M_{x2} (kNm)	M_{y1} (kNm)	M_{y2} (kNm)
BT 1-2-3	10	100	1	5	1	5
BT 4-5-6	200	1000	20	100	20	100

Table 3. Combinations of loadings and corresponding abbreviations for each loading pattern

LP1	LP2	LP3	LP4	LP5	LP6	LP7	LP8	LP9	LP10	LP11	LP12	LP13	LP14
P_1	P_2	P_1 M_{x1}	P_1 M_{x2}	P_2 M_{x1}	P_2 M_{x2}	P_1 M_{x1} M_{y1}	P_1 M_{x1} M_{y2}	P_1 M_{x2} M_{y1}	P_1 M_{x2} M_{y2}	P_2 M_{x1} M_{y1}	P_2 M_{x1} M_{y2}	P_2 M_{x2} M_{y1}	P_2 M_{x2} M_{y2}

Fatigue Assessment Approaches Utilized for Tubular T-joint

The irregularities in the geometry along the weld line and the variation in the thickness of parent plates cause to be concentrated on the stresses in the certain location of the welded structural system. The use of the finite element method for the simulation of welded structural system, unfortunately, fails to obtain a consistent stress distribution due to being completely dependent on the meshing attribution. Nevertheless, to predict the fatigue lifetime more accurately for the welded structural system, the best reasonable approach is to regularize accordingly the stresses of finite element considering the notch and thickness effects.

In this regard, there are two possible approaches for the evaluation of multi-principal axial stresses: i) combining two in-plane principal stresses, named as “critical plane stress analysis” (BSI 1993), ii)

summing the membrane and bending stresses taking into account of parent plate thickness, named as "equivalent structural stress analysis" (Dong, 2001; Dong and Hong, 2003). Although these two analysis approaches are valid for the larger loading cycles (e.g., 107) the weld geometry, and weld toe must be strictly modelled by use of equivalent structural stress-based fatigue approach rather than equivalent structural stress-based one. Particularly, the welding classification has to be defined for the critical plane stress-based fatigue approach neglecting the mean stress effect and the material properties of the parent plate.

Formulations of fatigue assessment approaches:

To estimate the fatigue lifetime, the S-N curve approach has a big attractive feature due to being easily correlated in accordance with the various joint types, loading conditions, etc. Particularly, the fatigue lifetime is easily computed using the critical plane stresses as

$$N = \frac{K_0}{S^m} \tag{1}$$

where S is the critical plane stress range, N is the fatigue lifetime, K_0 is a constant for a particular weld classification, m is 3 to represent a constant curve slope on log-log axes in a range of fatigue lifetime [10^5–10^7].

Although Eq. (1) is a very useful approach due to having a mesh-insensitive-computing procedure, requiring a new correlative regulation for every joint type, and loading condition makes it not to be a practical approach. Thus, the best way is to assign a different stress parameter. At this point, the equivalent structural stress begins to be utilized as an alternative to the critical plane stress. The working principles of the equivalent structural stress-based fatigue approach are managed depending on the parent metal thickness and the crack growth mechanism. Furthermore, the relative contribution of the membrane ($\sigma_m=F_y/(l*t)$) and bending stresses ($\sigma_b=6*M_x/(l*t^2)$) with respect to each other ($\sigma_s=\sigma_m+\sigma_b$) also play a big role for the estimation of fatigue lifetime depending on the welding length l, vertical force Fy and bending moment Mx in the equivalent structural stress-based fatigue approach. Thus, the use of S-N curve ($\Delta\sigma_s$-N) for the equivalent structural stress-based fatigue approach is governed by a two-stage growth model:

$$\frac{da}{dN} = C[f_1(\Delta K)_{a/t\leq 0.1} x f_1(\Delta K)_{a/t>0.1}] = C(M_{kn})^n(\Delta K)^m \tag{2}$$

where a stress intensity magnification factor M_{kn} and stress intensity factor ΔK corresponding to first stage of crack growth (0<a/t<0.1 "small crack") and second stage of crack growth (0.1<a/t<1 "long crack"), a and t are the magnitude of crack and the parent plate thickness. n and m are the constant growth exponent for the first stage of crack growth and the Paris Law exponent. Thus, after Eq. (3) is integrated, it is obtained:

$$N = \int_{a/t\to 0}^{a/t=1} \frac{da}{C(M_{kn})^n(\Delta K)^m} = \frac{1}{C}(t^{1-\frac{m}{2}})(\Delta\sigma_s)^{-m}(I(r)) \quad (3)$$

where I(r) is a dimensionless function depending on a ratio of bending and membrane stresses ($r=\Delta\sigma_b/(\Delta\sigma_b+\Delta\sigma_m)$), $\Delta\sigma_s$ is the structural stress range. It is noted that it is possible to write the structural stress range $\Delta\tau s$ for a shear dominated loading instead of the structural stress range $\Delta\sigma_s$. The other governing parameter is related to the probability of failure depending on the number of standard deviations below the mean life. In this study, this criterion is determined as 50% for two fatigue assessment approaches. Moreover, the repetitive loading cases are assumed as a constant amplitude loading with a minimum load of zero, in other words [1,0] or R=0 presented in the context of Abaqus.

Discussion

Effects of Loading and Boundary Conditions on Fatigue Damage and Lifetime

The fatigue analysis is performed for each of these loading and boundary combinations, which are presented in Figure 3 and Tables (1-3), separately. Thus, considering the fatigue damage, it is possible to determine the most critical cases for the steel skeletal system, which supports the wind turbines.

In this framework, the fatigue lifetimes, which are the outcome from performing two different fatigue evaluation approaches for each of loading and boundary combinations are sketched in Figure 4. The infinite fatigue lifetime corresponding to no fatigue damage is visualized without any numerical value beyond 10^{10} in Figure 4. It is noted that the fatigue lifetime for each combination of loading and boundary conditions are evaluated using toe 1 and toe 2 for SSF and CPF, respectively (see Figure 2).

Considering of Table 4 and Figure 4, the preliminary remarks are drawn considering the combinations of loading and boundary conditions, for example, LP1&BT1 and itemized as:

According to the location of fatigue damage

- The fatigue damage, which is obtained using the assessment of SSF does not occur for the lower loading conditions under almost all combinations of boundary conditions (see the term “ND” for LP1&BT1, LP1&BT2, LP1&BT3 etc. in Table 4).
- The fatigue damage, which is obtained using the assessment of CPF occurs for all combinations of loading and boundary conditions.
- The critical element no’s, which outcome from SSF and CPF assessments is consistently obtained as (9918, 9919 and 9931) and (9967, 9968, 9981, 13478 and 13491) for almost all combinations of loadings and BT1, BT2, and BT3 type boundary conditions (see Table 4). It is noted that the critical element no’s, which outcome from CPF assessments becomes to be as 13478 and 13491 for the lower loading conditions and BT1, BT2 and BT3 type boundary conditions.
- Considering SSF assessment, it is mentioned that the lower loading conditions prevent the occurrence of fatigue damage (see the term “ND” for LP1&BT4, LP3&BT4, LP1&BT5, and LP3&BT5, etc. in Table 4). In the case of the higher loading conditions, the inclusion of out-of-plane

bending moment into the current the loading conditions for the boundary conditions BT4 and BT5 does not cause the fatigue damage, which is obtained using SSF assessment, due to the existence of fixed-type boundary condition (see the term "ND" for LP7&BT4, LP8&BT4, LP7&BT5 and LP8&BT5 in Table 4). Another interesting result is also noted that the exclusion of fixed-type boundary condition prevents fatigue damage for the case of lower out-of-plane bending, in-plane bending moment and axial loading combination (see the term "ND" for LP7&BT3 in Table 4).

- Considering SSF assessment, an increase in the rigidity plays a big role to be occurred the fatigue damage only in the critical element no 9931 for almost all types of loading and boundary conditions (see Table 4). Considering CPF assessment, an increase in the rigidity causes to be occurred the fatigue damage in the critical element no 9990, 9991, 9992, and 9993 for almost all types of loading and boundary conditions (see Table 4). However, in accordance with CPF assessment, the location of fatigue damage is completely removed from the element no 13478 for the boundary type BT4, BT5 and, BT6, which is utilized to represent the higher rigidity, due to the relatively an increase in either the in-plane bending moment or out-of-plane bending moment along with the in-plane bending moment.
- The most critical element no corresponding to the related fatigue analysis cases are also tabulated in Table 4. The stress contour plots with the deformed shapes at the end of structural analysis are presented for the most critical cases of loading and boundary conditions, LP4&BT1 and LP4&BT4 (see Figure 5a-5b). The fatigue log-lives at the end of fatigue analysis considering the fatigue assessment methods SSF and CPF are also presented for the most critical cases of loading and boundary conditions, LP4&BT1 (see Figure 6a-6b). Some critical nodes are also presented for both toe 1 in brown color and toe 2 in green color in Figure 2.

According to the fatigue lifetime

- The fatigue lifetimes obtained using SSF assessment become to be higher than the other fatigue assessment approach, CPF (see Figure 4).
- As an expected situation, an increase in the severity degree in the loading conditions causes a decrease in the fatigue lifetime depending on the loading combinations. Particularly, an inclusion of out-of-plane bending into the loading combination makes a dramatic degradation in the fatigue lifetime (see the fatigue lifetimes in Figure 4).
- Considering the fatigue lifetimes, whereas the fixed-type boundary conditions increase the negative effect of the out-of-plane bending moment for the boundary conditions BT1 and BT2, the pinned-type boundary condition decreases this negative effect resulting in an increase in the fatigue lifetime (see the fatigue lifetimes for BT1 and BT2 along with BT3 in Figure 4). However, an increase in the rigidity makes the fixed-type boundary conditions to be more advantageous with respect to the pinned-type boundary condition and thus provides an elevation in the fatigue lifetime for the boundary

conditions BT4 and BT5 even if being the negative effect of out-of-plane bending moment (see the fatigue lifetimes for BT4-BT6 in Figure 4).

Table 4. Critical element no obtained for each of boundary and loading conditions set models

Loading Patterns (LP)	Boundary Types (BT)											
	BT1		**BT2**		**BT3**		**BT4**		**BT5**		**BT6**	
	SSF	**CPF**	**SSF**	**CPF**	**SSF**	**CPF**	**SSF**	**CPF**	**SSF**	**CPF**	**SSF**	**CPF**
LP1	ND	13491	ND	13491	ND	13491	ND	9991	ND	9990	ND	9990
LP2	9918	13491	9918	13491	9918	13491	9931	9991	9931	9990	9931	9990
LP3	ND	13491	ND	13491	ND	13491	ND	13491	ND	13491	9931	13491
LP4	9931	13478	9931	13478	9931	13478	9931	13491	9931	13491	9931	13491
LP5	9918	13491	9918	13491	9918	13491	9931	9992	9931	9992	9931	9992
LP6	9918	9967	9918	9967	9918	9967	9931	13491	9931	13491	9931	13491
LP7	9918	9968	9918	9968	ND	9968	ND	9991	ND	9991	9931	9991
LP8	9918	9981	9918	9981	9918	9981	ND	9987	ND	9970	9931	9969
LP9	9919	9967	9919	9967	9919	9967	9931	13491	9931	13491	9931	13491
LP10	9918	9968	9918	9968	9918	9968	9931	9991	9931	9991	9931	9993
LP11	9918	9968	9918	9968	9918	9968	9931	9991	9931	9991	9931	9991
LP12	9918	9968	9918	9968	9918	9968	9931	9988	9931	9988	9931	9991
LP13	9918	9967	9918	9967	9918	9967	9931	13491	9931	13491	9931	13491
LP14	9918	9968	9918	9968	9918	9968	9931	9991	9931	9991	9931	9991

ND: No Damage, SSF: structural stress-based fatigue approach, CPF: critical plane stress-based approach

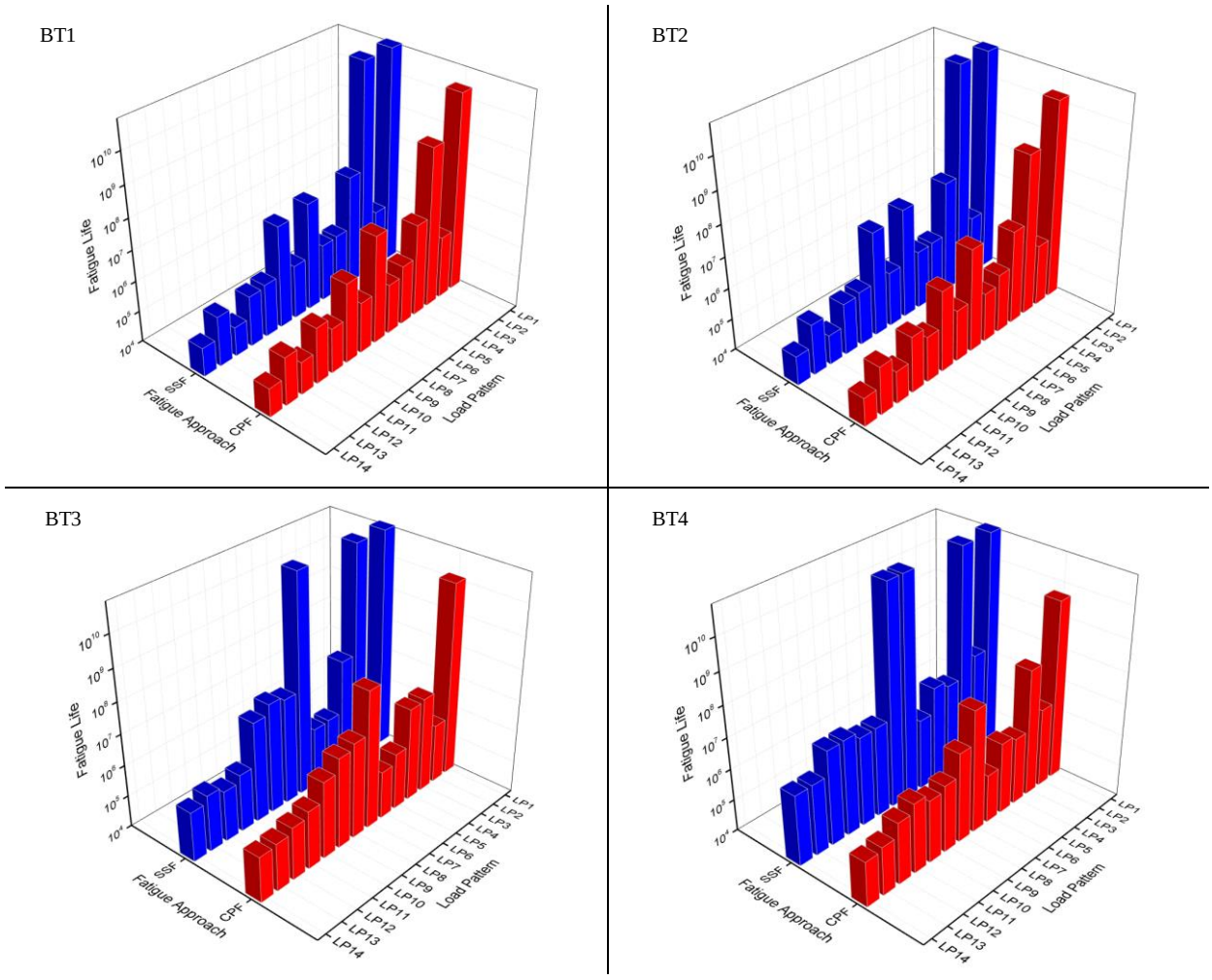

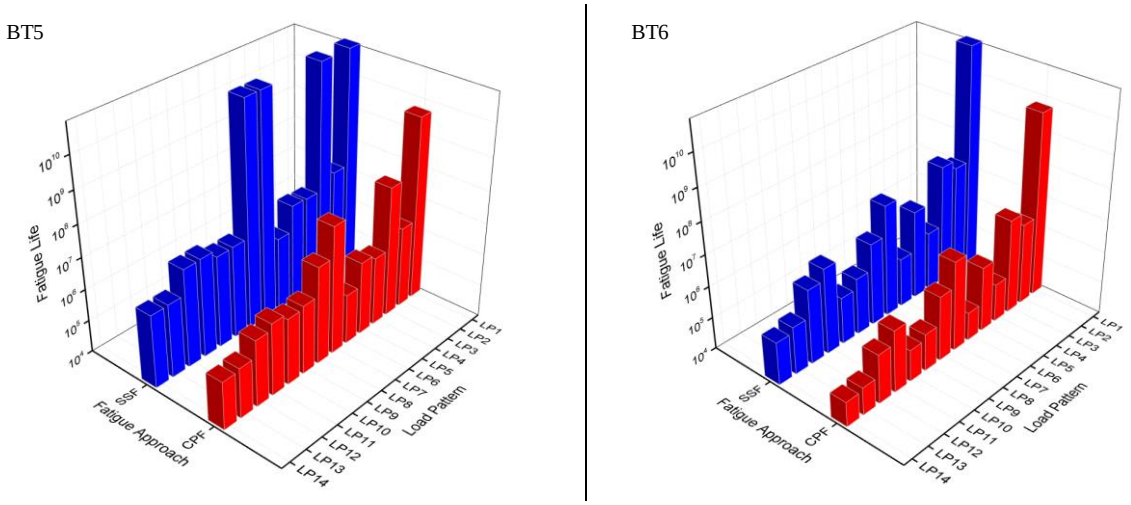

Figure 4. Fatigue lifetime for each boundary type (BT) obtained using the fatigue approaches

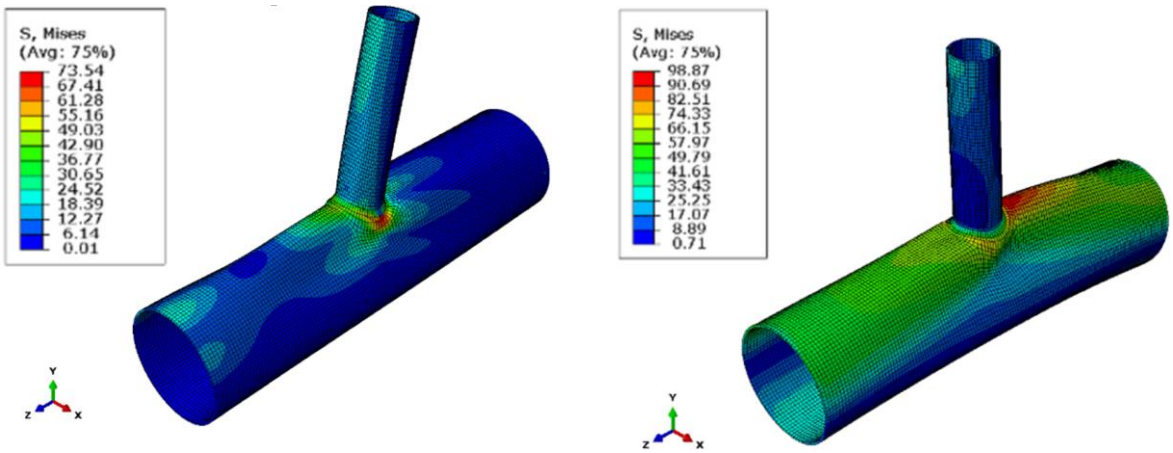

(a) (b)

Figure 5. Stress distribution for model under LP4&BT1 (a) and LP4&BT4 (b)

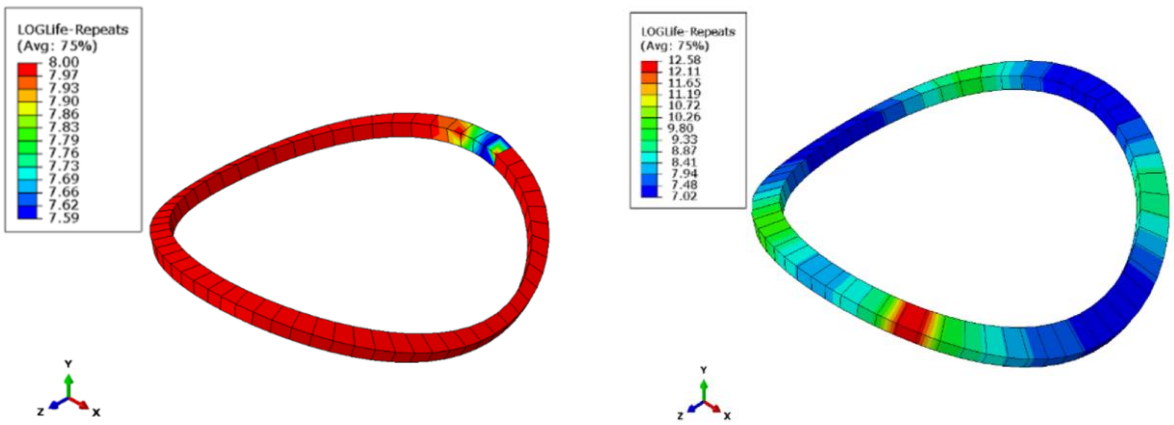

(a) (b)

Figure 6. Fatigue lifetimes obtained using SSF (a) CPF (b) approaches for model under LP4&BT1

Conclusion

This study investigates the loading and boundary conditions on the fatigue lifetime depending on the fatigue damage for T-type joint connection of tubular lattice girder. In this regard, a total of 14 different loading combination sets are applied for 6 structural systems with different boundary condition combination sets. Then, the following important remarks are briefly summarized as:

- The assessment method named SSF for the lower loading and all boundary conditions cannot provide a consistent evaluation for the fatigue damage.
- The increase in the in-plane bending moment causes to be gathered the fatigue damage on the crown and saddle regions of T-connection considering the assessment methods of SSF and CPF. However, the increase in the rigidity causes to be occurred the fatigue damage on the crown region of T-connection considering the assessment methods of CPF.
- The fatigue lifetimes obtained using SSF assessment become to be higher than the fatigue assessment approach, CPF.
- An inclusion of out-of-plane bending moment into any loading cases causes correspondingly to decrease the fatigue lifetime of the structural system.
- The inclusion of the fixed-type boundary conditions rather than the pinned-type one into the structural system causes a negative contribution to the fatigue behavior of the structural system in a way of decreasing its fatigue lifetime. However, through an increase in the rigidity of the structural system, the inclusion of the fixed-type boundary conditions into the structural system provides to be an increase in its fatigue lifetime.

As a next work, the fatigue analysis will be extended including the adjoining regions beyond the end of the welding line in a way of altering the mesh size of the finite element model. Moreover, the discontinuities in the weld line and weld geometry will be investigated on the effect of fatigue lifetime.

Declaration of Competing Interests

The authors declare that they have no competing interests that could have influence the work reported in this paper.

Credit Author Statement

Gokhan Yucel: Visualization, Writing-Original draft preparation, Writing - Review & Editing, Formal Analysis. Tugrul Talaslioglu: Conceptualization, Methodology, Supervision, Investigation, Writing-Original draft preparation, Writing - Review & Editing.

*This study was presented as a summary paper at the International Conference on Engineering, Natural and Applied Sciences (ICENAS'21) held online on 24-26 November 2021.

References

Abaqus. Dassault Systemes Simulia Corp. Jonhston, RI, USA, 2019.

American Welding Society. AWS D1.1/D1.1M:2015 An American National Standard Structural Welding Code-Steel.

Aygul M. Fatigue evaluation of welded details- Using the finite element method. Doctoral dissertation, Chalmers University of Technology, 2013 Gothenburg, Sweden.

BSI. BS 7608:1993 Code of Practice for Fatigue Design and Assessment of Steel Structures." British Standards Institution, 1993.

Cui W. A state-of-the-art review on fatigue life prediction methods for metal structures. Journal of Marine Science and Technology 2002; 7(1): 43-56.

Dong P. A structural stress definition and numerical implementation for fatigue analysis of welded joints. International Journal of Fatigue 2001; 23(10): 865-876.

Dong P., Hong JK. Analysis of hot spot stress and alternative structural stress methods. in Proceedings of the International Conference on Offshore Mechanics and Arctic Engineering – OMAE 2003; pp. 213–24.

Feng R., Xu J., Chen Z., Roy K., Chen B., Lim JB. Numerical investigation and design rules for stress concentration factors of stainless-steel hybrid tubular joints. Thin-Walled Structures 2021; 163, 107783.

Fuštar B., Lukačević I., Dujmović D. Review of fatigue assessment methods for welded steel structures. Advances in Civil Engineering 2018.

Hobbacher AF. Erratum to: Recommendations for fatigue design of welded joints and components. Springer, Cham 2019.

Hosseini AS., Zavvar E., Ahmadi H. Stress concentration factors in FRP-strengthened steel tubular KT-joints. Applied Ocean Research 2021; 108, 102525.

Gao K., Liu G. Novel nonlinear time-varying fatigue reliability analysis based on the probability density evolution method. International Journal of Fatigue 2021; 149, 106257.

Japanese Society of Steel Construction (JSSC). Fatigue design recommendations for steel structures 2012.

Jia LJ., Hanbin G. Ultra-low-cycle fatigue failure of metal structures under strong earthquakes. Springer 2019; 177-196.

Kajolli R. A new approach for estimating fatigue life in offshore steel structures. Master's thesis, University of Stavanger, 2013 Norway.

Lee YL., Mark B., Hong TK. Metal fatigue analysis handbook. Elsevier, 2011.

Maheswaran J. Fatigue life estimation of tubular joints in offshore jacket according to the SCFs in DNV-RP-C203, with comparison of the SCFs in ABAQUS/CAE. Master's thesis, University of Stavanger, 2014, Norway.

Mann JY. Bibliography on the fatigue of materials. Components and Structures. 1st ed. 1970

Pergamon.

Pinto H., Álvaro P., Ignacio A. Exponential model for damage accumulation in closed cell aluminum foams. Revista de La Construccion 2015; 14(2): 80-85.

UNI EN. BS EN 1993-1-9:2005- Eurocode 3: Design of Steel Structures-Part 1-9: Fatigue. in Eurocode 3, 2005.

Wei X., Zongyi W., Lin X., Chentai W. Review of fatigue assessment approaches for tubular joints in CFST trusses. International Journal of Fatigue 2018; 113, 43-53.

OKÜ Fen Bilimleri Enstitüsü Dergisi
5(Özel Sayı):15-25, 2022

OKU Journal of The Institute of Science and Technology, 5(Special Issue):15-25, 2022

Osmaniye Korkut Ata Üniversitesi Fen Bilimleri Enstitüsü Dergisi

Osmaniye Korkut Ata University Journal of The Institute of Science and Technology

Akkuyu Nükleer Reaktörlerinde Kullanılabilecek olan Bazı Kontrol Çubuğu Tiplerinin Radyasyon Koruma Parametrelerinin İncelenmesi

Yusuf KAVUN[1*], Ahmet ÖZTÜRK[2], Eyyüp TEL[3]

[1]Kahramanmaras Sutcu Imam Univ, Vocational School of Health Services, Dept. of Medical Imaging Tech., Kahramanmaraş, Turkey
[2] Kahramanmaras Sutcu Imam Univ, Inst. of Science, Dept. of Material Science and Engineering, Kahramanmaras, Turkey
[3] Osmaniye Korkut Ata University, Physics Department, 80000, Osmaniye

[1]https://orcid.org /0000-0001-9635-4388
[2]https://orcid.org/0000-0003-1543-8534
[3]https://orcid.org/0000-0002-5422-3301
*Corresponding author: yusufkavun@gmail.com

Araştırma Makalesi

Makale Tarihçesi:
Geliş tarihi: 08.12.2021
Kabul tarihi:13.01.2022
Online Yayınlanma: 23.02.2022

Anahtar Kelimeler:
Control rod
B4C
ZrB2
TiB2
HfB2
Phy-X

ÖZET

Kontrol çubukları, nükleer reaktörlerde çekirdekte oluşacak fisyonun kontrol edilmesi için kullanılır. Farklı reaktör tasarımlarında çeşitli enerjilerde bulunabilen nötronlar nedeniyle farklı kontrol çubuğu malzemeleri kullanmalıdır. Nötronları absorbe edebilen B_4C, ZrB_2, TiB_2 veya HfB_2 gibi kimyasal bileşiklerden yapılabilen bu malzemeler, çeşitli enerjilerdeki nötronlar için farklı absorpsiyon özelliklerine sahiptir. Bu çalışmada Akkuyu Nükleer Reaktörlerde kullanılabilecek kontrol çubukları araştırılmıştır. Bu kontrol çubuklarının yapısında B_4C, ZrB_2, TiB_2 veya HfB_2 gibi kimyasal bileşiklerin bulunabileceği ve lineer ve kütle zayıflama katsayıları (LAC, MAC), yarım ve onuncu değer kalınlıkları (HVL, TVL) ve ortalama serbest yol (MFP), atom numarası, elektron yoğunluğu (Zeff, Neff) ve etkin iletkenlik (Ceff) enerji parametreleri Phy-X yazılımı kullanılarak teorik olarak 1 keV ile 20 MeV arasında hesaplanmıştır.

Investigation of Radiation Protection Parameters of Some Control Rod Types that Can Be Used in Akkuyu Nuclear Reactors

Research Article

Article History:
Received: 08.12.2021
Accepted: 13.01.2022
Published online: 23.02.2022

Keywords:
Control rod
B4C
ZrB2
TiB2
HfB2
Phy-X

ABSTRACT

Control rods are used in nuclear reactors to control fission in the core. Different reactor designs must use different control rod materials because of the neutrons that can be found at various energies. These materials, which can be made of chemical compounds such as B_4C, ZrB_2, TiB_2 or HfB_2 that can absorb neutrons, have different absorption properties for neutrons of various energies. In this study, control rods that can be used in Akkuyu Nuclear Reactors were investigated. It has been taken into account that chemical compounds such as B_4C, ZrB_2, TiB_2 or HfB_2 may be present in the structure of these control rods, and the linear and mass attenuation coefficients (LAC, MAC), half and tenth value thicknesses (HVL, TVL) and mean free path (MFP), the atomic number, electron density (Zeff, Neff) and effective conductivity (Ceff) energy parameters have been calculated theoretically between 1 keV and 20 MeV using Phy-X software.

To Cite: Kavun Y., Öztürk A., Tel E. Investigation of Radiation Protection Parameters of Some Control Rod Types that Can Be Used in Akkuyu Nuclear Reactors. Osmaniye Korkut Ata Üniversitesi Fen Bilimleri Enstitüsü Dergisi 2022; 5(Özel sayı): 15-25.

Introduction

Nuclear reactors are facilities where heat energy is produced by using radioactive materials as fuel and electrical energy is produced from this energy (Cox et al., 2020). Unlike other power plants, due to the use of radioactive materials, more stringent security measures need to be taken, and therefore their technology must be continuously improved to include security measures (Lee, 2020).

Without talking about the control of the radioactive particles emerging in the reactor and the reactor control devices, we need to know the physics of the nuclear reactor system and reveal the technologies of these parts. There is a central core in the reactors, where the neutron is created in a controlled manner and the fission chain reactions that occur in the reactor are controlled. The neutrons produced by fragmentation are slowed down in thermal reactors until they decrease to thermal speeds using a moderator in the core. Graphite or heavy water is used for this slowing process. ^{235}U is mostly used in these thermal reactors and ^{235}U, which is a very important fissile material, is more likely to be decomposed by thermal neutrons than fast neutrons (Shultis and Faw, 2010; Lee, 2020; Mohanakrishnan et al., 2021).

The neutrons formed as a result of fission in the reactor core are initiated by the withdrawal of neutron absorbers such as boron or cadmium from the core or by adding another fuel element or using neutron reflectors. Retracting devices called control rods is the most commonly used method here (William Ray, 1963; Cockbame and Gültekin, 1966).

They can be collected in 3 groups as safety bars, closing bars and adjustment bars. Safety bars are located around the ember and provide safety by being placed around the ember during fueling or maintenance. The closing rods are withdrawn at a constant speed when the reactor starts to operate and these rods are held around the core during operation. If the core becomes critical, the safety bars are lowered and reactor operation can be stopped. Adjusting rods are used to bring the reactor to a critical point (Cockbame and Gültekin, 1966.).

Akkuyu Nuclear Power Plant is a VVR1200 type power plant and is a 3rd generation power plant (Fischer and Tiras, 2020). Within the scope of this study, the radiation absorption properties of possible control rod materials that can be used in this power plant were investigated with the Phy-X software (Şakar et al., 2020). For this purpose, linear and mass attenuation coefficients (LAC, MAC), half and tenth value layers (HVL, TVL), mean free path (MFP), effective atomic number and electron density (Z_{eff}, N_{eff}) and effective conductivity (C_{eff}) energy parameters of radiation particles interacting with B_4C, ZrB_2, TiB_2 and HfB_2 materials between 1 keV to 20 MeV energy have been theoretically calculated.

Material and Method

The Phy-X program (Özpolat et al., 2020), which is Photon Protection and Dosimetry (PSD) software available online at https://phy-x.net/PSD, has been developed for the calculation of parameters related

to Shielding and dosimetry. By using the program in the range of 1 keV-100 GeV, linear and mass attenuation coefficients (LAC, MAC), half and tenth value layers (HVL, TVL), mean free path (MFP), effective atomic number and electron density (Zeff, Neff), the effective conductivity (Ceff) energy absorption and exposure buildup factors (EABF, EBF) can be calculated. In addition, the energies of some well-known radioactive sources such as 22Na, 55Fe, 60Co, 109Cd, 131I, 133Ba, 137Cs, 152Eu and 241Am and characteristic X-ray energy data of elements such as Cu, Rb, Mo, Ag, Ba and Tb are also available in the program. These energies can be determined by the user and used in calculations (Özpolat et al., 2020). The Beer-Lambert Law (Eskalen et al., 2020) is given in Eq. 1, by using this obtained absorption coefficient (μ), the Mass Attenuation Coefficient (Agar, 2018; Kavun et al., 2019) can be calculated, which defines the probability of interaction between gamma photons and mass per unit area.

$$\mu = \ln\left(\frac{I_0}{I}\right) / (-x) \quad (\mathrm{cm}^{-1}) \tag{1}$$

The Mass Attenuation Coefficient (MAC) (μ_m) is given in Eq.2:

$$\mu_m = \frac{\mu}{\rho} = \sum w_i \left(\frac{\mu}{\rho}\right)_i \quad (\mathrm{cm}^2/\mathrm{g}) \tag{2}$$

Here, I and I_0 are unabsorbed and absorbed photon intensities; $\mu(\mathrm{cm}^{-1})$ and $\mu_m(\mathrm{cm}^2/\mathrm{g})$ are linear and mass attenuation coefficients; x (cm) is the thickness; w_i is the weight fraction and ρ is density (Agar, 2018; Kavun et al., 2021). HVL, TVL, MFP parameters are found using the absorption coefficient (μ) (Özpolat et al., 2020).

Result and Discussion

In the scope of this study, the radiation absorption properties of possible control rod materials that can be used in this power plant were investigated with the Phy-X software. For this purpose, linear and mass attenuation coefficients (LAC, MAC), half and tenth value layers (HVL, TVL), mean free path (MFP), effective atomic number and electron density (Z_{eff}, N_{eff}) and effective conductivity (C_{eff}) energy parameters of radiation particles interacting with B_4C, ZrB_2, TiB_2 and HfB_2 materials between 1 keV to 20 MeV energy have been theoretically calculated.

As seen in Table 1 and Figure 1 for B_4C, the LAC values have been started from 3633.904 cm^{-1} at 1 keV to 0.036 cm^{-1} at 20 MeV. It was observed that the linear attenuation values decreased as the energy increased. Accordingly, there is a similar situation in the MAC values obtained by using the LAC value. In the logarithmic calculated HVL and TVL values, these values increased as the energy increased. But, there is a fluctuation in N_{eff}, C_{eff} and Z_{eff} values as seen in Figure 1.

Table 1. Calculation results of B_4C

Energy	**MAC**	**LAC**	**HVL**	**TVL**	**MFP**	**Neff**	**Ceff**	**Zeff**
MeV	*cm²/g*	*1/cm*	*cm*	*cm*	*cm*	*electrons/g*	*S/m*	
0.001	1442.026	3633.904	0.00019	0.00063	0.00028	2.88E+23	5.25E+08	5.29
0.002	447.043	1126.549	0.00062	0.00204	0.00089	2.89E+23	5.26E+08	5.30
0.002	190.770	480.740	0.00144	0.00479	0.00208	2.89E+23	5.26E+08	5.30
0.003	56.163	141.531	0.00490	0.01627	0.00707	2.89E+23	5.26E+08	5.31
0.004	23.290	58.692	0.00019	0.00063	0.00028	2.89E+23	5.27E+08	5.31
0.005	11.732	29.564	0.023	0.078	0.034	2.90E+23	5.27E+08	5.31
0.006	6.714	16.920	0.041	0.136	0.059	2.90E+23	5.27E+08	5.31
0.008	2.831	7.134	0.097	0.323	0.140	2.89E+23	5.27E+08	5.31
0.010	1.498	3.775	0.184	0.610	0.265	2.89E+23	5.26E+08	5.30
0.015	0.553	1.394	0.497	1.652	0.717	2.88E+23	5.23E+08	5.28
0.02	0.332	0.836	0.829	2.753	1.195	2.86E+23	5.21E+08	5.25
0.03	0.217	0.547	1.266	4.207	1.827	2.85E+23	5.18E+08	5.22
0.04	0.186	0.467	1.483	4.926	2.139	2.84E+23	5.17E+08	5.21
0.05	0.171	0.431	1.609	5.344	2.321	2.84E+23	5.16E+08	5.21
0.06	0.162	0.408	1.697	5.639	2.449	2.84E+23	5.16E+08	5.20
0.08	0.150	0.379	1.831	6.082	2.642	2.83E+23	5.16E+08	5.20
0.1	0.142	0.357	1.940	6.445	2.799	2.83E+23	5.16E+08	5.20
0.2	0.127	0.319	2.173	7.218	3.135	2.83E+23	5.16E+08	5.20
0.2	0.116	0.291	2.378	7.901	3.431	2.83E+23	5.16E+08	5.20
0.3	0.100	0.253	2.740	9.103	3.954	2.83E+23	5.16E+08	5.20
0.4	0.090	0.227	3.060	10.164	4.414	2.83E+23	5.16E+08	5.20
0.5	0.082	0.207	3.352	11.134	4.835	2.83E+23	5.16E+08	5.20
0.6	0.076	0.191	3.624	12.037	5.228	2.83E+23	5.16E+08	5.20
0.8	0.067	0.168	4.128	13.712	5.955	2.83E+23	5.16E+08	5.20
1	0.060	0.151	4.590	15.247	6.621	2.83E+23	5.16E+08	5.20
2	0.049	0.123	5.641	18.739	8.138	2.83E+23	5.16E+08	5.20
2	0.042	0.105	6.579	21.854	9.491	2.83E+23	5.16E+08	5.20
3	0.033	0.084	8.224	27.318	11.864	2.83E+23	5.16E+08	5.20
4	0.029	0.072	9.643	32.032	13.911	2.83E+23	5.16E+08	5.20
5	0.025	0.064	10.885	36.159	15.704	2.83E+23	5.16E+08	5.20
6	0.023	0.058	11.979	39.793	17.282	2.84E+23	5.16E+08	5.20
7	0.021	0.054	12.952	43.024	18.685	2.84E+23	5.16E+08	5.20
8	0.020	0.050	13.819	45.906	19.937	2.84E+23	5.16E+08	5.20
9	0.019	0.048	14.590	48.468	21.049	2.84E+23	5.16E+08	5.20
10	0.018	0.045	15.286	50.778	22.053	2.84E+23	5.16E+08	5.21
11	0.017	0.044	15.910	52.852	22.953	2.84E+23	5.16E+08	5.21
12	0.017	0.042	16.478	54.739	23.773	2.84E+23	5.16E+08	5.21
13	0.016	0.041	16.988	56.434	24.509	2.84E+23	5.16E+08	5.21
14	0.016	0.040	17.451	57.969	25.176	2.84E+23	5.16E+08	5.21
15	0.015	0.039	17.870	59.362	25.781	2.84E+23	5.16E+08	5.21
16	0.015	0.038	18.249	60.621	26.327	2.84E+23	5.16E+08	5.21
18	0.015	0.037	18.910	62.818	27.281	2.84E+23	5.16E+08	5.21
20	0.014	0.036	19.464	64.657	28.080	2.84E+23	5.17E+08	5.21

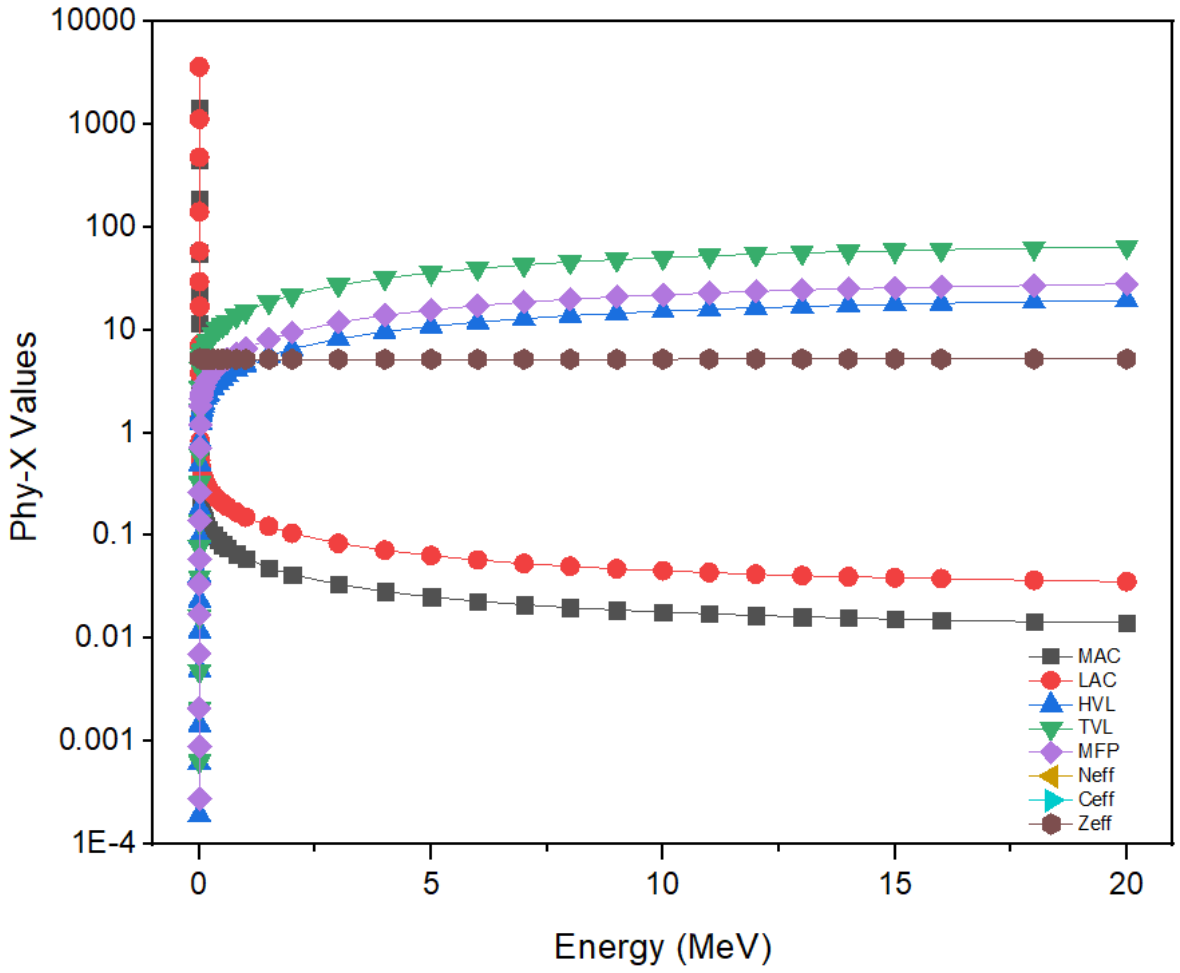

Figure 1. Radiation shielding results of B_4C using Phy-X software

For ZrB_2, the LAC values started from 22140.303 cm^{-1} at 1 keV to 0.219cm^{-1} at 20 MeV as seen in Table 2 and Figure 2. Similarly, The MAC values fluctuated around 3638.505 to 0.036 cm^2/g in these energy ranges. The HVL, TVL and MFP values starts from 0.00003, 0.00010 and 0.00005 cm to 3.169, 10.528 and 4.572, respectively. N_{eff}, C_{eff} and Z_{eff} values have similar behavior as seen in Figure 2. They have taken different values in 1 keV to 20 MeV range.

Table 2. Calculation results of ZrB_2

Energy *MeV*	**MAC** *cm^2/g*	**LAC** *1/cm*	**HVL** *cm*	**TVL** *cm*	**MFP** *cm*	**Neff** *electrons/g*	**Ceff** *S/m*	**Zeff**
0.001	3638.505	22140.303	0.00003	0.00010	0.00005	4.41E+23	1.94E+09	27.53
0.002	1391.005	8464.268	0.00008	0.00027	0.00012	4.70E+23	2.06E+09	29.34
0.002	686.829	4179.354	0.00017	0.00055	0.00024	4.88E+23	2.14E+09	30.49
0.003	1441.569	8771.945	0.00008	0.00026	0.00011	6.14E+23	2.70E+09	38.34
0.004	691.345	4206.834	0.00016	0.00055	0.00024	6.17E+23	2.71E+09	38.56
0.005	386.333	2350.837	0.00029	0.00098	0.00043	6.20E+23	2.72E+09	38.70
0.006	238.323	1450.195	0.00048	0.00159	0.00069	6.21E+23	2.73E+09	38.79
0.008	110.111	670.028	0.00103	0.00344	0.00149	6.23E+23	2.74E+09	38.89
0.010	60.203	366.334	0.002	0.006	0.003	6.23E+23	2.74E+09	38.91
0.015	19.997	121.684	0.006	0.019	0.008	6.20E+23	2.72E+09	38.75
0.02	58.570	356.398	0.002	0.006	0.003	6.36E+23	2.79E+09	39.73
0.03	20.130	122.491	0.006	0.019	0.008	6.32E+23	2.78E+09	39.46

0.04	9.240	56.224	0.012	0.041	0.018	6.24E+23	2.74E+09	38.98
0.05	5.023	30.564	0.023	0.075	0.033	6.13E+23	2.69E+09	38.30
0.06	3.057	18.599	0.037	0.124	0.054	5.99E+23	2.63E+09	37.40
0.08	1.420	8.638	0.080	0.267	0.116	5.62E+23	2.47E+09	35.12
0.1	0.807	4.912	0.141	0.469	0.204	5.20E+23	2.29E+09	32.49
0.2	0.330	2.009	0.345	1.146	0.498	4.25E+23	1.87E+09	26.58
0.2	0.203	1.233	0.562	1.868	0.811	3.65E+23	1.61E+09	22.83
0.3	0.125	0.763	0.908	3.017	1.310	3.12E+23	1.37E+09	19.47
0.4	0.099	0.604	1.148	3.812	1.656	2.92E+23	1.28E+09	18.23
0.5	0.086	0.522	1.329	4.414	1.917	2.83E+23	1.24E+09	17.68
0.6	0.077	0.468	1.480	4.915	2.134	2.78E+23	1.22E+09	17.39
0.8	0.066	0.400	1.735	5.762	2.503	2.74E+23	1.20E+09	17.11
1	0.058	0.354	1.955	6.496	2.821	2.72E+23	1.19E+09	16.98
2	0.047	0.287	2.415	8.021	3.484	2.71E+23	1.19E+09	16.93
2	0.041	0.252	2.752	9.142	3.970	2.75E+23	1.21E+09	17.16
3	0.036	0.218	3.186	10.584	4.597	2.87E+23	1.26E+09	17.92
4	0.033	0.202	3.425	11.376	4.941	3.01E+23	1.32E+09	18.79
5	0.032	0.195	3.549	11.789	5.120	3.15E+23	1.38E+09	19.66
6	0.032	0.192	3.607	11.981	5.203	3.28E+23	1.44E+09	20.46
7	0.031	0.191	3.621	12.030	5.224	3.40E+23	1.49E+09	21.21
8	0.032	0.192	3.611	11.995	5.209	3.51E+23	1.54E+09	21.89
9	0.032	0.193	3.585	11.908	5.172	3.60E+23	1.58E+09	22.51
10	0.032	0.195	3.549	11.791	5.121	3.69E+23	1.62E+09	23.07
11	0.032	0.197	3.510	11.660	5.064	3.78E+23	1.66E+09	23.58
12	0.033	0.200	3.468	11.521	5.004	3.85E+23	1.69E+09	24.04
13	0.033	0.202	3.427	11.385	4.945	3.92E+23	1.72E+09	24.46
14	0.034	0.205	3.387	11.252	4.887	3.98E+23	1.75E+09	24.83
15	0.034	0.207	3.348	11.121	4.830	4.03E+23	1.77E+09	25.17
16	0.034	0.209	3.309	10.993	4.774	4.08E+23	1.79E+09	25.48
18	0.035	0.214	3.237	10.752	4.669	4.17E+23	1.83E+09	26.02
20	0.036	0.219	3.169	10.528	4.572	4.24E+23	1.86E+09	26.48

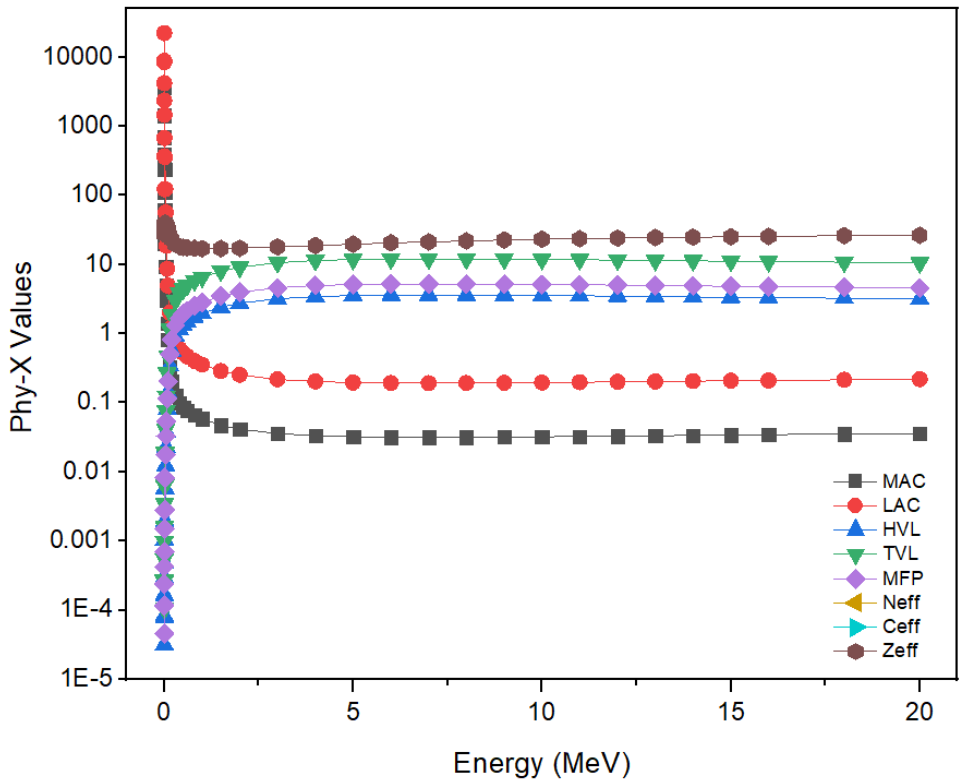

Figure 2. Radiation shielding results of ZrB_2 using Phy-X software.

In Table 3 and Figure 3, TiB_2 calculation results can be seen. The LAC values changed between 20000.205 cm^{-1} to 0.108 cm^{-1} for 1 keV and 20 MeV. These changes affected the MAC values. It was changed between 4424.824 cm^2/g and 0.024 cm^2/g in the same energy range. The HVL, TVL and MFP values started from 0.00003, 0.00012 and 0.00005 cm to 6.430, 21.360 and 9.277 cm, respectively. The fluctuation seen for N_{eff}, C_{eff} and Z_{eff} values in previous calculations is also available here.

Table 3. Calculation results of TiB_2

Energy *MeV*	**MAC** *cm²/g*	**LAC** *1/cm*	**HVL** *cm*	**TVL** *cm*	**MFP** *cm*	**Neff** *electrons/g*	**Ceff** *S/m*	**Zeff**
0.001	4424.824	20000.205	0.00003	0.00012	0.00005	4.42E+23	1.44E+09	17.01
0.002	1561.234	7056.778	0.00010	0.00033	0.00014	4.56E+23	1.49E+09	17.53
0.002	728.936	3294.791	0.00021	0.00070	0.00030	4.64E+23	1.52E+09	17.86
0.003	243.410	1100.213	0.00063	0.00209	0.00091	4.76E+23	1.55E+09	18.29
0.004	110.529	499.591	0.00139	0.00461	0.00200	4.83E+23	1.58E+09	18.57
0.005	474.063	2142.763	0.00032	0.00107	0.00047	5.60E+23	1.83E+09	21.53
0.006	299.572	1354.066	0.00051	0.00170	0.00074	5.61E+23	1.83E+09	21.58
0.008	140.122	633.352	0.001	0.004	0.002	5.62E+23	1.83E+09	21.62
0.010	76.629	346.362	0.002	0.007	0.003	5.62E+23	1.83E+09	21.63
0.015	24.862	112.374	0.006	0.020	0.009	5.60E+23	1.83E+09	21.56
0.02	11.014	49.781	0.014	0.046	0.020	5.56E+23	1.81E+09	21.38
0.03	3.489	15.769	0.044	0.146	0.063	5.38E+23	1.76E+09	20.70
0.04	1.580	7.142	0.097	0.322	0.140	5.11E+23	1.67E+09	19.64
0.05	0.888	4.012	0.173	0.574	0.249	4.77E+23	1.56E+09	18.36
0.06	0.577	2.608	0.266	0.883	0.383	4.43E+23	1.45E+09	17.05
0.08	0.325	1.469	0.472	1.568	0.681	3.87E+23	1.26E+09	14.87
0.1	0.231	1.043	0.665	2.208	0.959	3.49E+23	1.14E+09	13.43
0.2	0.152	0.688	1.007	3.346	1.453	3.07E+23	1.00E+09	11.80
0.2	0.126	0.569	1.218	4.048	1.758	2.93E+23	9.55E+08	11.25
0.3	0.103	0.463	1.496	4.969	2.158	2.83E+23	9.25E+08	10.90
0.4	0.090	0.407	1.703	5.657	2.457	2.81E+23	9.16E+08	10.79
0.5	0.082	0.368	1.881	6.249	2.714	2.79E+23	9.12E+08	10.75
0.6	0.075	0.339	2.042	6.785	2.947	2.79E+23	9.10E+08	10.73
0.8	0.066	0.297	2.336	7.760	3.370	2.78E+23	9.08E+08	10.70
1	0.059	0.266	2.603	8.648	3.756	2.78E+23	9.07E+08	10.69
2	0.048	0.217	3.196	10.617	4.611	2.78E+23	9.08E+08	10.70
2	0.042	0.188	3.689	12.253	5.322	2.80E+23	9.12E+08	10.76
3	0.034	0.156	4.456	14.804	6.429	2.85E+23	9.29E+08	10.95
4	0.031	0.138	5.017	16.668	7.239	2.91E+23	9.48E+08	11.18
5	0.028	0.128	5.429	18.036	7.833	2.97E+23	9.68E+08	11.41
6	0.027	0.121	5.733	19.045	8.271	3.03E+23	9.88E+08	11.65
7	0.026	0.116	5.955	19.782	8.591	3.09E+23	1.01E+09	11.87
8	0.025	0.113	6.119	20.328	8.828	3.14E+23	1.02E+09	12.08
9	0.025	0.111	6.236	20.714	8.996	3.19E+23	1.04E+09	12.28
10	0.024	0.110	6.324	21.009	9.124	3.24E+23	1.06E+09	12.46
11	0.024	0.109	6.384	21.207	9.210	3.28E+23	1.07E+09	12.63
12	0.024	0.108	6.428	21.353	9.274	3.32E+23	1.08E+09	12.79
13	0.024	0.107	6.454	21.440	9.311	3.36E+23	1.10E+09	12.93
14	0.024	0.107	6.472	21.501	9.338	3.40E+23	1.11E+09	13.06
15	0.024	0.107	6.477	21.517	9.345	3.43E+23	1.12E+09	13.19
16	0.024	0.107	6.477	21.516	9.344	3.46E+23	1.13E+09	13.30
18	0.024	0.107	6.462	21.467	9.323	3.51E+23	1.15E+09	13.51
20	0.024	0.108	6.430	21.360	9.277	3.56E+23	1.16E+09	13.69

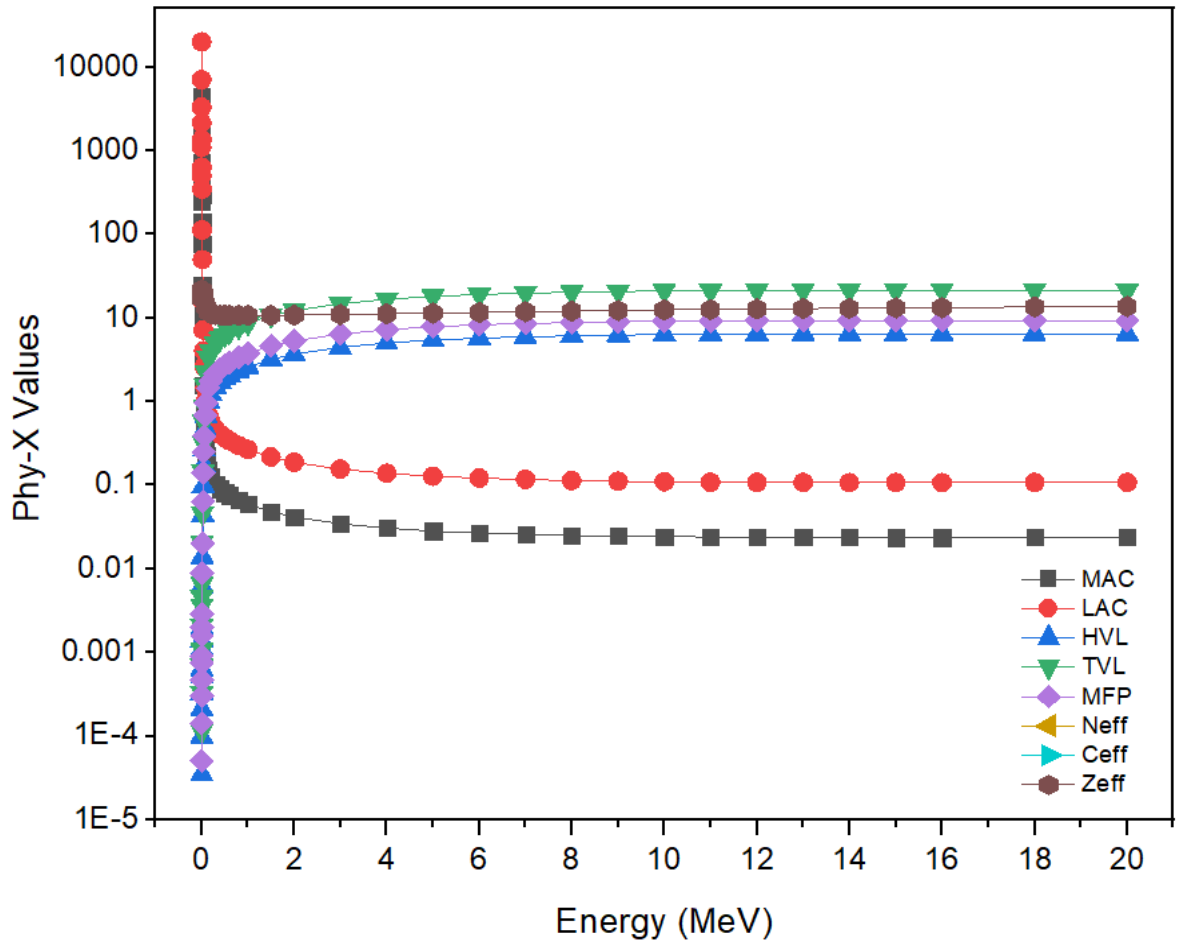

Figure 3. Radiation shielding results of TiB_2 using Phy-X software

Finally, for HfB_2, The LAC values obtained as 32632.138 cm^{-1} and 0.558 cm^{-1} for 1 keV to 20 MeV in Fig.4 and Table 4, respectively. Depending on LAC values, the MAC values have been obtained as 3107.823 and 0.053 cm^2/g. The obtained HVL, TVL and MFP values have been increased as the energy increased. Similar fluctuation in N_{eff}, C_{eff} and Z_{eff} values for this energy range is also available here.

Table 4. Calculation results of HfB_2

Energy *MeV*	**MAC** *cm^2/g*	**LAC** *1/cm*	**HVL** *cm*	**TVL** *cm*	**MFP** *cm*	**Neff** *electrons/g*	**Ceff** *S/m*	**Zeff**
0.001	3107.823	32632.138	0.00002	0.00007	0.00003	4.13E+23	3.13E+09	45.79
0.002	1368.924	14373.706	0.00005	0.00016	0.00007	4.65E+23	3.52E+09	51.49
0.002	3225.291	33865.557	0.00002	0.00007	0.00003	6.07E+23	4.60E+09	67.18
0.003	1582.288	16614.024	0.00004	0.00014	0.00006	6.23E+23	4.73E+09	69.05
0.004	792.119	8317.249	0.00008	0.00028	0.00012	6.28E+23	4.76E+09	69.55
0.005	457.167	4800.253	0.00014	0.00048	0.00021	6.31E+23	4.78E+09	69.86
0.006	289.977	3044.757	0.00023	0.00076	0.00033	6.33E+23	4.79E+09	70.06
0.008	140.359	1473.771	0.00047	0.00156	0.00068	6.35E+23	4.81E+09	70.30
0.010	205.395	2156.645	0.00032	0.00107	0.00046	6.44E+23	4.88E+09	71.37
0.015	115.071	1208.246	0.00057	0.00191	0.00083	6.46E+23	4.90E+09	71.57
0.02	54.328	570.441	0.001	0.004	0.002	6.45E+23	4.89E+09	71.43
0.03	18.737	196.743	0.004	0.012	0.005	6.40E+23	4.85E+09	70.87
0.04	8.785	92.238	0.008	0.025	0.011	6.31E+23	4.79E+09	69.93

0.05	4.905	51.498	0.013	0.045	0.019	6.20E+23	4.70E+09	68.63
0.06	3.068	32.210	0.022	0.071	0.031	6.05E+23	4.58E+09	66.99
0.08	6.572	69.008	0.010	0.033	0.014	6.30E+23	4.77E+09	69.74
0.1	3.719	39.051	0.018	0.059	0.026	6.17E+23	4.67E+09	68.30
0.2	1.331	13.976	0.050	0.165	0.072	5.73E+23	4.34E+09	63.42
0.2	0.667	7.001	0.099	0.329	0.143	5.21E+23	3.95E+09	57.75
0.3	0.283	2.973	0.233	0.775	0.336	4.32E+23	3.28E+09	47.86
0.4	0.173	1.818	0.381	1.267	0.550	3.74E+23	2.83E+09	41.40
0.5	0.127	1.332	0.520	1.729	0.751	3.38E+23	2.57E+09	37.48
0.6	0.102	1.076	0.644	2.141	0.930	3.16E+23	2.40E+09	35.04
0.8	0.077	0.812	0.853	2.835	1.231	2.92E+23	2.21E+09	32.35
1	0.064	0.676	1.026	3.407	1.480	2.80E+23	2.12E+09	30.96
2	0.049	0.517	1.340	4.451	1.933	2.70E+23	2.05E+09	29.90
2	0.044	0.458	1.515	5.033	2.186	2.75E+23	2.08E+09	30.44
3	0.039	0.415	1.671	5.553	2.411	2.95E+23	2.24E+09	32.67
4	0.039	0.405	1.710	5.680	2.467	3.17E+23	2.40E+09	35.13
5	0.039	0.408	1.701	5.650	2.454	3.38E+23	2.56E+09	37.43
6	0.039	0.415	1.672	5.553	2.412	3.56E+23	2.70E+09	39.47
7	0.040	0.424	1.634	5.428	2.357	3.73E+23	2.82E+09	41.27
8	0.041	0.435	1.593	5.293	2.299	3.87E+23	2.93E+09	42.86
9	0.043	0.446	1.553	5.158	2.240	4.00E+23	3.03E+09	44.26
10	0.044	0.458	1.513	5.028	2.183	4.11E+23	3.11E+09	45.50
11	0.045	0.470	1.476	4.904	2.130	4.21E+23	3.19E+09	46.59
12	0.046	0.481	1.441	4.786	2.079	4.29E+23	3.26E+09	47.57
13	0.047	0.492	1.408	4.677	2.031	4.37E+23	3.32E+09	48.44
14	0.048	0.503	1.378	4.576	1.987	4.44E+23	3.37E+09	49.22
15	0.049	0.513	1.350	4.485	1.948	4.51E+23	3.42E+09	49.91
16	0.050	0.523	1.325	4.400	1.911	4.56E+23	3.46E+09	50.52
18	0.052	0.541	1.280	4.253	1.847	4.66E+23	3.53E+09	51.58
20	0.053	0.558	1.241	4.124	1.791	4.74E+23	3.59E+09	52.46

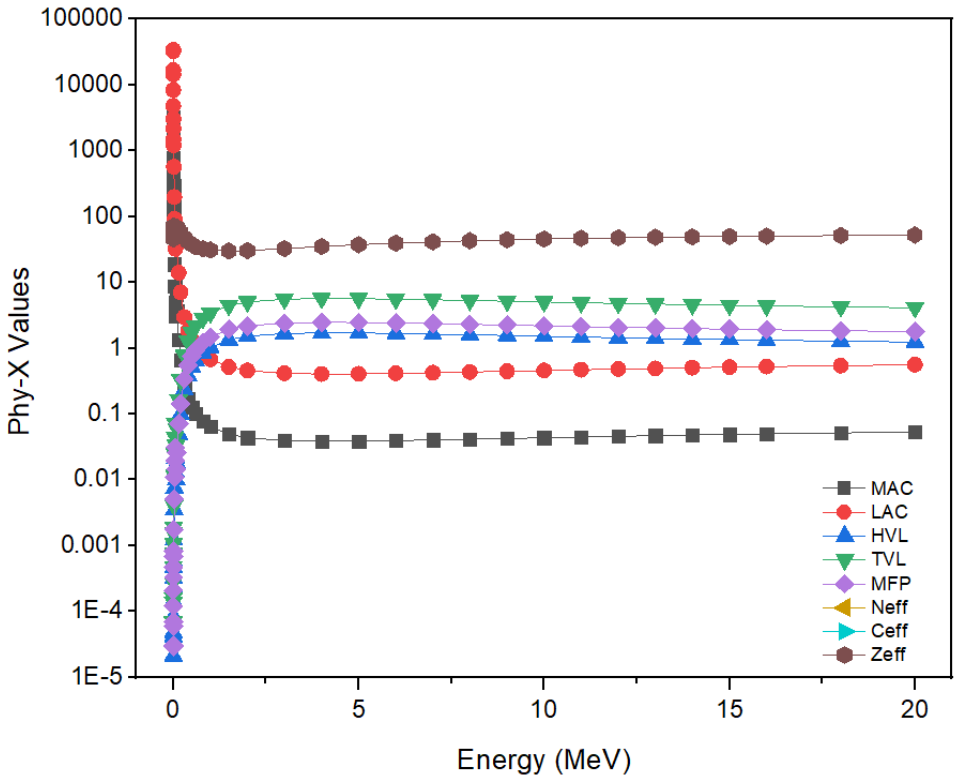

Figure 4. Radiation shielding results of HfB_2 using Phy-X software

Conclusions

The radiation absorption properties of B_4C, ZrB_2, TiB_2 or HfB_2 control rod materials that can be used in this power plant were investigated in this study by using the Phy-X software. To obtain attenuation properties, linear and mass attenuation coefficients (LAC, MAC), half and tenth value layers (HVL, TVL), mean free path (MFP), effective atomic number and electron density (Zeff, Neff) and effective conductivity (Ceff) energy parameters of radiation particles interacting with B_4C, ZrB_2, TiB_2 and HfB_2 materials between 1 keV to 20 MeV energy have been theoretically calculated.

According to the results obtained using the Phy-X software, LAC values decrease as the energy increases. A similar behavior is observed in the MAC values obtained using this LAC value. Here, the effect of energy on mass is clearly seen. HVL, TVL and MFP values increase as the energy increases. There are fluctuations in Neff, Ceff and Zeff values. Thus, the radiation absorption properties of these materials have been demonstrated and it has been theoretically obtained that they have effective absorption properties at low energies.

Acknowledgment

This study was supported by the Scientific Research Projects Coordination Unit of Kahramanmaraş Sütçü İmam University. Project numbers 2020/7-18 M, 2020/7-19 M and 2021/3-2 YLS.

Statement of Conflict of Interest

Authors have declared no conflict of interest.

Author's Contributions

The contribution of the authors is equal.

*This study was presented as a summary paper at the International Conference on Engineering, Natural and Applied Sciences (ICENAS'21) held online on 24-26 November 2021.

References

Agar O. Study on gamma ray shielding performance of concretes doped with natural sepiolite mineral. Radiochimica Acta 2018; 106(12): 1009-1016.

Cockbame DR., Gültekin E. Nükleer reaktörlerin kontrolü ve cihazlandırılması. TJDK 1966; 631(3): 21-27.

Cox J., Brown M., Hughes C. National renewable energy laboratory: Nuclear Energy with flexible operation, high VRE, and emission-constrained scenarios. Flexible Nuclear Energy for Clean Energy Systems 2020.

Fischer V., Tiras E. Water-based liquid scintillator detector as a new technology testbed for neutrino studies in Turkey. Nuclear Instruments and Methods in Physics Research Section A:

Accelerators, Spectrometers, Detectors and Associated Equipment 2020; 969: 163931.

Eskalen H., Kavun Y., Kerli S., Eken S. An investigation of radiation shielding properties of boron doped ZnO thin films. Optical Materials 2020; 105: 109871.

Kavun Y., Eskalen H., Kerli S., Kavgaci M. Fabrication and characterization of GdxFe2O3(100-x) /PVA (x=0, 5, 10, 20) composite films for radiation shielding. Applied Radiation and Isotopes 2021; 177: 109918.

Kavun Y., Uruş S., Tutuş A., Eken S., Özbek R. Investigation of radiation absorption properties of tungstate and molibdate doped wallpapers. Cumhuriyet Science Journal 2019; 40(4): 846-885

Lee JC. Nuclear reactor: Physics and Engineering. Nucl. React. Phys. Eng. 2020; 1–631.

Mohanakrishnan P., Singh OP., Umasankari K. Physics of nuclear reactors. 1st ed. Academic Press; 2021.

Özpolat ÖF., Alım B., Şakar E., Büyükyıldız M., Kurudirek M. Phy-X/ZeXTRa: A software for robust calculation of effective atomic numbers for photon, electron, proton, alpha particle, and carbon ion interactions. Radiation and Environmental Biophysics 2020; 59: 321-329.

Şakar E., Özpolat ÖF., Alım B., Sayyed MI., Kurudirek M. Phy-X / PSD: Development of a user friendly online software for calculation of parameters relevant to radiation shielding and dosimetry. Radiation Physics and Chemistry 2020; 166: 108496.

Shultis JK., Faw RE. Radiation shielding and radiological protection. In: Handbook of Nuclear Engineering. Springer US Publishing 2010.

William ER. Fabrication of control rods for nuclear reactors. 1st ed. Rowman and Littlefield; 1963

OKÜ Fen Bilimleri Enstitüsü Dergisi
5(Özel Sayı): 26-39, 2022

OKU Journal of The Institute of Science and Technology, 5(Special Issue):26-39, 2022

Osmaniye Korkut Ata Üniversitesi Fen Bilimleri Enstitüsü Dergisi

Osmaniye Korkut Ata University Journal of The Institute of Science and Technology

Simülasyon Destekli Tesis Yerleşim Tasarımı ve İyileştirme Çalışmaları: Bir Tekstil Firması Örneği

Muhammed ORDU[1*], Emrah KORHAN[2]

[1] Osmaniye Korkut Ata Üniversitesi, Mühendislik Fakültesi, Endüstri Mühendisliği Bölümü, 80000, Osmaniye
[2] Erciyes Üniversitesi, Mühendislik Fakültesi, Endüstri Mühendisliği Bölümü, 38039, Kayseri

[1] http://orcid.org/0000-0003-4764-9379
[2] http://orcid.org/0000-0001-7685-756X
*Sorumlu yazar: muhammedordu@osmaniye.edu.tr

Araştırma Makalesi

Makale Tarihçesi:
Geliş tarihi: 08.11.2021
Kabul tarihi:13.01.2022
Online Yayınlanma: 23.02.2022

Anahtar Kelimeler:
Tesis yerleşimi tasarımı
Simülasyon
Karar destek sistemi
Verimlilik
Tekstil

ÖZET

Günümüzde fabrikalar, rekabetçilik yeteneklerini artırmak ve kar marjlarını yükseltmek için birim zamanda daha fazla ürün üretmeyi amaçlamaktadırlar. Bu doğrultuda, daha yüksek satış gelirlerine ulaşırken gider kalemlerini de değerlendirmek zorunda kalmaktadırlar. İşletme operasyonlarından kaynaklanan maliyetler ise göz ardı edilebilmektedir. Fabrika içerisindeki gereksiz aktiviteler, tesis yerleşim planlarındaki düzensizlikler ve zaman kayıpları gibi faktörler fabrikaların üretim verimliliğini düşüren ama giderilebilecek nedenlerdir. Bu çalışmada, bir tekstil fabrikasının kesim departmanında tesis yerleşim tasarımı amaçlanmış ve bir ayrık olaylı simülasyon yöntemi geliştirilerek önerilen tasarım ile mevcut yerleşim düzeni performans ölçütleri açısından karşılaştırılmıştır. Öncelikle, ilgili departmanda proses diyagramı oluşturulmuş ve operasyon bileşenlerine ayrılmıştır. Zaman etüdü çalışması ile her bir aktiviteye ait süre ve mesafeler kaydedilmiştir. Bileşenler arasındaki günlük taşıma sayılarını gösteren from-to matrisleri oluşturulmuştur. Daha sonra bileşenler arasında ilişkiler diyagramı elde edilmiştir. Bileşenler hesaplanan sayısal ağırlıklarına göre yerleşim önceliklerine göre sıralanmışlardır. İkinci aşamada ise departmandaki stokastik süreçler dikkate alınarak bir simülasyon modeli kurulmuştur. Model doğrulandıktan sonra önerilen tasarım için güncellenmiştir. Elde edilen sonuçlara göre, önerilen yerleşim planlamasına göre departmandaki üretim verimliliği yaklaşık %14 artmıştır. Bu çalışma, fabrikaların sürekli olarak yerleşim düzenlemesine ihtiyaç duyduğunu ve simülasyon yöntemi ile daha iyi bir şekilde performans ölçümü yapıldığını ortaya koymaktadır.

Simulation Based Facility Layout Design and Improvement Studies: A Case of Textile Company

Research Article

Article History:
Received: 08.11.2021
Accepted: 13.01.2022
Published online: 23.02.2022

Keywords:
Facility layout design
Simulation
Decision support system
Productivity
Textile

ABSTRACT

Nowadays, factories aim to produce more products per unit time in order to increase their competitiveness and increase their profit margins. Accordingly, they have to take into account their expense items while achieving higher sales revenues. The costs arising from business operations can be ignored. Factors such as unnecessary activities in the factory, irregularities in the facility layout plans and time losses are the reasons that reduce the production efficiency of the factories but can be eliminated. In this study, facility layout design in the cutting department of a textile factory was aimed and the proposed design was compared with the existing layout in terms of performance criteria by developing discrete event simulation method. First of all, the process diagram was built in the related department and divided into operation components. The duration and distances of each activity were recorded by the time study analysis. From-to matrices showing the daily

transport numbers between the components were generated. Then, the relationship diagram between the components was obtained. Components are ordered according to their layout priorities according to their calculated numerical weights. In the second stage, a discrete event simulation model was established considering the stochastic processes in the department. After the model was validated, it was modified for the proposed design. The results show that the production efficiency in the department has increased by approximately 14% according to the proposed layout planning. This study reveals that factories always need to update facility layout design and simulation methods allows decision makers conduct better performance measurements.

To Cite: Ordu M., Korhan E. Simülasyon Destekli Tesis Yerleşim Tasarımı ve İyileştirme Çalışmaları: Bir Tekstil Firması Örneği. Osmaniye Korkut Ata Üniversitesi Fen Bilimleri Enstitüsü Dergisi 2022; 5(Özel sayı):26-39.

Giriş

Günümüzde işletmeler insan ve malzeme akışını kolaylaştırmak ve malzeme taşıma maliyetlerini düşürmek için uygun tesis yerleşimi yapmak zorundadırlar. Özellikle imalat sektöründe yer alan şirketler için tesis yerleşim tasarımı, rekabetçi küresel ortamda maliyetlerin kontrol edilebilmesi için önemli bir unsur haline gelmiştir (Naik ve Kallurkar, 2016). İyi bir tesis tasarımı üretim süreçlerinin etkinliğini ve verimliliğini arttırmaktadır. İşletme maliyetlerinin önemli bir kısmını malzeme taşıma maliyetleri oluşturmaktadır (Tompkins ve ark., 1996). Bu yüzden tesis yerleşiminden kaynaklı gereksiz taşımalar öncelikli olarak çözülmesi gereken sorunların başında yer almaktadır. Tesis yerleşimlerinde genellikle tasarım ihtiyacı, yeni bir tesis alanına gereksinim duyulduğunda ya da yeni ekipmanlara tesis sahası içerisinde yer verilmesi durumlarında ortaya çıkmaktadır (Baykasoğlu ve ark., 2006). Tesis yerleşimde yapılacak olan düzenlemelerin kötü olması, üretim süreçleri arasındaki stokların artmasına, gereksiz malzeme taşıma işlemlerinin yapılmasına ve iş akışının yavaşlamasına neden olmaktadır (Chiang ve Chiang, 1998).

Tesis yerleşimi tasarımına sistematik bir yaklaşımla bakmak gerekmektedir. Tasarım yapılırken sistemin içerisinde yer alan tüm unsurlar bütünsel bir bakış açısı ile değerlendirilmelidir (Yanık Uğurlu, 2013). Bu kapsamda karşılaşılan ilk problem, belli amaçlar doğrultusunda tesis içerisinde yer alan bölümlerin konumlandırılmasıdır (Lacksonen, 1994). Konumlandırma probleminin çözülmesi ile tesis içerisindeki yerleşim planı oluşturulmaktadır. Geleneksel düşünceye göre, bundan sonraki süreçte ise işletmenin ürettiği ürün tiplerine ve akış sürecine özgü olarak malzeme aktarma sistemi tasarlanmaktadır. Çağdaş düşünceye göre yerleşim planı ve malzeme aktarma sistemlerinin eş zamanlı olarak yapılması gereklidir. Çünkü aktarma donanımlarının tip ve kapladıkları alan yerleşim planını etkileyebilmektedir.

Yapılan çalışmanın amacı, bir işletmenin üretim süreçlerinin gerçekleştirildiği bir bölgede, tesis içi yerleşim planı yaptıktan sonra, yapılan iyileştirmelerin gerçek anlamda işletmeye olan katkısını simülasyon ortamında ortaya çıkarmaktır. Böylece tesis yerleşimi tasarımı kapsamında yapılan önerilerin uygulanabilirliği açısından etkinliği tespit edilmiş olacaktır. Çalışmada ilk olarak tesis yerleşim tasarımına yönelik literatür çalışmalarına yer verilmiştir. Daha sonra yerleşim planı için kullanılacak olan yöntem açıklanmış ve işletmenin sayısal verileri girdi olarak bu yöntemde

kullanılmıştır. Yöntemden elde edilen sonuçlarla yeni bir yerleşim planı oluşturulmuştur. Yerleşim planı ile yapılan değişiklikler simülasyon ortamında değerlendirilmiştir ve son olarak simülasyon sonuçlarına göre yeni yerleşim planının gerçek katkısı ortaya çıkarılmıştır.

Çalışmanın diğer bölümleri ise şu şekilde organize edilmektedir. İlgili literatür 2. Bölümde incelenirken çalışmada kullanılan iki aşamalı yaklaşım 3. Bölümde detaylı bir şekilde açıklanmaktadır. 4. Bölümde bulgular tartışılırken 5. Bölümde çalışma sonuçlandırılmakta ve gelecek çalışmalara yönelik fırsatlar sunulmaktadır.

Literatüre Bakış

Tesis yerleşim tasarımı ve planlanması üzerine literatürde çok sayıda çalışma bulunmaktadır. Örneğin, Naqvi ve ark., (2016) tesis planlama sürecinde yalın üretim ilkelerini dikkate alarak sistematik bir yerleşim planlaması ile verimliliği artırmışlardır. Akbilek (2017) bir üretim işletmesinde tesis yerleşimini akış odaklı olarak yeniden tasarlamıştır. Li ve ark. (2018) ise dinamik bir tesis planlamada insan faktörünü dikkate almışlardır. Uluskan ve Özyalıner (2021) işletmedeki süreç kalitelerine kaizen yöntemi uygulamışlar ve yapılan iyileştirmeler neticesinde ergonomik yönler dikkate alınarak tesis yerleşim tasarımı yapmışlardır.

Kapasiteli tesis yerleşim problemleri NP-Hard yapıya sahip oldukları için optimal sonuca ulaşmak adına sezgisel metotlardan faydalanılan çok sayıda çalışma bulunmaktadır. Bunlardan biri de tepe-tırmanma ve tavlama benzetimi metotlarıyla inceleme yapılan çalışmalardır (Yiğit ve Türkbey, 2003). Arostegui ve ark. (2006) tesis yerleşim problemini en iyi şekilde çözmeye yönelik olarak çok sayıda sezgisel yöntemi kıyaslamışlar ve çoğu durumda tabu arama algoritmasının, simüle edilmiş benzetimli tavlama ve genetik algoritmalarından daha iyi performans gösterdiklerini açıklamışlardır. Şahin (2008) dinamik tesis düzenleme problemini çözmek için bir tavlama benzetimi sezgiseli geliştirmiştir. Gülsüm ve ark. (2009) çalışmalarında, genetik algoritmadan faydalanarak tesis yerleşimi tasarımı ve bunun üzerine bir uygulama yapmışlardır. Golmohammadi ve ark. (2016) hücresel imalat sistemleri için geliştirdiği tesis planı için hiyerarşik genetik algoritma yöntemini kullanmıştır. Tefek ve Beşkirli (2019) tesis yerleştirme probleminde optimum sonuç elde edebilmek için yapay arı kolonisi algoritmasını kullanmışlardır. Aynı zamanda, Bozorgi ve ark. (2015) tabu arama, Hu ve Yang (2019) parçacık sürü optimizasyonunu ve Wei ve ark. (2019) genetik algoritmayı kullanmışlardır.

Matematiksel modelleme yöntemleri de tesis yerleşim çalışmalarında dikkate alınmaktadır. Örneğin, Akça ve Şahin (2018) çalışmalarında bir askeri tesisteki personel güvenliğini etkileyen önemli bölümlerin yerleşimini dikkate almak ve taşıma maliyetlerini azaltmak için çok amaçlı tesis tasarımı problemi kapsamında matematiksel modelleme kurmuşlardır. Allahyari ve Azab (2018) ise bir tesis yerleşim problemi için tavlama benzetim algoritmasını matematiksel modelleme ile birlikte düşünmüştür.

Bazı çalışmalar ise tesis içi yerleşim düzenlemesini simülasyon tekniğini kullanarak yapmışlardır. Örneğin, Aksaraylı ve Altuntaş (2009) bir üretim ortamının malzeme taşıma odaklı farklı tesis

planlarını ortaya koymuş ve geliştirdikleri simülasyon modeliyle performanslarını analiz etmişlerdir. Pourhassan ve Raissi (2017) simülasyon tabanlı bir optimizasyon yaklaşımı geliştirmiş ve dinamik bir tesis planlama problemine uygulamışlardır. Chen ve Tiong (2019) ise bir modüler üretim sisteminde tesis yerleşimini tavlama benzetim algoritmasını kuyruk teorisi ile birlikte ele almıştır.

Materyal ve Metot

Bu çalışma iki aşamadan oluşmaktadır. Birinci aşama, bir tekstil firmasının kesim departmanının tesis yerleşim tasarımı ve planlamasıdır. Bu aşamada, işletmenin üretim operasyonları ve malzeme akış süreci analiz edilmektedir. İş bileşenlerinin birbirleri arasındaki ilişki diyagramları çıkarılmakta ve birimler arası taşıma sayıları elde edilmektedir. Yapım şablon yöntemi ile üretimde kayıplara neden olan aktiviteler bertaraf edilerek yeni bir tesis planı oluşturulmaktadır. İkinci aşama ise departmanın mevcut ve önerilen yerleşimlerinin simülasyon yöntemiyle modellenmesidir. Bu simülasyon modeli ile önerilen tesis yerleşim planının ne düzeyde bir iyileştirme sağladığını kritik performans göstergeleri üzerinden ölçülmesini sağlamaktadır.

Yapım Şablon Yöntemi ile Tesis Yerleşim Planlaması

Çalışmanın ilk aşamasında yapım şablon yöntemi ile yeni bir tesis yerleşim planı belirlenmektedir. Bunun için öncelikle işletmenin kesim departmanının üretim operasyonları ve malzeme-insan hareketliliği, tesiste kullanılan ekipmanlar ve kapladıkları alanlar belirlenmektedir. Tablo 1 kesim departmanının proses diyagramını ve zaman etüdü çalışmasına ait uzaklık ve ortalama süreleri vermektedir.

Tablo 1. Proses diyagramı

İş Tanımı	Uzaklık (m)	Ortalama Süre (dk)
Kesime hazır kumaşın kesim bölümüne taşınması	10,4	3,2
Kumaş serimi	-	35,8
Çizim kâğıdının serimlerin üzerine ütü ile yapıştırılması	-	2,5
Serimlerin kesim hattının sonuna taşınması	11,6	1,9
Serimlerin otomatik kesim makinesini beklemesi	-	2,8
Serimlerin kesim makinesinin girişine yerleştirilmesi	-	2,0
Kesim süreci	-	43,5
Kesilen parçaların parti masalarına taşınması	2,0	10,2
Metolama (Etiketleme) işlemi	-	20,4
Parçaların raflara taşınması	15,1	4,8

Şekil 1 kesim departmanının üretim operasyonlarını akış diyagramı ile göstermektedir. İlgili departmanda 3 adet kesim hattı bulunmaktadır. Stok alanı 2'den gelen hammadde kumaşlar Taşıyıcı 1-2 veya Palete aktarılmaktadır. Kesim Hattı 1 ve 2'de üretim süreci insan gücü ile yürütülmekte iken Kesim Hattı 2'de serim ve kesim makineleri kullanılmaktadır. Kesim Makinesi ise Kesim Hattı 1 ve 2'de kullanılmaktadır. Kesim Hattı 3'te ise serimi yapılan kumaşlar insan gücü ile kesilmektedir. Kesim işlemi kesim makinesi ile yapılacak hatlarda çizimler ağ bağlantısı ile Kesim Makinesine gönderilmektedir. Kesim işlemi bittikten sonra kesilen parçalar Aktarma Masalarına alınmaktadır. Daha sonra Partileme Masalarına aktarılan malzemeler etiketlenmektedir. Bir sonraki departmana

gönderilmek üzere Raflara yerleştirilmektedir. Tablo 2 departmandaki iş bileşenlerini ve bunlara atanan kodları göstermektedir.

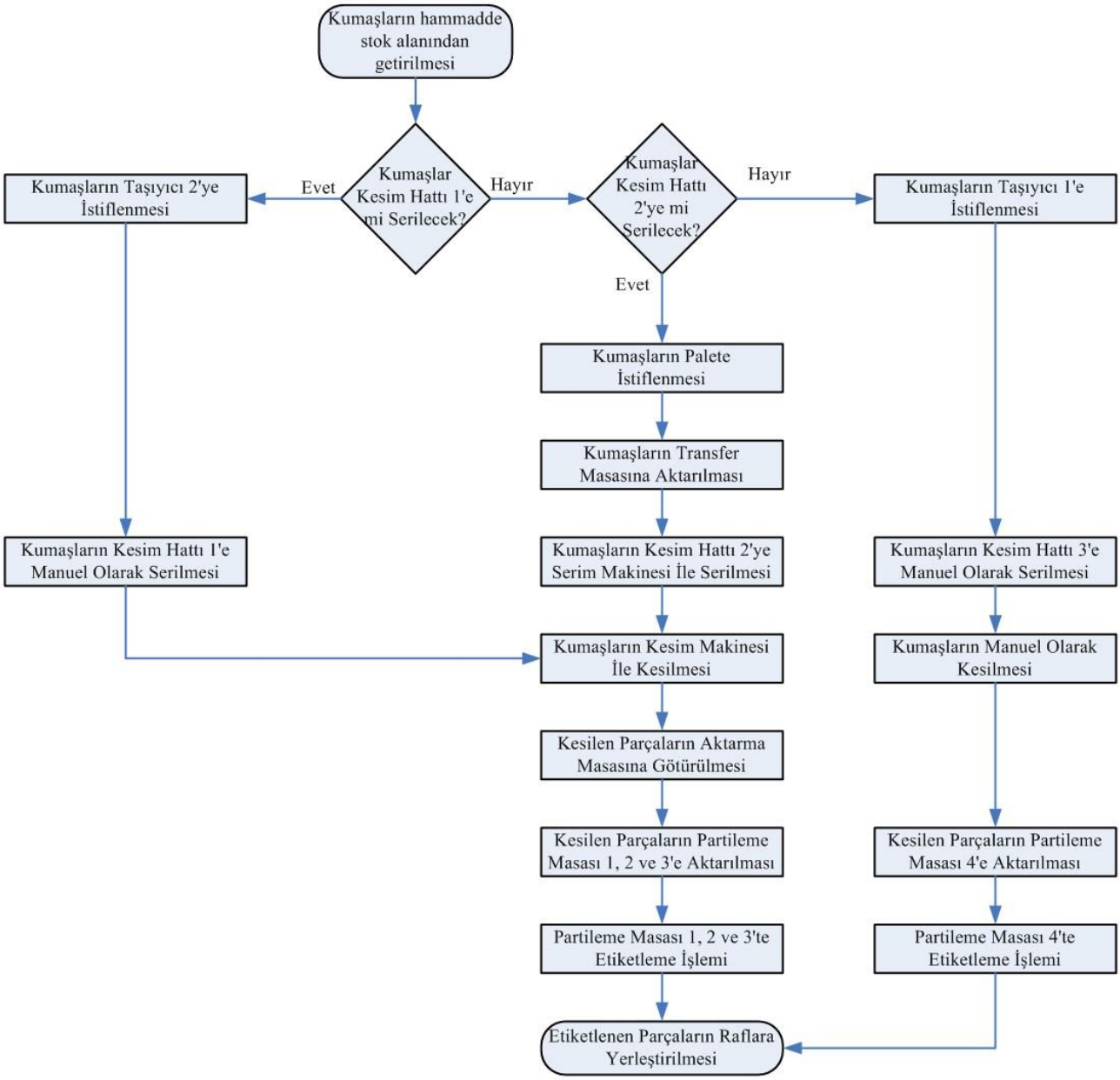

Şekil 1. Üretim operasyonlarının kavramsal haritası

Üretim prosesi analiz edildikten ve iş bileşenleri belirlendikten sonra from-to matrisinin oluşturulması gerekmektedir. Bu matris ile iş bileşenleri arasındaki günlük malzeme taşıma sayıları elde edilmektedir. Günlük sefer sayılarını gösteren bu from-to matrisi Tablo 3'te verilmektedir. Buna göre, Kesim hattı (K1) 1'den Stok Alanı (S1) 1'e günlük olarak ortalama 28 defa malzeme taşıması yapılmaktadır. Üretim proseslerinden de anlaşılacağı üzerine Rafa gelen sevkiyatlar sadece Partileme Masası (PM) 1-4'ten yapılmaktadır.

Tablo 2. Bileşenler ve kodları

Bileşenler	Bileşen Kodu	Bileşenler	Bileşen Kodu
Kumaş serim makinesi	M1	Taşıyıcı 1	T1
Kumaş kesim makinesi	M2	Taşıyıcı 2	T2
Kesim hattı 1	K1	Partileme masası 1	PM1
Kesim hattı 2	K2	Partileme masası 2	PM2
Kesim hattı 3	K3	Partileme masası 3	PM3
Stok alanı 1	S1	Partileme masası 4	PM4
Stok alanı 2	S2	Transfer masası	TM
Stok alanı 3	S3	Aktarma masası	AM
Palet	P	Masa artıkları kutusu	MAK
Malzeme dolabı	MD	Raf	R

Tablo 3. Günlük sefer sayılarını gösteren from-to matrisi

Bileşen Kodu	M1	M2	K1	K2	K3	S1	S2	S3	P	MD	T1	T2	PM1	PM2	PM3	PM4	TM	AM	MAK	R
M1		-	5	-	-	-	-	-	-	-	-	-	-	-	-	-	-	-	-	-
M2	-		-	-	-	-	-	-	-	-	-	-	-	-	-	-	-	12	-	-
K1	-	7		-	-	28	-	-	-	1	-	-	-	-	-	-	-	-	-	-
K2	-	5	-		-	28	-	-	-	1	-	-	-	-	-	-	-	-	-	-
K3	-	-	-	-		11	-	-	-	1	-	-	-	-	-	3	-	-	-	-
S1	-	-	-	-	-		-	-	-	-	-	-	-	-	-	-	-	-	-	-
S2	-	-	-	-	-	-		-	28	-	11	28	-	-	-	-	-	-	-	-
S3	-	-	-	-	-	-	-		-	-	-	-	-	-	-	-	-	-	-	-
P	-	-	-	-	-	-	-	-		-	-	-	-	-	-	-	28	-	-	-
MD	-	-	1	1	1	-	-	-	-		-	-	1	1	1	-	-	-	-	-
T1	-	-	-	-	11	-	-	-	-	-		-	-	-	-	-	-	-	-	-
T2	-	-	28	-	-	-	-	-	-	-	-		-	-	-	-	-	-	-	-
PM1	-	-	-	-	-	-	-	-	-	1	-	-		-	-	-	-	-	-	5
PM2	-	-	-	-	-	-	-	-	-	1	-	-	-		-	-	-	-	-	3
PM3	-	-	-	-	-	-	-	-	-	1	-	-	-	-		-	-	-	-	4
PM4	-	-	-	-	-	-	-	-	-	-	-	-	-	-	-		-	-	-	3
TM	-	28	-	-	-	-	-	-	-	-	-	-	-	-	-	-		-	-	-
AM	-	-	-	-	-	-	-	-	-	-	-	-	5	3	4	-	-		12	-
MAK	-	-	-	-	-	-	-	-	-	-	-	-	-	-	-	-	-	-		-
R	-	-	-	-	-	-	-	-	-	-	-	-	-	-	-	-	-	-	-	

Yeni tesis yerleşim planında iş bileşenlerinin en uygun bir yere atanabilmesi için birbirleriyle olan ilişkilerini iyi bir şekilde analiz etmek gerekmektedir. Bunun için kesim departmanındaki iş bileşenlerinin birbirleriyle olan ilişkileri Şekil 2'de verilen ilişkiler diyagramı ile ortaya konmaktadır. İlişkiler diyagramında işaretleyici olarak harfler kullanılmıştır. Harflerin sayısal değerleri ve yakınlık derecesi Tablo 4'te gösterildiği gibidir. Kumaş kesim makinesi daha önce de belirtildiği gibi Kesim Hattı 1 ve 2'de kullanıldığı için bu iş bileşenleri arasında "Kesinlikle Gerekli (A)" ilişkisi bulunmaktadır. Kesim Hattı 3'te kullanılmadığı için "Normal (O)" ilişkisi uygun görülmüştür.

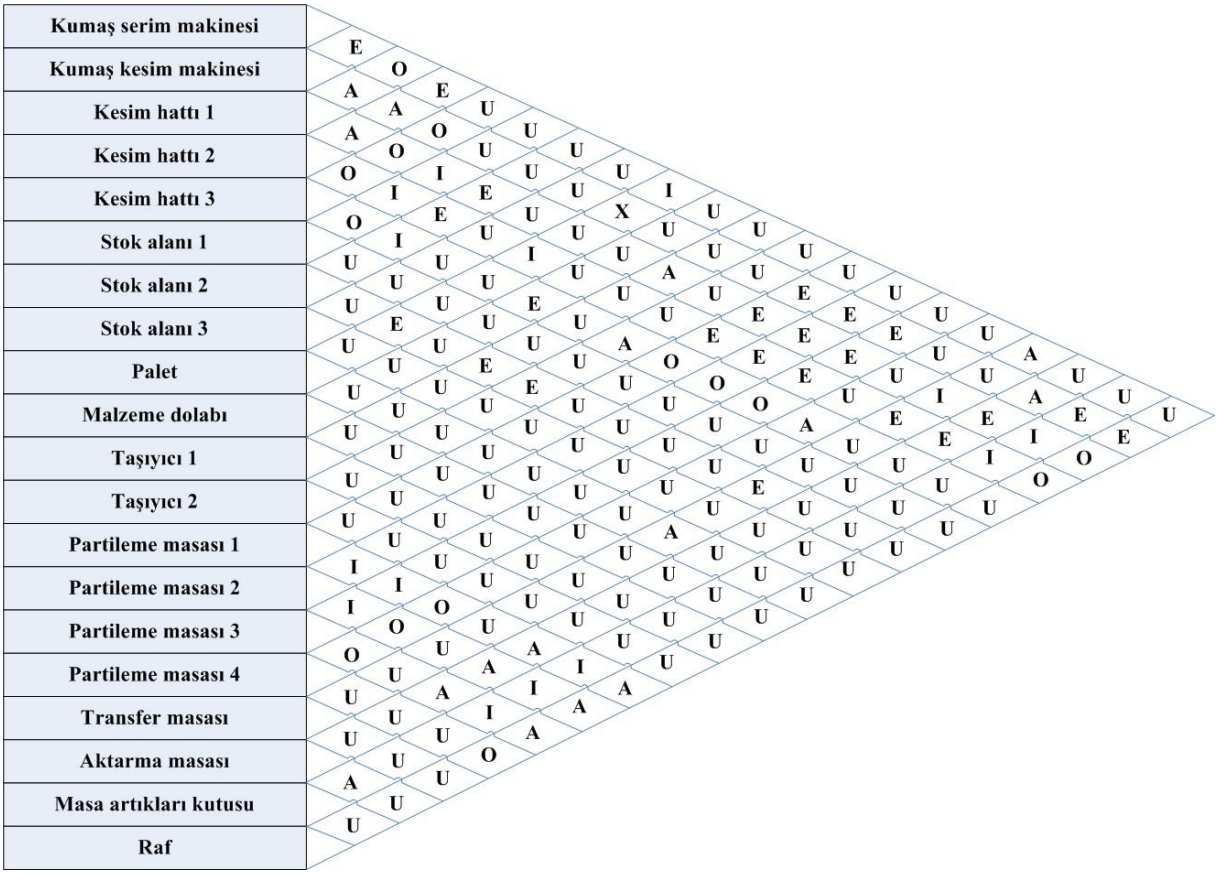

Şekil 2. İlişkiler diyagramı

İlişkiler diyagramının oluşturulmasından sonra diğer bileşenlerle en çok ilişki içerisinde olan iş bileşeninin belirlenmesi gerekmektedir. Tablo 4'te verilen nümerik değerler ile her bir iş bileşenin sayısal ağırlığı hesaplanmaktadır. Örneğin, M1 kodlu iş bileşeninin diğer bileşenler ile ilişkisi: "EOEUUUUIUUUUUUUAUUU". Her bir harfe karşılık gelen nümerik değerler toplanır. M1 iş bileşeninin sayısal ağırlık değeri (SAD) Eşitlik (1)'deki gibi bulunur:

$$SAD_{M1} = 3 + 1 + 3 + 0 + 0 + 0 + 0 + 2 + 0 + 0 + 0 + 0 + 0 + 0 + 0 + 4 + 0 + 0 + 0 = 13 \qquad (1)$$

Tablo 5 ise tüm iş bileşenlerinin sayısal ağırlık değerlerini göstermektedir.

Tablo 4. İşaretçiler, sayısal değerleri ve yakınlık dereceleri (Dereli ve Baykasoğlu, 2019)

Harf	Nümerik Değer	Yakınlık Derecesi
A	4	Kesinlikle gerekli
E	3	Özellikle gerekli
I	2	Önemli
O	1	Normal
U	0	Önemli değil
X	-1	İstenilmez
XX	-2, -3, -4?	Kesinlikle istenilmez

Tablo 5. Bileşenler ve sayısal ağırlıkları

Bileşen Kodu	Bileşenlerin Sayısal Ağırlıkları	Bileşen Kodu	Bileşenlerin Sayısal Ağırlıkları
M1	13	T1	7
M2	30	T2	7
K1	36	PM1	25
K2	36	PM2	25
K3	20	PM3	25
S1	5	PM4	8
S2	20	TM	16
S3	0	AM	22
P	10	MAK	17
MD	3	R	18

Bundan sonra iş bileşenlerinin yerleşim önceliklerinin tespit edilmesi gerekmektedir. Bunun için, Tablo 6'da önceliği tayin edilmiş bileşenler sırasında her bir iş bileşeninin kendinden önceki iş bileşenleriyle olan ilişkisi dikkate alınmaktadır. Örneğin, M1 iş bileşeni 10. Sütunda yer almaktadır. Kendinden önceki 9 iş bileşeni ile ilişki harfleri şu şekildedir: "OEEUUUUUU". Sayısal Ağırlık Değeri ise Eşitlik (2)'deki gibi bulunur:

$$SAD_{M1} = 1 + 3 + 3 + 0 + 0 + 0 + 0 + 0 + 0 = 7 \quad (2)$$

Tüm iş bileşenlerin sayısal ağırlık değerleri ve yerleşim önceliği Tablo 7'de gösterilmektedir.

Tablo 6. Bileşenlerin yerleşim önceliklerinin tespit edilmesi

Bileşen Kodu	Önceliği Tayin Edilmiş Bileşenler																			Sayısal Ağırlık
	K1	K2	M2	AM	PM1	PM2	PM3	R	MAK	M1	TM	P	S2	K3	PM4	TM1	TM2	S1	S3	MD	
M1	O	E	E	U	U	U	U	U	U												7
M2	A	A																			8
K2	A																				4
K3	O	O	O	U	O	O	O	U	U	U	U	U	I								8
S1	I	I	U	U	U	I	U	U	U	U	U	U	U	O	U	U	U				7
S2	E	E	U	U	U	U	U	U	U	U	E	E									12
S3	U	U	U	U	U	U	U	U	U	U	U	U	U	U	U	U	U	U			6
P	U	I	X	U	U	U	U	U	U	I	A										9
MD	U	U	U	U	U	U	U	U	U	U	U	U	U	E	U	U	U	U	U		3
T1	A	U	U	U	U	U	U	U	U	U	U	U	E	U	U						7
T2	U	U	U	U	U	U	U	U	U	U	U	U	E	A	U	U					7
PM1	E	E	E	A																	13
PM2	E	E	E	A	I																15
PM3	E	E	E	A	I	I															17
PM4	U	U	U	U	O	O	O	O	U	U	U	U	U	A							8
TM	I	E	U	U	U	U	U	U	U	A											9
AM	E	E	A																		10
MAK	I	I	E	A	I	I	I	U													17
R	O	O	E	U	A	A	A														17

Tablo 7. Bileşenlerin yerleşim öncelik sıraları

Yerleşim Öncelik Sırası	Bileşen Kodu	Yerleşim Öncelik Sırası	Bileşen Kodu
1	K1	11	PM4
2	PM3	12	M2
3	R	13	K3
4	MAK	14	M1
5	PM2	15	S1
6	PM1	16	T1
7	S2	17	T2
8	AM	18	S3
9	TM	19	K2
10	P	20	MD

Simülasyon Modeli

Şekil 1'de kesim departmanının üretim operasyonlarının kavramsal haritası verilmiştir. Bu üretim operasyonlarının girdi parametreleri ve bunlara bağlı istatistiki değerleri ise Tablo 1'de gösterilmektedir. Bu bilgiler ışığında ilgili departmanın ayrık zamanlı simülasyon modeli Simul8 yazılımı kullanılarak geliştirilmiştir. İlgili model Şekil 3'te sunulmaktadır. Bu modele göre, kumaşlar sisteme girdikten sonra üç farklı stok alanına istiflenmektedir: Taşıyıcı 1 – 2 ve Palet. İşçiler, kumaşları Taşıyıcı 2'den alıp Kesim Hattı 1'e manuel olarak sermektedir. Paletteki kumaşlar ise transfer masasına aktarılmakta ve buradan da Kumaş Serim Makinesi ile Kesim Hattı 2'ye serilmektedir. Kesim Hattı 1 ve 2'deki serilmiş kumaşlar sırasıyla Kesim Makinesi tarafından kesilmektedir. Kesilen kumaşlar aktarma masasına istiflenmektedir. Daha sonra Partileme Masası 1, 2 ve 3'ten birine aktarılarak işçiler tarafından etiketleme işlemi yapılmaktadır. Diğer yandan hammadde olarak gelen kumaşlar ihtiyaç durumuna göre işçiler tarafından manuel olarak Kesim Hattı 3'e serilmekte ve yine manuel olarak kesilmektedir. Bu kesim hattında kesilen kumaşlar sadece Partileme Masası 4'e aktarılmakta ve burada etiketleme işlemi gerçekleştirilmektedir. Partileme Masalarından etiketlenen kumaşlar bitmiş ürün stok alanına götürülmektedir.

Simülasyon modelimizin ısınma periyodu Welch Yöntemi (Law ve Kelton, 2000) ile 10 gün olarak bulunmuş ve optimum replikasyon sayısı Sabit Örneklem Büyüklüğü Prosedürü (Law ve Kelton, 2000) ile 20 olarak hesaplanmıştır.

Modelimizin geçerlilik ve doğruluk analizleri sırası ile yapılmıştır. Kavramsal harita ve simülasyon modelimizin nesne yerleşimi ve birbirleri arasındaki bağlantılar işletme çalışanları ile doğrulanmıştır. Elde edilen simülasyon sonuçları mevcut veriler ile karşılaştırılmış ve sapmalar %5'ten az bulunmuştur.

Önerilen yeni yerleşim planı simülasyon modelinde senaryo olarak uygulanmıştır. Mevcut yerleşim planı ile yeni önerilen tesis planı toplam akış şiddeti performans ölçütü üzerinden karşılaştırılmış ve bir sonraki bölümde bu sonuçlar açıklanarak tartışılmıştır.

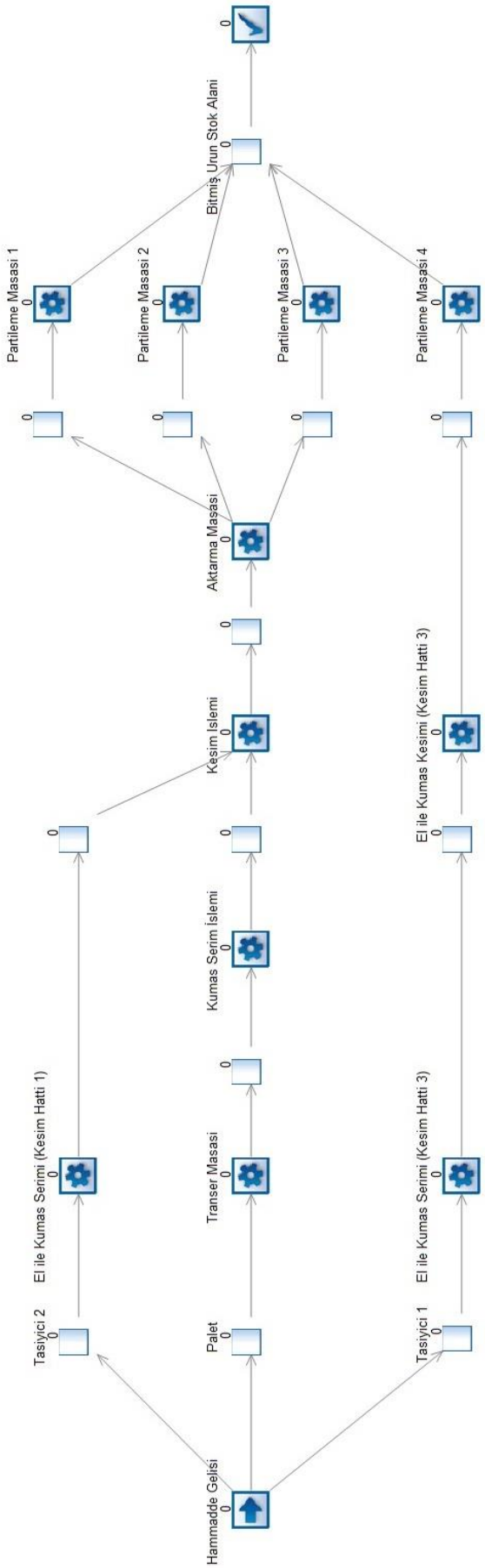

Şekil 3. Simülasyon modeli

Bulgular ve Tartışma

Çalışmamızda yapım şablon yöntemi kullanılarak ilgili tekstil firmasının kesim departmanı için önerilen yeni yerleşim planı simülasyon yöntemi ile modellenmiştir. Performans ölçütü olarak toplam akış şiddeti tercih edilmiştir. Toplam akış şiddetinin formülü Eşitlik (3) ile gösterilmektedir.

Toplam Akış Şiddeti = Sefer Sayısı x Mesafe (3)

Tablo 8, mevcut yerleşim ve önerilen yerleşim planları için hesaplanan toplam akış şiddetlerini göstermektedir. Yeni yerleşim planında Kesim Hattı 2 yer değiştirmemiştir. Stok Alanı 1, Kesim Hattı 2'ye göre biraz uzaklaşmış ve bundan dolayı, aralarındaki akış şiddeti 1176 birim artış göstermiştir. Kesim Hattı 1 ile Stok Alanı 1 arasındaki akış şiddeti %62 oranında azalmıştır. Yeni yerleşim planında Kesim Hattı 3'ün konumu Stok Alanı 1'in konumuna yaklaşmıştır. Bundan dolayıdır ki, Kesim Hattı 3 ile Stok Alanı 1'in arasındaki akış şiddeti ise 4092 birim azalmıştır. Stok Alanı 2 ile Taşıyıcı 1 arasındaki akış şiddeti %46 oranında azalırken Taşıyıcı 1 arasında ise %72'lik bir artış yaşanmıştır. Diğer yandan Kesim Hattı 3 ile Partileme Masası 4 yeni tesis planında birbirinden uzaklaşmış ve buna bağlı olarak akış şiddeti ise 0'dan 6528 birime çıkmıştır. Son olarak, Raf ile Partileme Masaları arasındaki akış şiddetleri önemli düzeyde azalmıştır. Yeni yerleşim planındaki toplam akış miktarı mevcut yerleşime göre yaklaşık %14 oranında azalmıştır.

Tablo 8. Fayda Analizi

Alternatifler	Bileşenler	S1	T1	T2	PM4	R	Toplam
Mevcut Yerleşim	K1	46452	-	-	-	-	46452
	K2	61796	-	-	-	-	61796
	K3	30217	-	-	-	-	36745
	S2	-	16016	22568	-	-	38584
	PM1	-	-	-	-	11585	11585
	PM2	-	-	-	-	7560	7560
	PM3	-	-	-	-	10884	10884
	PM4	-	-	-	-	9102	9102
	Toplam Akış Şiddeti (Sefer Sayısı x Mesafe)						222708
Önerilen Yerleşim	K1	17472	-	-	-	-	17472
	K2	62972	-	-	-	-	62972
	K3	26125	-	-	6528	-	32653
	S2	-	8635	38920	-	-	47555
	PM1	-	-	-	-	8675	8675
	PM2	-	-	-	-	5709	5709
	PM3	-	-	-	-	8416	8416
	PM4	-	-	-	-	7770	7770
	Toplam Akış Şiddeti (Sefer Sayısı x Mesafe)						191222
	Verimlilik Oranı (%)						%14.14

Sonuç

Bu çalışmada, bir tekstil firmasının kesim departmanın tesis yerleşiminden ve üretim akışından kaynaklanan darboğazları tespit etmek ve malzeme akışını kolaylaştırmak amaçlanmıştır. Bunun için iki aşamalı bir yaklaşım geliştirilmiştir. İlk aşamada, yapım şablon yöntemi kullanılarak yeni bir tesis tasarımı planlanmıştır. Bu süreçte, departmanın iş bileşenleri tespit edilmiş, proses diyagramı çıkarılmış ve iş bileşenlerinin birbirleri arasındaki ilişki analiz edilmiştir. Daha sonra iş bileşenleri

arasındaki günlük ortalama sefer sayıları ve mesafeler ölçülmüştür. Bileşenlerin sayısal ağırlıkları hesaplanarak yerleşimde öncelikleri tayin edilmiştir. İkinci aşamada ise, departmanın simülasyon modeli geliştirilmiştir. Doğruluğu onaylandıktan sonra model yeni yerleşim planına göre çalıştırılmıştır. Sonuç olarak, mevcut ve önerilen yerleşim planlarının toplam akış şiddetleri hesaplanmıştır. Yeni tesis planına göre verimliliğin arttığı gözlemlenmiştir.

Bu çalışma, ilgili departmanda üretilen malzemelerin üretim sürelerinin ve takt zamanlarının düşmesini ve birim zamanda üretilen malzeme miktarlarının artmasını sağlamıştır. Çalışma, ilgili fabrikanın sadece kesim departmanı ile sınırlandırılmıştır. Diğer departmanlarında çalışmaya entegre edilmesi ile gelecek çalışmalara ışık tutacaktır. Ayrıca, farklı sezgisel yöntemlerinde kullanılması ile farklı tesis planlarının önerilmesi ve bununda simülasyon yöntemi ile performanslarının kıyaslanması mümkün olabilecektir. Ayrıca, yalın üretim teknikleri işletmelerin performansını arttırmada etkin yöntemlerden biridir. Fakat, bu çalışmada yalın üretim teknikleri (5S gibi) kullanılmamıştır. Bu husus, gelecek çalışmalarda dikkate alınarak daha etkin bir tesis içi yerleşim düzenlemesi yapılabilecektir.

Çıkar Çatışması Beyanı

Makale yazarları aralarında herhangi bir çıkar çatışması olmadığını beyan ederler.

Araştırmacıların Katkı Oranı Beyan Özeti

M. Ordu makaleye %60, E. Korhan ise %40 oranda katkı sağlamış olduklarını beyan eder.

* Bu çalışma, 24-26 Kasım 2021 tarihlerinde çevrimiçi olarak gerçekleştirilen International Conference on Engineering, Natural and Applied Sciences (ICENAS'21) konferansında özet bildiri olarak sunulmuştur.

Kaynakça

Akbilek N. Gıda makineleri endüstrisinde akış odaklı tesis yerleşimi uygulaması. Sakarya Üniversitesi Fen Bilimleri Enstitüsü Dergisi 2017; 21(5): 951-960.

Akça M., Şahin R. Çok amaçlı karma tam sayılı tesis yerleşim problemi modeli ve askeri tesiste uygulama. Pamukkale Üniversitesi Mühendislik Bilimleri Dergisi 2018; 24(1): 117-123.

Aksarayli M., Altuntaş S. Malzeme taşıma odaklı planlama için üretim sistemlerindeki tezgah yerleşim düzenlerinin benzetim analizi ile karşılaştırılması. Pamukkale Üniversitesi Mühendislik Bilimleri Dergisi, 2009; 15(2): 203-214.

Allahyari MZ., Azab A. Mathematical modeling and multi-start search simulated annealing for unequal-area facility layout problem. Expert Systems With Applications 2018; 91: 46-62.

Arostegui Jr MA., Kadipasaoglu SN., Khumawala BM. An empirical comparison of tabu search, simulated annealing, and genetic algorithms for facilities location problems. International Journal of Production Economics 2006; 103(2): 742-754.

Baykasoğlu A., Dereli T., Sabuncu I. An ant colony algorithm for solving budget constrained and unconstrained dynamic facility layout problems. Omega 2006; 34(4): 385-396.

Bozorgi N., Abedzadeh M., Zeinali M. Tabu search heuristic for efficiency of dynamic facility layout problem. The International Journal of Advanced Manufacturing Technology 2015; 77: 689-703.

Chen C., Tiong LK. Using queuing theory and simulated annealing to design the facility layout in an AGV-based modular manufacturing system. International Journal of Production Research 2019; 57(17): 5538-5555.

Chiang WC., Chiang C. Intelligent local search strategies for solving facility layout problems with the quadratic assignment problem formulation. European Journal of Operational Research 1998; 106(2-3): 457-488.

Dereli T., Baykasoğlu A. Üretim sistemleri ve tesis planlama. 5. Basım. Ercan Öztemel (ed.) Endüstri Mühendisliğine Giriş. İstanbul: Papatya Yayıncılık Eğitim 2019.

Golmohammadi AM., Bani-Asadi H., Esmaeeli H., Hadian H., Begheri H. Facility layout for cellular manufacturing system under dynamic conditions. Decision Science Letters 2016; 5(2016): 407-416.

Gülsün B., Tuzkaya G., Duman C. Genetik algoritmalar ile tesis yerleşimi tasarımı ve bir uygulama. Doğuş Üniversitesi Dergisi 2009; 10(1): 73-87.

Hu B., Yang B. A particle swarm optimization algorithm for multi-row facility layout problem in semiconductor fabrication. Journal of Ambient Intelligence and Humanized Computing 2019; 10: 3201-3210.

Lacksonen TA. Static and dynamic layout problems with varying areas. Journal of the Operational Research Society 1994; 45(1): 59-69.

Law AM., Kelton WD. Simulation modeling and analysis. New York: McGraw – Hill 2000.

Li J., Tan X., Li J. Research on dynamic facility layout problem of manufacturing unit considering human factors. Mathematical Problems in Engineering 2018; 2018: 1-13.

Naik SB., Kallurkar S. A literature review on efficient plant layout design. International Journal of Industrial Engineering 2016; 7(2): 43-51.

Naqvi SAA., Fahad M., Atir M., Zubair M., Shehzad MM. Productivity improvement of a manufacturing facility using systematic layout planning. Cogent Engineering 2016; 3: 1-13.

Purhassan MR., Raissi S. An integrated simulation-based optimization technique for multi-objective dynamic facility layout problem. Journal of Industrial Information Integration 2017; 8: 49-58.

Şahin R. Dinamik tesis düzenleme problemi için bir tavlama benzetimi sezgiseli. Gazi Üniversitesi Mühendislik Mimarlık Fakültesi Dergisi 2008; 23(4): 863-870.

Tefek MF., Beşkirli M. Tesis yerleştirme (p-Hub) probleminin yapay arı kolonisi kullanılarak çözülmesi. Avrupa Bilim ve Teknoloji Dergisi 2019; 193-200.

Tompkins JA., White JA., Bozer YA., Tanchoco JMA., Trevino J. Facilities planning. 2nd ed. USA: John Wiley and Sons; 1996.

Uluskan M., Özyalıner MT. Otomotiv sektöründe kaizen yöntemi ile tesis yerleşim tasarımı ve reba analizi. Eskişehir Osmangazi Üniversitesi Mühendislik ve Mimarlık Fakültesi Dergisi 2021; 29(1): 1-19.

Yanık Uğurlu S. Tesis planlama. Erişim adresi: http://auzefkitap.istanbul.edu.tr/kitap/endustrimuhlt_ue/tesisplanlama.pdf, 2013.

Wei X., Yuan S., Ye Y. Optimizing facility layout planning for reconfigurable manufacturing system based on chaos genetic algorithm. Production & Manufacturing Research 2019; 7(1): 109-124.

Yiğit V., Türkbey O. Tesis yerleşim problemlerine sezgisel metotlarla yaklaşım. Gazi Üniversitesi Mühendislik Mimarlık Fakültesi Dergisi 2003; 18(4): 45-56.

OKÜ Fen Bilimleri Enstitüsü Dergisi
5(Özel Sayı):40-49, 2022

OKU Journal of The Institute of Science and Technology, 5(Special Issue):40-49, 2022

Osmaniye Korkut Ata Üniversitesi Fen Bilimleri Enstitüsü Dergisi

Osmaniye Korkut Ata University Journal of the Institute of Science and Technology

Chemical Analysis of Natural Dyestuff Extracted from Peanut Skin

Halil ÖZDEMİR[1*]

[1]Osmaniye Korkut Ata University, Osmaniye Vocational School, Textile Technology Program, 80000, Osmaniye, Turkey

[1]https://orcid.org/0000-0001-8575-7317
[*]Corresponding author: halilozdemir@osmaniye.edu.tr

Research Article

Article History:
Received: 09.12.2021
Accepted: 14.01.2022
Published online: 23.02.2022

Keywords:
Peanut skin
Natural dyestuff
Extraction
HPLC analysis
UV-visible spectrometric analysis

ABSTRACT

Most of the peanuts which from the legumes family is the most important agricultural product of Osmaniye province and its surroundings are consumed as snacks. It is also used in the food industry as peanut butter and peanut oil and is also used as an additive. Peanut skin obtained as a by-product of food production in the peanut industry is mostly used as animal feed. Peanut skin, which is rich in protein, fat, carbohydrates and polyphenols, is known to be a powerful antioxidant. Therefore, it is thought that it can be used easily in foods or dietary supplements. In the study, the presence of natural dyestuff in the peanut skin was investigated. Because peanuts are very rich in flavonoids and phenolic acids. For this purpose, as results of the analyzes made in HPLC and UV-Visible Spectrophotometer, it was determined that there are catechin and anthocyanin (Cyanidin) in the peanut skin. In addition, the amount of dyestuff in raw and roasted peanuts was also compared and it was determined that more dyestuff could be extracted from raw peanuts.

Yerfıstığı Tohum Kabuğundan Ekstrakte Edilmiş Doğal Boyarmaddenin Kimyasal Analizi

Araştırma Makalesi

Makale Tarihçesi:
Geliş tarihi: 09.12.2021
Kabul tarihi: 14.01.2022
Online Yayınlanma: 23.02.2022

Anahtar Kelimeler:
Yer fıstığı tohum kabuğu
Doğal boyama
Ekstraksiyon
Renk ölçümü
Haslık

ÖZET

Osmaniye ili ve çevresinin en önemli tarım ürünü olan baklagiller familyasından yerfıstığının büyük bir kısmı atıştırmalık olarak tüketilmektedir. Ayrıca fıstık, ezme ve fıstık yağı olarak da gıda sektöründe yer almakta ve katkı maddesi olarak da kullanılmaktadır. Fıstık endüstrisinde gıda üretiminin yan ürünü olarak elde edilen yerfıstığı kabuğu ise çoğunlukla hayvan yemi olarak kullanılmaktadır. Protein, yağ ve karbonhidratlar ile polifenoller açısından zengin olan fıstık kabuğunun güçlü bir antioksidan olduğu bilinmektedir. Bu yüzden gıdalarda veya diyet takviyelerinde rahatlıkla kullanılabileceği düşünülmektedir. Çalışmada, flavonoid ve fenolik asitler açısından zengin olduğu bilinen fıstık kabuğundaki doğal boyar maddenin varlığı araştırılmıştır. Bu amaçla HPLC ve UV-Görünür Spektrofotometrede yapılan analizler sonucunda fıstık kabuğunda kateşin ve antosiyanin (Cyanidin) olduğu belirlenmiştir. Çalışmada ayrıca ham ve kavrulmuş yer fıstığındaki boyar madde miktarları da karşılaştırılmış, ham yerfıstığından daha fazla boyar madde elde edilebileceği ortaya çıkarılmıştır.

To Cite: Özdemir H. Chemical Analysis of Natural Dyestuff Extracted from Peanut Skin. Osmaniye Korkut Ata Üniversitesi Fen Bilimleri Enstitüsü Dergisi 2022; 5(Özel sayı): 40-49.

Introduction

Peanut (*Arachis hypogaea* L.), which is among the oilseed plants, is defined as a functional food beneficial for human health because it contains one or more components and nutrients such as oil, protein, carbohydrates and various vitamins/minerals (Özalp and Kürklü, 2020).

Most of the peanut, which is the most important agricultural product of Osmaniye province and its surroundings in terms of its contribution to trade and industry, is consumed as a snack, as well as used in the food industry, especially as an additive in peanut oil, peanut butter, confectionery and confectionery. The plant contains 45-60% oil, 20-30% protein, 18% carbohydrates, vitamins and mineral substances in its seeds (Figure 1). Peanut skin is a conventional valuable plant that can be used in hardboard production, as a feed filler, in mushroom cultivation, as fuel, as a filler in wood production, in charcoal production, as roughage in cattle breeding, as litter and mulch in poultry farming, and to obtain adsorbent by carbonizing the bark (Afrin, 2015; Zeren, 2015).

It is stated that peanut, which is defined as a functional food because of its content of one or more bioactive compounds beneficial for human health, such as resveratrol and phytosterol, as well as antioxidant vitamins and minerals, plays a role in the prevention and treatment of chronic diseases such as obesity, diabetes and cardiovascular diseases. Peanut skin has also gained importance in recent years. It is thought that peanut skin can prevent some diseases in terms of health, due to its high catechin, procyanidin content and its anti-inflammatory effect (Özalp and Kürklü, 2020).

Peanut skin becomes waste in the production of both peanut oil and unshelled peanuts by breaking and separating the skin. After removing the peanut oil, the pulp contains the peanut skin that comprises natural dyestuffs, as well as protein and other substances. In addition, in the production of peanut kernels, a significant amount of peanut skin is obtained as waste during skin cracking and sorting.

Due to the increase in the use of chemically synthesized dyestuffs in the last century, natural dyeing has come to the point of disappearance. However, with the realization that some synthetic dyestuffs and pigments used in textile finishing companies threaten human health and cause environmental pollution due to their toxic and carcinogenic properties, the use of natural dyestuffs has come to the fore in recent years. The use of natural dyestuffs obtained from plants in nature has started to increase due to their biodegradability, non-toxicity and not causing any problems for human health and waste water contaminants. (Osman et al., 2011; Canpolat et al., 2013; Dayıoğlu et al., 2015)

Within the scope of the study, natural dyestuffs were tried to be obtained from peanut skin, since catechins and procyanidins in the peanut skin are in flavonoid structure as functional products. In addition, the effect of roasting applied to peanut on the extracted dyestuff was tried to be determined.

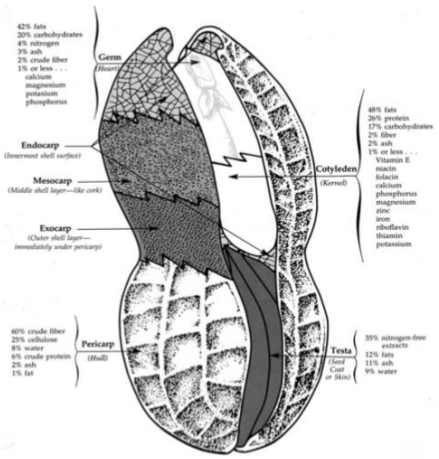

Figure 1. Chemical components of peanuts (Afrin, 2015)

Previous Studies

In review of Özalp and Kürklü (2020), they examined the nutrient content of peanuts and their relationship with diseases, stated that peanut skin has also gained popularity recently and contains high amounts of catechin and procyanidin.

In the article by Constanza et al. (2012), they manufactured spray-dried powders from peanut skin extracts. They determined that these powders contain procyanidin and have high antioxidant activity and create high added value. They also determined that the addition of maltodextrin during production caused the formation of polymeric compounds. Compared to the ground bark, these powders produced higher antioxidant capacity, phenolics and higher solubility. Finally, they proved that peanut skin can be used as a natural source of antioxidants.

In study by Lewis et al. (2013), they determined that peanut skin extracted with acetone or ethanol contained high levels of procyanidins and other phenolic compounds.

In the article by Yu et al. (2005), they investigated the effects of direct peeling, boiling and roasting peeling methods on the total phenolic and total antioxidant activities (TAA) of peanut skin extracts using different solvents. The composition of the extracts was determined by HPLC. As a result, substances such as phenolic acid, flavonoid and stilbene were detected in the peanut skin.

In the article by Yu et al. (2006), peanut skins were extracted according to direct peeling, boiling and roasting methods. Total phenolic (TP), total antioxidant activity (TAA) and free radical scavenging capacity of peanut skin extracts were determined. Peanut skin, a by-product, has been found to be an inexpensive source of antioxidants. It has been said that this product can be used in food or supplements.

In their article by Lee et al. (2009), they were examined the anthocyanins such as “pelargonidin, peonidin and cyanidin” were determined when the HPLC chromatograms of soybeans extract, which come from the same legume family as peanuts.

Wang et al. (2016) used anthocyanin extracts obtained from mulberry fruits to examine the dyeability of cotton fabrics. For anthocyanins, UV-vis spectra and HPLC retention times were examined to determine the chemical structure and it was found to be a cyanidin-derived anthocyanin.

Qin et al. (2010) investigated anthocyanins thought to be found in mulberry pigment. Firstly, fresh mulberry fruits were extracted and LC-MS, HNMR, HPLC-PAD and UV-Visible Spectroscopy instruments were used for the analysis of natural dye pigments. According to the results of the chemical analysis, it was determined that the anthocyanins in the mulberry pigment were cyanide.

Giusti and Wallace (2009) stated in their book chapter "Flavonoids as Natural Pigments" that there is a large consumer demand for natural red colors in the textile finishing industry and that flavonoids can be an alternative to synthetic dyes. Anthocyanins are also found in many fruits (such as strawberries) and vegetables, and they have explained that they give different colors from orange to red and violet.

Materials and Method

Supply of peanut skins and preparation

Virginia type peanuts were supplied through a company in Osmaniye, which produces both snacks and peanut butter. After the peanuts are collected from the field, kept in the sun and ventilated, they are subjected to pre-control and cleaning in the Sorting Machine. At this stage, unheated raw peanut skin (not roasted), which is separated from the machine as waste, can be supplied. During the roasting process at ~140^{o}C for the production of snacks, roasted peanut skin can be obtained from the machine as waste. Roasted and unroasted (raw) peanut skins supplied for use in the experiments were kept in the sun to remove the existing moisture and foreign materials were removed by sifting through a coarse sieve. Afterwards, the skins were passed through a laboratory grinder and sieved again in order to be used in tests such as HPLC and UV-Spectrophotometer and extraction processes.

Extraction

For unroasted and roasted peanut skins, 200 mg of powdered skins were mixed using 100 ml of Methanol in a magnetic stirrer at 1000 rpm for 5 hours on average at 30 ^{o}C and the extract was obtained by filtering on filter papers. Then, the solvent was removed using the evaporator, and it was tried to obtain dry natural dyestuff by using a vacuum pump and a vacuum oven.

Ultraviolet-visible field spectroscopy

Unknown substances can be identified and concentrations of known substances determined using UV-VIS spectroscopy. In order to determine the visible absorption spectra of the peanut skins, spectroscopic analysis with UV/Visible Spectrophotometer was performed in the "Thermo Scientific Evolution 220 UV-Visible Spectrophotometer" test device.

Identification of components by high-performance liquid chromatography (HPLC), Sample preparation

The dyestuff content of organic dyes and pigments can be determined by analyzing them by HPLC (high performance liquid chromatography).

The steps for sample preparation are summarized below;

- ✓ Sample 1, sample weight for peanut seed skin: 14.30 mg, injection volume 100 µL,
- ✓ Sample number 2, sample weight for heat-treated peanut seed skin: 14.40 mg, injection volume is 100 µL.
- ✓ The samples were hydrolyzed 37% (1: 1: 2, v / v / v) in 600 µL of H_2O/MeOH/HCl held at 100 °C for 8 minutes to remove the organic dyestuff. The samples were then evaporated under a gentle stream of nitrogen (65°C). The dry residue was dissolved in 500 µL MeOH / H_2O (2:1, v/v) and the samples were centrifuged. Samples were prepared for HPLC analysis by injecting 100 µL of each sample by further dilution if necessary and then centrifuging at 4000 rpm/25^{o}C/10 minutes (DATU, 2020).

HPLC-DAD Analysis

The technical specifications of the device used for the analysis and the analysis are summarized below;

- ✓ Chromatographic measurements in High Pressure Liquid Chromatography were performed using the Agilent 1200 series system (Agilent Technologies, Hewlett-Packard, Germany) including the G1311A Quat pump, G1322A Degasser, G1329A autosampler, G13166 TCC and G1315D Diode Array Detector.
- ✓ DAD detection was accomplished by scanning from 191 to 799 nm with a resolution of 2 nm.
- ✓ Chromatographic peaks were ascertained at eight different points between 255 and 620 nm.
- ✓ One Nova Pak C18 analytical column (39 × 150 mm, 4 µm, Part No WAT 086344, Waters) was used.
- ✓ Analytical and protective columns were kept at 30 °C and "Agilent Chemstation" data station was used.
- ✓ Two solvents "Solvent A: H_20 - 0.1% TFA and solvent B: CH3CN - 0.1% TFA" were used for the chromatographic separation of the hydrolyzed samples (DATU, 2020).

Results and Discussion

As a result of the extraction process; 0.2750 g dyestuff was obtained from the unroasted (raw) powder skin and 0.1291 g dyestuff was obtained from the roasted powder skin (Figure 2).

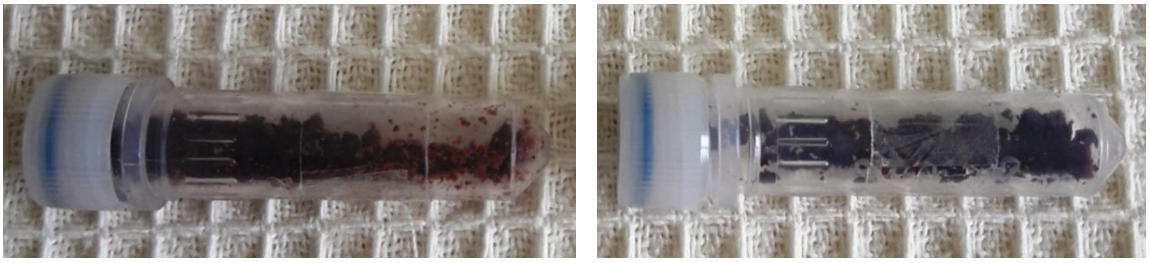

Natural Dyestuff 1 Natural Dyestuff 2

Figure 2. Unroasted peanut skin (Natural Dye 1), roasted peanut skin (Natural Dye 2)

As a result of the extractions, it was revealed that more amount natural dyestuffs were obtained from unroasted peanut skin.

As a consequence of the spectroscopic analysis with a UV/Visible Spectrophotometer, the absorption spectrum of the raw peanut skin was found to be 3.54 at 380 nm, 1.25 at 520 nm and 1.10 at 560 nm, as seen in Figure 3. The spectrum results detected at 520 nm wavelength were similar to the HPLC results.

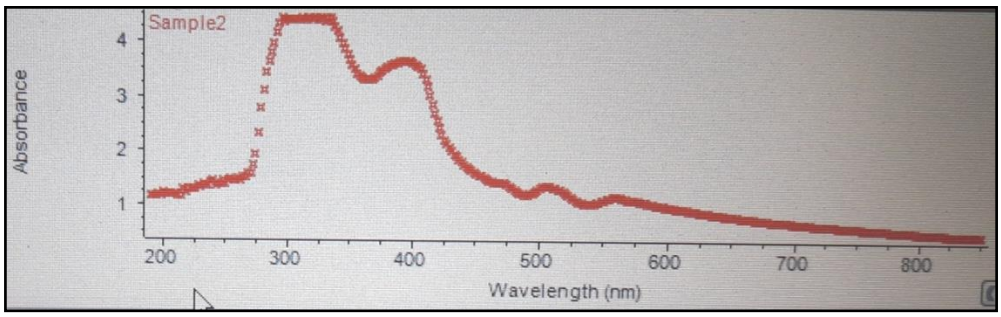

Figure 3. The absorption UV–Vis spectra of peanut skin

The chromatograms and spectra determined as a result of the High Pressure Liquid Chromatography (HPLC-DAD) method are shown in Figure 4-7. It was determined that the dyestuffs were the same in both samples, which were prepared and analyzed under the same experimental conditions (amount, volume and injection volume). However, it was determined that the dyestuffs detected in the raw peanut skin sample had higher peak values (mAU) than the dyestuffs detected in the heat treated (roasted) sample (Figure 7). Qualitative dyestuff analysis results by HPLC are summarized with graphics below;

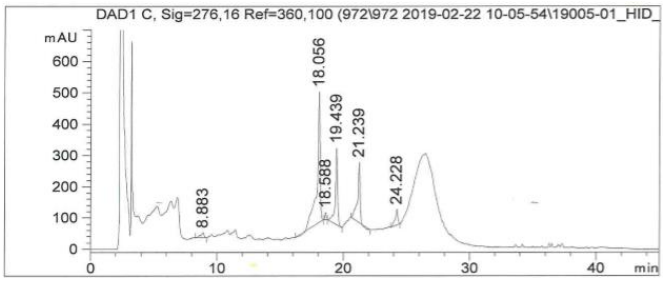

Figure 4. Raw peanut skin chromatogram

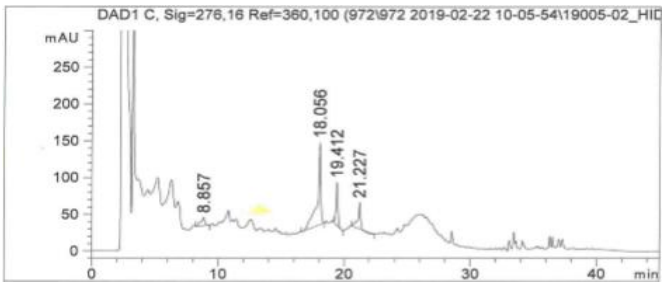

Figure 5. Heat-treated (roasted) peanut skin chromatogram

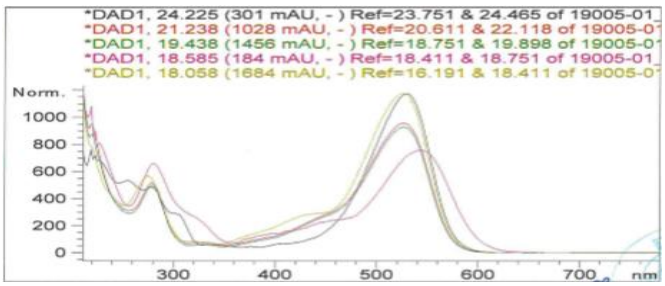

Figure 6. Overlapping of dyestuffs in raw peanut skin

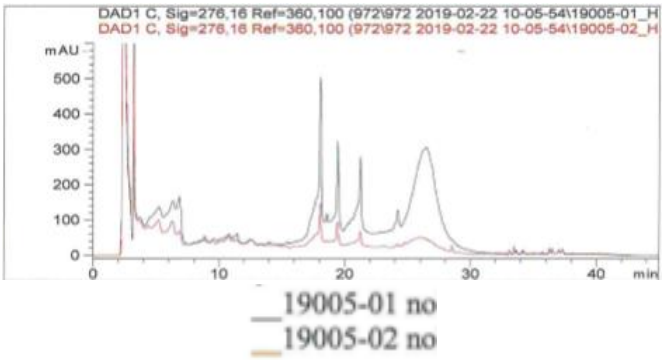

Figure 7. Comparison of chromatograms of raw (01) and heat-treated (roasted) (02) peanut skins

Phenolic acid and anthocyanin groups were determined in both samples subject to analysis. The maximum absorbance (λmax) values of the dyestuffs are shown in Table 1.

Table 1. The maximum absorbance (λmax) values of the dyestuffs

No	Detention Time (minutes)	Maximum absorbance value (nm)	Chemical Group	Dyestuff	References
1	8,883	231, 280, 309	Phenolic acid	Catechin	Constanza et al., (2012)
2	18,056	275, 320sh, 525	Anthocyanin	Cyanidin	Lewis et al., (2013)
3	18,588	281, 543	Anthocyanin	Cyanidin	Yu et al., (2005)
4	19,439	279, 329sh, 527	Anthocyanin	Cyanidin	Lee et al., (2009)
5	21,239	279, 329sh, 526	Anthocyanin	Cyanidin	Wang et al., (2014)
6	24,228	255, 279, 301sh, 529	Anthocyanin	Cyanidin	Qin et al., (2010)
					Giusti and Wallace, (2009)

According to the reference sources (Yu et al., 2005; Giusti and Wallace, 2009; Lee et al., 2009; Qin et al., 2010; Constanza et al., 2012; Lewis et al., 2013; Wang et al., 2014) for the determination of the

dyestuff in Table 1, when the chromatogram absorbance values, retention times, UV-spectra and λmax values were evaluated, results supporting this study were obtained. Especially in studies where HPLC analyzes are carried out to identify the compounds in the peanut skin; It can be said that the detection of phenolic acid and flavonoid determined by Yu et al. (2005), high levels of procyanidin in the studies of Constanza et al. (2012) and of Lewis et al. (2013) are consistent with the results of our study. As a result, it was determined that the natural dyestuff in the peanut skin is Anthocyanin/Cyanidin belonging to the Flavonoid pigment group (Figure 8).

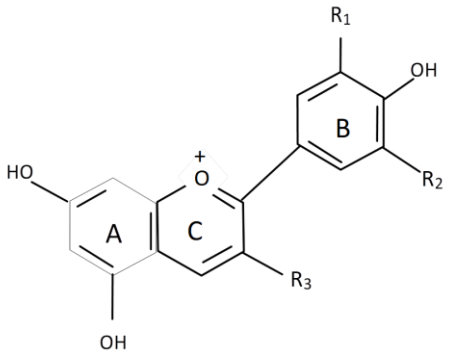

Name	R1	R2	λmax[a](nm)	Color
Pelargonidin	H	H	520	Orange
Cyanidin	OH	H	535	Red
Delphinidin	OH	OH	545	Purple
Peonidin	OCH_3	H	532	Red
Petunidin	OCH_3	OH	543	Purple
Malvidin	OCH_3	OCH_3	542	Purple

a:Absorbance maxima in the visible spectrum in methanol with 0.01 % HCl

Figure 8. Molecular structure of anthocyanins (Giusti and Wallace, 2009)

Conclusion

In our study on the determination of the natural dyestuff in the peanut skin, it has been determined that the natural dyestuff obtained in unroasted (raw) and roasted peanuts is the same with chromatograms and spectra obtained by HPLC-DAD method. As a result of the extraction processes it was revealed that more natural dyestuffs were obtained from unroasted peanut skin. A literature search was made and compared according to the determination of dyestuffs according to the retention time (minutes) and maximum absorbance (nm) values in the chromatograms. The results obtained indicated that the dyestuff in the peanut skin was mainly "Cyanidin" belonging to the "Anthocyanin" group, which is the most important group of "Flavonoid" pigments. It was observed that the spectral results of the raw peanut skin at a wavelength of 520 nm were similar to the HPLC results.

As a result, roasting at high temperatures is the most important process of peanut enterprises in terms of energy cost, taste, consumption and customer satisfaction. However, due to the high temperature processing of peanuts, the anthocyanin compounds in the peanut skin can be damaged and this may adversely affect the quality and efficiency of the natural dyestuff. When anthocyanins are subjected to heat treatment, they undergo hydrolysis of the glycosidic bond which leads to loss of color. In addition, the beneficial effects of peanuts in terms of health may decrease with the damage of beneficial substances such as tannin in the peanut skin with high temperature (Giusti and Wallace, 2009).

Thanks

The project numbered “OKÜBAP-2018-PT2-004” named “Extraction of Natural Dyes from Peanut Skin and Determination of Dyeing Properties” was supported by Osmaniye Korkut Ata University Scientific Research Projects Unit (BAP). I would like to thank the Cultural Heritage Preservation and Natural Dyes Laboratory (DATU), Osmaniye Korkut Ata University Central Research Laboratory and Öz Yeksek Peanut (Osmaniye) for their unwavering support for the study.

Conflict of Interest Statement

The author declares that there is no conflict of interest.

Contribution Rate Statement Summary of Researcher

The author declares that he has contributed 100% to the article.

*This study was presented as a summary paper at the International Conference on Engineering, Natural and Applied Sciences (ICENAS'21) held online on 24-26 November 2021.

References

Canbolat Ş., Acar K., Merdan N. *Sambucus ebulus* L. (şahmelik) bitkisinden ekstrakte edilmiş doğal boyarmadde ile ipekli materyallerin boyanması. İstanbul Ticaret Üniversitesi Fen Bilimleri Dergisi 2013; 12(23): 103-114.

Constanza KE., White BL., Davis JP., Sanders TH., Dean LL. Value-added processing of peanut skins: antioxidant capacity, total phenolics, and procyanidin content of spray-dried extracts. J. Agric. Food Chem. 2012; 60: 10776-10783.

DATU (Kültürel Mirası Koruma ve Doğal Boya Laboratuvarı). 2020. Analizler/Boyarmadde Analizi. https://www.datulab.com/tr/servislerimiz/analizler. Erişim Tarihi: 15.10.2021.

Dayıoğlu H., Kut D., Merdan N., Canpolat Ş. Effect of dyeing properties of fixing agent and plasma treatment on silk fabric dyed with natural dye extract obtained from *Sambucus ebulus* L. plant. Procedia - Social and Behavioral Sciences, World Conference on Technology, Innovation and Entrepreneurship 2015; 195: 1609-1617.

Giusti MM., Wallace TC. Flavonoids as natural pigments. Thomas B./Rita M. (Ed.), Hanbook of natural colorants. Wiley Series in Renewable Resources 2009; 257-272.

Lee JH., Kang NS., Shin SO., Shin SH., Lim SG., Suh DY., Baek IY., Park KY., Ha TJ. Characterization of anthocyanins in the black soybean (*Glycine max* L.) by HPLC-DAD-ESI/MS analysis. Food Chemistry 2009; 112: 226-231.

Lewis WE., Harris GK., Sanders TH., White BL., Dean LL. Antioxidant and anti-inflammatory effects of peanut skin extracts. Food and Nutrition Sciences 2013; 4: 22-32.

Nazia A. Phytochemical and biological investigation of *Arachis hypogaea*. A thesis report, Department of Pharmacy, East West University, pp: 108, Bangladesh, 2015.

Osman E., El-Zaher NA. Effect of mordant type on thermal stability and fastness properties of silk fabric dyed with natural dye "*Sambucus nigra*". Research Journal of Textile and Apparel 2011; 15(2): 61-70.

Özalp BB., Kürklü NS. Fonksiyonel bir gıda: Yer fıstığı ve sağlığa yararları. Akademik Gıda 2020; 18(3): 323-330.

QIN C., Li Y., Niu W., Ding Y., Zhang R., Shang X. Analysis and characterization of anthocyanins in mulberry fruit. Czech J. Food Sci. 2010; 28(2): 117-126.

Wang H., Tang Z., Zhou W. A method for dyeing cotton fabric with anthocyanin dyes extracted from mulberry (*Morus rubra*) fruits. Coloration Technology 2014; 132: 222-231.

Yu J., Ahmedna M., Göktepe I. Effects of processing methods and extraction solvents on concentration and antioxidant activity of peanut skin phenolics. Food Chemistry 2005; 90: 199-206.

Yu J., Ahmedna M., Göktepe I., Dai J. Peanut skin procyanidins: compositions and antioxidant activities as affected by processing. Journal of Food Composition and Analysis 2006; 19: 364-371.

Zeren ZC. Yerfıstığı tohumlarından enzimatik sulu ekstraksiyon ile yağ eldesi ve optimizasyonu. İstanbul Teknik Üniversitesi Fen Bilimleri Enstitüsü Kimya Mühendisliği Anabilim Dalı Yüksek Lisans Tezi, Sayfa No:57, İstanbul, Türkiye, 2015.

OKÜ Fen Bilimleri Enstitüsü Dergisi
5(Özel sayı):50-65, 2022

OKU Journal of The Institute of Science and Technology, 5(Special issue):50-65, 2022

Osmaniye Korkut Ata Üniversitesi Fen Bilimleri Enstitüsü Dergisi

Osmaniye Korkut Ata University Journal of The Institute of Science and Technology

Design and Implementation of Computer Vision Based Autonomous Vehicle Prototype

Emre DANDIL[1*], Bilal ARAL[2]

[1,2]Department of Computer Engineering, Faculty of Engineering, Bilecik Seyh Edebali University, Bilecik, Turkey

[1] https://orcid.org/0000-0001-6559-1399
[2] https://orcid.org/0000-0002-8756-5850
*Corresponding author: emre.dandil@bilecik.edu.tr

Research Article

Article History:
Received: 12.12.2021
Accepted:14.01.2022
Published online: 23.02.2022

Keywords:
Autonomous vehicles
Computer vision
Raspberry Pi
Cascade classifier
Traffic sign recognition
Lane tracking

ABSTRACT

In recent years, since automotive makers, IT providers, commercial electronic chip manufacturers have entered a rapid investment race for autonomous vehicles (AVs), they have started to be used in many infrastructures. AVs are automobiles that can drive themselves using the automatic control systems while cruising by sensing the road, traffic flow and surroundings without the need for a driver. AVs can detect objects around them using technologies such as radar, lidar, GPS, audiometry and computer vision. In this study, the design and implementation of a computer vision-based autonomous vehicle prototype is proposed. The developed prototype can perform lane tracking and traffic sign control by processing images obtained from the camera, and can detect objects around it with the distance sensor. In the AV prototype, the Raspberry Pi 3B+ module is used to process the images and control the motors, and the cascade classifier is used to recognize the traffic signs. In the performed tests, traffic signs are recognized in 7 different scenarios and the performances are compared. According to the results, the accuracy rate is 94,8% in the tests performed with only one traffic sign. As a result, the autonomous vehicle prototype developed in this study can successfully recognize traffic signs and move on the determined route in different scenarios.

Bilgisayarla Görme Destekli Otonom Araç Prototipinin Tasarımı ve Uygulaması

Araştırma Makalesi

Makale Tarihçesi:
Geliş tarihi: 12.12.2021
Kabul tarihi: 14.01.2022
Online Yayınlanma: 23.02.2022

Anahtar Kelimeler:
Otonom araçlar
Bilgisayarla görme
Raspberry Pi
Kaskad sınıflandırıcı
Trafik işareti tanıma
Şerit takibi

ÖZET

Son yıllarda, otomotiv üreticileri, bilgi teknolojileri sağlayıcıları, ticari elektronik çip üreticileri otonom araçlar (OA) için bir yatırım yarışına girdiklerinden, OA birçok altyapıda kullanılmaya başlamıştır. OA seyir halindeyken, otomatik kontrol sistemlerini kullanarak sürücüye ihtiyaç duymadan yolu, trafik akışını ve çevreyi algılayarak kendi kendine gidebilen otomobillerdir. OA, radar, lidar, GPS, odyometri ve bilgisayarla görme gibi teknolojileri kullanarak etrafındaki nesneleri algılayabilir. Bu çalışmada, bilgisayarla görme tabanlı bir otonom araç prototipinin tasarımı ve uygulaması önerilmektedir. Geliştirilen prototip, kameradan elde edilen görüntüleri işleyerek şerit takibi ve trafik işareti kontrolü gerçekleştirebilmektedir ve mesafe sensörü ile etrafındaki nesneleri algılayabilmektedir. Geliştirilen OA prototipinde görüntüleri işlemek ve motorları kontrol etmek için Raspberry Pi 3B+ modülü ve trafik işaretlerini tanımak için kaskad sınıflandırıcı kullanılmıştır. Yapılan testlerde trafik işaretleri 7 farklı senaryoda tanınmış ve performansları karşılaştırılmıştır. Sonuçlara göre tek trafik işareti ile yapılan testlerde doğruluk oranı %94,8'dir. Sonuç olarak, bu çalışmada geliştirilen otonom araç prototipi, trafik işaretlerini başarıyla tanıyabilmektedir ve farklı senaryolarda belirlenen rotada hareket edebilmektedir.

To Cite: Dandıl E., Aral B. Design and Implementation of Computer Vision Based Autonomous Vehicle Prototype. Osmaniye Korkut Ata Üniversitesi Fen Bilimleri Enstitüsü Dergisi 2022; 5(Özel sayı): 50-65.

Introduction

Autonomous vehicle (AV) technology has made rapid progress, especially in recent years, thanks to its advanced hardware and software systems. AVs are capable of fully automatic driving without any human intervention. In these technologies, solutions are sought for problems such as reducing the number of traffic accidents, increasing the mobility of the elderly and disabled, reducing gas emissions into the atmosphere and using infrastructures more effectively (Fagnant and Kockelman, 2015; Van Brummelen et al., 2018). It can be said that one of the important reasons in the development of AV technology is the very high rate of driver-related traffic accidents due to reasons such as fatigue, distraction, and excited driving (Van Brummelen et al., 2018). In addition, it provides a number of benefits such as safety, time efficiency, reducing traffic congestion, efficient use of resources, environmental impacts and increased mobility (Haboucha et al., 2017).

In addition to saving time for drivers to monitor the road continuously, AVs can also provide more effective use of time in activities such as sleeping, eating, relaxing or working while driving. More efficient parking is also possible with these vehicles at the same time. In addition, since a regular traffic flow will be optimized with AVs, it is predicted that with the reduction of traffic congestion, the amount of CO_2 released and fuel consumption will also decrease (Haboucha et al., 2017). Thanks to AVs, it is expected that the total vehicle fleets will decrease significantly, as a result of paving the way for children, the elderly and the disabled to travel by vehicle (Burns, 2013; Anderson et al., 2014; Meyer et al., 2017). Thus, it is clear that AVs will not only transform transportation, but also cause major changes in cities. Today, many vehicle companies are now investing in AVs. It is predicted that AVs will also significantly change the transportation market worldwide (Wiseman, 2021).

In terms of driver assistance systems, AVs are equipped with six different levels as Level 0, Level 1, Level 2, Level 3, Level 4 and Level 5 depending on whether there is any automatic system or fully autonomous driving systems (Gouda et al., 2021; NHTSA, 2021). While there is no autonomous system at Level 0, Level 5 represents vehicles with driverless fully automatic equipment. In recent years, companies such as Google, Tesla, Nissan and Volvo have been producing assistive driver technologies and additional equipment, as well as producing autonomous vehicles. In addition to the rapid growth of AV technologies from 2020, it is estimated that between 2022 and 2025, AVs will be seen in the markets (Fagnant and Kockelman, 2015).

Evaluating the status of AVs today, it was a major milestone for AVs when DARPA (Defense Advanced Research Projects Agency) launched a Grand Challenge in 2004. The goal was for AVs to be able to travel a route of 150 miles. After success for this challenge, the same team performed improvements so that AVs can deal with traffic issues. Especially since 2014, after Google's self-driving cars have come a long way successfully (Anthony, 2014), many vehicle manufacturers have started to work on self-driving vehicles (Fagnant and Kockelman, 2015). In addition, in recent years, the use of AVs has started to become widespread in many different fields such as defense, mining and agriculture.

Since AVs have become more prominent especially in recent years, the rate of research has increased rapidly after 2013. Studies on this subject have generally focused on security, cost, and feasibility for AVs. In a proposed comprehensive study on AVs, (Fagnant and Kockelman, 2015) suggested the use of these tools, opportunities, potential problems, and policies needed (Harper et al., 2016) estimated the increase in travel with AVs for people with disabilities who are unable to travel due to medical conditions (Haboucha et al., 2017) on the other hand, investigated the factors that determine the decisions of users in choosing AVs in their studies. In a study conducted on the cost of AVs (Wadud, 2017), the cost analysis of owning these fully automatic vehicles was evaluated. In another study, (Van Brummelen et al., 2018) they examined current technologies used for AVs. Apart from these, there are also many studies proposed for the AV prototype in the literature (Hossai et al., 2017) proposed an IoT-based AV prototype using computer vision. In another study, (Deac et al., 2018) developed a Raspberry Pi powered miniature AV. For the use of deep learning methods in AVs, (Bechtel et al., 2018) developed a low-cost, deep neural network-based autonomous car (Rossi et al., 2020), on the other hand, developed an AV prototype for real-time detection of road lines. In another study, (El-Tawab et al., 2020) developed an IoT-supported AV prototype, allowing it to move in a certain route.

In this study, a computer vision based AV prototype is developed that can detect lane tracking and traffic sign control, and detect objects around it with a distance sensor, using images obtained from the camera. In this prototype structure, Raspberry Pi 3B+ hardware module is used to process images and control the motors. In the study, cascade classifier is used to detect traffic signs. In the second section of the study, information about the used materials and the proposed methods are presented. In the third section, the experimental results and application practices of the designed AV are explained. In the last section, the findings and the obtained results are evaluated.

Material and Methods

In this study, a computer vision based AV prototype shown in Figure 1 was developed. With the developed AV prototype, traffic signs can be recognized and objects around the vehicle can be detected. There are two infrastructures in the system, namely hardware and software. Images and videos obtained from the camera hardware in AV are processed on the Raspberry Pi module with the developed software infrastructure, enabling the vehicle to tracking the lane accurately on the road and to recognize the traffic signs.

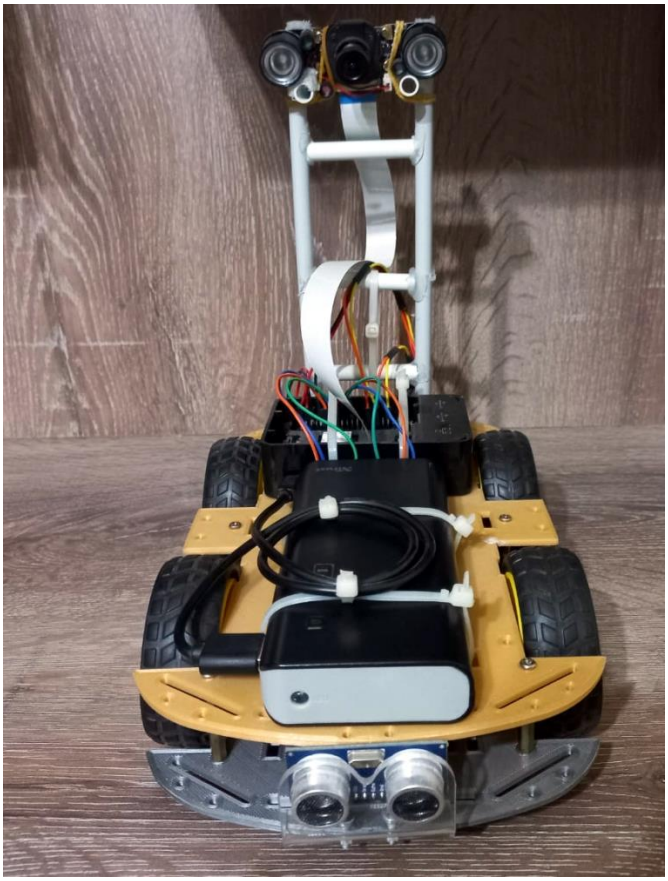

Figure 1. The AV prototype designed in this study

Hardware infrastructure

The representative circuit diagram showing the hardware infrastructure of the AV prototype developed in this study is presented in Figure 2. In the design of the developed prototype, the Raspberry Pi 3B+ model was used as the decision unit to process the images and control the vehicle. LN298N module is used as motor driver circuit. Two HC-SR04 ultrasonic distance sensors were used to detect objects, one to the front and the back of the developed AV prototype. A night vision supported camera module developed for the Raspberry Pi card was used to capture images from the vehicle. After connecting the Raspberry Pi 3B+ on the car kit, DC motors were connected with the LN298N motor driver circuit. 12V DC adapter was used for testing the motors and driver circuit. After the directions of the motors were tested, the power supply connections were made. A 10000 mAh portable charger was used to power the Raspberry Pi board and was connected to the 2.1 A output of the charger. Two 18650 mAh Li-ion batteries were used for the motor driver. For ease of use, two charging modules and a power switch were added to the battery spacer.

Software infrastructure

Using the software infrastructure of the developed AV prototype, the images coming from the camera hardware were processed, so that the recognition of traffic signs and lane tracking of the vehicle were realized successfully. While the Haar Cascade Classifier was used to recognize traffic signs on an

image dataset prepared in the study, the Hough Transform method was used to find the road lines to track the lanes while the vehicle was moving on the road.

Haar Cascade Classifier

Object detection method using Haar feature-based cascade classifiers was proposed by (Viola and Jones, 2001). Viola-Jones algorithm works fast and can reach high accuracy by using rectangular features to identify the object in the image (Dandıl and Özkul, 2019). A dataset is needed to train the Viola-Jones algorithm. The training set has to contain both positive images with the desired object and negative images without it. In order to detect the object in the positive image, as seen in Figure 3, sub-windows of 24*24 pixels are slid across the entire image and an object search is performed. Thus, during the training of the cascade classifier, feature extraction from images is performed using Haar Cascade.

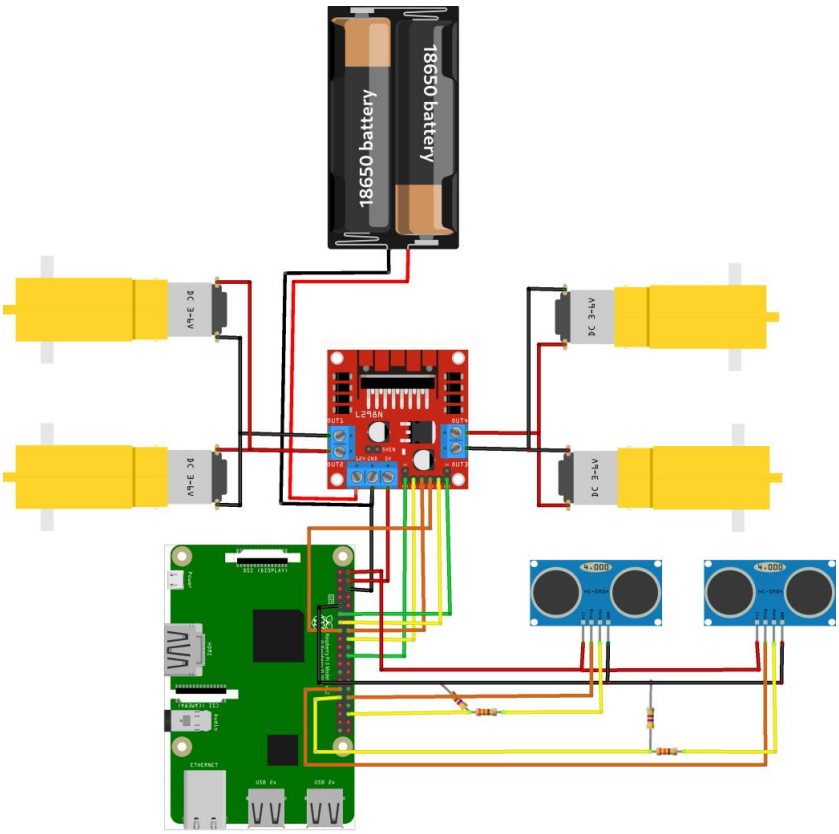

Figure 2. Hardware infrastructure of the developed AV prototype

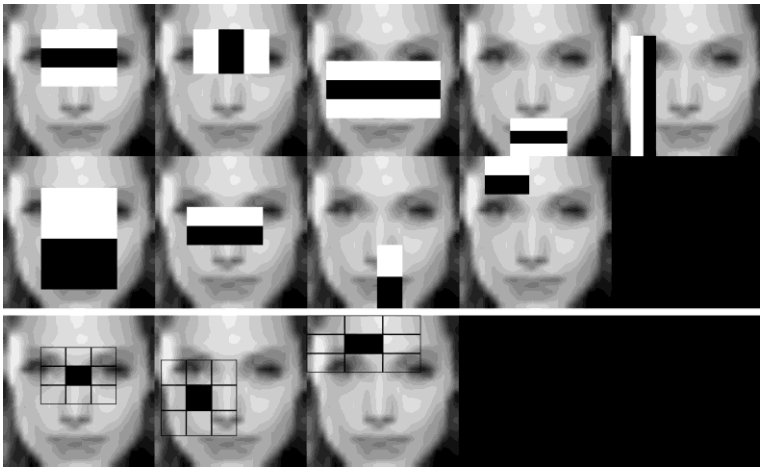

Figure 3. Extracting features from image using Haar Cascade during cascade classifier training (OpenCV, 2021b)

Image Dataset of Traffic Signs

An image dataset was created for the recognition of traffic signs by using the Haar Cascade Classifier on the AV prototype developed in our study. In order for the prototype designed in the study to be recognized correctly, seven different traffic sign models such as right turn, left turn, stop, road work, 30 km/h maximum speed limitation, 50 km/h maximum speed limitation and 80 km/h maximum speed limitation were created for the recognition of traffic signs. The models created for the traffic sign were prepared by sticking the printouts of the traffic signs taken from the Traffic Signs Handbook (KGM, 2015) of General Directorate of Highways (KGM) onto a cardboard material. In addition, the models are mounted on 12 cm long plastic pipes with a plastic cap at the bottom. Figure 4 shows some traffic sign models prepared within the scope of the study.

Figure 4. Some traffic sign models prepared within the scope of the study

The traffic sign dataset was prepared using the images obtained from the above models. For each traffic sign, a dataset consisting of 7000 images in total, consisting of 500 positive images with traffic

signs from different angles and 500 negative images without traffic signs was created. On the obtained images, the parts containing traffic signs were cropped and then sized as 64*64 pixels. Some of the positive images prepared for the stop sign are given in Figure 5.

Figure 5. Stop sign images captured at different angles from the image dataset

Hough Transform

Hough transform is an algorithm developed by (Hough, 1962) and proposed to recognize complex lines in images. Over time, many improvements and new methods for Hough transform have been developed (Mukhopadhyay and Chaudhuri, 2015). In this study, Hough transform was applied to determine the lines of interest in the path route of the AV.

Design and Implementation of AV Prototype

In this study, Haar Cascade Classifier was used to recognize traffic signs. All image processing applications applied to perform lane tracking operations were carried out with programming language (Python, 2021) using (OpenCV, 2021a) and (NumPy, 2021) libraries. The OpenCV library was used for the recognition of traffic signs and lane tracking application used in the AV prototype designed in this study. In the study, the training of the Haar classifier was carried out using Cascade Trainer GUI (Ahmadi, 2021) software on the prepared dataset. In addition, Gentle AdaBoost (GAB) was used to reduce the time loss of scanning in the image.

A path was prepared for the AV prototype developed in the study, as seen in Figure 6. Images of the dataset used for the recognition of traffic signs with the AV prototype were collected on this path. Images were transferred to the Raspberry Pi based module with the camera on the vehicle. As a result of the experimental studies, it was determined that the height of the camera from the ground has to be 24 cm and the angle of the camera with respect to the X axis has to be 18 degrees in order to obtain the images from the camera in the most appropriate way.

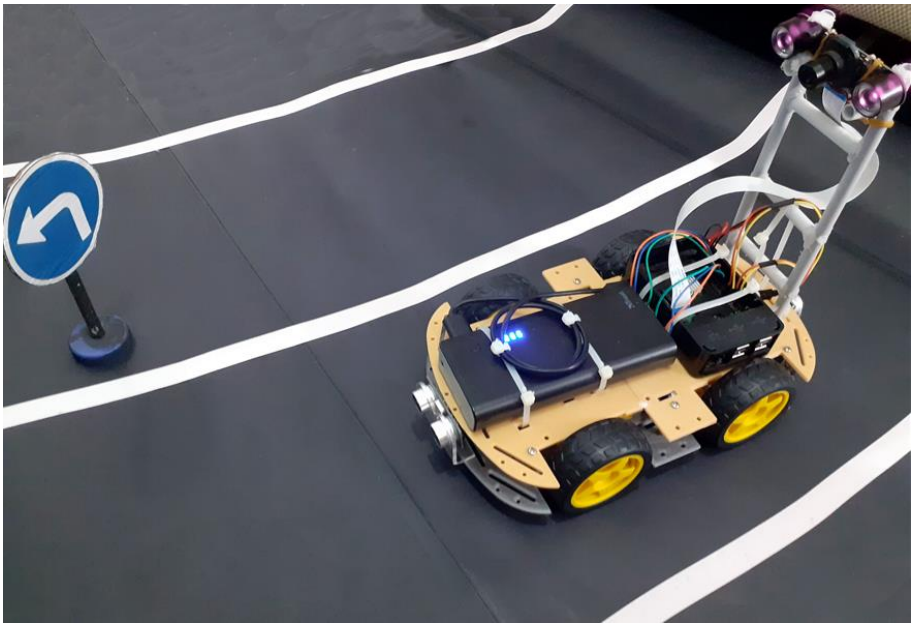

Figure 6. The path designed for the AV prototype developed in this study

In Figure 7, there is a flowchart showing the operation of the designed and implemented AV prototype. As can be seen from this flowchart, motor and sensor connections are adjusted when the system is started. After the system starts to work, a query is made whether there is a traffic sign in the image obtained from the camera. If the traffic sign is not detected on the image and the data coming from the sensors is not less than the determined distance, the following angle is calculated by applying lane tracking operations on the image. The movement of the vehicle is provided according to the scenarios determined by the angle information obtained from here.

Two different computer vision processes are operated in the developed AV prototype. The first of these is to track the lane on the AV route and the other is to recognize the traffic signs with the Haar Cascade Classifier. For lane tracking, finding the edge, extracting the region of interest, determining the straight lines, determining the lane vectors and creating the following vector were applied sequentially. At this stage, firstly, the image obtained from the camera was converted to a gray scale image. Then, according to the light of the environment in which the system was operated, a certain value thresholding process was applied to the related image. The edge detection process was completed with the Canny edge detection algorithm on the black and white image resulting from the thresholding. The edges detected by Canny in some road images obtained from the AV camera are shown in Figure 8.

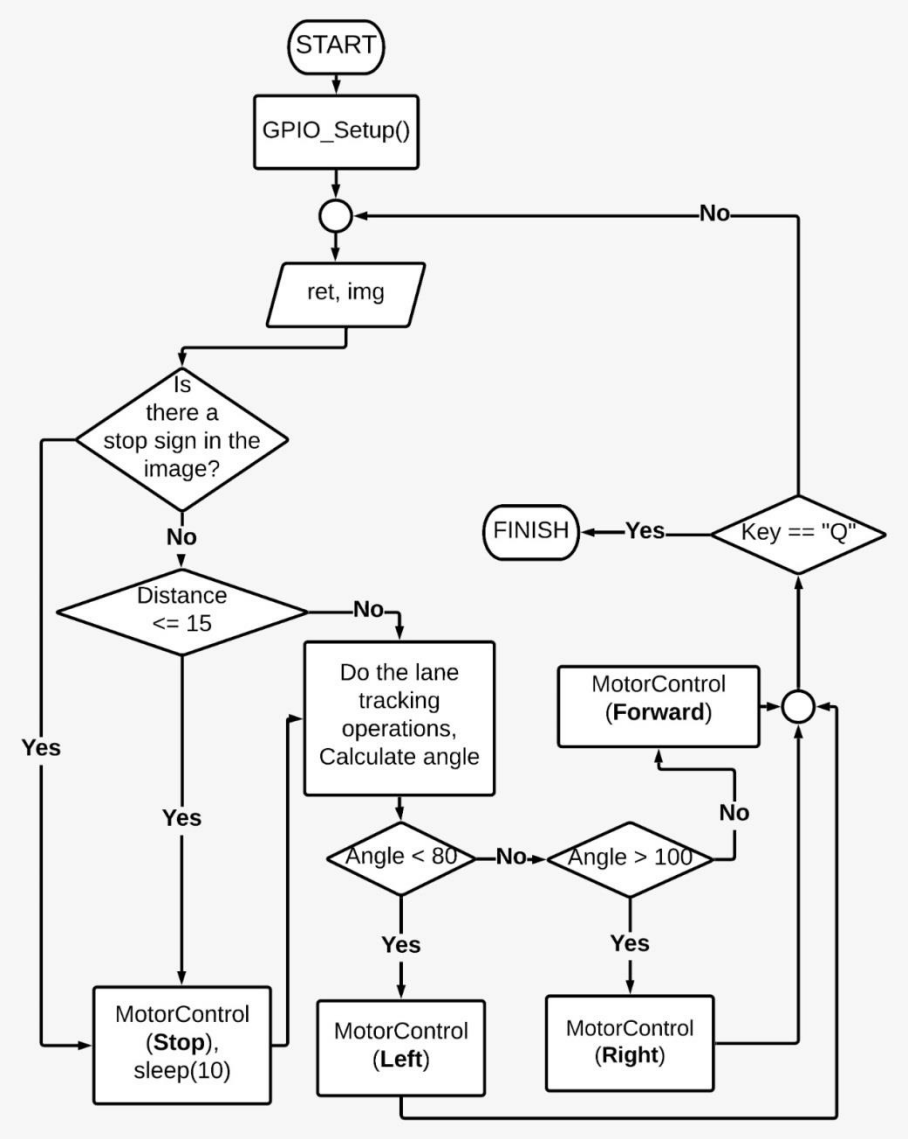

Figure 7. Flowchart diagram of the designed AV prototype

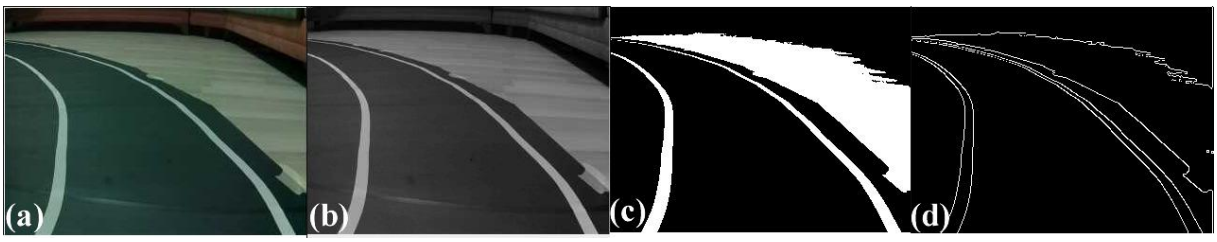

Figure 8. Detecting edges with Canny in some road images obtained from AV camera. (a) RGB image, (b) gray-level image, (c) thresholding and (d) edge detection

It is sufficient to track the lane in a limited area (region of interest), since using the entire image obtained after edge detection operations in lane tracking can tire the system and the lane lines can appear very close to each other due to perspective after a certain distance. In order to determine the region of interest on the image, the appropriate region was extracted by performing a bitwise-and operation with a mask. Removing the region of interest on the in-lane tracking image is shown in Figure 9. After the region of interest was determined, the Hough transform was used to determine the

lines in the region of interest. The determination of the lines in the region of interest with the Hough transform is shown in Figure 10.

Figure 9. Determination of the region of interest on the image for lane tracking

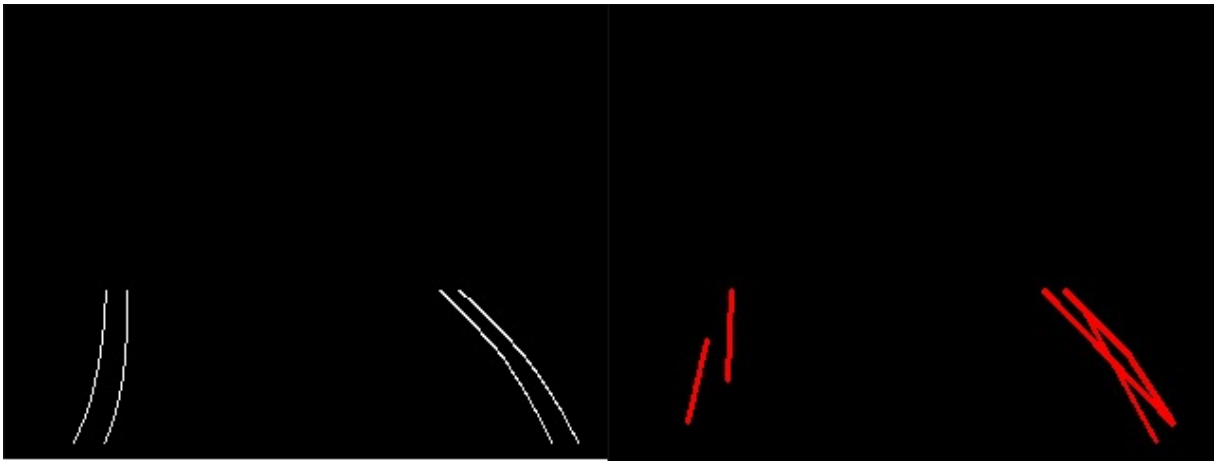

Figure 10. Determination of lines in the region of interest with Hough transform

Figure 11. Determination of lane vectors

The slopes of the lines obtained as a result of the Hough Transform were calculated and divided into two separate parts as right and left. By calculating the mean vectors of the two separated line segments, the vectors of the right and left lanes were calculated. Calculated lane vectors are indicated as seen in image Figure 11. By using the obtained lane vectors, the average of the distances of the two vectors to each other was obtained, as in Figure 12, to obtain the tracking vector. After calculating the

slope of the obtained tracking vector, the angle it made with the X axis was calculated. The resulting angle value was used to control the direction of the vehicle. Thus, it was ensured that the AV moves to the right in the range of 0-80 degrees, to the left in the range of 100-180 degrees, and straight in the range of 80-100 degrees.

Figure 12. Determination of the tracking vector

For real-time lane tracking in the developed AV prototype, the steps applied for lane tracking on Raspberry Pi from the images obtained from the camera are shown in Figure 13. In the Raspberry Pi environment shown in the figure, scripts developed in Python programming language for lane tracking were applied for finding the edge, extracting the region of interest, determining the straight lines, determining the lane vectors and creating the following vector operations, respectively.

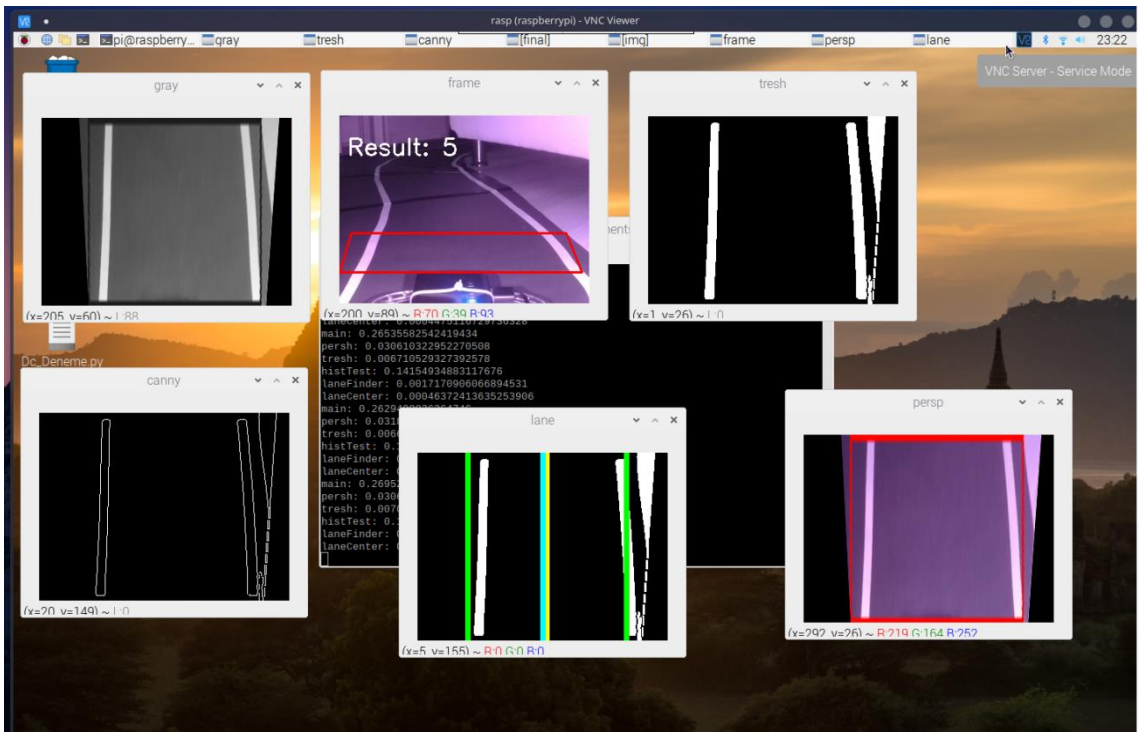

Figure 13. Lane tracking on Raspberry Pi using the developed AV prototype

With the AV prototype designed and implemented in this study, another process performed after lane tracking on the path is the recognition of traffic signs. By using Haar Classifier on the prepared dataset, the Stop traffic sign was successfully recognized as in Figure 14 and the lanes on the path were marked and tracked. With the developed AV prototype, right turn, left turn, stop, road work, 30 km/h maximum speed limitation, 50 km/h maximum speed limitation and 80 km/h maximum speed limitation traffic signs were recognized successfully.

Figure 14. Recognition of 'Stop' traffic sign by using Haar Classifier with AV on the prepared dataset

In the developed AV prototype model, performance tests were carried out for FPS (frame per second) in seven different scenarios (S1, S2, S3, S4, S5, S6 and S7) to recognize seven different traffic signs on the path. In this experimental study, the FPS values obtained from the AV prototype were compared, depending on the number of recognized traffic signs, while the vehicle's lane tracking operations and distance sensors were constantly on and off. Performance test results for recognized traffic signs are shown in Table 1 based on average FPS. According to these findings obtained after the test, it is seen that the vehicle has average FPS values of 6.11 in the best scenario and 1.54 in the worst scenario. Since some of the experiments reached according to the results in this table did not give the expected results, the S7 scenario in which only one traffic sign was detected in other experimental studies was chosen within the scope of our study.

Table 1. Performance test results based on average FPS for traffic signs

	Scenario						
Traffic signs	**S1**	**S2**	**S3**	**S4**	**S5**	**S6**	**S7**
Road work	on	off	off	off	off	off	off
Max 30 km/h speed limitation	on	on	off	off	off	off	off
Max 50 km/h speed limitation	on	on	on	off	off	off	off
Max 80 km/h speed limitation	on	on	on	on	off	off	off
Right turn	on	on	on	on	on	off	off
Left turn	on	on	on	on	on	on	off
Stop	on	on	on	on	on	on	on
FPS (average)	***1.54***	***1.72***	***1.93***	***2.27***	***2.94***	***3.83***	***6.11***

In another experimental study carried out for the AV designed in this study, experimental studies were performed on a test path with a length of approximately 3.5 m and a slope of 30 degrees in the horizontal plane, in a scenario consisting of two stop signs and an obstacle, by including 10 seconds of waiting time at each obstacle and stop sign. In this test, it was observed that the vehicle completed the path in approximately 86 seconds. In order to measure the performance of the developed AV to recognize traffic signs, 1000 video frames of traffic signs from different angles were obtained from the camera and tested in real time. Different traffic signs in 948 images out of 1000 images tested were successfully recognized by the developed AV. Accordingly, the success of the developed AV in recognizing traffic signs were calculated with an accuracy of 94.8%.

Conclusion

In this study, a computer vision based AV prototype was designed and implemented. Using the highly successful Haar Cascade Classifier, the traffic signs were recognized, and the lane tracking of the vehicle was successfully achieved by using image processing techniques on the images obtained from the camera. In addition, it was achieved that the vehicle can cruise safely with the distance sensors.

In the experimental studies, traffic signs were recognized in seven different scenarios and the performance of the AV was compared in terms of FPS. According to the findings, it has been seen that the Raspberry Pi board alone cannot meet the desired needs in real-time image processing theologies. Experimental studies with different up-to-date equipment are expected to be more successful. In this carried out study, in experimental studies with only one traffic sign, recognition of traffic signs was achieved with an accuracy of 94,8%. In addition, it has been observed that the light level of the environment where the images are obtained is a major factor in the detection of traffic signs and the success of lane tracking operations. In the study, it is predicted that if a more powerful hardware is used instead of the used Raspberry Pi card, the accuracy performance and real-time operating speed can be higher. In future studies, it is planned to recognize more traffic signs on a more advanced AV prototype in terms of hardware and software.

Acknowledgment

A part of this study was presented as a Project Study at Department of Computer Engineering, Faculty of Engineering, Bilecik Seyh Edebali University.

Statement of Conflict of Interest

Authors have declared no conflict of interest.

Author's Contributions

The contribution of the authors is equal.

*This study was presented as a summary paper at the International Conference on Engineering, Natural and Applied Sciences (ICENAS'21) held online on 24-26 November 2021.

References

Ahmadi A. Cascade classifier GUI. Available online: https://amin-ahmadi.com/cascade-trainer-gui/. (Accessed on: 29.01.2021)

Anderson JM., Nidhi K., Stanley KD., Sorensen P., Samaras C., Oluwatola OA. Autonomous vehicle technology: A guide for policymakers. 2014; Rand Corporation.

Anthony S. Google's self-driving car passes 700,000 accident-free miles, can now avoid cyclists, stop at railroad crossings. 2014; Available online: https://www.extremetech.com/extreme/181508-googles-self-driving-car-passes-700000-accident-free-miles-can-now-avoid-cyclists-stop-for-trains. (Accessed on: 20.10.2021)

Bechtel MG., McEllhiney E., Kim M., Yun H. Deeppicar: A low-cost deep neural network-based autonomous car. 2018 IEEE 24th international conference on embedded and real-time computing systems and applications (RTCSA), 28-31 August 2018, pp:11-21, Hakodate, Japan.

Burns LD. A vision of our transport future. Nature 2013; 497(7448): 181-182.

Dandıl E., Özkul İ. Futbol maçları için bilgisayarlı görü destekli gol karar sistemi (golkasis): Bir prototip çalışma. Gazi Üniversitesi Fen Bilimleri Dergisi Part C: Tasarım ve Teknoloji 2019; 7(1): 213-224.

Deac MA., Al-doori RWY., Negru M., Dănescu R. Miniature autonomous vehicle development on raspberry pi. 2018 IEEE 14th International Conference on Intelligent Computer Communication and Processing (ICCP), 6-8 September 2018, pp: 229-236, Cluj-Napoca, Romania.

El-Tawab S., Sprague N., Mufti A. Autonomous vehicles: Building a test-bed prototype at a controlled environment. 2020 IEEE 6th World Forum on Internet of Things (WF-IoT), 2-16 June 2020, pp: 1-6, New Orleans, LA, USA.

Fagnant DJ., Kockelman K. Preparing a nation for autonomous vehicles: opportunities, barriers and policy recommendations. Transportation Research Part A: Policy and Practice 2015; 77: 167-181.

Gouda M., Chowdhury I., Weiß J., Epp A., El-Basyouny K. Automated assessment of infrastructure preparedness for autonomous vehicles. Automation in construction 2021; 129: 103820.

Haboucha CJ., Ishaq R., Shiftan Y. User preferences regarding autonomous vehicles. Transportation Research Part C: Emerging Technologies 2017; 78: 37-49.

Harper CD., Hendrickson CT., Mangones S., Samaras C. Estimating potential increases in travel with autonomous vehicles for the non-driving, elderly and people with travel-restrictive medical conditions. Transportation Research Part C: Emerging Technologies 2016; 72: 1-9.

Hossai MRT., Shahjalal MA., Nuri NF. Design of an IoT based autonomous vehicle with the aid of computer vision. 2017 International Conference on Electrical, Computer and Communication Engineering (ECCE), 16-18 February 2017, pp: 752-756, Cox's Bazar, Bangladesh.

Hough PV. Method and means for recognizing complex patterns. 1962; Google Patents.

KGM. Karayolları Genel Müdürlüğü (KGM) Trafik İşaretleri El Kitabı. 2015; Available online: https://www.kgm.gov.tr/SiteCollectionDocuments/KGMdocuments/Trafik/IsaretlerElKitabi/TrafikIsaretleriElKitabi2015.pdf. (Accessed on: 29.10.2020)

Meyer J., Becker H., Bösch PM., Axhausen KW. Autonomous vehicles: The next jump in accessibilities?. Research in transportation economics 2017; 62: 80-91.

Mukhopadhyay P., Chaudhuri BB. A survey of hough transform. Pattern recognition 2015; 48(3): 993-1010.

NHTSA. National Highway Traffic Safety Administration-Automated Vehicles for Safety. Available online: https://www.nhtsa.gov/technology-innovation/automated-vehicles-safety. (Accessed on: 20.10.2021)

NumPy. Available online: https://numpy.org/doc/stable/. (Accessed on: 04.04.2021)

OpenCV. Available online: https://opencv.org/. (Accessed on: 29.01.2021)

OpenCV. Cascade classifier training. Available online: https://docs.opencv.org/4.5.4/dc/d88/tutorial_traincascade.html. (Accessed on: 29.01.2020)

Python. Available online: https://www.python.org. (Accessed on: 29.01.2021)

Rossi A., Ahmed N., Salehin S., Choudhury TH., Sarowar G. Real-time lane detection and motion planning in raspberry pi and arduino for an autonomous vehicle prototype. arXiv preprint arXiv:2009.09391 2020.

Van Brummelen J., O'Brien M., Gruyer D., Najjaran H. Autonomous vehicle perception: The technology of today and tomorrow. Transportation Research Part C: Emerging Technologies 2018; 89: 384-406.

Viola P., Jones M. Rapid object detection using a boosted cascade of simple features. 2001 IEEE computer society conference on computer vision and pattern recognition (CVPR 2001), 8-14 December 2001, pp: I-511-I-518, Kauai, HI, USA.

Wadud Z. Fully automated vehicles: A cost of ownership analysis to inform early adoption. Transportation Research Part A: Policy and Practice 2017; 101: 163-176.

Wiseman Y. Autonomous vehicles, Encyclopedia of Information Science and Technology, Fifth Edition 2021; IGI Global, pp:1-11.

OKÜ Fen Bilimleri Enstitüsü Dergisi
5(Özel Sayı):66-79, 2022

OKU Journal of The Institute of Science and Technology, 5(Special Issue):66-79, 2022

Osmaniye Korkut Ata Üniversitesi Fen Bilimleri Enstitüsü Dergisi

Osmaniye Korkut Ata University Journal of The Institute of Science and Technology

Akışkanlaştırıcı Katkı Oranının Betonların Aşınma Direnci Üzerine Etkisinin Araştırılması

Behçet DÜNDAR[1], Emriye ÇINAR RESULOĞULLARI[2*], Cebrail KAPLAN[3]

[1,2,3]Osmaniye Korkut Ata University, Faculty of Engineering, Department of Civil Engineering, 80000, Osmaniye, Turkey

[1]https://orcid.org/0000-0003-0724-9469
[2]https://orcid.org/0000-0002-9435-2968
[3]https://orcid.org/0000-0002-7403-5463
*Sorumlu yazar: emriyecinar@osmaniye.edu.tr

Araştırma Makalesi

Makale Tarihçesi:
Geliş tarihi: 10.12.2021
Kabul tarihi:14.01.2022
Online Yayınlanma: 23.02.2022

Anahtar Kelimeler:
Beton
Akışkanlaştırıcı katkı
Dayanım
Aşınma dayanımı

ÖZET

Günümüz teknolojisinde betonun taze veya sertleşmiş özelliklerini şekillendiren çeşitli kimyasal katkı maddeleri bulunmaktadır. İstenilen beton özelliklerini elde etmek için kimyasal katkılar tek başına veya birkaç katkının bir arada kullanılmasıyla eklenebilir. Kullanım dozajları istenilen performans kriterlerini sağlayacak ve aynı zamanda betonun taze ve sertleşmiş özelliklerini bozmayacak şekilde seçilmektedir. Bu çalışmada, en çok kullanılan akışkanlaştırıcı katkı kullanımının betonun fiziksel, mekanik ve aşınma dayanımına etkisi araştırılmaktadır. Bu amaç doğrultusunda, akışkanlaştırıcı katkıyı %0,5, %1, %1,5 ve %2 oranlarında kullanılarak üretilen betonların fiziksel, mekanik ve aşınma dayanımı özellikleri incelenmiştir. Beton numunelerinin üretiminde su/çimento oranı ve çimento miktarı sırasıyla 0,5 ve 350 kg/m^3 olarak sabit tutulmuştur. Agrega olarak 0-4 mm taneli kırma kum ve 4-16 mm tane büyüklüğünde agrega kullanılmaktadır. Kimyasal katkı oranının etkisini görmek amacıyla Arşimet, kılcal su emme, ultrason geçiş hızı, böhme (aşınma), schmidt ve basınç dayanımı testlerine tabi tutulmuştur. Su emme ve gözeneklilik yüzdelerinin en düşük olduğu değerler sırasıyla %3.18 ve %9.32 olarak %1 akışkanlaştırıcı katkı maddesi içeren numunede görülmüştür. Ultrases geçiş hızı, schmidt test çekici ve en yüksek basınç dayanımı değerleri sırasıyla 4901 m/s, 26.1 ve 57.14 MPa olarak %1 akışkanlaştırıcı katkı içeren 28 günlük numunede gözlendi. Kimyasal katkı oranının artması ile aşınmaya bağlı ağırlık kayıpları azalmıştır.

Investigation of the Effect of Plasticizer Additive Ratio on the Abrasion Resistance of Concretes

Research Article

Article History:
Received: 10.12.2021
Accepted: 14.01.2022
Published online: 23.02.2022

Keywords:
Concrete
Plasticizer additive
Strength
Abrasion resistance

ABSTRACT

In today's technology, there are various chemical additives that shape the fresh or hardened properties of concrete. Chemical additives can be added alone or by using a combination of several additives to obtain the desired concrete properties. Usage dosages are chosen in a way that will meet the desired performance criteria and at the same time will not impair the fresh and hardened properties of the concrete. In this study, the effect of the most used plasticizer additives on the physical, mechanical and abrasion resistance of concrete is investigated. For this purpose, physical, mechanical and abrasion resistance properties of concretes produced by using plasticizer additive at 0.5%, 1%, 1.5% and 2% ratios were investigated. In the production of concrete samples, the water/cement ratio and cement amount were kept constant as 0.5 and 350 kg/m^3, respectively. As aggregate, crushed sand with 0-4 mm grains and aggregate with 4-16 mm grain size are used. In

order to see the effect of chemical additive ratio, archimedes, capillary water absorption, ultrasound transmission rate, böhme (abrasion), schmidt and compressive strength tests were subjected to. The lowest water absorption and porosity percentages were observed in the sample containing 1% plasticizer additive as 3.18% and 9.32%, respectively. Ultrasonic pulse velocity, Schmidt hammer and the highest compressive strength values were observed as 4901 m/s, 26.1 and 57.14 MPa, respectively, in the 28-day-old sample containing 1% plasticizer additive. With the increase in the chemical additive ratio, the weight losses due to abrasion decreased.

To Cite: Dündar B., Resuloğulları EÇ., Kaplan C. Investigation of the Effect of Plasticizer Additive Ratio on the Abrasion Resistance of Concretes. Osmaniye Korkut Ata Üniversitesi Fen Bilimleri Enstitüsü Dergisi 2022; 5(Özel sayı): 66-79.

Introduction

Improving the various properties of concrete, providing convenience in production and transportation, etc. the use of chemical additives for these purposes has become quite common in recent years. It is known that various chemical additives are used in cement mortars and concretes both to contribute to the properties of fresh concrete and to increase the strength and durability performance of hardened concrete (Jeknavorian et al., 1998; ASTM C465-19). The functions of chemical additives are classified as normal or highwater reduction, retarding setting, accelerating setting and entraining air (Jeknavorian et al., 1998; Erdoğan et al., 2007). This classification water reducers are used to reduce the w/c ratio or to obtain more workable fresh concrete with a constant w/c ratio and are called plasticizers. Plasticizers are of great importance to the construction industry as the most widely used organic cement additive. The addition of plasticizers in concrete increases the workability of the concrete, reduces the amount of mixing water, changes the rheology of the mixture, and causes delay in setting (Chernyshev et al., 2018).

Adding water to facilitate the placement of fresh concrete adversely affects the concrete performance (Topçu et al., 2006). In order to prevent this effect, it is necessary to easily place the fresh concrete without adding extra water. To achieve this workability in fresh concrete, plasticizer additives are used (Topçu et al., 2006; Stecher et al., 2019). By adding the plasticizer additive to the concrete, agglomeration of the cement particles is prevented or minimized. As the cement particles disperse, the water trapped between them is released and becomes available for workability and cement hydration. However, the surface area of the cement particle exposed to hydration also increases (Jun, 2008). By keeping the w/c ratio constant in the mixing calculation, it is expected that a more fluid and easily placed concrete will be obtained without any loss of strength when different ratios of plasticizer are used (Haruna and Fall, 2020). The fact that good placement and compaction reduces the volume of voids within the concrete is an important factor for the durability of a concrete (Ali and Qureshi, 2019; Sathyan and Anand, 2019). In a concrete where the placement process is facilitated and compression is applied successfully; Improvements are seen in terms of durability due to ensuring a homogeneous mixture, obtaining a smooth surface, and preserving integrity. The fact that the service life of a reinforced concrete structural element is directly related to its durability performance causes researchers to focus on this issue. The fact that the share of maintenance and repair works in

construction activities is as high as 40% in developed countries clearly reveals that there are serious problems in terms of durability (Baradan and Aydın, 2013). The reason for the durability problems in the load-bearing structural elements is the various deteriorations in the concrete. Factors that cause deterioration in concrete are mechanical, physical, chemical and biological factors, and the effect of wear is one of the damages caused by mechanical means (Gökçer et al., 2015). Abrasion refers to material losses caused by frictions affecting concrete surfaces, and the surface properties of concrete are of great importance for resistance to abrasion (Naik et al., 2002; Aydın, 2016; Lau et al., 2019; Pranav et al., 2020). Abrasion deterioration in concrete is caused by factors such as gravel, sand and ice slides, wind, and water. Abrasion deterioration causes serious loss of bearing capacity in reinforced concrete structural elements and poses a great threat to important structures. In order to prevent this effect, the abrasion resistance of concrete should be increased.

The aim of this study is to investigate the effect of plasticizer additive ratio on wear resistance. A lot of research has been done on the use of plasticizer additives, which is one of the frequently used chemical additives, but there are not many articles investigating wear resistance. For this purpose, the physical, mechanical and abrasion resistance properties of concretes were investigated by adding plasticizer additives in different ratios into the concrete. In concrete production, the water/cement ratio was kept constant as 0.5, and plasticizer chemical additives were added at 0.5%, 1%, 1.5% and 2% rates. Concrete samples were subjected to slump, water absorption, porosity, ultrasonic, böhme (abrasion), schmidt and compressive strength tests.

Material and Method

Material

CEM I-42,5/R type Portland Cement (PC) produced in accordance with the TS EN 197-1 (2012) standard was used as the binder in the preparation of the samples. The chemical analysis of the cement used was taken from the producer factory, and its physical and chemical properties are given in Table 1.

In the experimental study, potable city mains water of Osmaniye province, which complies with the conditions specified in TS EN 1008 (2003), was used as mixed water. In concrete production, 16 mm was determined as the largest grain size, and 0-4 mm crushed sand and 4-16 mm limestone-based crushed stone with appropriate gradation were used. Surface dry water-saturated densities of fine and coarse aggregates are 2.67 and 2.70 gr/cm^3, respectively. The suitability of crushed sand used in the experiments for use in the experiments was checked in accordance with TS 706 EN 12620+A1 (2009) standards.

Table 1. Chemical and physical analysis of CEM I 42,5 R Portland cement.

Chemical Analysis	(%)
CaO	62.72
SiO_2	20.00
Al_2O_3	4.92
Fe_2O_3	3.76
MgO	1.84
SO_3	2.65
K_2O	0.73
Na_2O	0.26
Loss on Ignition (%)	2.54
Insoluble Residue (%)	-
Physical Properties	
Specific Gravity (g/cm^3)	3.11
Specific Surface (Blaine) (cm^2/g)	3250
Socket Start (min)	145
Socket End (min)	220
Volume Expansion (mm)	1
Compressive Strength (MPa) 28 days	49.5

Chemical additives in accordance with ASTM C494 standard are used in concrete production. The chemical additive used is lignosulfonate-based plasticizer with water reducing effect. The density of the plasticizer additive is 1.12 g/cm^3, the chlorine content is <0.1% and the pH value is 7.23 at 20 °C. It is used at rates of 0.5%, 1%, 1.5% and 2% by weight, depending on the amount of cement. The amount of material required for the preparation of concrete samples is given in Table 2.

Table 2. Amount of material required for 1 m^3 concrete

Sample Name	**Cement (kg)**	**Water (kg)**	**Crushed Sand (kg)**	**Aggregate (kg)**	**Chemical Additive (kg)**
0.5K	350	175	1041	832	1.75
1.0K	350	175	1039	831	3.50
1.5K	350	175	1037	829	5.25
2.0K	350	175	1035	827	7.00

Method

Concrete samples produced with a water/cement ratio of 0.5 and a cement amount of 350 kg/m^3 and containing plasticizer additives at different rates (0.5%, 1%, 1.5%, 2%) are slump, Archimedes, ultrasonic, böhme (abrasion), schmidt and pressure subjected to strength tests.

Slump Test

While producing the concrete samples, the workability of the concretes was checked by applying the slump test. The experiment was carried out by filling a cone-shaped metal mold with standard dimensions with fresh concrete in three layers and skewering each layer 25 times. The amount of slump in the concrete was measured by pulling up the truncated cone filled with fresh concrete (TS EN 12350-2, 2019).

Compressive Strength

In order to determine the compressive strength of concrete samples, cube samples of 150x150x150 mm dimensions were produced. Concrete samples, which completed their setting by waiting in the mold, were removed from the molds at the end of 24 hours and cured for 7 and 28 days, and their compressive strengths were determined. The compressive strengths were applied according to the TS EN 12390-4 (2019) standard with the aid of a 200-ton capacity device.

Böhme (Abrasion) Test

For the friction wear loss test, cube shaped test specimens with 71 mm side lengths were prepared in accordance with TS 2824 EN 1338 (2005). It was subjected to the abrasion test with the bohme device shown in Figure 1. In these samples, the contacting and opposing side should be parallel and flat. In the experiments, 20 g of abrasive powder is sprinkled on the friction strip and loaded with 294 N by means of a steel lever. After 22 cycles, sanding dust and sample wastes are cleaned from the disc that stops automatically. Again, 20 gr of abrasive powder is sprinkled on the friction strip and the sample is rotated 90º around the vertical axis. The test, consisting of 22 cycles for each sample, is applied to the sample 16 times. After the test sample is thoroughly cleaned, the sample is weighed on a precision balance and the weight loss is noted.

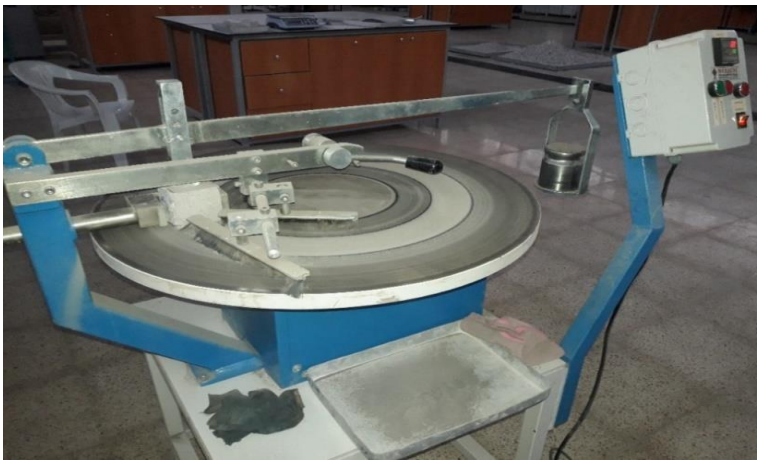

Figure 1. Böhme experimental setup

Water Absorption and Porosity

The porosity and water absorption properties of all samples were determined in accordance with the TS EN 1170-6 (1999) standard with the aid of scales working with the Archimedean principle. The samples were removed from the curing pool at the end of 28 days, and their weight in the water was recorded by placing them in the wire basket on the specific gravity stand. The surfaces of the samples removed from the water were dried using a cloth and the dry surface saturation weights were taken. The samples were dried for 24 hours in an oven operated at 105 ºC and turned into an oven dry. The temperature of the samples taken out of the drying oven was expected to decrease to room temperature and then the oven dry weights were weighed.

Ultrasonic Pulse Velocity

Ultrasonic Pulse Velocities of the samples were calculated using an Ultrasonic tester (P-wave). The TS EN 12504-4 (2021) standard is based on the Ultrasonic Pulse Velocity test applied in the oven-dry state. The distance between the two surfaces of the samples was measured with the help of a caliper and processed on the device, and ultrasonic gel was used to prevent air gaps on the surfaces to be measured. The sample was placed between the probes (transmitter-receiver) and aligned, and the device was operated. The transit time of the sound wave in the device is recorded. With the help of the distance in the measurement direction and the sound transmission time measured by the device, the necessary calculations were made, and the Ultrasonic Pulse Velocities were calculated and noted.

Figure 2. Ultrasonic transmission rate determination

Schmidt Test Hammer

Schmidt hammer test was carried out on concrete samples with dimensions of 100x100x100 mm. 12 readings were taken from each sample, and attention was paid to ensure that there was a minimum of 20 mm between each reading point and 40-50 mm space was left from the edges. After making 12 readings, the arithmetic average of the remaining 10 readings was taken, ignoring the largest and smallest values. In this way, an average R value representing the test surface was obtained. In the implementation of the experiment, the TS EN 12504-2 (2021) standard was used.

Results and Discussion

Slump Test

During the production of concrete samples, the data of the slump test applied to the fresh concrete mixtures are given in Figure 3. It is seen that the amount of slump obtained from concrete samples increases as the use of plasticizer additives increases. The highest slump value was observed in the concrete with 15.5 cm and 2% plasticizer admixture. Consistent with the data obtained, Benaicha et al. (2019) showed in their study that the workability of fresh concrete improves as the amount of plasticizer used increases.

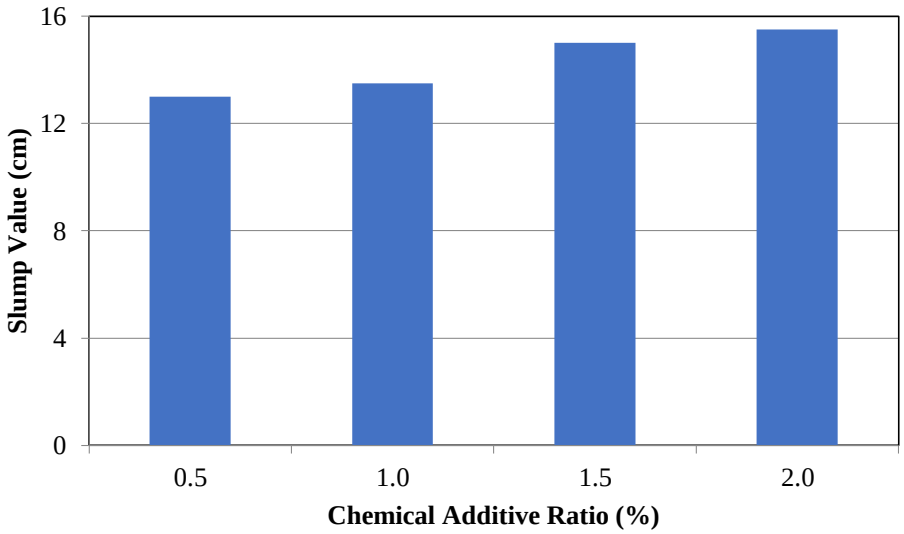

Figure 3. Slump values of concrete samples

Compressive Strength

The 7- and 28-day compressive strength values of the samples are given in Figure 4. According to the test results of the 7-day samples, the highest compressive strength value was 50.7 MPa in the sample with 1% plasticizer additive, while the lowest compressive strength value was 47.72 MPa in the sample with 2% plasticizer additive added. According to the test results of the 28-day samples, while the highest compressive strength value was 57.14 MPa in the sample with 1% plasticizer additive, the lowest compressive strength value was observed in the sample with 2% plasticizer additive as 53.41 MPa. The 1% plasticizer admixture used in the concrete sample caused the concrete sample to mix more homogeneously and settle better than the other samples, thus minimizing the porous structure and thus achieving higher strength without reducing the water/cement ratio. Consistent with these findings, Klein and Simon (2006) observed in their study that the use of plasticizers at recommended rates has a positive effect on the short and long-term compressive strength of concretes. While it was observed that the ideal plasticizer use was 1% in terms of compressive strength, it was observed that the consistency could be significantly improved by experiencing negligible strength drops as a result of using higher rates (1.5% and 2%).

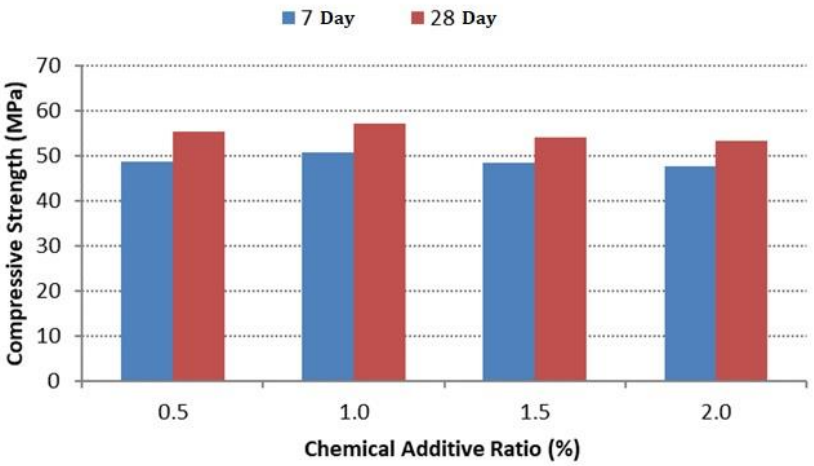

Figure 4. Compressive strength values of concrete samples

Böhme (Abrasion) Test

The weight loss percentages of the concrete samples calculated after the abrasion test are given in Figure 5. When the plasticizer additive is used at 0.5%, 1%, 1.5% and 2% ratios, it is seen that the weight loss percentages are 5.45%, 5.19%, 3.99% and 3.55%, respectively. It has been observed that the surface properties of concrete have a significant effect on its performance under the influence of wear. Although the use of plasticizer ratio more than 1% increased the void ratio in the internal structure, it resulted in obtaining samples with extremely smooth surfaces. With the increase of plasticizer addition, obtaining smoother surfaces in the samples increased the surface strength of the concrete samples. This resulted in a reduction in surface wear, resulting in a reduction in weight losses due to wear. There are studies in the literature that argue and reveal that wear resistance is affected by surface properties rather than the strength of concrete (Silva et al., 2019). When the data were examined, it was observed that the weight loss seen in the concrete sample produced with the addition of 2% plasticizer additive was 34.86% lower than the weight loss observed in the concrete sample produced with the addition of 0.5% plasticizer additive.

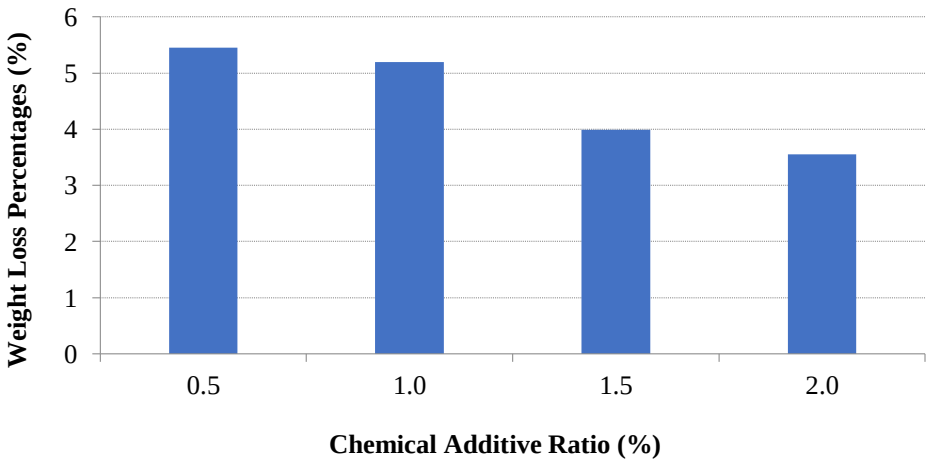

Figure 5. Böhm weight loss values of concrete samples

Water Absorption and Porosity

Water absorption and porosity percentages of concrete samples are given in Figure 6 and 7. According to the Archimedean test results, it is seen that the lowest water absorption percentage value is read as 3.18% in the sample containing 1% plasticizer additive. The highest water absorption percentage was read as 3.29% in the sample containing 2% additive. In porosity values, similar to the results in water absorption percentages; while the lowest value was observed as 9.32% in the sample containing 1% plasticizer additive, the highest value was observed as 9.58% in the sample containing 2% plasticizer additive. It is seen that while the void ratio and water absorption values decrease with 1% plasticizer additives, they increase with the use of 1.5% and 2% additives. The lowest water absorption and porosity observed in the sample containing 1% plasticizer additive indicates that the best settlement is achieved in the concrete using 1% plasticizer additive and the voids in the internal structure remain at a minimum level.

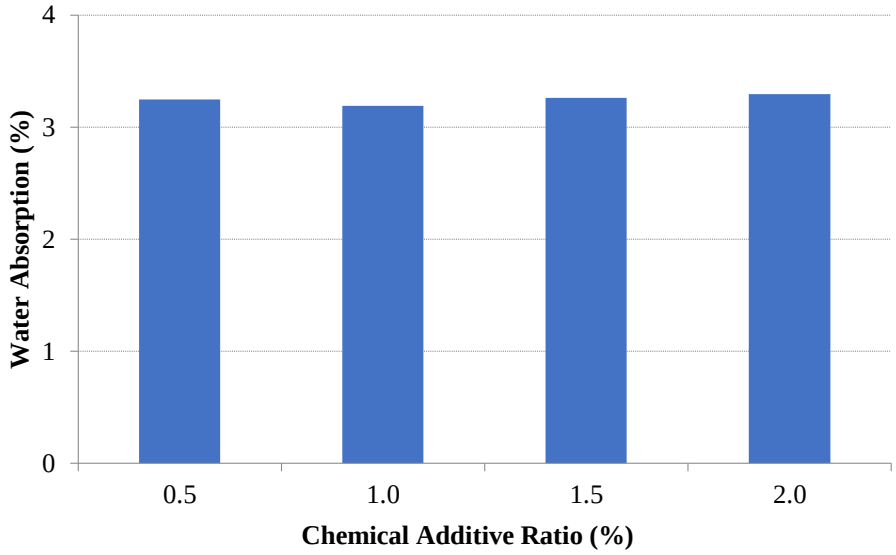

Figure 6. Water absorption percentages of concrete samples

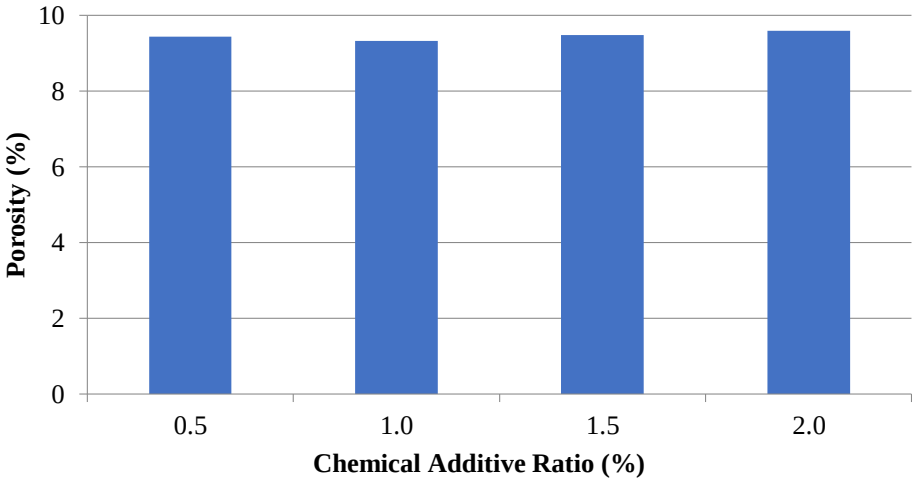

Figure 7. Porosity percentages of concrete samples

Ultrasonic Pulse Velocity

Ultrasonic Pulse Velocity of concrete samples is given in Figure 8. The highest transition velocity was measured as 4901 m/sec in concrete samples with 1% plasticizer additive. The lowest Ultrasonic Pulse Velocity was measured as 4672 m/sec in concretes with 2% plasticizer additive added. The Ultrasonic Pulse Velocity increases or decreases in relation to the void amount of the object and gives an idea about the strength of the concrete. While it is seen that the ultrasonic Pulse Velocity takes low values in the samples with void structure, high results are obtained in the samples with few voids. Many studies in the literature indicate that Ultrasonic Pulse Velocities decrease with an increase in the void ratio (Mendes et al., 2020). The fact that the highest ultrasonic transmission velocity was measured as 4901 m/s in the concrete sample containing 1% plasticizer additive supports that the porous structure remains at a minimum level in this sample. All concrete is classified as high-quality concrete as it is higher than 4000 m/s.

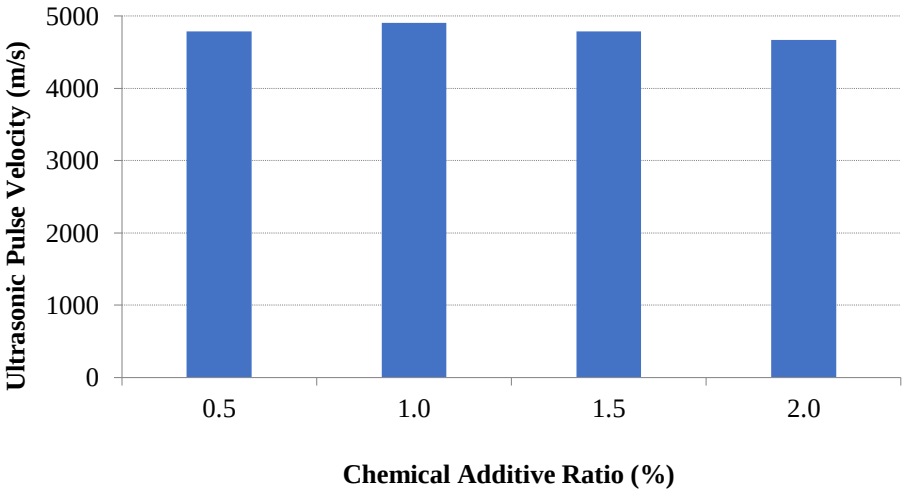

Figure 8. Ultrasonic pulse values of the samples

Schmidt Test Hammer

Schmidt test hammer readings of concrete samples are given in Figure 9. The highest value was read as 27.2 in the sample containing 2% chemical additive. The lowest value was read as 24.2 in the sample containing 0.5% chemical additive. Like the Ultrasonic Pulse Velocity, the data from the Schmidt test hammer readings also give an idea about the mechanical property of the concrete. Schmidt rebound value expresses the surface hardness, which has an effective role on the abrasion resistance of concretes. Considering the results obtained from the concrete samples, it is seen that the Schmidt rebound values are also high in the samples with lower weight losses due to abrasion. Topsakal and Özel (2012) stated in their study that there is a relationship between surface hardness and slump value. The data obtained showed that increasing the workability with the use of plasticizer additives can increase the surface hardness of the concrete.

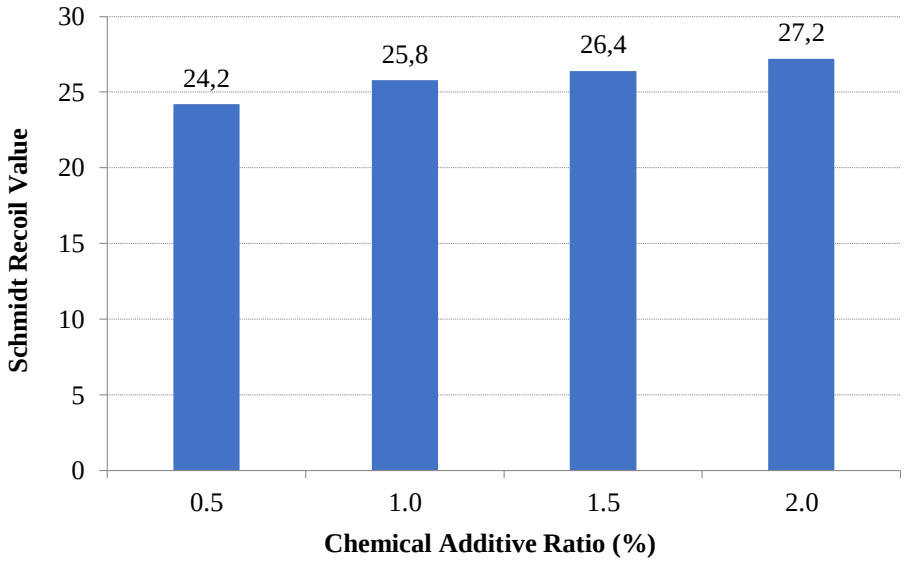

Figure 9. Schmidt hammer readings of samples

Conclusion and Recommendations

- As seen in the results of ultrasonic transmission velocity and compressive strength tests, the use of 1% plasticizer admixture enabled the concrete to achieve the best performance in terms of mechanical and physical properties. Considering this situation, the ideal plasticizer usage rate for the permeability and strength properties of concrete can be evaluated as 1%.
- In our study, besides the mechanical and physical properties, the wear deterioration, which is a durability problem, was also examined and it was determined that the use of plasticizer additives greatly improved the resistance of concrete against abrasion.
- According to the Archimedean test results, it is seen that the lowest water absorption percentage value is read as 3.18% in the sample containing 1% plasticizer additive. The highest water absorption percentage was read as 3.29% in the sample containing 2% additive.
- In porosity values, similar to the results in water absorption percentages; While the lowest value was observed as 9.32% in the sample containing 1% plasticizer additive, the highest value was observed as 9.58% in the sample containing 2% plasticizer additive.
- It is seen that while the void ratio and water absorption values decrease with 1% plasticizer additives, they increase with the use of 1.5% and 2% additives. The lowest water absorption and porosity observed in the sample containing 1% plasticizer additive indicates that the best settlement is achieved in the concrete using 1% plasticizer additive and the voids in the internal structure remain at a minimum level.
- The highest transition velocity was measured as 4901 m/sec in concrete samples with 1% plasticizer additive. The lowest ultrasonic pulse velocity was measured as 4672 m/sec in concretes with 2% plasticizer additives. The highest ultrasonic pulse velocity was measured as

4901 m/sec in the concrete sample containing 1% plasticizer additive, which also supports that the porous structure remained at a minimum level in this sample.

- When the plasticizer additive is used at 0.5%, 1%, 1.5% and 2% ratios, it is seen that the weight loss percentages are 5.45%, 5.19%, 3.99% and 3.55%, respectively. It has been observed that the surface properties of concrete have a significant effect on its performance under the influence of wear. Using more than 1% plasticizer ratio increased the void ratio in the internal structure but resulted in samples with extremely smooth surfaces.
- The obtaining of smoother surfaces in the samples with the increase of the plasticizer addition caused a decrease in the surface abrasions, resulting in a decrease in the weight losses due to abrasion.
- According to the compressive strength test results of 7-day samples, the highest value was seen as 50.7 MPa in the sample with 1% plasticizer additive.
- The results obtained as a result of the study; It has been shown that the workability properties are improved without a significant decrease in compressive strength values with the use of plasticizer additives, so that the concretes that are placed more easily have smooth surfaces and high surface strengths and become more resistant to abrasion.

Conflict of Interest Statement

The article author declares that there is no conflict of interest.

Contribution Rate Statement Summary of Researchers

The contribution of the authors is equal.

*This study was presented as a summary paper at the International Conference on Engineering, Natural and Applied Sciences (ICENAS'21) held online on 24-26 November 2021.

References

Ali B., Qureshi LA. Influence of glass fibers on mechanical and durability performance of concrete with recycled aggregates. Construction and Building Materials 2019; 228: 116783.

ASTM C465-19, Annual Book of ASTM Standards, 04.01.

ASTM C494/C494M-19, Annual Book of ASTM Standards, 04.02.

Aydın F. GFRP kutu profil aşınma özelliklerinin farklı dayanımlardaki betonlar ile karşılaştırılması, International Symposium on Innovative Technologies in Engineering and Science 2016; 3: 374-383.

Baradan B., Aydın S. Betonun durabilitesi (Dayanıklılık, Kalıcılık), Hazır Beton Kongresi, 2013; 54-68.

Benaicha M., Hafidi Alaoui A., Jalboud O., Burtschell Y. Dosage effect of superplasticizer on self-compacting concrete: correlation between rheology and strength, Journal of Materials Research and Technology, 2019; 8(2): 2063-2069.

Chernyshev AN., Jonsson M., Forsberg K. Characterization and degradation of a polyarylether based superplasticizer for use in concrete barriers in deep geological repositories. Applied Geochemistry, 2018; 95: 172-181.

Erdoğan TY., Erdoğan ST. Kimyasal katkı maddeleri ve tarihi geçmişleri. Yapılarda Kimyasal Katkılar Sempozyumu 2007; 2: 21-34.

Gökçer B., Yıldız S., Keleştemur O. Cam lif takviyeli çimento harçlarının aşınma direnci üzerine atık mermer tozunun etkisi, International Sustainable Buildings Symposium 2015; 2: 123-128.

Haruna S., Fall M. Time-and temperature-dependent rheological properties of cemented paste backfill that contains superplasticizer, Powder Technology 2020; 360: 731-740.

Ismail MK., Hassan AA. Abrasion and impact resistance of concrete before and after exposure to freezing and thawing cycles", Construction and Building Materials 2019; 215: 849-861.

Jeknavorian AA., Mabud MA., Barry EF., Litzau JJ. Novel pyrolysis-gas chromatography: mass spectrometric techniques for the characterization of chemical additives in Portland cement and concrete, J. Anal. Appl. Pyrolysis 1998; 46: 85-100.

Jun SD. Effect of a newly developed lignosulphonate superplasticizer on properties of cement pastes and mortars, Master's Thesis, National University of Singapore, Engineering Department of Civil Engineering, Singapore 2008.

Klein K., Simon D. Effect of specimen composition on the strength development in cemented paste backfill. Can. Geotech. J., 2006; 43(3): 310-324,

Lau CK., Lee H., Vimonsatit V., Huen WY., Chindaprasirt P. Abrasion resistance behaviour of fly ash based geopolymer using nanoindentation and artificial neural network. Construction and Building Materials 2019; 212: 635-644.

Mendes JC., Barreto RR., Costa LCB., Brigolini GJ., Peixoto RAF. Correlation between ultrasonic pulse velocity and thermal conductivity of cement-based composites. Journal of Nondestructive Evaluation, June 2020.

Naik TR., Singh SS., Ramme BW. Effect of source of fly ash on abrasion resistance of concrete. Journal of Materials in Civil Engineering, 2002; 14: 417-426.

Pranav S., Aggarwal S., Yang E., Sarkar AK., Singh AP., Lahoti M. Alternative materials for wearing course of concrete pavements: a critical review. Construction and Building Materials, 2020; 236: 117609.

Sathyan D., Anand K.B. Influence of superplasticizer family on the durability characteristics of fly ash incorporated cement concrete, Construction and Building Materials 2019; 204: 864-874.

Silva CV., Zorzi JE., Cruz RCD., Dal Molin DCCD. Experimental evidence that micro and macrostructural surface properties markedly influence on abrasion resistance of concretes, 2019; 422-423: 191-200.

Stecher J., Plank J. Novel concrete superplasticizers based on phosphate esters. Cement and Concrete Research, 2019; 119: 36-43.

Topçu İB., Canmaz M., Karakurt C. Beton üretiminde kimyasal katkı kullanımı. Politeknik Dergisi 2006; 9(1): 59-63.

Topsakal A., Özel C. Kendiliğinden yerleşen betonlarda çökme kaybının ve kalıplama zamanının sertleşmiş beton özellikleri üzerindeki etkisi. SDU International Technologic Science 2012; 4(2): 124-134.

TS 2824 EN 1338, Zemin Döşemesi için Beton Kaplama Blokları-Gerekli Şartlar ve Deney Metotları, TSE, Ankara Türkiye, 2005.

TS 706 EN 12620+A1, Beton Agregaları, TSE, Ankara Türkiye, 2009.

TS EN 1008. Beton-Karma suyu Numune alma, deneyler ve beton endüstrisindeki işlemlerden geri kazanılan su dahil, suyun, beton karma suyu olarak uygunluğunun tayini kuralları TSE, Ankara Turkey 2003.

TS EN 1170-6. Ön yapımlı beton mamuller-Cam elyaf takviyeli çimento (ctç) deney metodu-Bölüm 6: Suya daldırma yoluyla su emme ve kuru yoğunluk tayini, TSE, Ankara Türkiye, 1999.

TS EN 12350-2. Beton - Taze beton deneyleri - Bölüm 2: Çökme (slump) deneyi TSE, Ankara Türkiye, 2019.

TS EN 12390-4. Beton-Sertleşmiş beton deneyleri-Bölüm 4: Basınç dayanım deney makinelerinin özellikleri TSE, Ankara Türkiye, 2019.

TS EN 12504-2. Yapılarda beton deneyleri – Bölüm 2: Tahribatsız muayene – geri sıçrama sayısının belirlenmesi TSE, Ankara Türkiye, 2021.

TS EN 12504-4. Beton deneyleri-Bölüm 4: Ultrases geçiş hızının tayini, TSE, Ankara Türkiye, 2021.

TS EN 197-1. Cement- Stage 1: General cements – component, TSE, Ankara Turkey, 2012.

OKÜ Fen Bilimleri Enstitüsü Dergisi
5(Özel Sayı):80-95, 2022

OKU Journal of The Institute of Science and Technology, 5(Special Issue):80-95, 2022

Osmaniye Korkut Ata Üniversitesi Fen Bilimleri Enstitüsü Dergisi

Osmaniye Korkut Ata University Journal of The Institute of Science and Technology

Estimating Dam Reservoir Level Change of Istanbul Alibey Dam with The Fuzzy SMRGT Method

Enes Erkan ER[1*], Fatih ÜNEŞ[2], Bestami TAŞAR[3]

[1,2,3]İskenderun Technical University, Faculty of Engineering, Department of Civil Engineering,31200, Hatay, Turkey

[1]https://orcid.org/0000-0001-9982-9443
[2]https://orcid.org/0000-0001-5751-6970
[3]https://orcid.org/0000-0003-4842-3937
*Corresponding author: eer.mfbe20@iste.edu.tr

Research Article

Article History:
Received: 07.12.2021
Accepted: 14.01.2022
Published online: 23.02.2022

Keywords:
Dam reservoir level
Prediction
Fuzzy
ANN
Regression

ABSTRACT

Accurate estimation of the dam reservoir level is very important for the planning and operation of water structures. In this study, monthly dam reservoir level data between the years of 1989 and 2020 obtained from the State Hydraulic Works (DSI) was used to estimate the monthly dam reservoir level change. For the monthly dam reservoir level estimation, it has been tried to be estimated using the Simple Membership Functions and Fuzzy Rules Generation Technique (Fuzzy-SMRGT), Artificial Neural Networks (ANN) and the classical Multiple Linear Regression (MLR) methods. Alibey Dam located in Sultangazi district of Istanbul was chosen as the study area. The monthly evaporation, water entering into the lake, consumption of drinking water and amount of water discharged from the dam amounts were used to estimate the monthly Alibey Dam average dam reservoir level. The model results were compared with the actual observation data. When statistical criteria were evaluated, it was seen that artificial intelligence approaches and regression method were successful in estimating the dam reservoir level and gave close estimation results.

İstanbul Alibey Barajının Baraj Rezervuar Seviye Değişiminin Bulanık SMRGT Yöntemiyle Tahmin Edilmesi

Araştırma Makalesi

Makale Tarihçesi:
Geliş tarihi: 07.12.2021
Kabul tarihi:14.01.2022
Online Yayınlanma: 23.02.2022

Keywords:
Baraj rezervuar seviyesi
Tahmin
Fuzzy
ANN
Regresyon

ÖZET

Baraj rezervuar seviyesinin doğru bir şekilde tahmin edilmesi, su yapılarının planlanması ve işletilmesi için çok önemlidir. Bu çalışmada, aylık baraj rezervuar seviyesi değişimini tahmin etmek için Devlet Su İşleri'nden (DSİ) alınan 1989-2020 yılları arasındaki aylık baraj rezervuar seviyesi verileri kullanılmıştır. Aylık baraj rezervuar seviyesi tahmini için Basit Üyelik Fonksiyonları ve Bulanık Kural Oluşturma Tekniği (Fuzzy-SMRGT), Yapay Sinir Ağları (YSA) ve klasik Çoklu Doğrusal Regresyon (ÇDR) yöntemleri kullanılarak tahmin edilmeye çalışılmıştır. Çalışma alanı olarak İstanbul ili Sultangazi ilçesinde bulunan Alibey Barajı seçilmiştir. Aylık buharlaşma, aylık göle giren su, aylık içme suyu tüketimi ve aylık barajdan deşarj edilen su miktarı, aylık Alibey Barajı baraj rezervuar seviyesi ortalamasını tahmin etmek için kullanılmıştır. Model sonuçları gerçek gözlem verileriyle karşılaştırılmıştır. İstatistiksel kriterler değerlendirildiğinde yapay zekâ yaklaşımlarının ve regresyon yönteminin baraj rezervuar seviyesinin tahmininde başarılı olduğu ve yakın tahmin sonuçları verdiği görülmüştür.

To Cite: Er EE., Üneş F., Taşar B. Estimating Dam Reservoir Level Change of Istanbul Alibey Dam With The Fuzzy SMRGT Method. Osmaniye Korkut Ata Üniversitesi Fen Bilimleri Enstitüsü Dergisi 2022; 5(Özel sayı): 80-95.

Introduction

Water has the most important position in human life for sustaining life. However, especially with the global climate change experienced in recent years, the increasing water problems and their solutions have gained more importance. It has become inevitable to take some precautions due to the remarkable decrease in the amount of water usage. For these reasons, it is necessary to take precautions to know the potential of existing water resources and to use more efficiently (Küçükerdem, 2019). It is quitesubstantialto estimate the amount of water entering and leaving the system during the design and operation of water structures. Recently, prominent artificial intelligence models are used to estimate these data (Salam, 2018).

There are many studies in the literature with the development of a prediction model related to water structures and hydrology using artificial intelligence methods. Şener et al. (2014) of the changes in Burdur Lake dam reservoir level using the, regression analysis created prediction models Fuzzy Logic (FL)methods with precipitation and evaporation data. They observed that the FL method gave more successful results than the regression method. Aydemir (2020), estimatedthe dam reservoir level of Terkos Dam Lake with the FL. In his study, the most accurate estimation of water values in the future was investigated by establishing a modeling mechanism with the ANFIS method, with the help of water values from 2001-2012 in Terkos Dam. Üneş (2010), the dam reservoir level was estimated with artificial neural networks. Üneş et al. (2018a) estimated the amount of evaporation in the Cambridge reservoir basin with the ANN method, which is one of the artificial intelligence techniques. Üneş et al. (2018a) created models to predict ground dam reservoir level fluctuations with the ANN with the data of the Minnesota observation well station in the USA. On the other hand, Üneş et al. (2018b) evaluated and compared daily reference evapotranspiration by ANN and empirical methods. Üneş et al. (2019a) estimated the dam reservoir level fluctuations by selecting Millers Ferry Dam on the Alaba River in the USA. It has been observed that FL ANFIS models give better results than classical and other artificial models. Üneş et al. (2019b) estimated modeling of dam reservoir volume using Generalized Regression Neural Network (GRNN), SVM and M5decision tree models. Üneş et al. (2019c) created ground dam reservoir level estimation models with the fuzzy logic method. Üneş et al. (2019d) estimated the artificial neural network method for the estimation of the ainfall-runoff relationship. Demirci et al. (2017) estimated the ground dam reservoir level using the ANN with the data they obtained from the General Directorate of State Hydraulic Works (DSI) in the Kumlu district of the Amik Plain of Hatay (Demirci et al., 2018) estimated the reservoir capacity of the Brook Dam in Massachusetts, USA, using adaptive neuro fuzzy (NF) and multiple linear regression (MLR) models. NF andMLR results were compared to each other.

Arslan et al. (2020) estimated the Keban dam lake level change using adaptive neural fuzzy inference system (ANFIS) and support vector machines (SVM) methods. Kilinc (2004) tried to predict monthly inflows, total evaporations and end-of-month volumes of a reservoir by using the ANN in the operation of dam reservoirs in Istanbul. The estimation results were

compared with the results of classical methods. Turhan (2021), a comparative evaluation of the use of artificial neural networks in modeling the precipitation- flow relationship in water resources management. Latif et al. (2021) he studied the reservoir water balance simulation model using machine learning algorithm. Iraji et al. (2020) estimated the reduction in reservoir volume using an artificial neural network. Paul et al. (2019) a comparative study of wavelet transforms and MLR, KNN (K-Nearest Neighbors), ANN and ANFIS models in monthly flow estimation.Other studies on artificial intelligence in the field of hydraulics (Gemici, 2013; Kocabaş, 2013; Ozel 2020).

In this study, monthly evaporation amount (E_t), amount of water coming into the lake (LW_t), drinking water consumption (DW_t) and discharged water amount (DDW_t) from the dam reservoir were used to estimate the monthly dam reservoir level (DRL_t) change of Alibey Dam. Fuzzy-SMRGT + a fuzzy logic method, Multiple Linear Regression methods (MLR) and Artificial Neural Networks (ANN) were used.

Material and Methods

Study Area

In this study, Alibey Dam, which is located in Sultangazi district of Istanbul province of Turkey, was given in Figure 1 it was built between 1975-1983 for the purpose of supplying drinking water, utility water and industrial water. The volume of the dam body, which is an earth-fill type, is 1.900.000 m^3, its height from the river bed is 30,00 m, the lake volume at normal dam reservoir level is 66,80 hm^3, and the lake area at normal dam reservoir level is 4,66 km^2. An average of 39 hm^3 of drinking water is provided annually from the Alibey Dam. The 31-year monthly measurement data of the Alibey Dam, which is of great importance in its region, for the years 1989-2020 were used. Figure 2 shows that the changes in dam reservoir level. The changes in Dam Reservoir level between the years of1989 and 2020.

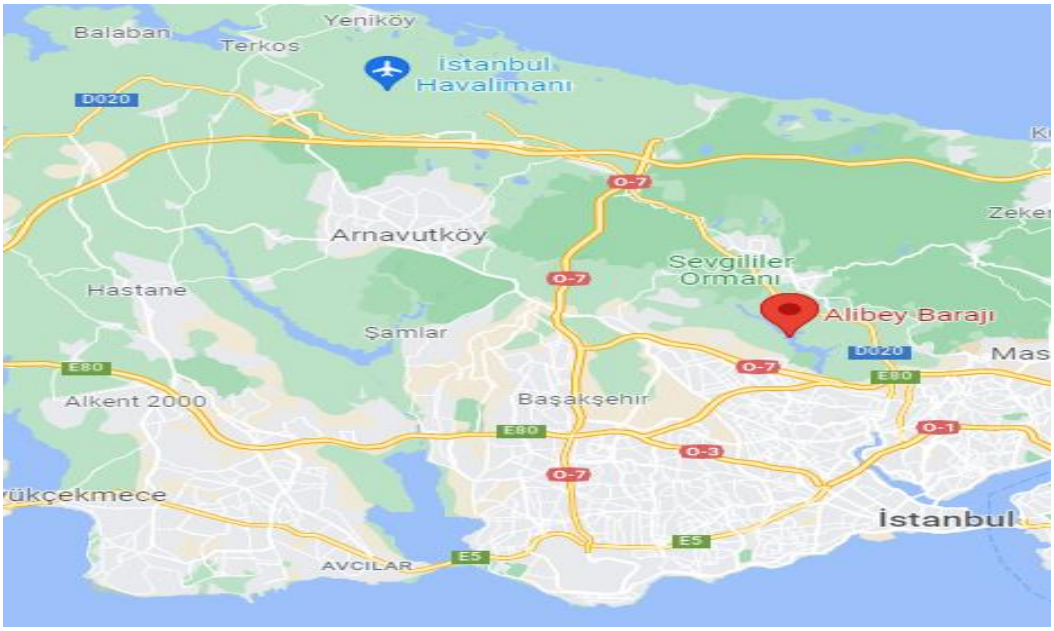

Figure 1. The location of Alibey Dam

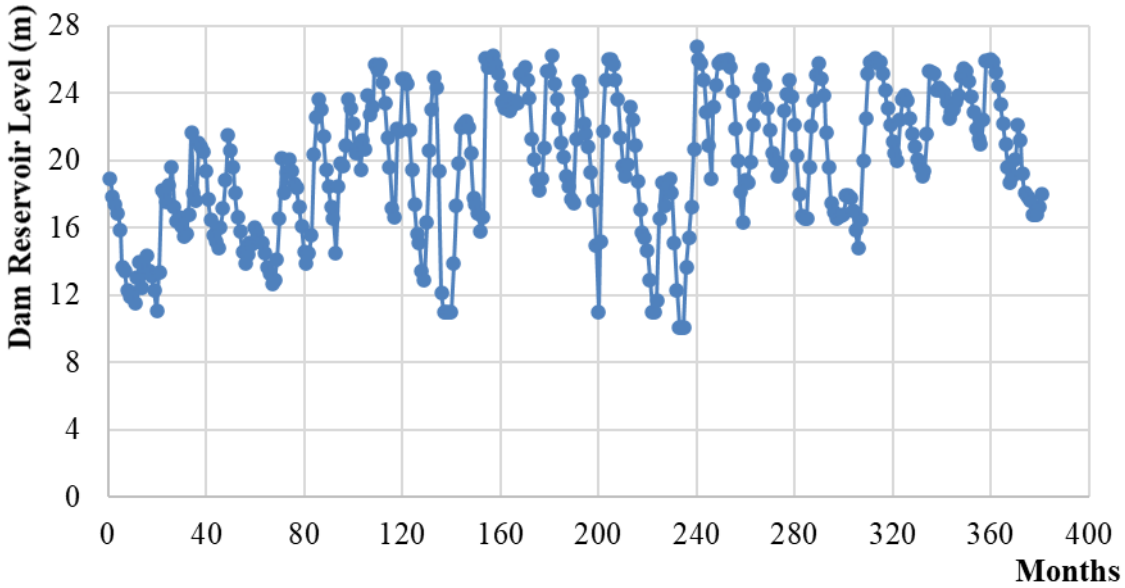

Figure 2. Dam reservoir level (m) variations between 1989 and 2020 years

Multiple Linear Regression (MLR) Method

The multiple linear regression method is a method used to analyze the relationship between one dependent variable and the independent variables. MLR deals with the linear relationship between more than one independent variable and one dependent variable. It is a very common method (Turhan et al., 2016; Tsakiri et al., 2018). If we show the independent variables X and the dependent variable Y, it can be formulated as shown below:

$$Y = A_0 + A_1 * X_1 + A_2 * X_2 \ldots . + A_i * X_i + B \quad (1)$$

Artificial Neural Networks (ANN)

ANN is a computer program created by taking advantage of the ability of the human brain to work and think. Thanks to the ANN, solutions are easily offered to complex problems. Although successful results have been achieved in solving the problems, the assignment of weights in the model is based on black box logic. That is, it is not known how the weights are assigned. The ANN is a method used to solve problems that cannot be expressed mathematically and is defined as a black box model. The general formula of the ANN model is given in Equation 2:

$$Y = f(\sum_{i=1}^{n} Xi * Wi + b_i) \quad (2)$$

In Equation 2, Y shows the dependent variable, X values show the independent variables, W model's layer weights and b model's bias value.

Fuzzy Logic

In real life, very complex events cannot be expressed mathematically. All theories and equations are expressed approximately in real life. The logic developed in order to make these uncertainties more understandable verbally is called FL (Uygunoğlu, 2005). This approach was first mentioned by Zadeh in 1965 in his article "Fuzzy Set" (Zadeh, 1996). FL system; It consists of input, database, fuzzification unit, fuzzy inference mechanism, rule base, defuzzification unit and output (Jang, 1997).

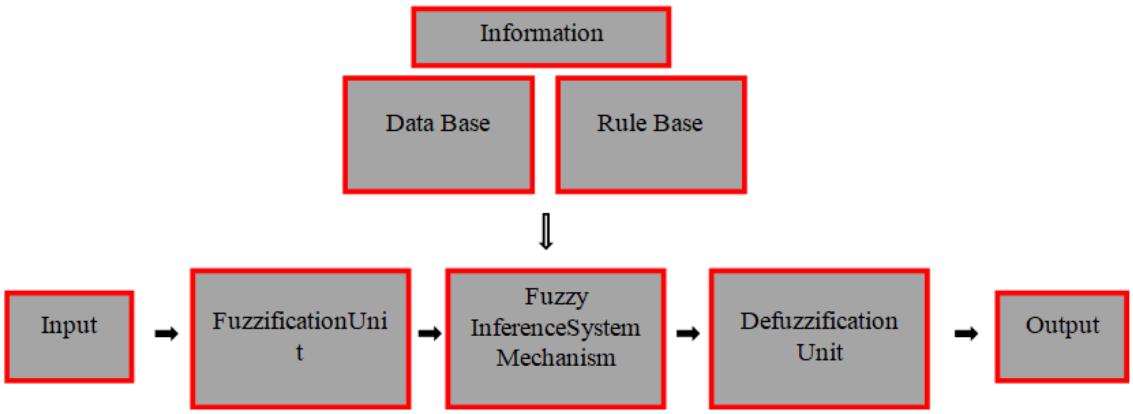

Figure 3. A general fuzzy logic system (Güner, 2014)

Input/Database: Contains input variables affecting the event to be analyzed and all information about them. This information can be numerical or verbal.

Fuzzification Unit: It is the unit in which the necessary transformation is made so that the data coming from the Input/Database section can be processed in the fuzzy extraction mechanism. Membership functions are executed in this unit.

Fuzzy Rule Base Unit: It contains all the rules that can be written as a logical IF-THEN type that binds inputs in the database to output variables.

Fuzzy Inference System Mechanism: This unit is a mechanism that includes all the operations that ensure that the system behaves with a single output by collecting all the partial relations established between the input and output fuzzy sets in the fuzzy rule base. This engine aggregates the implications of each rule and determines how the whole system will output under the inputs.

Defuzzification Unit: It is the unit in which the fuzzy output values (values in the [0-1] Range) are converted to the problem-specific scale at the input.

Output: It is the solution brought by the fuzzy logic system to the problem. It is obtained by passing the fuzzy output formed by the fuzzy extraction mechanism through the defuzzification unit (Uygunoğlu and Ünal, 2005).

In this study, Fuzzy SMRGT method was used in the creation and solution of the Fuzzy Logic model. The fuzzy SMRGT method was first proposed by Fuat Toprak in 2009. The biggest advantage of this method is that the model determines both the fuzzy rule (FRs) base and the membership functions (MFs) together with a very simple technique (Beduk, 2012). On the other hand, since it is completely based on expert opinion, it enables the model to be established without any data. The Fuzzy SMRGT method was first used to calculate the open channel cutoff in the hydraulic field. Afterwards, many studies were carried out in various fields (Hamidi 2013; Toprak, 2013; Toprak, 2015; Altaş, 2018; Bayri, 2018; Çakır, 2018; Derya, 2018; Toprak, 2018).

In the Fuzzy SMRGT method, firstly, the independent variables affecting the dependent variable are determined for the event at hand. Maximum and minimum value ranges are determined for each variable. Then the shape of the membership function is decided. The center and width of the membership functions are determined by their key values for each argument. These key values are the inputs of the fuzzy model. Thus, the Fuzzy SMRGT model is valid for the range of values corresponding to the centroid of the first and last membership function for each independent variable. A table is to give the key values of the outputs and the number of fuzz rules.

$$X_R = X_{\max} - X_{\min} \tag{3}$$

$$UW = \frac{X_R}{n_u} \tag{4}$$

$$EUW = \frac{X_R}{n_u} + A \tag{5}$$

$$A = \frac{UW}{2} \tag{6}$$

$$K_1 = X_{\min} + \frac{EUW}{3} \tag{7}$$

$$K_2 = X_{\max} - \frac{EUW}{3} \tag{8}$$

$$C_i = \frac{X_R}{2} + X_{\min} \tag{9}$$

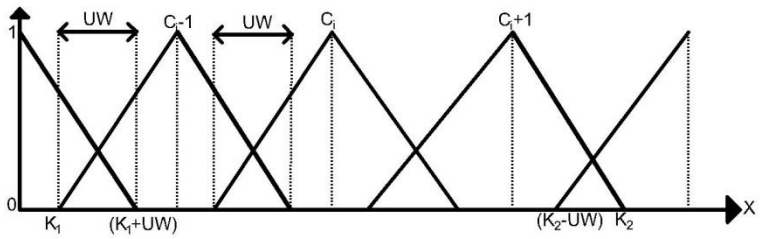

Figure 4. Boundary parameters of the Fuzzy SMRGT method

Table 1. Membership functions and key values range for each parameter

	DDW_t	E_t,	DW_t	LW_t	DRL_{t-1}	DRL_t
N_u	8	8	8	8	8	8
V_{max}	24,62	0,54	15,02	40,01	26,77	26,77
V_{min}	0	0	0	0	10,09	10,09
$V_r=V_{max}-V_{min}$	24,62	0,54	15,02	40,01	16,68	16,68
U_w	3,07	0,06	1,87	5	2,08	2,08
E_{uw}	4,62	0,10	2,81	7,5	3,13	3,13
K_1	1,54	0,03	0,94	2,50	11,13	11,13
K_1+U_w	4,62	0,10	2,82	7,50	13,22	13,22
C_i-1	6,16	0,14	3,76	10,00	14,26	14,26
$C_i-1+E_{uw}-U_w$	7,69	0,17	4,70	12,50	15,30	15,30
$K_2=Ci-1+E_{uw}$	10,77	0,24	6,58	17,51	17,39	17,39
C_i	12,31	0,27	7,51	20,01	18,43	18,43
$C_i+E_{uw}-U_w$	13,85	0,31	8,45	22,51	19,47	19,47
$K_{3+}U_w=C_i+E_{uw}$	16,93	0,38	10,33	27,51	21,56	21,56
C_i+1	18,47	0,41	11,27	30,01	22,60	22,60
K_4-U_w	20,00	0,45	12,21	32,51	23,64	23,64
K_4	23,08	0,51	14,09	37,51	25,73	25,73

In this table, the unit width (UW), kernel value (C_i), key values (K_i), range of variation (V_R), base width (E_{UW}) and nu represent the number of right triangles for each membership function.

Table 2. Statistical values of the models

	DDW_t	E_t,	DW_t	LW_t	DRL_{t-1}	DRL_t
			TRAINING			
V_{max}	24,62	0,54	15,02	40,01	26,77	26,77
V_{min}	0	0	0	0	10,09	10,09
SD	9,17	0,017	6,33	35,49	18,07	18,09
SC	5,46	1,24	0,86	2,32	-0,15	-0,15
			TEST			
V_{max}	10,64	0,49	7,06	24,45	26,11	26,11
V_{min}	0	0	0	0,227	14,78	14,78
SD	2,93	0,025	2,61	16,9	10,17	10,03
SC	4,93	0,686	0,2	2,57	-0,34	-0,33

In this table, measured max value (Vmax), measured min value (Vmin), standaid deviation (SD) and skewness coefficient (SC).

Model Result and Evaluations

In this study, monthly dam reservoir level changes were estimated using Fuzzy SMRGT, MLR and ANN methods. The performances of the obtained results were compared. A total of 381 monthly data for the years 1989-2020 of the Alibey Dam for 31 years were used. In the study, 75% of all data wastraining 25% is reserved for testing. 285 months of data were used for training and 96 months of measurement data for testing. In the Fuzzy SMRGT MLR and ANN model applications, the dam reservoir level value was estimated by using the monthly evaporation amount, the amount of water coming into the lake, the consumption of drinking water and the amount of water discharged.

In all models, 285 months of data were trained and 96 months of data were applied in the testing phase. The test results obtained were compared with the dam reservoir level results. The results according to these comparisons are given in Table 1.

To compare the performance of the models used to predict dam reservoir levels, mean absolute error (MAE), root mean squared errors (RMSE), and correlation coefficient (R) were used (Sahoo et al., 2019; Idrees et al., 2021). These statistical criteria are given in equations (10) and (11), respectively.

$$RMSE = \sqrt{\frac{1}{N}\sum_{i=1}^{N}(\mathrm{DRLt}i_{measured} - \mathrm{DRLt}i_{prediction})^2} \quad (10)$$

$$MAE = \frac{1}{N}\sum_{i=1}^{N}\left|\mathrm{DRLt}i_{measured} - \mathrm{DRLt}i_{prediction}\right| \quad (11)$$

Where N is the number of data in the test phase and DRL_t represents the dam reservoir level value. Statistical MAE, RMSE and R values of the models used in the study are given in Table 3.

Table 3. Statistical results of models

Model	Model Inputs	MAE	RMSE	R
MLR	E_t, LW_t, DW_t, DDW_t, DRL_{t-1}	0,814	1,071	0,952
ANN	E_t, LW_t, DW_t, DDW_t, DRL_{t-1}	0,830	1,046	0,951
SMRGT	E_t, LW_t, DW_t, DDW_t, DRL_{t-1}	0,803	1,033	0,955

MAE: Absolute mean error, RMSE: Root mean squared R: Correlation coefficient.

When Table 3 is examined, it is seen that MLR model, ANN model and Fuzzy SMRGT model give very close results.

Multiple Linear Regression Model Results

In MLR model applications, the average monthly evaporation (E_t), the water coming into the lake (LW_t), the consumption of drinking water (DW_t), the water discharged from the dam (DDW_t) and monthly average dam reservoir level time series (DRL_{t-1}) amounts were used for the estimation of the monthly average dam reservoir level (DRL_t). The distribution and scatter plots of the MLR model are shown in Figures 4 and 5, respectively. As seen in Figures 5 and 6, when the MLR model is applied for test data, it is seen that the model results are close to the real values and the correlation coefficient is 0,9526.

$$Y = 1{,}01 + 0{,}04 * DDW_t + (-2{,}25) * E_t + 0{,}05 * DW_t + 0{,}09 * LW_t + 0{,}92 * DRL_{t-1} \quad (12)$$

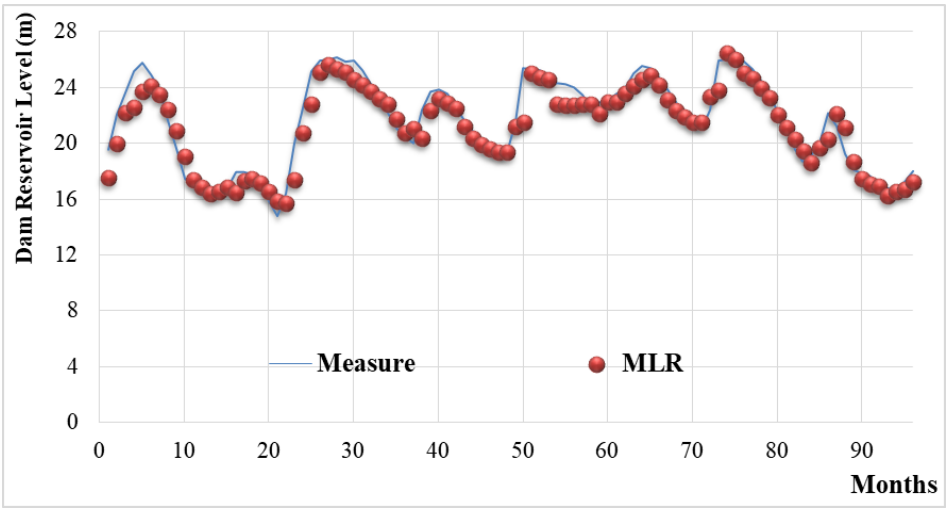

Figure 5. Measurement and MLR distribution plot for monthly average dam reservoir level

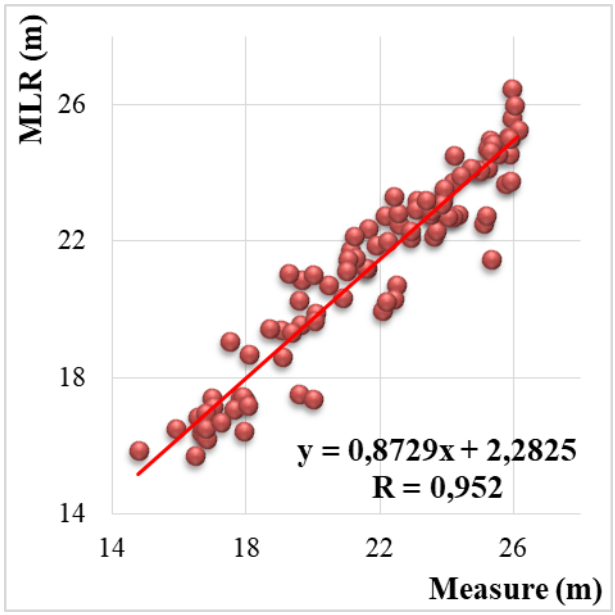

Figure 6. Measurement and MLR scatterplot for monthly average dam reservoir level

Artificial Neural Networks Model Results

In this study, the parameters of the average monthly evaporation (E_t) amount, the amount of water coming into the lake (LW_t), the consumption of drinking water (DW_t) and the amount of water discharged from the dam (DDW_t) obtained and regulated by DSI in ANN model applications, are used for the estimation of the monthly average dam reservoir level (DRL_t). ANN model distribution and scatter plots are shown in Figures 7 and 8, respectively. As seen in Figures 6 and 7, when ANN is applied for test data, it is seen that the model results are close to the real values and the correlation coefficient is 0,951 the fact that the ANN method is very close to the MLR method shows that this method is successful in this study.

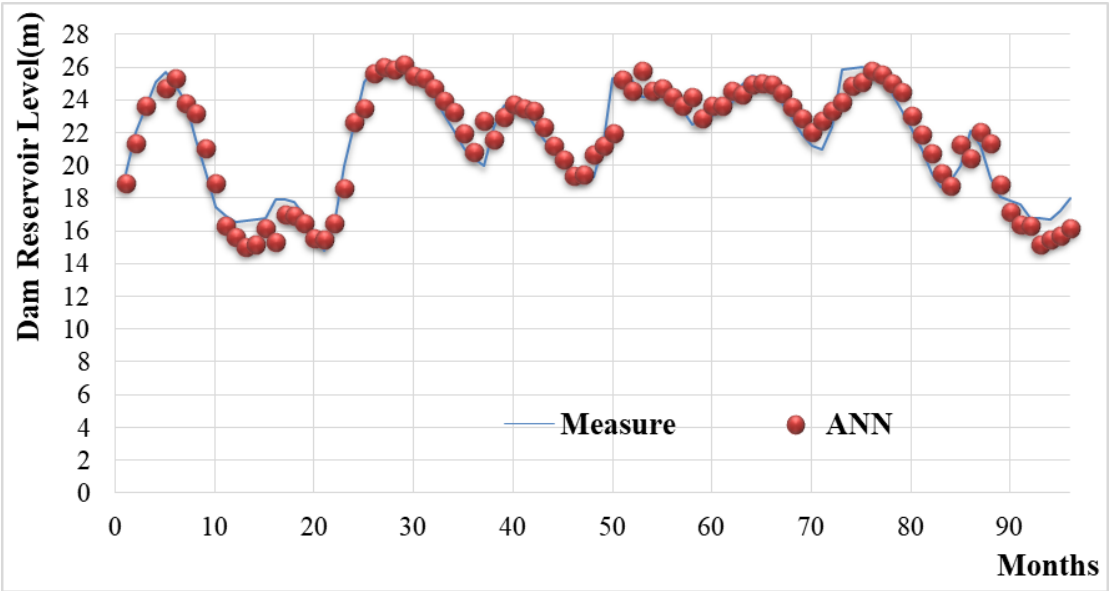

Figure 7. Measurement and ANN distribution plot for monthly average dam reservoir level

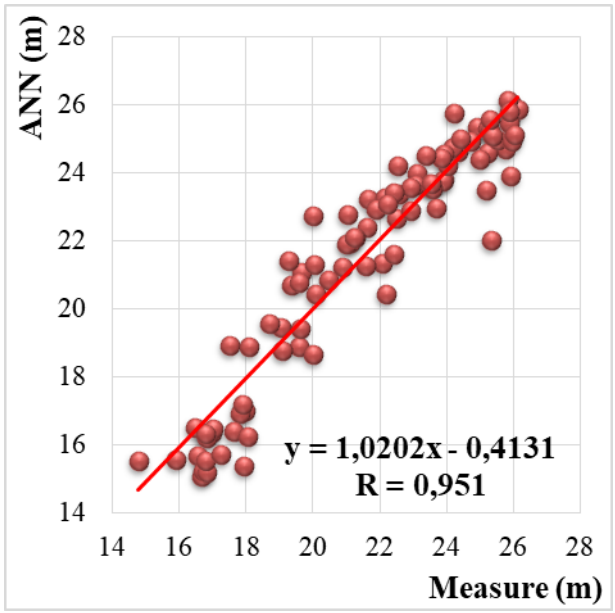

Figure 8. Measurement and ANN scatter plot for monthly average dam reservoir level

Fuzzy SMRGT Model Results

In this study, the parameters of the average monthly evaporation (E_t) amount obtained and regulated by DSI, the amount of water coming into the lake (LW_t), the consumption of drinking water (DW_t) and the amount of water discharged (DDW_t) from the dam were used for the estimation of the monthly average dam reservoir level (DRL_t) in the Fuzzy SMRGT model applications. The Fuzzy SMRGT model distribution and scatter plots are shown in Figures 8 and 9, respectively. As seen in Figures 9 and 10, when applied for Fuzzy SMRGT test data, it is seen that the model results are close to the true values and the correlation coefficient is 0,955. Fuzzy SMRGT method gave slightly better results than ANN and MLR methods. These results show that the Fuzzy SMRGT method can be used.

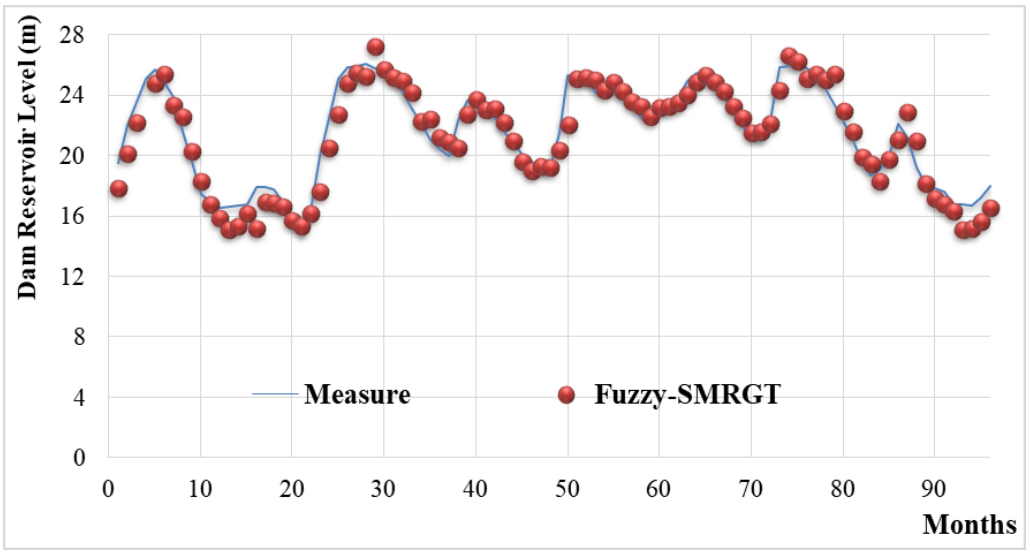

Figure 9. Measurement and SMRGT distribution plot for monthly average dam reservoir level

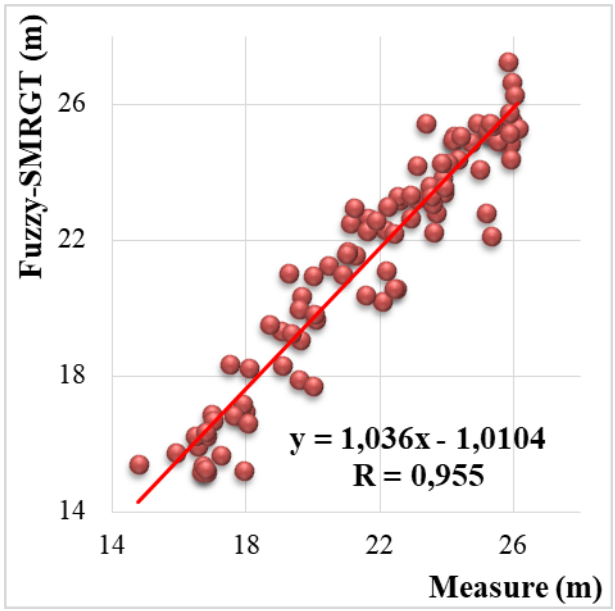

Figure 10. Measurement and SMRGT scatterplot for monthly average dam reservoir level

Result and Discussion

In this study, the monthly average dam reservoir level of Alibey Dam in Sultangazi District of Istanbul between 1989 and 2020 was estimated using the monthly evaporation amount, the amount of water coming into the lake, the consumption of drinking water and the amount of water discharged from the dam. Fuzzy SMRGT, ANNand MLR models were used for dam reservoir level estimation and the models were compared with each other. In the Fuzzy SMRGT, ANN and MLR models, 285 data out of a total of 381 data were applied for training and 96 data were applied for testing. The results obtained with the model were compared with the measurement values. Correlation coefficient (R), (MSE) and (MAE) were calculated for the performance evaluation of Fuzzy SMRGT, ANN and MLR Models. It has been observed that the Fuzzy model gives better results than the ANN model and gives very close results to the traditional MLR model.

The results show that when a Fuzzy SMRGT model is developed for a selected reservoir, monthly reservoir level change, hydroelectric energy calculations and determination of water resources management show that these model results can be used in water resource management studies. In this sense, it is thought that all three models can be used in dam level estimation.Models selected for the level estimation of the Alibey Dam reservoir made correct estimations with results close to each other.In this sense, it is thought that the results of this study can be used by the relevant institutions for future regulation studies for this reservoir.

As a result, Alibey dam is a very important dam in terms of meeting the water needs of the European side of Istanbul. Working with artificial intelligence for the first time on Alibey dam reveals how important this study is. The fact that the Fuzzy SMRGT method gives good results compared to the

ANN and MLR methods shows that the Fuzzy SMRGT method can be preferred in dam reservoir volume studies.

Acknowledgment

In this study, hydrological data measured by the State Hydraulic Works (DSI-TURKEY) was used. The authors thank DSI for measuring and transmitting hydrological data.

Conflict of Interest Statement

The article author declares that there is no conflict of interest.

Contribution Rate Statement Summary of Researchers

All authors declare that they have contributed equally to the article.

*This study was presented as a summary paper at the International Conference on Engineering, Natural and Applied Sciences (ICENAS'21) held online on 24-26 November 2021.

References

Altaş E., Aydın MC., Toprak ZF. Açık kanal akımlarında su yüzü profilinin bulanık SMRGT yöntemiyle modellenmesi. Dicle Üniversitesi Mühendislik Fakültesi Mühendislik Dergisi 2018; 9(2): 975-981.

Arslan H., Üneş F., Demirci M., Taşar B., Yılmaz A. Keban baraj gölü seviye değişiminin Anfis ve destek vektör makineleri ile tahmini. Osmaniye Korkut Ata Üniversitesi Fen Bilimleri Enstitüsü Dergisi 2020; 3(2): 71-77.

Aydemir M. Yapay sinir ağları ile bütçe gelirlerinin tahmini. İnönü Üniversitesi Sosyal Bilimleri Enstitüsü, Yüksek Lisans Tezi, 2020.

Bayri G. Zeminlerin basit üyeli fonksiyonlar ve bulanik kurallar üretim tekniği (SMRGT) ile sınıflandırılması. Bitlis Eren Üniversitesi Fen Bilimleri Enstitüsü, Yüksek Lisans Tezi, 2018.

Beduk F., Aydin ME., Ozcan S. Degradation of malathion and parathionby ozonation, photolytic ozonation, and heterogeneous catalytic ozonation processes. CLEAN–Soil, Air, Water 2012; 40(2): 179-187 (in Turkish).

Çakır Aydın D. İşitsel peyzajda ses çevresi memnuniyet düzeyinin bulanık mantık ile tahmin edilmesi: Diyarbakır Suriçi uygulaması. İstanbul Teknik Üniversitesi Fen Bilimleri Enstitüsü Mimarlık Anabilim Dalı, Doktora Tezi, 2018 (in Turkish).

Karakaya D. Akış katsayısının bulanık SMRGT yöntemi ile modellenmesi. Dicle Üniversitesi Fen Bilimleri Enstitüsü, Yüksek Lisans Tezi, 2018 (in Turkish).

Demirci M., Unes F., Kaya YZ., Mamak M., Tasar B., Ispir E. Estimation of ground water level using artificia neural networks: a case study of Hatay-Turkey. In 10th International Conference Environmenta Engineering Lithuania, 2017 (in Turkish).

Demirci M., Unes F., Kaya YZ., Tasar B., Varcin H. Modeling of dam reservoir volume using Adaptive neuro fuzzy method. Aerul si Apa. Componente ale Mediului 2018; 145-152 (in Turkish).

Gemici E., Ardiçlioğlu M., Kocabaş F. Akarsularda debinin yapay zeka yöntemleri ile modellenmesi. Erciyes Üniversitesi Fen Bilimleri Enstitüsü Fen Bilimleri Dergisi 2013; 29(2): 135-143.

Güner N., Çomak E. Lise öğrencilerinin matematik dersine yönelik tutumlarının bulanık mantık yöntemi ile incelenmesi. Pamukkale Üniversitesi Mühendislik Bilimleri Dergisi 2014; 20(5): 189-196.

Hamidi N., Toprak ZF., Gülsever H., Sungur M. Kuraklık indisinin SMRGT yöntemi ile modellenmesi. III. Türkiye İklim Değişikliği Kongresi İstanbul, Tik dek 2013; 3-5 (in Turkish).

Iraji, H., Mohammadi M., Shakouri B., Meshram SG. Predicting reservoir volume reduction using artificial neural network. Arabian Journal of Geosciences 2020; 13(17): 1-13.

Idrees MB., Jehanzaib M., Kim D., Kim TW. Comprehensive evaluation of machine learning models for suspended sediment load in flow prediction in a reservoir. Stochastic Environmental Research and Risk Assessment 2021; 1-19.

Jang JSR., Sun CT., Mizutani E. Neuro-fuzzy and soft computing-a computational approach to learning and machine intelligence [BookReview]. IEEE Transactions on automatic control 1996; 42(10): 1482-1484.

Kılınç İ. İstanbul'daki baraj haznelerinin işletilmesinde yapay sinir ağları kullanılması. İstanbul Teknik Üniversitesi Fen Bilimleri Enstitüsü İnşaat Anabilim Dalı, Doktora Tezi, 2004.

Kocabaş F., Ünal B., Ünal S., Fedakar HI., Gemici E. Fuzzy genetic approach for modeling of the critical submergence of an intake. Neural Computing and Applications 2013; 23(1): 73-82 (in Turkish).

Küçükerdem TS., Kilit M., Saplıoğlu K. Bulanık çıkarım sistemlerinde kullanılan küme sayılarının K-ortalamalar ile belirlenmesi ve baraj hacmi modellenmesi: Kestel barajı örneği. Pamukkale Üniversitesi Mühendislik Bilimleri Dergisi 2019; 25(8): 962-967.

Latif SD., Ahmed AN., Sherif M., Sefelnasr A., El-Shafie A. Reservoir water balance simulation model utilizing machine learning algorithm. Alexandria Engineering Journal 2021; 60(1): 1365-1378.

Ozel HU., Gemici BT., Gemici E., Ozel HB., Cetin M., Sevik H. Application of artificial neural networks to predict the heavy metal contamination in the Bartin River. Environmental Science and Pollution Research 2020; 27(34): 42495-42512 (in Turkish).

Poul AK., Shourian M., Ebrahimi, H. A comparative study of MLR, KNN, ANN and ANFIS models with wavelet transform in monthly stream flow prediction. Water Resources Management 2019; 33(8): 2907-2923.

Sahoo BB.,Jha R., Singh A., Kumar D. Long short-termmemory (LSTM) recurrent neural network forlow-flow hydrological time series forecasting. Acta Geophysica 2019; 67(5): 1471-1481.

Salam ZKAA., Keskin ME. Yapay sinir ağları ile Dibis barajı'nın seviye tahmini. Mühendislik Bilimleri ve Tasarım Dergisi 2018: 6(4): 564-569.

Şener E., Morova N. Bulanık mantık ve doğrusal regresyon analizleri ile Burdur gölü su seviyesi değişimlerinin modellenmesi. Süleyman Demirel Üniversitesi Fen Bilimleri Enstitüsü Dergisi 2014; 15(1): 60-66.

Taşar B., Ünes F., Demirci M., Kaya YZ. Yapay sinir ağları yöntemi kullanılarak buharlaşma miktarı tahmini. Dicle Üniversitesi Mühendislik Fakültesi Mühendislik Dergisi 2018; 9(1): 543-551.

Tsakiri K., Marsellos A., Kapetanakis S. Artificial neural network and multiple linear regression for flood prediction in Mohawk River, New York. Water 2018; 10(9): 1158.

Toprak ZF., Songur M., Hamidi N., Gulsever H. Determination of losses in water-networks using a new fuzzy technique (SMRGT). Global Journal on Technology 2013; 3: 833-840.

Toprak S., Arife A., Toprak ZF. SMRGT yöntemi ile bulanıklaştırılmış veriler için bulanık doğrusal regresyon. Erciyes Üniversitesi Fen Bilimleri Enstitüsü Fen Bilimleri Dergisi 2015; 31(3): 1-7.

Toprak ZF., Toprak A., Aykaç Z. Bulanık SMRGT yönteminin pratik uygulamaları. Dicle Üniversitesi Mühendislik Fakültesi Mühendislik Dergisi 2017; 8(1): 123-132.

Turhan E., Çağatay HÖ. Eksik akım verilerinin tahmin modelinin oluşturulmasında yapay sinir ağlarının kullanımı: Asi Nehri-Demirköprü akım gözlem istasyonu örneği. Çukurova Üniversitesi Mühendislik-Mimarlık Fakültesi Dergisi 2016; 31(1): 93-106.

Turhan E. A comparative evaluation of the use of artificial neural networks for modeling the rainfall–runoff relationship in water resources. Management. Journal of Ecological Engineering 2021; 22(5): 166-178 (in Turkish).

Uygunoğlu T., Ünal O. Seyitömer uçucu külünün betonun basınç dayanımına etkisi üzerine bulanık mantık yaklaşımı. Yapı Teknolojileri Elektronik Dergisi 2005; 1(1): 13-20 (in Turkish).

Ünes F. Dam reservoir level modeling by neural network approach: A case study. Neural Network World 2010; 20(4): 461 (in Turkish).

Üneş F., Doğan S., Taşar B., Kaya YZ., Demirci M. The evaluation and comparison of daily reference evapotranspiration with ANN and empirical methods. Natural and Engineering Sciences 2018a; 3(3): 54-64 (in Turkish).

Üneş F., Demirci M., Mertcan Z., Taşar B., Varçin H., Ziya YZ. Determination of groundwater level fluctuations by artificial neural networks. Natural and Engineering Sciences 2018b; 3(3): 35-42 (in Turkish).

Üneş F., Demirci M., Taşar B., Kaya YZ., Varçin H. Estimating dam reservoir level fluctuations using data-driven techniques. Polish Journal of Environ Mentals Studie 2019a; 28(5): 3451-3462.

Üneş F., Demirci M., Taşar B., Kaya YZ., Varçin, H. Modeling of dam reservoir volume using generalized regression neural network, support vector machines and m5 decision tree models. Applied Ecology and Environmental Research 2019b; 17(3): 7043.

Üneş F., Maruf AG., Taşar B. Groundwater level estimation for Dörtyol region in Hatay. International Journal of Environment, Agriculture and Biotechnology 2019c; 4(3): 859-864 (in Turkish).

Üneş F., Keskin L., Demirci M. Artificial neural network's method for prediction of rainfall-runoff relation: Regional practice. Natural and Engineering Sciences 2019d; 4(3): 220-230. (in Turkish).

Zadeh LA. Fuzzy sets. In Fuzzy sets, Fuzzy logic and Fuzzy systems: selected papers by Lotfi A Zadeh 1965, pp. 394-432.

OKÜ Fen Bilimleri Enstitüsü Dergisi
5(Özel Sayı):96-107, 2022

OKU Journal of The Institute of Science and Technology, 5(Special Issue):96-107, 2022

Osmaniye Korkut Ata Üniversitesi Fen Bilimleri Enstitüsü Dergisi

Osmaniye Korkut Ata University Journal of The Institute of Science and Technology

An Investigation for the Performance of the Design of Hot Forging Die and Workpiece

Ece Destina BEKLETENLER[1*], Simge İRIZALP[2], Murat DELİBALCI[3]

[1,3] İZELTAS İzmir El Aletleri Sanayi ve Ticaret Inc., 35070, İzmir
[2]Manisa Celal Bayar Universitesi, Mühendislik Fakültesi, Makine Mühendisliği Bölümü, 45140, Manisa

[1]https://orcid.org/0000-0003-2384-1307,
[2]https://orcid.org/0000-0002-0339-5699,
[3]https://orcid.org/0000-0002-9537-3920
Corresponding author: ece.bekletenler@izeltas.com.tr

Research Article

Article History:
Received: 06.12.2021
Accepted: 15.01.2022
Published online: 23.02.2022

Keywords:
Hot forging
Process cost
Die and workpiece design
Finite volume analysis

ABSTRACT

Hot forging is a metalworking process in which metals are plastically deformed above their recrystallization temperature, allowing the material to retain its deformed shape as it cools. In today's industry, the performance of the tools used during the hot forging process has always been a subject of interest. Although it is known that, the tool life used affects 10% of the design costs of the total budget, 80% of the total production costs are determined during the design stages. For this reason, minimizing mechanical stress and changing the die design, so as to optimize the tool life and reduce the cost, have been attractive. In this study, finite volume analysis was performed on 31CrV3 steel using the multi-stage forming process of hot closed die forging using Simufact Forming v16 software. 56NiCrMoV7 hot work tool steel was used as die material and X153CrMoV12 as template blade raw material. In this article, 3 state variables, effective plastic strain, equivalent stress and temperature were evaluated for two different die designs of multi-stage forming processes such as pre-forming, final forging, and cutting. The results were compared for cost for single and dual dies. For both die designs, the initial temperature of the billet is 1100-1200 ºC and the die temperature is 100-110 ºC. Finally, comparative analyzes of both die designs for three state variable parameters were performed in terms of mechanical properties and cost. The main focus is on calculating mechanical properties and cost based on available process parameters using subroutines during the incorporation of different die designs. According to the results obtained from the simulation study, the manufacturability of the product has been proven, the effect of the changes in the die and workpiece design on the cost have been investigated, and the final performance has been revealed by evaluating the profit rate.

Sıcak Dövme Kalıp ve İş Parçasının Tasarımının Performansı Üzerine Bir Araştırma

Araştırma Makalesi

Makale Tarihçesi:
Geliş tarihi: 06.12.2021
Kabul tarihi:15.01.2022
Online Yayınlanma: 23.02.2022

Anahtar Kelimeler:
Sıcak dövme
Proses maliyeti

ÖZET

Sıcak dövme, metallerin yeniden kristalleşme sıcaklıklarının üzerinde plastik olarak deforme edildiği ve malzemenin soğudukça deforme şeklini korumasını sağlayan bir metal işleme sürecidir. Günümüz endüstrisinde sıcak dövme işlemi sırasında kullanılan takımların performansı her zaman ilgi konusu olmuştur. Kullanılan takım ömrünün toplam bütçenin tasarım maliyetlerinin %10'unu etkilediği bilinmesine rağmen, toplam üretim maliyetlerinin %80'inin tasarım aşamalarında belirlendiği bilinmektedir. Bu

Kalıp ve iş parçası tasarımı
Sonlu hacimler analizi

nedenle, takım ömrünü optimize etmek ve maliyeti azaltmak için mekanik stresi en aza indirmek ve kalıp tasarımını değiştirmek cazip olmuştur. Bu çalışmada, Simufact Forming v16 yazılımı yardımıyla, kapalı kalıpta sıcak dövmenin çok aşamalı şekillendirme prosesi kullanılarak, 31CrV3 çeliği üzerinde sonlu hacim analizi yapılmıştır. Kalıp malzemesi olarak 56NiCrMoV7 sıcak iş takım çeliği, şablon bıçak hammaddesi olarak X153CrMoV12 kullanılmıştır. Bu makalede, ön şekillendirme, son dövme ve kesme gibi çok aşamalı şekillendirme proseslerinin iki farklı kalıp tasarımı için 3 durum değişkeni, efektif plastik gerinimi, eşdeğer gerilmesi ve sıcaklık değerlendirilmiştir. Sonuçlar, tekli ve ikili kalıplar için maliyet açısından karşılaştırılmıştır. Her iki kalıp tasarımı için de iş parçasının başlangıç sıcaklığı 1100-1200 ºC ve kalıp sıcaklığı 100-110 ºC'dir. Sonuç olarak, üç durumlu değişken parametre için her iki kalıp tasarımının mekanik özellikler ve maliyet açısından karşılaştırmalı analizleri yapılmıştır. Ana odak noktası, farklı kalıp tasarımlarının dahil edilmesi sırasında alt rutinler kullanılarak mevcut proses parametrelerine dayalı mekanik özelliklerin ve maliyetin hesaplanmasıdır. Simülasyon çalışmasından elde edilen sonuçlara göre ürünün üretilebilirliği ispatlanmış, kalıp ve iş parçası tasarımındaki değişikliklerin maliyete etkisi araştırılmış ve elde edilen kar oranı değerlendirilerek nihai performans ortaya konmuştur.

To Cite: Bekletenler ED., İrizalp S., Delibalcı M. An Investigation for the Performance of the Design of Hot Forging Die and Workpiece. Osmaniye Korkut Ata Üniversitesi Fen Bilimleri Enstitüsü Dergisi 2022; 5(Özel sayı): 96-107.

Introduction

Hot forging is one of the popular methods in which the workpiece is deformed under impact or pressure by means of tools called dies. Closed die hot forging is one of the most adopted methods for creating complex shaped parts with satisfactory geometric accuracy. More than 60% of industrial parts are produced with this method, due to its high strength and part production speed (Kumar and Kumar, 2019). Parameters such as temperature, raw material geometry and die design are effective in reducing production costs and increasing part quality. If the design and manufacture of parts are based on experience, the process can result in time loss and high costs. Optimizing the design of the part and die is essential to reduce the cost of the forging process and make it suitable for other production methods. (Maarefdoust and Kadkhodayan, 2010). The closed die hot forging process and the process affecting the cost improvements are shown in Figure 1 (Campi et al., 2020).

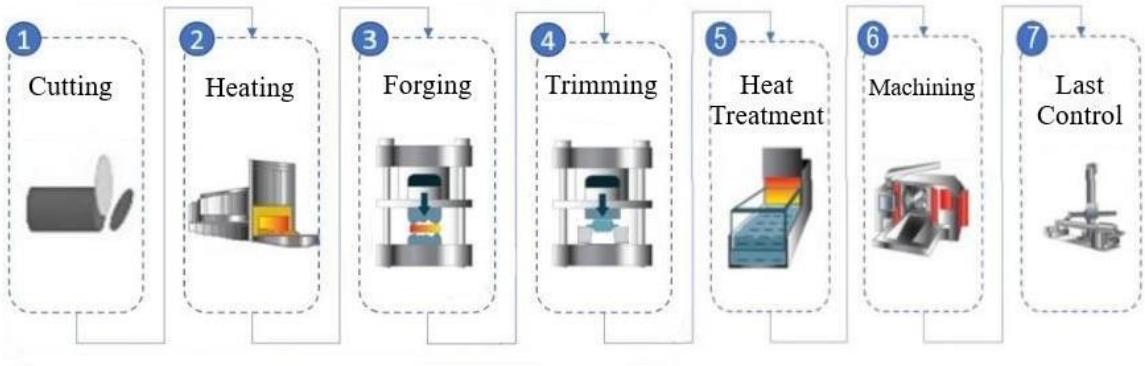

Figure 1. Hot forging process in a closed die (Campi et al., 2020)

Tool costs in hot forging can constitude 30% of the total process cost. Besides, tool production costs (die production cost) can directly affect the process parameters (repair, press downtime, scrap, rework, etc.). The most important factors to determine the tool life are die material, heat treatment and hot forging process control. In the production of hot forging dies, the material constitudes 5-15% of the total process cost and 5-15% of the heat treatment cost (Chander and Chawla, 2017). Figure 2 shows the die steel and machining costs according to the total tooling costs.

Figure 2. Tooling cost illustration (Chander and Chawla, 2017)

Cost estimation is a design task that provides the classification of cost items of both materials and processes prior to the manufacturing process (Campi, 2020). Today, companies have to provide product, and tool costs in a quality manner at competitive prices. With the advancement of technology and the development of computer-aided engineering (CAE) technology in the forging industry, production efficiency and product quality have been increased by reducing the product development cycle and product cost (Jha, 2016). Hot forging method can be simulated with two different methods as finite element method (FEM) and finite volume method (FVM). Santos et al. (2001) used FEM to determine the size of the billet material of the workpieces and the forces to be applied. The authors argued that, numerical simulation can actually aid modification and reduce the trial and error step in preparing tools for forging. The FVM and FEM method can also provide an important answer in predicting the process and defects. The place of die design and FEM analysis in the hot forging process flowchart are shown in Figure 3. Takemasu et al. (1996) designed the optimum preform die for the flashless forging of a connecting rod and proving the manufacturability by simulating with FEM by reducing pre-process trials. Meng et al. (2010) simulated the forging process combined with an optimization procedure to obtain optimal parameters of the geometry of the forging dies. Such forging processes are affected by material waste, die design, energy-saving, lubricant design, etc. Many different studies have been conducted on parameters. In this study, the manufacturability of the 25 × 28 mm double ended open-jaw wrench short pattern product, which was currently produced by using the single workpiece hot forging method, with dual workpieces in the simulation environment using CAE software, and the effect of die and workpiece design on the product cost were investigated.

The cost of single and dual forging methods was calculated by considering the effect of die and workpiece design on cutting, heating, and forging processes in the hot forging process, and both their mechanical properties, unit product costs and tool costs were investigated.

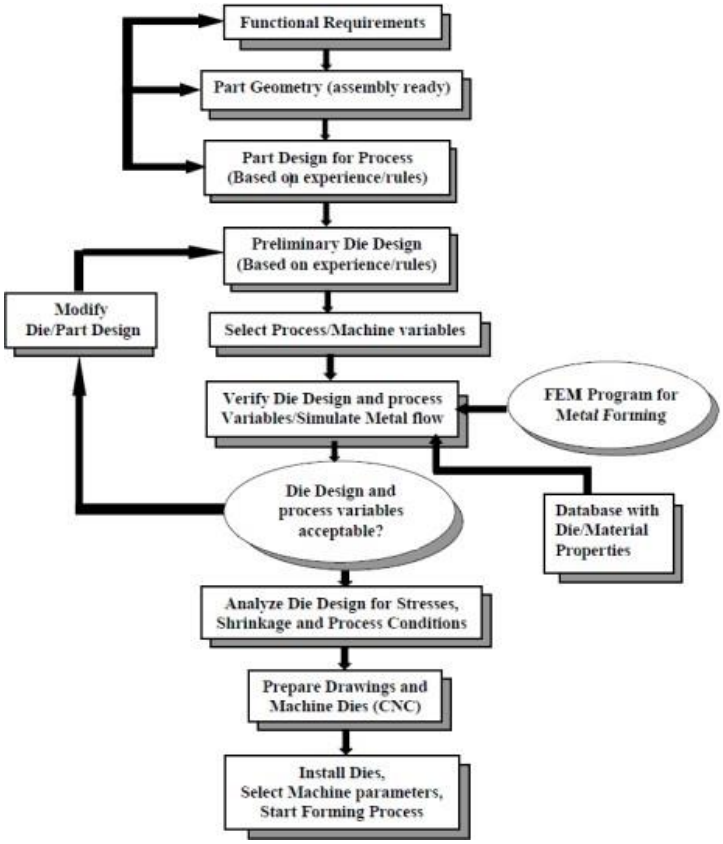

Figure 3. A flowchart illustrating forging process design (Altan and Shirgaokar, 2008)

Material and Method

In the study, a comprehensive research was conducted to understand the die design and forging process. For the short length product of the 25 × 28 mm double-edged wrench shown in Figure 4, 3D models of the dual die and workpiece were created. The workpiece forging temperature was 1100-1200 ℃ and the die temperature is 100-110 ℃. DIN 31CrV3 was used as workpiece raw material, DIN 56NiCrMoV7 hot work tool steel was used as forging die raw material, DIN X153CrMoV12 was used as template blade raw material. The chemical compositions of raw materials and die steels were determined by spectrometry analysis, which was shown in Table 1. A hammer with a capacity of 1200 kg was used as a forging bench. Machine capacity, workpiece forging temperature, die temperature and stroke numbers were kept constant and forging was carried out in single and dual dies. Only cutting and forging processes were based on cost estimation. Table 2 shows the parameters affecting the cutting and forging process costs.

Figure 4. 25 × 28 mm double ended open jaw wrench short pattern

Table 1. DIN 31CrV3, 56NiCrMoV7 and X153CrMoV12 chemical composition

STEEL	C%	Si%	Mn%	Cr%	Mo%	Ni%	V%
DIN 31CrV3	0.33-0.36	0.25-0.40	0.40-0.60	0.40-0.70	0.027	0.145	0.07-0.12
DIN 56NiCrMoV7	0.50-0.60	0.10-0.40	0.60-0.90	0.80-1.20	0.35-0.55	1.50-1.80	0.05-0.15
DIN X153CrMoV12	1.45-1.60	0.10-0.60	0.20-0.60	11.0-13.0	0.70-1.00	-	0.70-1.00

Table 2. Process parameters required for cost estimation

PROCESS NAME	PARAMETERS AFFECTING OF PROCESS COST
CUTTING	CUTTING BLADE RAW MATERIAL CUTTING BLADE PRODUCTION WORKPIECE RAW MATERIAL HOURLY WORKPIECE CUTTING CUSTOMS
FORGING	FORGING DIE RAW MATERIAL FORGING DIE PRODUCTION HOURLY LABOR COSTS

The products were produced by the multi-stage hot forging method. In multi-stage forging, the final shape of the product was obtained by deforming the initial geometry of the workpiece at various stages. In Figure 5, single and dual forging die models (upper and lower dies) and workpiece initial geometries are shown comparatively. Preforming, straight stroke, first and second shaping and finishing stages for multiple die forging simulations of 25 × 28 mm double-ended open jaw wrench short pattern product were simulated using Simufact Forming V16 and the manufacturability of the product was investigated. Besides, the cost estimations of cutting and forging processes, which were affected by the change in die and workpiece design were made. It is possible to classify the cost estimation methods as heuristic, analogical, parametric and analytical methods. Heuristic methods are based on past experiences. Analogical methods start from other products whose costs are calculated and make cost estimation using common parameters. Parametric methods, on the other hand, estimate the cost from the parameters used by the designers. Finally, analytical methods such as the activity-based forecasting method (ABC) allow the evaluation of the total cost of a product by decomposing the product's production steps into key tasks, operations, or activities with known (or easily calculated) costs (Rezaie et al., 2008). In this study, cost estimation was carried out with the activity-based costing

software used in Izeltas. The effect of die and workpiece design changes on unit product cost and tool cost was calculated and compared for single and dual die forging.

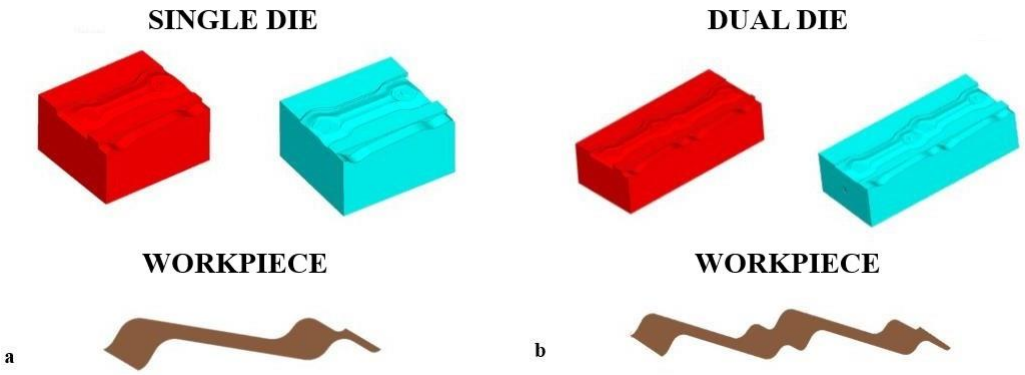

Figure 5. a) Single die and workpiece b) Dual die and workpiece

Results and Discussion

FVM is the underlying method of commercial simulation software, mostly derived for the solution of computational fluid dynamics and closed die forging with flash processes. Just like in FEM, the basic principle in FVM is to divide the geometry to be solved into parts and to find the general solution by combining the solutions, after making a solution for each of these parts (Kilerci, 2017). The simulation is used to study the flow of metal in the die cavity and to determine the energy required for the forming process. As a result of the simulation studies, the 25 × 28 mm double-ended open-jaw wrench short pattern length final product obtained after forging is shown in Figure 6. The final shape of the 25 × 28 double-ended open-jaw wrench short pattern product, which is forged in single and dual dies, is shown in Figure 7.

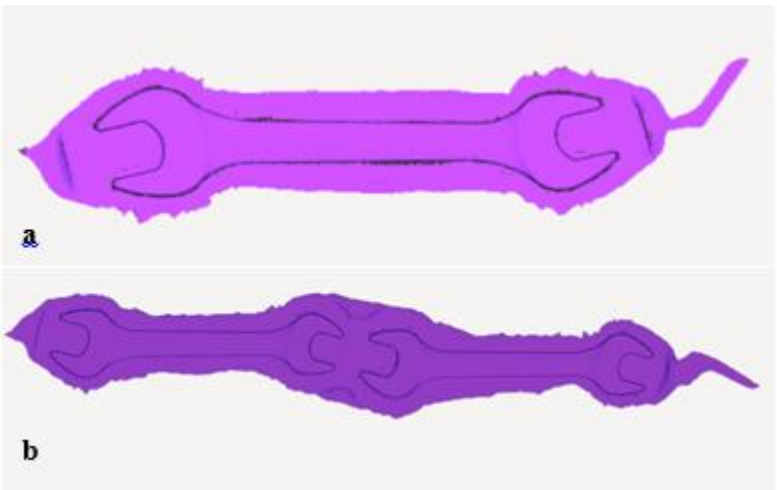

Figure 6. Single (a) and dual (b) 25 × 28 mm double-ended open-jaw wrench short pattern final shape obtained from simulation

Figure 7. Single (a) Dual (b) 25 × 28 mm double-ended open-jaw wrench short pattern final shape after hot forging

The press currently used has a total energy of 12936 J. The simulated force required for the single and dual die forging process is plotted in Figure 8, as a function of the press stroke. In the results shown in Figure 8, it was determined that, the dual forging die workpiece design was faultless, and the forging energy was within the energy limits of the currently used press. The peaks of the curves seen in the graphs show the energy transferred by the stroke of the press during the forging process. The rises correspond to the beginning of intensive material flow into the lateral openings − formation of the open-jaws After reaching the maximum value, the load sharply drops. This is known as the calibration step in which there is no vertical motion of the lower die (Milutinović et al., 2017). The fact that, the second curve is high in the product forged with a single mold is entirely at the discretion of the operator, therefore the energy percentages of the strokes are entered according to the program system according to the actual process applied in the company. Due to the deformation of the workpiece, the impact energies are assigned differently in single and dual forging. The differences in the stroke values vary depending on the plastic deformation in the material. With the changes made in the dual workpiece design, the force required for deformation has been reduced, due to the increase in the contact area and lateral loads. Since this is the opposite of a single workpiece, the stroke distance had to be increased in order to obtain the desired part properties.

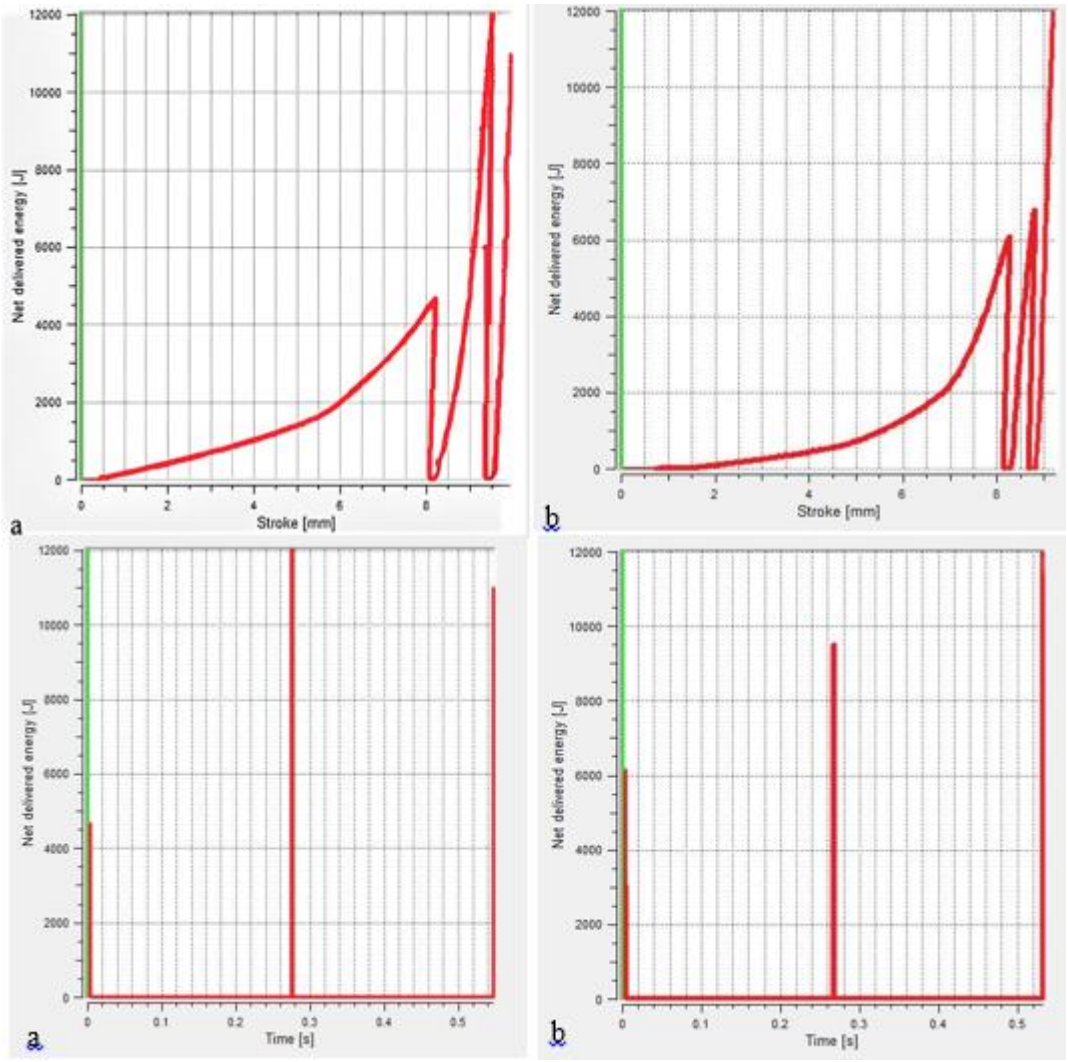

Figure 8. Net delivered energy from the hammer from the hammer depending on time and distance (a) single die (b) dual die

Equivalent stress and effective plastic strain results for both single forging and dual forging are shown in Figure 9, comparatively. Equivalent stress is slightly higher for single forging compared to dual forging. The gradual increase in die force, the reduction in effective plastic strain leading to minimal plastic deformation were present during the final forging stages for double forging as compared to single forging. This may limit grain structure improvement. According to the results shown in Figure 9, higher effective plastic strain values were obtained in the key body and burr region. The areas that undergo the most deformation are the burr line and the body part. High effective plastic strain values are seen where the deformation is high (plastic deformation). The reason why the effective plastic strain values are slightly higher in the dual forged product can be explained as the increase in the surface area of the workpiece geometry. Temperature values of workpieces for single and dual forging were given in Figure 10. The temperature field is more uniform in single forging. However it is noteworthy that, the part that affects the homogeneity is the burr region with a large surface area. In this case, the tendency of crack propagation may be in question for the circumference region, it is clear

that, the temperature distribution in the main workpiece is also homogeneous in dual forging (Milutinović et al., 2017).

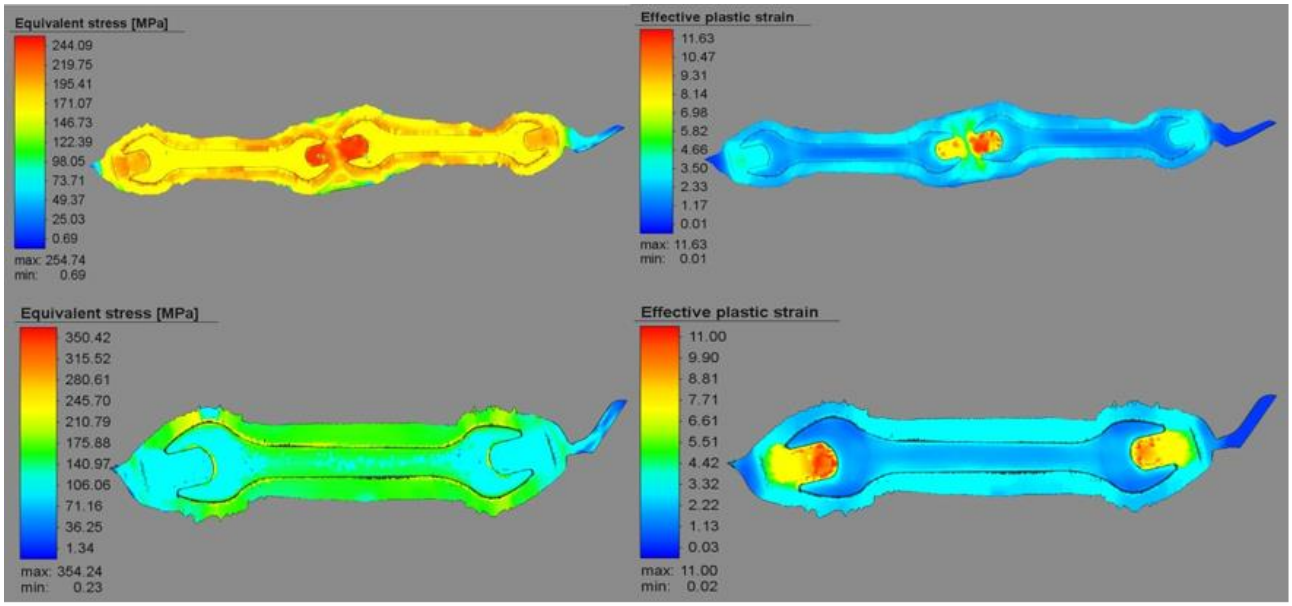

Figure 9. Comparison of equivalent stress and effective plastic strain for single and dual forging

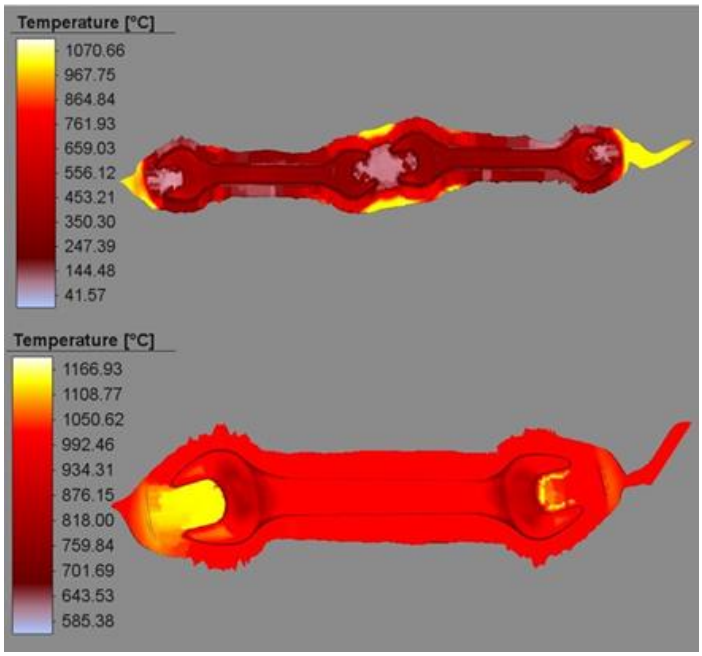

Figure 10. Temperature values for single and dual forging

The total costs of forging die, workpiece and cutting blade are calculated for single and dual forging die and given in Table 3. In line with the results, it was calculated that, 153000 products were produced during the total tool life with a single forging die and 544000 items could be produced with a dual die forging. According to the results, the dual forging dies increases the production of 25 × 28

mm double-ended open-jaw wrench short pattern products by 255% in the same cycle time. A similar study was investigated by Shirgaokar (2008). The author developed an FEA-based design and optimization sequence to improve material yield in multi-stage hot forging processes, using volume distribution analysis and achieved a 15% improvement in material yield for a sample process with preforming optimization alone. An additional 3-4% improvement is envisaged through the optimization of the blocking die design.

Table 3. Single and dual forging die, cutting blade and workpiece total cost

PROCESS DETAILS	TOTAL COST (€)
SINGLE DIE+WORKPIECE+CUTTING BLADE	160.930,42
DUAL DIE+WORKPIECE+CUTTING BLADE	271.907,73

In addition to these, the effect of the total die cost on the unit product cost was calculated and examined by considering the parameters given in Table 2. According to the data presented in Table 4, a profit of 0.052 € is obtained per unit product. The average life of a tool is two years, if it is used continuously. With the dual die, 391000 products will be over-forged in two years. The projected profit amount is foreseen as 20,332 € for 391000 products. Considering that the annual sales volume for the product under investigation is 50000, it will be possible to produce these products in 11 batches with a single die, while annual sales can be produced in 3 batches with a dual forging die. In this way, the forging machine will be freed, and an extra production bench will be provided for other products.

Table 4. Profit per unit product

SINGLE DIE UNIT COST	1,051 €
DUAL DIE UNIT COST	0,99 €
UNIT PROFIT	0,052 €

Conclusion

The main purpose of this study is to investigate the effect of the hot forging process stages on the mechanical properties and the product cost, and to prove the feasibility of design changes in the forging die and workpiece with a 3D simulation program. It has been researched that, production can be carried out with newly designed dies and workpieces without trial production costs in the virtual environment created before real production. As a result of the simulation studies, it has been proven that, production can be made by simply changing the die and workpiece design by using the same hammer and technique with the dual forging die. Equivalent stress is maximum during the final forging stages for single forging compared to dual forging. With the gradual increase in die force, a decrease in effective plastic strain leads to minimum plastic deformation, which thusly may limit grain structure refinement during final forging stages for dual forging compared to single forging. The final temperature distribution is homogenous in both forging processes. Burr region is also affected and

gradually increases in dual forging. After the simulation studies, the effects of cutting and forging parameters on tool and unit product costs were calculated. The products are actually produced with the newly designed die and workpiece. The results showed that this complex production process can be produced with the help of the software mentioned above, with less cost and time loss. As a result of the study, it is presented by proving that, high profitability can be obtained by simply changing the die and workpiece design using the same hammer and technique with dual forging dies. When the unit product profit obtained is calculated over the annual product sales, it is estimated that it will reach a high figure.

Acknowledgement

The authors would like to thank IZELTAS Izmir El Aletleri Sanayi ve Ticaret A.S. support of the study.

Conflict of Interest Statement

The authors of the article declare that there is no conflict of interest between them.

Contribution Rate Statement Summary of Authors

The authors declare that they have contributed 100% to the article.

*This study was presented as a summary paper at the International Conference on Engineering, Natural and Applied Sciences (ICENAS'21) held online on 24-26 November 2021.

References

Altan T., Shirgaokar M. Simulation based process design for improvement of profitability in the hot forging industry. In 19th International Forging Congress 2008; 615.

Campi F., Mandolini M., Favi C., Checcacci E., Germani M. An analytical cost estimation model for the design of axisymmetric components with open-die forging technology. The International Journal of Advanced Manufacturing Technology 2020; 110(7): 1869-1892.

Chander S., Chawla V. Failure of hot forging dies–an updated perspective. Materials Today Proceedings 2017; 4(2): 1147-1157.

Jha SK. Cost optimization of a forged steel crankshaft in global manufacturing environment. International Journal of Mechanical Engineering Research and Technology 2016; 2(2): 16-28.

Kilerci İ. Computer aided investigation of the effect of mechanical properties on metal forming production parameters. Manisa Celal Bayar Üniversitesi, Manisa, Doctoral Dissertation 2017.

Kumar OP., Kumar V. Optimization of the process parameters of forging of pitman arm. International Journal of Engineering Science Invention 2019; 8(08): 01-11.

Maarefdoust M., Kadkhodayan M. Simulation and analysis of hot forging process for industrial locking gear elevators. 14th International Conference on Applied Mechanics and Mechanical Engineering 2010; 14, 1-10.

Meng F., Labergere C., Lafon P. Methodology of the shape optimization of forging dies. International Journal of Material Forming 2010; 3(1): 927-930.

Milutinović M., Baloš S., Plančak M., Movrin D. Comparison of some mechanical properties and micro-topography of a component with non-axisymmetric geometry manufactured by cold orbital and hot forging. Journal of Materials Processing Technology 2017; 249: 179-192.

Rezaie K., Ostadi B., Torabi SA. Activity-based costing in flexible manufacturing systems with a case study in a forging industry. International Journal of Production Research 2008; 46(4): 1047-1069.

Santos AD., Duarte JF., Reis A., Rocha B., Neto R., Paiva R. The use of finite element simulation for optimization of metal forming and tool design. Journal of Materials Processing Technology 2001; 119(1-3): 152-157.

Shirgaokar M. Technology to improve competitiveness in warm and hot forging: Increasing die life and material utilization. The Ohio State University, Ohio Doctoral Dissertation 2008.

Takemasu T., Vazquez V., Painter B., Altan T. Investigation of metal flow and perform optimization in flashless forging of a connecting rod. Journal of Material Process Technology 1996; 59: 95-105.

OKÜ Fen Bilimleri Enstitüsü Dergisi
5(Özel Sayı):108-116, 2022

OKU Journal of The Institute of Science and Technology, 5(Special Issue):108-116, 2022

Osmaniye Korkut Ata Üniversitesi Fen Bilimleri Enstitüsü Dergisi

Osmaniye Korkut Ata University Journal of The Institute of Science and Technology

COVID-19 Real Time PCR Test Sonuçlarının PCR Cihazı ve CAtenA Smart PCR Bioinformatik Programı Üzerinden Değerlendirme Sürelerinin Karşılaştırılması

Ayşe Rüveyda UĞUR[1*], Habibe ÖVET[2]

[1]Medical Microbiology, Konya City Hospital, Konya, Turkey
[2]Medical Microbiology, Konya City Hospital, Konya, Turkey

[1]https://orcid.org/0000-0002-9622-6404
[2]https://orcid.org/0000-0001-8920-0612
*Sorumlu yazar: ayserugur@gmail.com

Araştırma Makalesi

Makale Tarihçesi:
Geliş tarihi: 17.12.2021
Kabul tarihi: 17.01.2022
Online Yayınlanma: 23.02.2022

Anahtar Kelimeler:
CAtenA Smart PCR
COVID-19
Veri analizi
Yapay zekâ
Analiz süresi

ÖZET

İlk kez Aralık 2019'da Çin'in Wuhan eyaletinde ortaya çıkan SARS-CoV-2 kaynaklı COVID-19 enfeksiyonu, tüm dünyada yıkıcı etkisini hala sürdüren bir pandemiye neden olmuştur. COVID-19 tanısında kullanılan standart tanı yöntemi nükleik asit çoğaltma yöntemidir. CAtenA Smart PCR, yapay zekâ kullanarak PCR veri analizi yapan ve kullanıcıya sonuç önerisinde bulunan bioinformatik bir programdır. Bu çalışmanın amacı, uzman hekimin PCR test verilerini cihaz başında değerlendirerek, sonuçları laboratuvar bilgi yönetim sistemine aktarma süresi ile CAtenA Smart PCR üzerinden değerlendirme süresi arasındaki farkın kıyaslanmasıdır. Konya Meram Devlet Hastanesi COVID-19 PCR Tanı Laboratuvarında 1 Eylül-30 Kasım 2021 tarihleri arasında çalışılmış ve her biri 94 farklı örnek ve iki iç kalite kontrolden oluşan 139 PCR çalışma verisi uzman hekimler tarafından PCR cihazından (Bio-Rad CFX96 Touch, Singapore) ve CAtenA programı (Ventura, Ankara, Turkey) üzerinden değerlendirilerek analiz süreleri kayıt altına alınmıştır. PCR cihazı üzerinden yapılan 139 teste ait ortalama analiz süresi 14,05 ± 7,55 dakika, CAtenA programı üzerinden yapılan ortalama analiz süresi 8,04 ± 3,93 dakika olarak bulunmuştur. Wilcoxon signed ranks testi ile istatistiksel analiz yapılmıştır. Analiz süreleri arasında anlamlı bir fark olduğu belirlenmiştir (p = 0,0001). Çalışma süreci, pozitiflik oranlarının veri analiz süresine etkisini görmek için yüksek pozitiflik ve düşük pozitiflik dönemi olmak üzere ikiye ayrılmıştır. İki grubun analiz süreleri arasında anlamlı fark olduğu belirlenmiştir (p = 0,0001). Bulguların vaka pozitiflik oranlarının PCR cihazı ve CAtenA üzerinden yapılan analiz sürelerini etkilediği görülmüştür. Sonuç olarak, PCR verilerini ön analizden geçirerek uzman onayına sunan ve sonuçları web tabanlı sonuç sistemine doğrudan aktarabilen CAtenA Smart PCR yapay zekâ programının, veri analiz süresini kısalttığı ve kullanıcıya kolaylık sağladığı belirlenmiştir.

Comparison of the Turnaround Times of COVID-19 Real Time PCR Data on the PCR Instrument and the Catena Smart PCR Bioinformatics Program

Research Article

Article History:
Received: 17.12.2021
Accepted:17.01.2022
Published online: 23.02.2022

Keywords:

ABSTRACT

The COVID-19 pandemic, which was caused by the SARS-CoV-2 virus, emerged in Wuhan, China in December 2019, and has had a detrimental impact worldwide. The nucleic acid amplification tests are the recommended method for the diagnosis of COVID-19. CAtenA Smart PCR is an artificial intelligence-based bioinformatics tool that assists with PCR data interpretation

CAtenA Smart PCR
COVID-19
Data analysis
Artificial intelligence
Turnaround time

and offers conclusion preferences before transaction to the web-based result systems. The aim of this study was to compare the turnaround times between the data analysis on a PCR instrument, including result submission, and the CAtenA Smart PCR-assisted analysis. The specialists assessed 139 PCR data sets, each with 94 samples and two internal controls, that were performed in the COVID-19 PCR Diagnostic Laboratory at Meram State Hospital in Konya between 1 September and 30 November 2021. The data analysis times for the PCR tool (Bio-Rad CFX96 Touch, Singapore) and the CAtenA Smart PCR Bioinformatics Program (Ventura, Ankara, Turkey) were recorded. The mean time duration of the 139 PCR data analyses for the PCR device was 14.05 ± 7.55 and 8.04 ± 3.93 minutes for the CAtenA. The Wilcoxon signed ranks test was used for the statistical analysis. The difference between the turnaround times for the PCR instrument and CAtenA Smart PCR was found to be statistically significant (p = 0.0001). We further divided the study period into two groups: the high-positivity phase and the low-positivity phase. We compared the two phases in order to assess the effect of the case positivity rates on the turnaround times. There was a significant difference between the turnaround times of the two groups (p = 0.0001). The findings showed that the positivity rate has affected the time duration of data analysis on both the PCR instrument and the CAtenA program. As a result, employing artificial intelligence-based CAtenA Smart PCR to interpret PCR data and send transactions to the web-based result systems reduces the time it takes to complete the task and gives the user more convenience.

To Cite: Uğur AR., Övet H. Comparison of the Turnaround Times of COVID-19 Real Time PCR Data on the PCR Instrument and the Catena Smart PCR Bioinformatics Program. Osmaniye Korkut Ata Üniversitesi Fen Bilimleri Enstitüsü Dergisi 2022; 5(Özel sayı): 108-116.

Introduction

The clinical microbiology laboratories perform a wide range of activities, from determining the pathogens in a patient's infection to assisting in the identification of global outbreaks, such as the COVID-19 pandemic. Throughout the ongoing pandemic, authorized COVID-19 diagnostic laboratories have been working as part of clinical microbiology laboratories at health care facilities. Currently, approximately 600 COVID-19 diagnostic laboratories are authorized in Turkey, with over 350,000 polymerase chain reaction (PCR) tests performed per day (URL_1). According to the World Health Organization, the PCR assay is one of the recommended diagnostic techniques for COVID-19 (URL_2). Real-time PCR technology allows for the simultaneous amplification, identification, and visualization of nucleic acids from a target microorganism. The COVID-19 has been at the forefront of research since its inception, and the real-time PCR assay is the most widely used nucleic acid amplification test in the world (Tasdelen and Ugur, 2021). Data from PCR tests are processed on the PCR device by a professional and entered into the Laboratory Information Management System (Laboratuvar Bilgi Yönetim Sistemi, LBYS), a web-based results entry and display tool. The PCR results are then automatically transmitted to the e-pulse Personal Health (e-nabız Kişisel Sağlık Sistemi, e-nabız) and Public Health Management Systems (Halk Sağlığı Yönetim Sistemi, HSYS) (Figure 1). CAtenA Smart PCR is a web-based bioinformatic application that uses artificial intelligence (AI) and integrates data from PCR instruments without the need for installation. A professional can either analyze data without depending on artificial intelligence-based tips or approve

its suggestions. After expert approval, the PCR results are transected to the LBYS, HSYS, and e-pulse (URL_3).

Figure 1. The process of collecting data, analyzing it, and submitting the results. The specialist should manually submit the results to the Laboratory Information Management System upon completion of the analysis on the PCR instrument. On the other hand, the approved results are automatically transacted to the Laboratory Information Management System via the CAtenA.

Laboratories are required to maintain the highest level of quality while increasing efficiency. All of the procedures performed by laboratories are becoming increasingly intertwined with bioinformatics. The use of artificial intelligence and bioinformatics effectively can improve the accuracy and timeliness of assays, while reducing laboratory workload, resulting in improved laboratory efficiency and reductions in healthcare costs (Rhoads et al., 2014; Egli et al., 2020). In laboratories, there has recently been an increase in demand for high-quality digital laboratory data. The aim of this study was to compare the turnaround times between the data analysis on a PCR instrument, including result submission, and the CAtenA Smart PCR-assisted analysis.

Material and Methods

Three specialists assessed a total of 139 PCR data sets, each of which included 94 samples and two internal controls, completed in the COVID-19 PCR Diagnostic Laboratory at Meram State Hospital in Konya between September and November 2021. All specialists had equal experience in PCR laboratory management. Only full plate assays were included in the study in order to equalize the performance required for the data analysis. Each specialist evaluated the same assay both on a PCR device-connected computer (Bio-Rad CFX96 Touch, Singapore) and on the CAtenA smart PCR Bioinformatics Program (Ventura, Ankara, Turkey). All PCR experiments were performed using Diagno5 plex NS SARS-CoV-2 Real-Time PCR Kit (A1 Life Sciences, Istanbul, Turkey). The study

period was further divided into two distinct groups according to the intensity of case positivity rates in Konya: one was termed the “high-positivity phase” (n = 80) in September, and the other as the “low-positivity phase” (n = 59) in November.

The specialists recorded the performed time duration of the data analysis for the PCR instrument and for the CAtenA. The time duration of the result entry procedure to the LBYS was added to the analysis time on the PCR instrument. The transaction to the LBYS was an integral part of the data analysis of the CAtenA.

Since the data were not regularly distributed, the Wilcoxon test, which is a nonparametric test, was utilized to determine if there was any significant difference between the turnaround times. The same statistical test was used to compare the turnaround times of the high- and low-positivity phases. A *p* value of less than 0.005 was used to determine statistical significance. SPSS 26 (IBM, USA) was used to conduct the statistical analysis.

Ethics approval for this study was obtained from the Necmettin Erbakan University Ethics Committee, Reference: 2021/3510 (7807).

Results and Discussion

In the present study, we found that the mean turnaround time of the 139 PCR data sets for the PCR instrument was 14.05 ± 7.55 min. The CAtenA Smart PCR had a mean turnaround time of 8.04 ± 3.93 min. for the 139 PCR data analysis (Table 1). The turnaround times on the CAtenA Smart PCR and the PCR instrument were determined to be statistically significant ($p = 0.0001$).

Table 1. The average turnaround times for 139 data sets' analyses.

	Mean (minutes)	**N**	**SD**	**Min.**	**Max.**
AI-based evaluation (CAtenA)	8.0400	139	3.92787	2.00	19.00
Data analysis on PCR Instrument	14.0468	139	7.55001	4.00	31.00

We further divided the study period into two groups: the high-positivity phase, which was shortly after the Delta variant of SARS-CoV-2 surge in September, and the low-positivity phase, which was assigned as the case where positivity rates declined in November in Konya. We compared the two periods in order to assess the effect of the case positivity rates on the turnaround times. The mean positive results per PCR assay in the high-positivity and the low-positivity periods were 21.36 ± 8.79 and 7.15 ± 3.69, respectively (Table 2). There was a significant difference between the turnaround times of the two groups ($p = 0.0001$). The findings showed that the positivity rate has affected the time duration of data analysis on both the PCR instrument and the CAtenA program (Table 3 and 4).

Table 2. Descriptive statistics for positivity rates in high- and low-positivity phases.

	Phase			Statistic	Std. Error
POSITIVES	Low-positivity	Mean		7.15	0.480
		95% Confidence Interval for Mean	Lower Bound	6.19	
			Upper Bound	8.11	
		5% Trimmed Mean		6.94	
		Median		6.00	
		Variance		13.614	
		Std. Deviation		3.690	
		Minimum		2	
		Maximum		20	
		Range		18	
		Interquartile Range		6	
		Skewness		0.900	0.311
		Kurtosis		1.165	0.613
	High-positivity	Mean		21.36	0.984
		95% Confidence Interval for Mean	Lower Bound	19.40	
			Upper Bound	23.32	
		5% Trimmed Mean		21.18	
		Median		21.00	
		Variance		77.424	
		Std. Deviation		8.799	
		Minimum		5	
		Maximum		42	
		Range		37	
		Interquartile Range		13	
		Skewness		0.183	0.269
		Kurtosis		-0.461	0.532

Table 3. A brief summary of group statistics for both AI-based (CAtenA) and PCR instrument-based evaluation time.

	Period Name	N	Mean	SD
AI-based evaluation (CAtenA)	Low-positivity Period	59	4.9671	1.87707
	High-positivity Period	80	10.3063	3.48005
Data analysis on PCR Instrument	Low-positivity Period	59	7.4493	4.28691
	High-positivity Period	80	18.9125	5.44057

Table 4. Statistical analysis between turnaround times of analyses in the high- and low-positivity periods.

	AI-based evaluation (CAtenA)	Data analysis on PCR Instrument
Mann-Whitney U	336.500	299.500
Wilcoxon W	2106.500	2069.500
Z	-8.669	-8.809
Asymp. Sig. (2-tailed)	0.000	0.000

Despite the availability of laboratories 24 hours a day, seven days a week, the workload at COVID-19 PCR diagnostic facilities has increased throughout the pandemic. Due to the exponential development in the number of COVID-19 cases around the world, the healthcare system is overloaded (Ding et al., 2021). Also, most countries have seen a significant rise in healthcare expenses, with more than doubling in the last decade (URL_4). In addition, the clinical microbiology laboratory is essential in identifying and preventing local infectious outbreaks (Kho et al., 2013). Timeliness is critical, since reducing the time it takes to notice an outbreak can dramatically reduce its negative impact (Sintchenko and Gallego, 2009).

The prompt completion of the PCR assays, as well as their error-free transaction to the system, is critical for the diagnosis, treatment, and follow-up of COVID-19, as well as controlling the pandemics. In order to communicate effectively with public health authorities and rapidly identify outbreaks, bioinformatics tools and artificial intelligence are essential (Xu et al., 2021).

Artificial intelligence, such as machine learning and deep learning, helps to strengthen the health system by allowing for the analysis of complicated and huge data sets processed in clinical laboratories (Peiffer-Smadja et al., 2020). For instance, applications that visually analyse gram stain-based images, stool microscopy, and digital bacterial cultures from growth medium have been successfully utilized (Rhoads et al., 2015). Artificial intelligence has recently begun to replace image analysis in a variety of data sources and applications in clinical microbiology laboratories (Smith et al., 2020; Asada et al., 2021). Furthermore, MALDI-TOF mass spectrometry (matrix-assisted laser desorption-ionization/time of flight mass spectrometry) and the use of artificial intelligence in whole genome analysis have broken new ground in the field of microbiology (van Oosten and Klein, 2020).

Applications used for molecular assays may vary in their interoperability and integration with the laboratory management systems. Based on our best knowledge, there is few data concerning the tools

enabling PCR data analysis with the aid of artificial intelligence and bioinformatics. The CAtenA Smart PCR is a tool that automates data flow and eliminates post-analytical errors caused by manual data entry, providing users with quick and reliable results (URL_3). Also, we previously assessed the high consistency between the expert analysis and the analysis of CAtenA too (Uğur and Taşdelen, 2021).

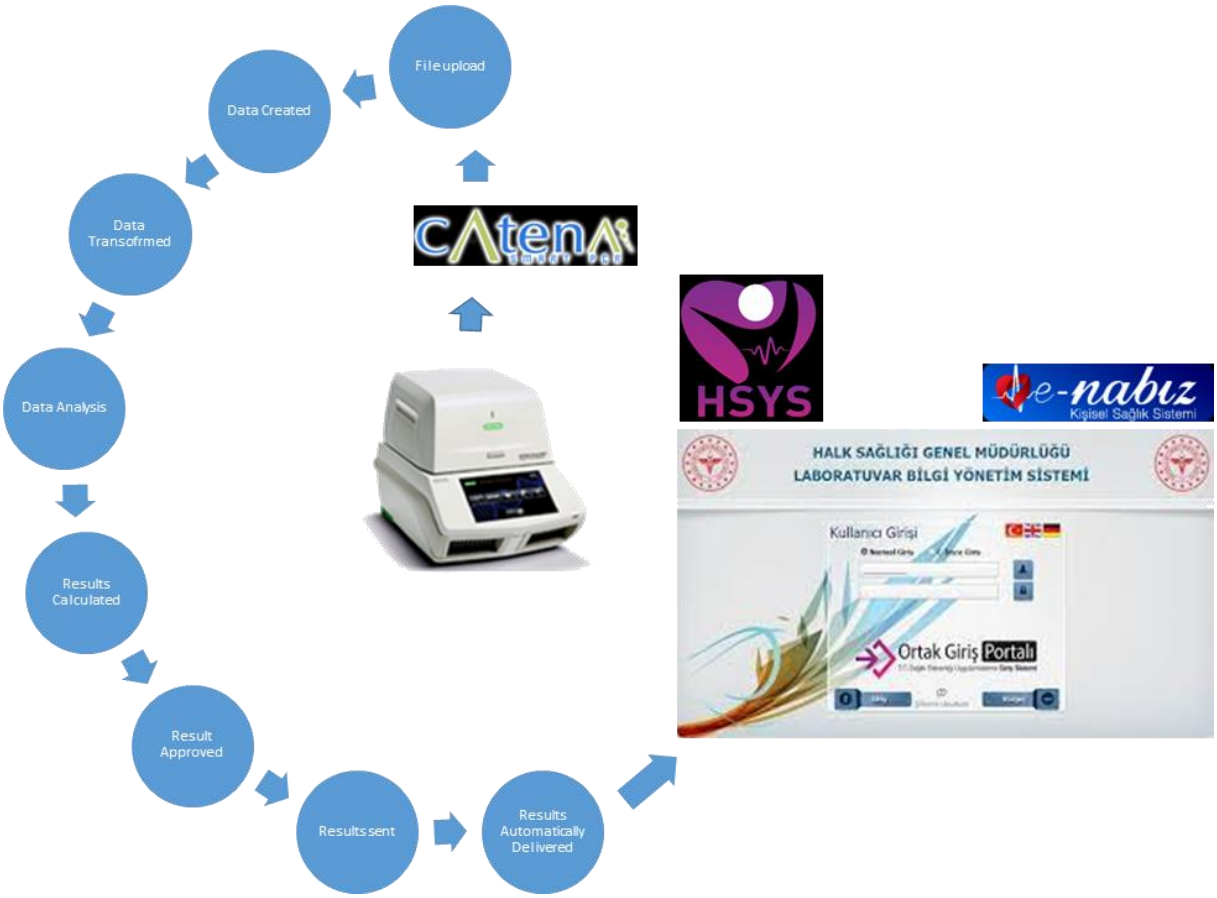

Figure 2. A schematic diagram of the workflow of the CAtenA Smart PCR.

In the present study, we found that using a bioinformatics tool integrated with artificial intelligence can significantly decrease the turnaround time of COVID-19 PCR tests, enabling more rapid completion of PCR tests. We also showed that, the duration of turnaround time decreased as the positivity rate declined. Another advantage was that the direct transaction of the results from the CAtenA to the LBYS could prevent post-analytical errors.

There are several limitations regarding our findings. The limited number of analyzed PCR data sets was one of the limitations of the present study. Our findings regarding factors affecting the turnaround times of data analyses were limited only by the positivity rates. The capacity and number of multiplex detections of SARS-CoV-2 variants, the sensitivity and specifity of the PCR kit, PCR device software specialties the quantity of inconclusive results (e.g., the recommendation of CAtenA for repeating tests), and experience of the user could all influence the length of the analysis. Another study restriction was that the data sets were examined by only three professionals. The fact that users' PCR

and program experience may have an impact on the PCR data analysis time. In the microbiology laboratory, AI has aided laboratory personnel in facilitating and speeding up diagnostic testing. The diversity, quality, and reliability of AI-based technologies, as well as the integration of AI into the clinical laboratory workflow, appear to be increasing in the not-too-distant future. Joint studies in multidisciplinary science fields such as medicine, computer, artificial intelligence, and bioinformatics are needed to develop and improve the qualification and capacity of diagnostic tests.

Conclusion

In the clinical microbiology laboratory, an ever-increasing amount of data must be created, evaluated, and interpreted. In conclusion, CAtenA Smart PCR artificial intelligence may aid users in interpreting PCR data and transacting to the LBYS, which speeds up the procedure and makes it more convenient for the user. The use of a bioinformatics tool in a laboratory allows for quick and consistent data entry. Artificial intelligence and bioinformatics tools will continue to improve patient and public health care in the future.

Statement of Conflict of Interest

Authors have declared no conflict of interest.

Author's Contributions

The contribution of the authors is equal.

*This study was presented as a summary paper at the International Conference on Engineering, Natural and Applied Sciences (ICENAS'21) held online on 24-26 November 2021.

References

Ding W., Nayak J., Swapnarekha H., Abraham A., Naik B., Pelusi D. Fusion of intelligent learning for COVID-19: A state-of-the-art review and analysis on real medical data. Neurocomputing 2021; 457: 40-66. https://doi.org/10.1016/j.neucom.2021.06.024

Egli A., Schrenzel J., Greub G. Digital microbiology. Clinical microbiology and infection: the official publication of the European Society of Clinical Microbiology and Infectious Diseases 2020; 26(10): 1324-1331. https://doi.org/10.1016/j.cmi.2020.06.023

Kho AN., Doebbeling BN., Cashy JP., Rosenman MB., Dexter PR., Shepherd DC., Lemmon L., Teal E., Khokar S., Overhage JM. A regional informatics platform for coordinated antibiotic-resistant infection tracking, alerting, and prevention. Clinical infectious diseases: An Official Publication of the Infectious Diseases Society of America 2013; 57(2): 254-262. https://doi.org/10.1093/cid/cit229

Peiffer-Smadja N., Dellière S., Rodriguez C., Birgand G., Lescure FX., Fourati S., Ruppé E. Machine learning in the clinical microbiology laboratory: has the time come for routine practice? Clinical microbiology and infection: the official publication of the European Society of Clinical Microbiology and Infectious Diseases 2020; 26(10): 1300-1309. https://doi.org/10.1016/j.cmi.2020.02.006

Rhoads DD., Novak SM., Pantanowitz L. A review of the current state of digital plate reading of cultures in clinical microbiology. Journal of Pathology Informatics 2015; 6: 23. https://doi.org/10.4103/2153-3539.157789

Rhoads DD., Sintchenko V., Rauch CA., Pantanowitz L. Clinical microbiology informatics. Clinical Microbiology Reviews 2014; 27(4): 1025-1047. https://doi.org/10.1128/CMR.00049-14

Sintchenko V., Gallego B. Laboratory-guided detection of disease outbreaks: three generations of surveillance systems. Archives of Pathology & Laboratory Medicine 2009; 133(6): 916-925. https://doi.org/10.5858/133.6.916

Smith KP., Wang H., Durant TJS., Mathison BA., Sharpeh SE., Kirby JE., Long SW., Rhoads DD. Application of artificial intelligence in clinical microbiology diagnostic testing. Clinical Microbiology Newsletter 2020; 42: 61-70.

Tasdelen A., Ugur AR. Artificial ıntelligence research on COVID-19 pandemic: A bibliometric analysis, 5th International Symposium on Multidisciplinary Studies and Innovative Technologies (ISMSIT) 2021; 693-699. doi: 10.1109/ISMSIT52890.2021.9604573.

Uğur AR., Taşdelen A. COVID-19 PCR testi veri analizinde CAtenA smart PCR bioinformatik programının sunduğu ön değerlendirme sonuçlarının uzman sonuçları ile uyumunun araştırılması. Avrupa Bilim ve Teknoloji Dergisi 2021; 327-330. DOI: 10.31590/ejosat.1024190

URL_1: https://covid19.saglik.gov.tr/TR-66935/genel-koronavirus-tablosu.html, (Date of Access: 30 November 2021).

URL_2: https://www.who.int/publications/i/item/laboratory-testing-of-2019-novel-coronavirus-(-2019-ncov)-in-suspected-human-cases-interim-guidance-17-january-2020, (Date of Access: 2 December 2021).

URL_3: https://ventura.com.tr/?page_id=1528, (Date of Access: 2 December 2021).

URL_4: https://data.oecd.org/healthres/health-spending.html, (Date of Access: 30 November 2021).

van Oosten LN., Klein CD. Machine learning in mass spectrometry: A MALDI-TOF MS approach to phenotypic antibacterial screening. Journal of Medicinal Chemistry 2020; 63(16): 8849-8856. https://doi.org/10.1021/acs.jmedchem.0c00040

Xu Z., Su C., Xiao Y., Wang F. AI for COVID-19: Battling the pandemic with computational intelligence. Intelligent Medicine 2021; 10.1016/j.imed.2021.09.001. doi:10.1016/j.imed.2021.09.001

OKÜ Fen Bilimleri Enstitüsü Dergisi
5(Özel Sayı):117-134, 2022

OKU Journal of The Institute of Science and Technology, 5(Special Issue):117-134, 2022

Osmaniye Korkut Ata Üniversitesi Fen Bilimleri Enstitüsü Dergisi

Osmaniye Korkut Ata University Journal of Natural and Applied Sciences

Effects of Stacking Sequence on the Structural Performance of Composite Overwrapped Pressure Vessels with Aluminium Liner

Taner COŞKUN[1*], Ömer Sinan ŞAHİN[2]

[1]Konya Technical University, Faculty of Engineering and Natural Science, Department of Mechanical Engineering, 42010, Konya/Turkey
[2]Konya Technical University, Faculty of Engineering and Natural Science, Department of Mechanical Engineering, 42010, Konya/Turkey

[1]https://orcid.org/0000-0002-4815-9278
[2]https://orcid.org/0000-0002-0999-7332
*Corresponding author: tcoskun@ktun.edu.tr

Research Article

Article History:

Received: 15.12.2021
Accepted: 18.01.2022
Published online: 23.02.2022

Keywords:

Dome profile
Filament winding
Geodesic trajectories
Pressure vessels
Stacking sequence

ABSTRACT

Pressure vessels are subjected to stresses in axial and radial directions during their service life, which causes undesirable damages. For that reason, it is highly important to design the fiber directions in composite overwrapped pressure vessels in such a way that can carry the loads occurring in both directions. In this context, composite pressure vessels with 20 mm polar opening radii were designed and composite layers were wound on the aluminium liner with 2 mm thickness. For the aluminium liner, the dome portions were designed with geodesic trajectories and the corresponding profile coordinates were obtained by solving the elliptical integral and using a circular arc. Helical and hoop winding layers were used together on the cylinder surface and the effect of stacking sequence on the structural performance was examined. In the current study, numerical models with six different stacking sequences of hoop winding and helical winding with aluminum liner were defined and thus mechanical properties such as stress, strain and failure indexes were determined. Furthermore, the effects of hoop winding layers utilization on the mechanical properties were investigated by comparing with the numerical model consisting of completely helical winding layers.As a result of the current study, it has been concluded that the hoop winding layers have favorable effects on mechanical properties. It has also been observed that the utilization of the hoop winding layers provides an improvement of approximately 31.42% in the failure index compared to the numerical model consisting of completely helical winding. Additionally, it was observed that although the stacking sequence for the hoop winding was highly effective on the interlaminar shear stress, it did not have much effect on the stress/strain results and the failure indexes.

İstifleme Sırasının Alüminyum Astarlı Kompozit Katmanlı Basınç Kaplarının Yapısal Performansına Etkileri

Araştırma Makalesi

Makale Tarihçesi:

Geliş tarihi: 15.12.2021
Kabul tarihi: 18.01.2022
Online Yayınlanma: 23.02.2022

ÖZET

Basınçlı kaplar hizmet ömürleri boyunca eksenel ve radyal yönlerde gerilmelere maruz kalmakta ve bu durum istenmeyen hasarlara neden olmaktadır. Bu sebepten dolayı kompozit katmanlı basınçlı kaplarda fiber

Anahtar Kelimeler:

Kubbe profili
Filaman sarım
Jeodezik yörünge
Basınç kapları
İstif sırası

yönlerinin her iki yönde oluşan yükleri taşıyabilecek şekilde tasarlanması oldukça önemlidir. Bu kapsamda 20 mm kutup ağzı yarıçapına sahip kompozit basınçlı kaplar tasarlanmış ve 2 mm kalınlığındaki alüminyum astar üzerine kompozit tabakalar sarılmıştır. Alüminyum astar için kubbe kısımları jeodezik yörüngelerle tasarlanmış ve eliptik integral çözülerek ve çember yay kullanılarak ilgili jeodezik profil koordinatları elde edilmiştir. Silindir yüzeyinde helisel ve çember sargı tabakaları bir arada kullanılmış ve istifleme sırasının yapısal performansa etkileri incelenmiştir. Bu çalışmada alüminyum astarlı altı farklı çember ve helisel sarım istif sırasına sahip sayısal modeller tanımlanmış ve böylece gerilme, gerinim ve hasar indeksleri gibi mekanik özellikler belirlenmiştir. Ayrıca, tamamen helisel sarım katmanlardan oluşan sayısal model ile karşılaştırılarak, çember sarım tabakaların mekanik özellikler üzerindeki etkileri araştırılmıştır. Mevcut çalışma sonucunda, çember sarım tabakaların mekanik özellikler üzerinde olumlu etkileri olduğu sonucuna varılmıştır. Ayrıca çember sarım tabaka kullanımının tamamen helisel sarımdan oluşan sayısal modele kıyasla hasar indeksinde yaklaşık %31.42 iyileşme sağladığı gözlemlenmiştir. Ek olarak, çember sarım tabakalar için istifleme sırasının katmanlar arası kayma gerilmesi üzerinde oldukça etkili olduğu fakat gerilme/gerinim sonuçları ile hasar indeksleri üzerinde çok fazla etkisi olmadığı gözlemlenmiştir.

To Cite: Coşkun T., Şahin ÖS. Effects of Stacking Sequence on the Structural Performance of Composite Overwrapped Pressure Vessels with Aluminium Liner. Osmaniye Korkut Ata Üniversitesi Fen Bilimleri Enstitüsü Dergisi 2022; 5(Özel sayı): 117-134.

Nomenclature

ρ	Density	**z**	Axial Coordinate
E	Young's Modulus	**R**	Cylinder Radius
G	Shear Modulus	$\mathbf{r_0}$	Polar Opening Radius
v	Poisson's Ratio	**α**	Filament Winding Angle
r	Radial Coordinate	$\mathbf{R_0}$	Circle Arc Radius

Introduction

Composite materials have many advantages over conventional materials such as high strength/weight ratio, fatigue and corrosion resistance (Takeichi et al. 2003; Zuttel, 2003). Due to these advantages, the utilization of composite materials in automotive, aviation, wind, petroleum, pressure vessels, medical and sports products is continuously increasing (Elmar and Bernhard, 2015). These materials are subjected to various stress levels in the usage areas and different damage mechanisms occur accordingly. Therefore, many studies have been carried out to determine the mechanical properties of composite materials. Yao et al. (2018) conducted a literature review on advanced surface treatment techniques and the production of carbon fiber reinforced thermoplastic composites. In this study, the advantages and disadvantages of using carbon fiber in thermoplastic composites were also examined and it was stated that carbon fibers have a lower density, higher strength and wear resistance compared to glass fibers. On the other hand, it was stated that unidirectional carbon fibers exhibit lower strain than glass fibers and are more expensive. In another study, Oromiehie et al. (2019) conducted a

literature review on the automated fiber placement method, which is one of the composite production techniques, and examined the effects of defects occurring during the production process on the final properties.

Many studies have been conducted in the literature to determine the mechanical properties of composite pipes. Gemi (2014; 2018) performed static burst and fatigue tests on glass fiber reinforced plastic composite pipes produced with various winding angles. Apart from that, Gemi et al. (2009) investigated the fatigue life of composite pipes with a ±75° winding angle. In the study conducted by Gemi et al. (2020), the mechanical properties and machinability characteristics of carbon and glass fiber reinforced hybrid composite pipes with various stacking sequences were experimentally investigated. In this context, composite pipes were subjected to hardness, ring tensile, burst and machinability tests. It was seen from the results that the stacking sequence was highly effective on the mechanical properties and the thrust force generated during drilling. Furthermore, considering the mechanical and machinability properties, the optimum stacking sequence was determined as glass/carbon/glass. In another study, Tasyurek and Tarakcioglu (2017) investigated the fatigue behavior of glass fiber reinforced composite pipes with a 55° winding angle and experimentally determined the effects of carbon nanotube addition with different mass ratios on the final results. Furthermore, the effects of surface cracks with different aspect ratios were also examined. It was determined that the use of carbon nanotubes improved the interlaminar adhesion quality, and hence the fatigue life of composite pipes. However, it was concluded that the carbon nanotubes ratio was effective on the results, and a significant improvement in the burst strength and fatigue life was achieved with the use of nanotubes at low mass ratios. In the study conducted by Gemi et al. (2021), the effects of low velocity impact on the strength of 54, 72 and 96 mm diameter glass fiber reinforced composite pipes were experimentally investigated. In this context, impacts were applied to the composite pipes at 4 different energy levels, and thus damage mechanisms and low-velocity impact behaviors were examined. As a result of the study, it was concluded that low velocity impact had less effect on strength and delamination became the dominant damage mechanism with increasing composite pipe diameter. Furthermore, it was observed that the damage mechanisms diversified, and the delaminated area increased with the ascending impact velocity. In another study conducted by Gemi et al. (2022), glass fiber reinforced composite pipes with 54, 72 and 96 mm diameters produced by the filament winding method were subjected to compression after impact tests. In this way, the losses in the axial strength of the specimens depending on the impact effect were determined experimentally, and also the damage mechanisms were examined. As a result, it was concluded that there were differences in the compression after impact damage responses for impacted and non-impacted composite pipes. While damage in non-impacted pipes was observed as local buckling in the flange region, it was determined that the delaminated area enlarged for the impacted specimens and resulted in splitting in the fiber direction with the effect of local buckling.

Hocine et al. (2009) carried out experimental and numerical analysis of the hydrogen pressure vessels obtained as a result of winding carbon fibers on an aluminium liner by filament winding method. In the analysis, only the cylindrical region was taken into account, and the effect of the fiber orientations on the structural performances was investigated by using three different filament winding angles. In addition, burst pressures were obtained for the pressure vessels with various winding angles is found based on the Tsai-Wu failure criterion. As a result of the study, the maximum burst pressure has been achieved for the 55-60° winding range. In another study conducted by Sepetcioglu (2021), graphene added basalt/epoxy composite pressure vessels were produced using the filament winding method. Specimens with ±55° fiber orientation were subjected to low-velocity impact tests at 7 different energy levels under 50 bar internal pressure, and thus their dynamic responses were investigated. As a result, an increase in the burst pressure for the pressure vessels has been observed with the contribution of graphene. It was also concluded that the graphene additive reduced the amount of absorbed energy for the pressure vessels. In the study conducted by Nebe et al. (2020), it was investigated experimentally and analytically how the stacking sequence affects the structural deformation, laminate quality and burst pressure in composite pressure vessels. As a consequence of the experimental studies, it was observed that the stacking sequence changed the burst pressure by about 67%.

Park and Sakai (2020) developed a 3D mathematical model that can calculate the stresses occurring in fiber-reinforced composite pressure vessels. They used the Tsai-Wu failure criterion to determine the burst pressure and plies in which the failure occurred. As a result of the optimization studies, it was determined that the stacking sequence has a significant effect on the burst pressure. In another study, Ozbek et al. (2019) subjected composite pipes produced by using glass, basalt, and glass/basalt fibers with different fiber orientations to the compression test and examined the failure modes, energy absorption capacities and crush behaviors. It was determined that the increase in fiber orientations caused deterioration in energy absorption capacity and an improvement in crushing load. Furthermore, it has been observed that the pipes manufactured using glass fiber have the highest energy absorption capacity. Prabhakar et al. (2019) studied the mechanical properties of filament wound composite pipes such as buckling, burst, corrosion and durability. According to the minimum damage mechanisms observed with the burst analysis, it has been stated that a ±55 ° winding angle is the optimum value. It has also been determined within the scope of literary studies that 90% of the pipes are produced using glass fiber.

In this study, numerical models of composite overwrapped pressure vessels with six different stacking sequences were defined and analyses were carried out by using the Ansys ACP module. The geodesic dome profile was obtained by solving the elliptic integral. The helical winding angles along the dome and cylinder surface were determined and the structural performance of the pressure vessels was investigated. As a result of the analysis, the effects of hoop winding and stacking sequence on the mechanical properties were determined.

Material and Methods

In the current study, numerical analysis of the pressure vessels with 50 mm cylinder radius and 20 mm polar opening radii was performed. In the numerical models, the cylindrical region length was defined as 300 mm and the composite layers were wound on an aluminium liner with a thickness of 2 mm. 12 helical layers were defined along the dome surface. On the other hand, a total of 24 layers of composite layers containing various numbers of helical and hoop windings were defined along the cylinder surface. 150 Bar internal pressure was applied to the numerical models, and thus the mechanical properties of the composite overwrapped pressure vessels were investigated. In the analysis, the material properties were taken from the Ansys Engineering Data Sources. Epoxy E-Glass UD was used as the composite material and Aluminium Alloy was used as the liner material. Composite and liner material properties are shown in Tables 1 and 2, respectively. Furthermore, stress and strain limits for the composite material are shown in Table 3. Boundary conditions were defined considering the application areas as shown in Figure 1. Furthermore, mesh convergence studies were carried out, and the optimum mesh size and method were determined as 2 mm and quadrilaterals, respectively. In this context, 31356 nodes and 31200 quad elements were used in the numerical models.

Table 1. Composite material properties

Materials	**ρ** [kg/m^3]	**E_x** [GPa]	**E_y** [GPa]	**E_z** [GPa]	**ν_{xy}** [-]	**ν_{yz}** [-]	**ν_{xz}** [-]	**G_{xy}** [GPa]	**G_{yz}** [GPa]	**G_{xz}** [GPa]
Epoxy E-Glass UD	2000	45	10	10	0.3	0.4	0.3	5	3.85	5

Table 2. Aluminium liner material properties

Materials	ρ [kg/m^3]	E [GPa]	v [-]	G [GPa]
Aluminium Alloy	2770	71	0.33	2.67

Table 3. Stress and strain limits for composite material

Direction	**Orthotropic Stress Limits [MPa]**	**Orthotropic Strain Limits [mm/mm]**
Tensile X	1100	0.0244
Tensile Y	35	0.0035
Tensile Z	35	0.0035
Compression X	-675	-0.015
Compression Y	-120	-0.012
Compression Z	-120	-0.012
Shear XY	80	0.016
Shear YZ	46.15	0.012
Shear XZ	80	0.016

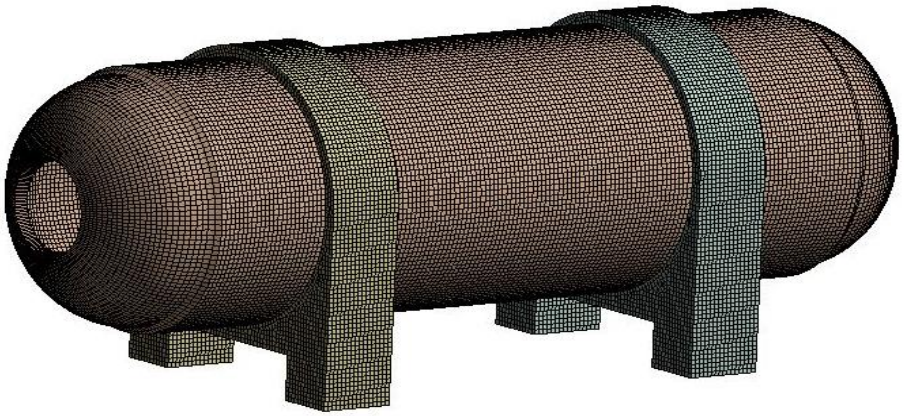

Figure 1. Visualization of the boundary conditions for the composite overwrapped pressure vessels

The geodesic curve represents the shortest distance between two points on any surface. When the composite yarns are wound in the geodesic path, since the fibers follow the stable trajectories, there is no need for friction force to keep the fibers in the defined winding trajectories. In the current study, the geodesic dome profile was obtained in two stages. In the first step, the elliptic integral given in Equation (1) was solved, and thus the axial and radial coordinates from the junction point of the cylinder with the dome to the constant curvature point were obtained (Kabir, 2000; Kumar and Kumari, 2012). The constant curvature point can be expressed as the coordinate at which the elliptic curve has the maximum radius.

$$\bar{z} = -\sqrt{1-\bar{r}_0^2}\int_1^{\bar{r}} \frac{\bar{r}^3}{\sqrt{\bar{r}^2-\bar{r}_0^2-\bar{r}^6(1-\bar{r}_0^2)}}\,dr \qquad (1)$$

Here, $\bar{z}$, $\bar{r}$ and $\bar{r}_0$ denote the dimensionless axial coordinates, radial coordinates and polar opening radii, respectively. As can be seen below, these values are obtained by dividing the axial coordinate, radial coordinate and polar opening radii by the cylinder radius, respectively. Schematic representations of the cylinder radius, polar opening radii, axial coordinates and radial coordinates are demonstrated in Figure 2 on the dome and cylindrical portions.

$$\bar{z} = \frac{z}{R}, \qquad \bar{r} = \frac{r}{R}, \qquad \bar{r}_0 = \frac{r_0}{R}$$

In the second step, a circular arc was used from the constant curvature point to the polar opening, thus completing the dome profile. The circular arc radius is the same as the constant curvature point radius and is obtained (Cai et al., 2019) using Equation (2).

$$R_\theta = \frac{R}{sin2\alpha_0} \qquad (2)$$

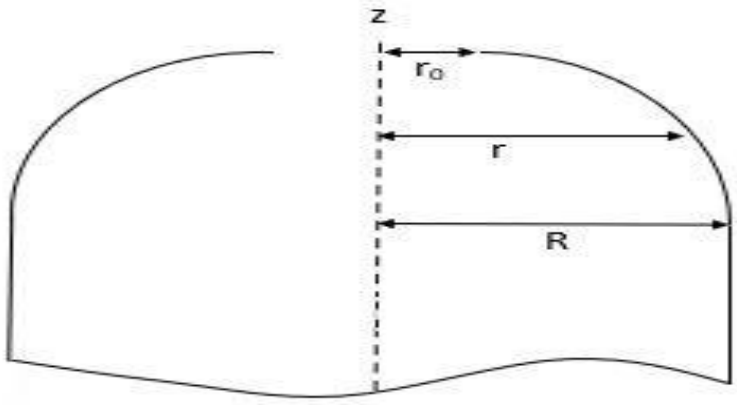

Figure 2. Schematic representation of the dome and cylindrical portions

Depending on the polar opening radii and cylinder radius, only one fiber orientation can be used in the pressure vessels with a geodesic dome profile. Although composite yarns are wound with a defined fiber orientation on the cylindrical surface, this situation is completely different for the dome surface. The filament winding angle is systematically increased up to 90° along the geodesic dome trajectory so that the composite yarns are wound tangentially to the polar opening. The helical winding angles along the cylinder and dome surface were determined (Zwillinger, 1998) using Equation (3). In this study, the helical winding angle of the cylindrical surface was obtained as ±23.58° depending on the polar opening radii and cylinder radius and the same winding angle was defined for all numerical models.

$$\alpha = \arcsin(\frac{r_0}{r}) \quad (3)$$

It is very well known that composite materials exhibit different strengths according to the longitudinal and transverse loading. Therefore, there may be cases where the helical winding is insufficient for the composite pressure vessels and additional hoop winding layers can be necessary to overcome safely the stresses occurring in the radial directions. For that reason, six different numerical models were defined to examine the effect of the stacking sequence and hoop winding layers on the mechanical properties and design more reliable pressure vessels. Six different stacking sequences used in the numerical analysis were demonstrated schematically in Figure 3.

Figure 3. Designations and schematic representation of six different stacking sequences

Results and Discussion

The geodesic dome profile with 20 mm polar opening radii is shown in Figure 4. The dome profile was created using an elliptical curve and a circular arc with a radius of 68.19 mm. Equation 1 was solved by using Matlab subroutine to define the first part of the dome profile and then a circle arc was used to complete the geodesic dome profile shown in Figure 1. On the other hand, the polar opening radii of the pressure vessels must be equal in order to make filament winding in the geodesic trajectories. For that reason, the same profile was used in both dome portions. Apart from that, the filament winding angle along the dome surface is shown in Figure 5. As can be seen from the figure, the fiber orientation at the r = 50 mm, which also represents the winding angle of the cylindrical region, is equal to ±23.58°. In addition, since the composite fibers pass tangentially to the polar opening, the filament winding angle is 90° at the r=20 mm.

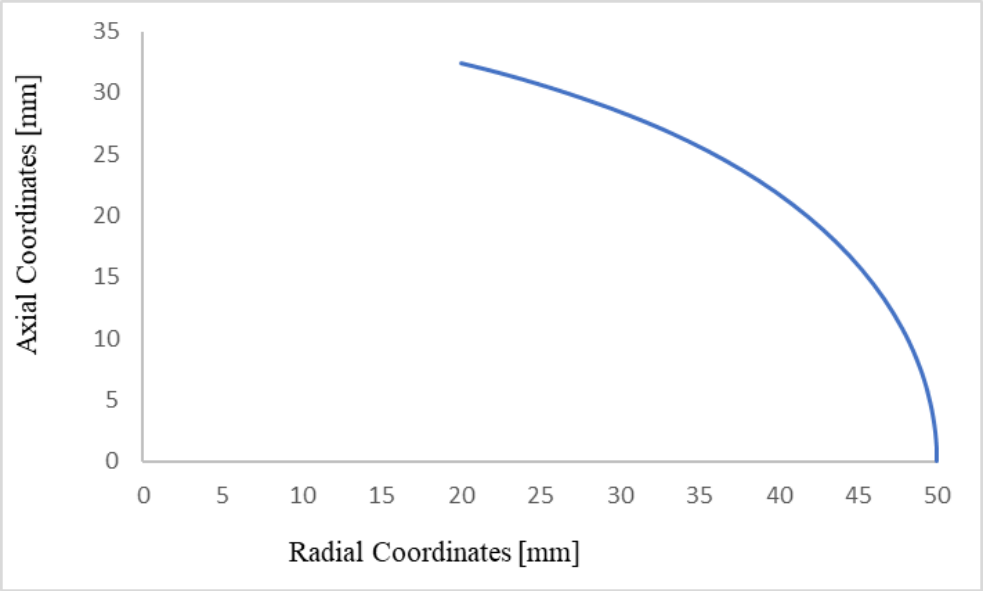

Figure 4. The geodesic dome profile for the pressure vessel with 20 mm polar opening radii

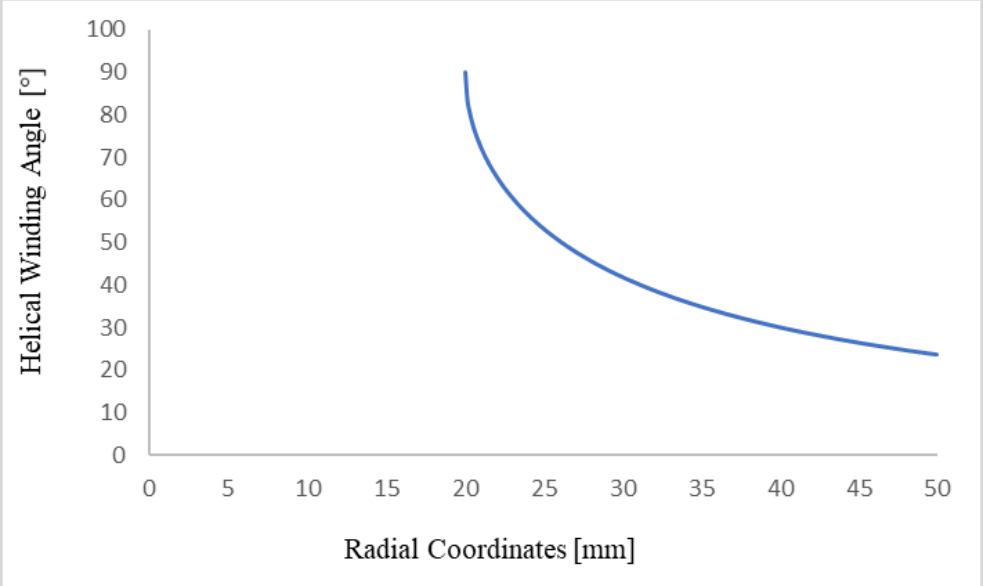

Figure 5. Helical winding angles for the pressure vessel with 20 mm polar opening radii

Since it is not possible to use hoop winding on the dome surface, only 12 helical winding layers are defined in all numerical models. For this reason, the mechanical properties in the dome portions were obtained completely the same for all models. Additionally, since the layers are defined as ±α ° in filament winding, composite layers with +α ° and -α ° fiber orientations generally exhibit the same mechanical properties. Therefore, the transverse and longitudinal stresses were only investigated for the 1st, 3rd, 5th, 7th, 9th and 11th layers in the current study. The maximum longitudinal and transverse stresses occurring on the composite layers from the inner to the outer plies respectively are shown in Figures 6 and 7. It is clearly seen that the lower longitudinal stresses occur in the inner plies and increase continuously towards the outer plies. On the other hand, the filament winding angles changes systematically along the dome surface in composite pressure vessels with a geodesic dome

profile (Butt et al., 2010). Depending on the polar opening and cylinder radii, the composite fibers entering the dome region with a certain winding angle reach 90° towards the polar opening edges. The systematically changing winding angle naturally causes differences in mechanical properties such as transverse/longitudinal stress and strain responses across the dome. This causes various strength properties to be exhibited and the burst pressure to differ in the dome parts (Madhavi, 2009). When Figure 6 is examined, it is seen that the maximum longitudinal stresses take place at the transition point of the dome and the cylinder, and there is a systematic reduction in the stresses towards the polar opening edges. This is an expected result and was completely attributed to the systematic increment of the filament winding angle towards the polar opening and the reduction in the axial stresses carried by the fibers. For instance, the longitudinal stresses were observed as 46.536 MPa in the cylinder-dome transition points for the SS-6 model, while it was determined as 0.38 MPa in the polar opening. Thus, significant changes took place in the longitudinal stresses for the dome parts depending on the winding angle variations. On the other hand, when Figure 7 is examined, it is seen that the transverse stresses are higher around the polar opening edges. This is because the winding angle is around 90° in the polar openings and the radial forces are carried by the fibers. Furthermore, it was observed that the transverse shear stresses decreased from the inner to outer layers. While the maximum transverse stress was obtained as 184.91 MPa in the 1st layer, it was determined as 170.3 MPa in the 11th layer.

Apart from that, longitudinal and transverse stresses for the composite overwrapped pressure vessels are shown in Figure 8. It is clearly seen that there was a decrement in longitudinal and an increment in transverse stresses with the utilization of hoop winding layers. The maximum longitudinal stresses were obtained as 122.46 and 131.92 MPa for the SS-1 and SS-6 stacking sequences, respectively. Thus, approximately 7.73% increment took place in the longitudinal stresses with the utilization of the hoop winding layers. Moreover, the maximum transverse stresses were obtained as 338.33 and 335.93 MPa for the SS-1 and SS-6 models, respectively. It was concluded from the results that the maximum stresses occur in the dome parts and therefore they are the most critical parts of the pressure vessels.

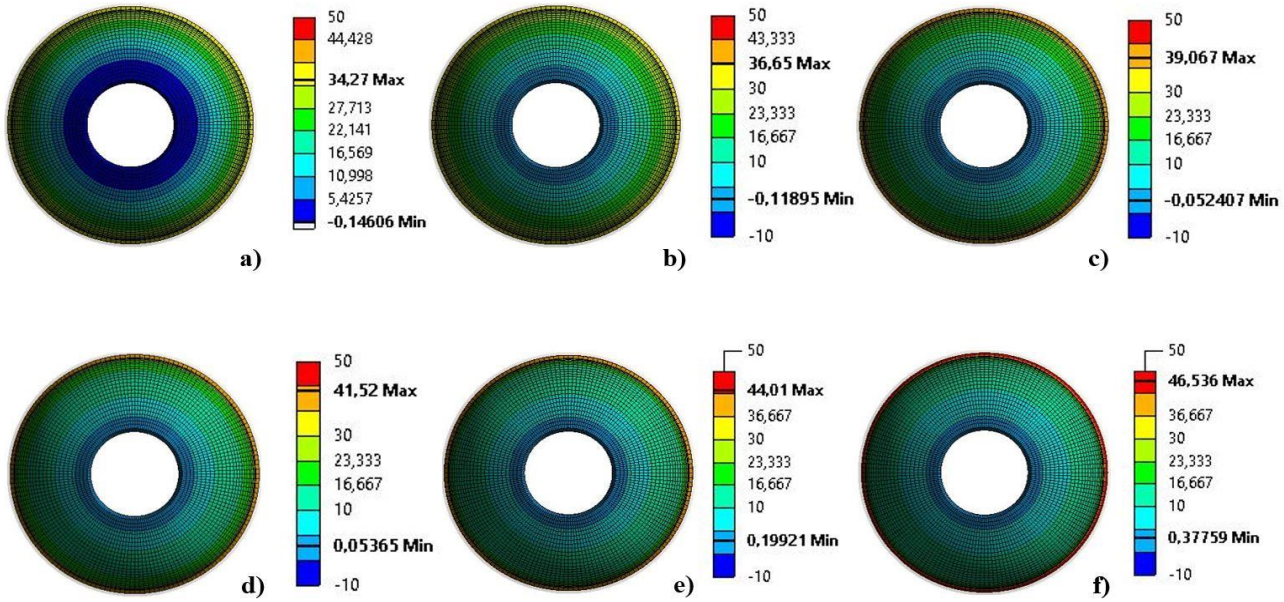

Figure 6. Maximum longitudinal stresses of the dome portions for a) 1st ply, b) 3rd ply, c) 5th ply, d) 7th ply, e) 9th ply and f) 11th ply

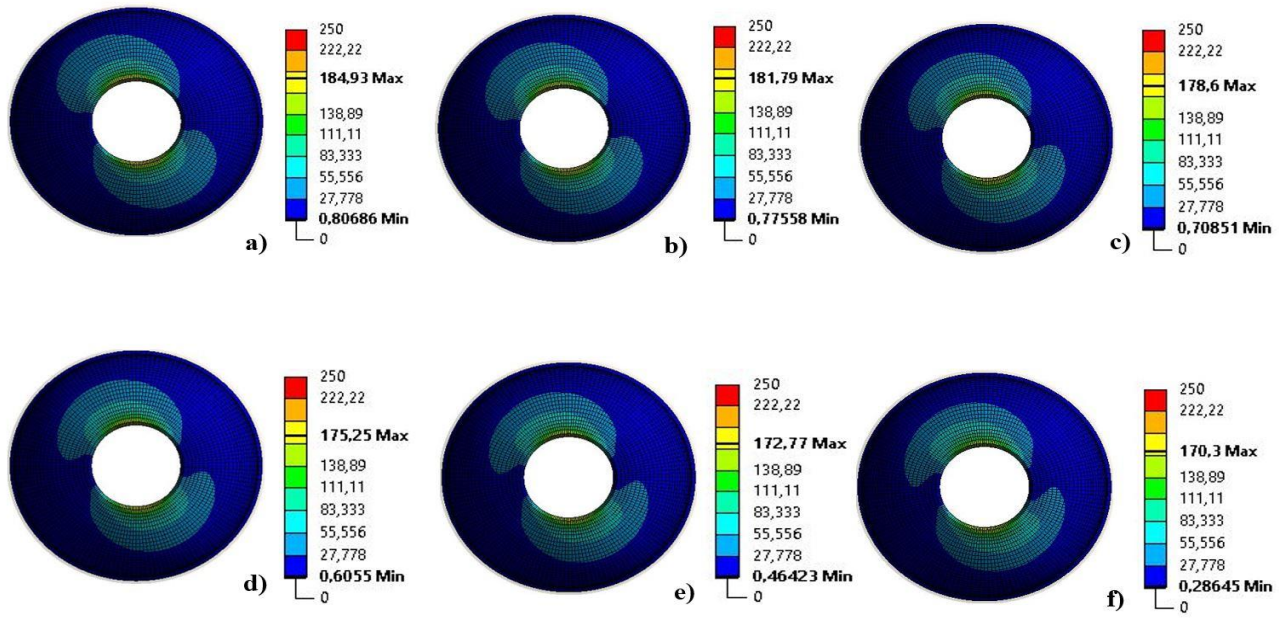

Figure 7. Maximum transverse stresses of the dome portions for a) 1st ply, b) 3rd ply, c) 5th ply, d) 7th ply, e) 9th ply and f) 11th ply

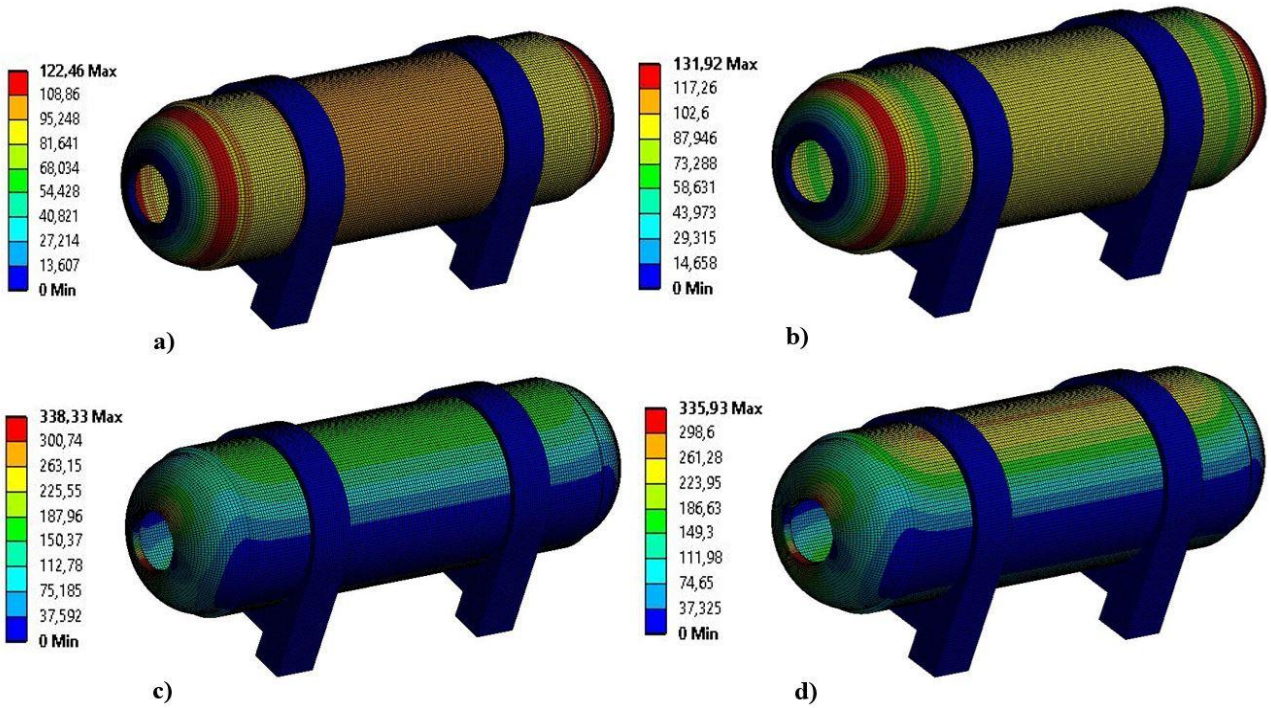

Figure 8. Maximum longitudinal stresses for a) SS-1, b) SS-6 and transverse stresses for c) SS-1, d) SS-6

The increase in the interlaminar shear stress is generally undesirable for the composite materials and leads to various damage mechanisms such as delamination. Therefore, the effects of stacking sequence on the interlaminar shear stresses were examined within the scope of the current study and it was aimed to reduce shear stresses take place in the composite pressure vessels. Interlaminar shear stresses for the numerical models with various stacking sequences are shown in Table 4. As can be clearly seen from the results, the utilization of hoop winding has a reasonably positive effect on the interlaminar shear stresses. For the SS-6 model which completely consists of helical layers, average interlaminar shear stress was obtained as 8.572 MPa. On the other hand, it was determined as 6.6 MPa for the SS-4 model. Thus, approximately 23.01% improvement was achieved in the interlaminar shear stress with the utilization of 12 hoop winding layers. On the other hand, it was concluded that the stacking sequence was not highly effective on the interlaminar shear stress. Among the models with the 12 hoop winding layers, the maximum average interlaminar shear stress was observed in the SS-2 model as 6.927 MPa while the minimum average interlaminar shear stress was observed in the SS-4 model as 6.6 MPa. Therefore approximately 4.72% reduction was achieved by varying stacking sequences. It has also been determined that the critical shear stresses on the structure can be reduced thanks to the use of hoop winding when the favorable effects are considered. Moreover, it has been determined that pressure vessels can be strengthened by optimizing the stacking sequences.

Table 4. Interlaminar shear stress for the composite layers with various stacking sequences

Plies	Interlaminar Shear Stress [MPa]					
	SS-1	**SS-2**	**SS-3**	**SS-4**	**SS-5**	**SS-6**
1-2	6.327	6.202	6.601	10.047	10.180	10.468
2-3	6.362	6.237	6.639	10.003	10.181	10.500
3-4	6.385	10.310	6.665	9.933	10.146	10.498
4-5	6.394	10.191	6.676	9.835	10.078	10.464
5-6	10.168	6.206	6.674	9.711	9.971	10.394
6-7	9.994	6.189	6.658	9.559	9.826	10.289
7-8	9.792	9.790	10.075	5.648	9.643	10.149
8-9	9.564	9.567	9.829	5.591	9.421	9.971
9-10	9.309	5.777	9.554	5.520	9.160	9.756
10-11	9.031	5.708	9.252	5.436	8.861	9.502
11-12	5.224	9.001	8.922	5.339	8.524	9.211
12-13	5.128	8.680	8.566	5.228	8.148	8.882
13-14	5.018	8.337	8.187	8.562	7.735	8.515
14-15	4.896	8.127	8.166	8.563	7.289	8.111
15-16	8.239	4.036	8.269	8.687	6.809	7.669
16-17	8.339	3.889	8.372	8.812	6.808	7.189
17-18	8.438	8.421	8.475	8.936	6.972	6.676
18-19	8.538	8.519	8.577	9.060	7.135	6.128
19-20	8.637	2.526	1.569	1.578	7.299	6.219
20-21	8.737	2.327	1.497	1.416	7.462	6.389
21-22	1.521	8.813	1.515	1.430	2.153	6.558
22-23	1.541	8.912	1.534	1.447	2.178	6.728
23-24	1.560	1.565	1.552	1.464	2.203	6.899
Average	6.919	6.927	6.688	6.600	7.747	8.572
Maximum	10.168	10.310	10.075	10.047	10.181	10.500

The longitudinal and transverse stress/strain results for the models with various stacking sequences are shown in Table 5. It was observed that there was no significant change in the results for the models with 12 helical and 12 hoop winding layers. Based on this it was concluded that the stacking sequence was not highly effective on the longitudinal and transverse stress/strain results. On the other hand, although no significant change in the transverse stress was observed in the SS-5 model, approximately 5.16% increment in the longitudinal stress was took place compared to the SS-1 model. Apart from that, 131.92 MPa longitudinal stress taken place in the SS-6 model which was designed with entirely helical layers and thus approximately 7.73% increase occurred compared to the SS-1 model. These

results show that the number of hoop winding layers is highly significant on the mechanical properties. Additionally, failure indexes for the cylindrical parts of the numerical models were investigated to determine how hoop winding layers affect the mechanical properties, and the results are shown in Figure 9. In the current study, inverse reverse factors which can be defined as an inverse of safety factor were found based on the Tsai-Wu failure criterion. Thus, it was aimed to reduce failure indexes by defining composite layers with various stacking sequences. As can be seen from the figure, similar results were obtained for the SS-1, SS-2, SS-3 and SS-4 models and it demonstrates that the stacking sequence was not significantly effective for the failure behavior. On the other hand, it was seen that this situation was completely different for the SS-5 and SS-6 models, and the decrease in the number of hoop winding layers caused deterioration in the failure indexes. The maximum inverse reverse factor has occurred on the cylinder surface as 0.8065 for the SS-5 model and approximately 25.91% deterioration took place compared to the SS-3 model. Moreover, the inverse reverse factor was obtained as 0.9341 for the SS-6 model and approximately 31.42% improvement was observed compared to the SS-3 model. It was revealed that the SS-6 models should be strengthened under internal pressures above 150 Bar.

Table 5. Longitudinal and transverse stress/strain results for various pressure vessels

	$\sigma_{L,max}$ [MPa]	$\sigma_{T,max}$ [MPa]	$\varepsilon_{L,max}$ [-]	$\varepsilon_{T,max}$ [-]
SS-1	122.46	338.33	0.0010784	0.0047274
SS-2	122.49	338.32	0.0010784	0.0047273
SS-3	122.41	338.35	0.0010785	0.0047277
SS-4	123.85	338.42	0.0011076	0.0047288
SS-5	128.78	336.97	0.0011082	0.0047085
SS-6	131.92	335.93	0.0011093	0.0046938

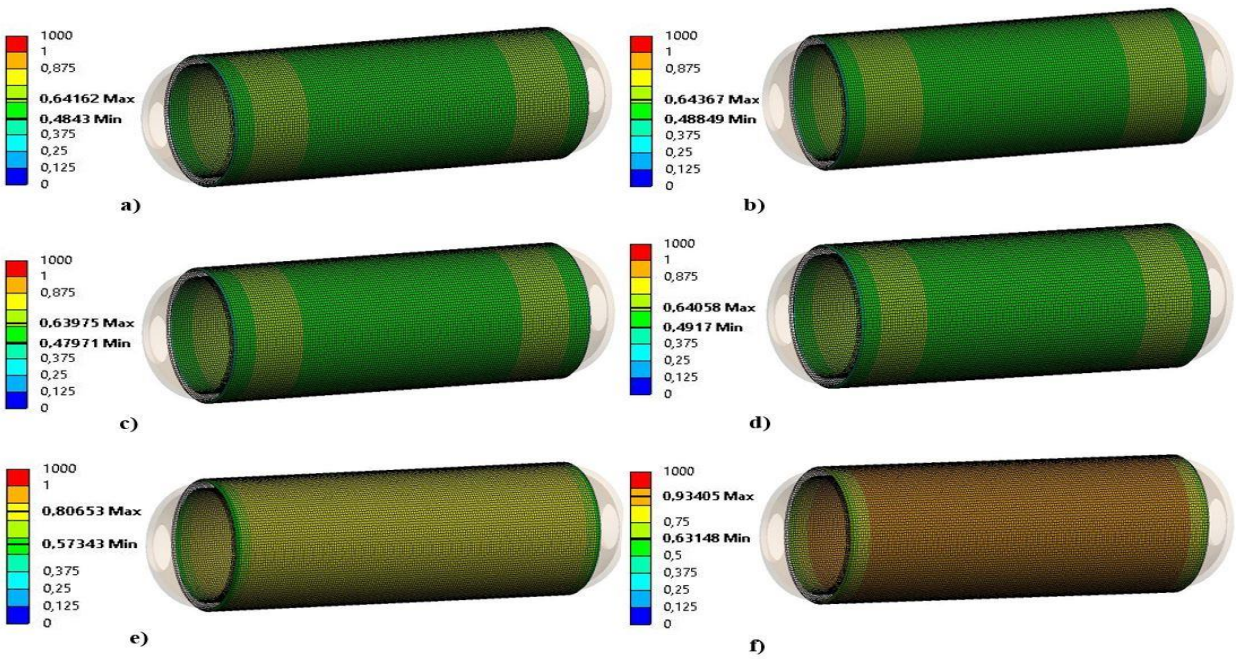

Figure 9. Inverse reverse factors of pressure vessels with various stacking sequences for a) SS-1, b) SS-2, c) SS-3, d) SS-4, e) SS-5 and f) SS-6

Conclusion

In the present study, the effects of the hoop winding layer and the stacking sequence on the strength of the composite overwrapped pressure vessels were investigated. In this context, six numerical models with different stacking sequences of the hoop and helical winding with liner were generated and numerical analyses were carried out with the help of the Ansys ACP module. In the numerical models, aluminium liners with geodesic dome profiles have been designed and then composite layers were defined on the liner surfaces. The stress/strain results for the dome and cylindrical portions were obtained and also the failure behaviors for the six numerical models were investigated. The outcomes achieved from the current study are as follows:

- It has been revealed that the utilization of hoop winding layers is highly effective on the interlaminar shear stresses and reduces the shear stresses. This is because shear stresses are maximum at ±45° and around fiber orientations, and thus the ±23.58° helical winding angles cause higher interlaminar shear stresses than the hoop winding layers. It has also been found that stacking sequences can be optimized to minimize the interlaminar shear stresses since higher shear stresses occur in the inner and outer laminates due to the bending effect.
- It is very well known that the only helical winding layers may be insufficient to meet the radial loads. Therefore, hoop winding layers have been used to strengthen composite pressure vessels against radial loads. As a result, it has been concluded that radial loads are safely carried by the hoop winding laminates, and significant improvement for the failure indexes has been achieved. In this way, maximum inverse reverse factors were obtained as 0.9341 and 0.6398 for the SS-6 and SS-3, respectively, and thus approximately 31.42% improvement in failure indexes has been achieved thanks to the 12 layers of hoop winding.

- From the current study, it was concluded that the dome profile is highly influential on the filament winding angles, and thus the mechanical properties of the composite overwrapped pressure vessels. Since the geodesic dome profile was used in our study, it is not possible to improve fiber orientations to more safely meet the axial and radial loads on the dome portions. Therefore, future studies include using non-geodesic dome trajectories to optimize filament winding angles throughout the dome. Furthermore, the design of hybrid layer overwrapped pressure vessels using carbon and glass fibers can be considered as future works.

Acknowledgement

This work has been performed within the scope of a master's thesis supported by Konya Technical University Graduate School of Natural and Applied Science.

Statement of Conflict of Interest:

Authors have declared no conflict of interest.

Author's Contributions:

The contribution of the authors is equal.

*This study was presented as a summary paper at the International Conference on Engineering, Natural and Applied Sciences (ICENAS'21) held online on 24-26 November 2021.

References

Butt AM., ul Haq SW. Comparative study for the design of optimal composite pressure vessels. Key Engineering Materials 2010; 442: 381-388.

Cai Q., Pu X., Dan L., Li X. Comparative study on multi-type domes of filament-wound composite pressure vessels. In IOP Conference Series: Materials Science and Engineering 2019; 677(2): 022062.

Elmar W., Bernhard J. Composites market report 2014.

Gemi DS., Sahin OS., Gemi L. Experimental investigation of the effect of diameter upon low velocity impact response of glass fiber reinforced composite pipes. Composite Structures 2021; 275: 114428.

Gemi DS., Sahin OS., Gemi L. Experimental investigation of axial compression behavior after low velocity impact of glass fiber reinforced filament wound pipes with different diameter. Composite Structures 2022; 280: 114929.

Gemi L. Düşük hızlı darbe hasarlı filaman sarım hibrid boruların iç basınç altında yorulma davranışı. Doktara Tezi, Selçuk Üniversitesi Fen Bilimleri Enstitüsü, Konya 2014.

Gemi L. Investigation of the effect of stacking sequence on low velocity impact response and damage formation in hybrid composite pipes under internal pressure. A comparative study. Composites Part B: Engineering 2018; 153: 217-232.

Gemi L., Koklu U., Yazman S., Morkavuk S. The effects of stacking sequence on drilling machinability of filament wound hybrid composite pipes: Part-1 mechanical characterization and drilling tests. Composites Part B 2020; 186: 107787.

Gemi L., Tarakcioglu N., Akdemir A., Sahin OS. Progressive fatigue failure behavior of glass/epoxy (±75) 2 filament-wound pipes under pure internal pressure. Materials & Design 2009; 30(10): 4293-4298.

Hocine A., Chapelle D., Boubakar ML., Benamar A., Bezazi A. Experimental and analytical investigation of the cylindrical part of a metallic vessel reinforced by filament winding while submitted to internal pressure. International journal of pressure vessels and piping 2009; 86(10): 649-655.

Kabir MZ. Finite element analysis of composite pressure vessels with a load sharing metallic liner. Composite structures 2000; 49(3): 247-255.

Kumar SS., Kumari AS. Design and failure analysis of geodesic dome of a composite pressure vessel. International Journal of Engineering Research and Technology 2012; 1(7): 1-8.

Madhavi M. Design and analysis of filament wound composite pressure vessel with integrated-end domes. Defence Science Journal 2009; 59(1): 73-81.

Nebe M., Asijee TJ., Braun C., van Campen JMJF., Walther F. Experimental and analytical analysis on the stacking sequence of composite pressure vessels. Composite Structures 2020; 247: 112429.

Oromiehie E., Prusty BG., Compston P., Rajan G. Automated fibre placement based composite structures: Review on the defects, impacts and inspections techniques. Composite Structures 2019; 224: 110987.

Ozbek O., Bozkurt OY., Erklig A. An experimental study on intraply fiber hybridization of filament wound composite pipes subjected to quasi-static compression loading. Polymer Testing 2019; 79: 106082.

Park YH., Sakai J. Optimum design of composite pressure vessel structure based on 3-dimensional failure criteria. International Journal of Material Forming 2020; 13(6): 957-965.

Prabhakar MM., Rajini N., Ayrilmis N., Mayandi K., Siengchin S., Senthilkumar K., Karthikeyan S., Ismail SO. An overview of burst, buckling, durability and corrosion analysis of lightweight FRP composite pipes and their applicability. Composite Structures 2019; 230: 111419.

Sepetcioglu H. Experimental study on the effect of graphene nanoplatelets on the low-velocity impact response of prestressed filament wound basalt-based composite pressure vessels. Polymer Composites 2021; 42: 5527-5540.

Takeichi N., Senoh H., Yokota T., Tsuruta H., Hamada K., Takeshita HT., Tanaka H., Kiyobayashi T., Takano T., Kuriyama N. Hybrid hydrogen storage vessel, a novel high-pressure hydrogen storage vessel combined with hydrogen storage material. International Journal of Hydrogen Energy 2003; 28(10): 1121-1129.

Tasyurek M., Tarakcioglu N. Enhanced fatigue behavior under internal pressure of CNT reinforced filament wound cracked pipes. Composites Part B: Engineering 2017; 124: 23-30.

Yao SS., Jin FL., Rhee KY., Hui D., Park SJ. Recent advances in carbon-fiber-reinforced thermoplastic composites: A review. Composites Part B: Engineering 2018; 142: 241-250.

Zuttel A. Materials for hydrogen storage. Materials Today 2003; 6(9): 24-33.

Zwillinger D. Handbook of differential equations. Gulf Professional Publishing 1998; 1.

OKÜ Fen Bilimleri Enstitüsü Dergisi
5(Özel Sayı):135-155, 2022

OKU Journal of The Institute of Science and Technology, 5(Special Issue):135-155, 2022

Osmaniye Korkut Ata Üniversitesi Fen Bilimleri Enstitüsü Dergisi

Osmaniye Korkut Ata University Journal of The Institute of Science and Technology

Investigation of the Flow Structures for Two Tandem Arrangements of Torpedo-Like Geometries

Ezgi AKBUDAK[1], Bülent YANIKTEPE[2*], Ertuğrul ŞEKEROGLU[3], Ömer KENAN[4], Muammer OZGOREN[5]

[1,2,3,4]Osmaniye Korkut Ata University, Faculty of Engineering, Department of Energy Systems Eng., Turkey
[5]Necmettin Erbakan University, Faculty of Engineering, Department of Mechanical Eng., Konya, Turkey

[1]https://orcid.org/0000-0002-7766-8303
[2]https://orcid.org/0000-0001-8958-4687
[3]https://orcid.org/0000-0002-6592-3872
[4]https://orcid.org/0000-0002-3919-6923
[5]https://orcid.org/0000-0002-9088-5679
*Corresponding Author: byaniktepe@osmaniye.edu.tr

Research Article

Article History:
Received: 17.12.2021
Accepted: 25.01.2022
Published online: 23.02.2022

Keywords:
Elliptical nose
PIV
Tandem arrangement
Torpedo-like geometry
Viscous flow

ABSTRACT

In this study, flow structures of a streamlined torpedo-like geometry having an elliptical nose and tampered stern at a length to the diameter aspect ratio of L/D=5 for a single and double tandem arrangement with various spacings have been investigated using Particle Image Velocimetry (PIV) method in a closed loop water channel. Reynolds number defined for the length of the geometry (L=200 mm), free stream water velocity of 100 mm/s was taken as Re=20000, the spacing (G) between two identical torpedo-like geometries is changed from 0 to 120 mm. Instantaneous 1000 images and their time-averaged results are comparatively presented for all configurations of the torpedo-like geometry. It is demonstrated that the tandem arrangements depending on the dimensionless spacing ratios (G/L) between 0 to 0.6 is significantly different from the single torpedo-like geometry for the flow patterns of instantaneous and time-averaged velocity field, dimensionless streamwise velocity component and streamline topology. For the contacting case in which the following model nose is placed on the trailing edge of the front model, the wake region of the back geometry is similar to the single model wake but the all of time-averaged flow patterns elongated and symmetrical flow patterns are slightly deformed. When flow area is provided between two models for spacing ratios of $0.15 \leq G/L \leq 0.30$, chaotic and rotational flow patterns occur due to the impinging of separated flow patterns from the front geometry to the nose of the downstream one. As the gap distance increases to the largest value at G/L=0.6, the wake region of both the single and tandem arrangement becomes almost identical. More detailed information for the flow characteristics of the examined torpedo-like geometry can be determined by using computational fluid dynamics after validation with PIV results in the present study.

Torpido Benzeri Geometrilerin İki Tandem Düzenlemesi İçin Akış Yapılarının İncelenmesi

Araştırma Makalesi

Makale Tarihçesi:
Geliş tarihi: 17.12.2021
Kabul tarihi: 25.01.2022
Online Yayınlanma: 23.02.2022

ÖZET

Bu çalışmada, çeşitli aralıklarla tek ve çift tandem düzenlemesi için uzunluk-çap en boy oranı L/D=5 olan, eliptik bir burna ve konik kıç kısmına sahip aerodinamik torpido benzeri bir geometrinin akış yapıları, bir kapalı çevrim su kanalı içinde Parçacık Görüntülemeli Hız ölçme (PIV), yöntemi kullanılarak

Anahtar Kelimeler:
Eliptik burun
PIV
Tandem düzenleme
Torpido benzeri geometri
Türbülanslı akış
Viskoz akış

incelenmektedir. Geometrinin uzunluğu için tanımlanan Reynolds sayısı (L=200 mm) Re=20000 değeri, serbest su akış hızı 100 mm/s, olarak alınmaktadır. İki özdeş torpido benzeri geometri arasındaki mesafe (G) 0-120 mm aralığında değişmektedir. Torpido benzeri geometrinin tüm konfigürasyonları için anlık ve 1000 görüntüden hesaplanan zaman ortalamalı sonuçlar karşılaştırmalı olarak sunulmaktadır. Boyutsuz boşluk oranlarına (G/L) 0 ila 0,6 arasındaki bağlı tandem düzenlemelerinin, anlık hız alanı (V), zaman ortalamalı hız alanı <V>, boyutsuz akış yönündeki hız bileşeni <u/U∞> ve akım çizgisi topolojilerinin <Ψ> tek torpido benzeri geometriden önemli ölçüde farklı olduğu gösterilmektedir. Öndeki modelin firar ucu arkadaki modelin burnuna temas durumu için arka geometrinin art izi bölgesi tek model art izine benzer, ancak tüm zaman ortalamalı akış yapıları uzamakta ve simetrik akış yapıları biraz deforme olmaktadır. Boyutsuz boşluk 0,15≤G/L≤0,30 aralık oranları için iki model arasında akış alanı sağlandığında, öndeki geometriden ayrılmış akış yapılarının arkadaki geometrinin burnuna çarpması nedeniyle karmaşık ve dönümlü akış yapıları oluşmaktadır. Boşluk oranı en büyük değer G/L=0,6'ya yükseldikçe hem tekli hem de art arda düzenlemesinin art izi bölgesi hemen hemen aynı hale gelmektedir. İncelenen torpido benzeri geometrinin akış özellikleri için daha ayrıntılı bilgi, bu çalışmadaki PIV sonuçlarıyla doğrulama yapıldıktan sonra hesaplamalı akışkanlar dinamiği kullanılarak belirlenebilmektedir.

To Cite: Akbudak E., Yanıktepe B., Sekeroglu E., Kenan Ö., Ozgoren M. Investigation of the Flow Structures for Two Tandem Arrangements of Torpedo-Like Geometries. Osmaniye Korkut Ata Üniversitesi Fen Bilimleri Enstitüsü Dergisi 2022; 5(Özel sayı): 135-155.

Introduction

The investigation related to unmanned vehicles in all fields of civil, industry, and military such as air, land, and sea applications for designing equipment, control systems, structures, aerodynamic and hydrodynamic behaviours has been performed by researchers for many years. Fluid mechanics applications have an important role to obtain an optimized geometry of aerodynamic and hydrodynamic characteristics of vehicles. Technological developments in all fields have been affected the production of manned or unmanned autonomous underwater vehicles (AUVs). Therefore, many researchers have been directed to design, apply and improve the new generations AUVs in defense, industry and research areas (Ozgoren et al. 2010; Rattanasiri et al. 2012; Tian et al. 2017; Akbudak et al. 2021; Kilavuz et al. 2022). One of the AUVs is a torpedo-like geometry that has to reach the pre-determined target with stored energy on the body in time. Controlling flow characteristics and diminishing the negative effects such as flow separation, fluid-structure interaction and larger unsteady drag forces require a detailed investigation. The obtained data can be used to control the maneuvering and cruising paths of AUVs for single or multiple arrangements. Rattanasiri et al. (2012) stated that AUVs performed many confidential missions with equipment such as different sensors, carried by many small AUVs instead of one large AUV resulting in better levels of resilience and redundancy. The arrangement of the movement of multiple AUVs in the flow environment was inspired by animals that swim and/or fly as herds. With the help of this observation, there are many research results that show more energetic performance benefits of the configurations such as different spacings of inline, tandem or staggered arrangement (Partridge et al. 1983; Hanrahan and Juanes 2001; Andersson and

Wallander, 2003; Alexander, 2004; Weihs, 2004; Rattanasiri et al. 2012). The drag characteristics of a pair of prolate spheroids having a length (L) of 1.2 m with a length-diameter ratio of 6:1 at a Reynolds Number (Re) of $3.2x10^6$ were examined by Molland and Utama (1997). They recorded that the drag coefficients according to the wetted surface area were 8%, 4% and 2% larger than that of a single spheroid, in consequence, for the spacing ratios of side by side arrangement for S/L of 0.27, 0.37 and 0.47. A numerical simulation study for multiple torpedo shape AUVs was done by Husaini (2009). It was displayed that the drag forces on both AUVs concerning the arrangement spacings were influenced significantly. Rattanasiri et al. (2012) conducted a study using same sized prolate spheroids and classified the results depending on the individual drag and combined drags with five regions which were low interaction region, parallel region, drafting region, echelon region, and push region. They recommended from their results that operators of AUVs can settle a possible fleet traveling arrangement accordingly energy consumption like swimming of dolphins.

A novel method that is Particle Image Velocimetry (PIV) has been using many fluid mechanic applications, recently. Yagmur (2016) studied the flow behaviors around a special torpedo-like geometry placed in a uniform flow for various angles of attack $\alpha=0^o$, 4^o, 8^o, 12^o and passive flow control modifying the geometry and adding tail via PIV and Computational Fluid Dynamics (CFD) by using ANSYS-Fluent program for Reynolds numbers of $Re=2x10^4$ and $Re=4x10^4$, time-dependently. Instantaneous and time-averaged vector fields, vorticity, contours for time-averaged scalar values of streamwise and cross-stream wise velocity components, and its root mean squares components, Reynolds stress correlation, Turbulence Kinetic Energy (TKE) scalar values and streamline topology were discussed. The results exhibited that the pressure coefficient took its maximum value ($C_P = 1$) at the stagnation point placed the leading edge of the torpedo-like geometry and it had negative values after the region that flow separation occurs along the fuselage region of the body for the torpedo-like geometry. With the increase in attack angles, both the drag and lift coefficients increased and lower pressure regions formed under the body. Because of the flow separation, Reynolds stress and TKE values in the trailing and leading region of the model became stronger with the increased attack angle. An experimental study with PIV method for comparison of different configurations of two spheres at Re= 5000 in a uniform flow was performed by Ozgoren et al. (2004), in which the turbulent flow characteristics around the both spheres were strongly dependent on the distance and arrangement angle. Another study by Yagmur et al. (2016), increasing angle of attack disrupted the symmetrical distribution of flow characteristics around the torpedo-like geometry so that the saddle point (S) at the tip of the nose of the geometry moved upwards, and that the trace area approached the body due to the increase in the Reynolds number. Kilavuz et al. (2021) investigated the flow characteristics of torpedo-like geometry placed near the free-surface for immersion ratios of $0.75 \leq h/D \leq 3.5$ and angles of attack $\alpha=0°$,4°, 8°, and 12°. Variation of Froude numbers (Fr) depending on the immersion ratio was found that Fr number and corresponding drag coefficient had higher values for the lower immersion ratio. Multiple arrangements of the circular cylinders, square cylinders, spheres, elliptic or oval

cylinders were investigated by Zobeyer et al. (2021), Hossain et al. (2021), Zhengi and Alam (2019), Ozgoren et al. (2014), Pinar et al. (2013), Ibrahim and Gomaa (2009), Georgios et al. (2006), Jianfeng et al. (2005), Mittal and Kumar (2001), Zdravkovich (1977). These articles highlighted the various phenomena, flow characteristics, forces and turbulence associated with vortex-induced oscillations depending on the distance between the bodies, Reynolds number, geometry shape and arrangement with experimental and numerical methods. Zdravkovich (1977) examined the flow-interaction results in a steady flow for various arrangements of two cylinders such as staggered, side-by-side and tandem. It was recorded that when more than one identical bluff body model was located in a fluid flow, the induced forces and vortex shedding structures are distinguishably different for a single geometry at the same Reynolds number. Furthermore, flow characteristics and flow-structure interaction are highly dependable on the arrangement between two fixed cylinders. Yaniktepe and Rockwel (2005), Mitchell and Delery (2001), Siegel et al. (2001), Polat et al. (2021), Ozalp et al. (2021) performed experimental studies using PIV method around unmanned combat air vehicle models in water channel and wind tunnel.

Investigation of flow characteristics of two tandem torpedo-like geometries which is a representative of fleet AUVs has been done using PIV method in uniform condition at Re=2x10^4. This will be one of the first study for the PIV application such a body arrangement, which has not been encountered in the literature. The results quantitively and comparatively have been presented depending on the spacing ratio by using instantaneous and time-averaged flow structures.

Material and Methods

The geometry and size of the torpedo-like model were determined to form a streamlined underwater vehicle model by using the Myring (1976) equations 1 and 2 given below.

$$r_N(x) = \frac{1}{2}D\left[1 - \left(\frac{x - L_N}{L_N}\right)^2\right]^{1/n} \quad (1)$$

$$r_S(x) = \frac{1}{2}D - \left[\frac{3D}{2{L_S}^2} - \frac{tan\theta}{L_S}\right](x - L_N - L_H)^2 + \left[\frac{D}{{L_S}^3} - \frac{tan\theta}{{L_S}^2}\right](x - L_N - L_H)^3 \quad (2)$$

Here, where n=2. The angular parameter of the tail is given in equation 2, where $\theta \cong 30°$ is taken. In these equations, x is the axial distance from the nose to the stern end. Myring angular parameter of the stern and the overall potential parameter of the geometry are taken as $\theta \cong 30°$ and n=2, respectively. The experiments were done at free-stream velocity of U_∞=100 mm/s corresponding to Reynolds numbers ($Re = U_\infty L/\upsilon$) 2.0x10^4, L=200 mm is the length and υ is the kinematic viscosity of water (υ=1x10^{-6} m^2/s^2). The PIV measurement was conducted using the water channel and a Nd:YAG laser

working in synchronization with a camera in the Advanced Mechanical Engineering laboratory of Osmaniye Korkut Ata University. The channel consisting of transparent Plexiglas to allow observation has a width of 0.8 m, length of 6 m, and depth of 1 m. During the experiment, water depth (h_W) is fixed as 80 cm. The 10 μm diameter silver coated hollow glass sphere particles with a density of around 1100 kg/m^3. The double pulse YAG laser with a 532 nm wavelength, a 145 mJ pulse energy and 15 Hz frequency were used to illuminate the flow field as seen in Figures 2 and 3. The experimental setup of the water channel for laser illumination and PIV measurement of field of views is shown in Figure 4. The space between the torpedo-like geometries is denoted by G. The thickness of the laser sheet was kept at approximately 1.5 mm. A Charged Couple Device (CCD) camera having 1600x1200 pixels resolution was used to capture images. Interrogation window areas of 32x32 pixels were used with 50% overlap for the double-frame images to produce velocity vectors. The obtained velocity field contained as many as 7326 (99x74) vectors. Throughout the measurement 1000 double-frame images were taken in 66.6 seconds. The obtained 1000 images containing instantaneous velocity vectors were used for the time-averaged velocity vector field, streamline topology and streamwise velocity component. The Dantec Dynamic Studio software was used to obtain the velocity field. Spurious velocity vectors (less than 3%) caused by shadows, reflections from the free-surface and model, laser sheet distortions and image processing were detected using the local median-filter technique, developed by Westerweel (1994). The uncertainty of velocity measurement in PIV is estimated to be around 2% as stated by Westerweel (1994) and Ozgoren (2006). From instantaneous PIV images, the time-averaged streamwise velocity is calculated as follows;

$$\langle u(i,j)\rangle = \frac{1}{N}\sum_{n=1}^{N} u_n(i,j) \tag{3}$$

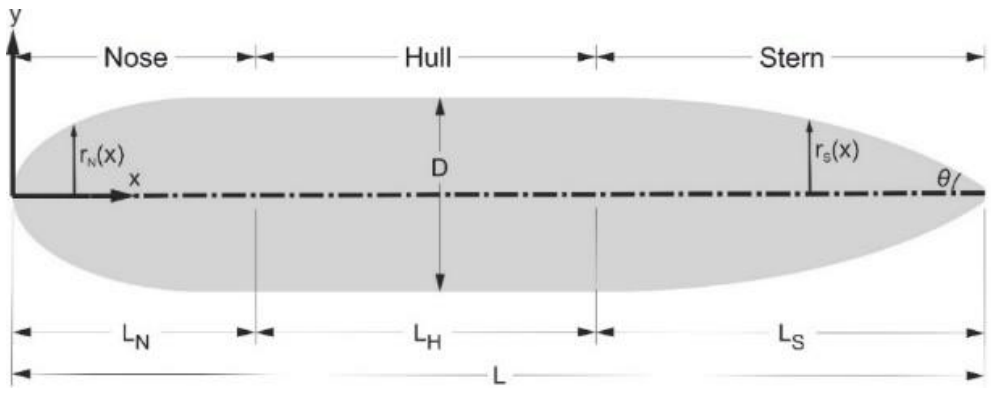

Figure 1. Parameters of a geometrical design of a torpedo-like geometry. The nose, hull and stern lengths of the model with a D=40 mm diameter are L_N=40 mm, L_H=80 mm and L_S=80 mm, respectively.

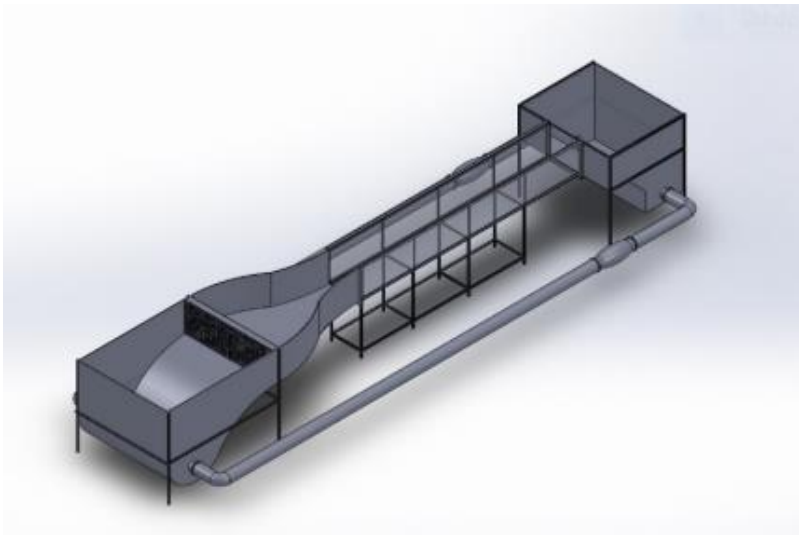

Figure 2. Water channel view for PIV measurement (Sekeroglu, 2019)

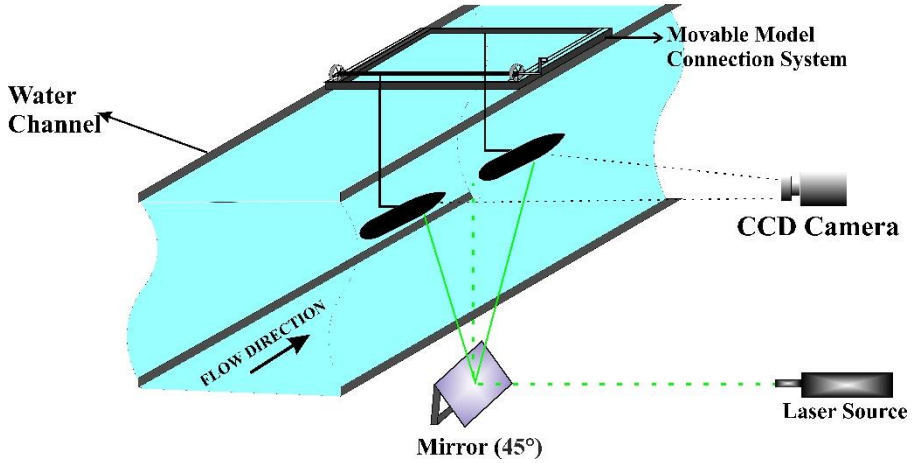

(a)

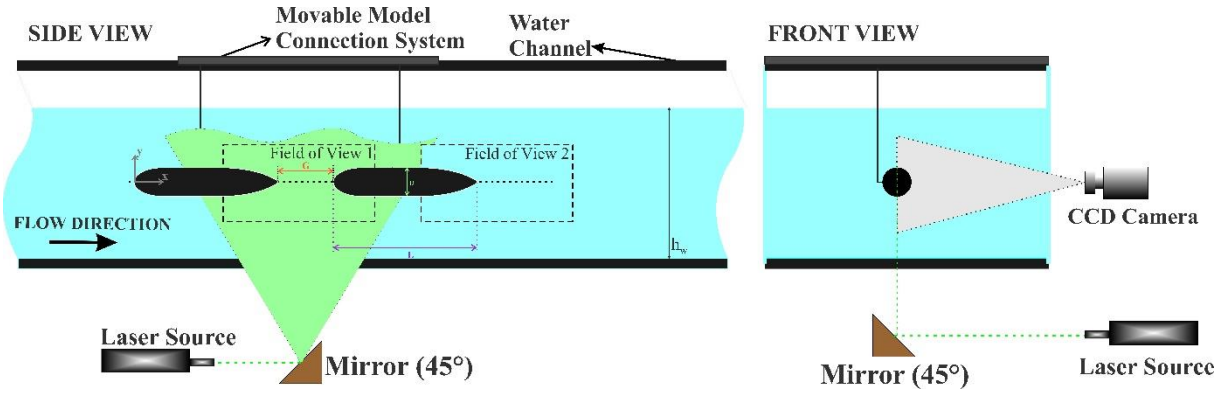

(b)

Figure 3. Experimental setup of the water channel for laser illumination and PIV measurement

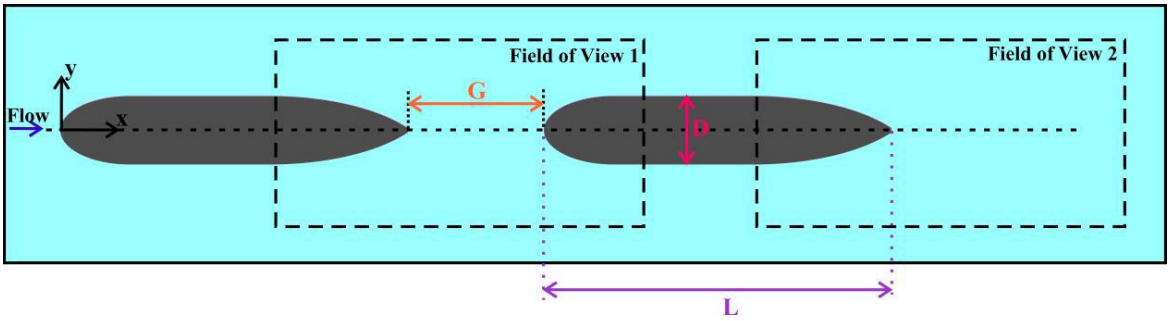

Figure 4. Field of views for the tandem arrangement of two torpedo-like geometries for PIV measurement

Results and Discussion

PIV results of a single torpedo-like geometry in the wake region (a) instantaneous velocity vector field (V) and time-averaged (b) velocity vector field <V>, (c) dimensionless streamwise velocity component (<u/U_∞>), and (d) streamline topology (<Ψ>) at Re=2x10^4 is presented in Figure 5. Instantaneous velocity vectors have a reversed flow and low level in the near wake of the downstream and then the flow progress in wavy motion. The time-averaged velocity vectors eliminate the alternating direction of the flow structures and the reserved flow region is restricted in approximately one diameter length. Time-averaged streamline topology includes a focus point and asymmetric pattern, which might be misalignment of the geometry during the experiment. The time-averaged streamwise velocity component does have a small negative value contour due to the lessening effect of the flow separation providing the streamlined body. Magnitudes of the contour levels increase gradually to reach almost the uniform velocity value. The vortex formation length in the wake region extends as long as one-length of the geometry.

In the wake region of the torpedo-like geometry, the stagnation point created by the diverging streamlines in the flow are indicated by the letter "S" for a saddle point, the point where the flow is accumulated at a single point by the convergence of the streamlines called Node and denoted with a letter "N", and the vortices formed by the streamlines of the rotational flow in the clockwise and anticlockwise directions called focus are indicated by the letter "F".

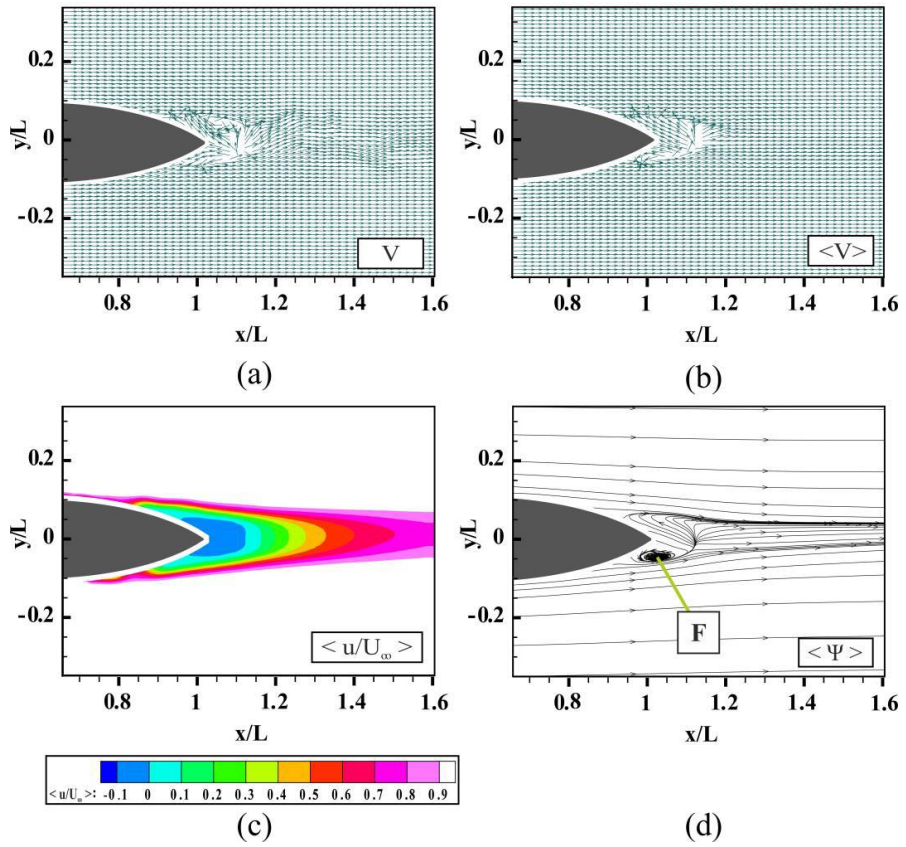

Figure 5. PIV results of an induvial torpedo-like geometry in the wake region (a) instantaneous velocity field (V) and time-averaged (b) velocity field <V>, (c) dimensionless streamwise velocity component (<u/U_∞>), and (d) streamline topology (<Ψ>) at Re=2x10^4.

Comparison of the spacing ratio in the range of 0≤G/L≤0.6 effects on instantaneous velocity vector field (V) for a tandem arrangement of two torpedo-like geometries at Re=2x10^4 is shown in Figure 6. As seen in Figure 6, if the torpedo-like geometries are far apart at G/L=0.6, the flow around either of them is similar to that of a single torpedo-like geometry. If the torpedo-like geometries are close or if the second torpedo-like geometry is neighbor to or within the wake of the front torpedo-like geometry, the interference between the two bodies can be one of the three types: proximity interference, wake interference, proximity and wake interference similar to the cases of the two tandem various bodies in the literature. Wake interference occurs for two torpedo-like geometries in tandem when the streamwise spacing between the two torpedo-like geometries is sufficiently large. The upstream torpedo-like geometry is unaffected by the presence of the downstream one. The trajectory of the upstream torpedo-like geometry at G/L=0.6 resembles a horizontal S shape as in the Von Karman Vortex Street. The downstream torpedo-like geometry lies in the wake of the upstream one and therefore suffers interference effects. When the downstream torpedo-like geometry is close to the upstream torpedo-like geometry and lies in its wake, both the geometries affect the flow past each other. This results in proximity and wake disturbance and can occur for the torpedo-like geometries in

tandem arrangement. All of these results are similar to the findings of the circular cylinders in the studies of Zdravkovich (1977), Mittal and Kumar (2001).

Torpedo-like geometry in the downstream placed in the wake region of the upstream torpedo-like geometry creates higher level turbulent flow characteristics compared to the single torpedo-like geometry. The separated flow from the upstream torpedo-like geometry impinges to the downstream one and tries to return back to the wake region between the two torpedo-like geometry whereas simultaneously the momentum of the incoming flow pushes the separated flow through the nose and fuselage of the downstream geometry. The PIV data are dominated by small-scale structures. In the wake region of downstream torpedo-like geometry, the accumulation of small vortices into larger ones seems to be an important feature of the forming of coherent structures. Such combination occurs most frequently when the shear layers from the upstream and downstream bodies are locally receptive to scales close to the subharmonic of existing scales in the flow as also stated by Cimbala et al. (1988). The wake view demonstrates the decay of the Von Karman Vortex Street, growth of secondary structures and finally recovering to the uniform condition. Hydrodynamic instability of the wake profile is responsible for interference and the formation of the downstream structure. The big vortex structure in the far wake is a result of accumulation of Kelvin Helmholtz vortices into bigger vortical structures. As the wake shrinks with downstream distance, the size of the big structures must also decay. Hydrodynamic instability of the developing wake profile causes this phenomenon. Hydrodynamic flow characteristics such as drag and lift forces change significantly when the separated flow crumbles the nose of a body.

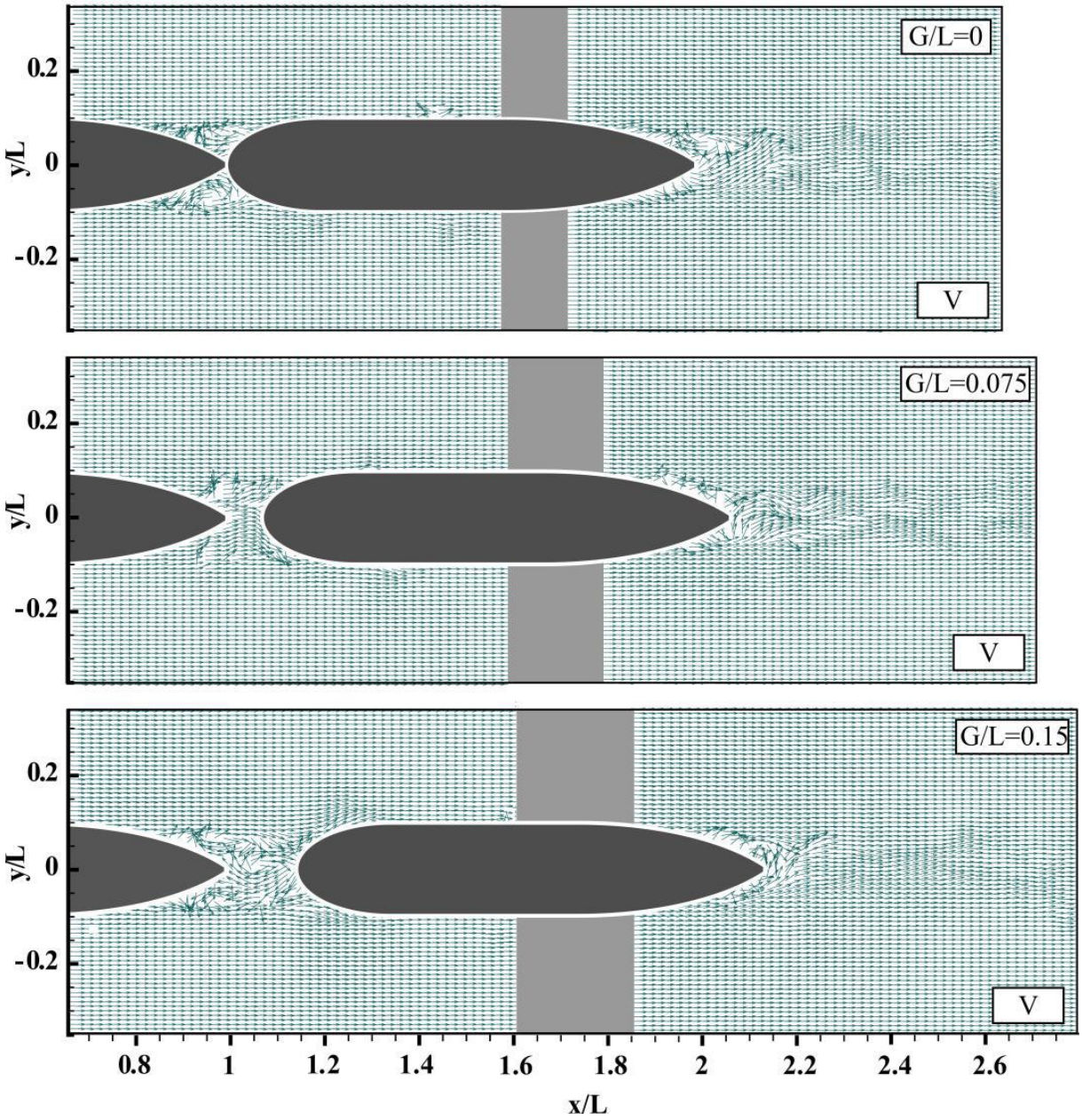

Figure 6a. Comparison of the spacing ratio in the range of $0 \leq G/L \leq 0.15$ effects on instantaneous vector field (V) for a tandem arrangement of two torpedo-like geometries at $Re=2x10^4$.

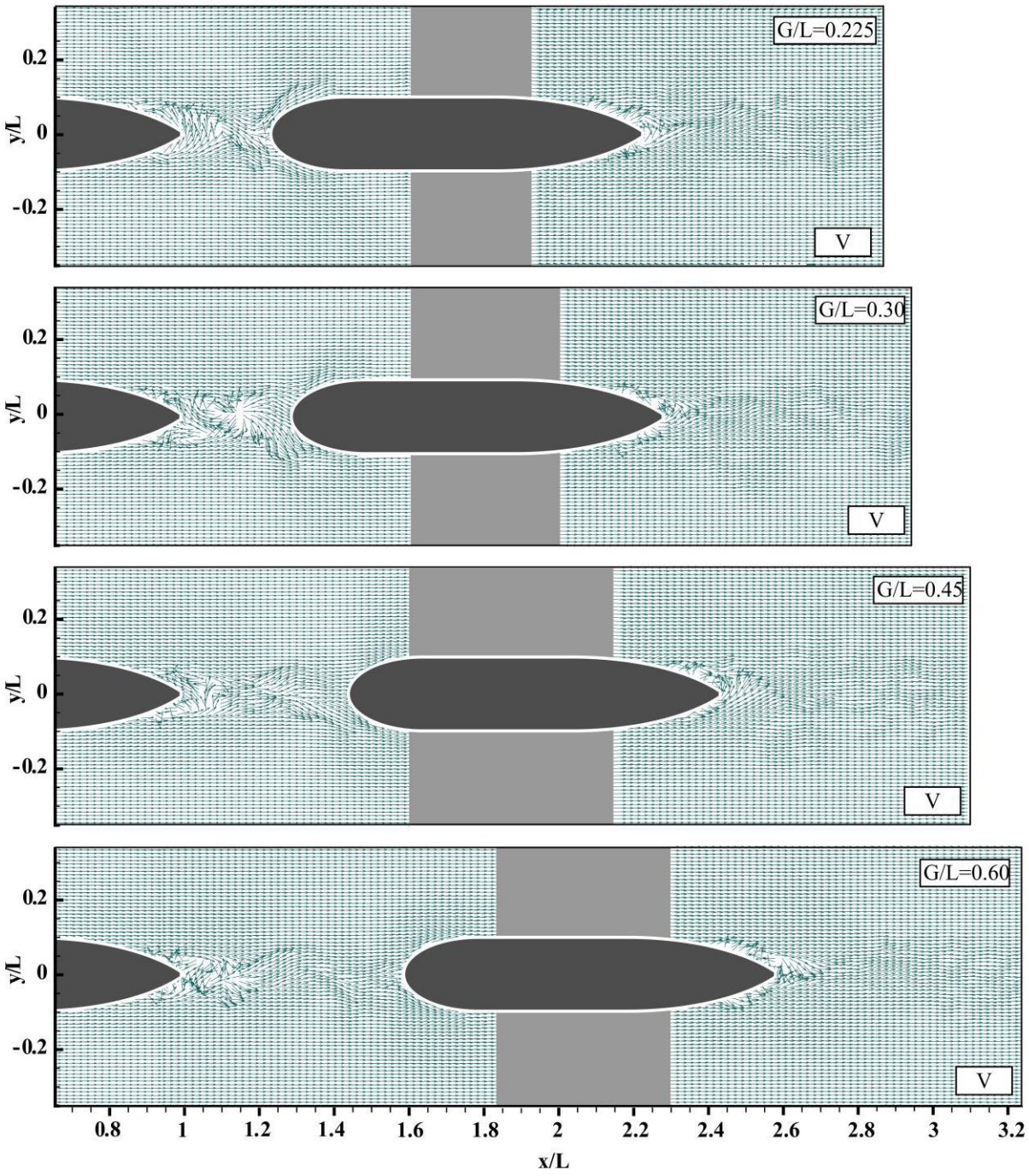

Figure 6b. Continued of 6a for the spacing ratio in the range of $0.225 \leq G/L \leq 0.6$

Comparison of the spacing ratios in the range of $0 \leq G/L \leq 0.15$ effects on the dimensionless time-averaged vector field <V>, time-averaged streamline topology <Ψ> and the time-averaged streamwise velocity $\langle u/U_\infty \rangle$ for a tandem arrangement of two torpedo-like geometries at $Re=2x10^4$ is given in Figures 7, 8 and 9. The time-averaged vector field <V> in Figure 7a for spacing ratio G/L=0, the effect of the upstream model in the FoV_1 region distorts the velocity vectors in the flow direction and tends to form a swirling flow around the stern, the flow follows the hull of the downstream and separates through the wake. Wake region of the downstream torpedo-like geometry is similar for the

cases of G/L=0, G/L=0.075 and G/L=0.15 while the wake region of the upstream body forms a complex velocity field for G/L=0.075 and G/L=0.15. For G/L=0.075, in the FoV_1 image, the incoming flow in the lower part of the geometry is directed towards the wake region since the pressure in the intermediate region between the bodies is lower. Later, the accelerated flow hits the nose downstream and disperses around the nose. The time-averaged streamline patterns for G/L=0.075 create nodes (N_1 and N_2). The increased spacing ratio for G/L=0.15 decreases the impingement flow momentum on the downstream torpedo-like geometry and the streamline topology forms two limited foci (F_1 and F_2). That is one in a clockwise direction on the upper side and the other in an anti-clockwise direction in the lower side. The wake region of the downstream torpedo-like geometry for time-averaged streamline topology creates a saddle point (S_1) and a focus point (F_2).

Shedding flow goes upwards to the nose of the downstream model, the flow which tries to return by hitting the object, is directed up or down due to flow instability because it does not have the energy to move against the flow direction. As expected, time-averaged streamwise velocity variation near to the stern profile in Figure 9 is a sharp curve both induvial and tandem arrangement for spacing ratios larger than G/L=0.15. As the shear layers on either side of the wake begin to combine, the wake gradually recovers as seen in Figure 8. At the spacing ratio of G/L=0.6, the time-averaged streamline topology in the wake region of the downstream torpedo-like geometry is smaller and closer to the trailing-edge than the induvial body as shown in Figure 5. Variations and trends of streamwise velocity component $<u/U_\infty>$ in Figure 5c are smaller than two tandem torpedo-like geometries in Figure 9 since the interference effect on the upstream and downstream model disturbs the wake properties, considerably. Vortex formation in the wake region of the induvial torpedo-like geometry is faster than the tandem arrangement for larger than G/L=0.3. At spacing ratios of G/L=0.45 and 0.60, the three-dimensional separated flow from the upstream torpedo-like geometry is recovered and merged nearly 0.8D away from the stern edge and it is around 0.3D away for the downstream one as exhibited in Figure 8. Later, the separated flow strikes to the downstream torpedo-like geometry similar to the uniform flow condition so that it induces wake region of the downstream torpedo-like geometry seeming to be the induvial one in Figure 5.

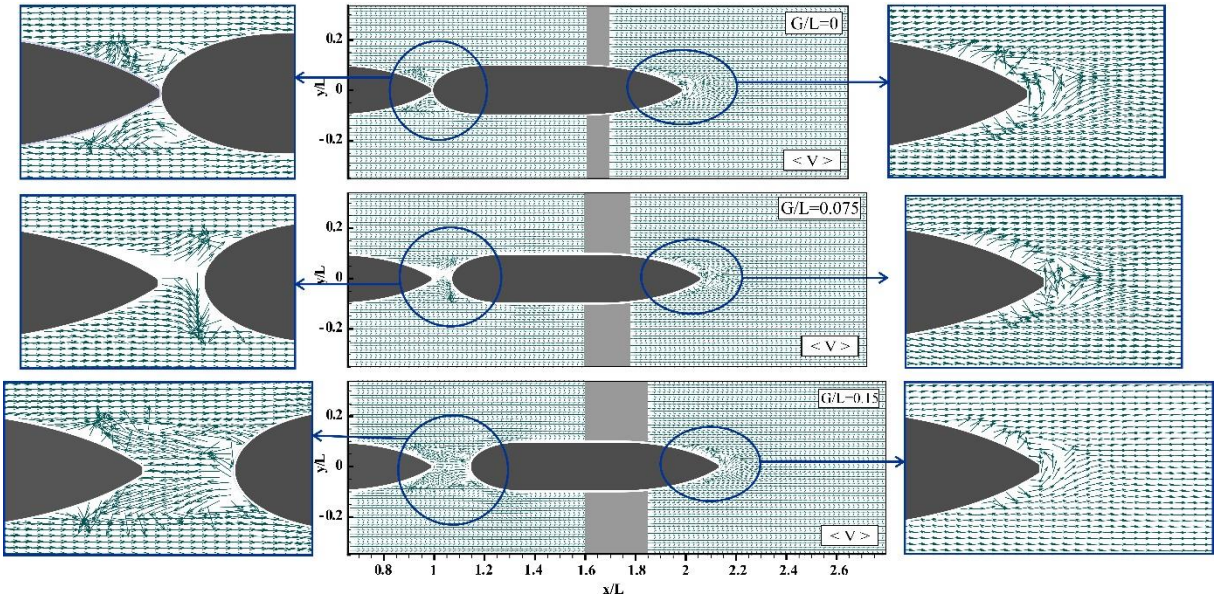

Figure 7a. Comparison of the spacing ratio in the range of $0 \leq G/L \leq 0.15$ effects on the time-averaged vector field <V> for a tandem arrangement of two torpedo-like geometries at $Re=2x10^4$. Left-hand side and right-hand side images show the focused flow region.

Overview of the time-averaged streamline topology, it is observed that the wake region both the upstream and downstream torpedo-like geometries reveal asymmetrical patterns for all spacing ratios due to the disturbance effect of the fluctuated turbulent flow. The vertical and three-dimensional size of the induvial wake region of the time-averaged velocity field is longer and bigger than the arrangement at spacing rations of G/L=0.30-0.45. Vortex shedding frequencies in the tandem arrangement may have more than one dominant frequency whereas the induvial torpedo-like geometry yields commonly only one dominant vortex shedding frequency. Three-dimensional relieving effect of the tampered stern either induvial torpedo-like geometry or the tandem arrangement forms a narrower and shorter wake region compared to the sharp-edged trailing body. Compared to the flow properties of the cylinder or sphere wake region for a tandem arrangement, the streamlined shape of the nose and stern of the torpedo-like geometry may cause lower forces fluctuations and less energy consumption during traveling.

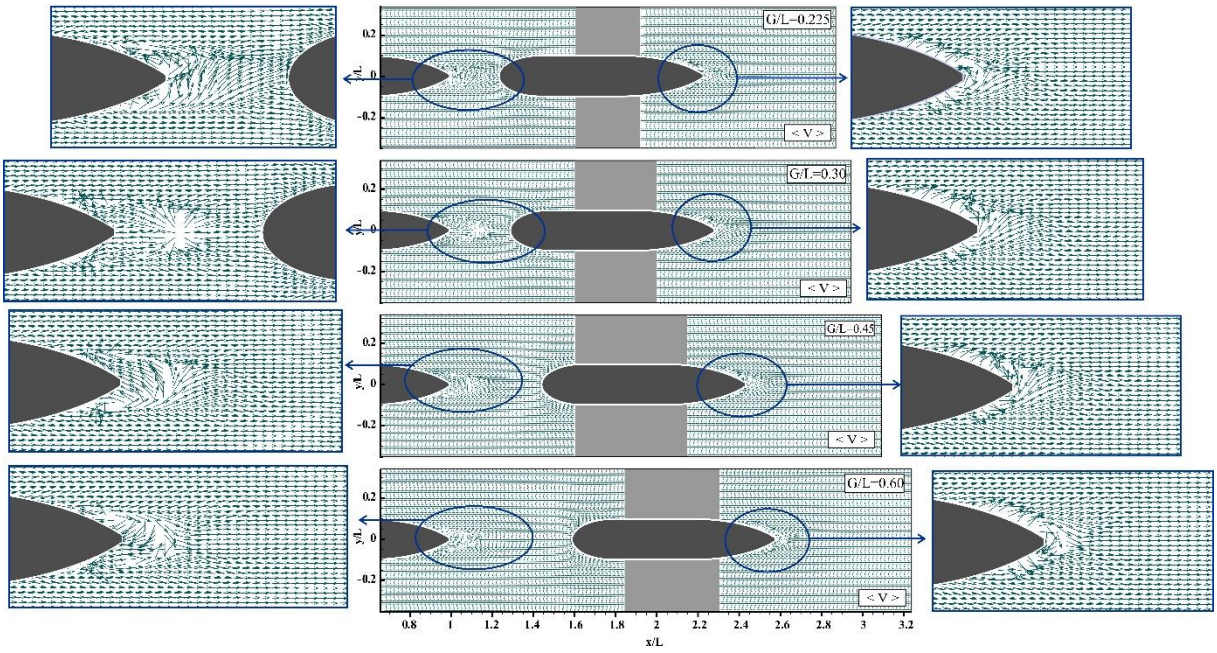

Figure 7b. Continued of 7a for the spacing ratio in the range of 0.225≤G/L≤0.6. Left-hand side and right-hand side images show the focused flow region.

It is demonstrated from the time-averaged velocity field in Figure 7, distance between upper and lower sides free-shear layer is shorter than the diameter of the torpedo-like geometry due to the retarded flow separation. Merging of the three-dimensional free-shear layer develops a saddle point that is locating different positions for both the geometries depending on spacing ratio. Magnitudes of the velocity inside the free-shear layer are lower than the uniform flow value downstream of the torpedo-like geometry due to the well-known wake region properties.

More detailed information on the topology of three-dimensional separated flows was given by Tobak and Peake (1982). In Figure 8a., three foci points (F_1, F_2 and F_3) and a saddle (S) are formed for the spacing ratio of G/L=0 and two foci behind the upstream torpedo-like geometry (F_1 and F_2) and present a symmetrical topology in the restricted region between the stern of upstream body and in front of the downstream body as seen in FoV_1. The effect of the flow striking the nose of the downstream model, asymmetrical wake occurs a clear appearance of saddle point (S) and focus (F_3) in the wake region of the FoV_2. When the spacing ratio is increased to G/L=0.15, uncompleted foci occur between two models and asymmetrical saddle point emerges in the wake region of the downstream body. Cross-comparison of the spacing ratios for G/L=0 and G/L=0.15 shows a larger circulation in F_1 for G/L=0.15 than F_1 for G/L=0 in the wake region of the upstream model. In Figure 8b., for G/L=0.225, the F_1 formed with the effect of the upstream turbulence is very small and close to the edge of the stern part of the upstream torpedo-like geometry. For G/L=0.30, a node point "N" is happened approximately 0.7D away from the tail-end of the upstream torpedo-like geometry.

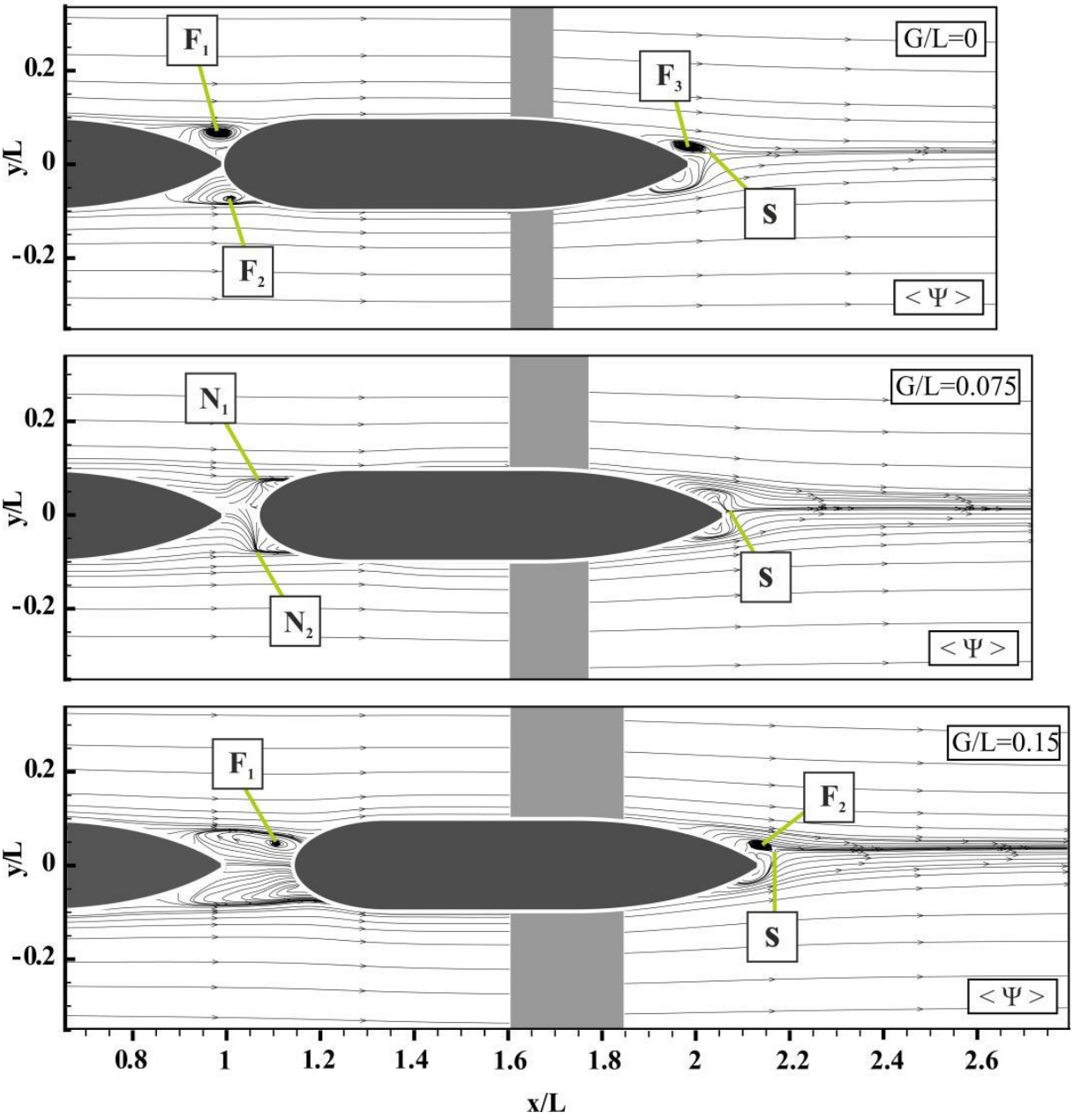

Figure 8a. Comparison of the spacing ratio in the range of $0.0 \leq G/L \leq 0.15$ effects on the time-averaged streamline topology $\langle \Psi \rangle$ for a tandem arrangement of two torpedo-like geometries at $Re=2x10^4$.

In Figure 9, negative contours of the time-averaged streamwise velocity $\langle u/U_\infty \rangle$ occur as small as $\langle u/U_\infty \rangle = -0.1$ in the wake region of the upstream torpedo-like geometry. The separated flow between the models for G/L=0.075 causes very fluctuated flows and their mean values eliminate each other so that the time-averaged values become closer to the zero values in the range of $0 \leq (\langle u/U_\infty \rangle) \leq 0.1$. The velocity profiles having a negative value indicate that a recirculation area occurs in the wake region. The recirculation region of the upstream torpedo-like geometry is larger than the downstream one in the flow direction. The minimum value of the $\langle u/U_\infty \rangle$ for an induvial torpedo-like geometry is

$<u/U_\infty>$=-0.05 while they are respectively $<u/U_\infty>$=-0.04 and $<u/U_\infty>$=-0.02 for the upstream and downstream of the torpedo-like geometries.

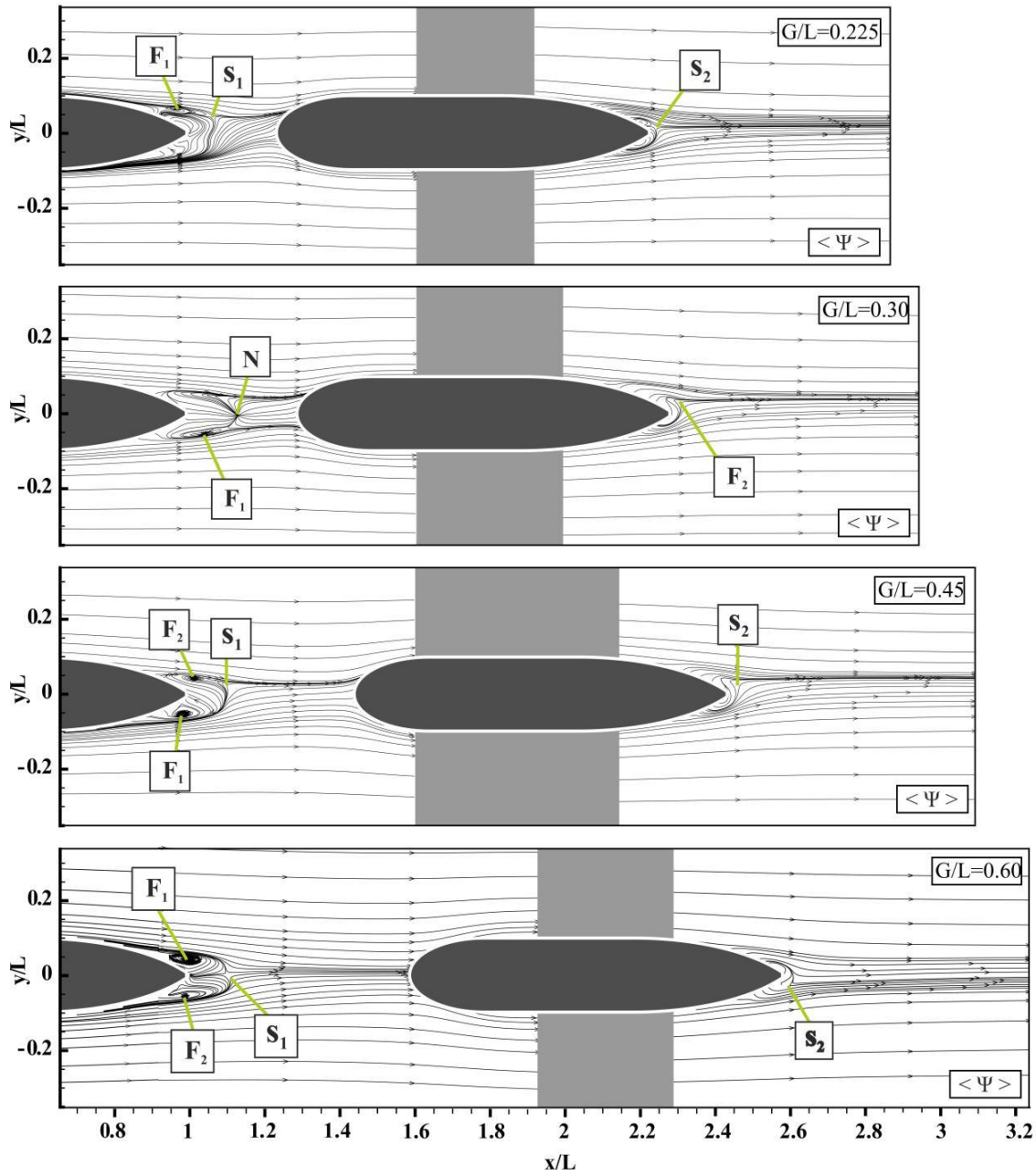

Figure 8b. Continued of 8a for the spacing ratio in the range of 0.225≤G/L≤0.6.

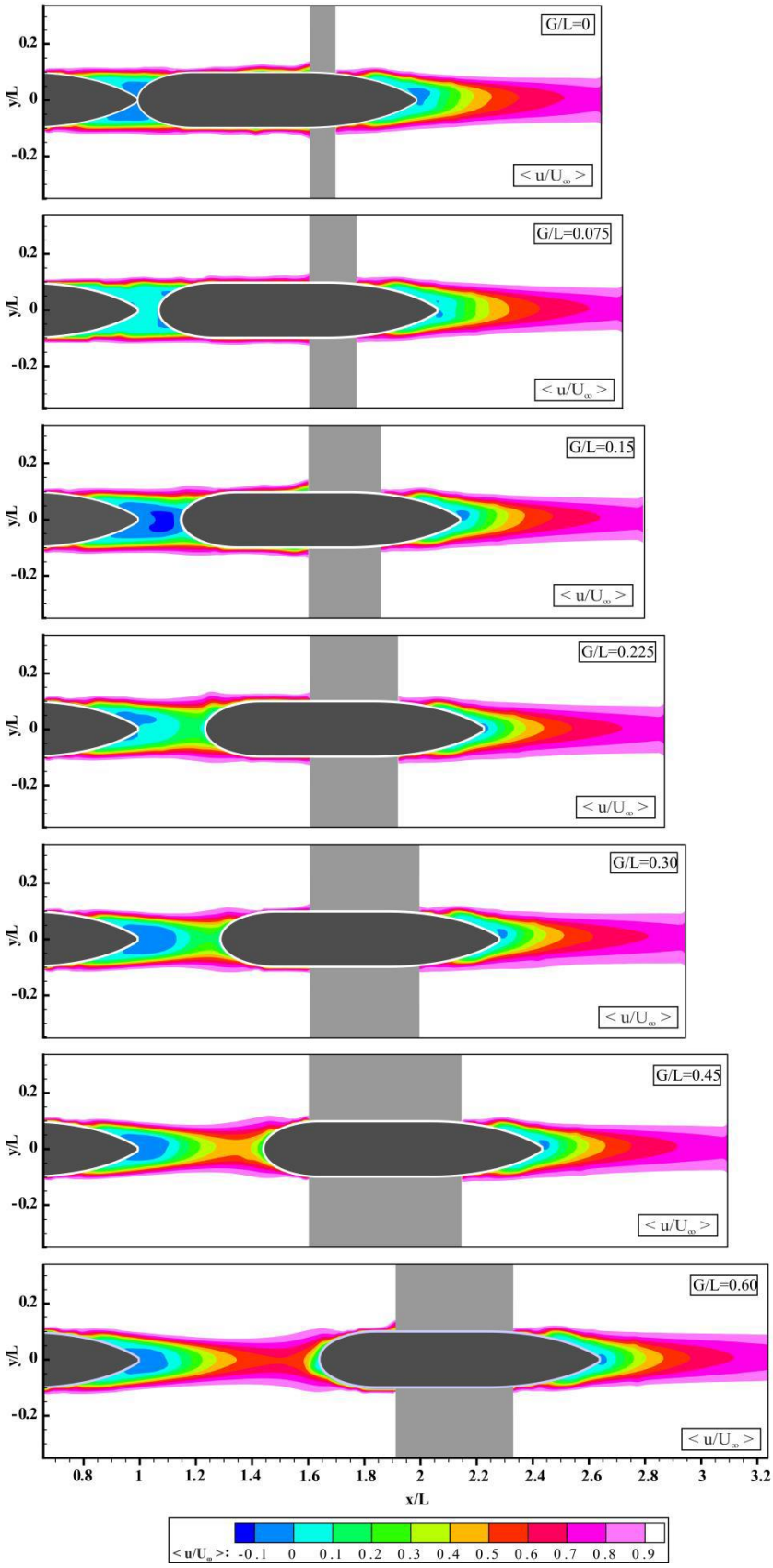

Figure 9. Comparison of the spacing ratio in the range of $0.0 \leq G/L \leq 0.60$ effects on the time-averaged streamwise velocity contours $\langle u/U_\infty \rangle$ for a tandem arrangement of two torpedo-like geometries at $Re=2x10^4$

Conclusion

In this study, PIV experiments were conducted to examine flow behaviours in a uniform flow condition around two torpedo-like geometries placed in a tandem arrangement in an open water channel at $Re=2x10^4$ based on the length of the body. The results for the induvial and tandem models are summarized as follows.

1) The instantaneous flow structures of instantaneous velocity vector fields around two tandem torpedo-like geometries continuously change due to the development of flow phenomena in the wake-influenced region and reveal an unsteady wavy structure in the wake region.

2) For the touching case at the spacing ratio of G/L=0 in the region between the trailing-edge of the upstream geometry and nose of the downstream one, the time-averaged streamline topology has two stable foci with a rotation inward direction, while asymmetrical streamline topology occurs in the wake region of the downstream model.

3) The concentrations of the rotational vector fields between the two bodies and in the wake region of the downstream model are more dominant for the small spacing ratio of $G/L<0.3$. For the spacing ratios of G/L=0.45 and 0.60, the flow passing the torpedo-like geometry has similar undulating motion in a swirling manner in the wake region of both models.

4) The flow characteristics show the size of the wake flow region, locations of the saddle, focus, foci and node as a function of the spacing ratios in the range of $0.30\leq G/L\leq 0.6$. It is seen that the wakes of both torpedo-like geometries were very complicated and sensitive to the spacing ratios due to the rotational flow impingement and the induced separation from the nose of the back geometry and finally occurrence of higher-level hydrodynamic forces.

5) The results revealed that the magnitudes of the time-averaged streamwise velocity gradually in the wake area of both geometries become almost identical as the spacing ratio increases to the G/L=0.6.

6) Time-averaged velocity vector fields, streamline topology and streamwise velocity component data will be useful to validate the numerical applications and later assess especially for lift and drag forces, flow-induced vibration effects and pressure variation.

Acknowledgment

The authors would like to acknowledge the Scientific and Technological Research Council of Turkey (TUBITAK) under Contract No. 214M318 and thank the Advanced Fluid Mechanics PIV laboratory of Osmaniye Korkut Ata University, Turkey for using the water channel and measurement systems.

Conflict of Interest

There is no conflict of interest between the authors.

Author's Contributions

The contribution of the authors is equal.

*This study was presented as a summary paper at the International Conference on Engineering, Natural and Applied Sciences (ICENAS'21) held online on 24-26 November 2021.

References

Akbudak E., Yaniktepe B., Sekeroglu E., Kenan O., Ozgoren M. Comparison of wake region flow characteristics for a tandem arrangement of two torpedo-like geometries. The International Conference on Engineering, Natural and Applied Science (ICENAS'21) Book of Abstracts 2021; November 24-26, 122, Osmaniye, Turkey.

Alexander RM. Hitching a lift hydrodynamically-in swimming, flying and cycling. Journal of Biology 2004; 3(2): 1-3.

Andersson M., Wallander J. Kin selection and reciprocity in flight formation?. Behavioral Ecology 2004; 15(1): 158-162.

Cimbala JM., Nagib HM., Roshko A. Large structure in the far wakes of two-dimensional bluff bodies. Journal of Fluid Mechanics 1988; 190, 265-298.

Hanrahan B., Juanes F. Estimating the number of fish in Atlantic bluefin tuna (Thunnus thynnus thynnus) schools using models derived from captive school observations. Fishery bulletin 2001; 99(3): 420-420.

Hossain MM., Nayeem MHK., Ali MAT. Numerical study of flow characteristics around rectangular cylinders in tandem. Journal of Mechanical Engineering, Automation and Control Systems 2021; 2(1): 36-43.

Husaini M., Samad Z., Arshad MR. CFD simulation cooperative AUV motion. Indian Journal of marine Sciences 2009; 38(3): 346–351.

Ibrahim TA., Gomaa A. Thermal performance criteria of elliptic tube bundle in crossflow. International Journal of Thermal Sciences 2009; 48(11): 2148-2158.

Jianfeng Z., Anlu R., Jian D., Wenqu C. Wake structures of two spheres in tandem arrangement at various gaps for Re= 300. Progress in Natural Science 2005; 15(2): 132-136.

Kılavuz A., Ozgoren M., Durhasan T., Sahin B., Kavurmacıoglu L., Akıllı H., Sarigiguzel F. Analysis of attack angle effect on flow characteristics around torpedo-Like geometry placed near the free-surface via CFD. Journal of Polytechnic 2021; 24 (4): 1579-1592

Kilavuz A., Sarigiguzel F., Ozgoren M., Durhasan T., Sahin B., Kavurmacioglu LA., Sekeroglu E., Yaniktepe B. The impacts of the free-surface and angle of attack on the flow structures around a torpedo-like geometry. European Journal of Mechanics-B/Fluids 2022; 92, 226-243.

Mitchell MA., Delery J. Research into vortex breakdown control. Progress in Aerospace Sciences 2001; 37(4): 385-418.

Mittal S., Kumar V. Flow-induced oscillations of two cylinders in tandem and staggered arrangements. Journal of Fluids and Structures 2001; 15(5): 717-736.

Molland AF., Utama IKAP. Wind tunnel investigation of a pair of ellipsoids in close proximity. Ship Science University of Southampton 1997.

Myring DF. A theoretical study of body drag in subcritical axisymmetric flow. Aeronautical quarterly 1976; 27(3): 186-194.

Ozalp C., Soyler M., Polat C., Saydam DB., Yaniktepe B. An experimental investigation of a rotationally oscillating cylinder. Journal of Wind Engineering and Industrial Aerodynamics 2021; 214, 104679.

Ozgoren M. Flow structure in the downstream of square and circular cylinders. Flow Measurement and Instrumentation 2006; 17(4): 225-235.

Ozgoren M. Flow structures around an equilateral triangle arrangement of three spheres. International Journal of Multiphase Flow 2013; 53, 54-64.

Ozgoren M., Dogan S., Canli E., Akilli H., Sahin B., Comparison of different configurations of two spheres at Re=5000 in a uniform flow. 17th International Symposium on Applications of Laser Techniques to Fluid Mechanics Lisbon, Portugal, 07-10 July, 2014, pp.1-12

Ozgoren M., Sahin B., Kahraman A., Akilli H., Canpolat C. Experimental investigation of flow characteristics of two tandem spheres placed in a uniform flow. Euromech Fluid Mechanics Conferance -8 (EFMC-8) 2010; September 13-16, s3-36, Germany.

Ozgoren M., Sahin B., Yayla S., Pınar E., Akar MA. Experimental investigation of flow structures around a tandem arrangement Spheres 16. Congress on Thermal Science and Technology with International Participation ,2007; 30 Mayıs-2 Haziran, 540-545, Kayseri, Turkey.

Partridge BL., Johansson J., Kalish J. The structure of schools of giant bluefin tuna in cape cad bay. Environmental Biology of Fishes 1983; 9, 253-262.

Papaioannou GV., Yue DK., Triantafyllou MS., Karnidakis G. Three-dimensionality effects in flow around two tandem cylinders. Journal of Fluid Mechanics 2006; 558, 387-413.

Polat C., Saydam DB, Soyler M, Ozalp C. Experimental investigation of flow around a rotating cylinder with PIV Technique. Osmaniye Korkut Ata University Journal of the Institute of Science and Technology, 2021; 4(3): 431-440.

Pinar E., Sahin B., Ozgoren M. Akilli H. Experimental study of flow structures around side-by-side spheres. Industrial & Engineering Chemistry Research 2013; 52(40): 14492-14503.

Rattanasiri P., Wilson PA., Phillips AB. Numerical investigation of the drag of twin prolate spheroid hulls in various longitudinal and transverse configurations. In2012 IEEE/OES Autonomous Underwater Vehicles (AUV) IEEE 2012; 1-7.

Sekeroglu E. Investigation of flow and power parameters of a vertical axis water turbine for river application (Master's thesis). Graduate School Of Natural and Applied Science Of Osmaniye Korkut Ata University, Master's thesis No. 592444, 2019, Osmaniye, Türkiye (in Turkish).

Siegel S., McLaughlin T., Morrow J. PIV measurements on a delta wing with periodic blowing and suction. In19th AIAA Applied Aerodynamics Conference 2001; 2436.

Tian W., Mao Z., Zhao F., Zhao Z. Layout optimization of two autonomous underwater vehicles for drag reduction with a combined CFD and neural network method. Complexity 2017.

Tobak M., Peake DJ. Topology of three-dimensional separated flows. Annual Review Of Fluid Mechanics 1982; 14(1): 61-85.

Weihs D. The hydrodynamics of dolphin drafting. Journal of Biology 2004; 3(2): 1-16.

Westerweel J. Efficient detection of spurious vectors in particle image velocimetry data. Experiments in Fluids 1994; 16(3): 236-247.

Yagmur S. Investigation of flow structure around torpedo like geometries. Graduate School Of Natural and Applied Science Of Selcuk University, Master's thesis, No.438592, Konya, Turkey, 2016.

Yagmur S., Goktepeli I., Ozgoren M., Kose F., Kavurmacioglu LA. Experimental investigation of attack angle effect on flow structure around leading and trailing edges of a torpedo-like geometry. Proceedings book, 2nd Global International Conference on Innovation in Marine Technology and the Future of Maritime Transportation (GMC2016) 2016; 57-66, Mugla/ Turkey.

Yaniktepe B., Rockwell D. Flow structure on diamond and lambda planforms: Trailing-edge region. AIAA Journal 2005; 43(7): 1490-1500.

Zdravkovich MM. Review of flow interference between two circular cylinders in various arrangements. Journal of Fluids Engineering 1977; 99(4): 618-633.

Zheng Q., Alam MM. Evolution of the wake of three inline square prisms. Physical Review Fluids 2019; 4(10): 104701.

Zobeyer H., Baki A., Nowrin SN. Interactions between tandem cylinders in an open channel: impact on mean and turbulent flow characteristics. Water 2021; 13(13): 1718.

OKÜ Fen Bilimleri Enstitüsü Dergisi
5(Özel Sayı):156-169, 2022

OKU Journal of The Institute of Science and Technology, 5(Special Issue):156-169, 2022

Osmaniye Korkut Ata Üniversitesi Fen Bilimleri Enstitüsü Dergisi

Osmaniye Korkut Ata University Journal of The Institute of Science and Technology

Experimental and Numerical Analysis of Energy Dissipation with Sluice Gate and Weirs in Trapezoidal Channel

Ercan GEMİCİ[1*], Numan KOCAMAN[2], Tuğba VURAL[3], Mert ZÜNGÖR[4]

[1]BartınUniversity, Faculty of Engineering, Architecture and Design, Department of Civil Engineering, 74110, Bartın
[2]Bartın Üniversitesi, Graduate School, Department of Civil Engineering, 74110, Bartın
[3]Bartın Üniversitesi, Graduate School, Department of Civil Engineering, 74110, Bartın
[4]Bartın Üniversitesi, Graduate School, Department of Civil Engineering, 74110, Bartın

[1]https://orcid.org/0000-0001-8464-4281
[2]https://orcid.org/0000-0003-4237-7677
[3]https://orcid.org/0000-0001-8713-3524
[4]https://orcid.org/0000-0002-1105-1511
*Corresponding author: egemici@bartin.edu.tr

Research Article

Article History:
Received: 15.12.2021
Accepted: 25.01.2022
Published online: 23.02.2022

Keywords:
Energy dissipation
Open channel
Velocity
Specific hydraulic head
Sluice gate
Weir

ABSTRACT

In open channels, only one of the sluice gates or weirs is often used for regulation purposes to limit the acceleration of flow through the channel and to help reduce the forces around the water structures. When the sluice gates are used single, depending on the tail water depth and the gate opening, all cases might experience free or submerged flow conditions and hydraulic jump might occur at the downstream. In this case, it is possible to damage the submerged or semi-submerged structures in this area due to the high flow velocity and high hydraulic energy at the downstream of the gate. The combination of weirs and gates can be preferred both to preserve the stability of the river bottom and to prevent damage to structures such as submerged pipes and transmission lines stretching across cross-sectional direction. In this study, the variation of the flow characteristics in the channel and around the pipeline extending across the channel cross-section was investigated when varying cross-sections weirs with the sluice gate are used together. Experimental flow velocity and water levels are measured for different discharges. These measurements were used to determine the boundary conditions of the computational fluid dynamics (CFD) software and to verify the flow property values obtained by CFD. After the verification, the velocity, pressure and specific hydraulic head values of the points that could not be measured experimentally with CFD software were also obtained. As a result of both experimental and numerical analysis, it has been seen that hydraulic head can be reduced significantly by using the gate and weir structures together. The effect of weir geometry on energy loss is clearly seen at high discharges. By using the two structures together, both the water depth in open channels will be kept at the desired level and possible damage due to water forces acting on underwater structures will be prevented.

Trapez Kanallarda Savak Kapağı ve Savaklarla Enerji Azaltımının Deneysel ve Sayısal Analizi

Araştırma Makalesi

Makale Tarihçesi:
Geliş tarihi: 15.12.2021
Kabul tarihi:25.01.2022
Online Yayınlanma: 23.02.2022

Anahtar Kelimeler:
Enerji azaltımı
Açık kanal
Hız

ÖZET

Açık kanallarda kanal boyunca akışın hızlanmasını sınırlamak ve su yapıları etrafındaki kuvvetleri azaltmaya yardımcı olmak için genellikle kapak veya savaklardan yalnız biri regülasyon amacıyla kullanılmaktadır. Savak kapakları yalnız kullanıldığında, kuyruk suyu derinliğine ve kapak açıklığına bağlı olarak serbest veya batmış akış koşulları meydana gelebilir ve mansapta hidrolik sıçrama oluşabilir. Bu durumda, kapağın mansabındaki yüksek akış hızı ve hidrolik enerji nedeniyle bu bölgedeki batık veya yarı batık yapıların zarar görmesi olasıdır. Kapak ve savakların beraber kullanımı,

Özgül hidrolik enerji
Savak kapağı
Savak

hem nehir tabanının stabilitesinin korunması hem de en kesit boyunca uzanan batık borular ve iletim hatları gibi yapılara zarar gelmemesi için tercih edilebilir. Bu çalışmada savak kapağı ile değişen en kesitli savaklar birlikte kullanıldığında kanalın ve kanal en kesiti doğrultusunda uzanan boru hattı etrafındaki akış özelliklerinin değişimi araştırılmıştır. Deneysel akış hızı ve su seviyeleri farklı debiler için ölçülmüştür. Bu ölçümler, hesaplamalı akışkanlar dinamiği (HAD) yazılımının sınır koşullarını belirlemek ve HAD ile elde edilen akış özelliği değerlerini doğrulamak için kullanılmıştır. Doğrulamanın ardından HAD yazılımı ile deneysel olarak ölçülemeyen noktaların hız, basınç ve özgül hidrolik enerji değerleri de elde edilmiştir. Hem deneysel hem de sayısal analizler sonucunda, kapak ve savak yapılarının birlikte kullanılmasıyla hidrolik enerjinin önemli ölçüde azaltılabileceği görülmüştür. Yüksek debilerde savak geometrisinin enerji kaybı üzerindeki etkisi açıkça görülmektedir. İki yapının birlikte kullanılmasıyla hem açık kanallardaki su derinliği istenilen seviyede tutulacak hem de su altı yapılarına etki eden su kuvvetleri nedeniyle olası hasarların önüne geçilecektir.

To Cite: Gemici E., Kocaman N., Vural T., Züngör M. Experimental and Numerical Analysis of Energy Dissipation with Sluice Gate and Weirs in Trapezoidal Channel. Osmaniye Korkut Ata Üniversitesi Fen Bilimleri Enstitüsü Dergisi 2022; 5(Özel sayı): 156-169.

Introduction

Sluice gates that allow water to swell or accumulate are important structures that keep the water level under control and prevent additional energy consumption in the water conveyance. They are frequently used in irrigation of agricultural lands, water intakes, river transport or as a sub-element of various water structures. Sluice gates raise the water level the upstream, which also causes the energy of the water to increase. High hydraulic head can cause various problems during the conveyance of water downstream. Hydraulic jump occurs in this region, the velocity and pressure of the water reach high values. High velocity and pressure forces damage both the river bed and the submerged or semi-submerged water structures within the river. In order to dissipate the energy, stilling pools in the river bed, arrangements in the river cross-section or additional water structures are constructed.

The flow passing under the gate is called free or submerged flow according to the conditions occurring downstream. The flow where only the water height at the upstream of the gate is effective and free jumping occurs at the downstream is free flow. Flows where the downstream water level affects the upstream water level and the downstream water level is higher than the gate opening are expressed as submerged flow. In the literature, there are many studies examining the flow characteristics for free flow (Silva and Rijo, 2017; Ferro, 2018; Petrila, 2002; Hoseini and Vatankhah, 2021; Dou et al., 2020) and submerged flow (Vaheddoost et al., 2021; Bijankhan et al., 2017; Sauida, 2014; Shayan and Farhoudi, 2013; Shaddehi and Bijankhan, 2020) after the gate and investigating the flow around the weir in various geometries (Haghiabi et al., 2021; Hu et al., 2018; Zounemat-Kermani and Mahdavi-Meymand, 2019; Zhang et al., 2018; Tullis, 2011). However, the number of studies is limited for situations where the gate and weir structure are used sequentially in channels that are not rectangular.

Abdelmonem et al. (2018) carried out an experimental study to increase the energy loss downstream of the sluice gate and to shorten the hydraulic jump length. Different gate openings, different discharges and different pendulum sill positions were used in the experiments using a 3 cm diameter pendulum sill behind the gate. It was stated that the pendulum should be placed in the first half of the hydraulic jump length to increase the energy loss.

Tan et al. (2008) examined the water level and discharge changes in unstable flows for the double-row movable sluice gate case in the form of upstream and downstream gate, and reported that the flow would be more stable if the water level in front of the gate was kept constant instead of the water level behind the gate. Liu et al. (2015) stated that the mechanical energy loss continues continuously by decreasing over time due to continuous scour in the river bed due to the under gate flow, but the discharge change passing under the gate is very small. Habibzadeh et al. (2011) who were proposed a theoretical model for the discharge coefficient in free and submerged rectangular gates have been stated that the formation of a circulating zone in the upstream pool causes turbulence and energy loss. Also they have been particularized that the energy loss is higher in submerged conditions, because the flow boundary is subject to very high shear layer drag in submerged gates. Cassan and Belaud (2012) investigated the turbulent flow near the gate structure on a smooth and rigid bed experimentally and numerically, and especially focused on submergence and large opening of gate. Erdbrink et al. (2014) investigated the mean pressure near the gate and turbulent kinetic energy with numerical simulations.

Weir characteristics have an important place in the flow pattern (Karimi et al., 2018). There are many studies investigating broad-crested weir flow with rectangular, triangular, trapezoidal, ogee, labyrinth, piano key, etc. cross-sections. Denys and Basson (2020) investigated the hydrodynamic behavior of rectangular piano key weirs. Al-Khatib and Gogus (2014) created a discharge estimation model with rectangular and compound cross-section broad-crested weirs. Imanian et al. (2021) investigated the free surface flow over a broad-crested weir under different hydraulic loads. Experimental part of their study has been consisted of the 3D velocity profile with Acoustic Doppler Velocimeter (ADV) around a rectangular weir placed in a 5 m long channel. In addition, the area on the weir was solved numerically with the OpenFOAM, which is open source CFD toolbox, using standard k-ε, RNG k-ε, realizable k-ε, k-ω SST and LRR turbulence models, and the numerical results have been compared with the experimental data.

In this study, it is aimed to reduce the high energy of the water transferred from upstream of the sluice gate to the downstream with different weir sections. Velocity measurements around the pipe were conducted with the ADV device for different discharges in the trapezoidal channel. Experimentally obtained data were also used to validate the numerical analyzes. Flow-3D commercial software was used as a numerical analysis model. The variation of velocity, pressure, specific hydraulic head, turbulent kinetic energy, shear velocity and shear stresses around the weir and pipe under different conditions were investigated.

Material and Methods

Experimental Setup

Laboratory experiments were carried out in a trapezoidal open channel setup in the Bartın University Civil Engineering Hydromechanics Laboratory. There is a thin, vertically movable sluice gate at the beginning of the channel. At the upstream of this sluice gate, the channel length is 5m, the bottom width is 0.5m, the height is 0.5m and the slope of the channel is 1:1. longitudinal bottom slope of the channel is 0.003. The experimental setup is shown in Figure 1.

(a) (b) (c)

Figure 1. Experimental Setup (a) no weir (b) V-weir (c) E-weir

Thickness of the rigid vertical sluice gate is 2.5 mm and the gate opening can be adjusted manually. Water circulation in the channel is achieved by the centrifugal pump that can supply water up to 108 L/s. Discharge can be adjusted with the valve on the pipe that conveys water to the high reservoir. The desired discharge in the channel can be controlled with ultrasonic and electromagnetic flow meters on the same pipe. In the experiments, the water surface profile was determined and velocities were measured with ADV.The ADV measures the velocity at a rate of approximately 10 Hz, averages the data, and records 1 s velocity-vector data. The acoustic Doppler velocimetry system provided instantaneous values of the two velocity components.It was oriented with the xy-plane being horizontal, the x direction aligned with the flow direction and positive downstream upwards.The point velocities were found by dividing the cross-section into pieces with 5 cm distances and making vertical velocity measurements at these points.Initially, the experiments were carried out under the conditions of a constant 3 cm sluice gate opening, at 30 and 66 m^3/h discharges, submerged flow where there are no weirs.Then, two weirs with different cross-sections for the same conditions were placed 2m downstream of the sluice gate.

Numerical Model

Numerical simulation of flow pattern was carried out using Flow-3D commercial software, which makes 3D flow modeling. There are different turbulence closure models in the software that applies the volume of fluid (VOF) method in solving problems with free surfaces. Flow-3D uses Reynolds equations derived from Navier-Stokes equations. These models are solved for the time-averaged turbulent flow field. Time-averaged turbulence quantities are mean velocities, turbulent kinetic energy, and Reynolds stress terms. According to the Boussinesq hypothesis, Reynolds stresses can be expressed in terms of mean velocity gradients$-\rho\overline{u_i'}\overline{u_j'}$in Reynolds-averagedNavier-Stokes (RANS) equations,

$$-\rho\overline{u_i'}\overline{u_j'} = \mu_t\left(\frac{\partial u_i}{\partial x_j}+\frac{\partial u_i}{\partial x_i}\right)-\frac{2}{3}\left(\rho k+\mu_t\frac{\partial u_k}{\partial x_k}\right)\delta_{ij} \quad (1)$$

Among Reynolds stress models, the two-equation eddy-viscosity equations usually solve the two additional transport equations and calculate the turbulent viscosity μ_t as a function of k (turbulent kinetic energy) and ε (turbulent dissipation rate) or k and ω (specific dissipation rate). In the standard k-ϵ model, the turbulent viscosity μ_t is:

$$\mu_t = \rho C_\mu \frac{k^2}{\varepsilon} \quad (2)$$

where ρ is the density of the fluid and C_μ is constant. The standard k-ε model does not take into account effects of streamline curvature.

RNG k-ε model brings improvements over the k-ε model with statistical techniques. This model also considers eddy and rotational effects by changing the turbulent viscosity. This model also considers eddy and rotational effects by changing the turbulent viscosity. In this study, the RNG k-ε model, which generally performs better in similar studies, was used (Ran et al., 2018).

The dimensions and flow conditions of the numerical model were constituted the same as the laboratory model. The three-dimensional geometries of the channel, gate and weirs were created using Salome Platform. Mesh of rectangular cells was used in the Flow-3D software. Meshes were checked for flow domain by the Flow-3D FAVOR application method that generates grids. Two mesh blocks were created to include the all channel volume and pipe volume. The size of the channel volume grid was first set to 0.05 – 0.015 m long (dense in the gate area), 0.01 m wide and 0.01 m high, and the number of all the grids was 6050000. The mesh surrounding the pipe consists of 46080 cells, each with a side of 0.0025 m. As the initial condition, 0.4 m height of water before the valve and 30 m^3/h and 66 m^3/h discharges were defined. Volume flow rate was taken at the upstream end and the outflow was selected at the downstream end as the boundary condition. Boundary condition at the channel side walls and the bottom was defined asawall. No-slip boundary condition was applied on solid boundary surfaces. At the upper boundary of the solution region and at the pipe boundary region, symmetry was taken as the boundary condition.

Results and Discussion

Model Validation

Verification of both experimental measurements and established model is necessary for a realistic analysis. For this reason, firstly, the accuracy of velocity measurements was calibrated by using the discharges obtained from two flow meters and the velocity values measured by ADV. The discharges obtained from the flow meter were entered into the model as boundary conditions. Mesh structure, cell

size and number of cells should be determined carefully to obtain accurate results. Therefore, considering the analysis time and experimental data, the optimum mesh conditions for which the model is acceptable were found by gradually improving it. For the 49 points shown in Figure 2-4, water depth differences which measured and obtained from the model were found in the range of 3,00% - 8,95% under 6 different conditions. As shown in Table 1 and Table 2, when the x-direction velocities obtained from the experimental and model are compared for a discharge of 30 and 66 m^3/h, the difference is less than 7.4%.

Table 1. Comparison of horizontal velocities obtained by the model and experiment (y=0.25m and Q=30 m^3/h)

	No weir			**E-weir**			**V-weir**		
x (m)	**u_{model} (m/s)**	**u_{exp} (m/s)**	**ε (%)**	**u_{model} (m/s)**	**u_{exp} (m/s)**	**ε (%)**	**u_{model} (m/s)**	**u_{exp} (m/s)**	**ε (%)**
-0.20	0.113	0.120	6.18	0.047	0.050	7.09	0.030	0.033	8.44
0.20	0.406	0.427	4.98	0.247	0.259	4.52	0.229	0.244	5.97
0.60	0.378	0.394	4.01	0.336	0.353	4.82	0.294	0.315	6.53
1.00	0.353	0.369	4.35	0.256	0.268	4.51	0.247	0.258	4.08
1.40	0.345	0.351	1.69	0.179	0.184	2.59	0.170	0.174	2.24
1.80	0.338	0.348	2.76	0.151	0.156	3.70	0.136	0.142	3.99
2.30	0.343	0.366	6.32	0.279	0.292	4.55	1.479	1.524	2.94
2.80	0.301	0.313	3.76	0.589	0.613	3.90	0.203	0.192	5.70
		Average:	**4.26**		**Average:**	**4.46**		**Average:**	**4.99**

Table 2. Comparison of horizontal velocities obtained by the model and experiment (y=0.25m and Q=66 m^3/h)

	No weir			**E-weir**			**V-weir**		
x (m)	**u_{model} (m/s)**	**u_{exp} (m/s)**	**ε (%)**	**u_{model} (m/s)**	**u_{exp} (m/s)**	**ε (%)**	**u_{model} (m/s)**	**u_{exp} (m/s)**	**ε (%)**
-0.20	0.102	0.108	5.21	0.039	0.045	13.39	0.034	0.039	12.60
0.20	1.297	1.313	1.24	0.477	0.504	5.28	0.414	0.447	7.38
0.60	1.206	1.235	2.31	0.585	0.614	4.73	0.517	0.533	2.91
1.00	1.208	1.251	3.42	0.505	0.548	7.80	0.498	0.507	1.77
1.40	1.029	1.108	7.15	0.324	0.346	6.30	0.315	0.341	7.51
1.80	1.104	1.135	2.72	0.239	0.251	4.74	0.230	0.256	10.34
2.30	0.558	0.619	9.86	0.217	0.247	12.05	1.310	1.372	4.52
2.80	0.514	0.572	10.17	1.299	1.364	4.73	1.425	1.463	2.60
		Average:	**5.26**		**Average:**	**7.38**		**Average:**	**6.20**

Water Surface Profiles

Flow pattern is described using water surface profiles measured along the centerline of the open channel. The water surface profile is used to determine the flow type and hydraulic jump characteristic. It is seen that there is a hydraulic jump after the sluice gate in Figure 2b and after the weirs in Figure 3-4. In both discharges conditions, both weirs are free flowing. M1 profile is formed between the sluice gate and the weirs for all discharges.

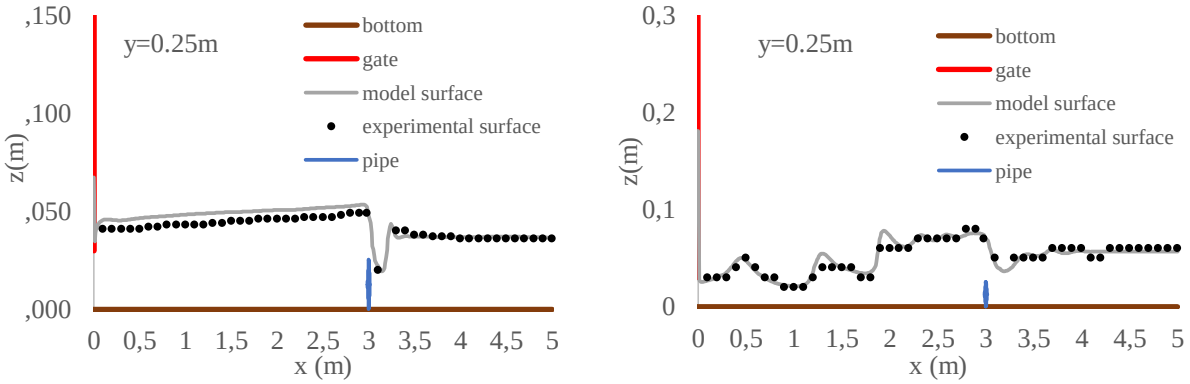

(a) (b)

Figure 2. Comparison of the water surface profile for no weir (a) Q=30 m^3/h (b) Q=66 m^3/h

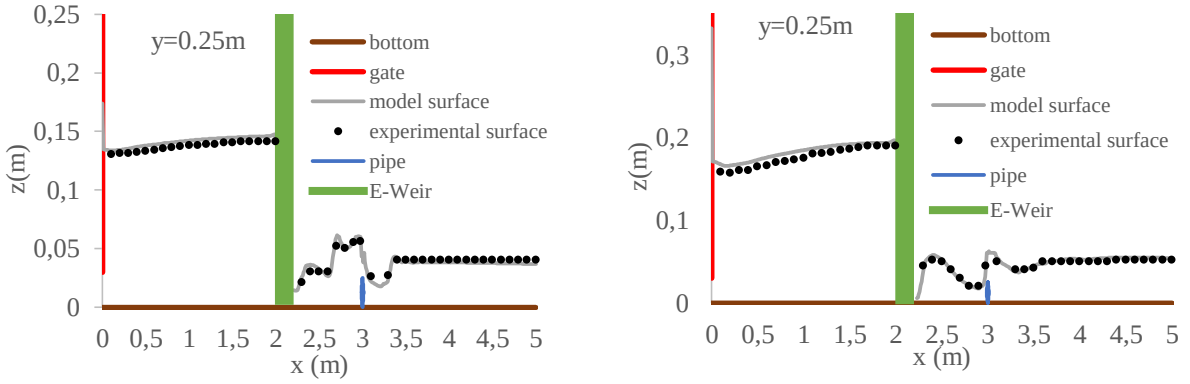

(a) (b)

Figure 3. Comparison of the water surface profile for E-weir (a) Q=30 m^3/h (b) Q=66 m^3/h

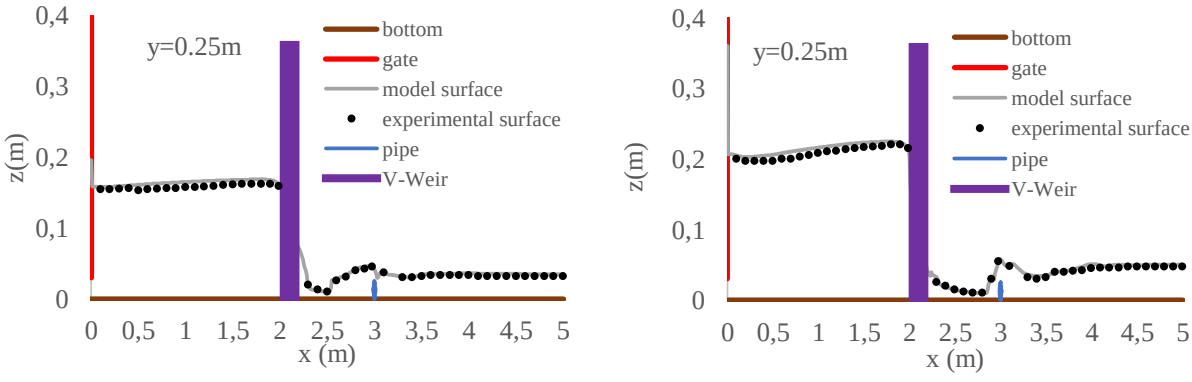

(a) (b)

Figure 4. Comparison of the water surface profile for V-weir (a) Q=30 m^3/h (b) Q=66 m^3/h

Velocity Distribution

Determination of velocity distribution is essential to modeling of hydraulic processes in open channel. The velocity distribution in open channel is affected by channel geometry, bed characteristics and in-river water structures. Water forces erode the channel bottom and can directly affect the water structure and damage it. It is seen in Figure 5b that the flow velocity after the gate is considerable amount high at major discharge and this high velocity continues until the middle of the channel. After the weir, it is seen in Figure 6-7 that the high velocity is faded out earlier.

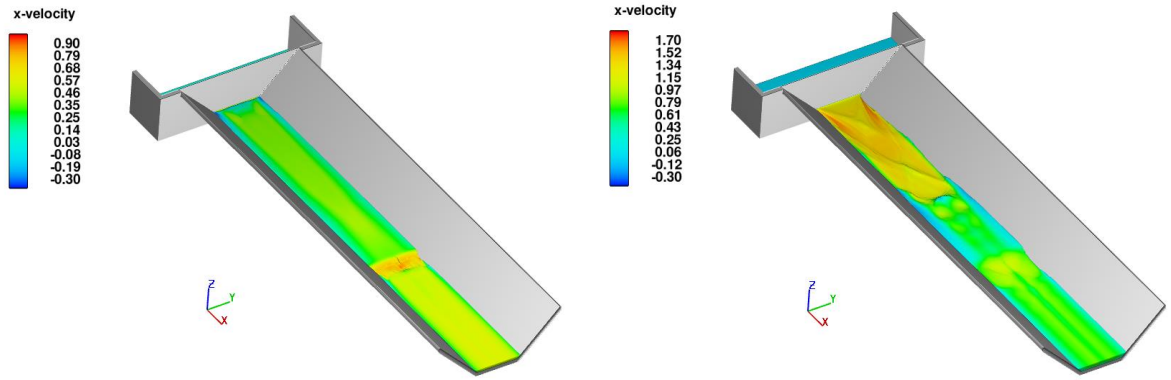

(a) (b)

Figure 5. 3D distribution of x velocity for no weir(a) Q=30 m^3/h (b) Q=66 m^3/h

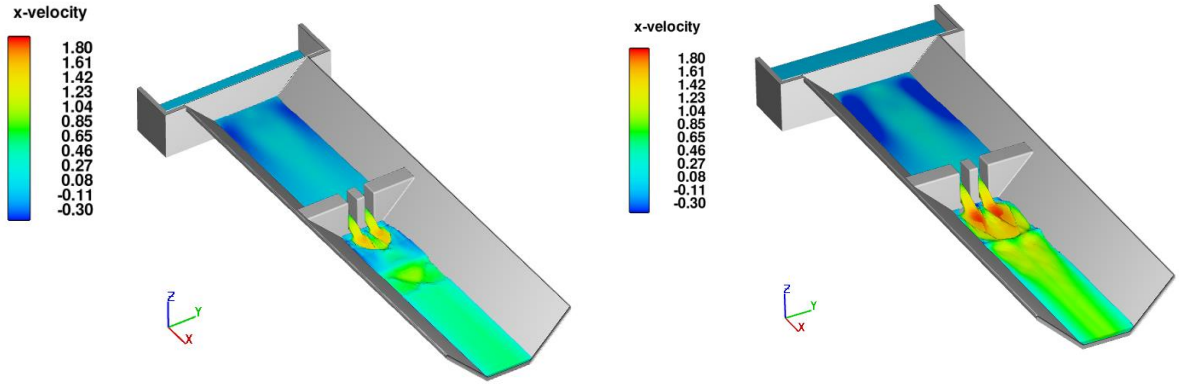

(a) (b)

Figure 6. 3D distribution of x velocity for E-weir(a) Q=30 m^3/h (b) Q=66 m^3/h

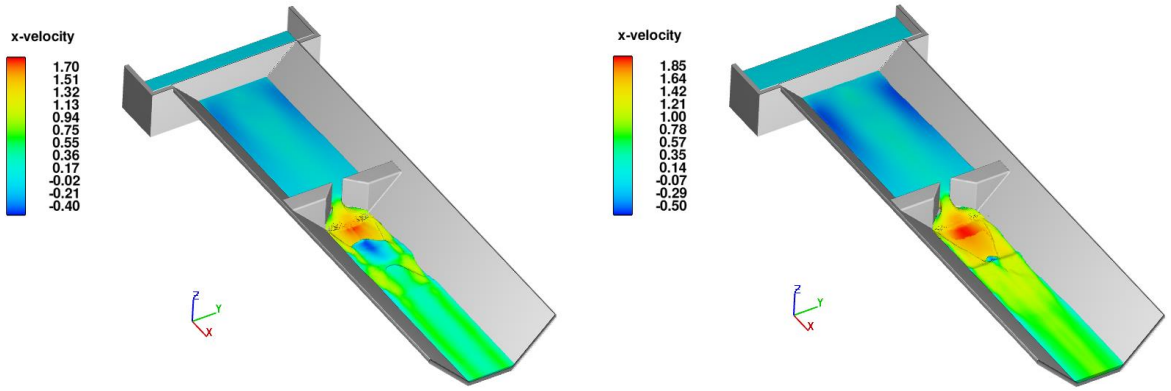

(a) (b)

Figure 7.3D distribution of x velocity for V-weir (a) Q=30 m^3/h (b) Q=66 m^3/h

Pressure force on the water structure is the most important parameter in the design of the structure. In this study, the focus is on the pressure distribution in front of the pipe, which placed 3 meters after the sluice gate, at the downstream of gate. In Figure 8b and Figure 9b are compared, it can be seen that the E-weir has decreased the pressure at the end regions of the pipe for high discharge. On the other hand, comparing Figure 8 and Figure 10, it is seen in that the V-weir has reduced the pressure in the middle regions of the pipe for both discharges.

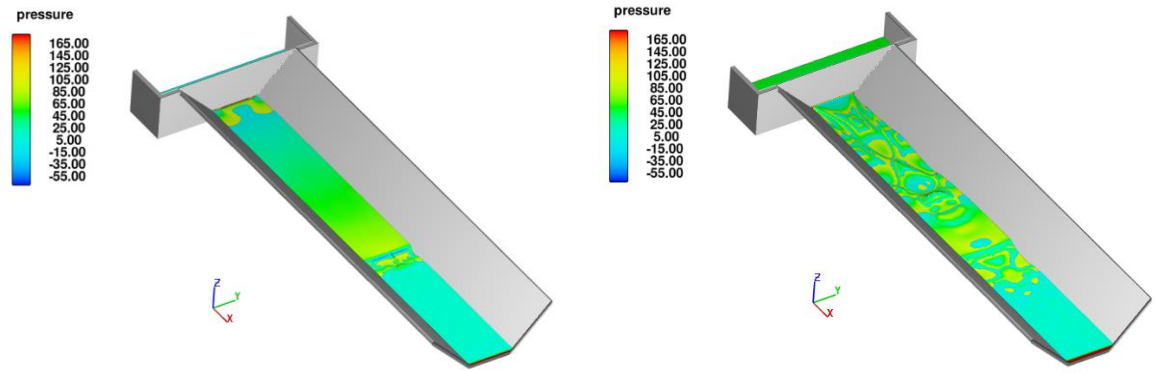

(a) (b)

Figure 8.3D distribution of pressure for no weir(a) Q=30 m^3/h (b) Q=66 m^3/h

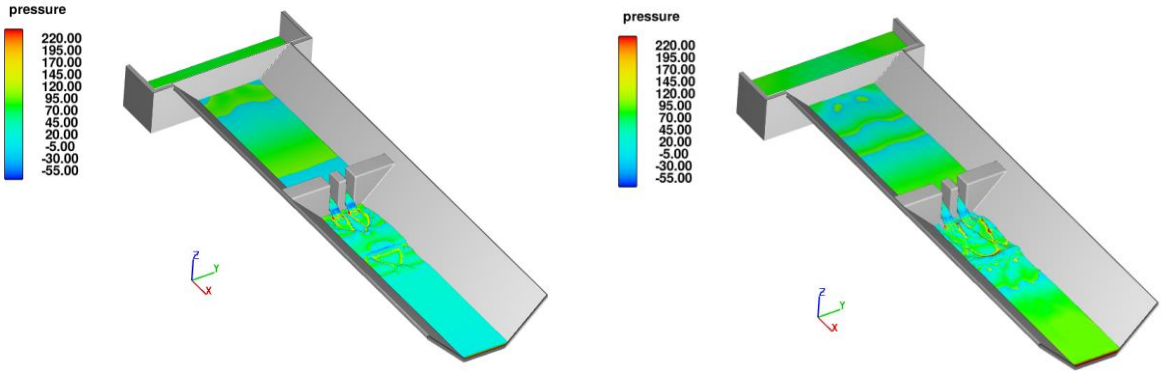

(a) (b)

Figure 9. 3D distribution of pressure for E-weir(a) Q=30 m^3/h (b) Q=66 m^3/h

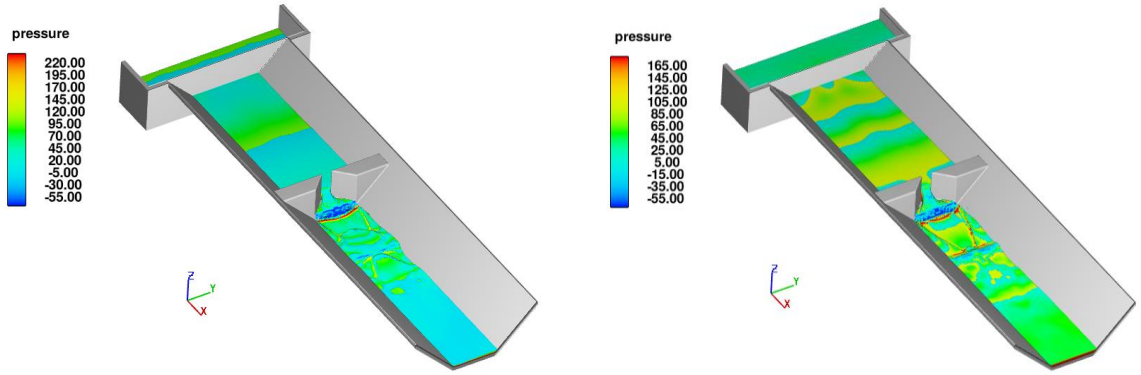

(a) (b)

Figure 10. 3D distribution of pressurefor V-weir(a) Q=30 m^3/h (b) Q=66 m^3/h

Specific Hydraulic Head Distribution

Forces on the structure are proportional to the magnitude of hydraulic head of the water. In open channels, specific hydraulic head is usually used instead of hydraulic head. Specific head was calculated by using Equation 3. D is water level, v is velocity and $g$is gravitational acceleration in Equation 3.

$$H_{specific} = D + \frac{v^2}{2g} \quad (3)$$

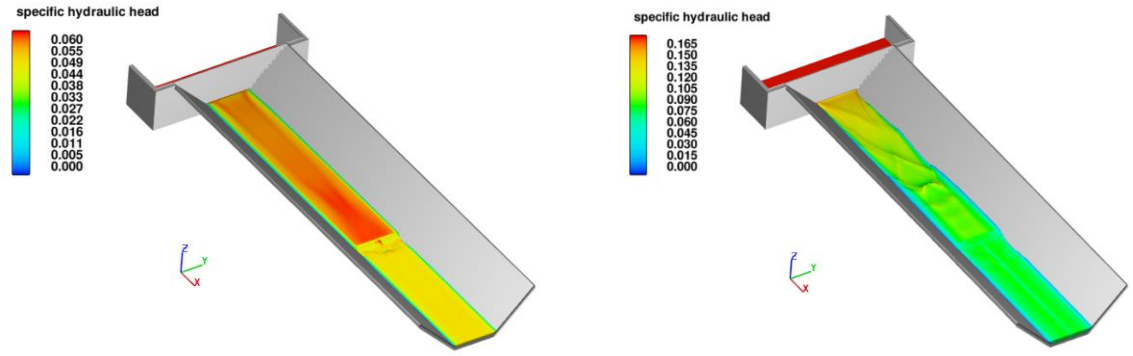

(a) (b)

Figure 11. 3D distribution of specific hydraulic head for no weir (a) Q=30 m^3/h (b) Q=66 m^3/h

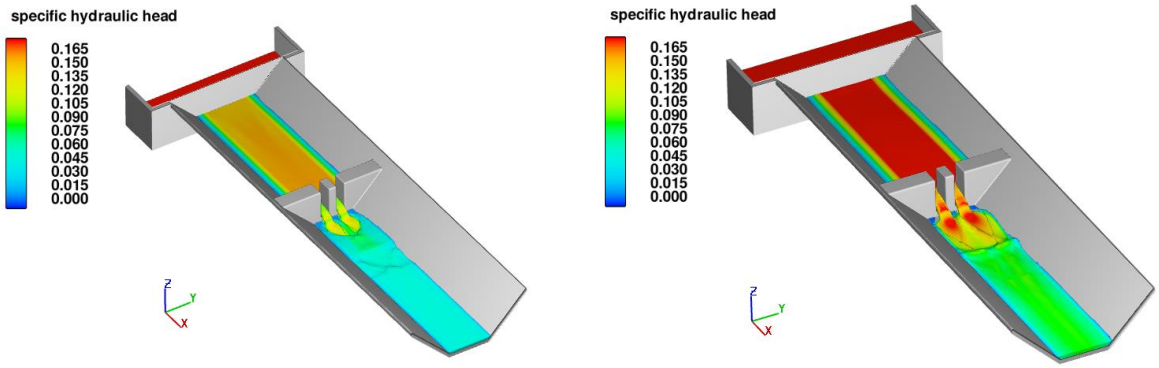

(a) (b)

Figure 12.3D distribution of specific hydraulic head for E-weir (a) Q=30 m^3/h (b) Q=66 m^3/h

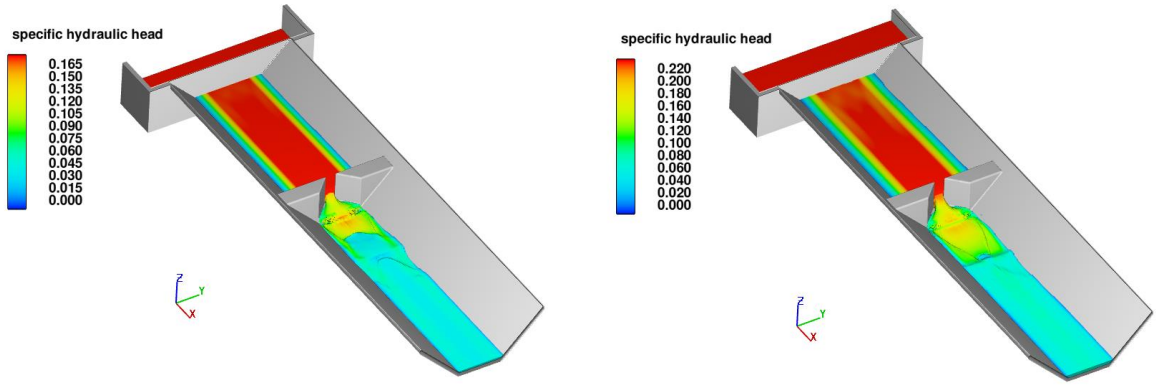

(a) (b)

Figure 13. 3D distribution of specific hydraulic headfor V-weir(a) Q=30 m^3/h (b) Q=66 m^3/h

Table 3. Variation of specific hydraulic head in front of the pipe (x=2.98m)

y (m)	Q=30 m^3/s					Q=66 m^3/s				
	Specific Hydraulic Head			Energy Dissipation		Specific Hydraulic Head			Energy Dissipation	
	No weir	V-weir	E-weir	V-weir ε (%)	E-weir ε (%)	No weir	V-weir	E-weir	V-weir ε (%)	E-weir ε (%)
0.00	0.0517	0.0620	0.0502	19.73	-2.90	0.0745	0.0680	0.0710	-8.73	-4.60
0.05	0.0551	0.0721	0.0554	30.90	0.54	0.0809	0.0783	0.0862	-3.28	6.46
0.10	0.0559	0.0616	0.0609	10.13	8.86	0.0852	0.0802	0.0904	-5.89	6.09
0.15	0.0562	0.0534	0.0659	-4.97	17.32	0.0868	0.0845	0.0836	-2.59	-3.70
0.20	0.0562	0.0491	0.0670	-12.70	19.13	0.0866	0.0747	0.0655	-13.78	-24.34
0.25	0.0570	0.0472	0.0678	-17.20	19.07	0.0860	0.0570	0.0583	-33.76	-32.25
0.30	0.0564	0.0492	0.0698	-12.77	23.73	0.0863	0.0752	0.0613	-12.85	-29.01
0.35	0.0561	0.0533	0.0657	-5.07	16.99	0.0865	0.0863	0.0895	-0.24	3.42
0.40	0.0558	0.0623	0.0603	11.62	8.05	0.0851	0.0833	0.0905	-2.11	6.32
0.45	0.0548	0.0716	0.0552	30.58	0.69	0.0809	0.0803	0.0828	-0.69	2.36
0.50	0.0514	0.0612	0.0499	19.12	-2.88	0.0745	0.0684	0.0663	-8.29	-11.07
			Average:	**6.31**	**9.87**			**Average:**	**-8.38**	**-7.30**

As can be seen from Table 3 and Figure 11-13 for high discharge values, specific hydraulic head decreases due to the effect of weirs, especially in the parts close to the middle of the pipe.

Conclusion

In this study, it is aimed to reduce hydraulic head around the downstream pipe by using different weirs with the effect of under sluice gate flow. The model errors slightly increase with the effect of secondary flow in the upstream of sluice gate, especially at high discharges. The average difference between experimental and numerical horizontal velocity values for all six situations at the velocity measurement points is below 7.4%. This shows that numerical models can be used for such problems. V-type weirs are more effective than E-type weirs in reducing velocity and pressure. Based on numerical results, for discharge of 66 m^3/h, the specific hydraulic head in front of the pipe was reduced with the effect of V-weir and E-weir by 8.38% and 7.3% on average, respectively. Weirs with

discharge of 30 m^3/h were not effective enough. The reason for this is that after the weirs at low discharge, the energy has increased because the water accumulates in front of the pipe. However, for cases where energy reduction is required only in the middle region, V-type weirs, which reduce the energy up to 17%, can be chosen. E-weirs and V-weirs can be preferred to shorten the hydraulic jump distance at high discharges.

Statement of Conflict of Interest

Authors have declared no conflict of interest.

Author's Contributions

The contribution of the corresponding author is 40% and contribution of other authors is equal and 20%.

*This study was presented as a summary paper at the International Conference on Engineering, Natural and Applied Sciences (ICENAS'21) held online on 24-26 November 2021.

References

Abdelmonem YK., Shabayek S., Khairy AO. Energy dissipation downstream sluice gate using a pendulum sill. Alexandria Engineering Journal 2018; 57(4): 3977-3983.

Al-Khatib, IA., Gogus M. Prediction models for discharge estimation in rectangular compound broad-crested weirs. Flow Measurement and Instrumentation 2014; 36, 1-8.

Bijankhan M., Kouchakzadeh S., Belaud G. Application of the submerged experimental velocity profiles for the sluice gate's stage-discharge relationship. Flow Measurement and Instrumentation 2017; 54, 97-108.

Cassan L., Belaud G. Experimental and numerical investigation of flow under sluice gates. Journal of Hydraulic Engineering 2012; 138(4): 367-373.

Denys FJ., Basson GR. Unsteady hydrodynamic behavior at piano key weirs. Journal of Hydraulic Engineering 2020; 146(5): 04020028.

Dou M., Qin C., Li G., Wang C. Research on calculation method of free flow discharge based on artificial neural network and regression analysis. Flow Measurement and Instrumentation 2020; 72, 101707.

Erdbrink CD., Krzhizhanovskaya VV., Sloot PM. Free-surface flow simulations for discharge-based operation of hydraulic structure gates. Journal of Hydroinformatics 2014; 16(1): 189-206.

Ferro V. Testing the stage-discharge relationship of a sharp crested sluice gate deduced by the momentum equation for a free-flow condition. Flow Measurement and Instrumentation 2018; 63, 14-17.

Habibzadeh A., Vatankhah AR., Rajaratnam N. Role of energy loss on discharge characteristics of sluice gates. Journal of Hydraulic Engineering 2011; 137(9): 1079-1084.

Haghiabi AH., Nou MRG., Parsaie A. The energy dissipation of flow over the labyrinth weirs. Alexandria Engineering Journal 2021; In Press.

Hoseini P., Vatankhah AR. Stage-discharge relationship for slide gates installed in partially full pipes. Flow Measurement and Instrumentation 2021; 77, 101838.

Hu H., Qian Z., Yang W., Hou D., Du L. Numerical study of characteristics and discharge capacity of piano key weirs. Flow Measurement and Instrumentation 2018; 62, 27-32.

Imanian H., Mohammadian A., Hoshyar P. Experimental and numerical study of flow over a broad-crested weir under different hydraulic head ratios. Flow Measurement and Instrumentation 2021; 80, 102004.

Karimi M., Attari J., Saneie M., Jalili Ghazizadeh MR. Side weir flow characteristics: comparison of piano key, labyrinth, and linear types. Journal of Hydraulic Engineering 2018; 144(12): 04018075.

Liu SH., Liao TT., Luo QS. Numerical simulation of turbulent flow behind sluice gate under submerged discharge conditions. Journal of Hydrodynamics 2015; 27(2): 257-263.

Petrila T. Mathematical model for the free surface flow under a sluice gate. Applied Mathematics and Computation 2002; 125(1): 49-58.

Ran D., Wang W., Hu X. Three-dimensional numerical simulation of flow in trapezoidal cutthroat flumes based on FLOW-3D. Frontiers of Agricultural Science and Engineering 2018; 5(2): 168-176.

Sauida MF. Calibration of submerged multi-sluice gates. Alexandria Engineering Journal 2014; 53(3): 663-668.

Shaddehi FR., Bijankhan M. Experimental study on free and submerged multi-jets. Flow Measurement and Instrumentation 2020; 75, 101805.

Shayan HK., Farhoudi J. Effective parameters for calculating discharge coefficient of sluice gates. Flow Measurement and Instrumentation 2013; 33, 96-105.

Silva CO., Rijo M. Flow rate measurements under sluice gates. Journal of Irrigation and Drainage Engineering 2017; 143(6): 06017001.

Tan GM., Ding ZL., Wang CD., Yao X. Gate regulation speed and transition process of unsteady flow in channel. Journal of Hydrodynamics 2008; 20(2): 231-238.

Tullis BP. Behavior of submerged ogee crest weir discharge coefficients. Journal of Irrigation and Drainage Engineering 2011; 137(10): 677-681.

Vaheddoost B., Safari MJS., Zeynali RI. Discharge coefficient for vertical sluice gate under submerged condition using contraction and energy loss coefficients. Flow Measurement and Instrumentation 2021; 80, 102007.

Zhang J., Chang Q., Zhang QH., Li SN. Experimental study on discharge coefficient of a gear-shaped weir. Water Science and Engineering 2018; 11(3): 258-264.

Zounemat-Kermani M., Mahdavi-Meymand A. Hybrid meta-heuristics artificial intelligence models in simulating discharge passing the piano key weirs. Journal of Hydrology 2019; 569, 12-21.

OKÜ Fen Bilimleri Enstitüsü Dergisi
5(Özel Sayı):170-184, 2022

OKU Journal of The Institute of Science and Technology, 5(Special Issue):170-184, 2022

Osmaniye Korkut Ata Üniversitesi Fen Bilimleri Enstitüsü Dergisi

Osmaniye Korkut Ata University Journal of The Institute of Science and Technology

Türkiye'nin Farklı Bölgelerdeki Güneş Enerjisi Potansiyelinin Analizi

Serenay EMİKÖNEL[1*], Ayşe KOCALMIŞ BİLHAN[2]

[1]Nevşehir Hacı Bektaş Veli Üniversitesi, Mühendislik Mimarlık Fakültesi, Elektrik Elektronik Mühendisliği Bölümü, 50200, Nevşehir
[2]Nevşehir Hacı Bektaş Veli Üniversitesi, Mühendislik Mimarlık Fakültesi, Elektrik Elektronik Mühendisliği Bölümü, 50200, Nevşehir

[1]https://orcid.org/0000-0002-2949-8397
[2]https://orcid.org/0000-0002-5008-6784
*Sorumlu yazar: serenayemikonel@gmail.com

Araştırma Makalesi

Makale Tarihçesi:
Geliş tarihi: 08.12.2021
Kabul tarihi: 05.02.2022
Online Yayınlanma: 23.02.2022

Anahtar Kelimeler:
Güneş enerjisi
Güneş enerji potansiyeli
Güneş ışınımı

ÖZET

Günümüzde küresel enerji krizi ve artan çevre kirliliği ile birlikte enerjinin ülkelerin gelişmişlik düzeylerini belirlemede en temel faktörlerden biri olduğunu göstermektedir. Özellikle pandemi döneminde günlük hayatın her alanında enerjiye duyulan ihtiyaç ve teknolojik araçların kullanımının artması, enerji kaynaklarının ve enerji üretim sürecinin önemini bir kez daha göstermiştir. Son zamanlarda yapılan araştırmalar, enerji ihtiyacı ve çevre kirliliğinin giderek daha fazla ön plana çıkmasıyla, yenilenebilir enerji kaynaklarının tüm dünyada geleneksel enerji kaynaklarının (fosil yakıtlar) yerini aldığını göstermektedir. Yenilenebilir enerji kaynakları kullanılarak fosil yakıtların kullanımı sonucu açığa çıkan CO_2 gazının çevreye verdiği zararı en aza indirmek mümkündür. Güneş ve rüzgâr gibi doğal kaynaklardan elde edilen enerji, çevreye verilen zararı en aza indirmesi, tükenmez bir enerji fırsatı sağlaması ve temiz bir enerji kaynağı olması nedeniyle fosil yakıtlara kıyasla önemli bir yere sahiptir. Yenilenebilir enerji kaynaklarından biri olan güneş enerjisi, herhangi bir yakıt veya hareketli parça gerektirmemesi, kullanım sırasında atık madde üretmemesi, çevre dostu olması, bol ve ücretsiz olması nedeniyle oldukça tercih edilen bir enerji kaynağıdır. Türkiye'nin coğrafi konumu güneş enerjisi kuşağında yer almaktadır. Bu nedenle hemen her bölgede kurulabilecek bir güneş enerjisi santralinin bölgesel enerjiye veya ülke ekonomisine katkı sağlayabileceği öngörülebilir. Bu çalışmada Türkiye'nin yedi farklı bölgesinden seçilen Siirt, Adana, Erzincan, Kırşehir, Kütahya, Balıkesir ve Amasya illeri için güneş enerjisi potansiyelleri araştırılmıştır. Araştırma sonuçlarına göre, farklı iklim koşullarında (kar, yağmur, bulut vb.) iller olsalar da benzer güneş radyasyon yoğunluklarının olduğu tespit edilmiştir. Bu da Türkiye'nin güneş enerjisi potansiyeli açısından ne kadar önemli olduğunu göstermektedir.

Analysis of Turkey's Solar Energy Potential in Different Regions

Research Article

Article History:
Received: 08.12.2021
Accepted: 05.02.2022
Published online: 23.02.2022

Keywords:
Solar energy
Solar energy potential
Solar irritation

ABSTRACT

Today, with the global energy crisis and the increasing environmental pollution, it shows that energy is one of the most basic factors in determining the development level of countries. The need for energy in every field of daily life and the increase in the use of technological tools, especially during the pandemic, has shown one more time the importance of energy sources and the energy production process. Recent studies show that, as energy shortage and environmental pollution become increasingly prominent, renewable energy is replacing conventional energy resources (fossil fuels) all around the world. By using renewable energy sources it is possible to minimize the damage to the environment caused by the CO_2 gas released as a result of the use of fossil fuels. The energy obtained from natural sources

such as the sun and wind has an important place compared to fossil fuels, as it minimizes the damage to the environment, provides an inexhaustible energy opportunity and, is a clean energy source. Solar energy, which is one of the renewable energy sources, is a highly preferred energy source because it does not require any fuel or moving parts, does not produce waste material during use, is environmentally friendly, and is abundant and free. The geographical location of Turkey is located in the solar energy belt. For this reason, it can be foreseen that a solar power plant that can be established in almost every region can contribute to regional energy or contribute to the country's economy. In this study, solar energy potentials were investigated for the provinces of Siirt, Adana, Erzincan, Kırşehir, Kütahya, Balıkesir, and Amasya, which were selected from seven different regions of Turkey. According to the results of the research, it has been determined that there are similar solar radiation intensities even if they are provinces in different climatic conditions (such as snow, rain, cloud, etc.). This shows how important Turkey is in terms of solar energy potential.

To Cite: Emikönel S., Bilhan AK. Analysis of Turkey's Solar Energy Potential in Different Regions. Osmaniye Korkut Ata Üniversitesi Fen Bilimleri Enstitüsü Dergisi 2022; 5(Özel sayı): 170-184.

Introduction

Nowadays, energy is one of the important factors which determine the level of developing countries (Taşkın and Korucu, 2014). The need for energy is increasing day by day due to reasons such as increasing population, industrialization, and pandemic (Şendemir, 2021). Many researches show that not only energy consumption is very important but also energy production is very important because of the use of energy in almost every aspect of our lives such as electronic vehicles, factories, electric cars, and street lighting in daily life (Kaya et al., 2018; Bilhan and Emikönel, 2021). Turkey which is one of the developing countries, the need for energy is increasing day by day (İzgeç, 2020). For this reason, many new renewable energy sources are developed and landed in many different areas.

As it is known, fossil fuels are widely used in energy production (Kaya et al., 2018). However, it also brings many negative consequences such as global warming, air pollution, formation of acid rain, and climate change caused by the CO_2 gas released by the use of fossil fuels (Dinçer, 2011; Atakul et al., 2015; Kılıç, 2015). However, it also brings back many negative outcomes such as global warming, air pollution, formation of acid rain, and climate change by the use of fossil fuels (Dinçer, 2011; Atakul et al., 2015; Kılıç, 2015). According to the prediction of many researchers and the World Energy Form, the limited reserves of fossil fuels will be exhausted in the next century due to the usage of coal, oil, natural gas, etc. in many areas (Kumar et al., 2010; Dinçer, 2011). In order to prevent the damage of fossil fuels to the environment and due to the limited fossil fuel resources, renewable energy sources have been more attractive in the last 50 years (Eltas, 2020; Bilhan and Emikönel, 2021).

The biggest advantage of renewable energy, it consists of natural processes and is available the next day (Kocakuşak, 2018; http://yegmweb.yegm.gov.tr/genc_cocuk/Yenilenebilir_Enerji_Nedir.aspx, 2021). The most popular renewable energy sources are hydro, sunlight, wind, biomass, geothermal, and hydrogen. Also, it is focused on the energy which is produced by the wave in recent studies (Yaman et al., 2019; Albayrak Karadağ, 2020).

Solar energy, which is one of the popular renewable energy sources, has an important place in energy production all over the world (Bilhan and Emikönel, 2021). Sun is an energy resource that basically consists of 92 % hydrogen and 8 % helium and some other elements. The fusion reaction occurs as a result of the conversion of hydrogen gas in the core of the Sun into helium gas. The radiant energy released by the formation of the fusion reaction is solar energy (İnan et al., 2018; https://enerji.gov.tr/bilgi-merkezi-enerji-gunes, 2021). In other words, the energy reflected from the sun on the 1 m^2 surface of the Earth in watts is solar energy (Bilhan and Emikönel, 2021). The intensity of solar energy outside the atmosphere is approximately 1370 W/m^2, but the amount reaching the earth varies between 0-1100 W/m^2 due to the atmosphere (Yolcan and Köse, 2020; https://enerji.gov.tr/bilgi-merkezi-enerji-gunes, 2021). According to the International Energy Agency (IEA), the solar energy which comes from the sun to earth in 90 minutes is enough to meet the energy need of the whole world for a year (Kılıç, 2015). This type of energy, which is obtained naturally during the hours of the sun, has started to be preferred in almost every field due to its unlimited nature and being an inexhaustible resource for centuries (Bulut et al., 2018; Eltas, 2020). The solar energy source has an important place in world energy demand. The International Energy Agency estimates that approximately 11% of global electrical energy production will be provided by solar energy in 2050 (Dinçer, 2011; Kırbaş et al., 2013).

In this study, the sunshine duration and solar radiation intensities of the provinces of Siirt, Adana, Erzincan, Kırşehir, Kütahya, Balıkesir, and Amasya, which we selected from seven different regions, were examined in accordance with the data obtained from the Ministry of Energy and Natural Resources to give information about the solar energy potential of our country. There are many studies on solar energy potential in the literature such as Çakmak and Altaş examined the solar energy data obtained from four different sources for the province of Erzincan in their study. Also in their study, the solar energy potentials of Erzincan and Germany were compared. As a result of the study, it was concluded that the province of Erzincan has a higher solar energy potential than Germany and that much more energy can be produced if the PV plants established in Germany are installed in Erzincan (Çakmak and Altaş, 2016). Aksungur et al. investigated the solar energy potential in Turkey and the world in their study and examined and compared the radiation intensities of the provinces of Isparta, Ankara, Erzincan, Birecik, Balıkesir, Yozgat, Yalova, which they selected from different regions of our country in the sunbelt. As a result of their research, they determined that there is not a big difference between the radiation values (Aksungur et al., 2013).

Solar Energy Potential in Turkey

Turkey is located between 26^0–45^0 east meridians with 36^0–42^0 northern parallels and has a surface area of 783,562 km^2. Turkey has a high solar energy potential because of its geographical location. Figure 1 shows Turkey's Solar Radiation Map created by the General Directorate of Renewable Energy (YEGM, 2020). In figure 1, the cities that can benefit the most from solar radiation are shown

in light and dark red colors, and the cities that can benefit from the least amount of solar radiation are shown in light and dark blue colors.

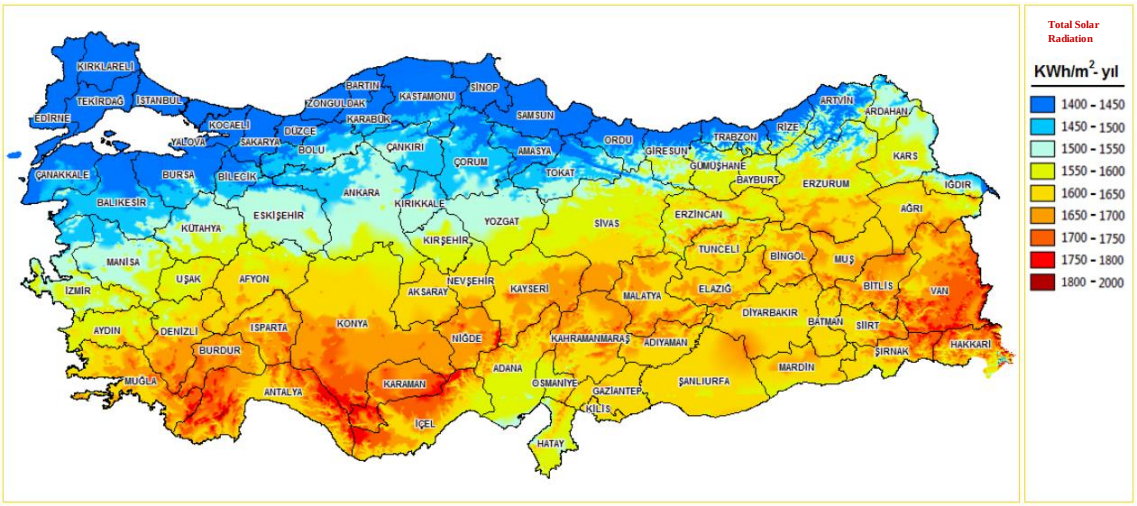

Figure 1. Turkey's Solar Energy Potential Atlas (GEPA)

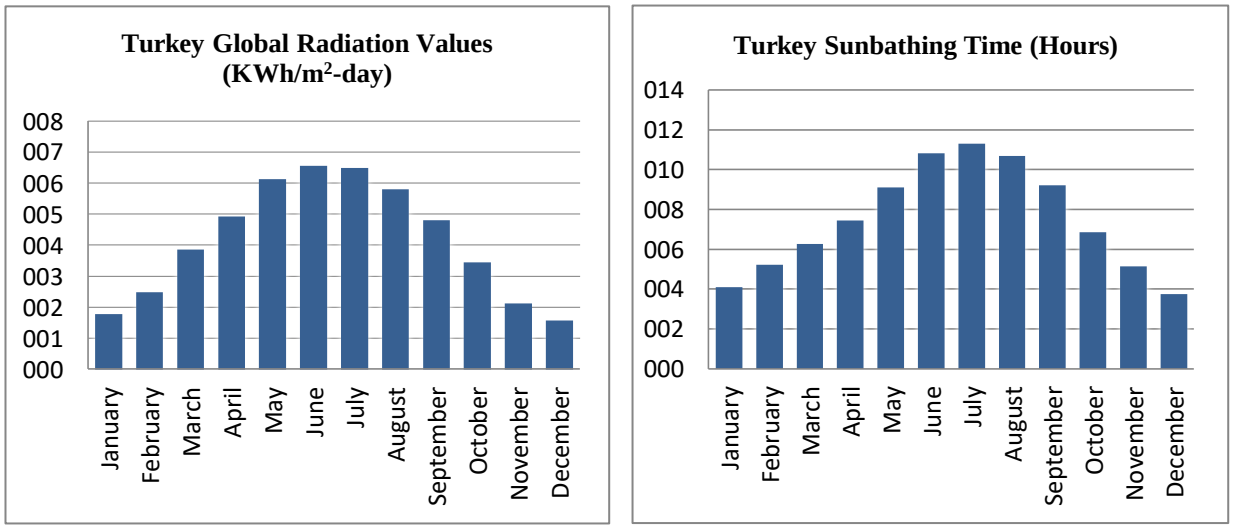

(a) (b)

Figure 2. (a) Turkey's global radiation values (KWh/m^2-day), (b) sunbathing duration (hours)

The average daily global radiation values on a monthly basis and the average monthly sunshine duration of Turkey are represented in Figure 2 (a) and (b), respectively (YEGM, 2020). In Fig. 2 (a), it is observed that the global radiation value reaches its highest value in June with 6.57 KWh/m^2-day. The average daily radiation intensity of Turkey on a monthly basis is 4.18 KWh/m^2-day and the annual average total is 1524.18 kWh/m^2-year (4.18x365) global radiation values. In Fig. 2 (b), it can be observed as while the highest sunshine duration was 11.31 hours in July, the lowest sunshine duration was 3.75 hours in December. Turkey's average daily sunshine duration on a monthly basis is 7.49 hours-days and it has an annual average total of 2736.89 hours-years (7.49x365) sunshine duration. Considering all these data, it is seen that Turkey has high solar energy potential.

Solar Energy Potentials of Provinces Selected from Seven Different Regions of Turkey

Siirt Province

The highest solar energy potential among the Regions of Turkey is the South-eastern Anatolia Region. The solar energy obtained from this region, where the sunbeam comes at a right angle most of the year, is 1460 KWh/m^2-year. The annual sunshine duration of the South-eastern Anatolia Region is 2993 hours (https://www.incitas.com.tr/bilgi-merkezi/blog/turkiyede-gunes-enerjisi-potansiyeli, 2021). The average global radiation values and sunshine durations on a monthly basis for the province of Siirt where is located in the Southeastern Anatolia Region are given in Figure 3 (a) and (b), respectively (YEGM, 2020). Fig. 3 (a) shows the highest radiation intensity is 6.78 KWh/m^2-day in June and the lowest radiation intensity is 1.79 KWh/m^2-day in December. Also, the monthly average sunshine duration of Siirt have been shown in Fig. 3 (b), too. As it can be seen from it, the highest value is 11.78 hours in July and the lowest value is 3.84 hours in January.

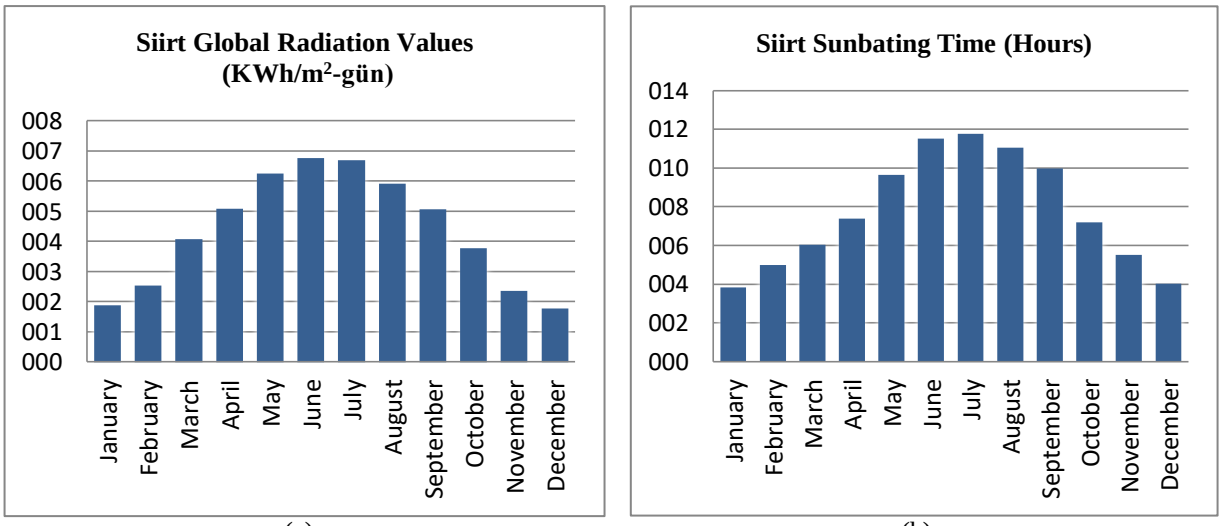

Figure 3. (a) Monthly global radiation values (KWh/m^2-day), (b) Monthly sunbathing durations (hours) in Siirt

It can be deduced from Figure 3 (a) and (b) that Siirt province has an annual average total of 2833 hours of sunshine and an annual average total of 1595 KWh/m^2-year radiation intensity. Considering these values, Siirt is in an important position among the places where its solar energy potential will benefit from solar energy (Bulut et al., 2018).

Adana Province

The Mediterranean Region is the second region with the highest radiation intensity in Turkey. In this region where the number of sunny days is high, the solar energy obtained is 1390 KWh/m^2-year and the total sunshine duration in a year is 2956 hours (https://www.incitas.com.tr/bilgi-merkezi/blog/turkiyede-gunes-enerjisi-potansiyeli, 2021)

The average global radiation values and sunshine durations on a monthly basis for the province of Adana where is located in the Mediterranean Region are given in Figure 4 (a) and (b), respectively (YEGM, 2020). Fig. 4 (a) shows the highest radiation intensity is 6.68 KWh/m^2-day in June and the lowest radiation intensity is 1.81 KWh/m^2-day in December. Also, the monthly average sunshine duration of Adana have been shown in Fig. 4 (b), too. In figure 4 (b), the sunshine duration of Adana province has the lowest sunshine duration with 4.21 hours in December, it reaches the highest value with 11.77 hours in July.

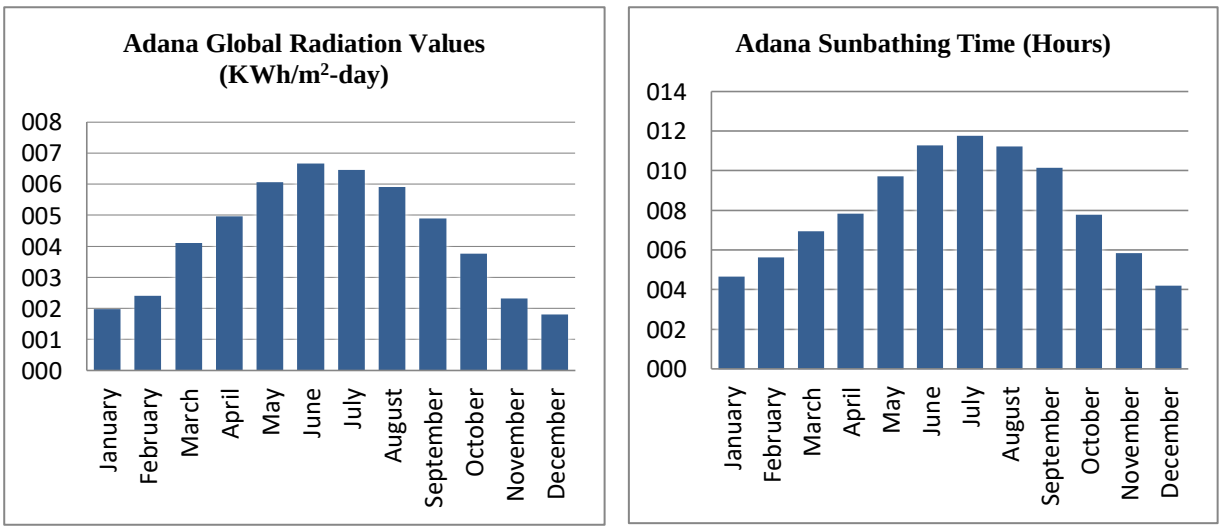

Figure 4. (a) Monthly global radiation values (KWh/m^2-day), (b) Monthly sunbathing durations (hours) in Adana

Adana has an annual average total of 2958 hours of sunshine and an annual average total of 1568 KWh/m^2-year radiation intensity. This shows that it has high solar energy potential.

Erzincan Province

The Eastern Anatolia Region is one of the regions with high radiation intensity. It has an annual average radiation intensity of 1365 KWh/m^2-year and an average annual sunshine duration of 2664 hours. The average global radiation values and sunshine durations on a monthly basis for the province of Erzincan where is located in the Eastern Anatolia Region are given in Figure 5 (a) and (b), respectively (YEGM, 2020). Fig. 5 (a) shows the highest radiation intensity is 6.37 KWh/m^2-day in June and the lowest radiation intensity is 1.55 KWh/m^2-day in December. As it is seen in Fig. 2 (b), the sunshine duration has a minimum of 3.27 hours in December, it reaches a maximum value of 10.67 hours in July.

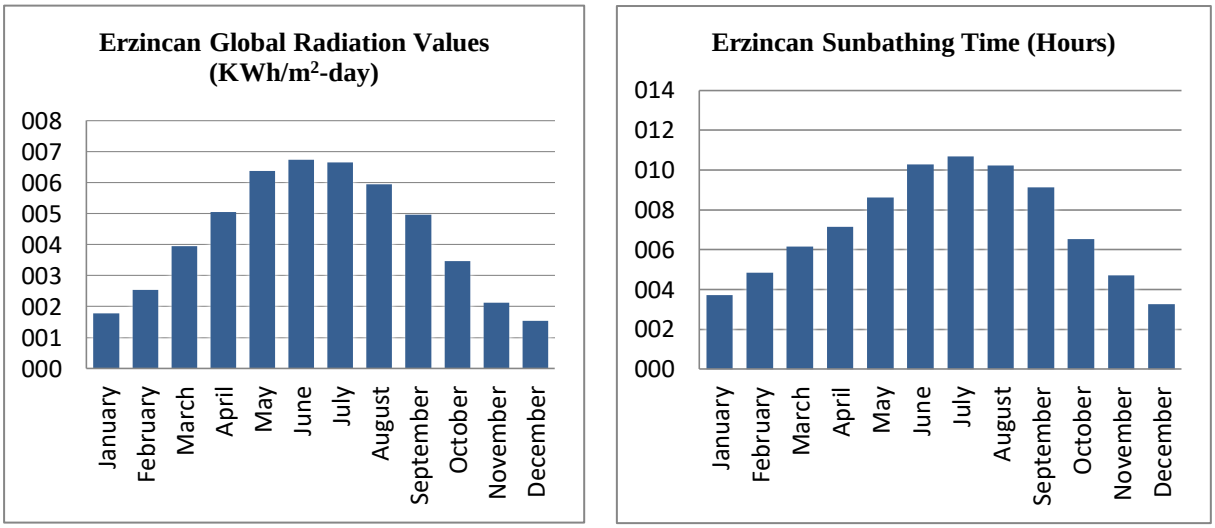

(a) (b)

Figure 5. (a) Monthly global radiation values (KWh/m^2-day), (b) Monthly sunbathing durations (hours) in Erzincan

The Erzincan has an annual average total sunshine duration of 2598 hours and an annual average total global radiation value of 1558.84 KWh/m^2-year. The province of Erzincan experiences a longer and hotter summer season compared to the surrounding provinces (Çakmak and Altaş, 2016). This means that Erzincan can benefit from more sun during the summer months.

Kırşehir Province

The Central Anatolia Region is the fourth region with high solar energy potential (https://www.powerenerji.com/turkiye-gunes-enerjisi-potansiyel-haritasi-bolge-il-guneslenme-sureleri.html, 2021). The solar energy obtained in this region is 1314 KWh/m2-year and the annual sunshine duration is 2628 hours.

The monthly average global radiation values and monthly average sunshine durations for the Kırşehir, which is are given in Figure 6 (a) and (b), respectively (YEGM, 2020). When the data in the Fig 6 (a) is examined, it has the highest radiation value with 6.47 KWh/m^2-day in June, while it has the least radiation value with 1.58 KWh/m^2-day in December. Considering the monthly sunshine duration of Kırşehir province in the Fig. 6 (b), July has the highest sunshine duration with 11.73 hours, while December has the least sunshine duration with 3.51 hours.

Kırşehir province has an annual average total of 2773 hours of sunshine and an annual average total of 1513 KWh/m2-year global radiation value. The one-year sunshine duration of Kırşehir province is above the one-year average total sunshine duration of Turkey.

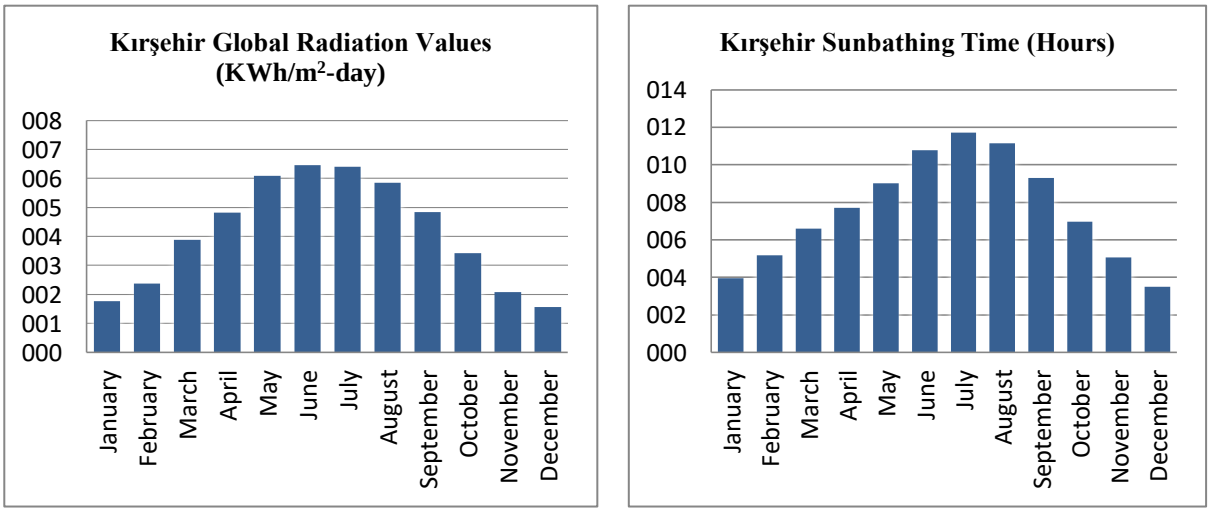

(a) (b)

Figure 6. (a) Monthly global radiation values (KWh/m^2-day), (b) Monthly sunbathing durations (hours) in Kırşehir

Kütahya Province

The Aegean Region ranks fifth in the solar energy potential ranking in Turkey. The Aegean Region has an annual average radiation intensity of 1304 KWh/m^2-year. The total sunshine duration in one year is 2738 hours. This is almost equivalent to the Turkey's average sunshine duration. The monthly average global radiation values and monthly average sunshine durations for the Kütahya in the Aegean Region are given in Figure 7 (a) and (b) (YEGM, 2020). Looking at the monthly average global radiation values of Kütahya in the Fig. 7 (a), it is determined that the highest radiation intensity is 6.48 KWh/m^2-day in June and the lowest radiation intensity is 1.51 KWh/m^2-day in December. In Fig. 7 (b), when the sunshine durations are examined, the highest value was 10.77 hours in July and the lowest value was 3.51 hours in December. The annual average total sunshine duration in Kütahya province is 2562 hours and the annual average total is 1493 KWh/m^2-year global radiation value

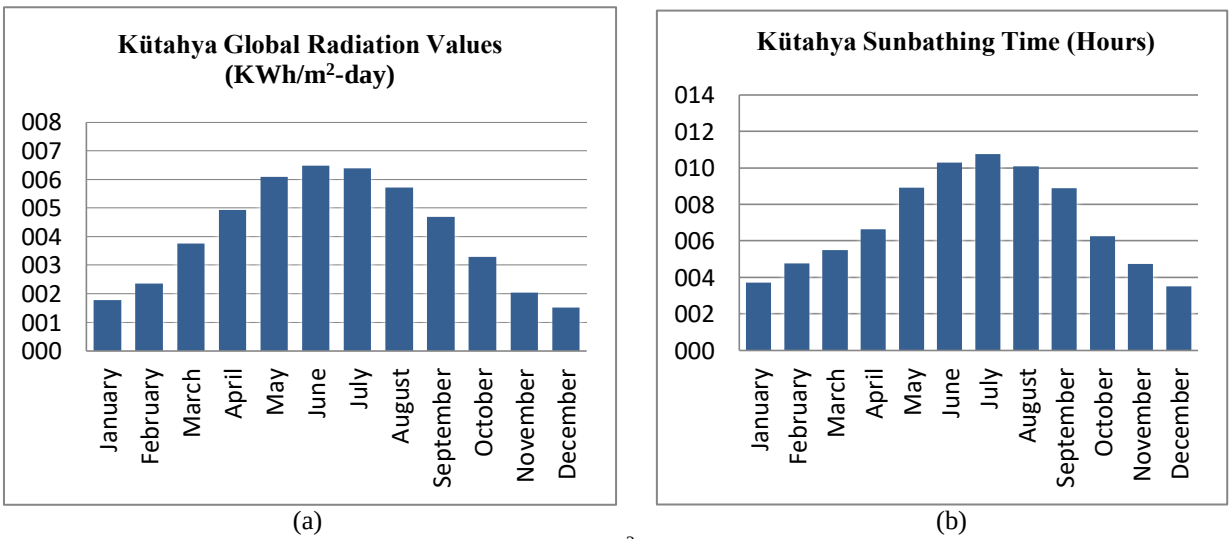

(a) (b)

Figure 7. (a) Monthly global radiation values (KWh/m^2-day), (b) Monthly sunbathing durations (hours) in Kütahya

Balıkesir Province

The solar energy obtained in the Marmara Region is 1168 KWh/m^2-year and the annual sunshine duration is 2409 hours. The average daily sunshine duration of Marmara Region is less than Aegean Region and is more than Black Sea Region.

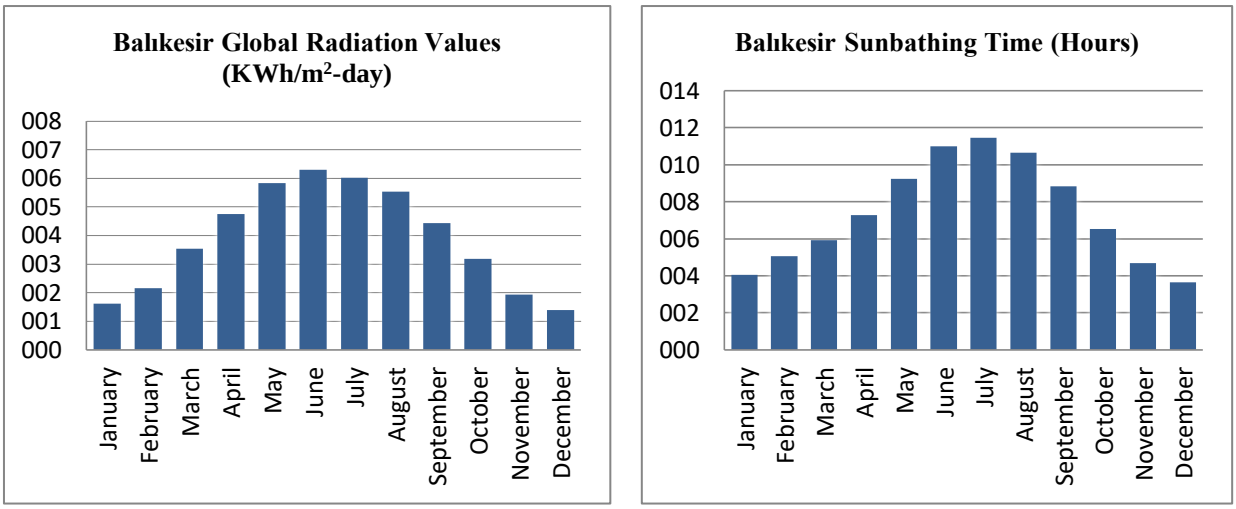

(a) (b)

Figure 8. (a) Monthly global radiation values (KWh/m^2-day), (b) Monthly sunbathing durations (hours) in Balıkesir

Fig. 8 (a) and (b) show the monthly average global radiation values and monthly average sunshine durations for Balıkesir in the Marmara Region, respectively (YEGM, 2020). Fig. 8 (a) shows that the monthly average global radiation values of Balıkesir has the highest radiation value with 6.29 KWh/m^2-day in June and the least radiation value with 1.39 KWh/m^2-day in December. The monthly average sunshine durations of Balıkesir reaches a minimum in December and a maximum in July as shown in Fig. 8 (b).

Balıkesir has an annual average total of 2690 hours of sunshine and an annual average total of 1421 KWh/m^2-year radiation intensity.

Amasya Province

The Black Sea Region has the lowest monthly average global radiation values. The Black Sea Region has an average annual radiation intensity of 1120 KWh/m^2-year. The total sunshine duration in one year is 1971 hours. Due to its geographical location, the number of sunny days is low in this region where the amount of precipitation is high (Bulut et al., 2018; Doğanay, 2021).Therefore, the region where we can benefit least from solar energy is the Black Sea Region (Bulut et al., 2018).

Figure 9 (a) and (b) show the monthly average global radiation values and monthly average sunshine durations for the Amasya in the Black (YEGM, 2020). When the Fig. 9 (a) is examined, it is observed that the radiation intensity of Amasya is the highest in June with a value of 6.14 KWh/m^2-day, and the lowest in December with a value of 1.36. In the Fig. 9 (b), it is seen that while Amasya has the

minimum sunshine duration in December with 3.19 hours, it reaches the maximum sunshine duration in June with 10.14 hours.

It is observed that Amasya has an annual average total of 2431 hours of sunbathing time and an annual average total of 1396 KWh/m2-year global radiation value. According to these values, Amasya is more fortunate than many other provinces in the region due to its geographical location (Kaynar, 2020). Ranking fourth in the region in terms of sunshine duration, Amasya reveals that it is the most suitable place to benefit from solar energy in the region (Kaynar, 2020).

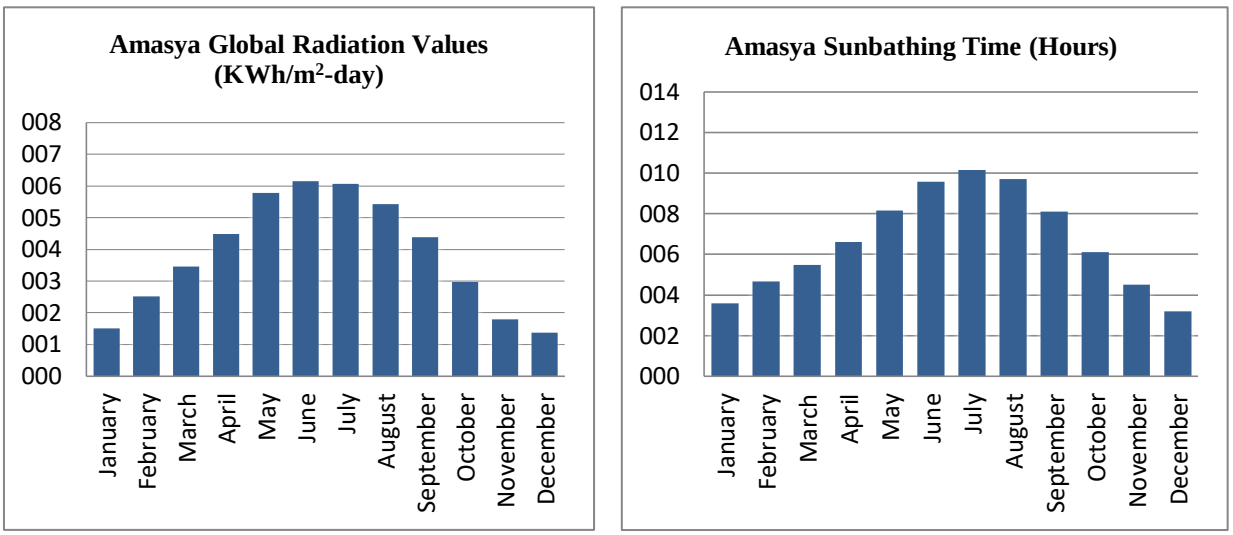

(a) (b)

Figure 9. (a) Monthly global radiation values (KWh/m^2-day), (b) Monthly sunbathing durations (hours) in Amasya

The radiation intensities and sunshine durations of the regions are summarized in Table 1 (https://www.powerenerji.com/turkiye-gunes-enerjisi-potansiyel-haritasi-bolge-il-guneslenme-sureleri.html, 2021). In Turkey, which is located in the sun belt, the solar energy potential decreases as we go from south to north (Doğanay, 2021). As it is seen from all Figures, the Southeast Anatolia Region has the highest solar energy potential and the Black Sea region has the least solar energy potential. This is because the Southeastern Anatolia Region is closer to the equatorial region and the Black Sea Region is the farthest from the equatorial region (Taşova, 2018).

Table 1. Radiation Intensities and Sunbathing Durations

Regions of Turkey	Radiation Intensities (KWh/m^2-year)	Sunbathing Duration (hour/year)
The South-Eastern Anatolia Region	1460	2993
The Mediterranean Region	1390	2956
The Eastern Anatolia Region	1365	2664
The Central Anatolia Region	1314	2628
The Aegean Region	1304	2738
The Marmara Region	1168	2409
The Black Sea Region	1120	1971

In Table 2, the radiation intensities and sunshine durations of the provinces of Siirt, Adana, Erzincan, Kırşehir, Kütahya, Balıkesir and Amasya, which are selected from seven different regions of Turkey, are summarized from the most irradiated to the least area. It is seen that the provinces in different regions have radiation intensities close to each other, even if they have different climatic conditions. This shows how important Turkey is in terms of solar energy potential. It can be predicted that a solar power plant that can be established in every region can contribute to regional energy or the national economy.

Table 2. Radiation Intensities and Sunbathing Durations of Province

Province	Radiation Intensities (KWh/m^2-year)	Sunbathing Duration (hour/year)
Siirt	1595	2833
Adana	1568	2958
Erzincan	1558	2598
Kırşehir	1513	2773
Kütahya	1493	2562
Balıkesir	1421	2690
Amasya	1396	2431

Result and Discussion

Turkey's solar energy potential is quite high due to its geographical location and location in the sunbelt. In this study, it is aimed to reveal the importance of solar energy and to give detailed information about the solar energy potential of Turkey. For this purpose, provinces (Siirt, Adana, Erzincan, Kırşehir, Kütahya, Balıkesir and Amasya) were randomly selected from seven different regions of Turkey.

In Table 3, the monthly global radiation values (KWh/m^2-day) and monthly sunshine duration (hours) of Siirt, Adana, Erzincan, Kırşehir, Kütahya, Balıkesir and Amasya are listed. All monthly values are shown in Figure 10 and Figure 11, respectively. In Figure 10 and 11, the x-axis shows the months as a

number such as 1 is for January, 2 is for February, 12 is for December. In Figure 10, the y-axis shows global radiation values. In Figure 11, the y-axis shows monthly sunbathing durations by hours.

Table 3. Radiation Intensities and Sunbathing Durations for all Province

	Global Radiation Values (KWh/m^2-day)						
	Siirt	Adana	Erzincan	Kırşehir	Kütahya	Balıkesir	Adana
January	1.89	1.98	1.78	1.78	1.77	1.61	1.50
February	2.54	2.42	2.54	2.38	2.36	2.15	2.51
March	4.09	4.12	3.95	3.89	3.75	3.54	3.45
April	5.10	4.98	5.05	4.83	4.93	4.75	4.48
May	6.27	6.07	6.37	6.09	6.08	5.83	5.78
June	6.78	6.68	6.74	6.47	6.48	6.29	6.14
July	6.71	6.46	6.65	6.42	6.38	6.01	6.07
August	5.93	5.91	5.95	5.85	5.72	5.53	5.42
September	5.07	4.90	4.96	4.84	4.69	4.42	4.38
October	3.79	3.78	3.47	3.43	3.28	3.18	2.97
November	2.37	2.33	2.13	2.08	2.04	1.93	1.78
December	1.79	1.81	1.55	1.58	1.51	1.39	1.36
	Monthly Sunbathing Durations (Hours)						
January	3.84	4.67	3.73	3.97	3.71	4.05	3.57
February	5.00	5.65	4.85	5.18	4.78	5.05	4.65
March	6.04	6.97	6.15	6.61	5.50	5.92	5.48
April	7.38	7.84	7.14	7.72	6.65	7.26	6.60
May	9.64	9.72	8.63	9.02	8.91	9.23	8.16
June	11.52	11.29	10.29	10.78	10.29	10.99	9.58
July	11.78	11.77	10.67	11.73	10.77	11.44	10.14
August	11.07	11.22	10.23	11.15	10.09	10.65	9.70
September	9.99	10.15	9.12	9.32	8.90	8.84	8.11
October	7.19	7.78	6.52	6.98	6.26	6.53	6.11
November	5.53	5.86	4.71	5.07	4.75	4.69	4.51
December	4.02	4.21	3.21	3.51	3.51	3.64	3.19

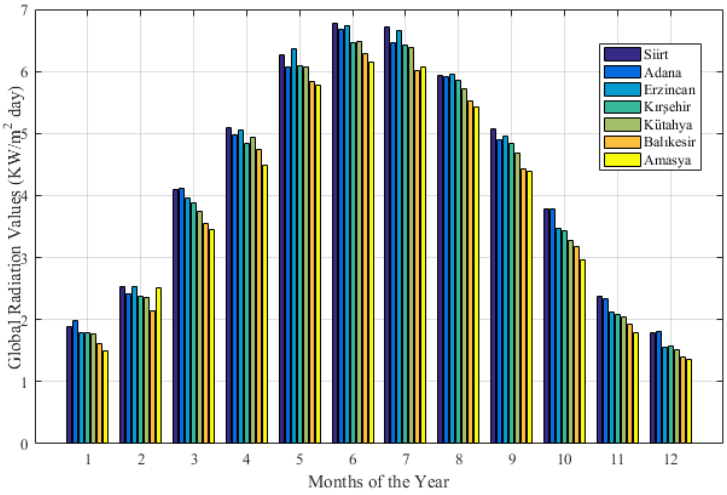

Figure 10. Monthly global radiation values (KWh/m2-day) of Siirt, Adana, Erzincan, Kırşehir, Kütahya, Balıkesir and Amasya

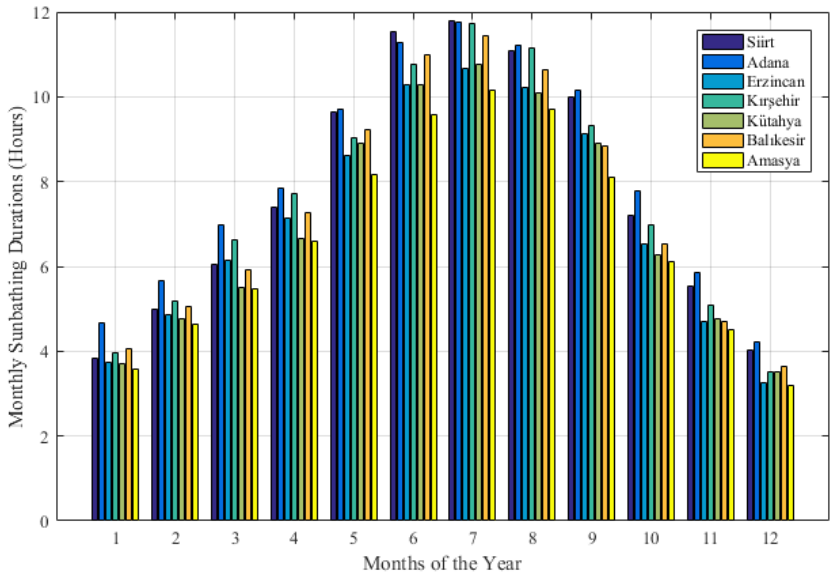

Figure 11. Monthly sunbathing durations (hours) of Siirt, Adana, Erzincan, Kırşehir, Kütahya, Balıkesir and Amasya

Conclusion

The increasing air pollution and fewness of fossil fuel sources have increased the interest in new environmentally friendly sources such as renewable energy sources. Solar energy is a type of energy obtained from natural sources and also it is ecofriendly. It is important to get best benefit with use of this type of energy, which provides unlimited energy. Turkey is located in the sun belt due to its geographical location. So, it has a very high solar energy potential according to many other countries. Turkey has an average daily radiation intensity of 4.18 KWh/m^2-day on a monthly basis and an annual average total of 1524.18 KWh/m^2-year (4.18x365) global radiation value. The average daily sunshine duration of Turkey on a monthly basis is 7.49 hours-days and has an annual average total of 2736.89 hours-years (7.49x365). Also, the solar energy potential increases as from north to south. The Southeastern Anatolia Region, where the sun's rays are the most, is in the first place among the regions that will benefit most from solar energy. Then Mediterranean Region where the number of sunny days is high comes in second place. Then Eastern Anatolia Region, Central Anatolia Region, Aegean Region, Marmara Region and Black Sea Region come, respectively.

In this study, not only has given more detailed information about the solar energy potential of Turkey, but also solar energy potentials of Siirt, Adana, Erzincan, Kırşehir, Kütahya, Balıkesir and Amasya were investigated and compared. Datas which were selected for seven different regions obtained from the Ministry of Energy and Natural Resources were used in this study. According to the result of the research, radiation intensities in all provinces are close to each other. However climatic conditions (such as snow, rain, etc.), landforms, floras are different from each other. These features indicate Turkey’s unique structure. Although Turkey has a high solar energy potential, other factors are effective in utilizing solar energy, too. Considering Turkey's radiation potential along with all these

factors, it can be predicted how a solar power plant that can be established in every region can contribute to regional energy or the economy of the country. In future studies, it is planned to examine the establishment of a solar power plant and grid connection in a suitable region with using the information in this article.

Statement of Conflict of Interest

Authors have declared no conflict of interest.

Author's Contributions

The contribution of the authors is equal.

*This study was presented as a summary paper at the International Conference on Engineering, Natural and Applied Sciences (ICENAS'21) held online on 24-26 November 2021.

References

Aksungur KM., Kurban M., Başaran Filik Ü. Türkiye'nin farklı bölgelerindeki güneş ışınım verilerinin analizi ve değerlendirilmesi. Enerji Verimliliği ve Kalitesi Sempozyumu, 2013.

Albayrak Karadağ Ö. Yenilenebilir enerji kaynaklarının değerlendirilmesinde kullanılan çok kriterli karar verme teknikleri ve değerlendirme kriterlerinin incelenmesi: 2017-2020. Atatürk Üniversitesi İktisadi ve İdari Bilimler Dergisi 2020; 34(4): 1287-1310.

Atakul Ş., Kalender MA., Gezici M., Eliçin AK. Güneş tarlası kurulumu. Tarım Makinaları Bilimi Dergisi 2015; 11(1): 55-60.

Bilhan AK., Emikönel S. Nevşehir ili güneş enerji potansiyelinin analizi ve kurulu güneş enerji santralleri. Avrupa Bilim ve Teknoloji Dergisi 2021; 24: 289-294.

Bulut N., Kuncan M., Horoz S. Türkiye'de güneş enerjisinin kullanım alanları ve Siirt güneş enerji potansiyeli. Ahtamara I. Uluslararası Multidisipliner Çalışmalar Kongresi, 25-26 Ağustos 2018, sayfa no:1315-1319, Van.

Çakmak R., Altaş İH. Erzincan'da güneş enerjisinden elektrik üretimi potansiyeli: Almanya ile karşılaştırılması. Uluslararası Erzincan Sempozyumu, 28 Eylül-1Ekim 2016, sayfa no:406-419, Erzincan.

Dinçer F. Türkiye'de güneş enerjisinden elektrik üretimi potansiyeli-ekonomik analizi ve AB ülkeleri ile karşılaştırmalı değerlendirme. Kahramanmaraş Sütçü İmam Üniversitesi Mühendislik Bilimleri Dergisi 2011; 14(1): 8-17.

Doğanay MM. Mardin bölgesi güneş (fotovoltaik) enerjisi potansiyel analizi. UMÜFED Uluslararası Batı Karadeniz Mühendislik ve Fen Bilimleri Dergisi 2021; 3(1): 86-117.

Eltas İ. Tek eksenli güneş takip sistemi veriminin Erzurum koşullarında belirlenmesi. Ordu Üniversitesi Fen Bilimleri Enstitüsü Yüksek Lisans Tezi, Ordu, Türkiye, 2020.

http://yegmweb.yegm.gov.tr/genc_cocuk/Yenilenebilir_Enerji_Nedir.aspx, 2021

https://www.incitas.com.tr/bilgi-merkezi/blog/turkiyede-gunes-enerjisi-potansiyeli

İnan İ., Akbulut İ., Aslan E. Enerji sorununun çözümünde yenilenemez ve yenilenebilir enerji kaynaklarının yeri ve önemi. Türk Dünyası Araştırmaları 2018; 120(237): 11-40.

İzgeç MM. Türkiye yenilenebilir enerji kapasitesi devreye alma işleminin darboğaz analizi. Fırat Üniversitesi Mühendislik Bilimleri Dergisi 2020; 32(2): 499-508.

Kaya K., Şenel MC., Koç E. Dünyada ve Türkiye'de yenilenebilir enerji kaynaklarının değerlendirilmesi. Teknolojik Uygulamalı Bilimler 2018; 13(3): 219-234.

Kaynar NK. Yenilenebilir enerji kaynaklarından güneş enerjisinin Amasya ilindeki potansiyeli. Bilge International Journal of Science and Technology Research 2020; 4(2): 48-54.

Kılıç FÇ. Güneş enerjisi. Türkiye'deki son durumu ve üretim teknolojileri. Mühendis ve Makina 2015; 56(671): 28-40.

Kırbaş İ., Çifci A., İşyarlar B. Burdur ili güneşlenme oranı ve güneş enerjisi potansiyeli. Mehmet Akif Ersoy Üniversitesi Fen Bilimleri Enstitüsü Dergisi 2013; 4(2): 20-23.

Kocakuşak R. Yenilenebilir enerji kaynaklarından güneş Enerjisinin, Türkiye'deki önemi ve ges kurulum araştırması. Maltepe Üniversitesi Sosyal Bilimler Enstitüsü Yüksek Lisans Tezi, İstanbul, Türkiye, 2018.

Kumar A., Kumar K., Kaushik N., Sharma S., Mishra S. Renewable energy in India: current status and future potentials. Renewable And Sustainable Energy Reviews 2010; 14(8): 2434-2442.

Power Enerji. https://www.powerenerji.com/turkiye-gunes-enerjisi-potansiyel-haritasi-bolge-il-guneslenme-sureleri.html

Şendemir M. Karabük ilinin yenilenebilir enerji kaynakları varlığına yönelik bir envanter çalışması. Karabük Üniversitesi Lisansüstü Eğitim Enstitüsü Yüksek Lisans Tezi, Karabük, Türkiye, 2021.

Yaman A., Yakın A. Behçet R. Van ili güneş ve hidroelektrik enerjilerinin potansiyeli ve ilin ekonomisine katkıları. Bitlis Eren Üniversitesi Fen Bilimleri Dergisi 2019; 8(1): 243-250.

YEGM. Yenilenebilir Enerji Kaynağı Genel Müdürlüğü. https://gepa.enerji.gov.tr/MyCalculator/Default.aspx, 2020.

Yolcan OO., Köse R. Türkiye'nin güneş enerjisi durumu ve güneş enerjisi santrali kurulumunda önemli parametreler. Kırklareli Üniversitesi Mühendislik ve Fen Bilimleri Dergisi 2020; 6(2): 196-215.

Taşkın O., Korucu T. Kahramanmaraş ili güneş enerjisi potansiyeli ve kullanım olanakları. KSÜ Doğa Bilimler Dergisi 2014; 17(4): 12-16.

Taşova M. Türkiye'nin güneş enerjisi parametre değerleri ve güneş enerjisinden faydalanma olanakları. İleri Teknoloji Bilimleri Dergisi 2018; 7(3): 10-17.

T.C. Enerji ve Tabii Kaynaklar Bakanlığı, https://enerji.gov.tr/bilgi-merkezi-enerji-gunes

OKÜ Fen Bilimleri Enstitüsü Dergisi
5(Özel Sayı):185-195, 2022

OKU Journal of The Institute of Science and Technology, 5(Special Issue):185-195, 2022

Osmaniye Korkut Ata Üniversitesi Fen Bilimleri Enstitüsü Dergisi

Osmaniye Korkut Ata University Journal of The Institute of Science and Technology

RF Stalam Drying Automation

Duygu Durdu KOÇ[1*], Kübra YILMAZ[2], Arif ŞENER[3]

[1]Ulusoy Textile Industry and Commerce Incorporated Company Adana/Turkey, Adana Alparslan Turkes Science and Technology University, Faculty of Engineering, Department of Mechanical Engineering, 01250, Adana, Turkey
[2]Ulusoy Textile Industry and Commerce Incorporated Company Adana/Turkey, Adana Alparslan Turkes Science and Technology University, Faculty of Engineering, Department of Industrial Engineering, 01250, Adana, Turkey
[3]Ulusoy Textile Industry and Commerce Incorporated Company Adana/Turkey

[1]https://orcid.org/0000-0002-4400-5714
[2]https://orcid.org/ 0000-0003-1040-1097
[3]https://orcid.org/0000-0003-0726-0027
*Corresponding author: duygu@samtekstekstil.com

Research Article

Makale Tarihçesi:
Geliş tarihi: 15.12.2021
Kabul tarihi:21.01.2022
Online Yayınlanma: 23.02.2022

Keywords:
Drying automation
Yarn bobbin
PLC
Radio frequency drying
Textile

ABSTRACT

The basis of the textile industry is yarn production. Many processes are applied to the yarn during the production phase. The last and most important of these processes is the drying process. There are various drying methods for the drying process and RF-Satalam dryers are discussed in this study. There are electrodes above and below the conveyor belt in these dryers. With the help of these electrodes, the water in the wet bobbin is evaporated by friction force and removed from the yarn. All process steps such as belt speed, drying parameters, electrode position of the machine determined by the machine operator have been automated with the developed system. With the barcode read to the system, it brings the data from the ERP database to the PLC system, where the raw weight of the wet coil is calculated and the tape speed and electrode level are determined.

RF Stalam Kurutma Otomasyonu

Araştırma Makalesi

Article History:
Received: 15.12.2021
Accepted: 21.01.2022
Published online:23.02.2022

Anahtar Kelimeler:
Kurutma otomasyonu
İplik bobini
PLC
Radyo frekanslı kurutucu
Tekstil

ÖZET

Tekstil sektörünün temelini iplik üretimi oluşturmaktadır. İpliğe, üretim aşamasında birçok işlem uygulanmaktadır. Bu işlemlerden sonuncusu ve en önemlisi kurutma işlemidir. Kurutma işlemi için çeşitli kurutma yöntemleri olup bu çalışmada RF-Satalam kurutma makineleri ele alınmıştır. Bu kurutma makinelerinde yer alan taşıyıcı bandın altında ve üstünde elektrodlar yer almaktadır. Bu elektrodlar yardımıyla ıslak bobin içindeki su, sürtünme kuvveti ile buharlaştırılarak iplikten uzaklaştırılır. Makine operatörü tarafından belirlenen makinenin bant hızı, kurutma parametreleri, elektrot konumu gibi tüm işlem adımları geliştirilen sistem ile otomatik hale getirilmiştir. Sisteme okutulan barkod ile ERP veri tabanındaki verileri PLC sistemine getirir ve burada ıslak bobinin ham ağrılığının hesaplanması sağlanarak bant hızı ve elektrod seviyesi belirlenir. Böylece yapılan yanlış hesaplamaların önüne geçilerek yangın riski ortadan kaldırılmış, makinede oluşabilecek elektrik hasarlarının önüne geçilmiş ve sistem daha verimli hale getirilmiştir.

To Cite: Koç DD., Yılmaz K., Şener A. RF Stalam Drying Automation. Osmaniye Korkut Ata Üniversitesi Fen Bilimleri Enstitüsü Dergisi 2022; 5(Özel sayı): 185-195.

Introduction

The textile sector, which is one of the oldest branches of industry in our country, also constitutes an important part of exports. Turkey ranks sixth in the world in terms of installed capacity and number of spindles in the textile industry. This production capacity has made our country the largest textile producer in Europe. In this respect, it provides important gains to the country's economy. The increase in the production volume with each passing day brings about an increase in employment opportunities. The responsibilities of the textile companies in our country are increasing in order to ensure the continuity of the increase in this field and to continue to have a say in the textile sector in the world. In this context, textile companies in their production; they should be based on quality, correct production, sustainability and efficient energy use. While it has become inevitable for companies to produce new products / machines in line with these foundations, the improvements they will make have revealed their R&D activities.

Yarn production constitutes the basis of all activities of the textile sector. Therefore, yarn production constitutes the priority area in innovation studies. Yarns are materials that have a certain length, number of twists, fineness and can be dyed. The fibers that make up the threads are called fibers. The yarn industry has many processes and steps in the production phase. In the period until the final product is obtained, yarn; It is subjected to processes such as dyeing, printing, coloring and drying. The final stage, drying, is a process that requires significant energy and cost. In this process, which is carried out to remove moisture from the yarn, first of all, mechanical processes are applied. However, since mechanical methods alone are not sufficient, full drying is carried out by applying secondary methods (Ribeiro, 1995; Akarsalan, 2002; Akyol, 2007).

The quality of the yarn depends on the dyestuff and chemicals used in the dyeing of the yarn, the fixation process and drying as the last step. While a correct drying method makes the yarn higher quality, incorrect drying can cause the yarn to be of second quality, to be wasted or even to burn. Therefore, the drying process is a very costly and time-consuming process. Therefore, the possible ratio of the amount of water in the yarn should be removed by mechanical means. In addition, determining the state of the water contained in the yarn is an important parameter in the effectiveness of the drying method to be applied. Water can be found on textile products as indicated in Table 1. (Le, 1995; Güneban, 2005; Akyol, 2010; Akyol, 2011)

Table 1. Types of water on textile products

Dripping water	It is water that can flow down the product with its own weight by not making bonds with the fibers, which can be completely removed by mechanical drying methods.
Surface water	It is water that can bond on the surface of the product with its adhesion force, but only a certain part of it can be removed by mechanical methods.
Capillary water	It is water that binds to the surface of the fibers forming the threads by adhesion forces. However, some of them can be removed by mechanical means.
Inflatable water	It is the water that binds to the fiber molecules forming the yarn with dipole forces and causes the fiber to swell, but is removed from the product by thermal methods.
Hydroscopic moisture (crystal water)	A well-applied drying method is water, which must be present in a textile product at the end. If this amount of water is removed from the product, the hold of the product will deteriorate and it will not be possible to reintroduce it into the product at the same rate.

Drying in the yarn is the method of removing these amounts of water in the yarn from the yarn by means of heat transfer. This process has become the most important step of the yarn production stage in terms of cost, quality and efficiency. There are various drying methods and machines used in the textile industry to perform this process (Jhanji et al. 2015; Gallopi et al. 2017). In addition, there is a pre-drying process applied before the drying method. The purpose of this process is to save energy by reducing the amount of energy to be used in the drying process.

The pre-drying process is carried out with three different methods. These methods are as follows: Spinning is the method performed by passing the wet textile product between rollers with a certain speed. In this method, the amount of water contained in the product is removed by vacuuming. Centrifugation is a method in which surface water is removed from the wet product by utilizing centrifugal force. After one of these methods for pre-drying is applied to the yarn, for the actual drying; convection drying, conduction drying, infrared (infrared) drying or radiofrequency dryers are preferred.

In the drying method, in which air and other gases are used as the heat source, the heated and dehumidified air comes into direct contact with the textile product, allowing the water in the product to evaporate. Hot air or other gases used are passed over and between the product to be dried. Due to this feature, it is also known as the hot air drying technique (Akyol, 2011). These dryers; they are tensioned, conveyor belt and air cushioned, hot-fluelar, perforated drum dryers (Karakoca, 2017).

In these drying machines, the yarn bobbins placed for the machine are exposed to air at a certain temperature and pressure, first from the outside to the inside, and then from the inside to the outside, and the drying process is carried out.

In the conduction drying method, firstly, the rollers are heated with hot steam or oil, then the textile product to be dried is directly contacted with the surface of the roller and the drying process is performed. However, in this process, since the product directly contacts the surface of the heated roller, it may cause overheating (Karakoca, 2017). Therefore, necessary precautions should be taken to ensure that the heating before drying is homogeneous. It is not preferred due to the need to develop unique control methods and high investment costs.

Infrared drying method, also known as radiation drying, is a heat transfer method that takes place in the form of electromagnetic waves from a high-temperature surface. In this method, which is used in cases where it is desired to reduce the amount of water in the product below 25%, the temperature can rise above 500 ^{0}C. Therefore, the risk of over-drying is very high (Karakoca, 2017).

In radio frequency dryers, no heat is taken from the outside for the drying process. The water molecules on the product passing between two capacitor plates connected to the alternating current are in constant motion thanks to the high frequency. The heat energy generated by this movement causes the evaporation of the water molecules and ensures the drying of the product.

They are drying machines that are widely used for drying open fiber, tops, hank, bobbin and ready-made clothing products. In order for the drying to be economical, the free water on the product is removed by pre-drying and subjected to the main drying process in the radiofrequency (RF) dryer. Although the initial setup cost is high, it provides an important advantage by providing a fast and effective drying opportunity (Karakoca, 2017).

Material and Methods

In the textile sector, the fibers are dyed after being turned into yarn. After the dyeing process, the yarn is dried in order to give the yarn its final shape and to ensure the permanence of its colour and to remove the water in it. The main logic of the drying process is to remove the water in the solid. In this process, it is very important to create the most suitable method that will make the right drying without compromising the yarn structure, colour and quality by consuming minimum energy. Improvement studies were carried out on the RF-Stalam dryer, which is considered within the scope of this study, for a more accurate and efficient operation. The current situation was analysed and the needs were determined before the studies. In a standard yarn bobbin drying process, the bobbins are first placed in

centrifugal machines where centrifugal force is used to remove excess water on them. In these machines, excess water is removed by rotating the coils at 1500 rpm for an average of 3 to 6 minutes.

Figure 1. Yarn bobbin centrifugal dryer

Afterwards, while the yarn bobbins dyed in the current system are dried, the bobbins are placed on the tape on the RF-Stalam dryer. The operator calculates the raw product kilogram and wet product kilogram by taking the work orders of the yarn bobbins coming out of the dyeing process. The belt speed of the dryer is calculated and adjusted according to the wet coil kilogram.

Belt Speed Calculation is done with the following formula.

$$V_{belt\ speed}\,(mt/h) = (kW \times 1{,}2)/(B \times S)$$

B: Number of coils per meter (pcs)

Q: Amount of water in a coil (kg)

Except for these formulas based on, all hank dryers are dried at a constant speed of 40 kW and 4.5 m/h. 16 hanks are placed on a one meter long tape, 4 side by side, in 4 layers, and the electrode is adjusted to the highest level by the operator.

According to the values in Table 1, the tape speed is calculated and the sequence is made.

No cloth is placed on the tape for muff dyeing. However, in all other viscose blended dyeing's, a dry and clean polyester cloth should be placed on the tape. In the 10" stalam, the electrode is used at the upper level for 10" bobbins and at the lower level for 6" bobbins. In this calculation made manually by the operator in line with all this information, if the tape speed is faster than it should be, the bobbins can come out of the drying process moist before they dry, or if the tape speed is slower than it should be, the yarn bobbins. It may ignite inside the machine and cause a fire. In such a case, the process will start again and the yarns obtained from the new products will be dyed and dried again.

Table 2. RF-Stalam band velocity calculation table

FIBER	10" STALAM			
	kW	Bobbin per 1 meter	Electrode Level	Speed of Band (mt/h)
2x78/68 dtex/Nylon Half Matt	40	11x5=55	Low Level	12
Acrylic (10")	40	28		
Acrylic (6")	60	28		
Acrylic / Nylon (Light Color)	55	28		
Acrylic / Nylon (Middle-Dark Color)	55	28		
Acrylic / Cotton	60	28		
Acrylic / Polyester	40	28		
Acrylic / Wool	60	28		
B438 Vis / Nyl	55	21	Low Level	4,5
B438 Vis / Nyl (optical)	40	21	Low Level	4,5
Nylon	40	28		
Cotton (except for softening and optical stanining)	40	>1200 gr:28, <1200 gr:36		
Cotton or Viscon (softening and optical stanining)	40	28		
Cotton / Polyester	55	28		
Polyester	30	28		
Polyester / Viscon	55	28		
Viscon (except for softening and optical staining)	70	>1200 gr:28 <1200 gr:36		
Wool	60	28		
Nylon (Kod1569-Kod2079-Kod2153) 8"	40	28		
Polyester / Viscon (C92)	55	28		
Polyester (K2056)	30	28		
KOD3196 PES	30	18 Hank		

Figure 2. RF-Stalam drying

This results in extra costs and loss of time. Considering all these problems that may arise, it has become necessary to make an improvement on the system and to minimize the errors that may arise from the operator or the machine. In line with these needs, a new system has been developed in the study. Thanks to this system, an automation system has been introduced that automatically determines the operating rules of the machine according to the raw material. For this, first of all, the inputs and outputs needed in the hardware were evaluated within the scope of the study. Electrical, electronic and mechanical equipment has been determined. As shown in Figure 3, necessary electronic circuit designs have been made in accordance with the system and data.

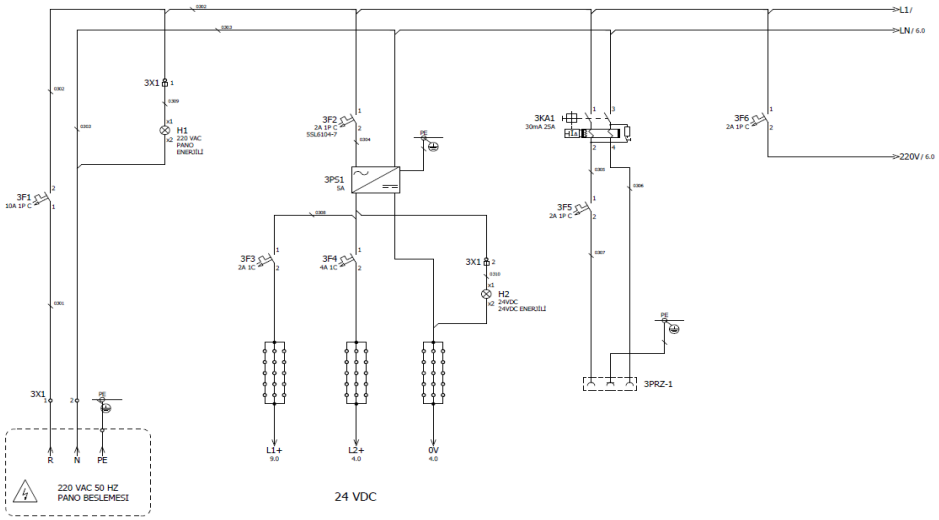

Figure 3. RF-Stalam Board Supply Line

In addition to the electronic circuit designs made, the system digital average was poured and the software system was developed. While developing the software, first of all, the parameters affecting the drying process were determined. These; raw material, bobbin weight, bobbin height. Thanks to the software developed as shown in Figure 4, all yarn types, their weights and the amount of water they contain are introduced to the system.

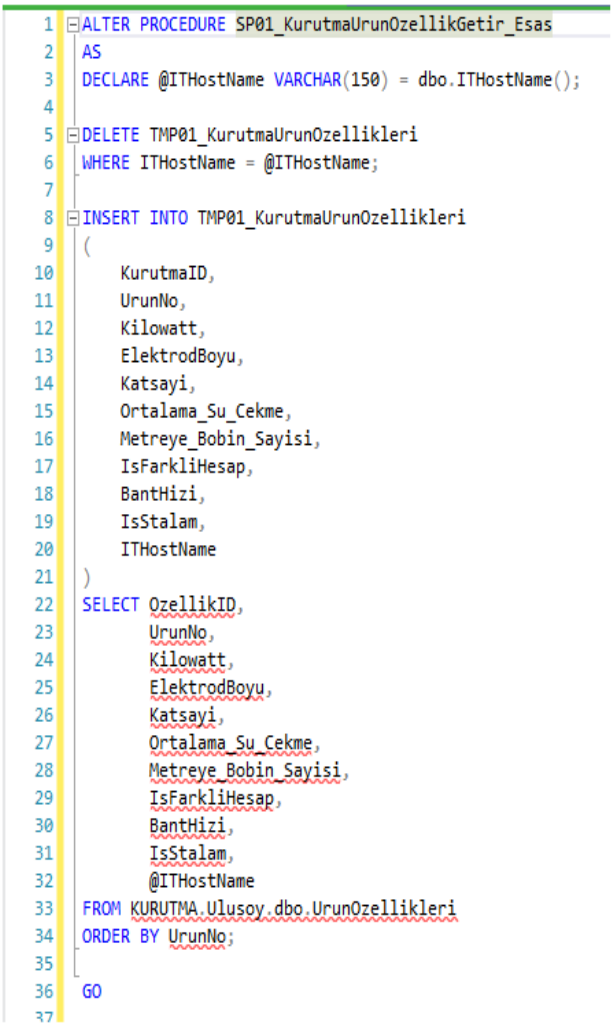

```
ALTER PROCEDURE SP01_KurutmaUrunOzellikGetir_Esas
AS
DECLARE @ITHostName VARCHAR(150) = dbo.ITHostName();

DELETE TMP01_KurutmaUrunOzellikleri
WHERE ITHostName = @ITHostName;

INSERT INTO TMP01_KurutmaUrunOzellikleri
(
    KurutmaID,
    UrunNo,
    Kilowatt,
    ElektrodBoyu,
    Katsayi,
    Ortalama_Su_Cekme,
    Metreye_Bobin_Sayisi,
    IsFarkliHesap,
    BantHizi,
    IsStalam,
    ITHostName
)
SELECT OzellikID,
       UrunNo,
       Kilowatt,
       ElektrodBoyu,
       Katsayi,
       Ortalama_Su_Cekme,
       Metreye_Bobin_Sayisi,
       IsFarkliHesap,
       BantHizi,
       IsStalam,
       @ITHostName
FROM KURUTMA.Ulusoy.dbo.UrunOzellikleri
ORDER BY UrunNo;

GO
```

Figure 4. Software that introduces the drying features to the system

Thus, it has become sufficient to read the lot numbers of the bobbin yarns into the system. The system automatically sends drying instructions to the dryer in line with the batch numbers read into the system.

Drying Product Features

Filter All

Product No	Product	Kilowatt	Electrode Size	Coefficient	Average Water Content	Bobbin per Square Metre	Different Account?	Speed of Band	Stalam?
218	Ne 24/1-ACRYLIC-RING-251-560 Z TM	40	45	1,7	10	28	☐		☐
218	Ne 24/1-ACRYLIC-RING-251-560 Z TM	60	1	1,2	10	28	☐		☑
219	Ne 20/1-ACRYLIC-RING-251-590 Z TM	60	1	1,2	15	28	☐		☑
219	Ne 20/1-ACRYLIC-RING-251-590 Z TM	40	45	1,7	15	28	☐		☐
984	Ne 16/1-ACRYLIC-RING-251-440 Z TM	40	45	1,7	10	28	☐		☐
984	Ne 16/1-ACRYLIC-RING-251-440 Z TM	60	1	1,2	10	28	☐		☑
1012	C000042-Nm 4.50-VISKON%70+COTTON%30-880 S TM	60	0	1,2	65	21	☐		☑
1018	C000050-Nm 8-POLYESTER-1000 S TM-0.70	30	0	1,2	15	28	☐		☑
1040	C000029-Nm 8-ACRYLIC-1000 S TM-0.70	40	0	1,2	10	28	☐		☑
1054	FETTUCCIA-Nm 2.40-ACRYLIC	40	0	1,2	10	28	☐		☑
1623	Ne 30/1-VISKON-RING-690 Z TM	40	60	1,5	65	21	☐		☐
1623	Ne 30/1-VISKON-RING-690 Z TM	70	1	1,2	65	21	☐		☑
1859	M01380A-Nm 23-FLOŞ%65+NAYLON%35-500 Z TM	55	1	1,2	50	28	☐		☑
1859	M01380A-Nm 23-FLOŞ%65+NAYLON%35-500 Z TM	40	45	1,5	50	28	☐		☐
1895	CORESPUN-Ne 30/2-VISKON%72+ELASTAN%28-330 S	30	1	1,2	50	9	☐		☑

Figure 5. Yarn grades introduced into the system

According to the system, the operator only reads the work order of the dyed yarn with a barcode reader, thanks to the barcode in the work order, the necessary data from the ERP database comes to the PLC and the PLC calculates the average raw weight of a bobbin, thanks to the bobbins placed in the weighing unit, the wet bobbin average is calculated on the PLC, and amount of water is found. The system calculates the belt speed according to the number of coils to be placed on the belt.

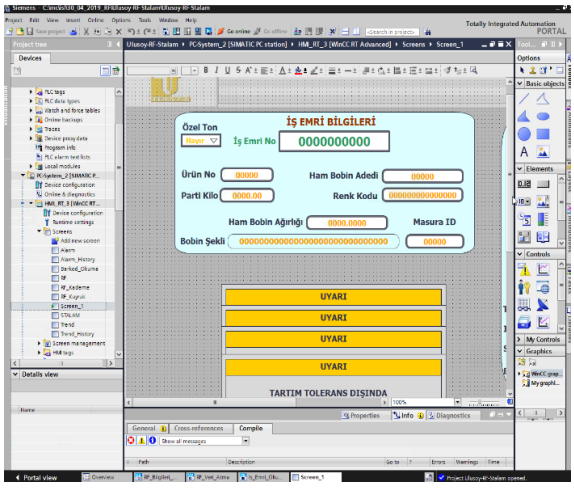

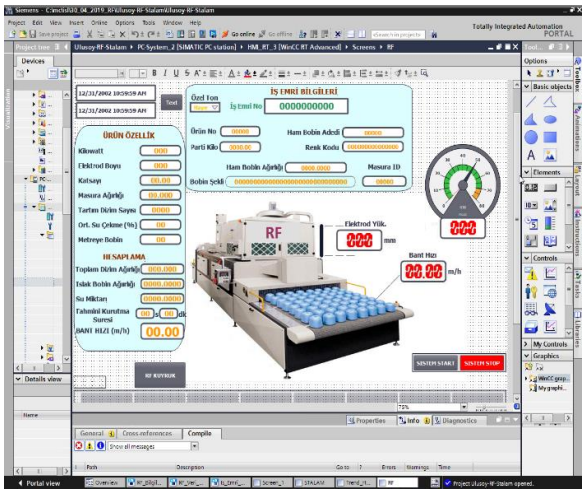

Figure 6. The screen of the developed system available to personnel

Thus, human errors arising from incorrect drying times calculation have been eliminated. Correct drying was ensured in one go, excess energy consumption was prevented and the cost per unit product was reduced.

Results and Discussion

Radiofrequency dryers are drying machines that are widely used in drying open fiber, tops, hank, bobbin and ready-made clothing products, where bulky textile products can be dried uniformly in a short time and in accordance with the desired humidity rate. Therefore, within the scope of this study, radiofrequency (RF) dryers are discussed in order to make drying economical.

Since the calculations are made and controlled by the system, the possibility of error is eliminated. Since the machine speed and drying power settings are automatically taken from the system, problems such as incomplete drying of the yarns or melting and burning of acrylic yarns are eliminated. The smoke produced by the combustion of acrylic yarns is toxic. Therefore, the system has become safer in terms of occupational safety and environment. The workload has been lightened and the system has been made independent from the personnel. Thus, the need for qualified personnel was eliminated. A waste-free and uninterrupted process was ensured. As a result, drying processes that make up 0.3% of the monthly total drying and result in burning were not seen after the field implementation of the project.

Conclusion

Since the calculations are made and controlled by the system, the probability of error has approached 0. Since the machine speed and drying power settings are automatically taken from the system, problems such as incomplete drying of the yarns or melting and burning of acrylic yarns are eliminated. Also the smoke produced by the combustion of acrylic yarns is toxic. Therefore, the system has become more secure in terms of occupational safety. The workload has been lightened. The need for qualified personnel has disappeared. A waste-free and uninterrupted process is provided.

Acknowledgment

Scope of work; Operating with 4 factories in Adana Organized Industrial Zone, Ulusoy Tekstil San. ve Tic. A.Ş., the RF-Stalam dryer, which is used after the bobbin dyeing processes, is discussed. Ulusoy Tekstil, which produces in the carpet, home textile, hand knitting and knitwear markets, dyes a total of 3.5 million kg of yarn on a yearly basis, 2.5 million kg of these yarns are bobbin dyed and are dried in RF-Stalam dryers after the process. This new study has been realized thanks to Ulusoy Tekstil's infrastructure and facilities, and I thank him for his help in the research.

Statement of Conflict of Interest

Authors have declared no conflict of interest.

Author's Contributions

The contribution of the authors is equal.

*This study was presented as a summary paper at the International Conference on Engineering, Natural and Applied Sciences (ICENAS'21) held online on 24-26 November 2021.

References

Akarsalan F. Tekstil mamul özelliklerinin kurutma etkinliğine etkisi. Yüksek Lisans Tezi, Süleyman Demirel Üniversitesi Fen Bilimleri Enstitüsü, 2002; Isparta.

Akyol E. Yün iplik bobinlerinin kuruma davranışının incelenmesi. Yüksek Lisans Tezi, Trakya Üniversitesi, 2011; Edirne.

Akyol U. İplik bobininin kurutulmasının teorik incelenmesi. Doktora Tezi, Trakya Üniversitesi Fen Bilimleri Enstitüsü, 2007; Edirne.

Akyol U., Cihan A., Shaliyes R. Thermophysical parameter estimation of a wool bobbin during convective drying process. Inverse Problems in Science and Engineering, 2010; 18: 227-240.

Güne ban H. Endüstriyel kurutma sistemleri. Türk Tesisat Mühendisleri Derneği Dergisi, 2005; 13:1-11.

Galoppi G., Ferrari L., Ferrara G., Carnevale EA. Experimental investigation on industrial drying process of cotton yarn bobbins: energy consumption and drying time. Energy Procedia 2017; 126: 361–368.

Jhanji Y., Gupta D. Thermo-physiological properties of polyester-cotton plated fabrics n relation to fibre linear density and yarn type. Fashion and Textiles 2015; 2: 16.

Karakoca A. İplik bobini kurutma işleminde sıcaklık alanının sonlu farklar yöntemi ile belirlenmesi. Yüksek Lisans Tezi, Namık Kemal Üniversitesi, 2017; Tekirdağ.

Le CV., Ly NG., Postle R. Heat and moisture transfer in textile assemblies. Part I: Steaming of Wool, Cotton, Nylon and Polyester Fabric. Textile Research Journal 1995; 65(4): 203-212.

Ribeiro J., Ventura JMP. Evaluation of textile bobbins drying processes: Experimental and Modelling Studies Drying Technology 1995; 13(1-2): 239-265.

Toroman S. İplik bobinlerinin kurutma davranışlarının deneysel olarak belirlenmesi. Yüksek Lisans Tezi, Namık Kemal Üniversitesi Fen Bilimleri Enstitüsü, 2011; Tekirdağ.

OKÜ Fen Bilimleri Enstitüsü Dergisi
5(Özel Sayı):196-205, 2022

OKU Journal of The Institute of Science and Technology, 5(Special Issue):196-205, 2022

Osmaniye Korkut Ata Üniversitesi Fen Bilimleri Enstitüsü Dergisi

Osmaniye Korkut Ata University Journal of The Institute of Science and Technology

Performance Analysis of A Single Stage Absorption Cooling System at Different Operating Temperatures

A. Burak YAVUZ[1], Osman KARA[2*], Bülent YANIKTEPE[3]

[1]Osmaniye Korkut Ata University, Kadirli Vocational School of Higher Education, Department of Mechanical, 80010, Osmaniye
[2,3]Osmaniye Korkut Ata University, Faculty of Engineering, Department of Energy Systems Engineering, 80010, Osmaniye

[1]https://orcid.org/0000-0002-8267-3086
[2]https://orcid.org/0000-0003-1501-677X
[3]https://orcid.org/0000-0001-8958-4687
* Corresponding author: osmankara@osmaniye.edu.tr

Research Article

Article History:
Received: 17.12.2021
Accepted:03.02.2022
Published online: 23.02.2022

Keywords:
Water-lithium bromide solution
Absorption refrigeration system
Coefficient of performance

ABSTRACT

Today, rapid developments are experienced in terms of energy consumption and energy efficiency in air conditioning systems. Among these systems, waste heat and renewable energy sources are used in absorption cooling systems. Although the initial investment cost of this system is high, the operating cost is low due to the use of waste heat. In this study, the effect of generator, condenser, absorber and evaporator temperatures on system performance (COP) in absorption cooling systems operating with single-stage $LiBr-H_2O$ fluid pair was investigated. The temperature effect was investigated using energy balances with the help of thermodynamic equations. It was found from the results that the system performance (COP) increased with increasing the generator temperature, and the system performance (COP) decreased with increasing the condenser and absorber temperatures. In addition, it was determined that the $LiBr-H_2O$ solution temperature and concentration changed in the system examined at different generator, condenser, absorber and evaporator temperatures, and crystallization occurred accordingly in some parameters.

Tek Kademeli Absorbsiyonlu Soğutma Sisteminin Farklı Çalışma Sıcaklıklarındaki Performans Analizi

Araştırma Makalesi

Makale Tarihçesi:
Geliş tarihi: 17.12.2021
Kabul tarihi: 03.02.2022
Online yayınlanma: 23.02.2022

Anahtar Kelimeler:
Lityum bromür-su çözeltisi
Absorbsiyonlu soğutma sistemi
Performans katsayısı

ÖZET

Günümüzde, İklimlendirme sistemlerinde enerji tüketimi ve enerji verimliliği açısından hızlı gelişmeler yaşanmaktadır. Bu sistemler içerisinde absorpsiyonlu soğutma sistemlerin de atık ısı ve yenilenebilir enerji kaynakları kullanılmaktadır. Bu sistemin ilk yatırım maliyetinin yüksek olmasına rağmen, atık ısı kullanımından dolayı işletme maliyeti düşüktür. Bu çalışmada tek kademeli $LiBr-H_2O$ akışkan çifti ile çalışan absorbsiyonlu soğutma sistemlerinde ısıtıcı, yoğuşturucu, soğurucu ve buharlaştırıcı sıcaklıklarının sistem performansı üzerine etkisi (COP) incelenmiştir. Sıcaklık etkisi termodinamik eşitlikler yardımı ile enerji denklikleri kullanılarak araştırılmıştır. Jenaratör sıcaklığının arttırılması ile sistem performansının (COP) arttığı, yoğuşturucu ve soğurucu sıcaklıklarının arttırılması ile sistem performansının (COP) azaldığı bulunmuştur. Ayrıca farklı jenaratör, yoğuşturucu, soğurucu ve buharlaştırıcı sıcaklıklarında incelenen sistemde $LiBr-H_2O$ eriyik sıcaklığının ve konsantrasyonun değiştiği, buna bağlı olarak bazı parametrelerde kristalizasyonun oluştuğu tespit edilmiştir.

To Cite: Yavuz AB., Kara O.,Yanıktepe B. Performance Analysis of A Single Stage Absorption Cooling System at Different Operating Temperatures. Osmaniye Korkut Ata Üniversitesi Fen Bilimleri Enstitüsü Dergisi 2022; 5(Özel sayı): 196-205.

Introduction

In recent years, with the increasing population and technological developments, the need for energy has also increased. Accordingly, increasing energy consumption has a negative effect on climate change, global warming and the decrease in energy reserves. In many areas, studies are carried out to reduce energy consumption or to use renewable energy sources (Yaniktepe, 2017). In particular, due to the intensive use of cooling systems both in daily life and in industrial facilities and in order to save energy, studies on this area have recently intensified (Özen, 2019). Absorption cooling systems have been developed due to the high electrical energy consumption in vapor compression cooling systems. In absorption cooling systems, energy saving is achieved by using energy sources such as solar energy, geothermal energy and waste heat (Cimşit, 2018). In absorption cooling systems, the electricity consumption demand is very low in the operation of the system with the use of renewable energy sources or the recovery of waste energy. Absorption cooling systems working with a single-stage $LiBr - H_2O$ fluid couple are one of the most widely used absorption cooling systems (Avanessian, 2014).

In the literature review on the subject, Kaynakli and Yamankaradeniz examined single-stage absorption cooling systems working with $LiBr - H_2O$ and $NH_3 - H_2O$ fluid pairs. They stated that under the same temperature conditions, the system using $LiBr - H_2O$ fluid couple is more efficient than the system using $NH_3 - H_2O$ fluid couple, but crystallization formation occurs at high generator temperatures in systems using $LiBr - H_2O$ fluid couple (Kaynakli and Yamankaradeniz, 2003). Liu et al. investigated the use of low-grade waste heat energy in the range of 90-150 ℃ of the absorption refrigeration system operating with $LiBr - H_2O$ fluid couple. They simulated various cooling temperatures and pressures (Liu et al., 2019). Han et al. investigated an absorption cooling system operating with $LiBr - H_2O$ fluid couple, which uses geothermal energy to cool a room where information communication technology devices are located. The temperatures of geothermal energy sources can reach 150 ℃ and above, and the places where information communication technology devices are located need to be cooled at all hours of the day. Therefore, they stated that absorption cooling technologies with geothermal resources can be used in places where cooling is needed (Han et al., 2020).

Erdinç et al. simulated an absorption cooling system working with a $LiBr - H_2O$ fluid couple. The effects of hot water, cooling water and water to be cooled temperatures on system performance were investigated (Erdinç et al., 2020). Alejandro et al. investigated a single-stage LiBr absorption chiller operated with a low heat source temperature. In their study, the authors developed an optimal control technique and significantly improved the system COP (Alejandro et al., 2018).

Kızılkan et al. investigated the thermoeconomic optimization of absorption cooling systems operating with $LiBr - H_2O$ fluid couple. Thermoeconomic optimization study was carried out to determine the optimum operating parameters of the system. It is important to determine the optimum operating parameters of a system. The authors optimized the main equipment of the absorption cooling system such as condenser, evaporator, generator, absorber heat exchangers. They also stated that the system performance should be calculated by considering not only economical but also thermodynamic properties while determining the optimum area. (Kızılkan et al., 2007). Soliman et al. investigated the operation of vehicle air conditioners using exhaust gas with a new generator design. They stated that absorption cooling systems working with $LiBr - H_2O$ fluid couple, using the exhaust gas temperature with the generator design, can operate at low engine speeds (Soliman et al., 2021).

In this study, the effect of generator, condenser, absorber and evaporator temperatures on the system performance (COP) in absorption refrigeration systems operating with a single-stage $LiBr - H_2O$ fluid couple was calculated with thermodynamic equations. In addition, the effects of different generator, condenser, absorber and evaporator temperatures on $LiBr - H_2O$ solution temperature and concentration were investigated, and accordingly, the temperatures at which crystallization occurred were determined.

Materials and Methods

The schematic representation of the absorption cooling system working with a single-stage $LiBr - H_2O$ fluid couple is shown in Figure 1. Cycle points are specified on the system. Considering the schematic representation of the absorption cooling system, the thermal capacities of the elements in the system were calculated using thermodynamic equations.

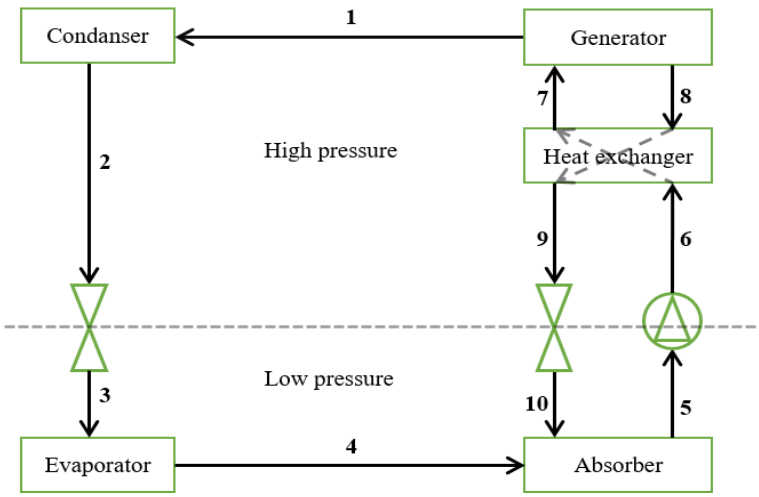

Figure 1. Schematic diagram of single state absorption refrigeration system

The capacities per unit mass of the evaporator and condenser were calculated using thermodynamic equations. Thermodynamic equations are given below.

$$q_{eva} = (h_4 - h_3) \quad (1)$$

$$q_{con} = (h_2 - h_1) \quad (2)$$

While calculating the generator capacity per unit mass, the heat exchanger balance, mass balances, rich solution concentration and lean solution concentration values were used (Kaynaklı and Yamankaradeniz, 2003).

$$m_7 = m_8 + m_1 \quad (3)$$

$$m_7 x_7 = m_8 x_8 \quad (4)$$

$$W_z = \frac{m_8}{m_1} = \frac{x_7}{x_8 - x_7} \quad (5)$$

$$W_f = \frac{m_7}{m_1} = \frac{x_8}{x_8 - x_7} \quad (6)$$

$$W_z(h_8 - h_9) = W_f(h_7 - h_6) \quad (7)$$

$$Q_{gen} = m_1 h_1 + m_8 h_8 - m_7 h_7 \quad (8)$$

$$q_{gen} = h_1 + W_z h_8 - W_f h_7 \quad (9)$$

Mass balances were used when calculating the capacity of the absorber per unit mass. The heat losses of the equipment in the system and the pump power can be neglected because they are of very small value (Avanessian, 2014). Accordingly, the system performance coefficient can be calculated with the following equations (Horuz, 1990).

$$Q_{abs} = m_5 h_5 - m_4 h_4 - m_{10} h_{10} \quad (11)$$

$$q_{abs} = W_f h_5 - h_4 - W_z h_{10} \quad (12)$$

$$COP = \frac{Q_{eva}}{Q_{gen}} \quad (13)$$

Results and Discussion

While determining the performance of the absorption cooling system working with a single-stage $LiBr - H_2O$ fluid couple, thermodynamic balances and mass balances were written with a computer program. The effects of thermodynamic values of evaporator, condenser, absorber, and generator at different temperatures on the cycle and system performance were investigated. Generator temperature 80℃, evaporator temperature 10℃, absorber and condenser temperature 40℃, the high pressure and the low pressure of cycle are taken 7.38 kPa, 1.22 kPa, respectively. Table 1 shows the temperature, pressure, enthalpy and concentration values of the cycle. The heat exchanger efficiency coefficient was accepted as 0.6. Table 2 shows the thermal capacities and system performance of the equipment in the system.

Table 1. Temperature and pressure values of system states

States	T (℃)	P (kPa)	h (kJ/kg)	X (%)
1	80,00	7,38	2643,00	-
2	40,00	7,38	167,53	-
3	10,00	1,22	167,53	-
4	10,00	1,22	2519,20	-
5	40,00	1,22	93,17	54,83
6	40,00	7,38	93,17	54,83
7	66,03	7,38	145,15	54,83
8	80,00	7,38	184,11	57,65
9	52,68	7,38	129,54	57,65
10	52,68	1,22	145,15	57,65

Table 2. Equipment capacities and system performance

Equipment	Thermal Capacities (kJ/kg)
Generator	3284,44
Condenser	2475,47
Evaporator	2351,47
Absorber	3160,44
COP	0,72

As seen in Table 2, the highest thermal capacity belongs to the generator among the equipment in the system. In addition to the temperature and enthalpy values of the generator, the rich and poor solution concentration values of the $LiBr - H_2O$ fluid couple also affect the generator thermal capacity. In Figure 2, concentration values are shown on the $LiBr - H_2O$ crystallization curve.

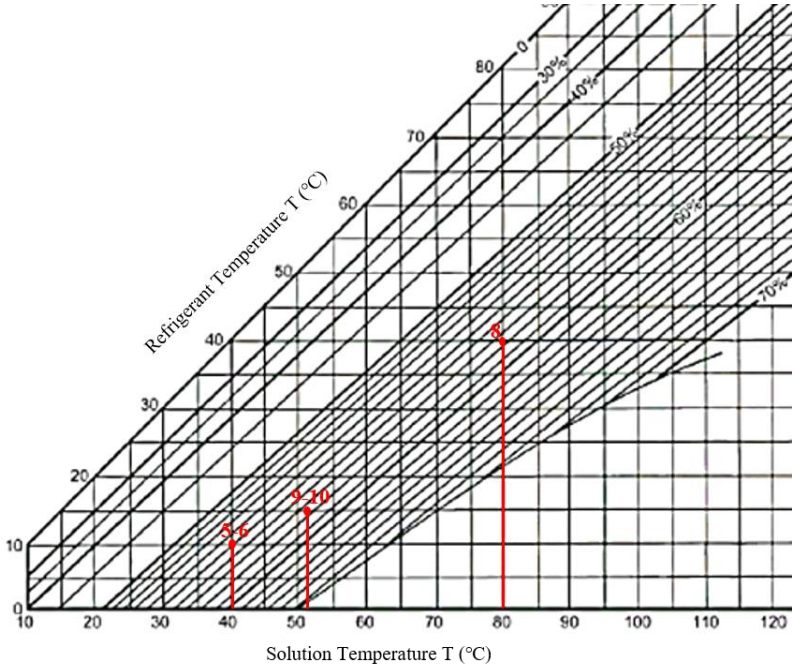

Figure 2. Crystallization curve of $LiBr - H_2O$ (Liao, 2014)

The effect of different generator temperatures on system performance is shown in Figure 3. While examining the effect of generator temperature on system performance, the evaporator temperature was taken as 10°C and the absorber and condenser temperature was taken as 40°C. As seen in Figure 3, the system performance increases as the generator temperature increases. However, if the generator temperature rises above 90°C, crystallization occurs. In the system, it was observed that the poor solution concentration remained constant with the increase in generator temperature. It was observed that the rich concentration increased depending on the generator temperature.

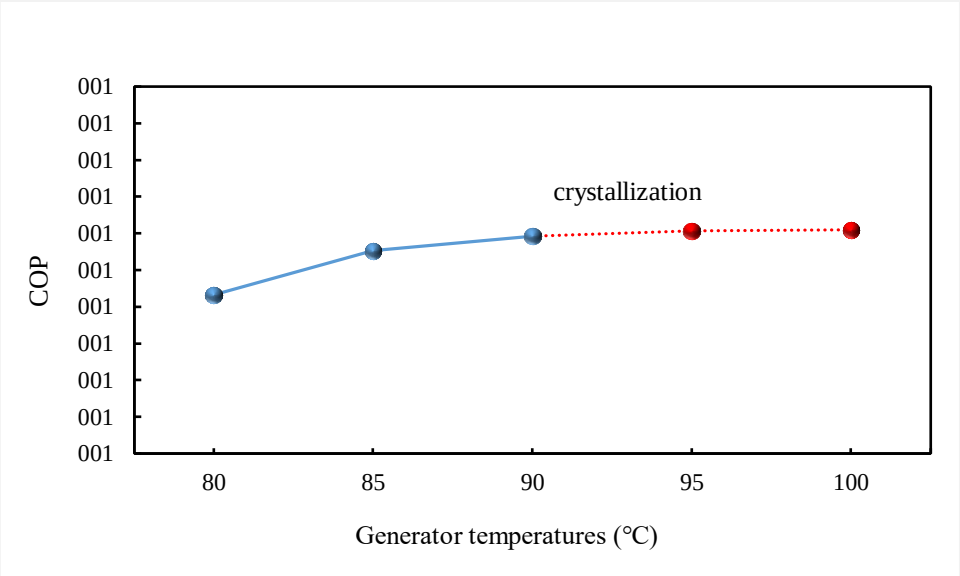

Figure 3. Effect of generator temperature on system performance

Figure 4 shows the effect of condenser and absorber temperature on system performance. While examining the effect of condenser and absorber temperatures on system performance, the evaporator temperature was taken as 10°C and the generator temperature was 80°C. The variation range of the condenser and absorber temperatures was taken as the same value. It was observed that the performance of the system decreased with increasing the condenser and absorber temperature. Although the system performance is high at low temperatures, crystallization occurs when the temperature drops below 35°C. This result shows a close agreement with that reported in the literature (Özen, 2019).

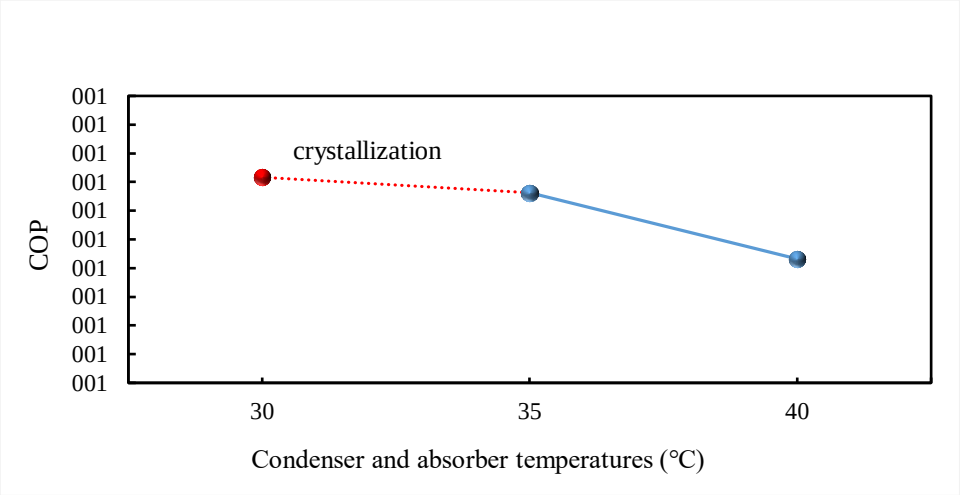

Figure 4. Effect of condenser and absorber temperature on system performance

The effect of evaporator temperature on system performance is shown in Figure 5. While examining the effect of evaporator temperature on system performance, generator temperature was taken as 80°C, absorber and condenser temperature was taken as 40°C. It was observed that the performance of the system increased with increasing the evaporator temperature. No risk of crystallization was encountered at the temperature values studied. The poor solution concentration increases with decreasing evaporator temperature. However, as the evaporator temperature drops below 7°C, the rich solution concentration and the poor solution concentration are very close to each other. In addition, it was observed that there was a sudden decrease in system performance as a result of the evaporator temperature below 7°C. The same trends were achieved by Kaynakli and Yamankaradeniz (Kaynakli and Yamankaradeniz, 2003).

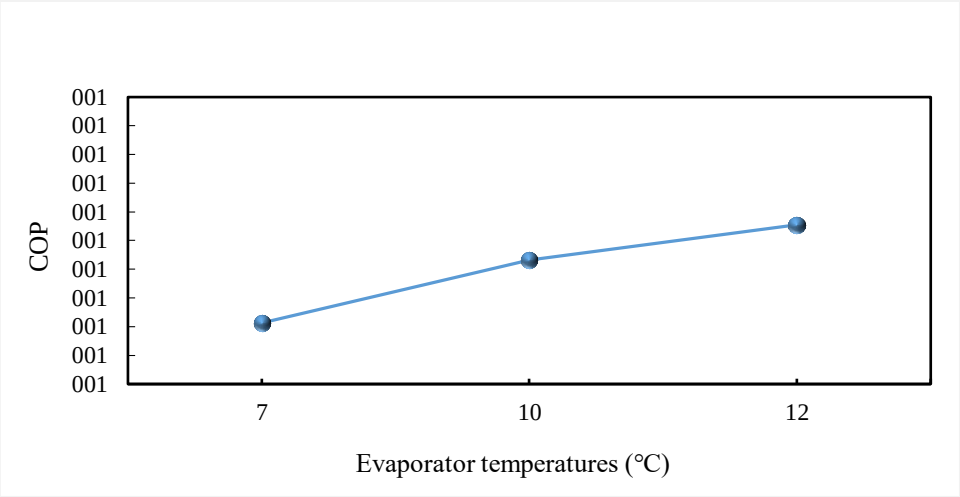

Figure 5. Effect of evaporator temperature on system performance

Conclusion

In this study, the effect of heater, condenser, absorber and evaporator temperatures on system performance (COP) in absorption cooling systems operating with a single-stage $LiBr - H_2O$ fluid couple was investigated. With the thermodynamic equations, it was observed that the system performance (COP) increases with increasing the generator and evaporator temperature in the system, and the system performance (COP) decreases with increasing the condenser and absorber temperatures. One of the biggest problems encountered in absorption cooling systems working with $LiBr - H_2O$ fluid couple is the danger of crystallization. In the examined system, crystallization occurs as a result of high generator temperatures. As the generator temperature increases, the rich concentration and the solution temperature at the generator inlet increase. If the rich solution concentration exceeds 70%, crystallization occurs. Depending on the heat exchanger efficiency coefficient, crystallization occurs when the condenser temperature is lower than 35°C. Therefore, in absorption cooling systems working with $LiBr - H_2O$ fluid couple, system design should be done at optimum temperatures, taking into account the formation of crystallization, regardless of system performance.

Statement of Conflict of Interest

Authors have declared no conflict of interest.

Author's Contributions

The contribution of the authors is equal.

*This study was presented as a summary paper at the International Conference on Engineering, Natural and Applied Sciences (ICENAS'21) held online on 24-26 November 2021.

Symbols

	subscripts
T : Temperature, ℃	abs : Absorber
Q : Termal power, kW	gen : Generator
q : Thermal capacity per unit mass, kJ/kg	con : Condenser
X : Concentration	eva : Evaporator
m : Mass flow rate, kg/s	f : Poor solution
P : Pressure, kPa	z : Rich solution

References

Avanessian T., Ameri M. Energy, exergy and economic analysis of single and double effect LiBr − H_2O absorption chillers. Energy and Buildings 2014; 73: 26-36.

Cimşit C. Thermodynamic analysis of vapour compression-absorption two stage refrigeration cycle. Karaelmas Science and Engineering Journal 2018; 8(1): 218-226.

Erdinç MT., Aktaş AE., Yılmaz A. Simulation of libr-water absorption refrigeration cycle cooling performance at various conditions. Çukurova University Journal of the Faculty of Engineering and Architecture 2020; 35(1): 211-219.

Han B., Li W., Li M., Liu L., Song J. Study on LiBr − H_2O absorption cooling system based on enhanced geothermal system for data center. Energy Reports 2020; 6(9): 1090-1098.

Horuz İ. Comparison of ammonia - water pair and lithium bromide - water pair from absorption coling systems. Master of Science in İnstitute of Science Uludağ Unıversity, page no:177, Bursa, Turkey,1990.

Kaynaklı Ö., Yamankaradeniz R. A comparision between H_2O − LiBr and NH_3 − H_2O solutions in single absorption refrigeration system. Dokuz Eylul University Faculty of Engineering Journal of Science and Engineering 2003; 5(2): 73-87.

Kızılkan Ö., Şencan A., Kalogirou SA. Thermoeconomic optimization of a LiBr absorption refrigeration system. chemical engineering and processing 2007; 46: 1376-1384.

Liao X. The development of an air-cooled absorption chiller concept and its integration in CHP systems. Degree of Doctor in İnstitute of Science Maryland University, page no: 172, College Park, USA, 2014.

Liu Z., Yang S., Deng C. Optimal design and analysis of a cascade LiBr − H_2O absorption refrigeration-transcritical CO_2 process for low-grade waste heat recovery. Energy Conversion and Management 2019; 192: 232-242.

Özen DN., Yağcıoğlu KÇ. Thermodynamic and exergy analysis of an absorption cooling system for LiBr − H_2O fluid couple. Selcuk University Journal of Engineering Science and Technology 2019; 7(1): 135-145.

Sabbagh AA., Gomez JM. Optimal control of single stage LiBr/water absorption chiller. International

Journal of Refrigeration 2018; 92: 1-9.

Soliman AS., Zhu S., Xu L., Dong J., Cheng P. Design of an $LiBr - H_2O$ absorption system using PCMs and powered by automotive exhaust gas. Applied Thermal Engineering 2021; 191: 116881.

Yaniktepe B., Kara O., Ozalp C. Technoeconomic evaluation for an installed small-scale photovoltaic power plant. International Journal of Photoenergy 2017; 2017: 1-7.

OKÜ Fen Bilimleri Enstitüsü Dergisi
5(Özel sayı):206-215, 2022

OKU Journal of The Institute of Science and Technology, 5(Special Issue):206-215, 2022

Osmaniye Korkut Ata Üniversitesi Fen Bilimleri Enstitüsü Dergisi

Osmaniye Korkut Ata University Journal of The Institute of Science and Technology

Electrochemical Production of Transition Metal-Based Electrocatalysts for Hydrogen Production

Eren ERGEN[1], Hüseyin NAZLIGÜL[2*], Başak Doğru MERT[3]

[1]Adana Alparslan Türkeş Science and Technology University, Faculty of Engineering, Department of Electrical and Electronic Engineering, 01250, Adana, Turkey
[2,3]Adana Alparslan Türkeş Science and Technology University, Faculty of Engineering, Department of Energy Systems Engineering, 01250, Adana, Turkey

[1]https://orcid.org/0000-0003-3804-0721
[2]https://orcid.org/0000-0003-3037-8568
[3]https://orcid.org/ 0000-0002-2270-9032
*Corresponding author: hnazligul@atu.edu.tr

Research Article

Article History:
Received: 09.12.2021
Accepted: 16.01.2022
Published online: 23.02.2022

Keywords:
Alkaline electrolysis
Hydrogen production
Renewable energy
Sustainable energy

ABSTRACT

Energy demand increases with increasing population and industrial developments. Unfortunately, non-renewable sources are used to meet a large portion of the demand. As a result of the negative effects, researchers have begun to investigate renewable sources by working in a variety of fields in order to ensure the energy and humanity's long-term sustainability. Renewable energy sources are very important for the future of the world. In this regard, we can claim that the convenient solution is “hydrogen” which is a promising energy carrier. In this study, alkaline electrolysis system was preferred due to the advantage of being easily integrated with renewable energy sources to meet the power requirements of the system. The platinum (Pt) and stainless steel (SS) electrodes were used as anodes. Graphite (G) and ternary transition metals (nickel, copper, cobalt) modified graphite (G/NiCoCu) electrodes were used as cathode. The modified electrodes were prepared by using a galvanostatic method. The various operation voltages were applied that varied from 2.3V to 3V in order to realize water splitting reaction. The amount of produced hydrogen gas was increased with increasing operation voltage. According to the experimental results, at 3V for 15 minutes of electrolysis time, the produced H_2 gas values were 15 mL, 11.13 mL and 13.12 mL for Pt - G (Cell-1), SS - G (Cell-2) and SS - G/ NiCoCu (Cell-3), respectively.

Hidrojen Üretimi için Geçiş Metali İhtiva Eden Elektrokatalizörlerin Elektrokimyasal Üretimi

Araştırma Makalesi

Makale Tarihçesi:
Geliş Tarihi: 09.12.2021
Kabul Tarihi: 16.01.2022
Online Yayınlama: 23.02.2022

Keywords:
Alkali elektroliz
Hidrojen üretimi
Yenilenebilir enerji
Sürdürülebilir enerji

ÖZET

Artan nüfus ve endüstriyel gelişmelerle birlikte enerji talebi de artmaktadır. Ne yazık ki, talebin büyük bir kısmını karşılamak için yenilenemeyen kaynaklar kullanılmaktadır. Olumsuz etkilerin bir sonucu olarak, araştırmacılar enerjinin ve insanlığın uzun vadeli sürdürülebilirliğini sağlamak için çeşitli alanlarda çalışarak yenilenebilir kaynakları araştırmaya başlamışlardır. Yenilenebilir enerji kaynakları dünyanın geleceği için çok önemlidir. Bu bağlamda, uygun çözümün gelecek vadeden bir enerji taşıyıcısı olan “hidrojen” olduğunu söyleyebiliriz. Bu çalışmada, sistemin güç ihtiyacını karşılamak için yenilenebilir enerji kaynakları ile kolayca entegre edilebilme avantajından dolayı alkali elektroliz sistemi tercih edilmiştir. Anot olarak platin (Pt) ve paslanmaz çelik (SS) elektrotlar kullanılmıştır. Katot olarak grafit (G) ve üçlü

(nikel, bakır, kobalt) geçiş metalleriyle modifiye edilmiş grafit (G/NiCoCu) elektrotlar kullanılmıştır. Modifiye elektrotlar, galvanostatik yöntem kullanılarak hazırlanmıştır. Suyun ayrışma reaksiyonunu gerçekleştirmek için 2,3V ile 3V arasında değişen çeşitli çalışma potansiyelleri uygulanmıştır. Artan uygulama potansiyeli ile üretilen hidrojen gazı ($H_{2(g)}$) miktarı artmıştır. Deneysel sonuçlara göre, 3V'de 15 dakikalık elektroliz süresi boyunca üretilen $H_{2(g)}$ miktarları, Pt - G (Hücre-1), SS - G (Hücre-2) ve SS - G/ NiCoCu (Hücre-3) için sırasıyla 15 mL; 11,13 mL ve 13,12 mL'dir.

To Cite: Ergen E., Nazlıgül H., Mert BD. Electrochemical Production of Transition Metal-Based Electrocatalysts for Hydrogen Production. Osmaniye Korkut Ata Üniversitesi Fen Bilimleri Enstitüsü Dergisi 2022; 5(Özel sayı): 206-215.

Introduction

Energy is an important element needed in people's daily lives and is also the infrastructure of technology. Unfortunately, this energy that we use to meet our needs and to develop technology has a certain limit. The increase in population rates, the increase in settlements and the increase in the demand for energy accelerate fossil fuel consumption. Humanity has used oil, coal, wood, fossil fuels, in short, non-renewable energy resources to meet the increasing demand for the centuries. The harmful products resulting from the consumption of fossil fuels, unfortunately, pollute our world (Barbir et al., 1990; Shafiee and Topal, 2009; Andres et al., 2011; Hanif et al., 2019; Martins et al., 2019; Waheed et al., 2019). In this context, we need renewable and sustainable energy in order to meet the needs and reduce the harmful effects on the environment. Thus, we will be able to reduce the level of risk and the damage we cause to the environment. Our country's physical-geographical location is very suitable for renewable energy production, and we are in a very efficient position, especially in terms of geothermal, solar and wind energy (Şenel and Koç, 2015; Koç et al., 2018; Çetin et al., 2019; Bekar, 2020; Güllü and Kartal, 2021). We should give much effort in this field, and we should contribute to the development of Turkey. Hydrogen should be convenient option in the energy arena of the future. Because the combustion of hydrogen produces merely water. It provides zero carbon emissions and has a high energy density, making it the most promising form of energy for the future. Although there are many methods for the production of hydrogen gas, alkaline water electrolysis method comes to the fore (Suermann et al., 2016). Because almost 99.9% pure hydrogen can be produced by this method (de Fátima Palhares et al., 2018). For the establishment and dissemination of industrial-scale systems, the overvoltage of the electrodes should be low, and the investment costs should be appropriate. Electrode selection is extremely important in the water decomposition process. While designing the electrodes, price-performance research was conducted for oxygen and hydrogen production efficiency. In the literature, Platinum (Pt) based materials are known as the most efficient electrocatalysts for hydrogen production due to their low overvoltage and high current density. However, Pt material is not in a cost-effective position. Therefore, we should produce electrocatalysts which are used as Pt alternatives for alkaline electrolysis. An electrode material that can act as an alternative to Pt electrodes and function effectively for hydrogen production has been extensively investigated. In this context, we chose to use SS on the anode side. Due to the affordability, chemical stability and catalytic properties of SS, it contributes to reducing the overpotential of hydrogen production compared to other

transition metals (Kim et al., 2017). On the cathode side, we preferred graphite (G). With its electrical conductivity, high corrosion resistance and low cost, it meets exactly the criteria we are looking for. Instead of using G lonely, based on the superior performance of dual coatings combining Ni-Co and Ni-Cu in the literature, triple coating on graphite was preferred and Ni-Co-Cu was used. Ni is one of the promising non-new metals with the highest current exchange density to the hydrogen evolution reaction, and recently, Ni-based alloy catalysts have been investigated to obtain high catalytic activity by electrolysis in alkaline water (Greeley et al., 2006; Aydın, 2021; Farsak and Aydın, 2021). Cu is the most suitable for alloying with Ni due to its low cost, high corrosion resistance and environmental friendliness (Ahn et al., 2013; Kumar and Shetti, 2018).

The main purpose of this study is to produce hydrogen gas by alkaline electrolysis process with energy obtained from a renewable energy source. At the same time, different types of anode materials were studied to improve the study. Two different anode materials (i.e., Pt and SS) were used for the electrolysis cell. Graphite and ternary metal deposited (i.e., nickel, copper, cobalt) graphite were used as the cathode. The main objectives of this study are explained as follows:

- To produce hydrogen gas by alkaline electrolysis process through different anodes and cathodes,
- To discover the most suitable material for electrolysis by comparing the anodes and cathodes.

Material and Method

In this study, graphite (G) electrode was preferred as cathode in our system due to its low cost. Copper wire was passed to one end of a graphite rod to provide conductivity. The electrode is 5 cm in length and embedded in polyester. The surface area of the prepared graphite electrode, which was not covered with resin in contact with the solution, is 0.36 cm^2. In Cell 1, a platinum (Pt) sheet with a surface area of 2 cm^2 was used as the anode electrode and graphite was used as the cathode. Stainless steel (SS) with a surface area of 0.78cm^2 was used as anode electrode in Cells 2 and 3, graphite and modified graphite were used as cathodes, respectively. To ensure conductivity, a 5 cm long copper wire was passed to the end of the Pt plate and the SS electrode. The SS electrode is embedded in the polyester so that only the surface area remains free. Except for the Pt electrode, the electrode surface was abraded up to 1200 degrees with sandpaper before electrodeposition processes. Then, each electrode was washed with acetone/ethanol mixture and distilled water. Two electrode techniques were used, several anodes were examined. In this work, ternary coating was favored on graphite and Ni-Co-Cu was employed, based on the outstanding performance of binary coatings combining Ni-Co and Ni-Cu in the literature (Solmaz et al., 2008; Solmaz et al., 2009; Demirdelen et al., 2020). Considering the literature, the coating's Co and Cu mole ratios should be kept low in comparison to the Ni mole ratio (Mert and Kardaş, 2011; Sun et al., 2021). The electrodeposition of nickel, cobalt and copper was performed by galvanostatically using Iviumstat Electrochemical Interface with a three-electrode configuration. In this system graphite was used as working electrode, nickel as counter electrode, and

an Ag/AgCl (3 M KCl) electrode was used as the reference electrode. A current density was 50 mA cm^{-2} and a coating thickness was 10 μm. Chemical composition of coating baths were; nickel bath 30% $NiSO_4.7H_2O$, 1% $NiCl_2.6H_2O$, and 1.25% H_3BO_3; cobalt bath 30% $CoSO_4.7H_2O$, 1% $CoCl_2.6H_2O$, 1.25% H_3BO_3; copper bath 26.67% $CuSO_4.5H_2O$, 1.25% H_3BO_3. NiCoCu ternary deposition was prepared by mixing in appropriate volumes to contain [Ni^{2+}], [Co^{2+}], [Cu^{2+}] ions at different concentrations in the deposition bath which was 50 mL. [Ni^{2+}]: [Co^{2+}]: [Cu^{2+}] mole ratio is 99: 0.5: 0.5.

Electrolysis was carried out using a direct current source and the amount of hydrogen produced both experimentally and theoretically at constant voltage. The theoretical calculations obtained by current-voltage curves with the help of Faraday Laws. A multimeter was used to determine the current flowing through the system. The cell components are given in Table 1.

Table 1. Working electrodes used in the electrolysis system in three different cells

Cell	Anode	Cathode
Cell-1	Pt	G
Cell-2	SS	G
Cell-3	SS	G/NiCoCu

The minimum potential required for electrode reactions to start is called the decomposition voltage. The theoretical decomposition voltage (E_d) can be found by calculating the electrode potentials corresponding to the equilibrium state of the anode and cathode with the Nernst Equation in Eq. (1) (Yazici et al., 1995);

$$E_d = E_{anode} - E_{cathode} \quad (1)$$

Theoretically, at 25 °C, the potential required for water to decompose is 1.23 V, where the evolution of hydrogen gas begins (Yörük et al., 2019). However, a higher potential must be applied because of the over voltages caused by the solution and electrode metal and the internal resistance of the voltage source and the cables used during the experiment. During the electrolysis of alkaline water, oxygen is released at the anode as in Eq. (2) and hydrogen gas is released at the cathode as in Eq. (3) (Kardaş et al., 2003).

Anode : $4OH^- \rightarrow O_2 + 2H_2O + 4e^-$ $E_A=0.401+0.0592pOH$ (PO_2=1.0 atm) (2)

Cathode : $4\ H_2O + 4e^- \rightarrow 4OH^- + 2H_2$ $E_C=-0.828+0.0592pOH$ (PH_2=1.0 atm) (3)

$2H_2O \rightarrow O_2 + 2H_2$ $E=E_A-E_C=1.229V$ (4)

In order to determine the decomposition voltages of the cells, Pt and SS electrodes on the anode sides; G and modified G electrodes on the cathode side were used in 1 M KOH solution. By using a direct current source, voltages between 1.3 V and 3 V were applied to the electrodes and applied to the system at 0.1 V intervals, and current potential curves were obtained by determining the current values

passing through the system. Since the theoretical split voltage is about 1.3 V, the studies started with 1.3 V and continued. After the decomposition voltage was determined as 1.8 V for Cell-1 and 1.9 V for Cell-2-3, hydrogen production volumes were observed at different voltage values. The amount of hydrogen production was investigated by placing the cylinder upside down on the cathode electrode where the hydrogen gas generation was located. The volumes of hydrogen produced were measured from 2.3 V to 3 V by increasing 0.1 V. The volume amounts displayed in the cylinder were noted at 3-minute intervals at each potential. Each voltage was applied to the system for 15 minutes. Considering that water vapor was collected in the cylinder in the same environment, the volume correction was made as follows (Kardaş et al., 2003);

$$P_{H_2} = P_T - P_{H_2O} \quad (5)$$

When the vapor pressure of water (P_{H_2O}) under these conditions is 23,756 mm Hg and the total atmospheric pressure (P_T) is 756 mm Hg, the pressure of hydrogen (P_{H_2}) gas under these conditions is determined as 732,244 mm Hg. Hydrogen volume (V_{H_2}) is;

$$V_{H_2} = \frac{732,244}{756} \text{ x } V_{measuring} \quad (6)$$

determined by the relation. The $V_{measuring}$ here is the total volume of gas collected experimentally in the cylinder.

Results and Discussion

Theoretically, the potential required for water decomposition at 25°C is 1.229 V. When the O_2 overvoltage (0.47 V) on Pt as the anode is added to this value, a potential of at least 1.70 V must be applied to the system to initiate the hydrogen gas evolution. The hydrogen gas was measured for the Cell-1 in 1 M KOH. Experimental decomposition voltage was calculated for each electrode in order to compare the volumes and the effectiveness of the deposition with each other. The decomposition voltage (E_d) for the Cell-1 (Pt anode-G cathode) electrode was 1.8 V and the overvoltage E_{over} was 0.5V in Eq. (7).

$$E_{over} = E_d - 1.3 = 1.7 - 1.3 \quad (7)$$
$$E_{over} = 0.4 \text{ V}$$

Hydrogen production volumes of Cell-1 at different voltage values are given in Table 2. The volumes of hydrogen produced were measured from 2.3 V to 3 V by increasing 0.1 V and the current values passing through the system at each potential are given. After 15 minutes, it was found to produce 15 mL of hydrogen with a Pt electrode.

Table 2. Total charge (Q) during 15 minutes electrolysis, theoretical (Vt) and experimental (Ve) hydrogen volumes at the end of 15 minutes for various voltages (E) for G electrode in case of Cell-1

E/V	Q (Coulomb)	Vt (mL)	Ve (mL)
2.3	39.0	4.54	3.50
2.4	50.0	5.79	4.75
2.5	63.0	7.29	6.25
2.6	73.5	8.54	7.50
2.7	86.5	10.04	9.00
2.8	99.5	11.54	10.50
2.9	129.5	15.04	14.00
3.0	138.0	16.04	15.00

The hydrogen gas was measured for the Cell-2 in 1 M KOH and given in Equation (11). The decomposition voltage was calculated for each electrode in order to compare the volumes and the effectiveness of the deposition with each other. The decomposition voltage (E_d) for the Cell-2 (SS anode-G cathode) electrode was 1.9 V and the overvoltage E_{over} was 0.6 V in Eq. (8).

$$E_{over} = E_d - 1.3 = 1.9 - 1.3 \quad (8)$$

$$E_{over} = 0.6 \text{ V}$$

Hydrogen production volumes of Cell-2 at different voltage values are given in Table 3. The volumes of hydrogen produced were measured from 2.3 V to 3 V by increasing 0.1 V and the current values passing through the system at each potential are given. After 15 minutes, it was found to produce 11.13 mL of hydrogen with an SS electrode.

Table 3. Total charge (Q) during 15 minutes electrolysis, theoretical (V_t) and experimental (V_e) hydrogen volumes at the end of 15 minutes for various voltages (E) for G electrode in case of Cell-2

E/V	Q (Coulomb)	Vt (mL)	Ve (mL)
2.3	23.88	2.77	2.42
2.4	33.48	3.88	3.58
2.5	56.52	6.56	6.30
2.6	65.16	7.56	7.26
2.7	74.52	8.65	8.13
2.8	82.80	9.61	9.20
2.9	88.36	10.26	10.16
3.0	97.74	11.34	11.13

The hydrogen gas was measured for the Cell-3 in 1 M KOH. Experimental dissociation voltage was calculated for each electrode in order to compare the volumes and the effectiveness of the coatings with each other. The decomposition voltage (E_d) for the Cell-3 (SS anode-G/NiCoCu cathode) electrode was 1.9 V and the overvoltage E_{over} was 0.6 V in Eq. (9).

$$E_{over} = E_d - 1.3 = 1.9 - 1.3 \quad (9)$$

$$E_{over} = 0.6 \text{ V}$$

Hydrogen production volumes of Cell-3 at different voltage values are given in Table 4. The volumes of hydrogen produced were measured from 2.3 V to 3 V by increasing 0.1 V and the current values passing through the system at each potential are given. After 15 minutes, it was found to produce 13.12 mL of hydrogen with an SS electrode.

Table 4. Total charge (Q) during 15 minutes electrolysis, theoretical (V_t) and experimental (V_e) hydrogen volumes at the end of 15 minutes for various voltages (E) for SS electrode in case of Cell-3

E/V	Q (Coulomb)	Vt (mL)	Ve (mL)
2.3	52.83	6.14	5.94
2.4	67.68	7.86	7.60
2.5	73.98	8.60	8.30
2.6	84.42	9.80	9.48
2.7	91.26	10.60	10.25
2.8	99.63	11.56	11.20
2.9	107.73	12.50	12.10
3.0	116.82	13.56	13.12

Hydrogen production of each cell was observed with a graduated cylinder filled with 1 M KOH electrolyte. The hydrogen performance of Pt-G (Cell-1), SS-G (Cell-2), and SS-G/NiCoCu (Cell-3) is compared in Figure 1. According to the study of Koca et al. (2019), in the alkaline electrolyte, Platinum (Pt) was utilized as the anode, CF, CF / Ni, CF / NiGa were utilized as the cathode electrodes, and 3V was operated in the cell for 30 minutes. The highest hydrogen production efficiency was detected for the Pt anode - CF/NiGa cathode which produced almost 0.92 mL hydrogen gas per minute. For the comparison of this study, the operation time was chosen as 15 minutes by the way the produced gas volume almost 13.75 mL. According to the study of Kaya et al. (Kaya et al., 2017), for steel and graphite electrodes at 4 V for concentration 5 wt. %, 10 wt. % and 15 wt. % KOH, 0.58 mL/min, 0.95 mL/min, 1.18 mL/min, hydrogen gas was accumulated, respectively. In this study, 15 mL, 11.13 mL and 13.12 hydrogen gas were produced, respectively, for 15 minutes by applying a voltage of 3 V. Although Cell-1 has the highest hydrogen production values at higher potentials (2.9 V and 3 V), for the lower potentials (from 2.3 V to 2.8 V), the Cell-3 was more favorable. Consequently, in the range of 2.3 V and 2.8 V, modified cathode (G/NiCoCu) enlarged catalytic activity.

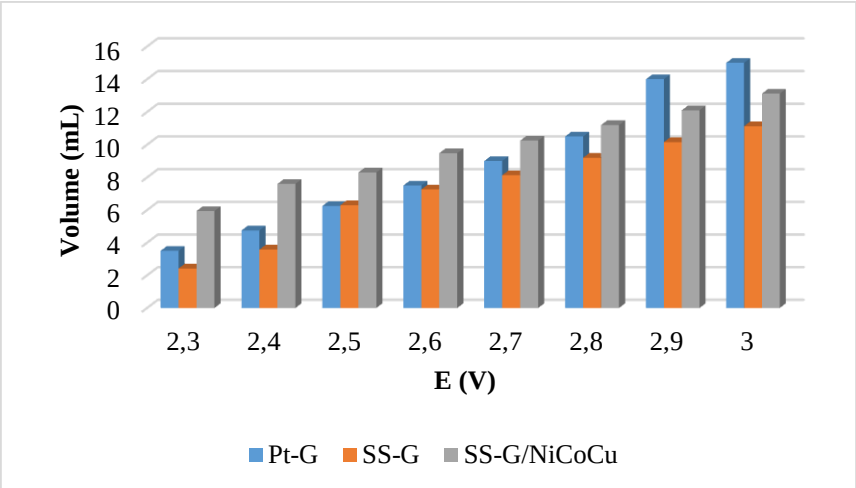

Figure 1. Comparison of hydrogen amounts produced by Pt-G, SS-G, and SS-G/NiCoCu electrodes after 15 minutes at 2.3 V to 3 V

Conclusion

We examined the several electrodes for producing hydrogen, which is trend topic and has recently attracted the concern of academics interested in renewable and sustainable energy. Results showed that, produced hydrogen gas values were 15 mL; 11.13 mL and 13.12 mL at 3V for 15 minutes electrolysis period, by using Pt-G (Cell-1); SS-G (Cell-2) and SS-G/NiCoCu (Cell-3), respectively. Although Cell-1 exhibited better efficiency than other electrodes at higher potentials, due to the high cost of Pt anode, SS anode was preferable. We recommend SS anode for hydrogen production, both in terms of cost and corrosion resistance. And we suggest the SS-G/NiCoCu electrode due to high hydrogen evolution performance, especially at lower potentials. In comparison to all cells, Cell-3 was observed to be the most convenient setup for alkaline electrolysis.

Acknowledgment

The authors are thankful to Adana Alparslan Türkeş Science and Technology University Research fund for financial support (Project Number: 21303005).

Statement of Conflict Interest

The authors have no conflicts of interest to declare.

Author's Contributions

The experimental studies were done by Eren ERGEN, discussion and writing of the manuscript was achieved by all author.

*This study was presented as a summary paper at the International Conference on Engineering, Natural and Applied Sciences (ICENAS'21) held online on 24-26 November 2021.

References

Ahn SH., Park HY., Choi I., Yoo SJ., Hwang SJ., Kim HJ., Jang JH. Electrochemically fabricated NiCu alloy catalysts for hydrogen production in alkaline water electrolysis. International Journal of Hydrogen Energy 2013; 38(31): 13493-13501.

Andres RJ., Gregg JS., Losey L., Marland G., Boden TA. Monthly, global emissions of carbon dioxide from fossil fuel consumption. Tellus B: Chemical and Physical Meteorology 2011; 63(3): 309-327.

Aydın Ö. A novel cathode catalyst for hydrogen evolution reaction: Ni–NiO@ Ru. Materials Chemistry and Physics 2021; 124850.

Barbir F., Veziroğlu TN., Plass Jr HJ. Environmental damage due to fossil fuels use. International Journal of Hydrogen Energy 1990; 15(10): 739-749.

Bekar N. Yenilenebilir enerji kaynakları açısından Türkiye'nin enerji jeopolitiği. Türkiye Siyaset Bilimi Dergisi 2020; 3(1): 37-54.

Çetin S., Turan E., Bayrakdar E. Türkiye'nin güneş enerjisi politikaları. Third Sector Social Economic Review 2019; 54(2): 949-968.

Demirdelen T., Ekinci F., Mert BD., Karasu İ., Tümay M. Green touch for hydrogen production via alkaline electrolysis: The semi-flexible PV panels mounted wind turbine design, production and performance analysis. International Journal of Hydrogen Energy 2020; 45(18): 10680-10695.

de Fátima Palhares DDA., Vieira LGM., Damasceno JJR. Hydrogen production by a low-cost electrolyzer developed through the combination of alkaline water electrolysis and solar energy use. International Journal of Hydrogen Energy 2018; 43(9): 4265-4275.

Farsak M., Aydın Ö. The snowflake-like structured NiO-Cu2O@ Fe/Ru catalyst for hydrogen fuel production. International Journal of Energy Research 2021; 45(5): 7561-7571.

Greeley J., Jaramillo TF., Bonde J., Chorkendorff IB., Nørskov JK. Computational high-throughput screening of electrocatalytic materials for hydrogen evolution. Nature Materials 2006; 5(11): 909-913.

Güllü M., Kartal Z. Türkiye'nin yenilenebilir enerji kaynaklarının 2030 yılına kadar tahmini. 19 Mayıs Sosyal Bilimler Dergisi 2021; 2(2): 288-313.

Hanif I., Raza SMF., Gago-de-Santos P., Abbas Q. Fossil fuels, foreign direct investment, and economic growth have triggered CO_2 emissions in emerging Asian economies: some empirical evidence. Energy 2019; 171: 493-501.

Kardaş G., Yazici B., Erbil M. Effect of some primary alcohols on hydrogen yield on platinum cathode in chloride solution. International Journal of Hydrogen Energy 2003; 28(11): 1213-1218.

Kaya MF., Demir N., Albawabiji SM., Taş M. Investigation of alkaline water electrolysis performance for different cost effective electrodes under magnetic field. International Journal of Hydrogen Energy 2017; 42: 17583-1759.

Kim SM., Jin SH., Lee YJ., Lee MH. Design of nickel electrodes by electrodeposition: effect of internal stress on hydrogen evolution reaction in alkaline solutions. Electrochimica Acta 2017; 252: 67-75.

Koca B., Çelik G., Kardaş G., Yazici B. NiGa modified carbon-felt cathode for hydrogen production. International Journal of Hydrogen Energy 2019; 44(27): 14157-14163.

Koç A., Yağlı H., Koç Y., Uğurlu İ. Dünyada ve Türkiye'de enerji görünümünün genel değerlendirilmesi. Mühendis ve Makine 2018; 59(692): 86-114.

Kumar M., Shetti NP. Magnetron sputter deposited NiCu alloy catalysts for production of hydrogen through electrolysis in alkaline water. Materials Science for Energy Technologies 2018; 1(2): 160-165.

Martins F., Felgueiras C., Smitkova M., Caetano N. Analysis of fossil fuel energy consumption and

environmental impacts in European countries. Energies 2019; 12(6): 964.

Mert ME., Kardaş G. Electrocatalytic behaviour of NiBi coatings for hydrogen evolution reaction in alkaline medium. Journal of Alloys and Compounds 2011; 509(37): 9190-9194.

Shafiee S., Topal E. When will fossil fuel reserves be diminished?. Energy Policy 2009; 37(1): 181-189.

Solmaz R., Döner A., Kardaş G. Electrochemical deposition and characterization of NiCu coatings as cathode materials for hydrogen evolution reaction. Electrochemistry Communications 2008; 10(12): 1909-1911.

Solmaz R., Döner A., Şahin İ., Yüce AO., Kardaş G., Yazıcı B., Erbil M. The stability of NiCoZn electrocatalyst for hydrogen evolution activity in alkaline solution during long-term electrolysis. International Journal of Hydrogen Energy 2009; 34(19): 7910-7918.

Suermann M., Schmidt TJ., Büchi FN. Cell performance determining parameters in high pressure water electrolysis. Electrochimica Acta 2016; 211: 989-997.

Sun C., Xu Q., Zou X., Cheng H., Lu XA. A new method to determine AgCl (1% mol)/Ag electrode potential versus the standard chloride electrode potential in a LiCl-KCl eutectic. Electrochemistry Communications 2021; 130: 107111.

Şenel MC., Koç E. Dünyada ve Türkiye'de rüzgâr enerjisi durumu-genel değerlendirme. Mühendis ve Makine 2015; 56(663): 46-56.

Waheed R., Sarwar S., Wei C. The survey of economic growth, energy consumption and carbon emission. Energy Reports 2019; 5: 1103-1115.

Yazici B., Tatli G., Galip H., Erbil M. Investigation of suitable cathodes for the production of hydrogen gas by electrolysis. International Journal of Hydrogen Energy 1995; 20(12): 957-965.

Yolcan OO., Köse R. Türkiye'nin güneş enerjisi durumu ve güneş enerjisi santrali kurulumunda önemli parametreler. Kırklareli Üniversitesi Mühendislik ve Fen Bilimleri Dergisi 2020; 6(2): 196-215.

Yörük Ö., Zıraman DU., Doğan ÖM., Uysal BZ. Çan linyitinden elektroliz yöntemi ile hidrojen üretiminde çeşitli parametrelerin etkisinin incelenmesi. Gazi Üniversitesi Fen Bilimleri Dergisi Part C: Tasarım ve Teknoloji 2019; 7(4): 957-968.

OKÜ Fen Bilimleri Enstitüsü Dergisi
5(Özel Sayı):216-226, 2022

OKU Journal of The Institute of Science and Technology, 5(Special Issue):216-226, 2022

Osmaniye Korkut Ata Üniversitesi Fen Bilimleri Enstitüsü Dergisi

Osmaniye Korkut Ata University Journal of The Institute of Science and Technology

Farklı Etilen Oranlarına Sahip EPDM Kauçuklarından Kükürt Vulkanizasyonuyla Üretilen Kauçukların Reolojik ve Mekanik Özelliklerinin İncelenmesi

Hakan ULUSOY[1], Feridun DEMİR[2*]

[1,2]Osmaniye Korkut Ata Üniversitesi Fen Bilimleri Enstitüsü Kimya Mühendisliği Anabilim Dalı, Osmaniye

[1]https://orcid.org/0000-0002-0558-9462
[2]https://orcid.org/0000-0001-6372-6958
*Sorumlu yazar: feridundemir@osmaniye.edu.tr

Araştırma Makalesi

Makale Tarihçesi:
Geliş tarihi: 15.12.2021
Kabul tarihi: 12.02.2022
Online Yayınlanma: 23.02.2022

Anahtar Kelimeler:
EPDM Kauçuk
Etilen oranı
Mekanik analiz
Sertlik değişimi
Reolojik davranış

ÖZET

Bu çalışmada, etilenin kauçukların reolojik ve mekanik özellikleri üzerindeki etkisi araştırılmıştır. Bu amaçla farklı oranlarda etilen içeren EPDM kauçukların karıştırılması ve kükürtle kürlenmesi ile kauçuklar üretilmiştir. Formülasyonlar, tüm numunelerin aynı sertliğe sahip olması için modifiye edilmiştir. Reometre analizi sonuçları, Suprene 512 F numunesinin maksimum kür torkunun (M/dN.m) diğer iki numuneden daha yüksek olduğunu, ancak kür süresinin %90'ının diğer iki numuneden daha geç olduğunu ortaya koymuştur. Çekme-uzama analizi, en yüksek etilen içeriğine sahip Suprene 512 F kauçuğunun Ts/MPa ve Eb/% oranlarının daha yüksek olduğunu ortaya koymuştur. Sertlik analizi, kauçuktaki etilen miktarındaki artışın, çekme kopma mukavemetindeki artışla doğru orantılı olduğunu ortaya koymuştur. Ayrıca kauçuktaki etilen oranının vulkanizasyon sonrası sertlik değişimini lineer olarak etkilediği görülmüştür. Kauçuk karışım formülasyonları yapılırken karışımdaki etilen oranının vulkanizasyon sonucu oluşan ürünün sertliğinde meydana gelen değişimi doğrudan etkileyeceği göz önünde bulundurulmalıdır.

Investigation of Rheological and Mechanical Properties of Rubbers Produced by Sulfur Vulcanization from EPDM Rubbers with Different Ethylene Ratios

Research Article

Article History:
Received: 15.12.2021
Accepted: 12.02.2022
Published online: 23.02.2022

Keywords:
EPDM Rubber
Ethylene ratio
Mechanical analysis
Hardness change
Rheological behavior

ABSTRACT

In this study, the effect of ethylene on the rheological and mechanical properties of rubbers was investigated. For this purpose, rubbers were produced by mixing EPDM rubbers containing ethylene in different ratios and curing with sulfur. The formulations were modified so that all samples had the same hardness. The results of the rheometer analysis revealed that the maximum cure torque (M/dN.m) of the Suprene 512 F sample was higher than the other two samples; however, 90% of the curing time was later than the other two samples. Tensile-elongation analysis revealed that the Ts/MPa and Eb/% ratios of Suprene 512 F rubber with the highest ethylene content were higher. The hardness analysis revealed that the increase in the amount of ethylene in the rubber was directly proportional to the increase in the tensile breaking strength. In addition, it was observed that the ethylene ratio in rubber linearly affected the hardness change after vulcanization. While making rubber blend formulations, it should be considered that the ethylene ratio in the mixture will directly affect the change in the hardness of the product formed as a result of vulcanization.

To Cite: Ulusoy H., Demir F. Investigation of Rheological and Mechanical Properties of Rubbers Produced by Sulfur Vulcanization from EPDM Rubbers with Different Ethylene Ratios. Osmaniye Korkut Ata Üniversitesi Fen Bilimleri Enstitüsü Dergisi 2022; 5(Özel sayı):216-226.

Introduction

Ethylene Propylene Diene Rubber (EPDM), a very important synthetic rubber in the industrial field, has very good heat, UV light, oxygen, and ozone resistance and has a saturated polymer backbone (Spanos et al. 2014). Specifically, EPDM rubber is used in automotive sealing gaskets (window, door, and body), o-rings, waterproof gaskets for joining tunnel segments, roofing gaskets for building constructions, etc; therefore, it has become one of the most widely used sealing elements in industry (Da Maia et al. 2013; Pourmand et al. 2016; Li et al. 2019; Tu et al. 2021). EPDM is a rubber with excellent elasticity, low temperature flexibility, and good electrical insulation properties due to its non-polar and saturated hydrocarbon backbone structure. In addition to these important features that are preferred in industrial applications, it has superior resistance to heat, oxygen, ozone, and UV. EPDM elastomers can vary according to the amount and type of diene used, as well as in different ethylene and propylene ratios (Brydson, 1978). The quantitative ratio of monomers gives the elastomer certain properties (Wheelan and Lee, 1981), such as the production of high green, strong polymers when high ethylene content is used. Ethylene content used at low and medium values produce softer and more elastic polymers. The higher the ethylene content, the more likely the polymer to get filler, and the better mixing and extrusion process (Abdou-Sabet and Fath, 1982). EPDM rubber products can be used as a supporting product in high cost parts in different usage areas of the industry. The change in the microstructure of rubbers brings about general structural effects, and as a result, these structural deteriorations can affect the degradation properties of the composites used with EPDM rubber mixture (Kole et al. 1993; Gamlin et al. 2011). Choosing rubber with the wrong ethylene ratio while making rubber mixture formulations may cause the risk of hardness change of the product at low temperatures, and financial losses in the materials or structures used together. Therefore, this effect should be taken into account when creating formulations and should be controlled with process parameters.

The aim of this study is to investigate the effect of the ethylene ratio in the rubber raw material on the rheological and mechanical properties of Dutral TER 4049 and Suprene 512F EPDM rubbers mixed at different rates after curing with sulfur.

Material and Methods

Materials

The EPDM rubber materials used in this study are Dutral TER 4049 produced by Universal, and Suprene 512 F produced by SK Global Chemical, and their properties are shown in Table 1.

Table 1. EPDM rubber properties.

Grade	Diene content ENB (%)	Ethylene content	Mooney (ML 1+4 125 °C) (MU)	Extender oil paraffinic (phr)
Dutral TER 4049	4.5	60	76	-
Suprene 512 F	4.5	69	63	-

The following additives are added to the mixture during rubber preparation. These are

- Carbon FEF N 550 (Omsk Carbon Group) and Pro 1500 (Alkim Petro Kimya) as fillers
- 1618RG Stearic acid and ZnO (Melos A.Ş.) as activators
- AFLUX 42 and PEG 4000 as process facilitators
- TMTD, MBTS, and CBS from Eigenmann & Veronelli as accelerators
- Sulfur as a vulcanization agent
- and Kezadol (80% CaO) from Kettlitzas moisture inhibitor

An industrial size Model X(S)N-110 Kneader was used to mix the rubber mixture. Model X(S)K800 was used as mill and Model XP-600 Batch off Cooler (Taixing Ruixing Rubber & plastic Machinery Co. Ltd.) was used as cooling machine. These machines constitute the machine park used in rubber production.

Formulations

Three different formulations were written by using two different types of EPDM rubber and the same hardness was adjusted in three formulations. Table 2 shows the content of rubbers in different formulations.

Table 2. Rubber mixtures prepared in different formulations (phr).

Content	Suprene 512 F	Suprene 512 F (%50)-Dutral TER 4049 (%50)	Dutral TER 4049
Rubber	100	100	100
Carbon (FEF N 550)	81.7	85	86.7
Paraffinic Oil	76.7	76.7	76.7
Active ZnO	6.7	6.7	6.7
Stearic Acid	2.5	2.5	2.5
AFLUX 42	2.0	2.0	2.0
PEG 4000	2.0	2.0	2.0
TMTD	1.17	1.17	1.17
MBTS	1.17	1.17	1.17
CBS	0.83	0.83	0.83
S	0.9	0.9	0.9
CaO	6.7	6.7	6.7

Methods

Preparation of EPDM blend mix

Three different formulations were prepared for this study. For each formulation prepared, the rubber raw material was chewed in a kneader machine at 90 °C for 1.5 min. Then, Carbon (FEF N 550), paraffinic oil, active zinc, stearic acid, AFLUX 42, and PEG 4000 were added into the kneader machine at the phr ratios determined in the formulation. The mixture was allowed to mix for 5.5 min. Then, the amount of activators (TMTD, MBTS, CBS) determined in the formulation were added and mixed for 3 more minutes. The mixture, which was mixed in the kneader machine for a total of 10 min, was transferred to the mill at 110 °C output temperature. The rubber mixture in the mill was aerated for 1 min and its temperature was reduced. A certain amount of sulfur was added to the rubber mixture in the mill, and the temperature was lowered. The rubber mixture, which was mixed in the mill for 1 min and 40 sec, was cut and started to be given to Batch off Cooler. Transfer of the entire rubber compound mixture from the mill to the Batch off Cooler took place in 2 min 34 sec. The mixture, which was mixed by rotating in a total of 5 min and 14 sec, was sent to Batch off Cooler as a 14 cm long and 2 cm thick strip. The rubber mixture, which was cooled in Batch off Cooler for 16 min, was left to rest for 6 h in a cold room at 16 °C.

Rheological Properties

The hardness and curing properties of the EPDM rubber mixture were investigated using the GLK3000-MDR Rheometer at the test temperature of 185 °C. At the same time, min torque (ML), max torque (MH), torque difference (MH-ML), scorch time, and curing time were determined.

Tensile Strength and Elongation at Break

The tensile-elongation tests, which were the mechanical properties of the prepared EPDM rubber mixtures, were examined with the GLK3000-T5 Tensile-Breaking device at 200 mm/min speed according to ISO 37. Machine parameters used when testing according to ISO 37 standard were as follows: speed: 200 mm/min; direction: move up; extension type: trace; and load average times: 3. Tensile strength (Ts/MPa) and elongation break (Eb/%) values of the sample were determined.

Hardness Properties

Different EPDM rubber mixtures prepared here were investigated according to ISO 48 using hardness discs vulcanized at 185 °C for 4 min and 12 sec. In addition, three discs from each of the samples made with 3 different mixtures were taken and kept in an oven for 24 h at -10 °C, and the effects of temperature changes on hardness were observed.

Results and Discussion

Tensile Analysis

The results of the tensile analysis of the formulation containing Dutral TER 4049 made with parameters are shown in Figure 1 and Table 3.

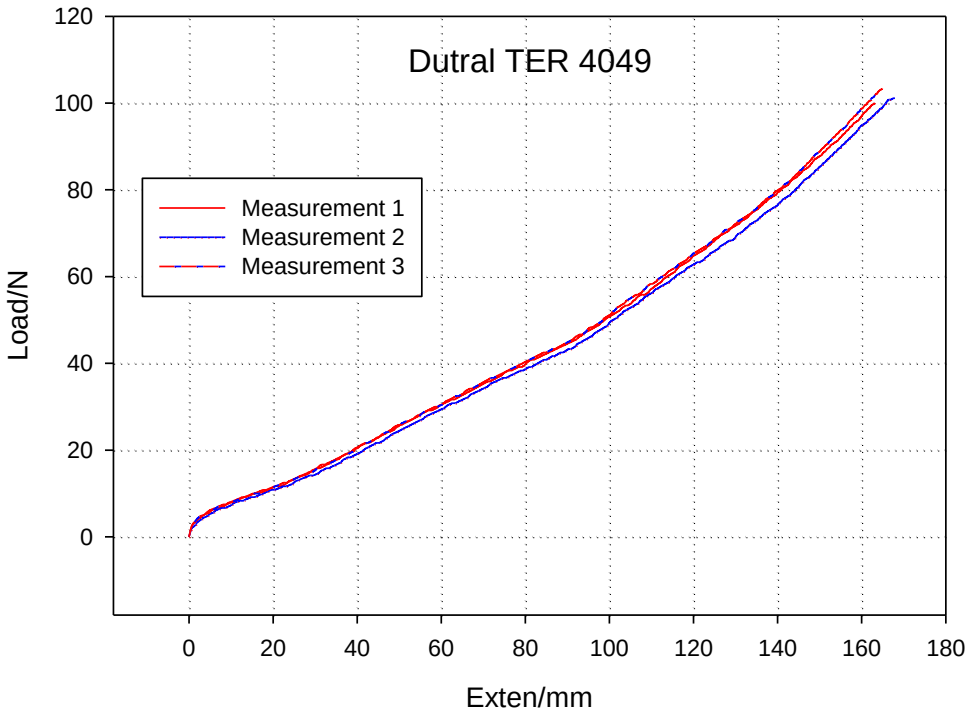

Figure 1. Tensile load of Dutral TER 4049.

Table 3. Tensile strength and elongation break analysis table for Dutral TER 4049 at different measurements.

Measurement	Thick/ mm	Width/ mm	Lo/ mm	Fmax /N	Lmax/ mm	Ts/M pa	Eb/ %	S50/ Mpa	S100/ Mpa	S200/ Mpa
1	1.95	4	25	72.78	171.62	9.33	686.5	0.7	1.1	2.37
2	1.95	4	25	80.56	178.9	10.33	715.6	0.8	1.23	2.52
3	1.95	4	25	84.17	176.64	10.79	706.6	0.91	1.39	2.78
A	1.95	4	25	79.17	175.72	10.15	702.9	0.8	1.24	2.56
V	0.00	0.0	0.0	5.82	3.73	0.75	14.9	0.11	0.15	0.21

The results of the tensile analysis of the formulation containing Suprene 512 F (50%) – Dutral TER 4049 (50%) made with the machine parameters are shown in Figure 2 and Table 4.

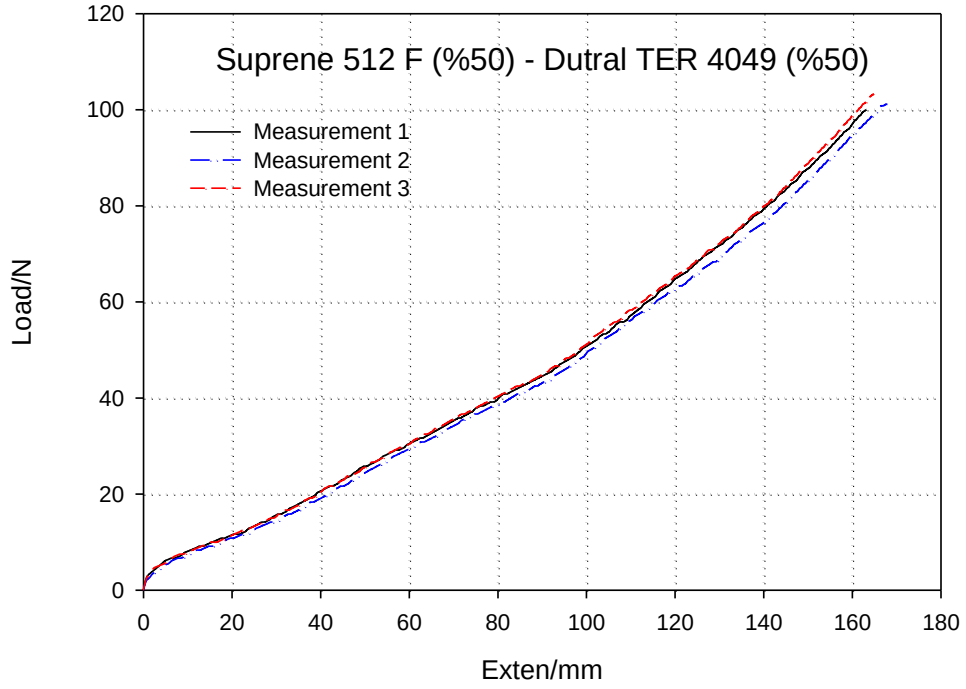

Figure 2. Tensile load of Suprene 512 F (%50) - Dutral TER 4049 (%50).

Table 4. Tensile strength and elongation break analysis table for Suprene 512 F (%50) - Dutral TER 4049 (%50) at different measurements.

Measurement	Thick /mm	Width/ mm	Lo/ mm	Fmax/ N	Lmax/ mm	Ts/Mpa	Eb/%	S50/ Mpa	S100/ Mpa	S200/ Mpa
1	1.95	4	25	89.72	158.62	11.5	634.5	1.1	1.67	3.26
2	1.95	4	25	95.00	165.68	12.18	662.7	1.07	1.67	3.24
3	1.95	4	25	78.61	145.59	10.08	582.4	1.05	1.62	3.2
A	1.95	4	25	87.78	156.63	11.25	626.5	1.07	1.65	3.23
V	0.00	0.00	0.0	8.37	10.19	1.07	40.8	0.03	0.03	0.03

The results of the tensile analysis using the ISO 37 standard for the formulation containing Suprene 512 F are shown in Figure 3 and Table 5.

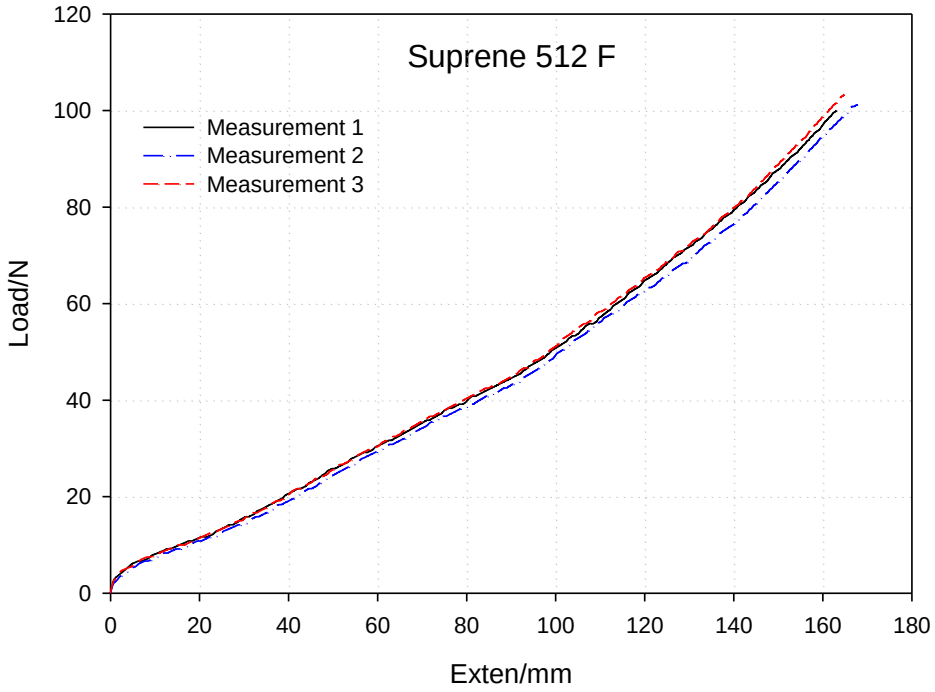

Figure 3. Tensile load of Suprene 512 F.

Table 5. Tensile strength and elongation break analysis table for different measurements of Suprene 512 F.

Measurement	Thick /mm	Width/ mm	Lo/ mm	Fmax/ N	Lmax/ mm	Ts/Mpa	Eb/%	S50/ Mpa	S100/ Mpa	S200/ Mpa
1	1.91	4	25	100	163.14	13.09	652.6	1.19	1.75	3.38
2	1.93	4	25	101.1	167.49	13.1	670.0	1.08	1.63	3.17
3	1.92	4	25	103.3	164.89	13.45	659.6	1.16	1.73	3.34
A	1.92	4	25	101.5	165.17	13.21	660.7	1.14	1.7	3.3
V	0.01	0.0	0.0	1.7	2.19	0.21	8.8	0.006	0.06	0.11

When the Tensile/Elongation analysis results of EPDM rubbers prepared in three different combinations were evaluated, it was observed that as the ethylene ratio increased, the tensile strength (Ts/Mpa) increased, but the elongation break force (Eb/%) decreased. Therefore, in the results of the Tensile-elongation analysis, the Ts/MPa value of the Suprene 512 F rubber with the highest ethylene content was observed to be quite high and the Eb/% value to be low. This indicated that the Suprene 512 F sample was mechanically stable. This is probably due to the increase in the number of bonds formed by the carbon atoms in the ethylene molecule and the sulfur used as the vulcanizing agent during the vulcanization of rubber, and is due to the fact that it increases the three-dimensional network formation by forming stable links between the sulfur and the chain segments that can be obtained by chemical reaction.

Rheological Measurements

Rheological measurements were carried out using the machine parameters Time: 3:00 m/s, Torque: 20.93 dN.m, and T: 185 °C. The rheological analysis results according to the parameters are given in Table 6 and Figure 4.

Table 6. Rheological test results of EPDM rubbers prepared at different formulations.

Sample	MH/dN.m	ML/dN.m	Ts1(m:s)	Ts90/(m:s)
Suprene 512 F	11.49	3.77	0.41	1.2
Suprene 512 F (%50) - Dutral TER 4049 (%50)	11.79	3.32	0.4	1.23
Dutral TER 4049	13.32	3.63	0.44	1.37

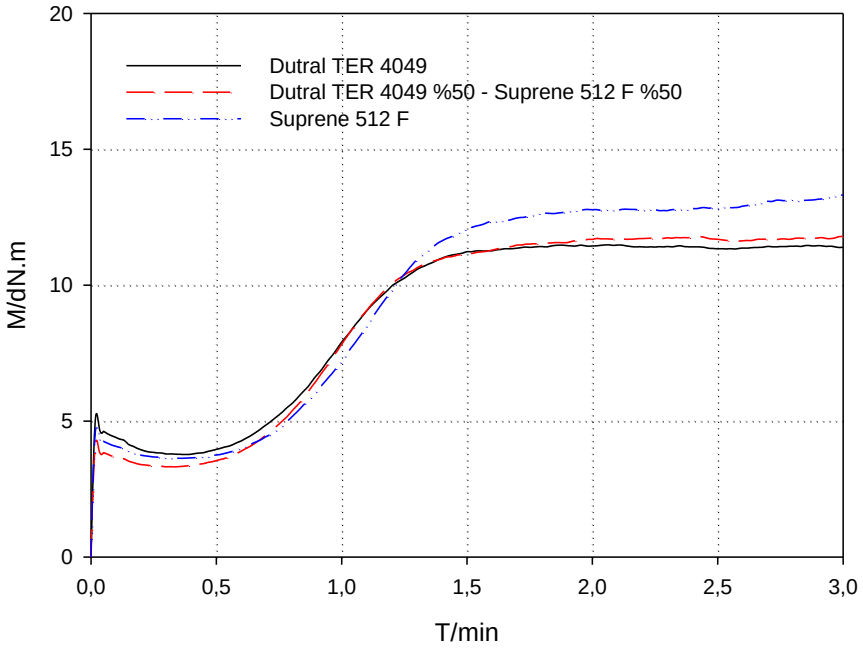

Figure 4. Rheological behaviors of the rubbers.

The results of the rheometer analysis revealed that the maximum cure torque (M/dN.m) of the Suprene 512 F sample was higher than the other two samples; however, 90% of the curing time was later than the other two samples. Comparing the rheological test results of EPDM vulcanizates in three different combinations, it has been observed that the excess of ethylene content plays a diluting role in the rubber and partially dissolves the rubber macromolecule, leading to a decrease in physical entanglement. On the other hand, excess ethylene may have reacted with free radicals produced by thermal degradation, joining the main-net of EPDM rubbers and forming double crosslinking networks. Crosslinking is commonly used to characterize an elastomer or vulcanized rubber, and to indicate three-dimensional network formation by forming stable links between chain segments that can

be obtained by chemical reaction with sulfur. This crosslinking is called chemical crosslinking, and is related to the mechanical properties of a rubber net such as crosslink density, tensile strength, and shear modulus or hardness. The tensile strength results of the study also increased with increasing ethylene content, indicating that there may be an increase in chemical crosslink density.

Hardness Analysis

The aging test was performed by keeping the samples in an oven at -10 °C for 48 h. Table 7 shows the hardness test results (i) before aging test at 22 °C, (ii) 48 h aging at -10 °C, and (iii) 6 h after aging test at 22 °C laboratory temperature.

Table 7. Shoremeter results of EPDM rubbers prepared in different formulations.

Sample	**Dutral TER 4049**			**Suprene 512 F (%50)-Dutral TER 4049 (%50)**			**Suprene 512 F**		
Before thermal aging (22°C)	51	51	52	55	55	55	57	57	56
Aging (-10 °C)	55	55	55	65	64	65	69	68	69
6 h after aging	55	56	55	60	60	60	62	62	62

The arithmetic mean of three different samples for each formulation measured in Table 7 is given in Table 8.

Table 8. The arithmetic mean of the shoremeter results.

Sample	**Dutral TER 4049**	**Suprene 512 F (%50)-Dutral TER 4049 (%50)**	**Suprene 512 F**
Before thermal aging (22°C)	51.33	55.00	56.66
Aging (-10 °C)	55.00	64.66	68.66
6 h after aging	55.33	60.00	62.00

In the hardness determination study performed at -10 °C and 24-hour conditioning period, it was observed that the hardness change of Suprene 512 F sample was higher than the others. This is due to the fact that the amount of ethylene in Suprene 512 F is higher than the others, and it causes crystallization in the structure at low temperatures. After conditioning, the hardness of Suprene 512 F, which was left in laboratory conditions at 24°C for 6 h, decreased to 62 SHA.

Conclusions

The increase in the ethylene ratio in the rubber showed a positive change in the mechanical and rheological properties of the produced material. This is probably due to the fact that the excess ethylene ratio increases the number of bonds formed by the sulfur used as the vulcanization agent during the vulcanization of the rubber, and it increases the three-dimensional network formation by

forming stable links between the sulfur and the chain segments that can be obtained by chemical reaction. In addition, the increase in the amount of ethylene in EPDM rubber caused crystallization at low temperatures and caused more percent hardness change. This sudden temperature-hardness change causes the rubber products, which are auxiliary materials, to damage the system, shorten their useful life, operate at low efficiency, or fail to meet the standards. Therefore, the reaction of the amount of ethylene to sudden temperature changes should be taken into account while forming the compound formulation. This is due to the fact that the amount of ethylene in Suprene 512 F is higher than the others, and it causes crystallization in the structure at low temperatures. While preparing rubber dough suitable for different demands, the ethylene ratio in the rubber raw material should be noted, considering the effects observed as a result of these experiments.

Acknowledgment

This study was carried out in the laboratories of Golday Kaucuk Company and Osmaniye Korkut Ata University. The authors would like to acknowledge these supports.

Author's Contributions

The contribution of the authors is equal.

*This study was presented as a summary paper at the International Conference on Engineering, Natural and Applied Sciences (ICENAS'21) held online on 24-26 November 2021.

References

Abdou-Sabet S., Fath MA. Thermoplastic elastomeric blends of olefin rubber and polyolefin resin. US Patent. 1982; 4: 311–628.

Brydson JA. Rubber Chemistry. Applied Science Publishers, London, 1978, 462.

da Maia JV., Pereira FP., Dutra JCN., Mello SAC., Becerra EAO., Massi M., da Silva Sobrinho AS. Influence of gas and treatment time on the surface modification of EPDM rubber treated at afterglow microwave plasmas. Applied Surface Science 2013; 285(Part B): 918–926.

Gamlin C., Dutta N., Ray-Choudhury N., Kehoeb D., Matisons J. Influence of ethylene–propylene ratio on the thermal degradation behavior of EPDM elastomers. Thermochimica Acta 2001; 367-368.

Kole S., Chaki TK., Bhowmick A., Tripathy D. Effect of compatibiliser, curing sequence and ageing on the thermal stability of silicone rubber, EPDM rubber and their blends. Materials Science 1993; 41(1): 109-116.

Li C., Wang Y., Yuan Z., Ye L. Construction of sacrificial bonds and hybrid networks in EPDM rubber towards mechanical performance enhancement. Applied Surface Science 2019; 484: 616–627.

Pourmand P., Linde E., Hedenqvist MS., Furo I., Dvinskikh SV., Gedde UW. Profiling of thermally aged EPDM seals using portable NMR, indenter measurements and IR spectroscopy facilitating separation of different deterioration mechanisms. Polymer Testing 2016; 53: 77–84.

Spanos P., Beelen J., Gogelein C. NR replacement by ultra-high molecular weight EPDM in dynamic applications. Rubber World 2014; 251(3): 21-27.

Tu J., Shi X., Jing Y., Zou H., Kadlcak J., Yong Z., Liu S., Liu G. Relationships of tensile strength with crosslink density forthe high-carbon black-filled EPDM compounds with various softeners. Polymer Engineering & Science 2021; 61(8): 2213–2221.

Wheelan A., Lee KS. Developments in Rubber Technology-2: Synthetic Rubbers. Applied Science Publishers, London, 1981.

OKÜ Fen Bilimleri Enstitüsü Dergisi
5(Özel Sayı):227-233, 2022

OKU Journal of The Institute of Science and Technology, 5(Special Issue):227-233, 2022

Osmaniye Korkut Ata Üniversitesi Fen Bilimleri Enstitüsü Dergisi

Osmaniye Korkut Ata University Journal of The Institute of Science and Technology

Sac ve Levhalar için Serbest Deformasyon Makinası

Seran KILIÇ ÖNEN[1], Ahmet ASLANDAĞ[2*]

[1,2]Kasso Mühendislik San ve Tic. A.Ş.

[1]https://orcid.org/ 0000-0001-8879-0454
[2]https://orcid.org/0000-0003-3277-1929
*Sorumlu yazar: ahmetaslandag@kasso.com.tr

Araştırma Makalesi

Makale Tarihçesi:
Geliş tarihi: 09.12.2021
Kabul tarihi:17.01.2022
Online Yayınlanma: 23.02.2022

Anahtar Kelimeler:
Sac levha
Sac levha şekillendirme
Germe ile şekillendirme
Uniform şekillendirme

ÖZET

Plastik şekillendirmede oldukça zor olan üç boyutlu form ve şekillerin elde edilmesinde, şeklin kontrolü ile birlikte deformasyonun sağlanabilmesi ancak olağanüstü şekillenme hareketleriyle mümkün olabilmekte ve 3 boyutlu görünümler elde edilebilmektedir. Saç levhayı çok küçük deformasyonlarla şekillendirmek ve derin ayrıntılarını görünür hale getirmek için Ar – Ge çalışmaları yapılarak teknolojik geliştirme sağlanabilmektedir. Deformasyondaki zorluklar sebebiyle, bu güne kadar karmaşık şekillerin ayrıntılı olarak elde edilmesi ancak iki eksenli şekillendirmelerle mümkün olabilmiştir. Halen metal şekillendirme, sektörünün önemli bir problemi olarak çözüm beklemektedir. Serbest deformasyon tekniğiyle üç boyutlu bir şeklin plastik şekil verme yöntemiyle mümkün hale getirilmesi amaçlanmış, malzemenin akışı kontrol edilerek ve estetik açıdan üç boyutlu akışlardan oluşan ürünlerin elde edilebilmesi için yeni bir plastik şekillendirme makinasının tasarımı yapılmıştır. Makine erkek şekillendirme kalıbı kullanarak, artırılmış ek form yöntemiyle seri üretime uygun serbest şekillerin elde edilmesini sağlayacaktır.

Free Deformation Machine For Sheets

Research Article

Article History:
Received: 09.12.2021
Accepted: 17.01.2022
Published online: 23.02.2022

Keywords:
Sheet metal
Sheet metal forming
Shaping by stretching
Uniform shaping

ABSTRACT

In obtaining three-dimensional forms and shapes, which are very difficult in plastic shaping, deformation can only be achieved with the control of the shape, but it is possible with extraordinary shaping movements and 3-dimensional views can be obtained. Technological development can be achieved by conducting R & D studies to shape the sheet metal with very small deformations and to make the deep details visible. Due to the difficulties in deformation, it has been possible to obtain complex shapes in detail until now only with biaxial shaping. It is still waiting for a solution as an important problem of the metal forming industry. With the free deformation technique, it was aimed to make a three-dimensional shape possible with the plastic forming method, and a new plastic forming machine was designed in order to control the flow of the material and to obtain products consisting of three-dimensional flows aesthetically. The machine will ensure that free shapes suitable for mass production are obtained with the increased additional form method by using a male forming mold.

To Cite: Önen SK., Aslandağ A. Sac ve Levhalar için Serbest Deformasyon Makinası. Osmaniye Korkut Ata Üniversitesi Fen Bilimleri Enstitüsü Dergisi 2022; 5(Özel sayı): 227-233.

Giriş

Plastik deformasyonla geometrik bir şekle sahip ürünün elde edilmesi için, dört yüzeyli, parametrik yüzeyde bütünsel veya yerel olarak uygulanmış, üç değişkenli matematiksel bir fonksiyona dayandırılmış ve tasarımdaki etkileri için sezgisel bir değerlendirme yapılmıştır (Rivers ve James, 2007). Serbest biçimli deformasyon algoritmasıyla, grafik işleme için uygun algoritmanın kullanarak, bir dakikadan daha kısa bir zamanda manyetik rezonansın görüntülerinin kayıtları elde edilebilmiş ve klasik bir uygulama ile kritik uygulamalarda veya büyük veri kümelerinin işlenmesinde önemli bir fayda sağlanmıştır (Lamousin ve Waggenspack, 1994). Rijit olmayan yüzeylerin izlenmesi problemi ele alınmış ve genel bir veriye dayalı ağ deformasyon çerçevesi oluşturulmuştur. Daha az varsayımla, yüzey ve dolayısıyla büyük deformasyonları etkin bir şekilde ele alıp çoğu serbest biçimli yüzeylere kolayca genelleme yapılmış ve referans yüzeyi temel yüzeye bölünmüştür. Gürültülü ortamlar için yüzey üzerinde doğal uyum alanlarındaki kısıtlamalar azaltılmıştır. Büyük deformasyonlara ve hızlı hareketlere maruz kalan, muhtemelen bağlantılı olmayan bileşenlerle açık ve kapalı yüzeyler üzerinde deneyler yapmış, nicel ve nitel değerlendirmeler gerçekleştirilmiştir (Pernot ve ark., 2005).

Elastikiyet teorisi, kauçuk, kumaş, kâğıt ve esnek metaller gibi deforme olabilen malzemeleri tanımlar. Rijit olmayan eğrilerin, yüzeylerin ve katıların davranışını zamanın bir fonksiyonu olarak modelleyen diferansiyel denklemler oluşturmak için esneklik teorisini kullanılmıştır. Elastik olarak deforme olabilen modeller mevcut olup çeşitli simülasyon modelleriyle elde edilmektedir. Uygulanan kuvvetlere, kısıtlamalara, sekil geometrisine ve mevcut zorluklara doğal çözümler getirilebilmiştir. Modeller temelde dinamiktir ve gerçekçi animasyon, temeldeki diferansiyel denklemlerin sayısal olarak çözülmesiyle oluşturulabilmiştir. Böylece şeklin tanımı ve hareketin tanımı birleştirilerek elde edilmiştir (Leon ve Veron, 1997). Serbest biçimli deformasyon güçlü bir modelleme aracıdır, ancak karmaşık deformasyonlar altında bir nesnenin şeklini kontrol etmek genellikle çok zordur.

Çoğu konvansiyonel sistemde Serbest Şekillendirme Deformasyonu (DŞD) ile ara yüz, basitçe matematik temelde doğrudan temsil edilebilmektedir. Şekillendirme operatörleri, kontrol noktalarına müdahale ederek deformasyonları yönetirler. Şekli tam olarak kontrol etmedeki zorluk, büyük ölçüde kontrol noktalarının şekillendirilen malzemeyi tam olarak temsil etmemesinden kaynaklanmaktadır. Deforme olan malzemenin kontrol noktalarını tam olarak takip edemez. İlaveten, kullanıcıya sunulan serbestlik derecesi sayısı çok fazla olabilir. Kullanıcının, nesneyi doğrudan manipüle ederek bir malzemenin serbest biçimli deformasyonunu kontrol etmesine olanak tanıyan, deformasyonunu daha iyi kontrol eden ve daha sezgisel bir ara yüze oluşturan bir yöntem elde edilmiştir (Cui ve Feng, 2015). Gerçek zamanlı veya büyük ölçekli çevrimdışı simülasyonlar için hacimsel, büyük deformasyon dinamiklerinin tasarıma uygun bir şekilde elde edilmesini sağlayan bir teknik mevcuttur. Bu teknikte şekil eşleştirme, kafes yapısı içinde deforme olabilen şekillerin eşleştirmesinin önceden belirlenmiş geometriye sahip normal bir eşleştirme yapılmıştır. Kafes köşeleri, bölge genişliği yoluyla akma miktarı ile belirtilen etkili mekanik sertlik ile yerel kafes bölgelerindeki katı şekil eşleştirme operatörlerinin yetenek ve marifetiyle başarılabilmektedir (Kenwright, 2015). Bilgisayar tabanlı

geometrik modellemenin ortaya çıkışından bu yana tasarımcılar, heykeltıraşların kil ile yaptığı çalışmaları büyük bir çoğunluğunu kolaca benzerlik sağlayan modelleme ve deformasyon araçları geliştirdiler (Hsu ve Hughes, 1992)

Mevcut serbest şekillendirme deformasyonlarının rasyonel olarak bir makine marifetiyle sağlanması amaçlanmıştır. Makine sahip olduğu esneklik ve kontrol sayesinde serbest şekillendirme formunu oluşturma tekniğini seri üretime uygulayabilecek ve küresel ölçekteki şekil kombinasyonlarını oluşturabilecektir.

Deformasyonun Ağı

Geometrik şeklin elde edilmesi öncesi grafik olarak şekillendirme mekanizması deformasyon gereken alanlarda kontrol noktaları oluşturulmalıdır. Kontrol noktalarının sayısı, hassas ayrıntı gerektiren alanlara göre belirlenip, şekil alacak yüzey üzerinde doğrusal olmayan bir şekilde kontrol edilebilir bir hacimde belirlenir. Kontrol noktaları dört yüzlü bir hacimin içinde üçgenler olarak bir grafik ağı oluşturulacak şekilde yerleştirilebilir. Dört yüzlü hacimi oluşturan kafesin köşeleri ve üçgeni oluşturan noktalar deformasyon başlangıcı olacaktır. Deformasyon köşeden köşeye doğru ilerleyerek matematik bir fonksiyon oluşturmalıdır. Şekil 1 de dört yüzlü köşelerine yerleştirilen üçgenleri ve kontrol noktalarını göstermektedir. Şekil 1: Dörtyüzlü, üçü her köşede veya tepe noktasında buluşan dört üçgen yüzden oluşan çokyüzlüdür. Altı kenarı ve dört köşesi vardır ve geometrik bir bölgenin basit, belirsiz olmayan bir temsilini sağlar (Kenwright, 2015).

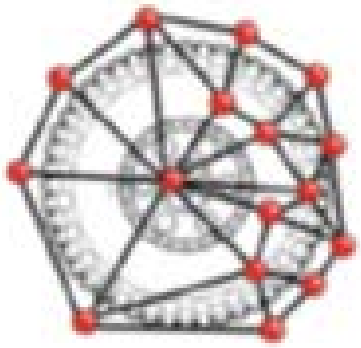

Şekil 1. Dört yüzlü hacım için kontrol noktaları (Kenwright, 2015)

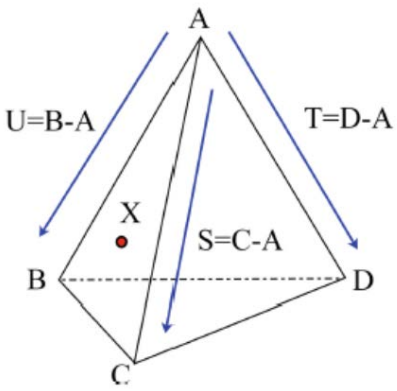

Şekil 2. Yüzeydeki bir noktanın tanımı (Kenwright, 2015)

Geometrik formu tanımlayan fonksiyonun elde edilebilmesi için oluşturulacak algoritma adımları; orijinal şekile, ince ayrıntı gerektiren alanlara daha fazla kontrol noktası ekleyerek, kontrol noktalarını dört yüzlü hacimler halinde üçgenlerle belirleme ve bu belirlenen algoritmayı kullanarak grafik köşeler ve bunlarla ilişkili dört yüzlüler için ağırlıkları formülle belirlenir (Kenwright, 2015):

$$U = B - A$$
$$S = C - A \qquad (1)$$
$$T = D - A$$

Burada A, B, C, D dört yüzlünün köşelerini, U, S ve T de üçgen kenarlarındaki deformasyonları göstermektedir.

SŞD kavramı tipik olarak tek biçimli bir ızgara olarak temsil edilir. Şekil 2'de gösterildiği gibi dört yüzlü (ABCD) dört köşesini ve (X) içindeki noktanın belirlenmesi (Kenwright, 2015);

$$X(s,t,u) = A + sS + tT + uU \qquad (2)$$

denklemiyle tanımlanır. Bir dörtyüzlü hücre için enterpolasyon fonksiyonu lineerdir ve kafes uzayı (2) eşitliği ile tanımlanmıştır. A, yerel koordinat sisteminin orijinidir ve S, T ve U, SŞD dörtyüzlüsünün kenarları boyunca uzanır. Kafesin herhangi bir iç noktası için $0 < s < 1,0 < t < 1$ ve $0 < u < 1$. s, t ve u'yu dörtyüzlü köşe noktalarından biri olarak A kümesiyle (3) eşitliğinden hesaplanabilir. (Ben Kenwright,2015).

$$\begin{aligned} S &= 0\ T.U\ (X - A) / T.U.S \\ t &= S.U\ (X - A) / S.U.T \\ u &= S.T\ (X - A) / S.T.U \\ X &= A + s.S + t.T + u.U \end{aligned} \qquad (3)$$

Burada s, t ve u, dört yüzlü içindeki nokta için skaler ağırlıklardır. Skaler ağırlıklar başlangıçta (yani herhangi bir deformasyon meydana gelmeden önce) hesaplanır. Kontrol noktaları (dörtyüzlünün köşeleri) hareket ettikçe, biçimlendirilme yeniden hesaplanır. Şekil 3. Simülasyon - Grafiksel ağı 12270 köşeleri, 23 kontrol noktası, 27 dörtyüzlünün; orijinal meshi, kontrol noktalarının yerleştirilmesi, dörtyüzlü kontrol noktaları, dörtyüzlü grafik köşeler belirlenerek, deformasyon oluşturulmuş ve bir otomobil jantındaki uygulaması gösterilmiştir.

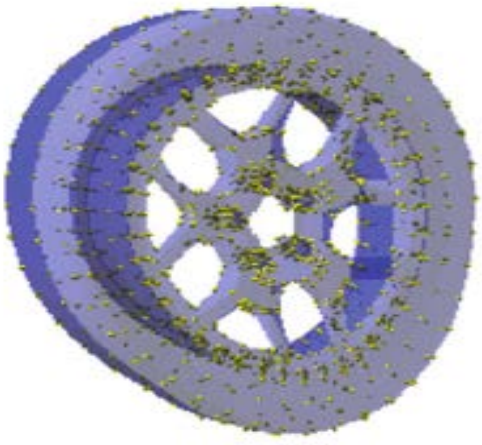

Şekil 3. Yerleştirilmiş kontrol noktaları (George ve Borouchaki, 1998)

Dört yüzlü hücrelerin çoklu seviyelerin hiyerarşisi ve komşu hücrelerin öncelikle ağırlıklı olarak şekillenmesini önlemek için küresel bağlamda formüller geliştirilebilir.

Serbest Şekillendirme Makinesi

Saç malzemeyi kuvvet etkisiyle dörtyüzlü yapısı oluşturmak için üç koordinat ekseninde aynı anda veya ardışık olarak artırılmış gerilme oluşturacak makine KASSO Mühendislik tarafından tasarlanmıştır. Tasarımda kuvvetin uygulanması, hareketin sağlanması ve formun oluşturulması hidrolik sistemle sağlanmaktadır. Hareketlerin önceliği, sıralaması ve kontrolü PC kontrolle sağlanmaktadır. Makine 3000 x 6000 mm boyutlarındaki saç malzemelere dörtyüzlü şekil verebilecek mekanik, kinematik ve aerodinamik şekilleri seri olarak üretebilecektir.

Tübitak destekli prototipin çalışma prensibini anlatan görseller aşağıda Şekil 4 de verilmiştir. Derin şekilli deformasyon ve şekillendirilecek ürün Şekil 5 de görülmektedir.

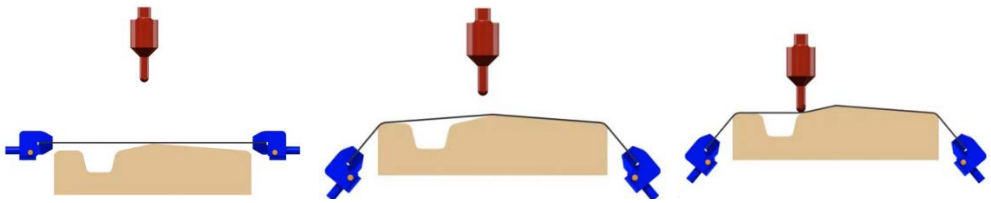

Şekil 4. Şekillendirme adımları. a- Yerleştirme, b- Gerdirme, c- Kuvvet uygulama

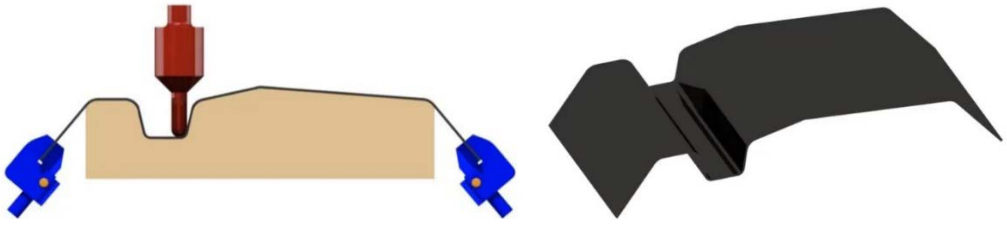

Şekil 5. a- Deformasyon ve b-Ürün

Serbest form deformasyonu yapacak makineye ait anal taslak aşağıda Şekil 6 da verilmiştir.

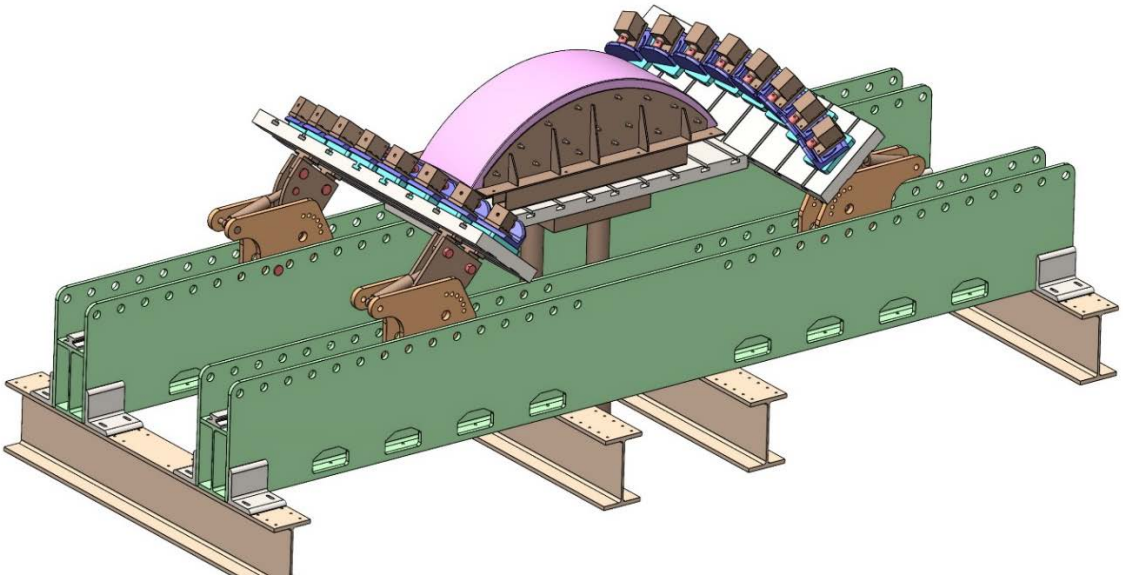

Şekil 6: Serbest form deformasyonu makinası

Sonuç ve Tartışma

Sonuç olarak, saç, plastik ve tekstil esaslı malzemelerde deformasyonlar oluşturmak için çok çeşitli yöntemler kullanılmaktadır. Doğrusal olmayan şekiller tek, iki ve üç eksenli makinalarla elde dilip sektör ihtiyaçları karşılanmaktadır. Yeni tasarımlar sayesinde çok farklı şekilli ürünler üretilmektedir. Makinaların tasarımında; ürüne verilecek şekil, mekanik, kinematik, aerodinamik özellikler ile hareketlerin otomasyonu, seri üretime uygunluk her geçen gün önem kazanmaktadır.

i. Dört yüzlü hücrelerin oluşturulması, oluşan geometrik şeklin ideal hale getirilmesi,
ii. Kenwright (2015) tarafından geliştirilen yazılımla dörtyüzlü yapısının bilgisayar yazılımı ve kontrolüyle gerçekleştirilmesi,
iii. Ürüne yönelik ve seri üretime uygun makinalara zamanın ruhuna uygun gereksinim duyulması,
iv. Bu gereksinim karışılmak için, doğrusal olmayan serbest biçimli bir deformasyon dağılımı mekanik olarak da elde edilmesi mümkün olabileceği,
v. Kontrol noktaları, onu gerektiren alanlarda ek ayrıntı düzeyine odaklanmak için şekil yüzeyine gerdirme yapılarak dağıtılması mümkün hale getirileceği,
vi. Otomatik olarak küçültülmüş bir poli dış bükey gövde oluşturmak ve grafik köşelerin dağılımına göre kontrol noktaları yerleştirmek, buna izin veren alanlarda da daha aerodinamik şekiller elde edilebileceği

Sonuç

Yassı levhalarda germe yöntemiyle şekillendirme amaçlanan bu makina ile istenilen dış bükey yüzeyler bu yöntemle verilebilmektedir. Bununla birlikte arttırımlı şekil verme yöntemi ile ise iç bükey yüzeylerde kalan yüzeylerin şekillendirmesini sağlamaktadır.

Teşekkür

"3210120" proje numaralı "Metal Levhalara Freeform Plastik Şekil Vermek Amaciyla Sadece Erkek Form Kalibi Kullanarak Arttirilmiş Ek Form Yöntemli Makine Tasarimi Ve İmalatI" başlıklı projede verilen Ar-Ge desteği için TÜBİTAK Teknoloji ve Yenilik Destek Programları Başkanlığı'na teşekkür ediyoruz.

Çıkar Çatışması Beyanı

Makale yazarları aralarında herhangi bir çıkar çatışması olmadığını beyan ederler.

Araştırmacıların Katkı Oranı Beyan Özeti

Yazarlar makaleye eşit oranda katkı sağlamış olduklarını beyan ederler.

* Bu çalışma, 24-26 Kasım 2021 tarihlerinde çevrimiçi olarak gerçekleştirilen International Conference on Engineering, Natural and Applied Sciences (ICENAS'21) konferansında özet bildiri olarak sunulmuştur.

Kaynaklar

Cui Y., Feng J. GPU-based smooth free-form deformation with sharp feature awareness. Mathematics Computer Science. doi:10.1016/j.cagd.2015.03.002Corpus ID: 19577162.

George OL., Borouchaki H. Delaunary triangulation and mech. Hermes, Paris, 1998

Hsu WM., Hughes J., Kaufman H. Direct manipulation of free-form deformations. Proceedings of the 19th Annual Conference on Computer Graphics and Interactive Techniques 1992; doi:10.1145/133994.134036 Corpus ID: 8864124.

Kenwright B. Free-form tetrahedron deformation. Computer Science 2015; doi:10.1007/978-3-319-27863-6_74 Corpus ID: 993068.

Lamousin HJ., Waggenspack NN. NURBS-based free-form deformations. IEEE Computer Graphics and Applications 1994; 14(6): 59-65.

Leon JC., Veron P. Semiglobal deformation and correction of free form surfaces using a mechanical alternative. The Visual Computer 1997; 13: 109-126.

Pernot JP., Guillet S., Léon JC., Falcidieno B., Giannini F. Shape tuning in fully free-form deformation features. J. Comput. Inf. Sci. Eng. 2005; 5(2): 95-103.

Rivers AR., James DL. Fast lattice shape matching for robust real-time deformation, ACM Transactions on Graphics 2007; 26(3): 82.

OKÜ Fen Bilimleri Enstitüsü Dergisi
5(Özel Sayı):234-251, 2022

OKU Journal of The Institute of Science and Technology, 5(Special Issue):234-251, 2022

Osmaniye Korkut Ata Üniversitesi Fen Bilimleri Enstitüsü Dergisi

Osmaniye Korkut Ata University Journal of The Institute of Science and Technology

Benchmark Fonksiyonları için Altın Kartal Optimizasyon Algoritmasının Parametrelerini Optimize Etme

Mehmet BEŞKİRLİ[1], Mehmet Fatih TEFEK[2*]

[1]Şırnak Üniversitesi, Mühendislik Fakültesi, Bilgisayar Mühendisliği Bölümü, Şırnak
[2]Osmaniye Korkut Ata Üniversitesi, Mühendislik Fakültesi, Bilgisayar Mühendisliği Bölümü, Osmaniye

[1]https://orcid.org/ 0000-0002-4842-3817
[2]https://orcid.org/0000-0003-3390-4201
*Sorumlu yazar: mehmetfatihtefek@osmaniye.edu.tr

Araştırma Makalesi

Makale Tarihçesi:
Geliş tarihi: 16.12.2021
Kabul tarihi: 09.02.2022
Online Yayınlanma: 23.02.2022

Anahtar Kelimeler:
Altın kartal optimizasyon
Algoritması
Parametre optimizasyonu
Kıyaslama fonksiyonları
Optimizasyon

ÖZET

Bu çalışmada, Altın Kartal Optimizasyon (AKO) algoritmasının performansını iyileştirmek için AKO algoritmasının parametreleri optimize edilmiştir. Bu sayede algoritmanın parametresinin en iyi değerinin elde edileceği ve elde edilen parametre değerleri için algoritmanın daha kararlı bir işlem gerçekleştireceği öngörülmektedir. Algoritmanın parametre optimizasyonu birçok çalışmada kullanılmaktadır. AKO algoritmasının iki farklı parametre değeri vardır. Bu parametreler sırasıyla saldırı ve seyirdir. Seyir parametre değeri [0.5-1], saldırı parametresi değeri [0.5-2] arasındadır. Algoritmanın her bir parametre değeri için 23 farklı kıyaslama fonksiyonu üzerinde deneysel çalışmalar yapılmıştır. Deneysel çalışma sonuçlarında en iyi parametrelerin değerleri belirlenmeye çalışılmıştır. Unimodal benchmark test fonksiyonlarında seyir parametresi 0.75 değeri ile iyi sonuçlar elde etmiştir. Saldırı parametresi ise fonksiyonlara bağlı olarak 1.5'e yaklaştığında optimum sonuca doğru yakınsadığı tablo ve grafiklerde verilmiştir. Benzer şekilde, multimodal kıyaslama testi sonuçlarında, seyir parametresi 0.75 değeri ile benzer şekilde iyi sonuçlar hesaplamıştır. Fonksiyonların özelliklerine bağlı olarak, değer 1.5'e yaklaştıkça saldırı parametresinin değerinin daha iyi bir çözüm bulduğu tablo ve grafiklerde gösterilmiştir.

Optimizing the Parameters of the Golden Eagle Optimizer Algorithm for Benchmark Functions

Research Article

Article History:
Received: 16.12.2021
Accepted: 09.02.2022
Published online: 23.02.2022

Keywords:
Golden eagle optimizer algorithm
Parameter optimizing
Benchmark functions
Optimization

ABSTRACT

In this study, in order to improve the performance of the Golden Eagle Optimization (GEO) algorithm, the parameters of the algorithm were optimized. In this way, it is predicted that the best value of the algorithm's parameter will be obtained and the algorithm will perform a more stable operation for the obtained parameter values. The algorithm's parameter optimization is used in many studies. There are two different parameter values of the GOE algorithm. These parameters are attack and cruise, respectively. Cruise parameter value is between [0.5-1] and attack parameter value is between [0.5-2]. Experimental studies were carried out on 23 different benchmark functions for each parameter value of the algorithm. In the experimental study results, the values of the best parameters were tried to be determined. It is shown in the tables and graphics that the solutions converge to the optimum result when the cruise parameter approaches 0.75 and the attack parameter 1.5 for the unimodal benchmark test functions. Similarly, for multimodal benchmark functions, it is seen in the tables and graphs that the attack parameter is 1.5 and the cruise parameter is 0.75.

To Cite: Beşkirli M., Tefek MF. Optimizing The Parameters of The Golden Eagle Optimizer Algorithm for Benchmark Functions. Osmaniye Korkut Ata Üniversitesi Fen Bilimleri Enstitüsü Dergisi 2022; 5(Özel sayı): 234-251.

Introduction

Optimization is the process of obtaining the best value of the objective function under certain constraints (Beşkirli and Dağ, 2022). Metaheuristic algorithms do not guarantee that they will obtain exact results for all optimization problems (Beşkirli and Dağ, 2020; Beşkirli et. al., 2020). However, they try to achieve the best results. Metaheuristic algorithms give better results than classical methods. In this study, Golden Eagle Optimization (GEO) algorithm was used. Although optimization algorithms try to achieve good results, the algorithm will be able to achieve better results with the improvements to be made on the algorithm. The best parameter level of the GEO algorithm was investigated in this study. It affects the success of the result to be obtained by parameter arrangement of the algorithm. For this reason, the parameter values that we think will be suitable for many problems in the literature have been applied to the benchmark functions and the best parameter values have been recommended. There are many studies in the literature on this subject. When these studies are examined, it is stated that the performance of the algorithm is at the highest level when the parameters of the algorithms are at the best value. Some of these studies are (Akay and Karaboga, 2012; Brest et. al., 2017; Brest et. al., 2008; Cicirello and Smith, 2000; Grefenstette, 1986; Luo et. al., 2016; Michalewicz and Schoenauer, 1996; Rao et. al., 2012; Zhangqi et al., 2011). Some studies on GOE in the literature are as follows: GOE algorithm was developed by Pan et al. (2022) and 3D UAV path planning process was performed. The method proposed by Pan et al. (2022) was called the GEO-DLS method and this method was used to improve the search capability of GEO. In GEO-DLS, it has been seen that the parameters are used with the values in the original form of GEO. A secure Ad Hoc optional distance vector routing protocol study with the improved GEO algorithm by Joshi and Biradar (2021). In this study, it was observed that no changes were made in the parameters of the GEO algorithm. Ilango et al. (2021) proposed a hybrid approach with GEO in order to achieve an optimum distribution over the distribution network. Thus, they aimed to minimize the cost through optimal allocation as parking space for electric vehicles. However, it was observed that no change was made in the parameter values of the GEO algorithm. Selimyan and Musavi (2021) used the GEO aggregation to design the organ transplant supply chain network problem. In this study, it has been seen that the parameters of the GEO algorithm are used in their original form. Abdel-Basset et al. (2022) made a comparison with the algorithms recently proposed by high-dimensional knapsack problems. These algorithms include the GEO method, but it has been observed that no changes have been made in the parameters of the GEO method. Vijh et al. (2021) solved the feature selection method for histological images using the GEO algorithm. An innovation has been made on the GEO algorithm, but it has been observed that no changes have been made on the parameters.

In this study, the parameter determination of the GEO algorithm was made by taking the cruise parameter between [0.5-1] and the attack parameter between [0.5-2] values. The improved parameters of the GEO algorithm are applied to 7 unimodal and 16 multimodal benchmark functions. When the

attack and cruise parameters were 1.5 and 0.75, respectively, better solutions were obtained than the original parameter values of GEO. Obtained results are given with tables and convergence curves.

Material and Methods

The Golden Eagle Optimizer Algorithm (GEO)

The golden eagle optimizer algorithm (GEO), one of the nature-inspired algorithms, was proposed by Muahmmadi-Balani (Mohammadi-Balani et. al., 2021) in 2021 based on the superior vision, high speed and very strong claws of golden eagles. During the hunting process of golden eagles, they first draw a circular trajectory for hunting and follow a straight path for hunting. The mathematical modeling of this algorithm is firstly the spiral movement of golden eagles. Afterwards, the prey selection process takes place. Then it is attacked. Then the travel vector is calculated. Then, the transition to new positions is made to replace the golden eagles. There is a transition from exploration to exploitation. A related image is given in Figure 1.

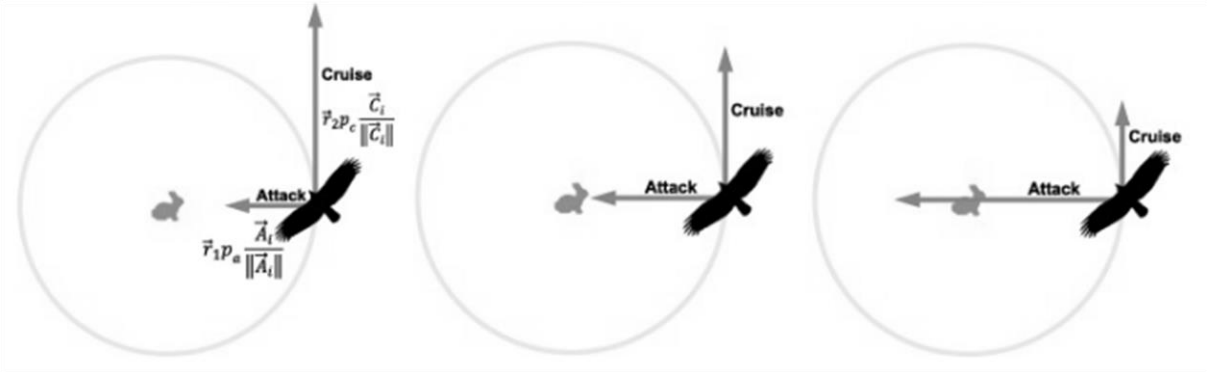

Figure 1. Correlation steps between exploration and exploitation in golden eagles (Mohammadi-Balani et al., 2021)

The main steps of golden eagles are shown in Figure 2. The prey is selected first, respectively. Then vector calculation for the attack is performed. Then the cruise plane is created. A vector is then randomly selected from the generated course plane. Finally, the process is terminated with the step vector.

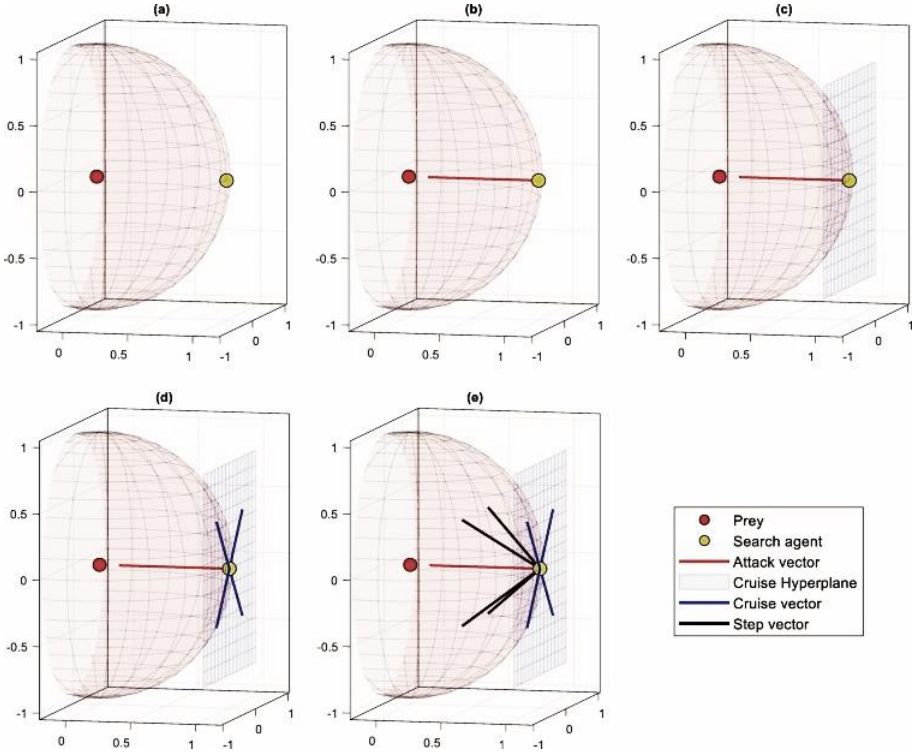

Figure 2. The main steps of golden eagles (Mohammadi-Balani et al., 2021)

Benchmark Functions

The parameters of the GEO algorithm were applied to 23 different benchmark problems to obtain the optimum value. These problems consist of unimodal and multimodal functions. Unimodal benchmark functions are given in Table 1. Multimodal benchmark functions are given in Table 2.

Table 1. Unimodal benchmark functions (D: Dimension)

Fn.	Name	D	Search Range	Function	f_{min}
F1	Beale	2	$[-4.5, 4.5]^D$	$f_1(x) = (1.5 - x_1 - x_1x_2)^2 + (2.25 - x_1 + x_1x_2^2)^2 + (2.625 - x_1 + x_1x_2^3)^2$	0
F2	Matyas	2	$[-10, 10]^D$	$f_2(x) = 0.26(x_1^2 + x_2^2) - 0.48x_1x_2$	0
F3	Three-hump camel	2	$[-5, 5]^D$	$f_3(x) = 2x_1^2 - 1.05x_1^4 + \frac{x_1}{6} + x_1x_2 + x_2^2$	0
F4	Exponential	30	$[-1, 1]^D$	$f_4(x) = -e^{\left(-0.5\sum_{i=1}^{n} x_i^2\right)}$	0
F5	Ridge	30	$[-5, 5]^D$	$f_5(x) = x_1 + 2\left(\sum_{i=2}^{n} x_i^2\right)^{0.1}$	-5
F6	Sphere	30	$[-100, 100]^D$	$f_1(x) = \sum_{i=1}^{N} x_i^2$	0
F7	Step	30	$[-5.12, 5.12]^D$	$f_7(x) = \sum_{i=1}^{n} (\lfloor x_i + 0.5 \rfloor)^2$	0

Table 2. Multimodal benchmark functions (D: Dimension)

Fn.	Name	D	Search Range	Function	f_{min}
F8	Drop Wave	2	$[-5.2, 5.2]^D$	$f_8(x) = -\frac{1+cos\left(12\sqrt{x_1^2+x_2^2}\right)}{0.5(x_1^2+x_2^2)+2}$	-1
F9	Egg holder	2	$[-512, 512]^D$	$f_9(x) = -(x_2+47)sin\left(\sqrt{\left\|x_2+\frac{x_1}{2}+47\right\|}\right) - x_1 sin\left(\sqrt{\|x_1-x_2-47\|}\right)$	-959.6407
F10	Himmelblau	2	$[-5, 5]^D$	$f_{10}(x) = (x_1^2+x_2-11)^2+(x_1+x_2^2-7)^2$	0
F11	Levi 13	2	$[-10, 10]^D$	$f_{11}(x) = sin^2(3\pi x_1)(x-1)^2\left(1+sin^2(3\pi x_2)\right) + (x_2-1)^2\left(1+sin^2(2\pi x_2)\right)$	0
F12	Ackley 1	30	$[-32, 32]^D$	$f_{12}(x) = 20 + e - 20\mathrm{e}^{\left(-0.2\sqrt{\frac{1}{N}\sum_{i=1}^{N} x_i^2}\right)} - e^{\left(\frac{1}{N}\sum_{i=1}^{N}\cos(2\pi x_i)\right)}$	0
F13	Griewank	30	$[-600, 600]^D$	$f_{13}(x) = \sum_{i=1}^{N}\frac{x_i^2}{4000} - \prod_{i=1}^{N}\cos\left(\frac{x_i}{\sqrt{i}}\right) + 1$	0
F14	Happy cat	30	$[-2, 2]^D$	$f_{14}(x) = \sqrt[8]{(\|x\|^2-n)^2} + \frac{1}{n}\left(\frac{1}{2}\|x\|^2 + \sum_{i=1}^{n} x_i\right) + \frac{1}{2}$	0
F15	Michalewicz	10	$[0, \pi]^D$	$f_{15}(x) = \sum_{i=1}^{n} sin(x_i)\left(sin\left(\frac{ix_i^2}{\pi}\right)\right)^{20}$	-9.6602
F16	Penalized 1	30	$[-50, 50]^D$	$f_{16}(x) = \frac{\pi}{n}\{10sin^2(\pi y_1) + \sum_{i=1}^{n-1}(y_i-1)^2[1+10sin^2(\pi y_{i+1})] + (y_n-1)^2\} + \sum_{i=1}^{n} u(x_i, 10, 100, 4)$ $y_i = 1+\frac{1}{4}(x_i+1)$ $u_{x_i,a,k,m} = \begin{cases} k(x_i-a)^m & x_i > a \\ 0 & -a \le x_i \le a \\ k(x_i-a)^m & x_i < a \end{cases}$	0
F17	Penalized 2	30	$[-50, 50]^D$	$f_{17}(x) = \frac{1}{10}\{sin^2(\pi x_1) + \sum_{i=1}^{n-1}(x_i-1)^2[1+sin^2(3\pi x_{i+1})] + (x_n-1)^2[1+sin^2(2\pi x_{i+1})]\} + \sum_{i=1}^{n} u(x_i, 5, 100, 4)$	0
F18	Periodic	30	$[-50, 50]^D$	$f_{18}(x) = 1 + \sum_{i=1}^{n} sin^2(x_i) - \frac{1}{10}e^{\left(\sum_{i=1}^{n} x_i^2\right)}$	0.9
F19	Qing	30	$[-500, 500]^D$	$f_{19}(x) = \sum_{i=1}^{n}\left(x_i^2 - i\right)^2$	0
F20	Rastrigin	30	$[-5.12, 5.12]^D$	$f_{20}(x) = \sum_{i=1}^{n}\left(x_i^2 - 10\,cos(2\pi x_i)\right) + 10\mathrm{n}$	0
F21	Rosenbrock	30	$[-5, 10]^D$	$f_{21}(x) = \sum_{i=1}^{n}\left(100\left(x_{i+1}-x_i^2\right)^2 + (1-x_i)^2\right)$	0
F22	Salomon	30	$[-100, 100]^D$	$f_{22}(x) = 1 - cos\left(2\pi\sqrt{\sum_{i=1}^{n} x_i^2}\right) + 0.1\sqrt{\sum_{i=1}^{n} x_i^2}$	0
F23	Yang 4	30	$[-10, 10]^D$	$f_{23}(x) = \left(\sum_{i=1}^{n} sin^2(x_i)\right)e^{\left(-\sum_{i=1}^{n} sin^2\sqrt{\|x_i\|}\right)}$	-1

Results and Discussion

To find the best parameter values, 23 different comparison functions were applied to the GEO algorithm. The best values obtained for the unimodal benchmark functions solution are given in Table 3-4. The best values obtained for the solution of multimodal benchmark functions are given in Table 7-8. Convergence curves obtained for unimodal benchmark functions according to different attack and

cruise parameter values are given in Tables 5 and 6, and multimodal benchmark functions are given in Table 9-10.

Table 3. Best values of unimodal functions according to attack and cruise parameters

		Values of Parameters					
Func.	**Attack**		**0.5**			**1**	
	Cruise	**0.5**	**0.75**	**1**	**0.5**	**0.75**	**1**
F1	Best	1.52E-03	1.89E-14	6.23E-18	8.71E-05	3.52E-06	**0.00E+00**
F2	Best	3.85E-09	1.03E-51	1.16E-22	1.55E-13	4.59E-100	9.20E-77
F3	Best	2.53E-13	2.13E-66	2.18E-28	**5.87E-189**	5.44E-20	1.02E-96
F4	Best	-9.53E-01	**-1.00E+00**	**-1.00E+00**	-9.86E-01	**-1.00E+00**	**-1.00E+00**
F5	Best	-2.57E+00	-4.40E+00	-4.16E+00	-2.59E+00	-1.00E+00	-4.91E+00
F6	Best	8.23E+02	2.94E-04	6.71E-03	6.74E+02	4.35E-10	8.31E-13
F7	Best	4.57E+00	3.53E-07	3.49E-05	3.36E+00	1.03E-11	2.26E-15

Table 4. Best values of unimodal functions according to attack and cruise parameters

		Values of Parameters					
Func.	**Attack**		**1.5**			**2**	
	Cruise	**0.5**	**0.75**	**1**	**0.5**	**0.75**	**1**
F1	Best	**0.00E+00**	**0.00E+00**	**0.00E+00**	**0.00E+00**	**0.00E+00**	**0.00E+00**
F2	Best	**2.14E-140**	9.90E-103	1.94E-73	5.87E-103	7.92E-75	1.74E-54
F3	Best	6.67E-182	2.30E-143	1.07E-104	7.92E-136	2.01E-103	2.71E-73
F4	Best	**-1.00E+00**	**-1.00E+00**	**-1.00E+00**	**-1.00E+00**	**-1.00E+00**	**-1.00E+00**
F5	Best	-4.78E+00	**-4.94E+00**	-4.77E+00	-4.86E+00	-4.76E+00	-4.37E+00
F6	Best	4.52E-09	**3.53E-14**	7.99E-10	1.43E-10	2.19E-08	4.82E-04
F7	Best	5.77E-11	**2.31E-16**	7.20E-13	2.13E-12	3.52E-11	1.25E-06

Table 5. Convergence curves by parameter values for unimodal benchmark functions (A: Attack, C: Cruise)

Values of Parameters						
A	**0.5**			**1**		
C	**0.5**	**0.75**	**1**	**0.5**	**0.75**	**1**
F1	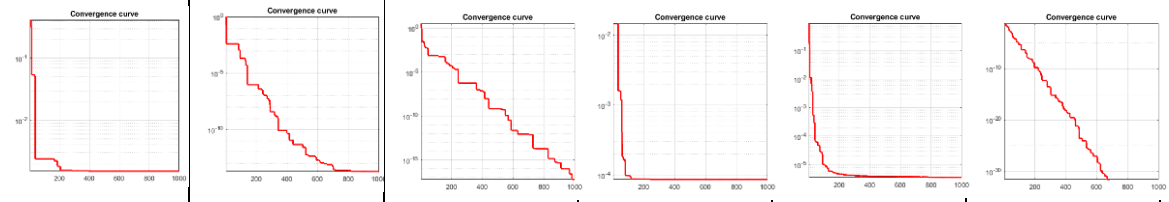					
F2	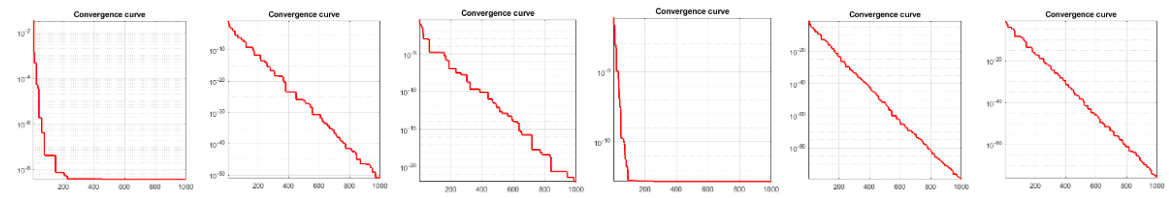					

F3	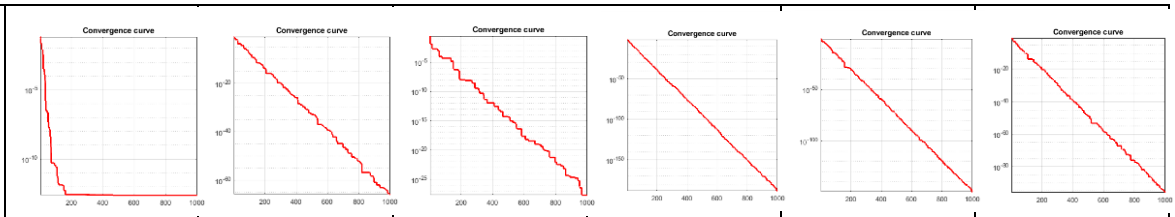
F4	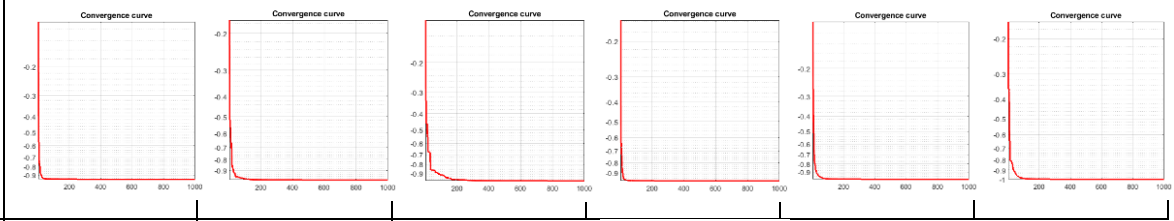
F5	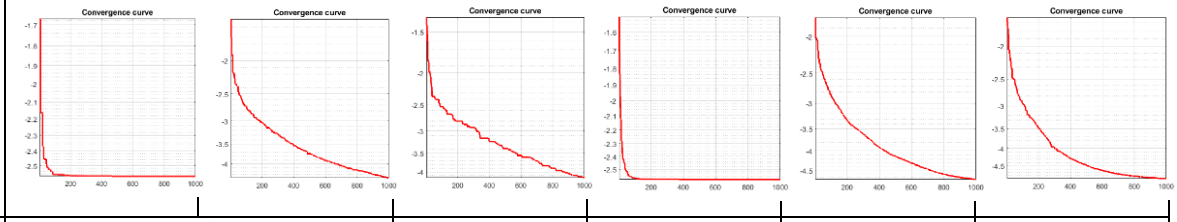
F6	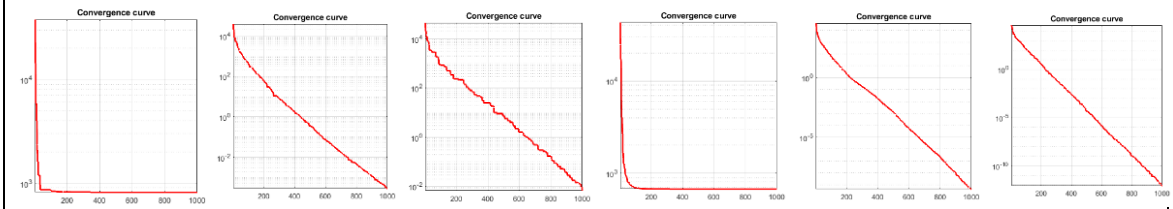
F7	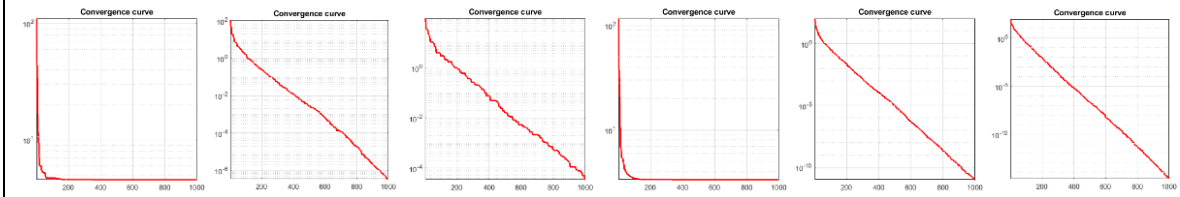

Table 6. Convergence curves by parameter values for unimodal benchmark functions (A: Attack, C: Cruise)

Values of Parameters						
A	**1.5**			**2**		
C	**0.5**	**0.75**	**1**	**0.5**	**0.75**	**1**
F1	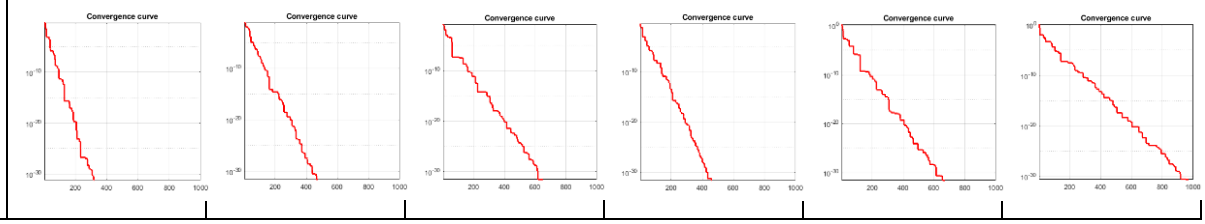					

F2	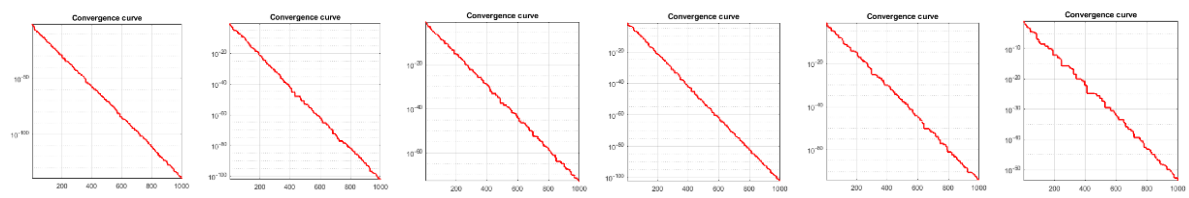					
F3	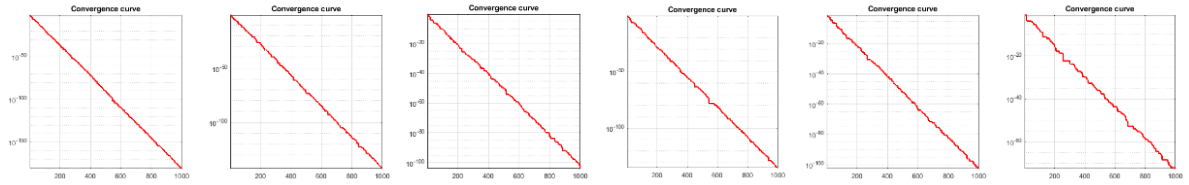					
F4	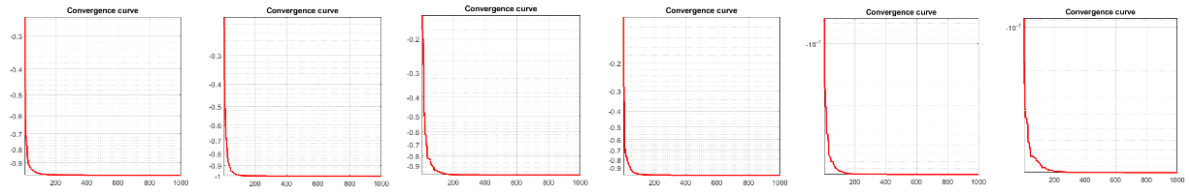					
F5	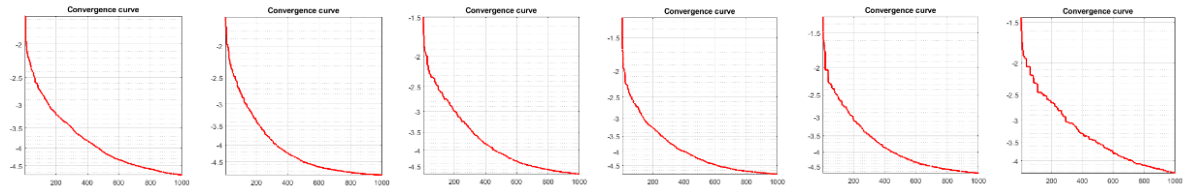					
F6	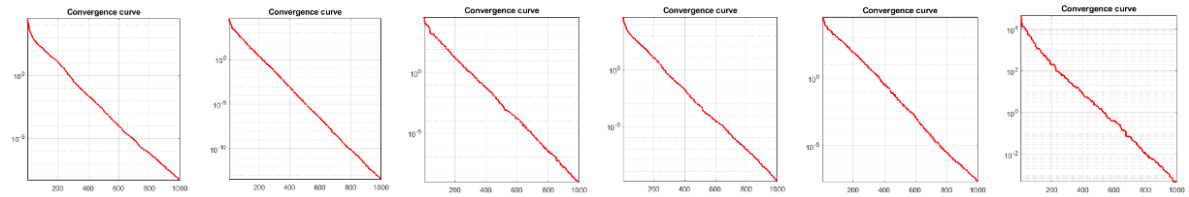					
F7	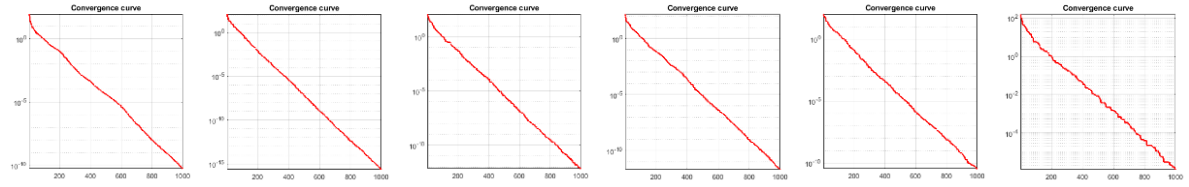					

When the results and convergence curves for the unimodal functions are examined, it is seen that the algorithm achieves the best value when the Attack and Cruise parameters are 1.5 and 0.75, respectively.

Table 7. Best values of multimodal functions according to attack and cruise parameters

		Values of Parameters					
Func.	**Attack**		**0,5**			**1**	
	Cruise	**0,5**	**0,75**	**1**	**0,5**	**0,75**	**1**
F8	Best	**-1.00E+00**	**-1.00E+00**	**-1.00E+00**	**-1.00E+00**	**-1.00E+00**	**-1.00E+00**
F9	Best	-9.12E+02	**-9.60E+02**	**-9.60E+02**	-8.95E+02	**-9.60E+02**	**-9.60E+02**
F10	Best	3.11E-08	**0.00E+00**	3.64E-03	**0.00E+00**	**0.00E+00**	**0.00E+00**
F11	Best	7.65E-08	**1.35E-31**	1.97E-19	4.16E-10	9.56E-29	**1.35E-31**
F12	Best	6.75E+00	2.32E+00	3.82E-02	6.25E+00	2.32E+00	3.65E-07
F13	Best	5.19E+01	3.06E-02	9.29E-02	3.21E+01	1.51E-02	8.10E-08
F14	Best	**1.83E-01**	2.94E-01	3.19E-01	2.44E-01	2.27E-01	2.46E-01
F15	Best	-7.14E+00	-8.68E+00	-6.05E+00	-8.95E+00	**-9.31E+00**	-8.57E+00
F16	Best	6.22E+00	7.35E-01	2.66E-03	3.92E+00	1.03E+00	2.09E-01
F17	Best	5.93E+01	4.38E-03	4.06E-03	3.54E+01	7.22E-03	1.10E-02
F18	Best	7.42E+00	7.32E+00	5.47E+00	7.26E+00	6.71E+00	3.97E+00
F19	Best	2.86E+07	2.87E+02	1.56E+03	1.52E+07	1.39E+00	2.19E-01
F20	Best	1.16E+02	1.15E+01	1.80E+02	7.63E+01	**1.09E+01**	2.09E+01
F21	Best	3.81E+04	4.35E+00	1.12E+02	1.83E+04	**2.39E+00**	6.91E+01
F22	Best	2.70E+00	4.00E-01	3.00E-01	3.20E+00	6.00E-01	**2.00E-01**
F23	Best	1.49E-11	2.63E-11	3.75E-11	7.17E-12	5.53E-21	6.14E-24

Table 8. Best values of multimodal functions according to attack and cruise parameters

		Values of Parameters					
Func.	**Attack**		**1.5**			**2**	
	Cruise	**0.5**	**0.75**	**1**	**0.5**	**0.75**	**1**
F8	Best	**-1.00E+00**	**-1.00E+00**	**-1.00E+00**	**-1.00E+00**	**-1.00E+00**	**-1.00E+00**
F9	Best	**-9.60E+02**	**-9.60E+02**	**-9.60E+02**	**-9.60E+02**	**-9.60E+02**	**-9.60E+02**
F10	Best	**0.00E+00**	**0.00E+00**	**0.00E+00**	**0.00E+00**	**0.00E+00**	**0.00E+00**
F11	Best	**1.35E-31**	**1.35E-31**	**1.35E-31**	**1.35E-31**	**1.35E-31**	**1.35E-31**
F12	Best	3.98E+00	**5.78E-08**	1.54E-05	8.68E-04	9.31E-01	9.30E-03
F13	Best	7.48E-03	**8.09E-09**	5.88E-06	9.86E-03	4.67E-05	1.80E-02
F14	Best	4.18E-01	2.77E-01	4.10E-01	2.37E-01	3.21E-01	2.19E-01
F15	Best	-9.13E+00	-9.24E+00	-8.94E+00	-8.35E+00	-8.77E+00	-7.67E+00
F16	Best	1.53E-01	1.04E-01	1.46E-07	**1.15E-07**	1.90E-07	1.15E-03
F17	Best	1.10E-02	**2.42E-10**	1.98E-07	6.91E-09	3.10E-07	7.00E-04
F18	Best	**1.56E+00**	1.58E+00	1.93E+00	1.98E+00	2.28E+00	1.80E+00
F19	Best	8.10E-01	**3.39E-03**	2.88E-01	3.08E-01	2.18E+00	6.07E+01
F20	Best	1.39E+01	4.38E+01	4.38E+01	3.88E+01	2.49E+01	1.44E+02
F21	Best	8.08E+01	6.85E+01	2.21E+01	5.48E-01	1.06E+01	9.73E+01
F22	Best	1.10E+00	3.00E-01	3.00E-01	5.00E-01	3.00E-01	4.01E-01
F23	Best	6.70E-22	**5.48E-27**	3.84E-21	4.02E-22	2.37E-19	3.07E-16

Table 9. Convergence curves by parameter values for multimodal benchmark functions (A: Attack, C: Cruise)

Values of Parameters						
A	**0.5**			**1**		
C	**0.5**	**0.75**	**1**	**0.5**	**0.75**	**1**
F8	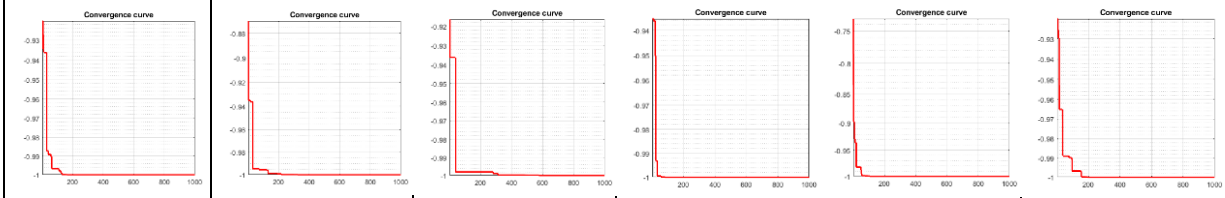					
F9	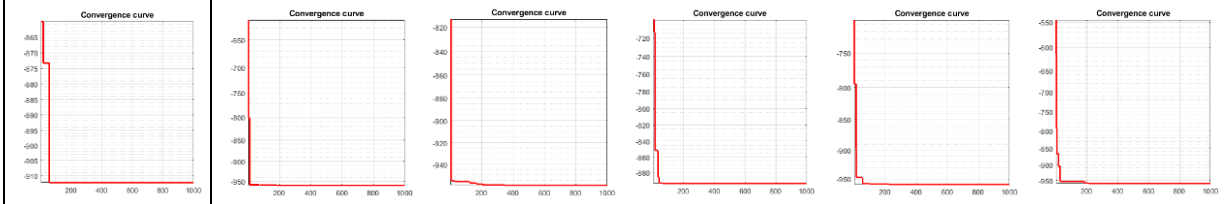					
F10	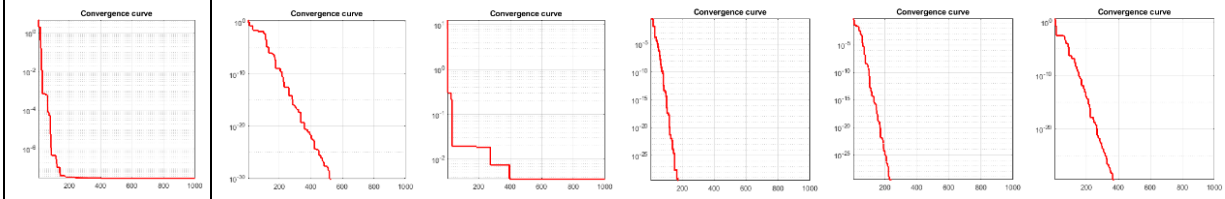					
F11	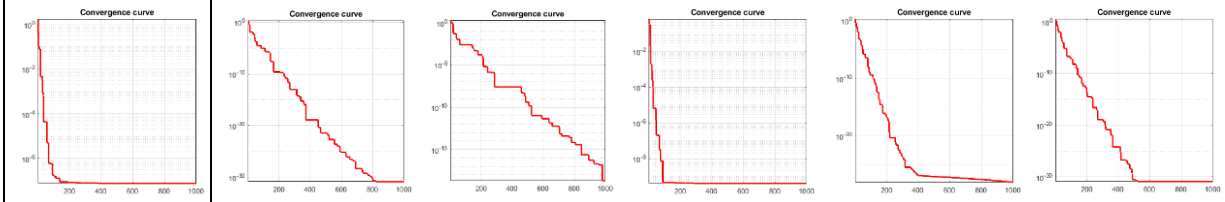					
F12	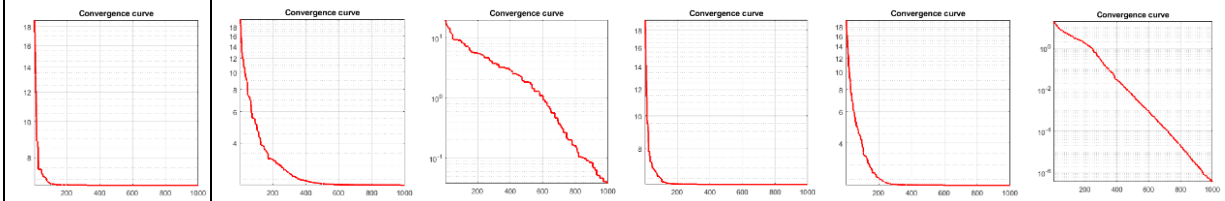					
F13	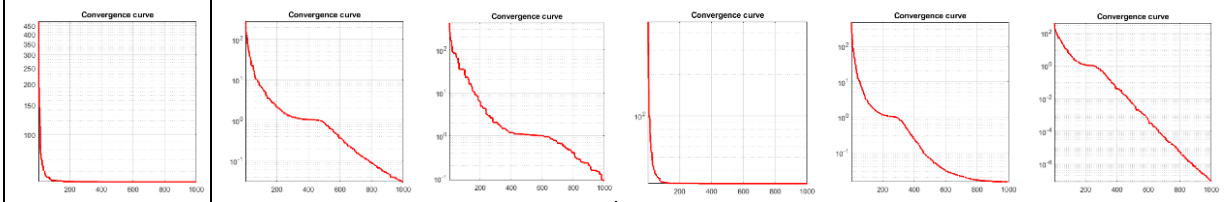					

F14	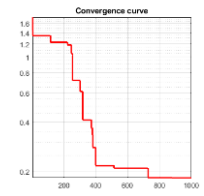	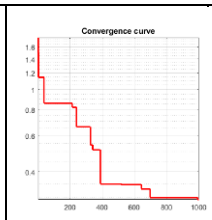	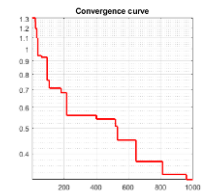	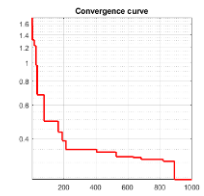	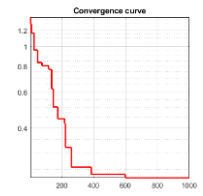	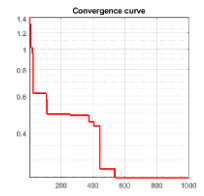
F15	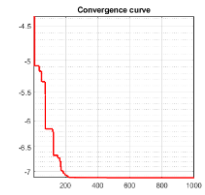	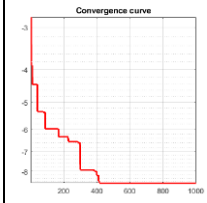	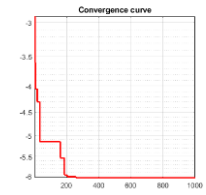	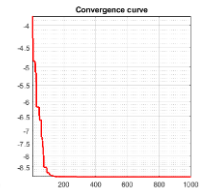	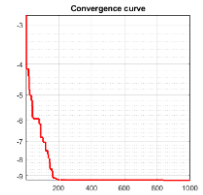	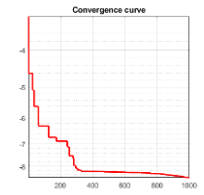
F16	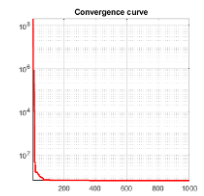	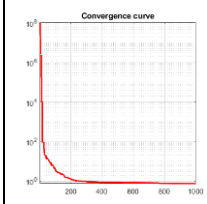	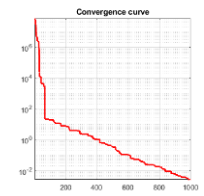	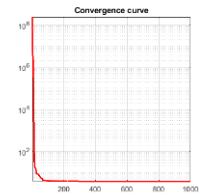	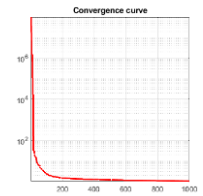	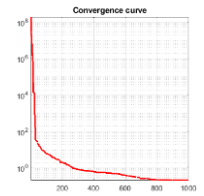
F17	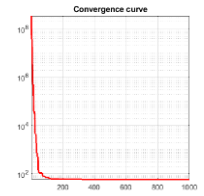	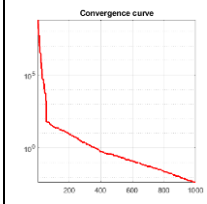	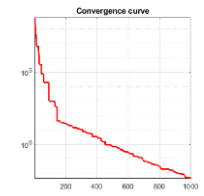	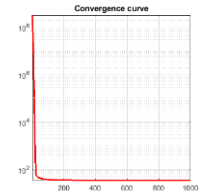	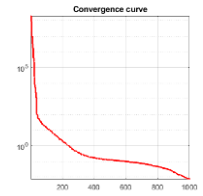	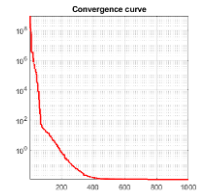
F18	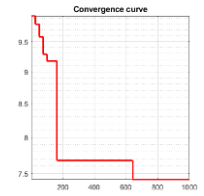	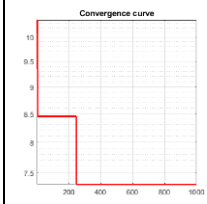	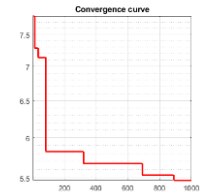	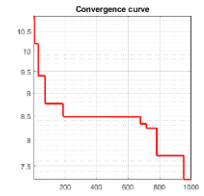	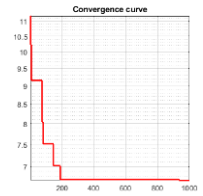	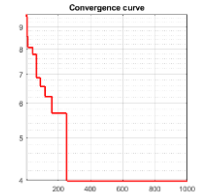
F19	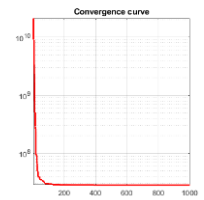	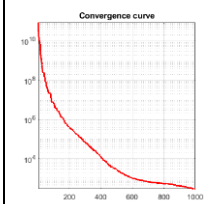	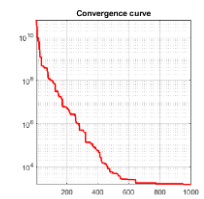	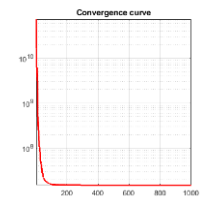	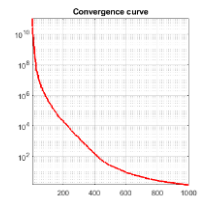	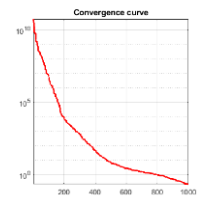
F20	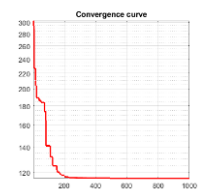	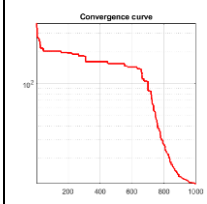	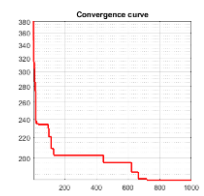	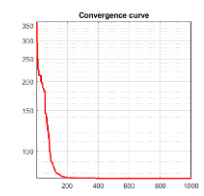	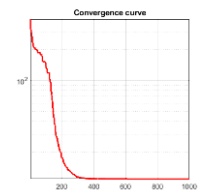	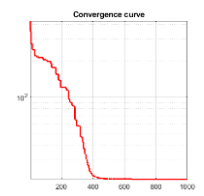

F21	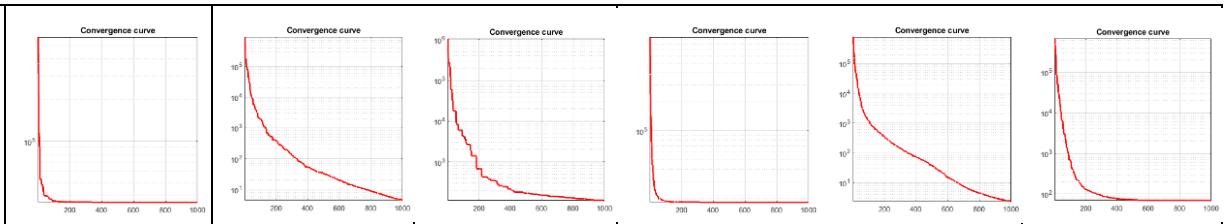					
F22	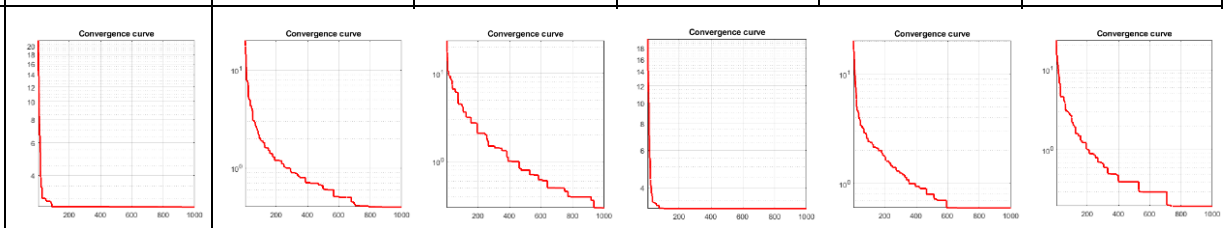					
F23	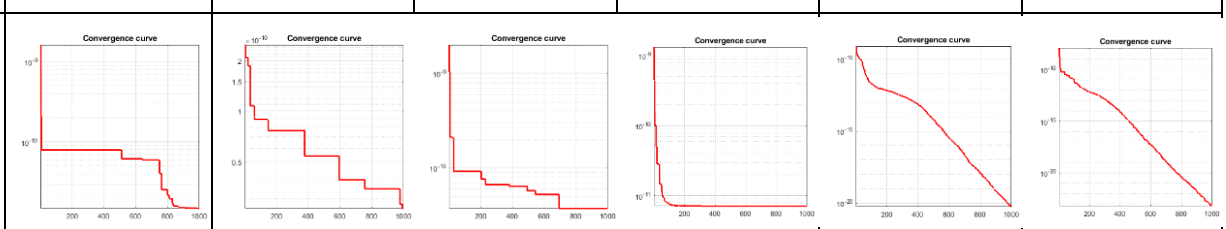					

Table 10. Convergence curves by parameter values for multimodal benchmark functions (A: Attack, C: Cruise)

Values of Parameters						
A	**1.5**			**2**		
C	**0.5**	**0.75**	**1**	**0.5**	**0.75**	**1**
F8	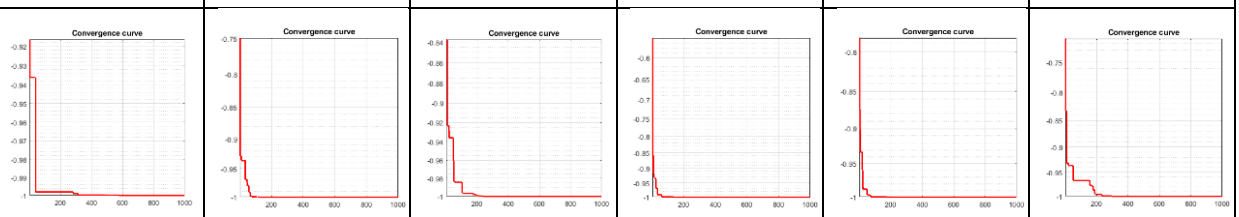					
F9	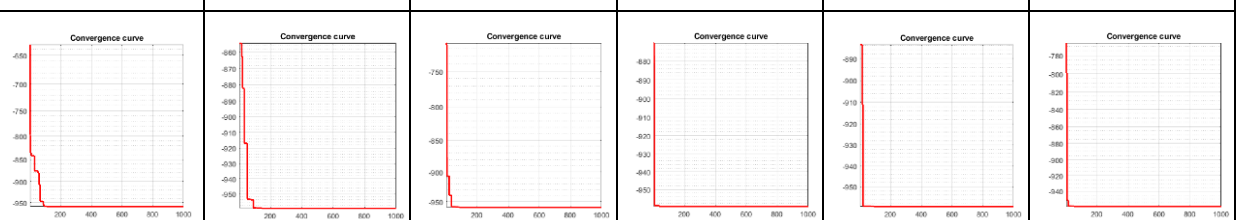					
F10	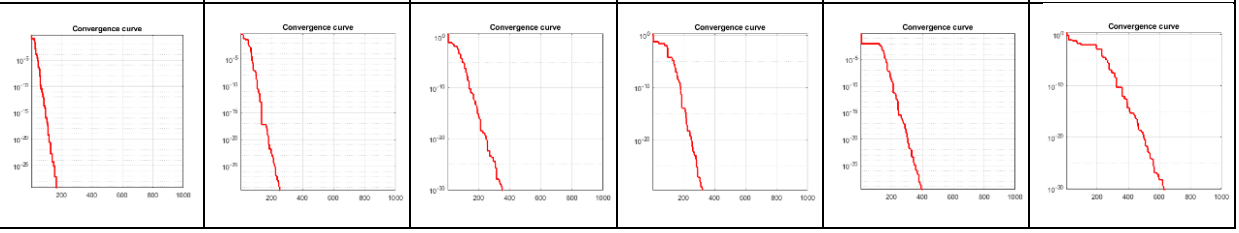					

F11	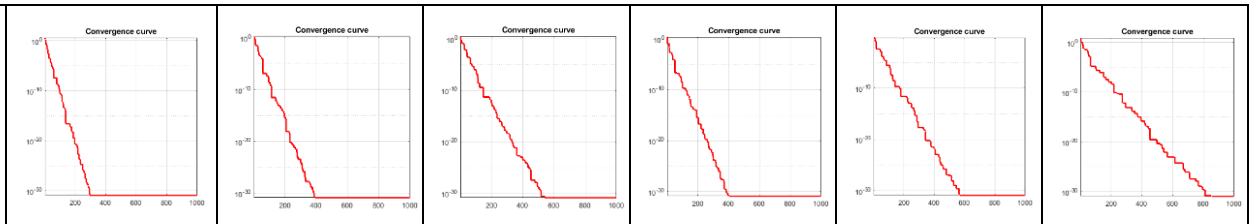					
F12	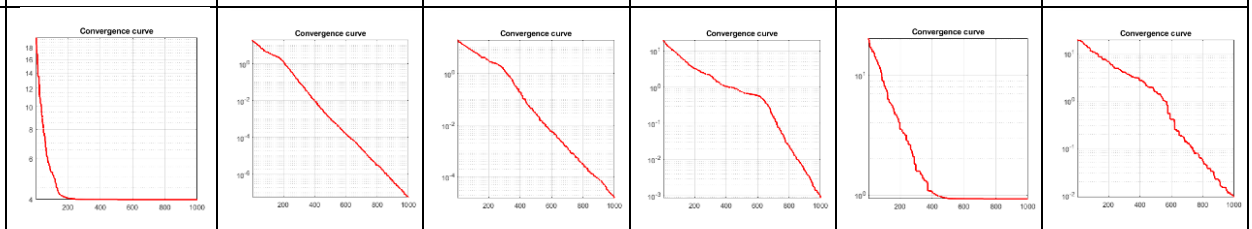					
F13	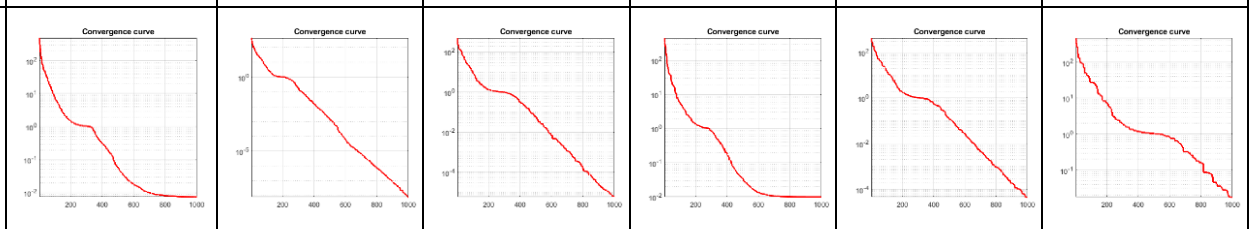					
F14	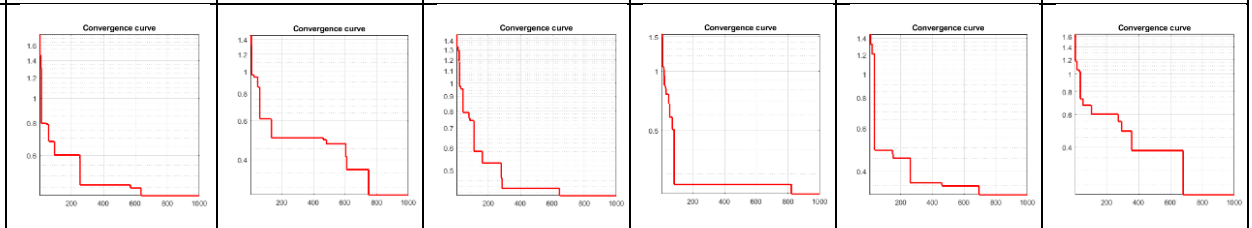					
F15	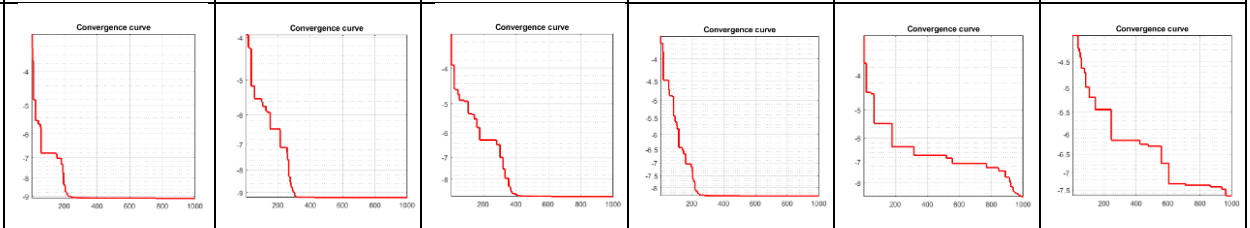					
F16	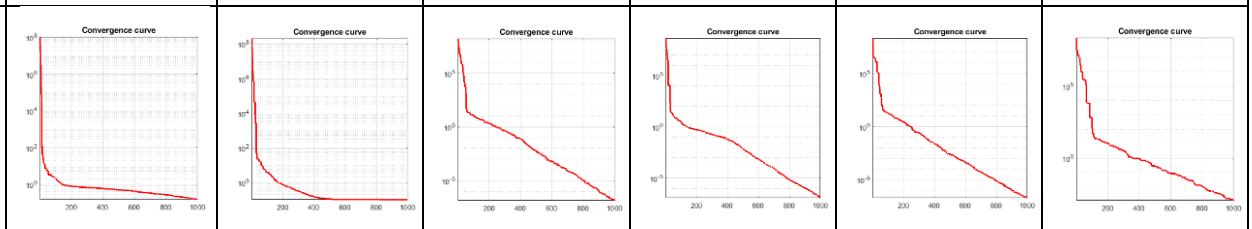					
F17	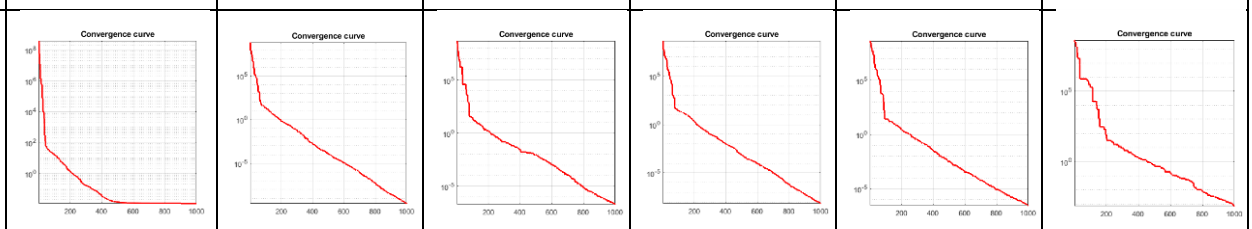					
F18	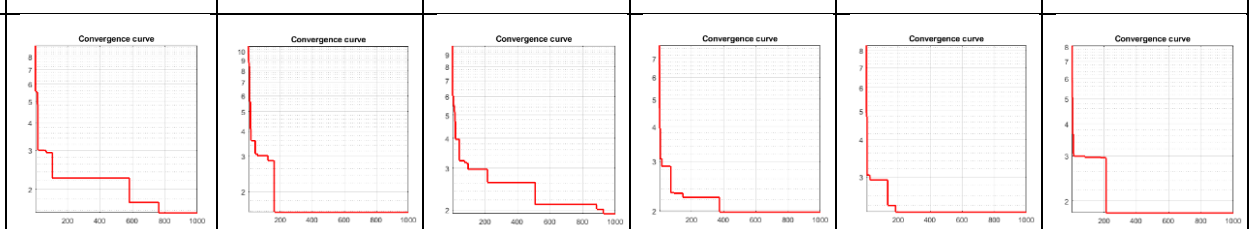					

F19	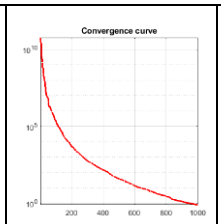	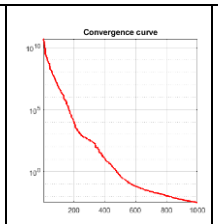	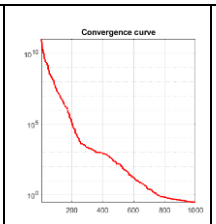	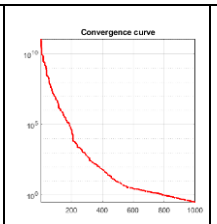	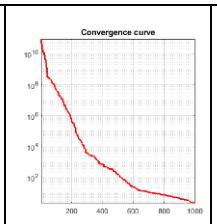	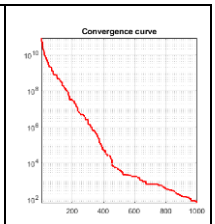
F20	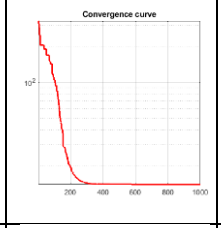	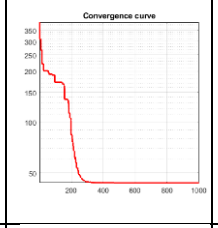	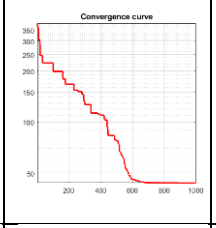	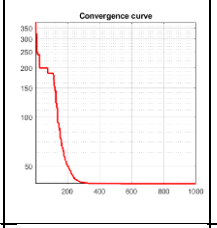	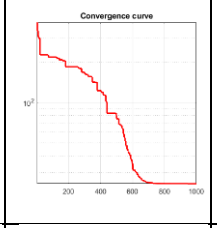	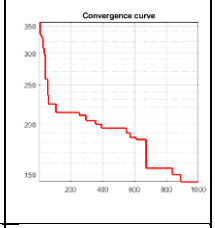
F21	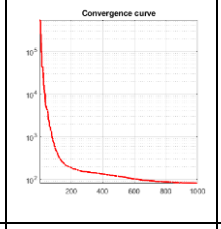	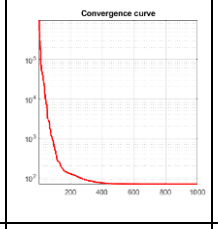	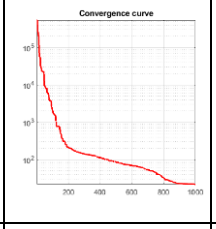	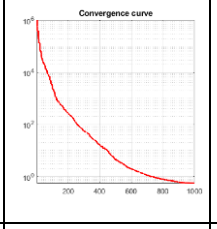	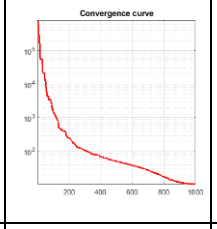	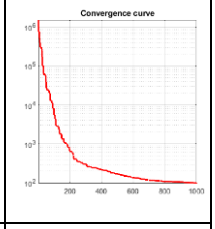
F22	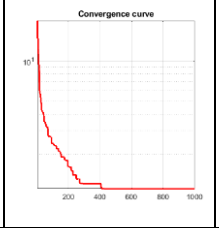	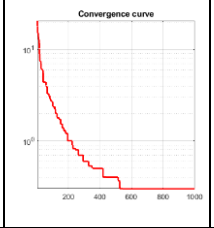	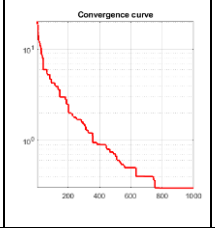	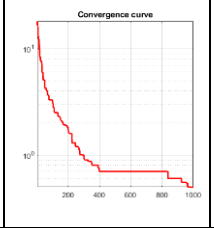	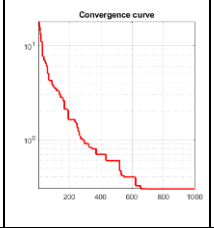	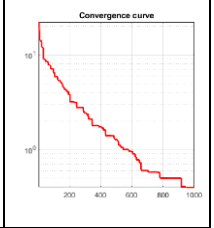
F23	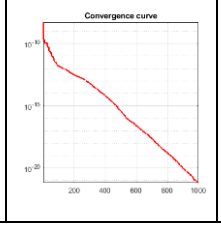	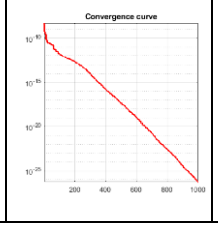	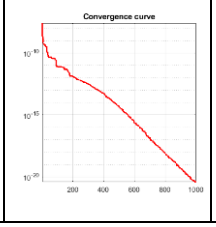	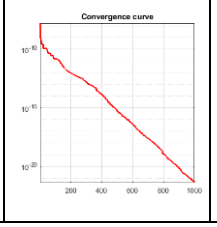	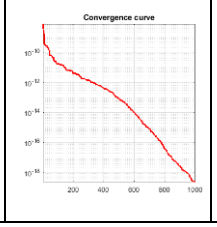	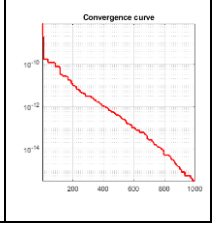

When the results and convergence curves for the multimodal functions are examined, it is seen that the algorithm achieves the best value when the Attack and Cruise parameters are 1.5 and 0.75, respectively.

In this study, cruise and attack parameters of the GEO algorithm are optimized using unimodal and multimodal benchmark functions. In Table 3 and Table 4, rank analysis based on the number of functions in which unimodal benchmark functions are successful is performed. In Figure 3, rank success numbers for Unimodal benchmark functions are given. According to the rank analysis, when the attack parameter of the GEO algorithm is 1.5 and the cruise parameter is 0.75, it is seen in Figure 3 that the best values are obtained in unimodal functions.

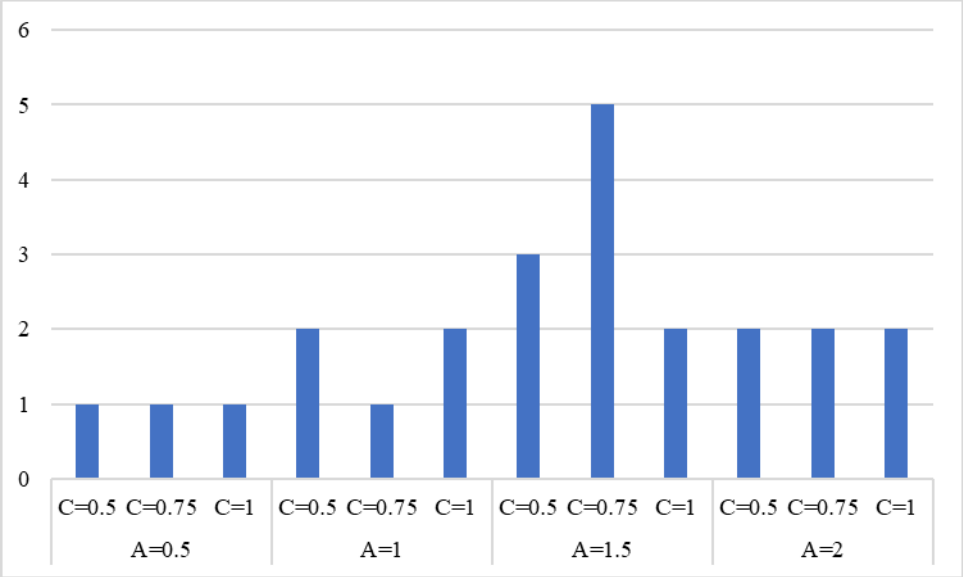

Figure 3. Rank Analyses for Unimodal Benchmark Functions (A: Attack, C: Cruise)

In Table 7 and Table 8, rank analysis based on the number of functions in which the multimodal benchmark functions were successful was performed. In Figure 4, rank success numbers for Multimodal benchmark functions are given. According to the rank analysis, when the attack parameter of the GEO algorithm is 1.5 and the cruise parameter is 0.75, it is seen in Figure 4 that the best values are obtained in multimodal functions.

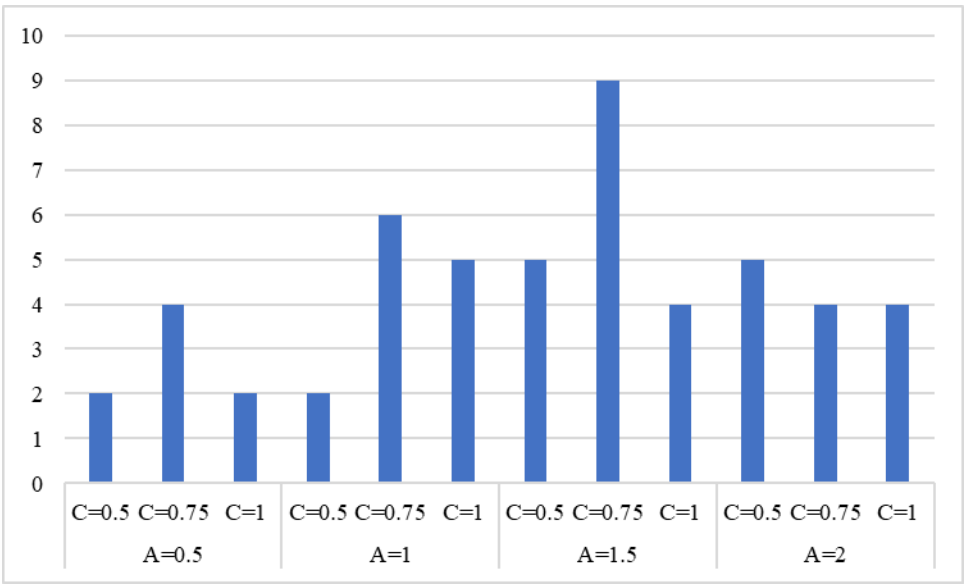

Figure 4. Rank Analyses for Multimodal Benchmark Functions (A: Attack, C: Cruise)

In the original article of the GEO algorithm, it was stated that the lowest objective function value was obtained in the range of attack parameter [0.5-2.0] and cruise parameter [1.0-0.5] (Mohammadi-Balani et al., 2021). The parameter values of GEO are taken as linear increasing for attack parameter and

linear decreasing for cruise parameter (Mohammadi-Balani et al., 2021). However, in this study, it is proved both in the tables and in Figures 3 and 4 that better results are obtained if the attack parameter is 1.5 and the cruise parameter is 0.75.

Conclusion

In this study, the best parameter value for the benchmark functions of the attack and cruise parameters of the golden eagle's optimization (GEO) algorithm is calculated. An evaluation was made according to the effect of these parameters on the functions. The attack parameter of the algorithm is between [0-2] and the cruise parameter is between [0-1]. As a result of the calculation on the functions of the algorithm, it is seen that the attack parameter is 0.75 and the cruise parameter is 1.5, and it is the best. The algorithm achieved the best results in both unimodal functions and multimodal functions at the specified parameter values. Separate convergence plots were found to be the best in these results. In the rank analysis, it has been determined that the GEO algorithm attack and cruise parameters are more successful in benchmark functions when they are 0.75 and 1.5, respectively. As a result, it is recommended that the golden eagles optimization algorithm achieves the best result in these parameter values and it is recommended to use these parameter values in overnight studies. In the next studies, it is aimed to solve real world problems by making improvements on the algorithm by using this parameter value and providing a performance shot.

Statement of Conflict of Interest

Authors have declared no conflict of interest.

Author's Contributions

The contribution of the authors is equal.

*This study was presented as a summary paper at the International Conference on Engineering, Natural and Applied Sciences (ICENAS'21) held online on 24-26 November 2021.

References

Abdel-Basset M., Mohamed R., Elkomy OM., Abouhawwash M. Recent metaheuristic algorithms with genetic operators for high-dimensional knapsack instances: A Comparative study. Computers & Industrial Engineering 2022; 166: 107974.

Akay B., Karaboga D. A Modified artificial bee colony algorithm for real-parameter optimization. Information sciences 2012; 192: 120-142.

Beşkirli A., Dağ İ. An efficient tree seed inspired algorithm for parameter estimation of Photovoltaic models. Energy Reports 2022; 8: 291-298.

Beşkirli A., Dağ İ. A new binary variant with transfer functions of Harris Hawks Optimization for binary wind turbine micrositing. Energy Reports 2020; 6: 668-673.

Beşkirli A., Özdemir D., Temurtaş H. A comparison of modified tree–seed algorithm for high-dimensional numerical functions. Neural Computing and Applications 2020; 32(11): 6877-6911.

Brest J., Maučec MS., Bošković B. Single objective real-parameter optimization: Algorithm jSO. IEEE congress on evolutionary computation (CEC), 5-8 June 2017, Donostia, Spain.

Brest J., Zamuda A., Boskovic B., Maucec MS., Zumer V. High-dimensional real-parameter optimization using self-adaptive differential evolution algorithm with population size reduction. IEEE Congress on Evolutionary Computation (IEEE World Congress on Computational Intelligence), 1-6 June 2008, Hong Kong, China.

Cicirello VA., Smith SF. Modeling GA performance for control parameter optimization. Proceedings of the Genetic and Evolutionary Computation Conference, 1-5 July 2000, Pittsburgh, USA.

Grefenstette JJ. Optimization of control parameters for genetic algorithms. IEEE Transactions on systems man Cybernetics 1986; 16(1): 122-128.

Ilango R., Rajesh P., Shajin FH. S2NA-GEO method–based charging strategy of electric vehicles to mitigate the volatility of renewable energy sources. International Transactions on Electrical Energy Systems 2021; 31(12): e13125.

Joshi SS., Biradar SR. A Novel golden eagle optimizer based trusted ad hoc on-demand distance vector (GEO-TAODV) routing protocol. International Journal of Computer Networks and Applications 2021; 8(5): 538-548.

Luo F., Zhao J., Dong ZY. A new metaheuristic algorithm for real-parameter optimization: natural aggregation algorithm. IEEE Congress on Evolutionary Computation (CEC), 24-29 July 2016, Vancouver, BC, Canada.

Michalewicz Z., Schoenauer M. Evolutionary algorithms for constrained parameter optimization problems. Evolutionary computation 1996; 4(1): 1-32.

Mohammadi-Balani A., Nayeri MD., Azar A., Taghizadeh-Yazdi M. Golden eagle optimizer: A nature-inspired metaheuristic algorithm. Computers Industrial Engineering, 2021; 152: 107050.

Pan JS., Lv JX., Yan LJ., Weng SW., Chu SC., Xue JK. Golden eagle optimizer with double learning strategies for 3D path planning of UAV in power inspection. Mathematics and Computers in Simulation 2022; 193: 509-532.

Rao R. V., Savsani V., Balic J. Teaching–learning-based optimization algorithm for unconstrained and constrained real-parameter optimization problems. Engineering Optimization 2012; 44(12): 1447-1462.

Salimian S., Mousavi S. A new intuitionistic fuzzy multi-criteria decision-making method for designing organ transplantation supply chain network problem: Golden eagle metaheuristic

algorithm. Journal of Industrial Engineering Research in Production Systems 2021; 9(18): 179-195.

Vijh S., Kumar S., Saraswat M. Efficient feature selection method for histopathological images using modified golden eagle optimization algorithm. 9th International Conference on Reliability, Infocom Technologies and Optimization (Trends and Future Directions)(ICRITO), 3-4 September 2021, Noida, India.

Zhangqi W., Xiaoguang Z., Qingyao H. Mobile robot path planning based on parameter optimization ant colony algorithm. Procedia Engineering 2011; 15: 2738-2741.

OKÜ Fen Bilimleri Enstitüsü Dergisi
5(Özel Sayı):252-261, 2022

OKU Journal of The Institute of Science and Technology, 5(Special Issue):252-261, 2022

Osmaniye Korkut Ata Üniversitesi Fen Bilimleri Enstitüsü Dergisi

Osmaniye Korkut Ata University Journal of The Institute of Science and Technology

Improving Emissions by An Auxiliary Air Conditioner in Liquid Hydrogen Powered Spark Ignition Engine Vehicles

Adem UGURLU[1*]

[1]Kırklareli University, Technology Faculty, Department of Mechatronics Engineering, 39000, Kırklareli.

[1]https://orcid.org/ 0000-0002-9531-3944
*Corresponding author: adem.ugurlu@klu.edu.tr

Research Article

Article History:
Received: 11.12.2021
Accepted: 20.01.2022
Published online: 23.02.2022

Keywords:
Liquid hydrogen
Air conditioning
Vehicles
Emissions

ABSTRACT

An Auxiliary Air Conditioner (AAC) system, which decreases the cabin air conditioning load of Liquid Hydrogen (LH_2) powered Spark Ignition Internal Combustion Engine Vehicles (SI ICEV), has been proposed in this study. Volatile Organic Compounds (VOC), Carbon Monoxide (CO), Nitrogen Oxides (NO_x), Particulate Matters (PM_{10} & $PM_{2.5}$), Sulfur Oxides (SO_x), and Carbon Dioxide (CO_2) emissions are theoretically calculated using GREET software developed by Argonne National Laboratory for decades between 2010 and 2050. The results of the study show that the proposed novel system decreases all emissions emitted from LH_2 SI ICEVs decreasing both Well-To-Pump (WTP) and Well-To-Wheel (WTW) emissions. These decreases are around 3 g/year for VOC, 20 g/year for CO, 13 g/year for NO_x, 1 g/year for both PM_{10} and $PM_{2.5}$, 1 g/year for SO_x, and 16 kg/year for CO_2.

Yardımcı Klima Kullanımı ile Sıvı Hidrojenle Çalışan Buji Ateşlemeli Motorlu Taşıtlarda Emisyonların İyileştirilmesi

Araştırma Makalesi

Makale Tarihçesi:
Geliş tarihi: 11.12.2021
Kabul tarihi:20.01.2022
Online Yayınlanma: 23.02.2022

Anahtar Kelimeler:
Sıvı hidrojen
Klima
Taşıtlar
Emisyonlar

ÖZET

Bu çalışmada, sıvı hidrojen (LH_2) ile çalışan buji ateşlemeli içten yanmalı motorlu taşıtların (SI ICEV) kabin klima yükünü azaltan bir yardımcı klima (AAC) sistemi önerilmiştir. Uçucu organik bileşikler (VOC), karbon monoksit (CO), azot oksitler (NO_x), partikül maddeler (PM_{10} & $PM_{2.5}$), kükürt oksitler (SO_x) ve karbon dioksit (CO_2) emisyonları, Argonne ulusal laboratuvarı tarafından geliştirilen GREET yazılımı kullanılarak 2010 ve 2050 yılları arasındaki her on yıl için teorik olarak hesaplanmıştır. Çalışmanın sonuçları, önerilen yeni sistemin LH_2 SI ICEV'lerden yayılan tüm emisyonları azalttığını ve hem kuyudan pompaya (WTP) hem de kuyudan tekerleğe (WTW) emisyonlarını azalttığını göstermektedir. Bu azalmalar VOC için 3 g/yıl, CO için 20 g/yıl, NO_x için 13 g/yıl, PM_{10} ve $PM_{2.5}$ için 1 g/yıl, SO_x için 1 g/yıl ve CO_2 için 16 kg/yıl civarındadır.

To Cite: Uğurlu A. Improving Emissions by An Auxiliary Air Conditioner in Liquid Hydrogen Powered Spark Ignition Engine Vehicles. Osmaniye Korkut Ata Üniversitesi Fen Bilimleri Enstitüsü Dergisi 2022; 5(Özel sayı): 252-261.

Introduction

Due to strict emission regulations and increasing energy demands, there has been great progress in the field of alternative fuels in recent years (Ciniviz and Köse, 2011; Tüccar et al., 2013; Akar et al., 2018). With its efficient and non-polluting nature, hydrogen is one of the first ones that come to mind

of these alternative fuels. Since there is naturally no carbon content in hydrogen fuel, emissions from the combustion of hydrogen in an internal combustion engine are water vapor and some NO_x gas if the combustion temperature is too high (Baltacioglu et al., 2016; Ozcanli et al., 2017; Ozcanli et al., 2018). Another important advantage of hydrogen, apart from the absence of carbon in its content, is its high mass-energy density. But, there are some problems preventing the intensive use of hydrogen as a fuel in vehicles, such as production costs, storage challenges, embrittlement and percolation issues in the hydrogen fuel lines and hydrogen tanks (Serin and Yıldızhan, 2018). It is estimated that these problems will be eliminated in time with the help of academic studies and market requests.

Since hydrogen liquefaction is a better way of storing hydrogen (Ansarinasab et al., 2017), the liquid form of hydrogen is used in several hydrogen applications. For instance, many hydrogen-powered vehicles use gaseous hydrogen, some examples like BMW 750hl and BMW Mini Hydrogen utilize hydrogen fuel in liquid form. Gasification of LH_2 results in waste of energy, which can be possibly used in refrigeration needs at a small cost with auxiliary equipment in those applications. One of the areas where this applies is Vehicle Air Conditioning (VAC) systems. Considering the comfort functions and safety, an Air Conditioning (AC) system is one of the vital systems of vehicles. But, due to the significant power consumption of mechanical compressors in AC systems, fuel consumption increases in vehicles. And this increase can be as much as around 12-17% due to the conditions such as driver factors, environmental factors, and road factors for mid-size and subcompact cars Lambert and Jones (2006), and Khayyam (2013) report in their studies. For this reason, decreasing the energy consumption of a VAC system will maintain to improve the vehicle's overall energy efficiency. To improve the energy efficiency of VAC systems, many methods and systems have been proposed so far. Several of these methods and systems include alternative systems to the conventional vapor compression cycles (Jiang et al., 2018; Gillet et al., 2018), new designs of compressors (Yang et al., 2017; Dahlan et al., 2014) and evaporators (Zhang and Canova, 2015), alternative driving sources to the engine of the vehicle (Pang et al., 2019), and some control methods such as PID (Zhang et al., 2010; Khayyam et al., 2011a), rule based (Khayyam et al., 2009), and fuzzy (Thompson and Dexter, 2005; Calvino et al., 2004; Sousa et al., 1997; Farzaneh and Tootoonchi, 2008; Khayyam et al., 2011b).

In this study, the use of an AAC in LH_2-powered SI ICEVs has been investigated on emission basis. The proposed system provides gaseous hydrogen for both powers for the engine and cooling for air conditioning. The analyses were conducted for the vehicles with and without the AAC in GREET software. Emission reductions were calculated for different scenarios of vehicle and fuel production technologies between 2010 and 2050. VOC, CO, NO_x, PM_{10}, $PM_{2.5}$, SO_x, and CO_2 emissions were compared for an average car specified in the software.

Methodology

The proposed AAC system has two main circuits: air and hydrogen. Hydrogen circuit supplies hydrogen fuel for spark-ignition internal combustion engine of the vehicle. The air circuit maintains cooling for the cabin of the vehicle. Temperature decrease of the air is established by the latent heat of the hydrogen passing through the evaporator part of the system and reducing the cabin cooling load of the vehicle. The more hydrogen flows to power the vehicle, the more cooled-down air is supplied to cool down the vehicle cabin. Hydrogen is stored in liquid form in the cryogenic tank under pressure. Gaseous hydrogen at atmospheric pressure is required by the engine. A pressure regulator reduces the hydrogen pressure. This pressure regulation step is followed by an evaporation process. Hydrogen is evaporated in an evaporator by an air flow blown along the outer surfaces of the evaporator. To decrease the AC cooling load, the cooled-down air is directed to the vehicle passenger compartment. This cooling load highly depends on the environmental factors such as: outside temperature and humidity, number of passengers, and sun light, etc.

Analyses of the emissions from LH_2-powered SI ICEVs with and without the AAC system have been performed according to the equations from Eq. (1) to Eq. (6) as follows. Eq. (1) gives the calculation method of the average gasoline consumption (L/s) of a gasoline-powered SI ICEV. FC_g (L/100 km) is determined according to the New European Driving Cycle (NEDC) and given by the vehicle manufacturers. The vehicle takes away of 11.007 km during the NEDC cycle in 1180 s (Pacheco et al., 2013). In this study, analyses of LH_2-powered SI ICEVs have been conducted using FC_g values between 0 and 30 L/100 km as consists to vehicles on the market. Therefore, values of $\dot{v}_g$ at different conditions can be calculated, and a simple comparison between gasoline-powered SI ICEV and LH_2-powered SI ICEVs can be establish through the analysis.

$$\dot{v}_g = \frac{\frac{FC_g \times 11.007}{100}}{1180} \quad (1)$$

The average gasoline consumption is calculated as seen from Eq. (2) in mass flow rate ($\dot{m}_g$) using ρ_g, which is the average density of gasoline. ρ_g is taken as between 0.72-0.78 kg/L from the literature (Cengel and Boles, 2005).

$$\dot{m}_g = \dot{v}_g \times \rho_g \quad (2)$$

Approximate vehicle hydrogen consumption is calculated using the equivalent heating value rate of gasoline and hydrogen ($r_{HV,h/g}$) as seen in Eq. (3) in mass flow rate ($\dot{m}_h$). Arithmetic means of lower heating values and higher heating values for both hydrogen and gasoline were calculated in this equivalent rate. Lower and higher heating values for gasoline are 44,000 kJ/kg and 47,300 kJ/kg, and they are 120,000 kJ/kg and 141,800 kJ/kg for hydrogen (Cengel and Boles, 2005). Since heating values of gasoline is lower than that of LH_2, the required amount of hydrogen mass flow rate is found approximately 0.3488 times lower than the mass flow rate of gasoline.

$$\dot{m}_h = \dot{m}_g \times r_{HV,h/g} \tag{3}$$

Eq. (4) shows how to calculate the cooling capacity of the system maintaining the liquid hydrogen to the engine at the exact amount. In this equation, $\dot{Q}_c$ presents the cooling amount (kJ/s) that the system absorbs from the air to be blown to the vehicle cabin, $\dot{m}_h$ is the approximate hydrogen mass flow rate (kg/s), and $h_{fg,h}$ is the enthalpy of vaporization (kJ/kg) of hydrogen. $h_{fg,h}$ is taken as 446 kJ/kg from the literature (Cengel and Boles, 2005). The formula gives results for the system that it works at 100% efficiency. Calculations are also maintained as if the system runs at 75%, 50%, and 25% efficiencies as well.

$$\dot{Q}_c = \dot{m}_h \times h_{fg,h} \tag{4}$$

The next part of the analysis includes COP calculation of the system as Eq. (5) shows. COP_R is the measurement of the system that is an air conditioning system in terms of performance. Peltier effect thermoelectric cooling is taken into consideration in the calculation of the COP value of the system. Thermoelectric coolers do not have compressors unlike conventional refrigerators and air conditioners. Similar to the thermoelectric coolers, the proposed system in this study includes no compressor, because they always have pressurized liquid hydrogen in their tanks. When the pressure of the liquid hydrogen becomes insufficient for the hydrogen flow, the tank is refilled with LH_2 in hydrogen fuel stations. It will be inconvenient to include the hydrogen consumption of the engine as the operating cost of the system in terms of energy consumption. The only energy the system consumes to create a cooling effect is the fan that circulates the air through the evaporator. The fan power (P_f) of the system used in the calculations is 24 W.

$$COP_R = \frac{\dot{Q}_c}{P_f} \tag{5}$$

AC savings (%) of the AAC system on vehicles at various cooling loads are calculated through Eq. (6). S_{AC} is the percent saving, $\dot{Q}_c$ is cooling capacity of the system (kW), and $\dot{L}_c$ is the cooling load of the vehicle (kW). $\dot{L}_c$ values are chosen according to the literature (Meier et al., 2018), which gives that

average cooling load values for standard, compact, and subcompact automobiles are 5.12 kW, 4.15 kW, and 3.62 kW, respectively. $\dot{L}_c$ values of vehicles are continuously variable values according to the factors such as the vehicle size, number of the occupants, and weather conditions. Therefore, 1 kW, 2 kW, 3 kW, 4 kW, 5 kW, and 6 kW values were taken to determine the AC saving values for different conditions. The study of Meier et al. (2018) is also compatible with those chosen values.

$$S_{AC} = \frac{\dot{Q}_c}{\dot{L}_c} \tag{6}$$

Finally, after the S_{AC} is determined for a variety of fuel consumptions, AAC efficiencies, and AC loads, reductions in the emissions are calculated and presented for years and vehicle technologies using an average value of S_{AC} together with the real values of emissions found out by running GREET software. At this stage, it was assumed that when the main AC system is turned on, it increases emissions by 15%. Among the calculated average S_{AC} values, it is taken as 2.7%. The average S_{AC} of the AAC system has been chosen by assuming the system is operating at 50% efficiency and the AC load of the vehicle is 3 kW.

Results and Discussion

For a gasoline consumption range of 0-30 L/100 km, gasoline-powered SI ICEVs have the highest hydrogen consumption of about 0.0007 kg/s. And this amount of hydrogen can supply 326 W cooling power to the cabin. The COP of this process will be 13.6. The amounts of cooling powers seem to be only enough at very low AC loads with humid weather and fewer occupants. When the AC load increases over the amounts of cooling capacities of the vehicles with this proposed system, it can only be used in the assistance of the main AC unit of the vehicle. The main air conditioner should operate at the rate which the air conditioning load exceeds the cooling capacity of the proposed system. According to the variations of AC savings in percent, on the other hand, the AAC system can decrease the AC load of the vehicle cabin up to the value of about 33% in 1 kW AC load with 100% efficiency operation of the system. This value is directly connected to the fuel consumption of the vehicle. When the fuel consumption decreases, the AAC system can assist the main AC system of the vehicle at a lower percentage. Averagely, if the AAC system operates at 50% efficiency, it can assist the main AC of the vehicle at 2.7% with a COP of 3.4. The average S_{AC} value of 2.7% will be used in the emissions calculations to find reductions when the AAC system is used in LH_2-powered SI ICEVs.

Table 1 shows VOC, CO, NO_x, PM_{10}, $PM_{2.5}$, SO_x, and CO_2 emissions from 2005, 2015, 2025, 2035, and 2045 model years LH_2-powered SI ICEVs with and without the AAC system in the years 2010, 2020, 2030, 2040, and 2050 according to GREET software and calculations are performed by using specified equations above. The AAC system reduces the AC load of the vehicles, thus decreasing fuel consumption, hence WTP emissions of the vehicles, which are given in g/km, decrease as well as

WTW emissions of the vehicles, which are operational emissions added to WTP emissions. As seen from Table 1, all the emissions decrease by year, thanks to the enhancements in both vehicle technologies and fuel production processes according to the scenarios in GREET. The decline in emissions is particularly evident between 2010 and 2020. Emissions between 2040 and 2050 remain almost the same. But, the proposed AAC system slightly decreases all emissions of SI ICEVs powered by LH_2 fuel due to the reduction in fuel consumptions of the vehicles. If we give the WTW emissions in the year 2010 as examples, these decreases are 3×10^{-4} g/km in VOC emissions, 21×10^{-4} g/km in CO emissions, 20×10^{-4} g/km in NO_x emissions, 3×10^{-4} g/km in PM_{10} emissions, 2×10^{-4} g/km in $PM_{2.5}$ emissions, 23×10^{-4} g/km in SO_x emissions, and 1.7 g/km in CO_2 emissions.

Table 1. Emissions of LH_2-powered SI ICEVs with and without the AAC system

Year	Vehicle	Emission	VOC [g/km]	CO [g/km]	NO_x [g/km]	PM_{10} [g/km]	$PM_{2.5}$ [g/km]	SO_x [g/km]	CO_2 [g/km]
2010	SI ICEV - LH_2 (2005)	WTP	0.0485	0.1281	0.3541	0.0683	0.0428	0.5707	416.2
		WTW	0.0768	0.5173	0.4829	0.0686	0.0431	0.5707	415.5
		WTP_{AAC}	0.0483	0.1276	0.3527	0.0680	0.0426	0.5684	414.5
		WTW_{AAC}	0.0765	0.5152	0.4809	0.0683	0.0429	0.5684	413.8
2020	SI ICEV - LH_2 (2015)	WTP	0.0348	0.0871	0.1236	0.0137	0.0079	0.1556	295.5
		WTW	0.0494	0.4062	0.1923	0.0140	0.0082	0.1556	295.0
		WTP_{AAC}	0.0347	0.0868	0.1231	0.0136	0.0079	0.1550	294.3
		WTW_{AAC}	0.0492	0.4046	0.1915	0.0139	0.0082	0.1550	293.8
2030	SI ICEV - LH_2 (2025)	WTP	0.0269	0.0683	0.0933	0.0104	0.0060	0.1168	228.1
		WTW	0.0361	0.2329	0.1370	0.0106	0.0062	0.1168	227.9
		WTP_{AAC}	0.0268	0.0680	0.0930	0.0103	0.0060	0.1163	227.2
		WTW_{AAC}	0.0360	0.2320	0.1364	0.0106	0.0062	0.1163	227.0
2040	SI ICEV - LH_2 (2035)	WTP	0.0238	0.0609	0.0816	0.0089	0.0053	0.0983	200.5
		WTW	0.0330	0.2255	0.1252	0.0091	0.0055	0.0983	200.2
		WTP_{AAC}	0.0237	0.0607	0.0812	0.0089	0.0052	0.0979	199.7
		WTW_{AAC}	0.0329	0.2246	0.1247	0.0091	0.0054	0.0979	199.4
2050	SI ICEV - LH_2 (2045)	WTP	0.0238	0.0614	0.0816	0.0087	0.0052	0.0944	199.1
		WTW	0.0330	0.2260	0.1253	0.0089	0.0054	0.0944	198.8
		WTP_{AAC}	0.0237	0.0612	0.0813	0.0086	0.0052	0.0940	198.3
		WTW_{AAC}	0.0329	0.2251	0.1248	0.0088	0.0054	0.0940	198.0

Fig. 1 shows the reductions of WTW VOC, CO, NO_x, PM_{10}, $PM_{2.5}$, and SO_x emissions when the proposed AAC system is used in LH_2-powered vehicles for the decades between 2010 and 2050. The values are calculated for vehicles traveling 15000 km/year. Almost all types of emissions are characterized by a high drop between 2010 and 2020 as clearly seen from the figure. This reduction is particularly noticeable in NO_x, PMs, and SO_x emissions. This can be interpreted that a significant improvement in fuel production and vehicle operation technologies was made between 2010 and 2020. The reductions of emissions decrease, again, for all emission types due to the decrease in emission levels over the years. Average reduction values for the emissions are 2.8 g/year for VOC, 19.5 g/year for CO, 12.9 g/year for NO_x, 1.4 g/year for PM_{10}, 0.8 g/year for $PM_{2.5}$, and 12.6 g/year for SO_x.

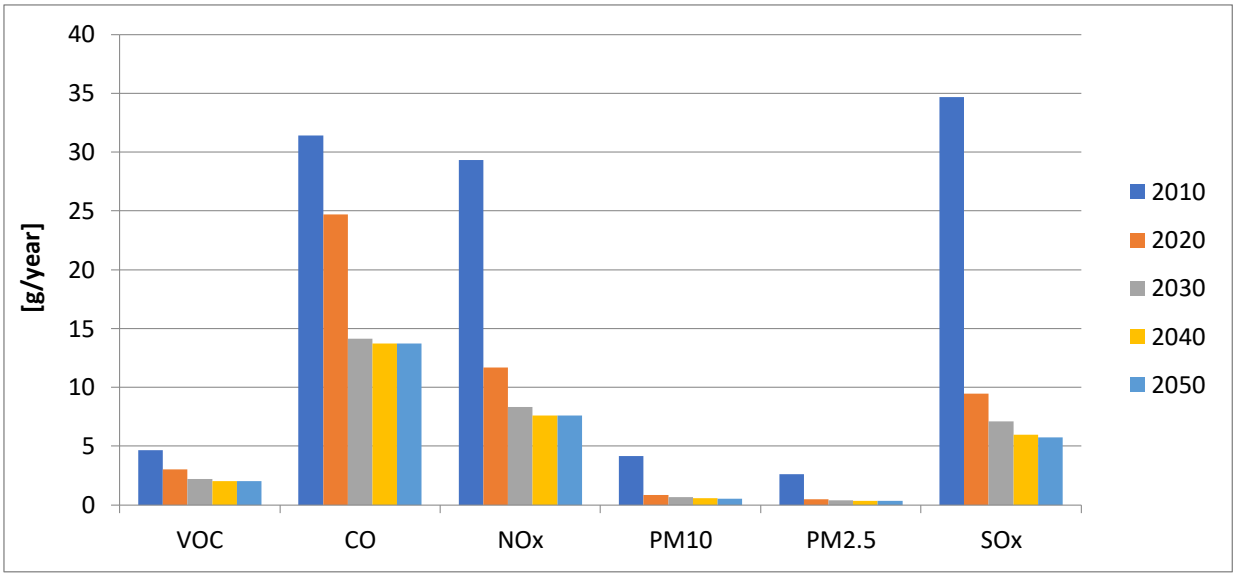

Figure 1. Reductions of emissions by years in LH_2-powered SI ICEVs with AAC

Reductions in CO_2 emissions of LH_2-powered SI ICEVs with AAC system over the years are shown in Fig. 2. Differently from the previous emission types, the reductions in CO_2 emission are given in kg/year as seen from the figure. It is assumed in the calculation that the vehicles take 15000 km/year. Using the proposed AAC system, CO_2 emissions of LH_2-powered SI ICEVs can be reduced over 16 kg/year averagely for the years between 2010 and 2050. This reduction is at the levels of 25.2 kg/year in 2010, and it decreases in every decade until 2050.

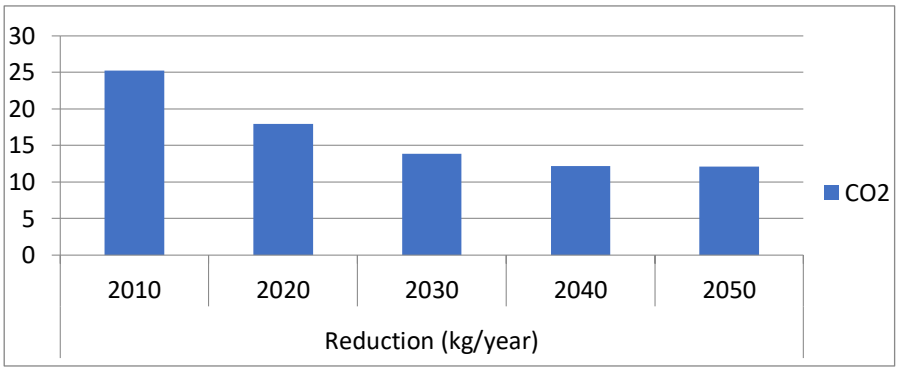

Figure 2. Reductions of CO_2 emissions by years in LH_2-powered SI ICEVs with AAC

Conclusion

In this study, an AAC system was proposed for LH_2-powered SI ICEVs, and an emission analysis was performed for the vehicles with and without the proposed system. GREET software was used in the analysis. VOC, CO, NO_x, PM_{10}, $PM_{2.5}$, SO_x, and CO_2 emissions are included for the target years of decades between 2010 and 2050 in the analysis. Both WTP and WTW values were calculated for the emissions. Therefore, it can be concluded from the study that:

- All emissions decrease due to the developments in vehicle technologies and fuel production processes from the year 2010 to 2050.

- The highest decrease in emission is between the years 2010 and 2020.

- The AAC system reduces all the emissions due to the decrease in the fuel consumption of the engine.

- The decrease in VOC, CO, NO_x, PM_{10}, $PM_{2.5}$, and SO_x emissions emitted from LH_2-powered SI ICEVs taking 15000 km/year using the AAC system is 8.3 g/year on average, which is a very low value. Average reduction in CO_2 emission, however, is over 16 kg/year.

It can be understood from the study that the proposed AAC system can be an auxiliary air conditioning system to the main air conditioning system of LH_2-powered SI ICEVs. They have acceptable cooling capacity values and COP rates. The widespread utilization of this system in LH_2-powered vehicles can lead to a further reduction in fuel consumption, emissions, and overall costs.

Competing Interests

The author declares that there is no competing interest in this study.

Authors Contributions

The author is the only writer of this study.

*This study was presented as a summary paper at the International Conference on Engineering, Natural and Applied Sciences (ICENAS'21) held online on 24-26 November 2021.

References

Akar MA., Kekilli E., Bas O., Yildizhan S., Serin H., Ozcanli M. Hydrogen enriched waste oil biodiesel usage in compression ignition engine. International Journal of Hydrogen Energy 2018; 43(38): 18046-18052.

Ansarinasab H., Mehrpooya M., Mohammadi A. Advanced exergy and exergoeconomic analyses of a hydrogen liquefaction plant equipped with mixed refrigerant system. Journal of Cleaner Production 2017; 144: 248-259.

Baltacioglu MK., Arat HT., Özcanli M., Aydin K. Experimental comparison of pure hydrogen and HHO (hydroxy) enriched biodiesel (B10) fuel in a commercial diesel engine. International Journal of Hydrogen Energy 2016; 41(19): 8347-8353.

Calvino F., Gennusa M., Roizzo G., Scaccianoce G. The control of indoor thermal comfort conditions: introducing a fuzzy adaptive controller. Energy and Buildings 2004; 36: 97-102.

Cengel YA., Boles MA. Thermodynamics: An Engineering Approach. McGraw-Hill 2005; New York.

Ciniviz M., Köse H. The use of hydrogen in internal combustion engine: a review. International Journal of Automotive Engineering and Technologies 2011; 1.

Dahlan AA., Zulkifli AH., Nasution H., Aziz AA., Perang MRM., Jamil HM. Zulkifli AA. Efficient and 'green' vehicle air conditioning system using electric compressor. Energy Procedia 2014; 61: 270-273.

Farzaneh Y., Tootoonchi AA. Controlling automobile thermal comfort using optimized fuzzy controller. Applied Thermal Engineering 2008; 28: 1906-1917.

Gillet T., Andres E., El-Bakkali A., Lemort V., Rulliere R., Haberschill P. Sleeping evaporator and refrigerant maldistribution: An experimental investigation in an automotive multi-evaporator air-conditioning and battery cooling system. International Journal of Refrigeration 2018; 90: 119-131.

Jiang L., Wang RZ., Li JB., Wang LW., Roskilly AP. Performance analysis on a novel sorption air conditioner for electric vehicles. Energy Conversion and Management 2018; 156: 515-524.

Khayyam H. Adaptive intelligent control of vehicle air conditioning system. Applied Thermal Engineering 2013; 51: 1154-1161.

Khayyam H., Kouzani AZ., Hu EJ. Reducing energy consumption of vehicle air conditioning system by an energy management system. The 4th International Green Energy Conference 2009; Beijing, China.

Khayyam H., Kouzani AZ., Hu EJ., Nahavandi S. Coordinated energy management of vehicle air conditioning system. Applied Thermal Engineering 2011a; 31: 750-764.

Khayyam H., Nahavandi S., Eric H., Kouzani A., Chonka A., Abawajy J., Marano V., Sam D. Intelligent energy management control of vehicle air conditioning via look-ahead system. Applied Thermal Engineering 2011b; 31: 3147-3160.

Lambert MA., Jones BJ. Automotive adsorption air conditioner powered by exhaust heat. Part 1: conceptual and embodiment design. Journal of Automobile Engineering 2006; 220: 959-972.

Meier K., Kurtz C., Weckerle C., Hubner M., Bürger I. Air-conditioning system for vehicles with on-board hydrogen. Applied Thermal Engineering 2018; 129: 1150–1159.

Ozcanli M., Akar MA., Calik A., Serin H. Using HHO (Hydroxy) and hydrogen enriched castor oil biodiesel in compression ignition engine. International Journal of Hydrogen Energy 2017; 42(36): 23366-23372.

Ozcanli M., Bas O., Akar MA., Yildizhan S., Serin H. Recent studies on hydrogen usage in Wankel SI engine. International Journal of Hydrogen Energy 2018; 43(38): 18037-18045.

Pacheco FA., Martins MES., Zhao H. New European Drive Cycle (NEDC) simulation of a passenger car with a HCCI engine: Emissions and fuel consumption results. Fuel 2013; 111: 733-739.

Pang W., Yu H., Zhang Y., Yan H. Solar photovoltaic based air cooling system for vehicles. Renewable Energy 2019; 130: 25-31.

Ruth DW. Simulation of modelling of automobile comfort cooling requirements. ASHRAE Journals 1975; 53-55.

Serin H., Yıldızhan Ş. Hydrogen addition to tea seed oil biodiesel: Performance and emission characteristics. International Journal of Hydrogen Energy 2018; 43(38): 18020-18027.

Sousa JM., Babuska R., Verbruggen HB. Fuzzy predictive control applied to air-conditioning system. Control Engineering Practice 1997; 5: 1395-1406.

Thompson R., Dexter A. A fuzzy decision-making approach to temperature control in air-conditioning systems. Control Engineering Practice 2005; 13: 689-698.

Tüccar G., Tosun E., Özcanlı M., Aydın K. Possibility of Turkey to transit Electric Vehicle-based transportation. International Journal of Automotive Engineering and Technologies 2013; 2: 64-69.

Yang X., Dong C., Qu Z. Design and dynamic analysis of a novel double-swing vane compressor for electric vehicle air conditioning systems. International Journal of Refrigeration 2017; 76: 52-62.

Zhang J., Qin G., Xu B., Hu H., Chen Z. Study on automotive air conditioner control system based on incremental-PID. Advanced Material Research 2010; 129(131): 17-22.

Zhang Q., Canova M. Modeling air conditioning system with storage evaporator for vehicle energy management. Applied Thermal Engineering 2015; 87: 779-787.

OKÜ Fen Bilimleri Enstitüsü Dergisi
5(Özel Sayı):262-274, 2022

OKU Journal of The Institute of Science and Technology, 5(Special Issue):262-274, 2022

Osmaniye Korkut Ata Üniversitesi Fen Bilimleri Enstitüsü Dergisi

Osmaniye Korkut Ata University Journal of The Institute of Science and Technology

Fabrication and Characterization of Mullite Reinforced CeO_2 Added ZrO_2 Ceramics

Mehmet Akif HAFIZOĞLU[1*], Ahmet AKKUŞ[2], Tahsin BOYRAZ[3]

[1]Dicle University, Faculty of Engineering, Department of Mechanical Engineering, 21280, Diyarbakır, Turkey
[2]Sivas Cumhuriyet University, Faculty of Engineering, Department of Mechanical Engineering, 58140, Sivas, Turkey
[3]Sivas Cumhuriyet University, Faculty of Engineering, Department of Metallurgical and Materials Engineering, 58140, Sivas, Turkey

[1]https://orcid.org/0000-0002-9689-3004
[2]https://orcid.org/0000-0002-6881-9333
[3]https://orcid.org/0000-0003-4404-6388
*Corresponding author: makif.hafizoglu@dicle.edu.tr

Research Article

Article History:
Received: 07.12.2021
Accepted: 14.02.2022
Published online: 23.02.2022

Keywords:
Zirconia
Cerium Oxide
Mullite
Characterization
Wear

ABSTRACT

We examined in this study whether there are phase differences in the CeO_2-ZrO_2 mixture depending on sintering temperatures and times. In addition, the effect of mullite was investigated on the mechanical, physical and microstructural properties of this mixture. Mullite ($3Al_2O_3.2SiO_2$) and 10 mol % cerium oxide doped zirconium dioxide (10 mol % CeO_2 - 90 mol % ZrO_2) powders were synthesized by conventional ceramic production technique. The mixtures were prepared by mechanical alloying method using zirconia ball mill in acetone environment. To synthesize mullite, Al_2O_3 and SiO_2 powders mixture was prepared with stoichiometric proportions and fired it in the air at 1600 ^oC for 3 h. And the ceria added zirconia composites were fired at 1300 ^oC for 2 h. Thus, ceria - zirconia and mullite composite phases were obtained and milling and sieving processes were carried out. Then, mullite-free and 10% by weight mullite reinforced cerium oxide added zirconia mixtures were prepared by powder metallurgy method. For 24 h, the mixtures were milled with zirconia ball mill in acetone environment and sieved by 75 µm sieve. The powders were pressed by uniaxial pressing after drying. The formed samples were sintered in a high temperature furnace in air conditions for 1 and 5 h at 1500 and 1600 ^oC sintering temperatures. Finally, microstructure examinations of the composites with SEM, phase analysis with XRD, hardness, three-point bending and wear tests were performed. In addition, the results of water absorption, porosity and density from physical properties were investigated.

Mullit Takviyeli CeO_2 Katkılı ZrO_2 Seramiklerinin İmalatı ve Karakterizasyonu

Araştırma Makalesi

Makale Tarihçesi:
Geliş tarihi: 07.12.2021
Kabul tarihi: 14.02.2022
Online Yayınlanma: 23.02.2022

Anahtar Kelimeler:
Zirkonya
Seryum oksit
Mullit
Karakterizasyon
Aşınma

ÖZET

Bu çalışmada CeO_2-ZrO_2 karışımında sinterleme sıcaklıkları ve sürelerine bağlı olarak faz farklılıkları olup olmadığını inceledik. Ayrıca mullitin bu karışımın mekanik, fiziksel ve mikroyapısal özelliklerine etkisi araştırılmıştır. Mullit ($3Al_2O_3.2SiO_2$) ve %10 mol seryum oksit katkılı zirkonyum dioksit (%10 mol CeO_2 - %90 mol ZrO_2) tozları geleneksel seramik üretim tekniği ile sentezlendi. Karışımlar, aseton ortamında zirkonya bilyalı değirmen kullanılarak mekanik alaşımlama yöntemiyle hazırlanmıştır. Mullit sentezi için, Al_2O_3 ve SiO_2 toz karışımı stokiyometrik oranlarda hazırlanmış ve 1600 ^oC'de 3 saat hava atmosferinde fırınlanmıştır. Serya katkılı zirkonya kompozitleri 1300 ^oC'de 2 saat fırınlanmıştır. Böylece serya - zirkonya ve mullit kompozit fazlar elde edilmiş, öğütme ve eleme işlemleri

gerçekleştirilmiştir. Daha sonra toz metalurjisi yöntemiyle mullitsiz ve ağırlıkça %10 mullit takviyeli seryum oksit katkılı zirkonya karışımları hazırlanmıştır. Karışımlar 24 saat aseton ortamında zirkonya bilyalı değirmende öğütülmüş ve 75 µm elekten elenmiştir. Tozlar kurutulduktan sonra tek eksenli presleme ile preslenmiştir. Oluşan numuneler hava atmosferinde bir yüksek sıcaklık fırınında 1500 ve 1600 ^{o}C sinterleme sıcaklıklarında 1 ve 5 saat sinterlenmiştir. Son olarak kompozitlerin SEM ile mikroyapı incelemeleri, XRD ile faz analizi, sertlik, üç nokta eğilme ve aşınma testleri yapılmıştır. Ayrıca fiziksel özelliklerden su emme, gözeneklilik ve yoğunluk sonuçları araştırılmıştır.

To Cite: Hafızoğlu MA., Akkuş A., Boyraz T. Fabrication and Characterization of Mullite Reinforced CeO_2 Added ZrO_2 Ceramics. Osmaniye Korkut Ata Üniversitesi Fen Bilimleri Enstitüsü Dergisi 2022; 5(Özel sayı): 262-274.

Introduction

Among ceramics, zirconia (ZrO_2) and its composites have become very popular for technological and many scientific studies because of their good mechanical properties, corrosion resistance, low thermal conductivities, higher temperature stabilities and higher chemical stabilities (Ceylan, 2006; Boyraz, 2008; Pekdemir, 2018). They are preferred as significant materials for refractory materials, high temperature furnaces, components that are resistant to wear, various cutting tools, dental studies and a lot of fields (Ceylan, 2006; Boyraz, 2008; Abi, 2009; Pekdemir, 2018). High-purity zirconia (ZrO_2) exhibits three polymorphs depending on temperature: monoclinic zirconia phase is stable at temperatures up to 1170 °C. After this temperature, the conversion from the monoclinic phase to the tetragonal phase begins and the tetragonal phase is stable at temperatures up to 2370 °C. From this temperature to the melting temperature of 2680 °C, it is in the cubic zirconia phase. (Boyraz, 2008; Abi, 2009). Depending on the cooling processes, conversion from the t-ZrO_2 phase to the m-ZrO_2 phase takes place. Transformation is very important as it causes volumetric changes of around 3% to 5% and thus cracks. Due to preventing this transformation and stabilizing the zirconia, it is common to use stabilizers. Addition of stabilizers to zirconia, lowers temperature of the transformations, reduces volumetric growth or shrinking and blocks the polymorphic transformations. By using stabilizers, it is possible to make stable the high-temperature phases at low temperatures too (Abi, 2009). Different stabilizers, such as, Al_2O_3, CaO, CeO_2, MgO, SiO_2, TiO_2, Y_2O_3 and even a combination of them, stabilize and hold stable the zirconia in the t-ZrO_2 and/or c-ZrO_2 forms at low temperatures (Hafızoğlu, 2021; Hafızoğlu, Akkuş and Boyraz, 2021; Hafızoğlu, Boyraz and Akkuş, 2021). It is possible to produce materials including only t-ZrO_2 or c-ZrO_2 or a mixture of these with m-ZrO_2 phases by adding different quantities of stabilizers. If less than sufficient stabilizing oxide is added, partially stabilized zirconia (PSZ) is obtained instead of fully stabilized zirconia. PSZ usually consists of two or more closely mixed phases. As a result of using stabilizers and obtaining fully or partially stabilized zirconia, could be achieved superb mechanical properties for example bending strength, hardness, fracture toughness (Cutler et al., 1992).

Zirconia exhibits better mechanical properties than other ceramics. However, like all other ceramics, it is fragile and cannot be formed at room temperature. Therefore, it is desirable to increase the

toughness of these materials. So, some energy absorbing mechanisms such as transformation toughening and fiber reinforcement are used in ceramic matrices (Boyraz, 2008).

Increasing fracture toughness with transformation toughness, works on the principle of a phase transformation caused by tension, by reducing the driving force that propagates existing cracks in the material structure (Boyraz, 2008). The best example for this can be indicated zirconia. Zirconia which is added to the ceramic main phase, keeps important role in increasing the fracture toughness and thus the bending strength with its tetragonal - monoclinic transformation toughening feature. With the discovery of the transformation toughening that occurs in zirconia, this material has found wide use. Because the main factor limiting the use of ZrO_2 in advanced engineering applications was the low toughness of this material. Increasing the toughness property with transformation toughness has also increased the interest in zirconia. The volume increase of 3 - 5%, which occurs with the tetragonal - monoclinic phase transformation in zirconia, prevents crack propagation, so increases the toughness of the material and its resistance to fracture (Boyacıoğlu, 2007). The t-m transformation in zirconia can occur in different ways. For example: t-ZrO_2 can be free as a single particle or crystal; It can also be found in a compacted form in a matrix as a precipitate phase. Tetragonal zirconia particle size and the matrix in which the particles are compacted are the most important factors. A critical t-ZrO_2 grain size is determined for ZrO_2 matrix phase. If the grain size is below this critical size, there will be no transformation; above, the t-m transformation occurs either continuously or as a result of applying a stress (Boyraz, 1998).

In the ceramic - ceramic mixed structure formation process, which is the other method of increasing the fracture toughness, the strength and toughness are increased by adding ceramic whiskers, fibers or particles to the main phase. This method is based on creating a physical barrier to the progressive crack. With higher tensile strength than polycrystalline material, whiskers are a good barrier to propagation cracking. So, the fracture toughness of zirconia can be increased more by adding some secondary phases for example nano particles, nano sized fibers or nano sheets into zirconia matrix (Liu et al., 2018). For the last decades, improvement of nanomaterials offers new alternatives to reinforce ceramics. Carbon nanotubes have attracted important attention as reinforcement materials because of their superior properties. However, at high temperatures, they are prone to react with oxide matrixes leading to degradation in some mechanical properties of carbon nanotubes and limited the reinforcing effect on the ceramics (Sun et al., 2005; Eichler et al., 2007). So, it is stated that incorporation of mullite which is another type of ceramic toughening method with its high temperature oxidation and corrosion resistance and the other superior properties, might be preferred (Liu et al., 2018). In the literature, mullite (3 Al_2O_3.2SiO_2) is described as the matchless stable middle crystalline phase for Al_2O_3-SiO_2 binary system, cost-friendly and exhibiting good refractory ability (El Ouatib et al., 2005; Kucuk and Boyraz, 2019). Mullite has received significant attention for technological applications because of its well properties like low coefficient of thermal expansion, high melting temperature, good resistance to creep, good chemical stability and satisfactory hardness (Kumar et al., 2015; Roy et

al., 2015). In short, fracture toughness of zirconia can be advanced with mullite reinforcement as the secondary phase into the ZrO_2 matrix and so, the other mechanical properties can be improved too (Liu et al., 2018). In addition, the temperature of sintering is also important, because of affecting some properties of ceramics through changing of the crystalline phases and microstructure (Denry and Kelly, 2008).

In this study, mullite ($3Al_2O_3.2SiO_2$) and 10 mol % cerium oxide doped zirconium dioxide powders were synthesized by conventional ceramic production technique. It was examined whether there are phase differences in the CeO_2-ZrO_2 mixture depending on sintering temperatures and times and the effect of mullite on the mechanical, physical and microstructural properties of this mixture.

Material and Methods

Mullite and ceria doped zirconia powders were produced by conventional ceramic production method in this study. All precursory powder materials were obtained from Company Eczacıbası (Al_2O_3 and SiO_2 powders), Merck (CeO_2) and Chemicals of Handan Yaxiang Trading Co. (ZrO_2). The powders were mixed in acetone environment by mechanical alloying method. The powders were heated for 24 hours in oven at 110 ºC before and after mixing. Mullite ($3Al_2O_3.2SiO_2$) and 10 mol% ceria doped zirconia (CeO_2-ZrO_2) powders were synthetized by sintering from the powders prepared with stoichiometric ratios of Al_2O_3, SiO_2, CeO_2 and ZrO_2 powders after homogenized in ball mill. Mullite ($3Al_2O_3.2SiO_2$) was synthetized for 3h at 1600 ^oC and 10 mol% ceria doped zirconia (CeO_2-ZrO_2) composite powders were synthetized for 2 h at 1300 ^oC. Thus, ceria - zirconia and mullite composite phases were obtained and milling and sieving processes were carried out. Then, mullite-free and 10% by weight mullite reinforced cerium oxide added zirconium oxide composites were prepared by powder metallurgy technique (hereinafter these mixtures will be named CeZ00M and CeZ10M respectively). The sample was coded as CeZ10M16005 (CeZ: Ceria doped zirconia; 10M: 10% Mullite addition and 16005: 1600 °C sintering temperature and 5 hours sintering time). After the composite powders were milled for 24 h in acetone environment with zirconia ball mill, sieved by 75 µm sieve and dried. Then, the composite mixtures were pressed to 56x12 mm sizes mold gap by uniaxial pressing machine at 200 MPa load. The pressed samples were sintered in a high temperature furnace (Protherm™ Furnace) and in air conditions for 1-5 h sintering times and 1500-1600 ^oC temperatures. The heating rate was 5 ^oC/min. Then, microstructure investigations with SEM, phase analysis with XRD, the hardness, 3-point bending and wear tests and physical properties that are water absorption, porosity, shrinkage and density results were examined on the composites.

The three-point flexural strength tests were executed with crosshead speed of 0.5 mm/min in a Shimadzu brand tensile-compression device. For each sample, measurements were taken five times and their average were taken as the bending strength results of the samples.

The strength calculations were made with the formula (1):

$$\sigma = 3/2*P*L / (b*h^2) \quad (1)$$

(In (1) the letters mean that, P: maximum load, L: the distance of between supports, h: height, b: width).

After 180, 320, 600, 1200 and 2500 grit sanding process, polishing is done for each sample. With Vickers hardness tester that was Mitutoyo brand, the measurements of hardness were executed by 1 kg load for 10 seconds. For each sample, measurements were taken five times and their average were taken as the hardness results of the samples (Önen and Boyraz, 2014; Akkuş and Boyraz, 2018; Boyraz and Akkuş, 2021). The wear tests of samples were executed with Plint brand wear tester. For wear tests, steel discs were used. For each sample, wear tests were executed at 400 rpm rate, 5, 10 and 15 min wear durations and 100 N force. The samples were measured with a precision scale of 10^{-4} g. After the assigned wear times, the samples were scaled again and the wear amounts were calculated (Akkuş and Boyraz, 2018; Boyraz and Akkuş, 2021). To determine the phases, XRD with Cu Kα radiation (Bruker AXS D8 Advance; 20kV-60kV, 6mA-80mA and $\theta = 10^{o}$-90^{o}, 0.002^{o}) was used. The phases of the samples seen in XRD patterns were defined with the Panalytical X'Pert program. The microstructural characterization of the samples was done with the Mira3XMU FE-SEM (Tescan, Czech Republic) brand scanning electron microscope machine and energy dispersion spectrum. The results were presented in various graphics and tables and some comments on these results were made.

Results and Discussion

Physical (shrinkage, water absorption, density and porosity tests) and mechanical (hardness, 3-point bending and wear) tests, SEM, EDS and XRD analysis results were included in this section. Calculations and measurements were repeated 5 times and arithmetic averages were taken. The shrinkage, porosity, water absorption, relative density and bulk density results are shown in Table 1, and also Fig. 1. In Fig. 1, the relative density values were taken at the rate of 1/3 of the actual values for the graph.

Table 1. Physical test results of CeZ00M and CeZ10M samples

Samples	Bulk density (g/cm^3)	Relative density (%)	Water absorption (%)	Porosity (%)	Shrinkage (%)
CeZ00M15001	5,21	88,80	2,08	11,20	12,35
CeZ00M15005	5,63	96,03	0,20	3,97	14,32
CeZ00M16001	5,80	98,87	0,18	1,13	15,17
CeZ00M16005	5,82	99,22	0,17	0,78	15,96
CeZ10M15001	4,84	88,22	1,39	11,78	12,57
CeZ10M15005	4,89	89,14	1,31	10,86	12,72
CeZ10M16001	4,92	89,68	1,25	10,32	13,14
CeZ10M16005	4,91	89,50	1,26	10,50	13,15

Ming-qing et al. (2002), produced the samples stabilized with 12 mol% CeO_2 by sintering at 1500 – 1600 ^oC temperatures for 3 hours. They stated that the highest density value was obtained from 16003 samples similarly our study.

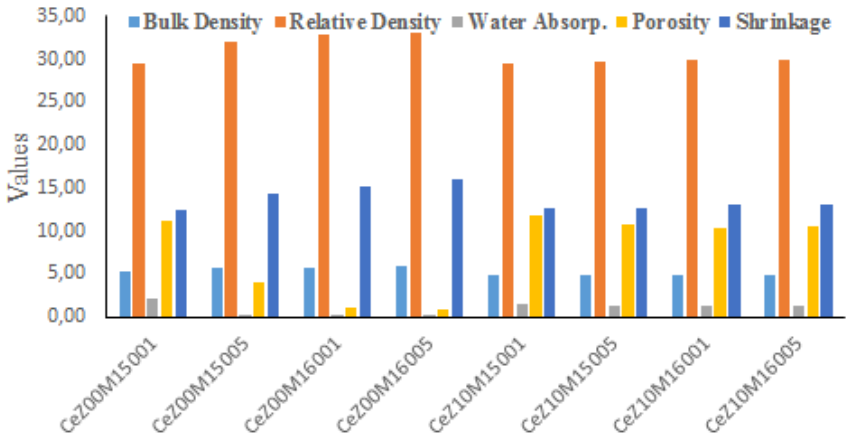

Fig. 1. Physical test results graph of CeZ00M and CeZ10M samples

When the results were examined, it was found that with increasing sintering temperature and time, the shrinkage values increased in general, and accordingly the water absorption and porosity values decreased; It is seen that experimental density and relative density values increase. In addition, it is seen that the shrinkage, experimental density and relative density values are lower and the water absorption and porosity values are higher in mullite added samples.

Table 2 and Fig. 2 indicated the hardness and three-point flexural or bending strength results of CeZ00M and CeZ10M samples.

Table 2. Hardness and three-point bending strength results of CeZ00M and CeZ10M samples

Samples	Hardness (HV)	3-Point bending strength (MPa)
CeZ00M15001	400,80	127,52
CeZ00M15005	511,30	140,95
CeZ00M16001	592,25	147,40
CeZ00M16005	595,20	77,28
CeZ10M15001	395,20	15,60
CeZ10M15005	400,55	16,54
CeZ10M16001	418,28	18,24
CeZ10M16005	376,70	15,06

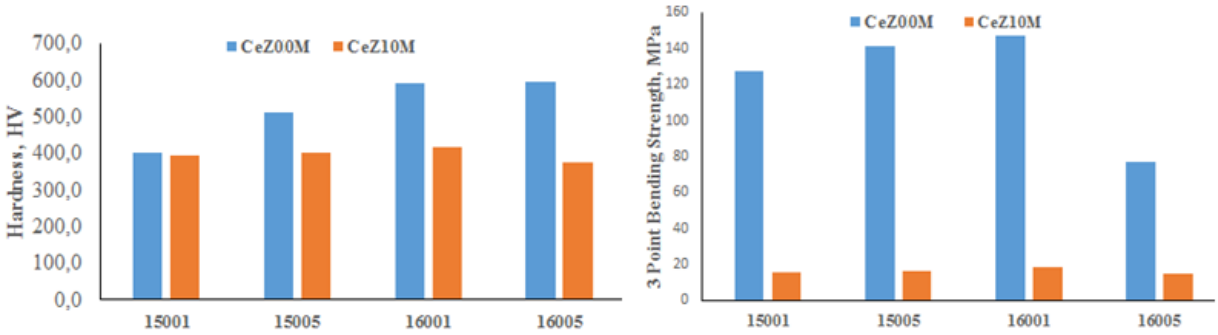

Fig. 2. Hardness and three-point bending strength graphics of samples

It is seen that the hardness values generally increase with increasing sintering temperature and time. The hardness values of the mullite added samples are lower and the CeZ10M16005 sample has the lowest hardness value despite the high sintering temperature and time. This is related to the pores that occur in the microstructure.

According to the 3-point bending test results, it is seen that the three-point flexural strength values increase with increasing sintering temperature and time in the samples, and the flexural strength values of the 16005 samples with and without mullite additives have the lowest values. In addition, it is understood that the three-point bending strength values of the mullite added samples are very low. It is thought that this situation is a result of the defects in the microstructure and possible phase changes depending on the sintering temperature, sintering time and mullite additive.

The wear tests of samples were executed with Plint brand wear tester. For wear tests, steel discs were used. For each sample, wear tests were executed at 400 rpm rate, 5, 10 and 15 min wear durations and 100 N force. The samples were measured with a precision scale of 10^{-4} g. After the assigned wear times, the samples were scaled again and the wear amounts were calculated. Wear results are seen in Table 3 and Fig. 3.

Table 3. Wear results of CeZ00M and CeZ10M samples

Samples	Wear Volume (mm^3), 100 N		
	5 min.	10 min.	15 min.
CeZ00M15001	0,995	1,847	2,874
CeZ00M15005	0,755	1,211	1,751
CeZ00M16001	0,318	0,404	0,756
CeZ00M16005	0,287	0,601	0,946
CeZ10M15001	1,650	2,781	4,754
CeZ10M15005	1,099	1,783	3,105
CeZ10M16001	0,451	1,065	1,553
CeZ10M16005	0,605	1,258	2,148

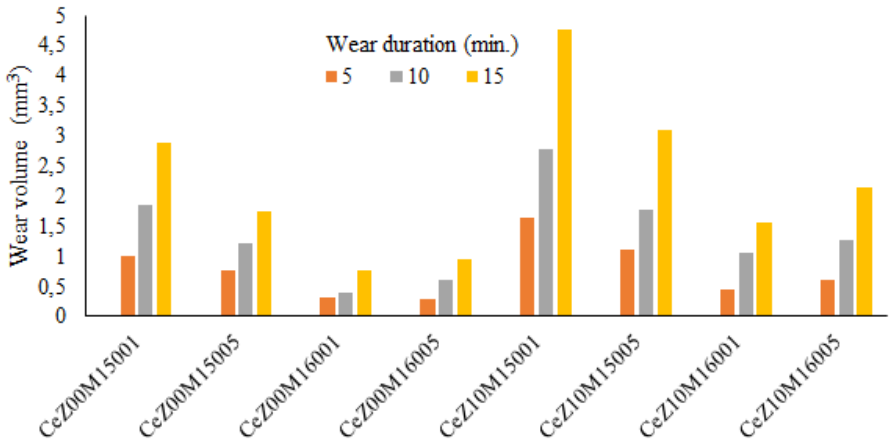

Fig. 3. Wear test results graph of samples

When the data obtained are examined, it is seen that the wear results vary depending on the bending strength, hardness and wear time of the specimens. In general, as the wear time increases, the amount of wear of the samples also increases; It is understood that the wear resistance of the samples with high hardness and bending strength is higher and the mullite additive negatively affects these samples and decreases the wear resistance. Although adhesive type wear is observed in the samples in general, it has been observed that with the increase in the wear time in some samples, cracks occur on the worn surface and very small pieces break off and cause abrasive wear.

The phase changes in the sample structure related with the temperature and time of CeZ00M and CeZ10M samples were analyzed and the basic phases that emerged in the structure were shown in Fig. 4.

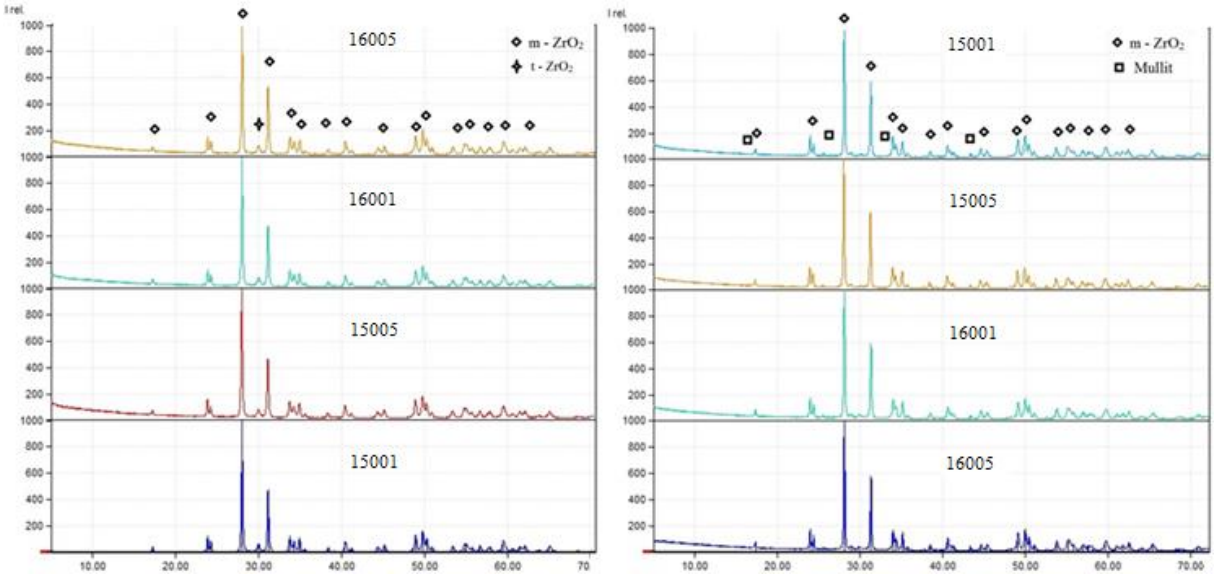

Fig. 4. XRD patterns of CeZ00M (left) and CeZ10M (right) samples

From XRD patterns of the samples, m-ZrO_2, t-ZrO_2 and mullite phases were detected. The m-ZrO_2 (JCPDS 37-1484), t-ZrO_2 (JCPDS 81-1544) and mullite (JCPDS 83-1881) phases were verified by comparison with JCPDS standard cards.

In our mullite-free (CeZ00M) samples, while the m-ZrO_2 phase decreased from 15001 to 16005 in the sample XRD patterns given in Figure 4; In the 16005 sample, the m-ZrO_2 phase increased compared to the other samples. The t-ZrO_2 phase is seen in the samples, albeit slightly. The fact that the 16005 sample has the lowest bending strength is because of the increase in the monoclinic phase and grain coarsening in this direction.

In our mullite added (CeZ10M) samples given in Figure 4, XRD patterns are the almost same and there is no t-ZrO_2 or c-ZrO_2 phase in the structure. In addition, macro cracks were formed in the mullite added samples during the production stage. Therefore, mullite additive affected these samples negatively and also reduced the mechanical properties. The decrease in flexural strength in CeZ10M16005 sample is thought to be due to excessive grain growth.

The microstructure image and elemental analyzes of CeZ00M16005 and CeZ10M16005 samples with EDS are given in Figure 5. From the SEM image given in Figure 5, we see that the grain size is significantly larger in the mullite added sample, which will adversely affect the microstructure. It can be predicted that this situation will have a negative effect on the hardness results of the specimens and decrease the hardness of the mullite added sample. As a matter of fact, in the experimental results, the hardness value of the CeZ10M16005 sample was found to be lower than the hardness value of the CeZ00M16005 sample.

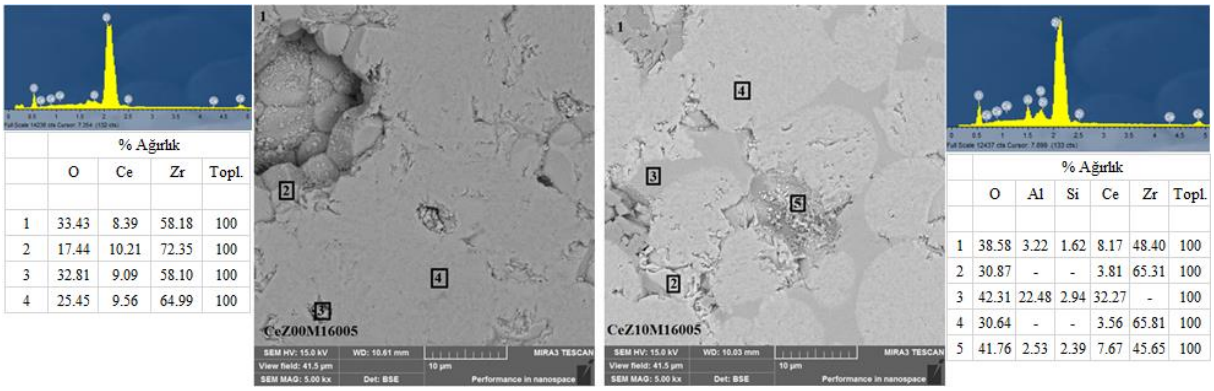

	% Ağırlık			
	O	Ce	Zr	Topl.
1	33.43	8.39	58.18	100
2	17.44	10.21	72.35	100
3	32.81	9.09	58.10	100
4	25.45	9.56	64.99	100

	% Ağırlık					
	O	Al	Si	Ce	Zr	Topl.
1	38.58	3.22	1.62	8.17	48.40	100
2	30.87	-	-	3.81	65.31	100
3	42.31	22.48	2.94	32.27	-	100
4	30.64	-	-	3.56	65.81	100
5	41.76	2.53	2.39	7.67	45.65	100

Fig. 5. SEM images and elemental analyzes of CeZ00M16005 and CeZ10M16005 samples

According to the EDS analyzes given in Fig. 5, the evaluation of the EDS analysis results on the CeZ00M16005 and CeZ10M16005 samples was made from general (1) and parts 2, 3, 4, 5. It has been observed that the results of the EDS elemental analysis made from the general field survey (1) and other parts are compatible with the contribution rates and XRD results made to the samples.

Conclusion

In our study, utilization of mullite in the production of ceria doped zirconia was explored. The effect of CeO_2 and mullite contribution to ZrO_2 main matrix was evaluated.

In all samples except CeZ10M16005, shrinkage, experimental and relative density and hardness values increased with increasing sintering temperature and time; It was observed that the porosity and water absorption values decreased. This situation in the CeZ10M16005 sample is thought to be a result of the pores formed in the microstructure and possible phase changes related to the decrease in the density value. In addition, with increasing sintering temperature and time, the three-point flexural strength values and wear resistance of the samples generally increased; On the other hand, it was observed that the wear resistance decreased and the flexural strength values got the lowest values in the 16005 samples with and without mullite additives.

From the XRD patterns, while m-ZrO_2 phase decreases from CeZ00M15001 to CeZ00M16005 samples; In the CeZ00M16005 sample, the m-ZrO_2 phase increased compared to the other samples. A small amount of t-ZrO_2 phase is seen in the samples. The fact that the CeZ00M16005 samples have the lowest bending strength is due to the increasing the monoclinic phase and grain coarsening in this direction. There is no significant difference in the XRD patterns of the mullite-doped samples and no t-ZrO_2 or c-ZrO_2 phase was detected in the structure. Therefore, we think that the decrease in flexural strength of mullite-added CeZ10M16005 sample is due to excessive grain growth.

The density value of mullite additive is lower than ZrO_2 - CeO_2 composite and it is more stable about shrinkage value at high temperatures compared to this composite. Therefore, in mullite added samples, shrinkage, experimental density, relative density and hardness values are lower, whereas water absorption and porosity values are higher. The SEM images show that the grain size is significantly

larger in the mullite added sample. This adversely affect the microstructure. It can be said that this situation has a negative effect on the hardness results of the specimens and decrease the hardness of the mullite added samples. Also, from the XRD patterns of mullite-added samples, it was seen that there is no t-ZrO_2 or c-ZrO_2 phase in the structure. This is a reason of lower bending strength values. In addition, macro cracks were formed in the mullite added samples during the production stage. Therefore, mullite additive affected these samples negatively and also reduced the mechanical properties which are hardness, bending strength and wear values.

In samples without mullite additives, m-ZrO_2 and t-ZrO_2 phases were detected, whereas m-ZrO_2 and mullite phases were found in samples with mullite additives. In these samples, no significant phase change was observed depending on temperature and time.

Acknowledgment

This work is supported by the Scientific Research Project Fund of Sivas Cumhuriyet University under the project number M-767. Authors would like to acknowledge Scientific Research Project Fund of Sivas Cumhuriyet University.

Statement of Conflict of Interest

No conflict of interest was declared by the authors.

Author's Contributions

The authors declare that they have contributed equally to the article.

*This study was presented as a summary paper at the International Conference on Engineering, Natural and Applied Sciences (ICENAS'21) held online on 24-26 November 2021.

References

Abi CB. An investigation on fracture toughness of traditional and technical ceramics. Afyon Kocatepe University, Doctoral dissertation, 194p, Afyon, 2009.

Akkus A., Boyraz T. Investigation of wear properties of CaO, MgO added stabilized zirconia ceramics produced by different pressing methods. Journal of Ceramic Processing Research 2018; 19(3): 249-252.

Boyacıoğlu T. Improvement of room temperature mechanical properties of various amount of metal oxide doping cubic zirconia (c-ZrO2) used as electrolyte material for solid oxide fuel cells. Gazi University, Master's thesis, 123p, Ankara, 2007.

Boyraz T. An investigation on physical and electrical properties of CaO/MgO-stabilized zirconia ceramics formed with different methods. Istanbul Technical University, Doctoral dissertation, 150p, İstanbul, 2008.

Boyraz T., Akkuş A. Investigation of wear properties of mullite and aluminium titanate added porcelain ceramics, Journal of Ceramic Processing Research 2021; 22(2: 226-231.

Boyraz T. Dental porcelain powders. Sakarya University, Master's thesis, 131p, Sakarya, 1998.

Ceylan A. The production of functionally graded SiAlON ceramics by tape casting method. Anadolu University, Doctoral dissertation, 204p, Eskişehir, 2006.

Cutler RA., Reynolds JR. Jones A. Sintering and characterization of polycrystalline monoclinic, tetragonal, and cubic zirconia. Journal of the American Ceramic Society 1992; 75(8): 2173-2183.

Denry I., Kelly JR. State of the art of zirconia for dental applications. Dental materials 2008; 24(3): 299-307.

Eichler J., Rödel J., Eisele U., Hoffman M. Effect of grain size on mechanical properties of submicrometer 3Y-TZP: fracture strength and hydrothermal degradation. Journal of the American Ceramic Society 2007; 90(9): 2830-2836.

El Ouatib R., Guillemet S., Durand B., Samdi A., Rakho LE. Moussa R. Reactivity of aluminum sulfate and silica in molten alkali-metal sulfates in order to prepare mullite. Journal of the European Ceramic Society 2005; 25(1): 73-80.

Hafızoğlu MA. Production, characterization and investigation of wear properties of zirconia ceramics with mullite additives and stabilized with different oxides. Sivas Cumhuriyet University, Doctoral dissertation, 248p, Sivas, 2021.

Hafızoğlu MA., Akkuş A., Boyraz T. Fabrication and characterization of mullite reinforced Y2O3 added ZrO2 ceramics. International Conference on Engineering Technologies (ICENTE'21), 18-20 November 2021, 124, Konya, Turkey.

Hafızoğlu MA., Akkuş A., Boyraz T. Fabrication and characterization of mullite reinforced CeO2 added ZrO2 ceramics. International Conference on Engineering, Natural and Applied Science (ICENAS'21), 24-26 November 2021, 128, Osmaniye, Turkey.

Kucuk I., Boyraz T. Structural and mechanical characterization of mullite and aluminium titanate reinforced yttria stabilized zirconia ceramic composites. Journal of Ceramic Processing Research 2019; 20(1): 73-79.

Kumar P., Nath M., Ghosh A.,Tripathi HS. Enhancement of thermal shock resistance of reaction sintered mullite–zirconia composites in the presence of lanthanum oxide. Materials Characterization 2015; 101: 34-39.

Liu PF., Li Z., Xiao P., Luo H., Jiang TH. Microstructure and mechanical properties of in-situ grown mullite toughened 3Y-TZP zirconia ceramics fabricated by gelcasting. Ceramics International 2018; 44(2): 1394-1403.

Ming-qing Y., Shi-gang F., Lian-meng Z., Shu-zhen S. Mechanical properties of ZrO 2 ceramic stabilized by Y 2 O 3 and CeO 2. Journal of Wuhan University of Technology-Materials Science Editorial 2002; 17(2): 14-18.

Önen U., Boyraz T. Microstructural characterization and thermal properties of aluminium titanate/spinel ceramic matrix composites. Acta Phys. Pol. A 2014; 125(2): 488-490.

Pekdemir AD. Preparation and characterization of boron carbide at low-temperature from boric acid and polyols. Ankara University, Doctoral dissertation, 178p, Ankara, 2018.

Roy J., Das S., Maitra S. Solgel-processed mullite coating—a review. International Journal of Applied Ceramic Technology 2015; 12: E71-E77.

Sun J., Gao L., Iwasa M., Nakayama T., Niihara, K. Failure investigation of carbon nanotube/3Y-TZP nanocomposites. Ceramics International 2005; 31(8): 1131-1134.